GFZ
Helmholtz Centre
POTSDAM

GeoMod2014

Modelling in Geosciences

Programme & Extended Abstracts

31 August - 5 September 2014

Editors:
Kirsten Elger
Øystein Thordén Haug
Malte Ritter

DFG Geo.X Geo.Sim

Recommended Citation

Elger, K; Haug, Ø. T.; Ritter, M. C. (Eds), (2014): Proceedings of GeoMod2014 – Modelling in Geosciences: Programme and Extended Abstracts 31 August–5 September 2014, GeoMod2014 – Modelling in Geosciences (Potsdam 2014), Potsdam: GFZ German Research Centre for Geosciences. DOI: http://doi.org/10.2312/GFZ.geomod.2014.001.

Disclaimer and Copyright

Imprint

Publisher
Helmholtz Centre Potsdam
GFZ German Research Centre for Geosciences
Telegrafenberg
14473 Potsdam
Published in Potsdam, Germany

Editors
Kirsten Elger
Øystein T. Haug
Malte C. Ritter

doi: 10.2312/GFZ.geomod.2014.001

About this book

This volume contains the extended abstracts of contributions presented during GeoMod 2014 at the Helmholtz Centre Potsdam GFZ German Research Centre for Geosciences (GFZ Potsdam), showing the state of the art of the tectonic modeling community.

GeoMod is a biennial conference dedicated to latest results of analogue and numerical modelling of lithospheric and mantle deformation. It started in 2002 in Milan as RealMod2002, then moved to Lucerne (GeoMod2004), Florence (2008), Lisbon (2010), and Lausanne (2012).

GeoMod2014 took place from 31 August to 3 September 2014 with 138 participants from 25 countries on all continents. The scientific programme of GeoMod2014 was organized in seven topical sessions listed below. The conference was followed by a 2-day short course on "Constitutive Laws: from Observation to Implementation in Models" (including lectures, lab visits, and practical exercises), as well as a 1-day hands-on tutorial on the ASPECT numerical modelling software.

GeoMod2014 focused on rheology and deformation at a wide range of temporal and spatial scales: from earthquakes to long-term deformation, from microstructures to orogens and subduction systems. For the first time, the discipline of volcanotectonics was included, while the (mantle) geodynamics community was more strongly represented than in previous editions. The bridge to field geology has traditionally been strong. At GeoMod 2014, fitting to the focus on rheology, the rock mechanics community was also represented. We thank our sponsors DFG, GFZ Potsdam and Geo.X, the conveners and all participants for contributing to a successful conference.

The GeoMod2014 Committee

The Scientific Committee
Onno Oncken
Georg Dresen
Stephan Sobolev
Matthias Rosenau
Karen Leever

The Organising Committee
Kirsten Elger
Franziska Alberg
Students support: Zahra Amirzada, Felix Eckelmann, Øystein Thordén Haug, Shaoyang Li, Malte Ritter, Tasca Santimano, Sarah Schröder, Johannes Wagner

Sessions, Conveners, and keynote speakers

(Seismo-)tectonics
Conveners: Boris Kaus (U Mainz), Onno Oncken (GFZ/FU Berlin),
Keynotes: Kelin Wang (Geological Survey Canada, Alberta), Bertrand Maillot (U Cergy-Pontoise)

Tectonics & Surface Processes
Conveners: Fabien Graveleau (U Lille), Niels Hovius (GFZ/U Potsdam),
Keynotes: Ritske Huismans (U Bergen), Stéphane Dominguez (U Montpellier II)

Volcanism and Volcanotectonics
Conveners: Olivier Galland (U Oslo), Eoghan Holohan (GFZ)
Keynotes: Rikke Pedersen (U Iceland), Olivier Roche (U BP Clermont-Ferrand)

Geodynamics
Conveners: Francesca Funiciello (U Roma Tre), Stephan Sobolev (GFZ),
Keynotes: Anne Davaille (U Paris-Sud), Bernhard Steinberger (GFZ)

Rheology
Conveners: Georg Dresen (GFZ/U Potsdam), Hiroki Sone (GFZ),
Keynotes: Yuri Fialko (U California), Laurent Montési (U Maryland)

Fluids and Deformation
Conveners: Stephen Miller (U Bonn), Marcos Moreno Switt (GFZ),
Keynotes: Boris Galvan (U Bonn), Takeshi Tsuji (U Kyushu)

Methods and Materials (poster-only session)
Conveners: Matthias Rosenau (GFZ), Marcel Frehner (ETH Zürich)

Short course on "Constitutive Laws: from Observation to Implementation in Models"
Lecturers: Onno Oncken (GFZ Potsdam), Matthias Rosenau (GFZ Potsdam), Fabio Corbi (GFZ Potsdam), Georg Dresen (GFZ Potsdam), Stephan Sobolev (GFZ Potsdam), Sascha Brune (U Sydney)

Hands-on tutorial on "ASPECT: a next-generation geodynamic modelling software"
(Advanced Solver for Problems in Earth's ConvecTion)
Lecturers: Anne Glerum (Utrecht University), Juliane Dannberg (GFZ Potsdam). Supervised by Wolfgang Bangerth (Texas A&M University, ASPECT main developer), Stephan Sobolev (GFZ Potsdam), Bernhard Steinberger (GFZ Potsdam).

Contents

GFZ
Helmholtz Centre
POTSDAM

GeoMod2014

Modelling in Geosciences

Programme & Extended Abstracts

31 August - 5 September 2014

Editors:
Kirsten Elger
Øystein Thordén Haug
Malte Ritter

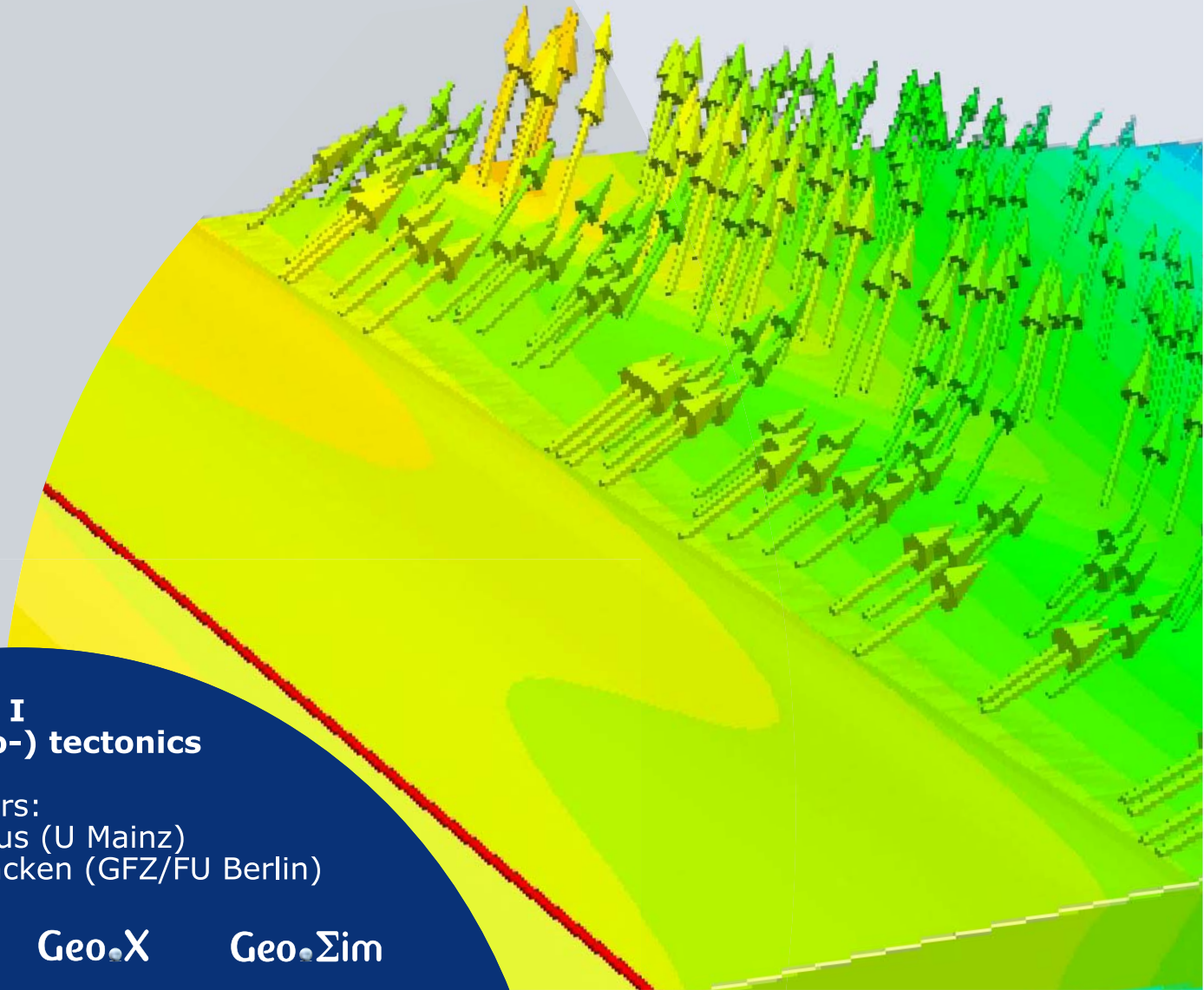

Session I
(Seismo-) tectonics

Conveners:
Boris Kaus (U Mainz)
Onno Oncken (GFZ/FU Berlin)

DFG GeoX GeoΣim

Session I.

(Seismo-)tectonics

Session Description: (Seismo-)tectonics

Conveners: Boris Kaus (U Mainz), Onno Oncken (GFZ/FU Berlin)

In the past decade, several great to giant subduction megathrust earthquakes have occurred (Sumatra 2004 and 2005, Chile 2010 and Japan 2011). Despite the fact that scientists knew that these subduction zones had the potential for megathrust earthquakes each new event had "surprises" in terms of size, duration, and complexity of the rupture, as well as the size of the associated tsunami or upper plate deformation. These events now belong to the group of very densely observed earthquakes, involving pre-seismic, co-seismic and post-seismic observations with integrated instrumentation and field observation encompassing seismology, geodesy, and geomorphology. These investigations have dramatically increased our understanding of the kinematics of the seismic cycle and thrown light on the underlying physical processes. Numerical and physical simulation in particular are benefitting from these results and are beginning to reveal driving mechanisms contributing to an advancement in theoretical understanding. We particularly solicit contributions that add to this development and to an improved understanding of the relationship between deformation accumulation at a wide range of temporal scales.

An investigation of seismicity and lithospheric features of the Zagros region, SW Iran, using coda wave attenuation

Mohsen Ahmadzadeh Irandoust[1], Habib Rahimi[2], Farhad Sobouti[1]

[1] *Department of Earth Sciences, Institute for Advanced Studies in Basic Sciences, Zanjan, Iran*
[2] *Institute of Geophysics, University of Tehran, Tehran, Iran*
e-mail: *m.ahmadzadeh@iasbs.ac.ir*
session: *(Seismo)-tectonics*

Abstract

In this study we used more than 2800 earthquakes to estimate coda wave quality factor, Q_c, in the Zagros Fold and thrust Belt and in the Sanandaj-Sirjan Metamorphic Zone. The coda quality factor was estimated using the single backscattering model. We investigated lateral and depth variation of Q_c in the study region. The average frequency relations for SSZ, Bandar-Abbas region and ZFTB are $Q_c = (124 \pm 5)f^{(0.82\pm0.02)}$, $Q_c = (111 \pm 2)f^{(0.99\pm0.01)}$ and $Q_c = (89 \pm 5)f^{(1.02\pm0.03)}$, respectively. The depth variations of Q_c show that there is a low velocity zone under SSZ and that the lithosphere of NW Zagros is thicker than other parts of ZFTB.
Key words: Quality factor, Attenuation, Seismicity, Coda, Zagros

Introduction

The Zagros mountains of SW Iran are one of the most seismically active intra-continental fold and thrust belts on Earth, and an important element in the active tectonics of the Middle East. Surface faulting associated with earthquakes is extremely rare, and most information about the active faulting comes from earthquakes. Hence, estimation of seismic wave attenuation (Q^{-1}) can be useful for the regions like Zagros. The seismic quality factor (Q) is strongly affected by the tectonic pattern of the lithosphere at any region. The characteristics of seismic coda waves are generally described by the average decay of the envelope in the tail portion of a seismogram. Based on the concept that the earth is assumed to be composed by the randomly distributed heterogeneities, the behavior of coda waves can be adequately explained by the scattering of primary elastic waves in a random medium (Aki and Chouet 1975). The coda quality factor values show frequency dependence as $Q_c = Q_0 f^n$ for $f > 1$ Hz, where Q_0 is Q_c at 1 Hz and n is the frequency relation parameter. Q_0 can be useful to quantify the seismicity of regions. Also n is indicative of the degree of heterogeneity of the crust and varies from 0.5 to 1.1 for most worldwide regions. Higher values of n indicate more heterogeneity and seismicity for a region.

Data and Methodology

In this study we have used over 2800 earthquake records of the Iranian National Seismic Network (INSN) and the Iranian Seismological Center (IRSC) to estimate the coda quality factor (Fig. 1). Features of the data are the following: (1) epicentral distances are less than 100 km, (2) focal depths are less than 20 km, (3) magnitudes are between 2.5 and 5.5, (4) period of data is from 2004 to 2012, and (5) sampling rate of digital seismic data is 50 Hz.

According to the single backscattering model (Aki and Chouet 1975), the coda amplitude can be expressed by $A(f,t) = C(f)t^{-\alpha}exp(-\pi ft/Q_c)$, where $A(f,t)$ is the time series of amplitudes of the

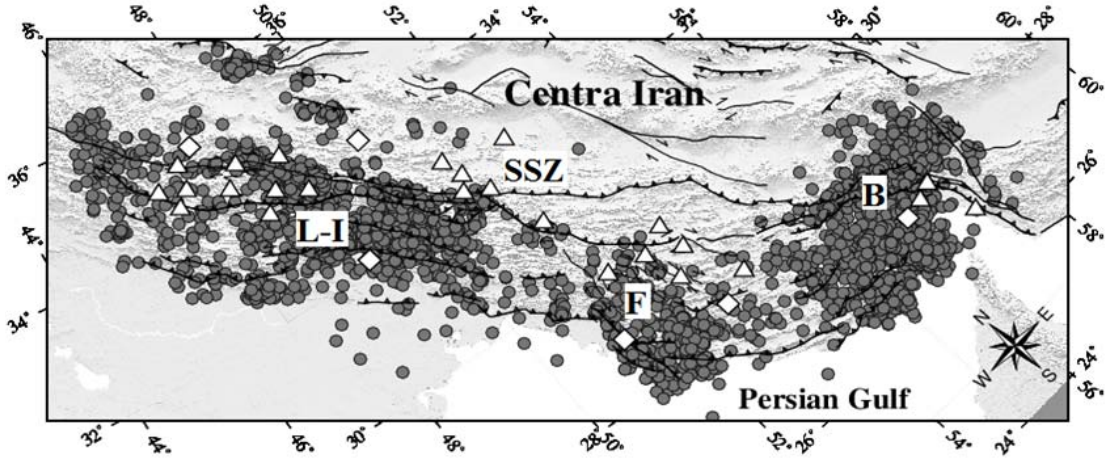

Fig. 1.: Location of stations and earthquakes in Zagros. Subregions of the study region, Bandar-Abbas (B, Fars (F), Lorestan-Izaeh (L-I) and SSZ are shown in the map.

filtered seismograms, $C(f)$ is the coda source factor which is considered as constant and α is the geometrical spreading factor ($\alpha = 1$ for body waves).Taking the natural logarithm of above equation and rearranging the terms, we get, $ln[A(f,t).t] = c - bt$, where $c = lnC(f)$ and $b = \pi f/Q_c$. Filtered seismograms are used for the detailed study of the decay of coda wave amplitudes with time to estimate Q_c values. The signals were filtered in seven frequency windows with central frequencies of 1.5, 3, 4.5, 6, 9, 12 and 18 Hz. To investigate the depth-dependence of attenuation, Q_c values were calculated for 18 lapse times ($5, 10, 15, \ldots$ 90s). Also we used the ellipsoidal volume sampled by coda waves at different lapse times to estimate the maximum scattering depths.

Results and Discussion

To investigate the lateral variation of upper lithosphere attenuation structure, we concentrated on the study of coda waves with shorter lapse times (e.g. 30 s), because they are less affected by deeper parts of the lithosphere. To compare the results in all stations distributed all over the region,Q_0 values are plotted in Fig. 2. In general, it could be seen that the average value of Q_0 in the seismically less active part of the study region, that is, SSZ, is greater than that in the active Zagros region. In the ZFTB there is no significant lateral variation in attenuation, except in the SE Zagros (the Bandar-Abbas region) which shows lower attenuation. The average frequency relations for SSZ, Bandar-Abbas region and ZFTB were obtained as: $Q_c = (124\pm5)f^{(0.82\pm0.02)}$, $Q_c = (111\pm2)f^{(0.99\pm0.01)}$ and $Q_c = (89\pm5)f^{(1.02\pm0.03)}$, respectively.

We have compared some of the results of Q_c studies obtained by various researchers worldwide. Our calculated Q_c values for the study region are comparable with active tectonic regions like Himalaya and SW Anatolia. Among Q_c studies in Iran, SSZ shows the lowest attenuation, while ZFTB shows a high attenuation like Alborz mountains (northern Iran). To investigate the variation of Q_c with depth, we calculated quality factors for 18 lapse time window length. Considering this fact that our study region is very wide and in order to have a good comparison of the spatial attenuation variation between different parts of the Zagros, we divided the region into 4 segments. The subregions are Bandar-Abbas (B), Fars (F), Lorestan-Izeh (L-I) and Sanandaj-Sirjan zone (SSZ) which are shown in Fig. 1. For each subregion, Fig. 3 shows variation of average Q_0 (quality factor at 1 Hz) and n (frequency relation parameter) with respect to lapse time and maximum depth of scattering. The results show that in general, Q_0 is an increasing function of lapse

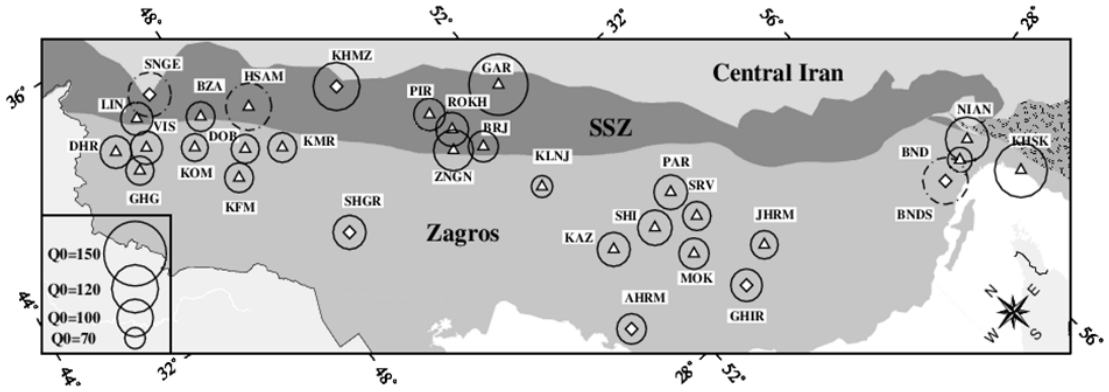

Fig. 2.: Map of Q_0 for 30 s time window lengths. Triangles and diamonds show stations located in Zagros and Sanandaj-Sirjan zone. Inset shows scale for Q_0.

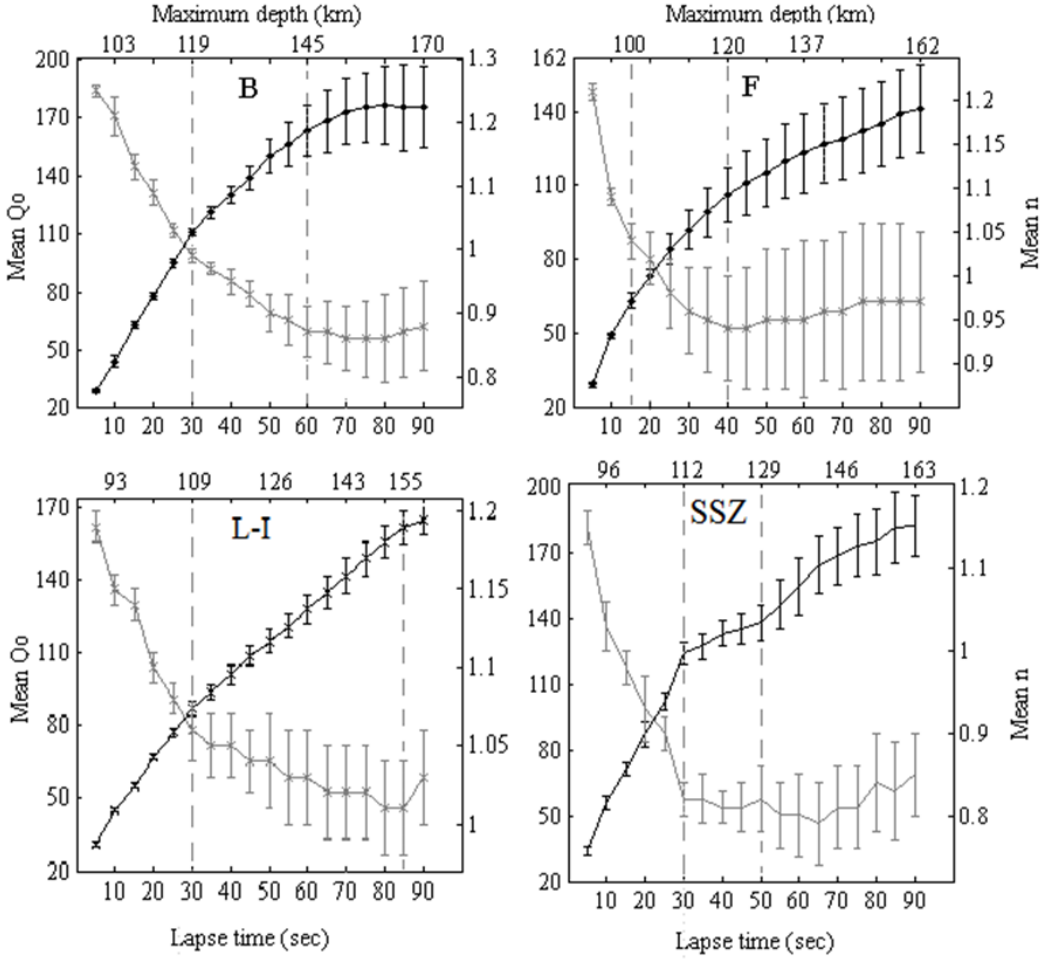

Fig. 3.: Variation of average Q_0, (Q_c in 1 Hz) and n (frequency relation parameter) with lapse time and maximum scattering depth in subregions of the study region, Bandar-Abbas (B), Fars (F), Lorestan-Izaeh (L-I) and Sanandaj-Sirjan Zone (SSZ).

time, while the n value is a decreasing function of lapse time. It seems reasonable that the larger the lapse time indicating the larger the volume of material with larger lateral and depth extent shows higher Q_c and decay of coda at a larger lapse time caries information about attenuation properties of deeper layers of the lithosphere.

Beneath SSZ and at the depth range of 50 to 80 km, there is a high correlation between the previously reported low velocity medium (Kaviani et al. 2007) and the observed sharp changes in the trend of the Q_0 and n curves. In the reported velocity structure in mind, unlike SSZ, under the crust of the Zagros, our results in different parts of the mountain range show no sharp changes in the trends of Q_0 and n. On the other hand, we observe a significant correlation between the reported lithosphere thicknesses (e.g. Priestly et al. 2012) and the trends of Q_0 and n in longer lapse times (i.e. larger depths). The NW Zagros has the thickest lithosphere. In this region the Q_0 curve shows an increasing slope up to a lapse time of 85 s. Other parts of Zagros with thinner lithosphere show a constant or gradually increasing trend of Q_0 and n at large lapse times.

Conclusion

Investigation of the variation of coda wave attenuation in the Zagros region shows our study region is comparable with seismically active tectonic regions of the world. And SSZ shows the lowest attenuation and seismicity among different tectonic areas of Iran. Also there is a correlation between the trends of Q_0 and n we obtained and the reported lithosphere thicknesses and velocity structure in the Zagros region.

References

Aki, K. and Chouet, B., 1975, Origin of coda waves: source, attenuation, and scattering effects, J. geophys. Res., 80, 3322–3342.

Kaviani, A., Paul, A., Bourova, A., Hatzfeld, D., Pedersen, H. and Mokhtari, M., 2007. A strong seismic velocity contrast in the shallow mantle across the Zagros collision zone (Iran), Geophys. J. Int., 171, 399–410.

Priestley, K., McKenzie, D., Barron, J., Tatar, M., and Debayle, E., 2012. The Zagros core: Deformation of the continental lithospheric mantle. Geochemistry, Geophysics, Geosystems, 13(11).

Coseismic Coulomb stress changes on intra-continental normal and thrust faults: insights from three-dimensional finite-element modelling

Meike Bagge[1], Andrea Hampel[1]

[1]*Leibniz Universität Hannover, Institut für Geologie, Callinstraße 30, 30167 Hannover, Germany*
e-mail: *bagge@geowi.uni-hannover.de, hampel@geowi.uni-hannover.de*
session: *(Seismo-) Tectonics*

Investigating the interaction of faults plays a crucial role in the assessment of future seismic risks. The calculation of Coulomb stress changes allows to quantify the stress changes on the so-called receiver faults in the surrounding of the fault that was ruptured during an earthquake. A positive Coulomb stress change implies that the earthquake has brought the receiver fault closer to failure while a negative value indicates a delay of the next earthquake (King et al. 1994; Stein 1999). So far, most studies focussed on calculating the Coulomb stress changes resulting from particular earthquakes such as the 2008 Wenchuan (China) or 2009 L'Aquila (Italy) events (Serpelloni et al. 2012, Parson et al. 2008, Wan & Shen 2010). Furthermore, gravity and the regional stress field were commonly neglected. Here we present a systematic analysis of the Coulomb stress changes on intra-continental dip-slip faults using three-dimensional finite-element models with arrays of normal and thrust faults, respectively. Our models allow the calculation of coseismic ("static") Coulomb stress changes on pre-defined fault planes, whose dip and position relative to each other can be varied. Gravity and a regional stress field are included in the models, which represent a 200 x 200 km wide lithosphere with viscoelastic behaviour of the lower crust and lithospheric mantle (Fig. 1).

Figure 2 shows the vertical and total horizontal coseismic displacement of the model surface and the coseismic total slip on the source fault plane (fault 6). In the thrust fault model, the coseismic

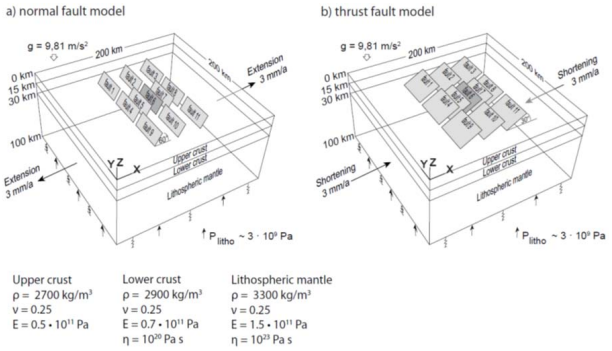

Fig. 1.: Perspective view of the three-dimensional reference model. The lithosphere is divided into an elastic upper crust, viscoelastic lower crust and viscoelastic lithospheric mantle. The source fault (fault 6, dark grey) and the ten receiver faults (light grey) are embedded in the upper crust. The 40-km-long faults dip with 60° in the normal fault reference model (a) and with 30° in the thrust fault reference model (b). The rheological parameters are density (ρ), Young's modulus (E), Poisson's ratio (μ) and viscosity (η). Gravity is included as body force. Isostatic effects are implemented by a lithostatic pressure (P_{litho}, black arrows) and an elastic foundation (springs) representing an asthenosphere. The bottom of the model is free to move in the vertical and horizontal directions and the model sides are fixed in the y-direction. We use a velocity boundary condition to create an extension (a) or shortening (b) of 6 mm/yr in the x-direction to initiate slip on the fault.

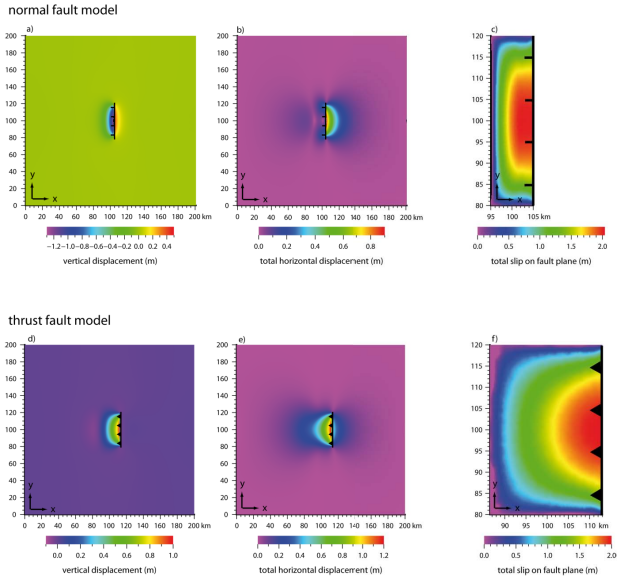

Fig. 2.: Coseismic vertical and total horizontal displacements at the model surface of the normal fault (a, b) and thrust fault (d, e) model. Coseismic slip on the source fault plane (fault 6) in the normal fault (c) and thrust fault (f) model.

vertical displacement shows mainly uplift of the hanging wall (Fig. 2 d). In the normal fault model, subsidence occurs in the hanging wall, whereas uplift is observed in the footwall (Fig. 2 a). The total horizontal displacement is highest in the hanging wall of the thrust fault model (Fig. 2 e) and in the footwall of the normal fault model (Fig. 2 b). Even though the fault planes have a rectangular shape, a typical elliptical slip distribution develops, with 2 m displacement at the surface and zero displacement at the fault tips and downdip edges (Fig. 2 e, f).

In a first series of experiments, we analysed the Coulomb stress changes resulting from coseismic slip of 2 m on the 40-km-long source fault. The preliminary results from both the thrust and normal fault models show that synthetic receiver faults parallel to the source fault experience primarily negative Coulomb stress changes with a symmetric distribution on each fault plane. In other words, these faults are located in a stress shadow zone. In contrast, faults positioned in the along-strike prolongation of the source fault undergo mostly positive Coulomb stress changes, i.e. they are located in a stress triggering zone. The Coulomb stress changes are largest at the fault tip that is closer to the source fault, resulting in an asymmetric Coulomb stress change distribution. Experiments with variable fault dip show that the distribution of the Coulomb stress change depends on the fault dip. Steeper receiver faults generally exhibit smaller Coulomb stress changes than shallow-dipping faults. In the future, we will use the fault-array models to evaluate the Coulomb stress changes arising from postseismic relaxation in the lower crust and lithospheric mantle and their dependence on the viscosity of these layers.

References

King, G. C., Stein, R. S. and Lin, J. (1994): Static stress changes and the triggering of earthquakes. - Bulletin of the Seismological Society of America, 84(3): 935-953.

Parsons, T., Ji, C. and Kirby, E. (2008): Stress changes from the 2008 Wenchuan earthquake and increased hazard in the Sichuan basin. - Nature, 454(7203): 509-510.

Serpelloni, E., Anderlini, L. and Belardinelli, M. E. (2012): Fault geometry, coseismic-slip distribution and Coulomb stress change associated with the 2009 April 6, Mw 6.3, L'Aquila earthquake from inversion of GPS displacements. - Geophysical Journal International, 188(2): 473-489.

Stein, R. S. (1999): The role of stress transfer in earthquake occurrence. - Nature, 402(6762): 605-609.

Wan, Y. and Shen, Z. K. (2010): Static Coulomb stress changes on faults caused by the 2008 Mw 7.9 Wenchuan, China earthquake. - Tectonophysics, 491(1): 105-118.

The role of pre-existing frictional weaknesses on the propagation of extensional fault

Lorenzo Bonini[1], Roberto Basili[2], Pierfrancesco Burrato[2], Vanja Kastelic[2], Giovanni Toscani[1], Silvio Seno[1], Gianluca Valensise[2]

[1] *Dipartimento di Scienze della Terra e dell'Ambiente, Università di Pavia, Italy*
[2] *Istituto Nazionale di Geofisica e Vulcanologia, Rome, Italy*
e-mail: *lorenzo.bonini@unipv.it*
session: *(Seismo-) Tectonics*

Introduction

Understanding the evolution of faults from their blind phase to a mature stage (i. e. surface-breaking faults) is fundamental in active tectonic studies because conventional analyses for identifying and characterizing the earthquake potential of large continental faults rely largely on surface evidence of faults.

In brittle crust, faults form and propagate by linking small tensile cracks. A plethora of studies dealt with fault propagation mechanisms using different approaches, from theoretical formulations to field analyses to numerical and analogue simulations (see Mandl, 2000; Scholz, 2000; and Gudmundsson, 2011 for a summary). In an isotropic material, the propagation of faults is controlled by rock toughness and applied stress. In nature, rocks exhibit intrinsic mechanical anisotropies that affect stress trajectories and consequently the nucleation and growth of faults. Examples of mechanical heterogeneities in nature are lithological changes, layering, fluids, inherited faults etc.

Here we focus on the role that pre-existing thin mechanical discontinuities with different orientations may play in the propagation of an extensional fault. We present a series of clay (wet kaolin) analog models simulating the evolution of a buried extensional structure. To analyze how mechanical discontinuities affect strain distribution and new extensional faults formation, we introduce in the models frictional weaknesses with different orientation (Fig. 1).

Method

Wet clay has been extensively used as analog material since the beginning of experimental geology (see Graveleau et al., 2012 for a review). During the past thirty years, wet kaolin has been selected as the preferred clay type for analogue models because its plasticity index and viscoelasticity are lower than other clay types (Withjack and Jamison, 1986; Eisenstadt and Sims, 2005; Henza et al., 2010; Cooke and van der Elst, 2012). In this study, we use wet kaolin with a density of $1.65\,\mathrm{g\,cm^{-3}}$, a water content of 60 % by mass, a shear strength ranging from 50 Pa to 120 Pa (Eisenstadt and Sims, 2005; Cooke and van der Elst, 2012), and a friction coefficient of 0.6. Under these experimental conditions and following well established scaling rules (e. g. Hubbert, 1937), 1 cm in the experiment is about 1 km in nature. The experimental apparatus simulates extensional displacements of a subsiding rigid block (Fig. 1) at an imposed rate of $0.005\,\mathrm{mm\,s^{-1}}$.

The peculiar properties of wet kaolin allow us to reproduce localized faulting, distributed deformations, and fault reactivation. Recently, Cooke et al., (2013) developed an experimental technique that introduces thin frictional weaknesses in the initial setup of the experiments by

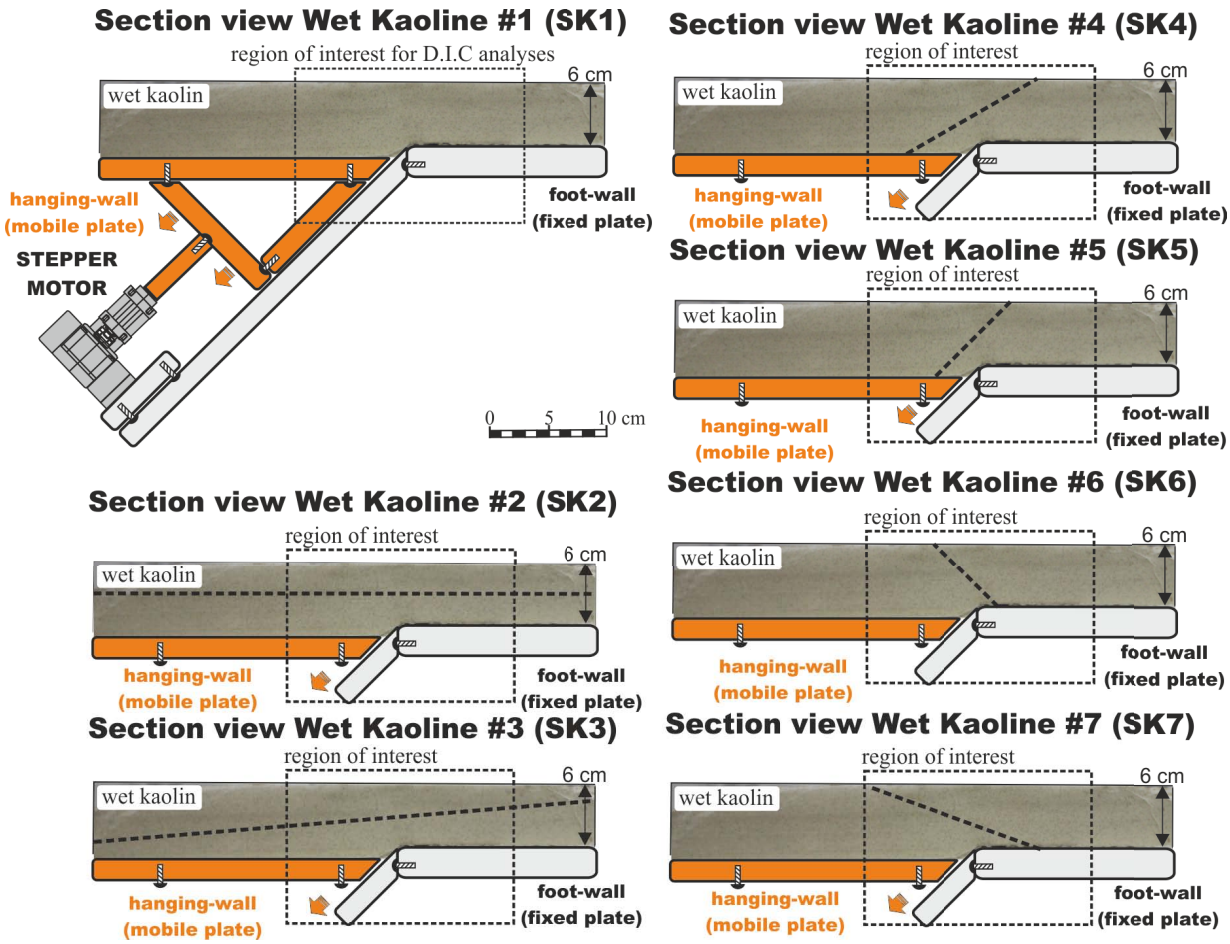

Fig. 1.: Initial setup of the experiments. Dashed lines represent pre-existing mechanical discontinuities introduced in the initial setup.

cutting clay with an electrified blade. The same method has been used by Bonini et al. (2014) in an extensional setting. We use such approach to reproduce pre-existing discontinuities in our models.

To monitor the evolution of the experiments we used an high-resolution camera taking pictures every 0.5 mm of displacement. Then we calculated the strain distribution using the Displacement Image Correlation method (D.I.C.).

Results

In the isotropic experiment (Sk 1), different systems of upward- and downward propagating faults all evolved to form high-angle faults with a listric geometry after 1.5 cm of extension. In all other experiments the results differ depending on the orientation of the mechanical discontinuity. For instance, in the experiments with an horizontal discontinuity (Sk 2) the new fault quickly propagates and buried slip is transferred to the surface by a single fault system after 1 cm of total displacement (0.5 cm before than in Sk 1 model). In the Sk 3 model, the upward-propagating fault slows down its propagation when it meets a low-angle discontinuity. The effect is opposite with respect to Sk 2 model, and a well-developed bending-moment fault appears at the surface of the models. In the Sk 4 model, the discontinuity dips 30°, and when the new upward-propagating fault meets it slip is deflected along it without forming a new fault in the uppermost part of the model. In the Sk 5 model, the initial 45°-dipping discontinuity is quickly reactivated and transfers all the displacement to the surface. Finally, the Sk 6 and Sk 7 experiments simulate inherited antithetic discontinuities; in these models, the upward-propagation of new faults is limited by the inherited discontinuities, and once again bending-moment faults develop at the surface.

Conclusions

Our models show that the nucleation and propagation of extensional faults may be affected differently depending on the orientation of pre-existing frictional weaknesses. The induced tensile stress ahead of upward-propagating faults is influenced by mechanical discontinuities that generate a rotation of the principal stress. This implies differences in (i) the growth rate of the new faults, (ii) the shape of the associated folds, and (iii) the development of bending-moments faults at the surface. In summary, the interaction between new and inherited faults may result (1) in limitations of the size of new structures and, therefore, of the associated earthquakes (down-dip segmentation), and (2) it may cause the reactivation of older fault segments and generate new surface breaks not directly connected to the master faults at depth (bending-moment faults). The 2009 L'Aquila seismic sequence is an example of how seismogenic ruptures on an extensional fault may be strongly controlled at depth by the interaction between new and inherited faults (see Bonini et al., 2014). Other recent damaging earthquakes caused by other types of faults (1983, Coalinga, U.S.A, M_w 6.5; 1989, Loma Prieta, U.S.A., M_w 6.9; 1994, Northridge, U.S.A, M_w 6.7; 2008, Wenchuan, M_w 7.9; 2010, Haiti) also showed a complex multi-level nature of the co- and post-seismic deformations caused by the interaction between seismogenic fault and thin mechanical discontinuities (e. g.: faults, weak layers). The analysis of the relationship between new faults and inherited weaknesses will improve seismic hazard assessment and structural interpretations of seismogenic faults in complex tectonic settings.

Acknowledgements

Work founded by Project Miur-Firb "Abruzzo" (code: RBAP10ZC8K_003)

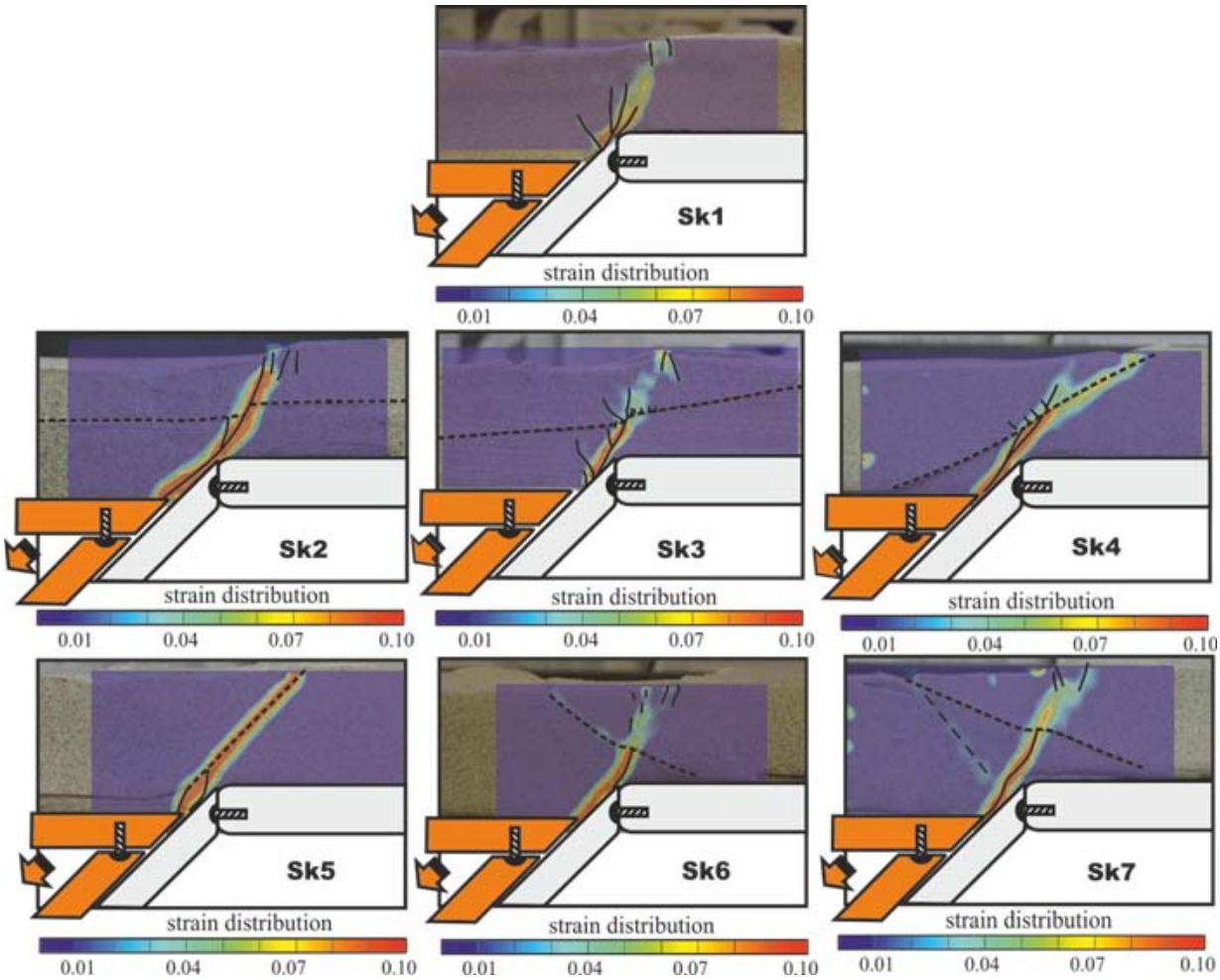

Fig. 2.: The strain distribution in the experiments at 1 cm of total displacement.

References

Bonini, L., Di Bucci, D., Toscani, G., Seno, S., Valensise, G. (2014). On the complexity of surface ruptures during normal faulting earthquakes: excerpts from the 6 April 2009 L'Aquila (central Italy) earthquake (M_w 6.3). Solid earth, 389-408, doi:10.5194/se-5-389-2014.

Cooke, M.L., van der Elst, J. (2012). Rheologic testing of wet kaolin reveals frictional and bi-viscous behavior typical of crustal materials. Geophysical research Letters, 39, L01308, doi:10.1029/2011GL050186.

Cooke, M.L., Schottenfeld, M.T., Buchanan, S.W. (2013). Evolution of fault efficiency at restraining bends within wet kaolin analog experiments. Journal of Structural Geology, 51, 180-192, http://dx.doi.org/10.1016/j.jsg.2013.01.010.

Eisenstadt, G., Sims, D. (2005). Evaluating sand and clay models: do rheological differences matter? Journal of Structural Geology, 27, 1399-1412, doi:10.1016/j.jsg.2005.04.010.

Graveleau, F., Malavieille, J., Dominguez, S. (2012). Experimental modelling of orogenic wedges: A review. Tectonophysics, 538-540, 1-66, doi:10.1016/j.tecto.2012.01.027.

Gudmundsson, A. (2011). Rock fractures in geological processes. Cambrige University Press, New York.

Henza A.A., Withjack, M.O., Schlische, R.W. (2010). Normal-fault development during two phases of non-coaxial extension: An experimental study. Journal of Structural Geology, 32, 1656-1667, doi:10.1016/j.jsg.2009.07.007.

Hubbert, M. K. (1937). Theory of scale models as applied to the study of geologic structures, Geol. Soc. Am. Bull., 48, 1459–1520.

Mandl, G. (2000). Faulting in brittle rocks: an introduction to the mechanics of tectonic faults, Springer Berlin.

Scholz, C. H. (2000). The mechanics of earthquakes and faulting, Cambridge University Press, 439 pp.

Withjack, M.O., Jamison, W.R. (1986), Deformation produced by oblique rifting, Tectonophysics, 126, 99–124, doi:10.1016/0040-1951(86)90222-2.

Analogue models of subduction megathrust earthquakes: analyzing the viscoelastic rheological parameter space with an innovative monitoring technique

Silvia Brizzi[1], Fabio Corbi[1, 2], Francesca Funiciello[1], Monica Moroni[3]

[1] *Dipartimento di Scienze, Sezione di Geologia, Università degli Studi "Roma Tre", L.go S. Leonardo Murialdo, I – 00146, Rome, Italy*
[2] *German Research Center for Geosciences, Section 2.1, Telegrafenberg – 14473, Potsdam, Germany*
[3] *Dipartimento di Ingegneria Civile Edile e Ambientale, Sapienza – Università di Roma, Via Eudossiana, 18 – 00148, Rome, Italy*
e-mail: *brizzi.silvia@gmail.com*
session: *(Seismo-) Tectonics*

The majority of global seismicity originates at subduction zones, both within the converging plates and along the plate interface. In particular, most of the events with Mw > 8.0 (usually known as mega-earthquakes) occurs along the subduction thrust fault, i. e., the frictional interface between the subducting and overriding plates. Consequently, subduction zones generate Earth's largest earthquakes and most destructive tsunamis, being responsible for about 90 % of the seismic moment globally released during the last century [e. g., Pachecho & Skyes, 1992]. Contrary to popular belief, mega-earthquakes are not rare events. Indeed, numerous megathrust events have occurred at subduction zones during the last decade, often revealing unexpected characteristics. As tragically demonstrated by 2011 Tohoku, 2008 Maule and 2004 Sumatra earthquakes, these events often impact densely populated coastal areas and cause large numbers of fatalities and damages to infrastructures.

Understanding mega-earthquakes behaviour is particularly challenging. While scientists have a general comprehension of the subduction thrust fault seismogenesis, its physics still remains poorly constrained. This is mainly due to the short (i. e., limited to the past century) instrumental seismic history, which does not provide enough temporal perspective on the recurrence time of these big events and can be misinterpreted using oversimplifying assumptions. Moreover, except for discrete and punctual observations (e. g., Japan Trench Fast Drilling Project) what is known about subduction thrust fault behaviour derive from indirect methodologies, such as InSAR deformation measurements, land geodetic data and geophysical studies of convergent margins. Over time, scientific community made great efforts to gain a better physical understanding of subduction seismic cycle, because this would have fundamental implications on seismic hazard assessment of convergent margins. In addition to the previously mentioned methodologies, numerical [e. g., Wang, 2007; Kaneko et al., 2010; van Dinther et al., 2013] and analogue modelling [e. g., Rosenau et al., 2009; 2010; Corbi et al., 2013] can also be used as key-tool to study subduction earthquake cycle. In particular, analogue models have been widely used to investigate processes related to small-scale/short-term and large-scale/long-term earthquake physics, because of the great advantage of overcoming the restricted direct observation in space and time related to subduction thrust fault behaviour. Moreover, with the advent of deformation monitoring techniques, analogue modelling has entered the stage of becoming a potentially quantitative method.

First properly scaled analogue experiments with realistic geometries (i. e., wedge-shaped) suitable for studying interplate seismicity have been realized using granular elasto-plastic [e. g., Rosenau et al., 2009] and viscoelastic materials [e. g., Corbi et al., 2013]. Viscoelastic laboratory experiments consist of a type A 2.5 wt.-% gelatin wedge, under-thrusted by a rigid steel conveyor plate (i. e., the analogue of subducting plate), with defined velocity-weakening and –strengthening regions. Type A gelatin is an innovative analogue material that has: a) proper rheological properties to simulate downscaled lithospheric rock behaviour [Di Giuseppe et al., 2009] and b) appropriate transparency, that allows non-intrusive and continuous monitoring of the evolution of the model. This new geodynamical approach simulates the basic physics governing the subduction seismic cycle and related rupture processes, in a simplified yet robust way, helping to contribute to our understanding of mega-earthquakes. Despite the strength of the methodology, analogue earthquakes are not perfectly comparable with natural observations, especially in terms of recurrence time, coseismic duration and slip. The aim of this study is, therefore, to improve subduction seismic cycle analogue models, implementing: a) rheological properties of the analogue material and b) images analysis technique adopted for the experimental monitoring. In particular, this has been achieved with subsequent steps schematically illustrated in fig. 1.

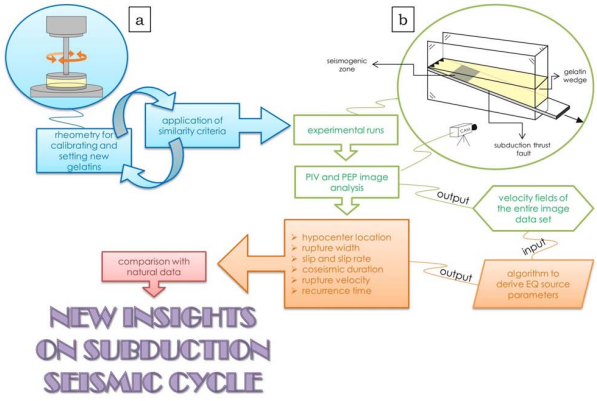

Fig. 1.: Workflow describing the main steps of the project; a) schematic drawing of parallel-plate rheometer used to determine the rheological properties of gelatin samples; b) schematic drawing of the experimental apparatus.

Although type A 2.5 wt% gelatin is the analogue material that best approximate lithospheric viscoelastic behaviour under laboratory conditions, in this work we aim at improving pre-existing experimental scaling factors. In order to quantify and compare periodicity and source parameters of analogue earthquakes as a function of lithospheric rheology, we use type A gelatin with greater concentration (i. e., 3 wt.-% and 6 wt.-%). The selection of new analogue materials, properly scaled with rheological viscoelastic behaviour of the lithosphere, has been realized with the approach commonly used in Material Science, i. e., measuring the deformation energy stored in the sample during the shear process and lost afterwards [e. g., Mezger, 2002]. The results of this work show that elastic and viscous properties of the analogue materials play important role in controlling seismogenic behaviour of subduction thrust fault, improving similarities with natural mega-earthquakes.

Models realized in this study have also been implemented in terms of monitoring system. In particular, model deformation has been derived by means of PEP (ParticlE and Prediction velocity) algorithm, belonging to PTV (Particle Tracking Velocimetry) techniques. Similarly to the usually adopted PIV (Particle Image Velocimetry) technique, PEP is an optical method used for extracting velocity field in fluid flows via the reconstruction of tracer particles seeding the media under investigation [e. g., Shindler et al., 2012]. PEP differs from classic cross-correlation techniques (i. e., PIV) in its ability to provide sparse velocity vectors at points coincident with particle barycentre positions. Velocity field is then evaluated from a Lagrangian point of view, allowing a larger spatial resolution (in the order of sub-pixel dimensions) compared to PIV. Outputs of PEP algorithm (i. e., velocity field of the images data set acquired during the experiments) are post-

processed using an ad hoc algorithm in order to obtain a set of seismologically relevant parameters, i. e., earthquake source parameters. In order to verify the implementation of monitoring system, experiments have also been analysed by means of PIV method, accordingly to Corbi et al. [2013]. Earthquake source parameters derived by PEP and PIV algorithm have also been compared in order to detect possible differences between the two methodologies. Preliminary results show that PEP algorithm is able to identify a greater number of analogue earthquakes, compared to PIV, detecting also smaller analogue earthquakes. Furthermore, spatio-temporal slip rate and cumulative slip distributions are defined with higher and sharper resolution in the space domain compared to PIV. PEP algorithm is then suitable to potentially gain new insights on seismogenic process of subduction thrust fault. Moreover, the ability to distinguish analogue earthquakes of different sizes may also have implications on successful applicability of scaling relationship, such as Gutenberg-Richter law, to experimental results.

References

Corbi, F., F. Funiciello, M. Moroni, Y. van Dinther, P. M. Mai, L. A. Dalguer & C. Faccenna (2013) – The seismic cycle at subduction thrusts: 1. Insights from laboratory models. J. Geophys. Res. Solid Earth, 118, 1483-1501, doi:10.1029/2012JB009481

Di Giuseppe, E., F. Funiciello, F. Corbi, G. Ranalli & G. Mojoli (2009) – Gelatins as rock analogs: A systematic study of their rheological and physical properties. Tectonophysics, 473(3-4), 391–403, doi:10.1016/j. tecto.2009.03.012.

Kaneko, Y., J.-P. Avouac & N. Lapusta (2010) – Towards inferring earthquake patterns from geodetic observations of interseismic coupling. Nat. Geosci., 3(5), 363–369, doi:10.1038/ngeo843

Pacheco, J. F. & L. R. Sykes (1992) – Seismic moment catalog of large shallow earthquakes, 1900 to 1989. Bull. Seismol. Soc. Am., 82, 1306–1349.

Rosenau, M., J. Lohrmann & O. Oncken (2009) – Shocks in a box: An analogue model of subduction earthquake cycles with application to seismotectonic forearc evolution. J. Geophys. Res., 114(B1), 1–20, doi:10.1029/2008JB005665.

Rosenau, M., R. Nerlich, S. Brune & O. Oncken (2010) – Experimental insights into the scaling and variability of local tsunamis triggered by giant subduction megathrust earthquakes. J. Geophys. Res., 115(B9), 1–20, doi:10.1029/2009JB007100.

Shindler, L., M. Moroni & A. Cenedese (2012) – Using optical flow equation for particle detection and velocity prediction in particle tracking. Applied Mathematics and Computation, 218, 8684–8694, doi:10.1016/j.amc.2012.02.030.

van Dinther, Y., T. V. Gerya, L. A. Dalguer, F. Corbi, F. Funiciello, & P. M. Mai (2013) – The seismic cycle at subduction thrusts: 2. Dynamic implications of geodynamic simulations validated with laboratory models. J. Geophys. Res. Solid Earth, 118, 15021525, doi:10.1029/2012JB009479.

Wang, K. (2007) – Elastic and viscoelastic models of crustal deformation in subduction earthquake cycles, in The Seismogenic Zone of Subduction Thrust Faults, MARGINS Theoretical and Experimental Earth Science Series, edited by T. H. Dixon & J. C. Moore, Columbia Univ. Press, New York.

Upscaling of micro- and meso-scale structures to local- and regional scales: implications for 3D implicit and explicit models of structurally complex deformation of multi-layered rocks

Mathias Egglseder[1], Alexander Cruden[1]

[1]*School of Geosciences, Monash University, Melbourne, Victoria 3800, Australia*
e-mail: *mathias.egglseder@monash.edu*
session: *(Seismo-) Tectonics*

An ideal geological model should account for all structures from the micro- to the regional scale using the principle that small-scale structures can be extrapolated to larger-scale structures and vice-versa. In reality, this task is not straightforward if the structural evolution of an area is complicated by overprinting ductile and brittle deformation events and contrasting rheological behaviors of rock types. In order to address this practical challenge, we will evaluate whether insights provided from micro- and meso-scale structures observed in thin sections and hand specimens can be upscaled to the geometry and spatial-timing relationships at a larger local to regional scale. Our approach is to visualize complexly-deformed hand specimens using explicit (Move, Midland Valley Ltd.) modelling techniques to characterize the 3D geometry of relevant structural features, supported by microstructural observations. The results are then compared with structural observations in outcrops and 3D mine-scale models using implicit (Leapfrog, AranzGeo Ltd.) modelling techniques, which offer spatial information on a larger scale.

The 3D deformation of multilayered rocks with different rheological properties has been studied using analogue and numerical modelling, but results to date have been difficult to apply to complex geologic settings. A complementary approach to improve understanding of the complex 3D deformation of multilayered rocks is to carry out 3D multiscale analysis and geometric modelling in a field area containing contrasting lithologies that has been affected by multiple deformation phases. These requirements are prevalent in deformed Neoarchean to Paleoproterozoic banded iron formations (BIF) of the Hamersley Province, Australia. Here, sedimentary rocks comprise mm to dm thick bands of alternating chert and iron oxide layers, interbedded with shales, carbonates and volcanic rocks. The stratigraphic succession is laterally consistent with no significant facies changes over large distances (Morris 1993), making the BIFs an ideal laboratory to study the deformation of multilayers with different rheological behaviors in three dimensions. The area is also well exposed and extensive subsurface data is available due to iron ore mining operations and exploration activities. Here we take advantage of 50 years of data acquisition by Rio Tinto Ltd. at the Mount Tom Price mine to create a 3D model of the deposit in order to characterize the 3D geometry of a key part of this structurally complex region. The rock units experienced several proposed shortening and extensional deformation stages with an only low grade metamorphic overprint (e. g. Taylor et al. 2001; Müller et al. 2005; Dalstra 2006; Morris & Kneeshaw 2011).

Our new structural approach attempts to challenge the many debated aspects of BIF formation, the structural evolution of the region and the enrichment processes that lead to BIF-hosted

Fig. 1.: Thin chert layers in shale show different deformation compared to thick overlying BIF layers.

Fig. 2.: Complex structural features of chert layers (red) in shales (black).

high-grade iron ore deposits. Different analysis techniques have been used to approach these topics incorporating basic field mapping and microscopy, 3D visualization using X-ray microscopy (XRM) and 3D modelling techniques to develop 3D models on all scales. Field observations indicate complex relationships between structural features, with simultaneous formation of brittle and ductile structures controlled by the rheological properties of the different rock units (Fig. 1 and Fig. 2). Folds are commonly non-cylindrical and faults die out rapidly vertically and horizontally, creating challenges for the recognition of overprinting relationships.

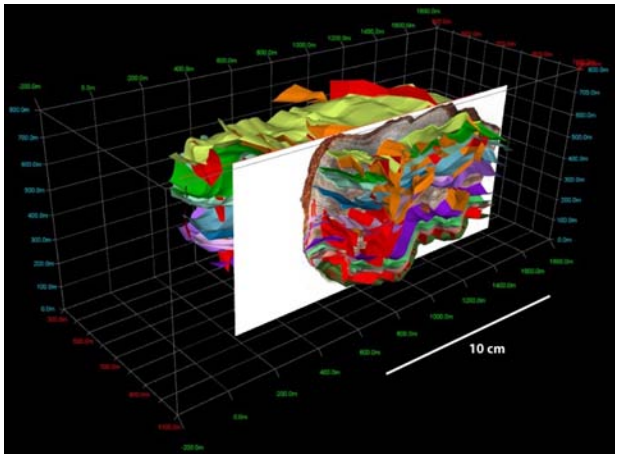

Fig. 3.: 3D Move (by Midland Valley Ltd.) model of complexly deformed specimen

In order to better resolve these structural relationships, serial sections of a complexly deformed hand specimen of BIF were digitized and then used to create an explicit 3D model with 3DMove (Midland Valley Ltd.) (Fig. 3). The model shows that structural features are controlled by differences in the rheological properties of chert and iron oxide layers, which has led to complex deformation patterns at all scales. The resulting structural analysis shows at least two deformation events. A first extensional event (D 1) led to the development of pinch-and-swell structures and boudinage of more competent cherty layers. A later (possibly two-stage) shortening event (D 2) is indicated by buckling, mullion structures and thrusting, which are mainly controlled by the rheological contrasts between rock units (Fig. 4).

Microscopic studies (optical and XRM) indicate significant removal of quartz, which leads to a reduction of layer thicknesses and hence a compacted sequence of iron oxides (Fig. 5) alongside reprecipitation as fibrous strain fringes (Passchier & Trouw 2005) in extensional domains associated with martite-crystals (martite: pseudomorph of hematite after magnetite). A cleavage also developed in the flattening plane and is indicated by a second generation of iron oxides precipitated by iron-rich fluids.

Similar structural features arising from rheological contrasts between chert, iron oxides and

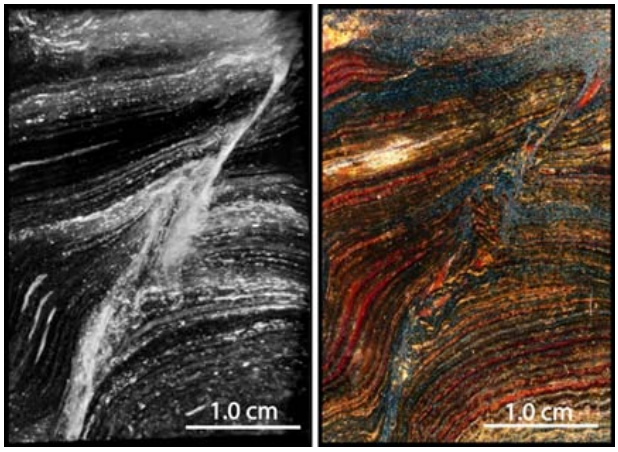

Fig. 4.: Complex structures compared; left: XRM image, right: photo scan

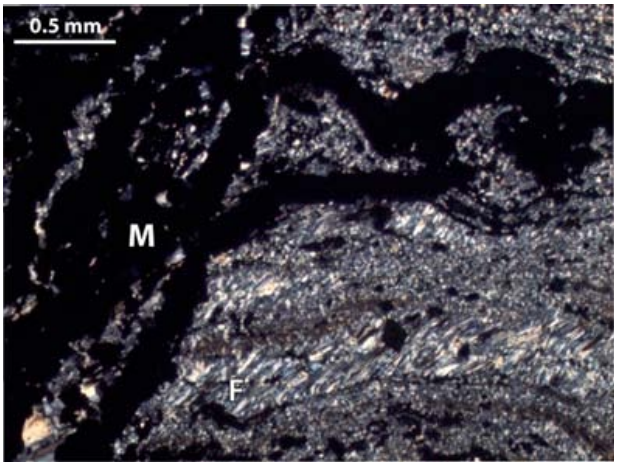

Fig. 5.: Dissolution of quartz leads to reduced iron oxide layers and reprecipitation as fibrous strain fringes (F), M: Martite

shales are also observed in outcrops and in deposit scale models (Fig. 6). Contrasting fluid flow properties between lithologies (e. g. BIF and shales) may also have played a major role leading to different styles of deformation and the development of a variety of fold and fault geometries (e. g., Marques et al. 2010).

The extrapolation of these smaller scale structures to larger scales using 3D modelling techniques depends on the complexity of the geology and the data available (Calcagno et al. 2008). To generate a 3D model of the Mount Tom Price mine (Fig. 7) we have used the implicit modelling

Fig. 6.: Complex relationships between boudins, folds and faults due to different rheological behaviour

software Leapfrog (AranzGeo Ltd.), which interpolates raw datasets of numeric and non-numeric data (e. g., lithological boundaries, geochemical, geophysical, mapping and structural data) using a single mathematical volume function (RBF: radial basis function) into a single coherent model. In contrast, the alternative explicit modelling techniques introduce inherent bias because models are typically built from already interpreted 2D cross-sections. The advantage of implicit modelling is that the interpolation process is relatively unbiased. However, it requires a consistently high data density and does not produce satisfactory results away from data points (see Fig. 7, isosurfaces are not well constrained at certain distances to the drill hole data) and is therefore not yet utilizable in the same resolution for regional scale models with fewer data points (no drill hole data).

Figure 7 shows a cross section through the main part of the Mount Tom Price iron ore deposit with the least amount of user-defined interpretation. The main structure is a major syncline with a SW-dipping normal fault on its NE limb, which appears to exploit shale layers as detachment horizons. In 3D and at the local and mine scale, the trends of this and other faults are often not clear, which could be explained by contrasts in rheological behaviour between shale- and BIF units. Relative large distances between exploration drill holes often do not permit observation

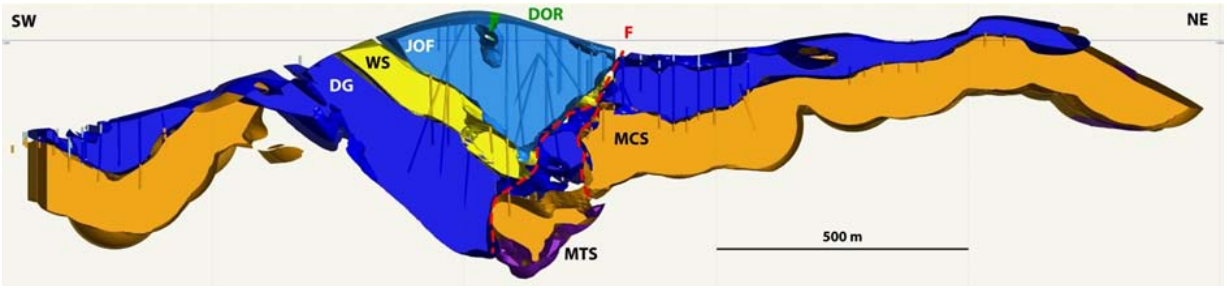

Fig. 7.: Cross section of the 3D Leapfrog model. Holes are subject to the distance to data points of drill holes. DOR: Dolerite, F: Fault, JOF: Joffre Mb. (BIF), MCS: Mt. McRae Shale, MTS: Mt. Sylvia Fm. (Shale/chert), WS: Whaleback Shale Member

of smaller scale structures.

Our preliminary analysis shows that similar structures can be observed on smaller and larger scales, e. g., thickness variations and the absence of individual layers due to extensional and compressional deformation, non-cylindrical and converging folds as well as vertically and horizontally discontinuous faults. Different lithologies are variably affected by synchronous folding and faulting and by simultaneous dissolution and reprecipitation on a microscale. These complimentary observations suggest that similar mechanisms of deformation are prevalent on all scales, which is an implication that would have arisen without extensive study of smaller scale structures.

We hypothesize that the above structural associations established a framework for later enrichments and replacements that led to the formation of high-grade iron ore. Since the 3D deformation of multilayers with contrasting thickness and lithology is not well understood, our approach also provides insights on the variable behaviors of different rock units on all scales. 3D analysis of the resulting structures at the meso-scale and their subsequent extrapolation to larger scales is an effective way to significantly improve the understanding of complex structural processes. Although 3D modelling tools are important and helpful for this analysis they cannot replace basic structural geology combined with different fields of geology (here: petrography, microtectonics, geochemistry). Consideration of all available geological data is crucial to create a realistic geological model, which is able to explain all observable features for academic as well as applied purposes.

References

Calcagno, P., Chilès, J.P., Courrioux, G., Guillen, A., 2008. Geological modelling from field data and geological knowledge. Physics of the Earth and Planetary Interiors, 171(1-4), 147–157.

Dalstra, H.J., 2006. Structural controls of bedded iron ore in the Hamersley Province, Western Australia – an example from the Paraburdoo Ranges. Applied Earth Science: IMM Transactions section B, 115(4), 139–145.

Marques, F.O., Burg, J.-P., Lechmann, S.M., Schmalholz, S.M., 2010. Fluid-assisted particulate flow of turbidites at very low temperature: A key to tight folding in a submarine Variscan foreland basin of SW Europe. Tectonics, 29(2), TC2005, doi:10.1029/2008TC002439.

Morris, R.C., 1993. Genetic modelling for banded iron-formation of the Hamersley Group, Pilbara Craton, Western Australia. Precambrian Research, 60, 243–286.

Morris, R.C. & Kneeshaw, M., 2011. Genesis modelling for the Hamersley BIF-hosted iron ores of Western Australia: a critical review. Australian Journal of Earth Sciences, 58(5), 417–451.

Müller, S.G., Krapež, B., Barley, M.E., Fletcher, I.R., 2005. Giant iron-ore deposits of the

Hamersley province related to the breakup of Paleoproterozoic Australia: New insights from in situ SHRIMP dating of baddeleyite from mafic intrusions. Geology, 33(7), 577-580.

Passchier, C.W. & Trouw, R.A.J., 2005. Microtectonics. 2nd edition, Springer Verlag, Berlin, Heidelberg, 366pp.

Taylor, D., Dalstra, H.J., Harding, A.E., Broadbent, G.C., Barley, M.E., 2001. Genesis of High-Grade Hematite Orebodies of the Hamersley Province, Western Australia. Economic Geology, 96, 837–873.

Influence of the seismogenic downdip width on supercycles at subduction thrusts

Robert Herrendörfer[1], Ylona van Dinther[1], Taras Gerya[1], Luis A. Dalguer[1,2]

[1]*ETH Zurich, Institute of Geophysics*
[2]*now at swissnuclear*
e-mail: *robert.herrendoerfer@erdw.ethz.ch*
session: *(Seismo-) Tectonics*

Introduction

Megathrust earthquakes exhibit a strong variability in size and extent both in strike and dip direction. For instance, in the north-east Japan subduction zone mainly M 7 earthquakes had ruptured a small part of the rupture area of the 2011 M 9.0 Tohoku earthquake that appears to have spanned the entire seismogenic zone downdip width [e. g. 5]. In some of the cases when a long record of past earthquakes is available, a recurring earthquake pattern seems to arise, which is called supercycle [1, 2]. It contains the occurrence of smaller earthquakes in between larger earthquakes. A better understanding of this variability in earthquake size would contribute to an improved hazard assessment in areas close to subduction zones. We observe that supercycles have been proposed for those subduction zones [1,2] with a large seismogenic zone downdip width [3] (Fig. 1), including the north-east Japan subduction zone. This suggests a potential role of the downdip width. In this numerical study we show that the downdip width is indeed the key parameter controlling the long-term seismicity at subduction thrusts.

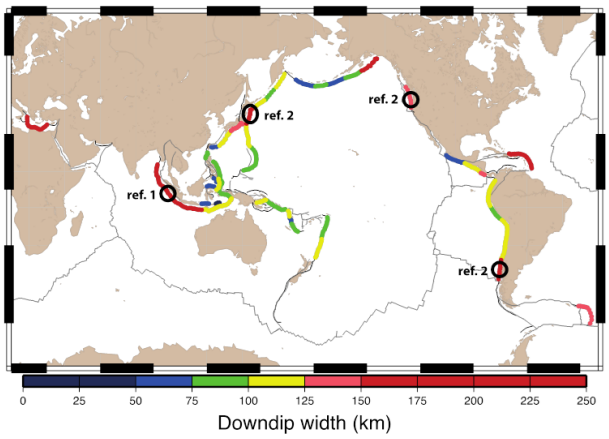

Fig. 1.: Downdip width of seismogenic zones and proposed supercycles. Supercycles have been proposed [1, 2] for seismogenic zones with an estimated wide downdip width [3]. Adapted from [3]. Colorscale corresponds to the distributionof the downdip widths, with red colors indicating subduction zones outside one standard deviation from the mean value.

Methods

To investigate the role of the seismogenic downdip width, we use a two-dimensional continuum, seismo-mechanical numerical model of a simplified subduction zone [4]. Under the assumption

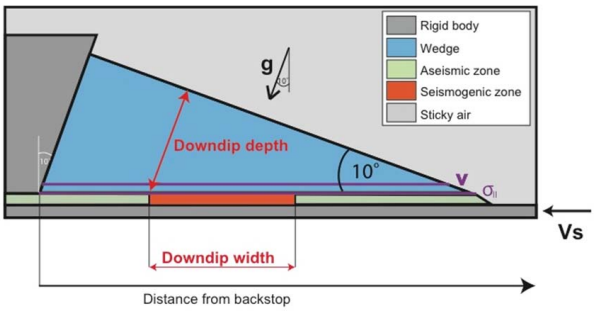

Fig. 2.: Numerical model setup. A visco-elastic wedge is underthrusted by a rigid plate with a subduction velocity of Vs and at a subduction angle of 10°. The interface between the wedge and the plate is modeled as a frictional boundary layer. In this layer, the seismogenic zone, modelled as velocity-weakening, is limited up- and downdip by aseismic zones, modelled as velocity strengthening. Horizontal displacement velocity is measured 1 cm above, stress and strength at the top of the frictional boundary layer.

of an incompressible medium, we solve for the conservation of mass and momentum and apply a visco-elasto-plastic rheology. The model setup (Fig. 2) consists of a visco-elastic wedge that is underthrusted by a rigid plate. In the frictional boundary layer between plate and wedge, we apply a pressure-dependent yield strength, a non-associative plastic flow law and a strongly rate-dependent friction. In this layer, a velocity-weakening seismogenic zone is limited up- and downdip by velocity-strengthening aseismic areas. Here, model results and parameters are scaled up to natural values. Main model limitations include the restriction to 2D, a non-adaptive time-step, and negligible wave propagation effects.

We compare different models using functions and parameters, averaged over the width of the seismogenic zone: cumulative sum of displacements tracks the evolution of elastic strain, strength excess depicts the stress state and the S parameter is the ratio of initial strength excess and stress change for each event. Furthermore, we calculate the average supercycle duration and the average number of events per supercycle. We qualitatively distinguish between sub-critical, pulse-like and crack-like ruptures by evaluating the propagation distance, local duration of coseismic displacements and the existence of healing during an event.

Results

In the reference model with a downdip width of 248 km (LW) supercycles evolve (Fig. 3 a). Interseismic deformation concentrated at the seismogenic zone limits, small sub-critical and pulse-like ruptures effectively increase the stress within the seismogenic zone to a critical state (Fig. 3 b-c). A supercycle is then completed by a large crack-like rupture (i. e. superevent), which strongly reduces stresses in the entire seismogenic zone. A model with a downdip width of 102 km (SW), in contrast, is characterized by ordinary cycles, mainly consisting of similar sized, quasi-periodical crack-like ruptures (Fig. 3). Increasing the seismogenic zone downdip width thus leads to a transition from ordinary cycles to supercycles as the number and variability of events increase (Fig. 4 a) as well as the size of and recurrence time between the largest events. It also leads to an increase of the median S parameter, indicating a transition from the dominance of crack-like ruptures to the dominance of pulse-like ruptures (Fig. 4 b).

Other factors which can be shown with our model to influence supercycles are 1) downdip depth of the seismogenic zone, 2) a large strength excess due to a relatively strong megathrust and 3) large stress drops due to a strongly rate-dependent friction.

With our 2D model we cannot rule out the hypothesis that the observation of supercycles might be a result of strength or frictional heterogeneities along the dip and strike of the megathrust or due to earthquake interactions from different segments.

Conclusions

In the reference model with a downdip width of 248 km (LW) supercycles evolve (Fig. 3 a). Interseismic deformation concentrated at the seismogenic zone limits, small sub-critical and pulse-like ruptures effectively increase the stress within the

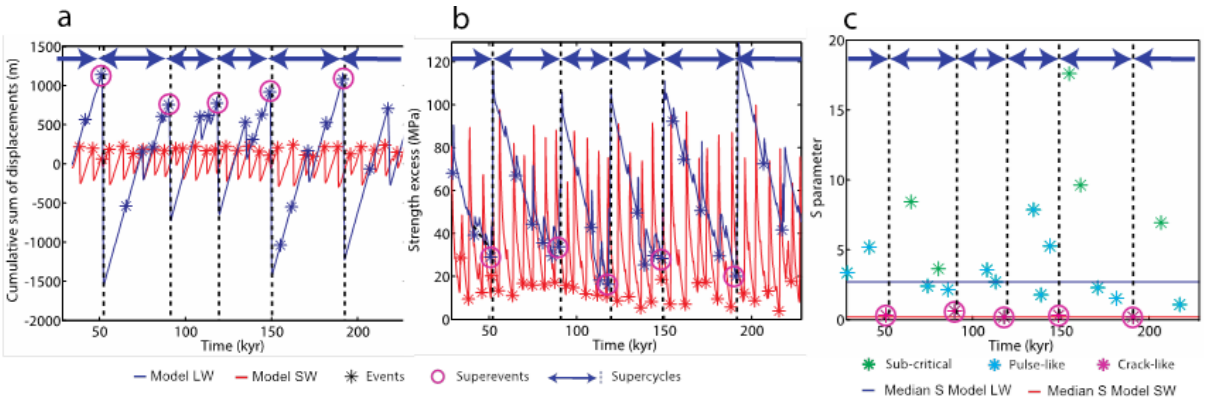

Fig. 3.: Results for reference models LW and SW. Functions and parameters, averaged over the downdip width of the respective seismogenic zone for model LW (downdip width=$248\,\mathrm{km}$) and for model SW (downdip width=$102\,\mathrm{km}$): a, Detrended, cumulative sum of displacements over time, b, evolution of strength excess (i.e. difference between yield strength and second invariant of deviatoric stress tensor), c, S parameter (ratio between initial strength excess and stress change) over time in model LW, while colors of each event indicate the rupture style. Horizontal lines show the median S value for model LW and model SW. Stars represent detected events. Purple circles show superevents. Blue arrows indicate the duration of supercycles in model LW.

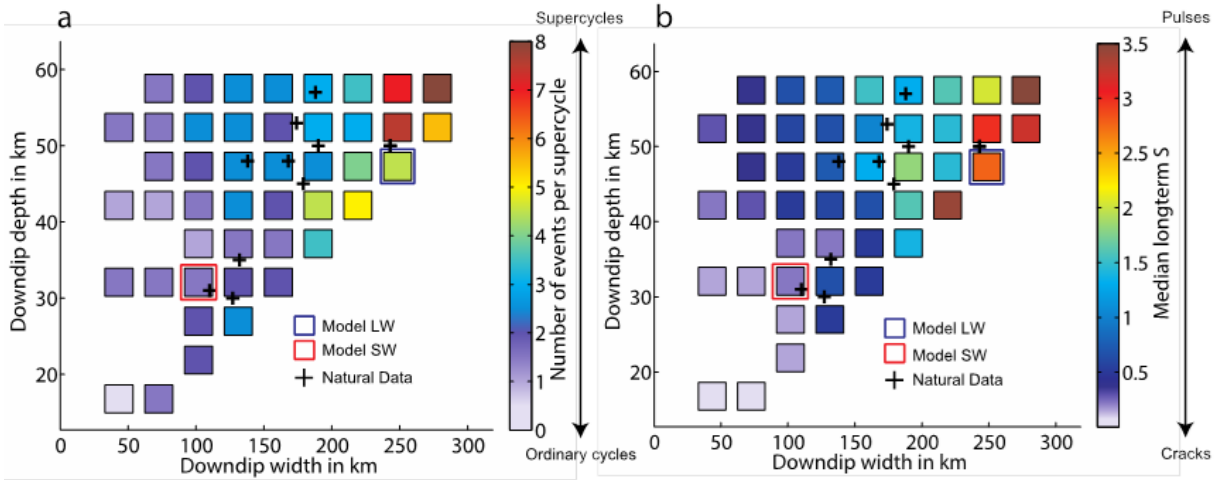

Fig. 4.: Results of the parameter study. Role of the downdip width and depth of theseismogenic zone for a, the number of events and, b, the median of the S parameter. Model LW and SW are highlighted with blue and red squares, respectively. Black crosses indicate natural seismogenic zones, determined by [3]. The increase of the number of events indicates the transition from simple cycles to supercycles, while the increase of the median S paramater indicates the transition from the dominance of cracks to pulse-like ruptures.

seismogenic zone to a critical state (Fig. 3 b-c). A supercycle is then completed by a large crack-like rupture (i. e. superevent), which strongly reduces stresses in the entire seismogenic zone. A model with a downdip width of 102 km (SW), in contrast, is characterized by ordinary cycles, mainly consisting of similar sized, quasi-periodical crack-like ruptures (Fig. 3). Increasing the seismogenic zone downdip width thus leads to a transition from ordinary cycles to supercycles as the number and variability of events increase (Fig. 4 a) as well as the size of and recurrence time between the largest events. It also leads to an increase of the median S parameter, indicating a transition from the dominance of crack-like ruptures to the dominance of pulse-like ruptures (Fig. 4 b).

Other factors which can be shown with our model to influence supercycles are 1) downdip depth of the seismogenic zone, 2) a large strength excess due to a relatively strong megathrust and 3) large stress drops due to a strongly rate-dependent friction.

With our 2D model we cannot rule out the hypothesis that the observation of supercycles might be a result of strength or frictional heterogeneities along the dip and strike of the megathrust or due to earthquake interactions from different segments.

References

[1] Sieh et al. Earthquake Supercycles Inferred from Sea-Level Changes Recorded in the Corals of West Sumatra. Science, 322(5908):1674-1678, 2008.

[2] Goldfinger et al. Superquakes and Supercycles. Seismological Research Letters, 84(1): 24-32, 2013.

[3] Heuret et al. Physical characteristics of subduction interface type seismogenic zones revisited. G3, 12(1), Q01004, 2011.

[4] van Dinther et al.The seismic cycle at subduction zone thrusts: 2. Dynamic implications of geodynamic simulations validated with laboratory models. J. Geophys. Res., 118:1502-1525, 2013.

[5] Simons et al. The 2011 Magnitude 9.0 Tohoku-Oki Earthquake: Mosaicking the Megathrust from Seconds to Centuries, Science, 332 (6036), 1421-1425 2011

Geomechanical modeling of fault geometry role on subduction earthquake cycle: Case study of Chilean margin

Shaoyang Li[1], Marcos Moreno[1], Jon Bedford[1], Matthias Rosenau[1], Daniel Melnick[2], Onno Oncken[1]

[1] *Helmholtz Centre Potsdam, GFZ German Research Centre for Geosciences, Telegrafenberg, Potsdam, Germany*
[2] *Institut für Erd- und Umweltwissenschaften, DFG-Leibniz Center for Surface Process and Climate Studies, Universität Potsdam, Potsdam, Germany*
e-mail: *shaoy@gfz-potsdam.de*
session: *(Seismo-) Tectonics*

Introduction

Understanding the mechanical processes governing magnitude, recurrence, and segmentation of earthquakes along a subduction margin is of paramount importance for assessing the margin's seismic hazard. Long-term variations in fault friction and geometrical undulations of the plate interface are thought to be the first order controls on system behavior and activation. Many studies from analogue and numerical modeling have quantitatively investigated the effects of fault heterogeneities on earthquake cycle behavior [1], but a clear understanding of main controlling parameters remain elusive. An observable permanent/plastic strain is built up over multiple seismic cycles, producing geological features such as terraces and peninsulas [2] providing some constraints for the models. Co-, post- and interseismic kinematics of a margin are likely to be mainly an expression of the frictional properties controlling the stick-slip behavior of the plate interface and relaxation phenomena in the mantle wedge and deeper viscoelastic portion of the subduction zone lithosphere. Challenges remain in separating the contributions of these overlapping relaxation phases and interface kinematic processes in the data.

Short-term heterogeneous coseismic slip distribution on faults may be due to heterogeneous pre-stress, geometric complexity, heterogeneous material properties, dynamic weakening mechanism [3-5]. Recent studies of the dynamic modeling of geometric effects, such as fault bending, fault stepover, fault roughness, and parallel offset of faults, on rupture propagation (e. g. [5-8]) indicate that rupture tends to decelerate or terminate at places where the fault geometry varies. Some of these studies emphasize the importance of initial stress but normally with pre-defined unrealistic stress field or principle stress orientation, which may not represent tectonic loading due to geometric complexity in detail or any frictional heterogeneity. Moreover, initial stress can largely affect the seismic rupture and the ability of breaking past kinks or branches in the fault system [5, 7, 9]. Therefore, fault geometry and structure can heavily affect interseismic stress accumulation along fault system as well as the stress released in large ruptures.

Modern precise geophysical measurements give reasonable constrains on fault geometry, material properties and kinematics. Furthermore, decades of space geodetic observations are allowing to accurately quantify transient deformation associated with the earthquake cycle process [10-12]. These kinematic observations offer an excellent chance to model how large plate boundary fault system is evolving with unprecedented precision. Integrating geophysical and geodetic data with

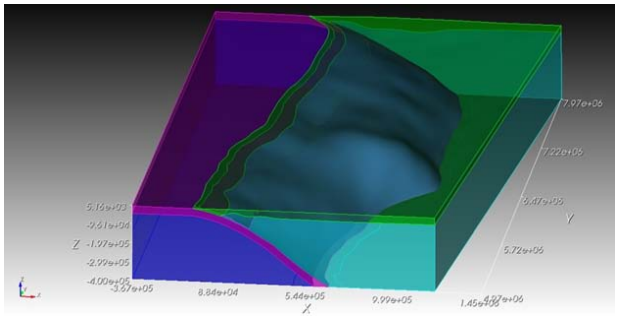

Fig. 1.: Geometry of whole Chilean subduction zone

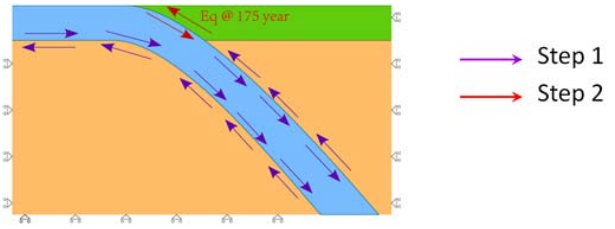

Fig. 2.: Two-step method of earthquake cycle modeling

numerical modeling shade some lights on mechanisms of earthquake cycle of large plate boundary fault system establishing new tools that were not available. In this context, we attempt to evaluate geometry effects on the earthquake cycle (without considering permanent friction heterogeneity [1]) using the Finite Element Method (FEM) (Figure 1) and all available geophysical and geodetic data for the entire Chilean interplate margin. We simulate an earthquake cycle to investigate the continuous complex geometry effects on pre-seismic stress heterogeneities, dynamic strong-holder-breaking rupturing, and long-term earthquake segmentations, hence long-term fault system seismic hazards. Our study emphasizes the importance of considering the geometrical complexity during all phases of the earthquake cycle.

Method

We construct a FEM including precisely all the geomechanical heterogeneities of the Chilean subduction zone (Figure 1) [13, 14]. Our models attempt to quantify the control of geometrical features on the buildup of high shear stress along a fault and their direct mechanical on seismic barrier or asperities. Therefore, we implemented a simple method with two forward steps: Firstly, we simulate tectonic loading of interseismic period with complex realistic geometry and geodetically derived plate convergence and forearc deformation. Here, we imposed a homogenous locking degree along the fault, and therefore only the geometrical features control lateral variations of strain accumulation. Secondly, we mimic a coseismic rupture releasing the interseismic accumulated stress in first step (shown as Figure 2). Hence our modeling emphasizes the importance of producing realistic pre-stress on a dynamic model, task that is not well described on literature.

Preliminary results

We successfully produce rough segmentations along whole Chilean subduction zone in our preliminary test of our model set up (Figure 3 b). Comparing to the nature earthquake history, we find out our model well reproduce large segmentation in south Chile where 1960 M_w 9.5 earthquake happens. However, our model cannot reproduce all details along the margin. This may due to inaccurate interseismic kinematics and the variation in reoccurrence period for different segments.

Future work

We plan to add complexity in both interseismic and coseismic model. By simulating gravity stresses as background stress, we can better constrain fault opening during coseismic simulations. Better interseismic models may involve realistic loading (variation of convergence along the trench) and reliable geodetic inverted locking degrees in seismogenic zones. Using dynamic method (i. e. explicit scheme of finite element method), our model can better catch the characters of megathrust earthquake rupturing, which result in subduction zone segmentations. We will calculate the distribution of locking and attempt to include the influence of the Andean Shortening

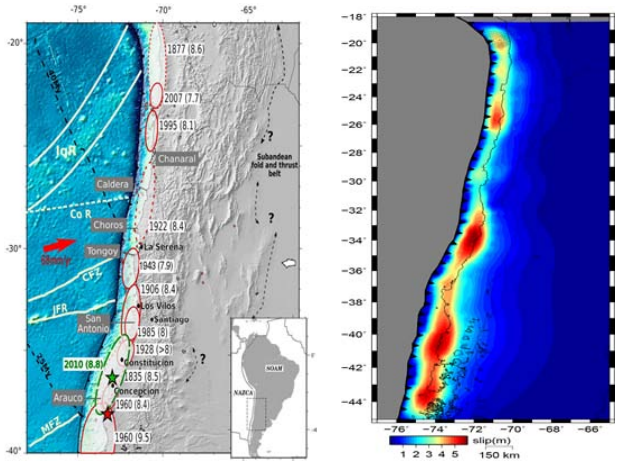

Fig. 3.: Comparison of surface deformation of our model with historical segmentation along whole Chilean margin. (a) Historical megathrust earthquakes segmentation [15]. [2] Preliminary result of surface deformation from our simple earthquake cycle model of geometry complex.

on the GPS signals. In this way, we will archive better final solution to compare the locking degree of short term crystal deformation based on GPS observations with the asperities and barrier patchwork from the stress release.

References

[1] Y. Kaneko, J. P. Avouac, N. Lapusta, Nature Geosci. 3, 363 (2010).

[2] D. Melnick, B. Bookhagen, H. P. Echtler, M. R. Strecker, Geological Society of America Bulletin 118, 1463 (November 1, 2006, 2006).

[3] C. H. Scholz, Nature 391, 37 (1998).

[4] P. M. Mai, G. C. Beroza, Journal of Geophysical Research-Solid Earth 107, (Nov, 2002).

[5] B. Duan, D. D. Oglesby, Journal of Geophysical Research: Solid Earth 111, B05309 (2006).

[6] Y. Kase, K. Kuge, Geophysical Journal International 135, 911 (December 1, 1998, 1998).

[7] B. Duan, D. D. Oglesby, BULLETIN OF THE SEISMOLOGICAL SOCIETY OF AMERICA 95, 1623 (2005).

[8] T. Candela, F. Renard, J. Schmittbuhl, M. Bouchon, E. E. Brodsky, Geophysical Journal International 187, 959 (2011).

[9] N. Kame, J. R. Rice, R. Dmowska, Journal of Geophysical Research: Solid Earth (1978–2012) 108, (2003).

[10] J. Klotz et al., Earth and Planetary Science Letters 193, 437 (2001).

[11] J. Bedford et al., Earth and Planetary Science Letters 383, 26 (2013).

[12] M. Moreno et al., Earth and Planetary Science Letters 321–322, 152 (2012).

[13] A. Tassara, H. J. Goetze, S. Schmidt, R. Hackney, J. Geophys. Res. 111, B09404 (2006).

[14] G. Hayes. (Nature Publishing Group, a division of Macmillan Publishers Limited. All Rights Reserved., 2010).

[15] M. Metois, A. Socquet, C. Vigny, J. Geophys. Res. 117, B03406 (2012).

The long term evolution of fold-and-thrust belts: consistency of numerical approaches and physical experiments

Bertrand Maillot

Laboratoire Géosciences et Environnement Cergy, Université de Cergy-Pontoise, France
e-mail: *bertrand.maillot@u-cergy.fr*
session: *(Seismo-) Tectonics*

The recent developments in numerical techniques to describe large slip on frictional surfaces and the formation of faults, have allowed us to simulate numerically the long term evolution of fold-and-thrust belts, which were so far only simulated with physical experiments. Therefore, the question of the fit between various numerical solutions (Buiter et al., 2006), and physical analogue experiments (Schreurs et al., 2006), has become central. This presentation will focus first on the production of experimental data that can be quantitatively compared to numerical simulations, and second on the development of a numerical method to simulate the experimental data and further used to predict the spatio-temporal activity of faults during the very long term growth of an accretionary wedge, thereby suggesting further experiments.

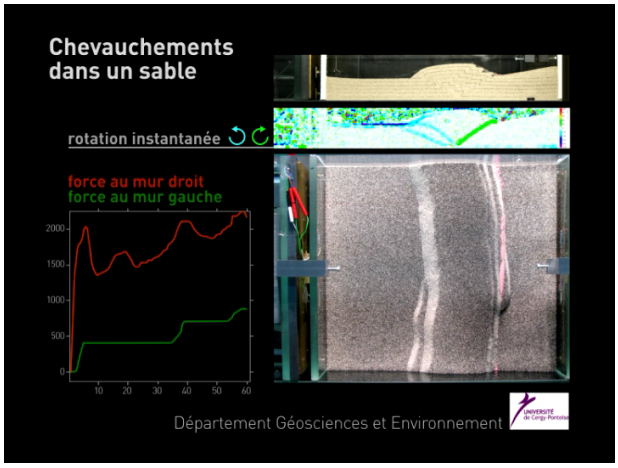

Fig. 1.: A typical thrusting experiment. Top right: lateral view through the glass side wall, with map of rotations below (obtained by PIV); bottom right: top view; bottom left: force measured at each end walls (red: right) during shortening (mm). (P. Souloumiac, PhD)

Experimental Data

Fig. 1 illustrates a basic thrusting experiment. Its simulation with a 2D numerical code raises a series of questions. Should the comparison be made with the side view, or with a cross-section in the center (that can be observed only post-mortem in the absence of a scanner)? What is the reproducibility of the experimental cross-section? How to measure quantitatively the fit of a simulation to a cross-section? These questions find general answers in the theory of inverse problems. I will present some of their specific aspects for a thrusting experiment using sand, among which the problem of building the sand pack, of side wall friction (Fig. 2), of force measurement, and a protocol to establish error bars that account for the lateral variability of thrusting.

Numerical approach by sequential limit analysis

Although numerical methods that solve the full mechanical problem (various FEM techniques), as well as DEM methods are rapidly progressing, the

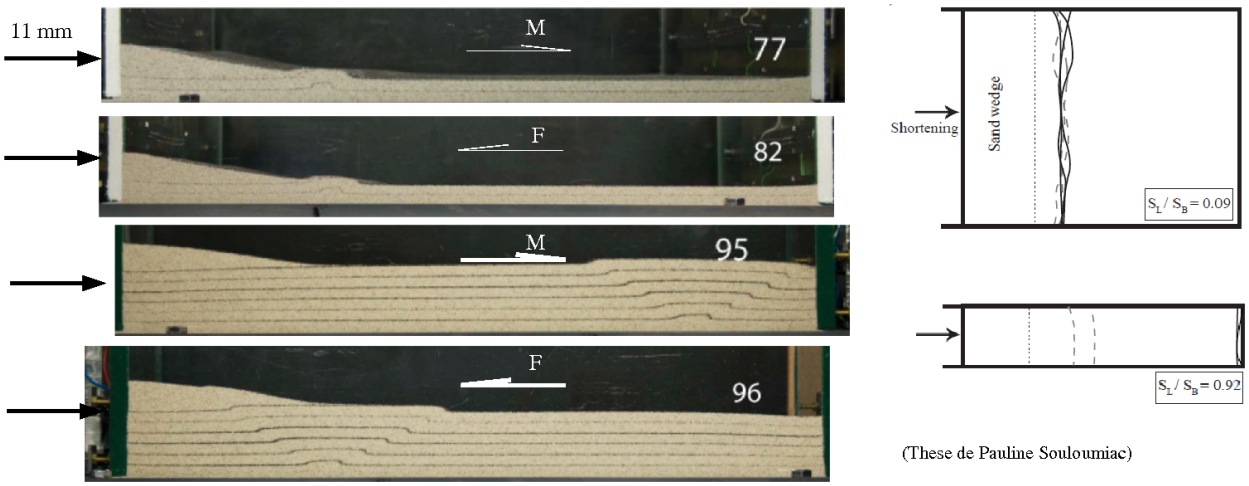

Fig. 2.: Illustration of side wall friction effects. M: mobile base configuration (equivalent to conveyor belt, or "pull" type of box); F: fixed base configuration (equivalent to boxes using a single moving wall, or "push" type). At low lateral to basal area ratio (SL/S_B), results are the same (top two photos), but at high SL/S_B values, thrusting occurs at opposite ends of the box (bottom two photos), demonstrating a strong bias. (P. Souloumiac, PhD)

kinematic approach of Limit Analysis, also called the maximum strength theorem (MST) (Maillot and Leroy, 2006), offers a simplified method to determine the active fault geometry accounting for mechanical balance and the Coulomb criterion (Cubas et al., 2008, Mary et al., 2013a, 2013b). Its sequential application leads to the Sequential Limit Analysis (SLA) method. I will briefly present the method and its ability to reproduce experiments (Fig. 3). The very long term growth by frontal accretion reveals a complex pattern of thrust ramp activity (called G-grams) grouped in families (Fig. 4). The introduction of ramp friction weakening, perturbs this pattern and creates periods of inactivity of ramps in the back of the wedge that were not previously documented. Current developments focus on gravitational instability in over-pressured materials (Yuan et al., 2014). Longer term developments will focus on a 3D implementation, and on varying material properties within the sedimentary pile.

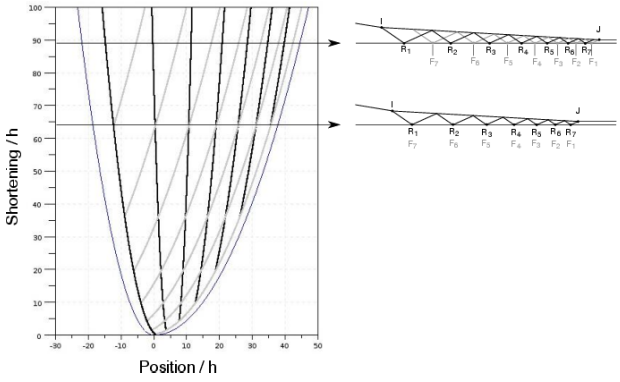

Fig. 4.: Spatio-temporal pattern of thrust ramp distribution (G-gram) during frontal accretion in a frictional wedge, showing "in phase" (at shortening=64) and "out-of-phase" periods (at shortening=89) between the families R and F of thrust ramps issued respectively from the deformation fronts at the back (point I) or the front (point J) of the wedge. (B. Mary, PhD).

Perspectives

Because SLA uses the same parameters as the Critical Coulomb Wedge theory, but provides the

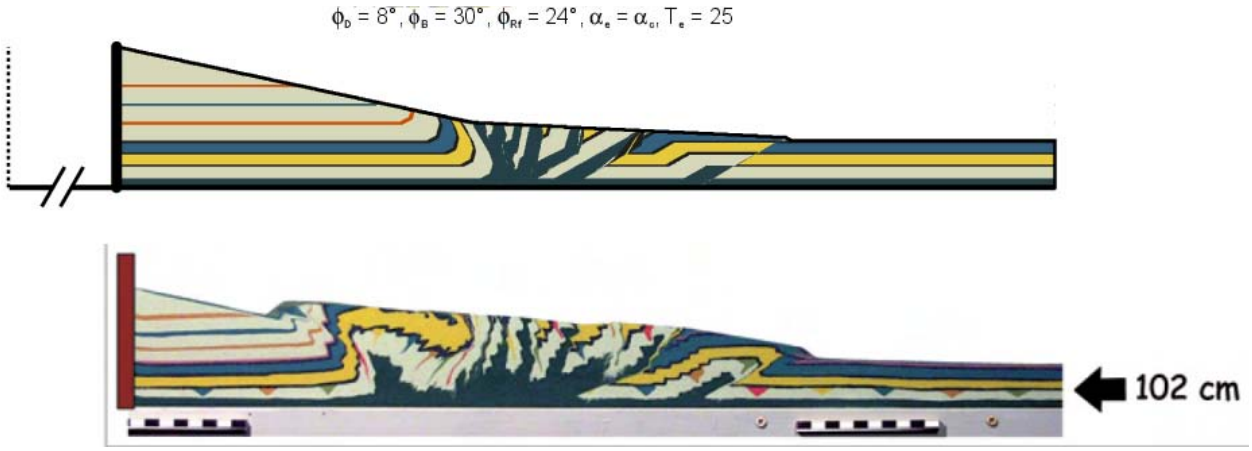

Fig. 3.: Comparison between a numerical simulation by Sequential Limit Analysis (SLAMTec), and a sand box experiment (Konstantinovskaya and Malavieille, 20xx) (B. Mary, PhD)

internal deformation during wedge growth, it can be seen as a generalisation of the CCW theory. Its predictions could be used as benchmarks for the more complex and general numerical methods, and suggest further experiments to compare to the spatio-temporal thrusting patterns mentioned above. Concerning experimental data, protocols to produce data with well defined statistical properties for comparison with 3D numerical simulations should now be developed, inspired by the 2D procedure. Overall, the comparison of experimental and numerical data in the framework of inverse problem theory, although not yet accessible for most numerical methods, is a very demanding and fruitful objective. It helps us to raise levels of both approaches, question their mutual consistency, and interpret the observed structures in terms of material parameters and boundary conditions.

References

Buiter, S.J.H, et al., The numerical sandbox: comparison of model results for a shortening and an extension experiment, The Geological Society of London Special Publication, 2006, 253, 29-64

Cubas, N., Barnes, C., Maillot, B. (2013), Inverse method applied to a sand wedge: estimation of friction parameters and uncertainty analysis, Journal of Structural Geology, 55, 101—113.

Cubas N., B. Maillot, C. Barnes, 2010. Statistical analysis of an experimental compressional sand wedge, Journal of Structural Geology, 32, 818–831, doi:10.1016/j.jsg.2010.05.010.

Cubas N., Y.M. Leroy, B. Maillot, Prediction of thrusting sequences in accretionary wedges, J. Geophys. Res., 113, B12412, doi:10.1029/2008JB005717, 2008.

Konstantinovskaya, E. & Malavieille, J. Erosion and exhumation in accretionary orogens : Experimental and geological approaches. Geochemistry, Geophysics, Geosystems, 2005, 6.

Maillot B., A sedimentation device to produce uniform sand packs, Tectonophysics, 593, 85—94, 2013, doi : 10.1016/j.tecto.2013.02.028.

Maillot B, Leroy YM. Kink-fold onset and development based on the maximum strength theorem. J. Mech. Phys. Solids. 2006, 54(10): 2030–2059.

Mary, B. C. L. Au delà du prisme critique de Coulomb par l'analyse limite séquentielle et contributions expérimentales, PhD thesis, Université de Cergy-Pontoise, France, 2012

Mary B.C., B. Maillot, Y.M. Leroy (2013), Predicting orogenic wedge styles as a function of analogue erosion law and material softening, Geochem. Geophys. Geosyst., 14, doi:10.1002/ggge.20262.

Mary BCL, Maillot B, Leroy YM. Deterministic chaos in frictional wedges revealed by convergence analysis. Int. J Num. Anal. Meth. Geom. 2013.

Pons A, Leroy YM. Stability of accretionary wedges based on the maximum strength theorem for fluid-saturated porous media . J. Mech. Phys. Solids . 2012, 60(4): 643–664.

Schreurs, G. et al., 2006: Analogue benchmarks of shortening and extension experiments, Buiter, S. & Schreurs, G. (Eds.) Geological Society Special publication, Analogue and Numerical Modelling of crustal scale processes., The Geological Society of London Special Publication, 2006, 253, 1-27

Souloumiac, P. Mécanismes 3D de ruine en géologie structurale : approche numérique et analogique. École Centrale Paris, 2009

Souloumiac P., B. Maillot, Y. M. Leroy, Bias due to side wall friction in sand box experiments, Journal of Structural Geology, 2012, doi:10.1016/j.jsg.2011.11.002.

Yuan, X., Y. M. Leroy, B. Maillot. Stability of over-pressured cohesive and frictional materials based on Sequential Limit Analysis, Extended Abstract, GeoMod 2014, this conference.

Cross-scale model of seismic cycle: first results

Iskander A. Muldashev[1], Stephan V. Sobolev[1]

[1] *GFZ German Research Centre for Geosciences, Potsdam, Germany*
e-mail: *muldashev@gfz-potsdam.de*
session: *(Seismo-) Tectonics*

Introduction

Origin and possible clustering of great earthquakes is perhaps one of the most exciting and mysterious problems in geophysics. Distribution in time of the largest earthquakes during observational period of about 100 years is highly uneven and shows two domains of increased release of seismic energy; during 50 s-60 s of last century and during the last decade, starting from great Sumatra earthquake of 2004. Interpretation of these data is highly controversial. Different statistical analyses suggest that such distribution indicates tendency for clustering of great earthquakes, or claim that this could be a realization of the random Poisson process, or that no robust statement on clustering can be made due to the small statistics for great earthquakes. Because it is unlikely that statistics of great earthquakes will significantly change in the next years, the uncertainty about clustering will remain. Therefore, other than purely statistical approaches should be found to tackle this problem.

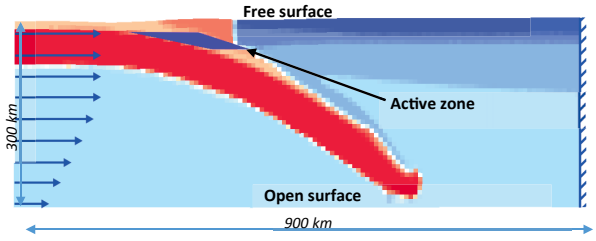

Fig. 1.: Setup of the 2D model of a subduction zone. Colours represent material phases. The region of the rate and state friction law is marked as active zone.

We take a modeling approach in which we attempt to model great earthquakes using numerical techniques that employ sophisticated rheology consistent with laboratory data of crustal and mantle rocks and are capable to describe geological time-scale deformation of lithosphere. Such geological time-scale models have been carried out for various tectonic settings using finite element modeling technique (Popov and Sobolev, 2008). Here we demonstrate first results of our modeling, which we consider as a preparation phase.

Modeling approach

First we make the model setup shown in Fig. 1, by modeling subduction process in the geological time-scale (107 years). We use finite element modeling technique (Popov and Sobolev, 2008) to model subduction during 4 Mln years, with the kinematic boundary conditions shown in Fig 1. To do so we employ visco-elasto-plastic rheology with constant low (0.01-0.05) friction coefficient in the uppermost part of the subduction slab, that is consistent with the idea of high pore-fluid pressure in subduction channel. The time step in such model is about 104 years. As a result we get the subduction model with appropriate stress distribution.

Second, we use geological time scale subduction model to simulate processes at the seismic cycle time scale (10-104 years). In these models we take geological time scale model, keep the same boundary conditions, but turn to much smaller time step (<10 years) and simultaneously introduce rate and state friction law (Dieterich, 1972;

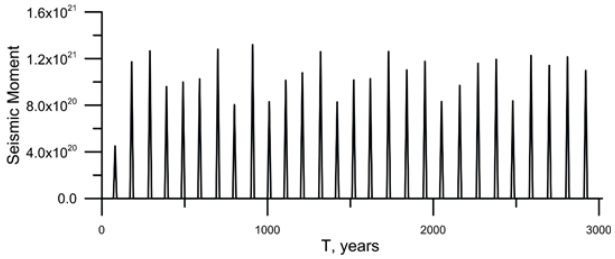

Fig. 2.: Seismic moment versus time for the typical model. Each "earthquake" represent one-time-step large displacement in "active zone" and in the adjacent deeper part of the interface between the slab and overriding plate.

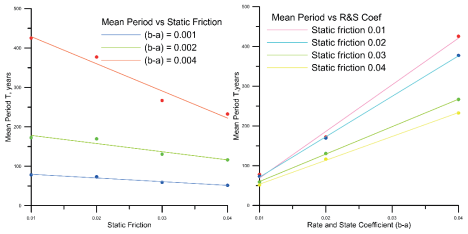

Fig. 3.: Mean period of earthquakes versus initial friction (left). Mean period of earthquakes versus rate and state coefficient (right).

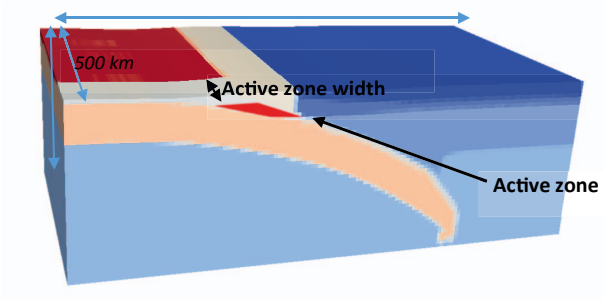

Fig. 4.: Setup of the 3D model of a subduction zone. Colours represent material phases. The region of the rate and state friction law is marked as active zone.

Scholtz, 1998) (in steady-state approximation) in the part of the uppermost layer of the subducting slab located in the depth range of (10 km to 42 km). This zone is labeled as "Active zone" in Fig. 1. The friction law is given by the relation:

$$\mu = \mu_0 - (b-a)log\Big(\frac{V}{V_0}\Big) \qquad (1)$$

Where μ_0 - static friction; a, b - experimentally determined variables; V - displacement rate; V_0 - initial displacement rate.

In the case when $(b-a) < 0$ the slip in "active zone" becomes unstable which leads to the stick-slip behavior (Scholtz, 1998), when instabilities (earthquakes) occur as one-time-step large displacements which are separated by period of slow inter-seismic deformation. Typical series of model earthquakes is shown in Fig. 2.

Parameter sensitivity

We performed a series of experiments to study sensitivity of models to different initial frictions and rate and state coefficients. Figure 3 shows dependencies of mean period between the earthquakes in model on static friction coefficient (Fig. 3, left) and on rate and state coefficient parameter (b-a) (Fig. 3, right).

As expected, we obtain almost linear relation between the earthquake period and (b-a) parameter. But interestingly, we also obtain week invers dependency of the earthquake period on static friction, that appears to be more pronounced at higher values of (b-a) parameter. We interpret this effect as the result of larger depth of brittle-ductile transition in the models with lower static friction that in turn causes deeper penetration of the rupture, larger average slip and larger time of accumulation of the next earthquake.

Next we study dependency of seismic moment (and average slip) of model earthquake on rupture area and compare the results with theoretical predictions. To do that we consider 3D model. Although we use 2D initial geological time-scale model, the active zone in the model is 3D (Fig. 4) with width varying from 100 km to 300 km. Rest of the model has static friction. In this setup static friction is 0.01 and (b-a) equals to 0.002. We use different sizes of finite elements in vertical cross-section (7 km) and in trench parallel direction (25 km to 50 km).

We obtain relations close to the theoretical expectation for the average stress drop of earthquake independent from its magnitude (Kanamori and Brodsky, 2004). For the smaller

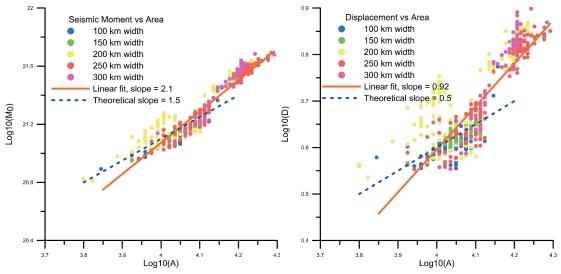

Fig. 5.: Logarithm of seismic moment of earthquakes versus logarithm of rupture area (left). .Logarithm of displacement during earthquake versus logarithm of rupture area (right).

earthquakes, whose rupture zones do not occupy the entire seismogenic zone, the average displacement is proportional to the square root of rapture area (A) and seismic moment is proportional to A3/2. For the large earthquakes the average displacement is proportional to the rapture area (A) and seismic moment is proportional to A2. These trends are also consistent with the observations (see Figure 11 in Kanamori and Brodsky (2004), suggesting that we are on the right way.

References

Dieterich, J. (1972), Time-dependence of rock friction. J. Geophys. Res. 77, 3690-3697.

Kanamori, H. and E.E. Brodsky (2004). The physics of earthquakes, Reports on Progress in Physics, v. 67, 1429-1496

A. A. Popov and S. V. Sobolev (2008), SLIM3D: A tool for three-dimensional thermomechanical modelling of lithospheric deformation with elasto-visco-plastic rheology. Physics of the Earth and Planetary Interiors 171, 55-75

Scholz, C. H. (1998), Earthquakes and friction laws, Nature, 391, 37-42.

Numerical modelling of the instantaneous subduction dynamics of the Banda Arc region

Casper Pranger[1,2], Cedric Thieulot[1], Arie van den Berg[1], Wim Spakman[1]

[1] *Mantle Dynamics Group, Department of Earth Sciences, Utrecht University, Budapestlaan 4, 3584 CD Utrecht, The Netherlands*
[2] *Now at Institute of Geophysics, ETH Zürich, Soneggstrasse 5, CH-8092 Zürich, Switzerland*
e-mail: *casper.pranger@erdw.ethz.ch*
session: *(Seismo-) Tectonics*

Introduction

The tightly curved Banda Arc (eastern Indonesia) plays a pivotal role in the convergent interaction of the Eurasian, Australian, and Pacific plates. Historically there have been two opposing hypotheses regarding its origin: either the arc has been formed by two opposite-dipping subduction zones joining at the apex, or a single slab has been wrought in its current position by surface kinematics and mantle processes. Using detailed tectonic reconstructions and mantle tomography, the latter view has recently gained substantial support by the work of Spakman and Hall (2010). Through numerical modelling of the instantaneous dynamics of the intricate subducting system, the research presented here aims to determine the factors that control the evolution of the single slab, but also to provide insight into the complexities of instantaneous numerical modelling of subduction in general. To aid the construction of very complex model geometries, we have developed a tool that allows us to digitally draw faults, slab sections, and plate outlines based on tomography, surface topography, and Wadati-Benioff zone geometry. The tool communicates with the finite element mesh generator, which then gives a composite mesh with highly desirable properties. Our results give a basic one-slab-model that satisfies both the predictions of the Spakman and Hall model and the stress state from CMT solutions and seismic fast directions. Better agreement can be attained by varying the buoyancy structure,

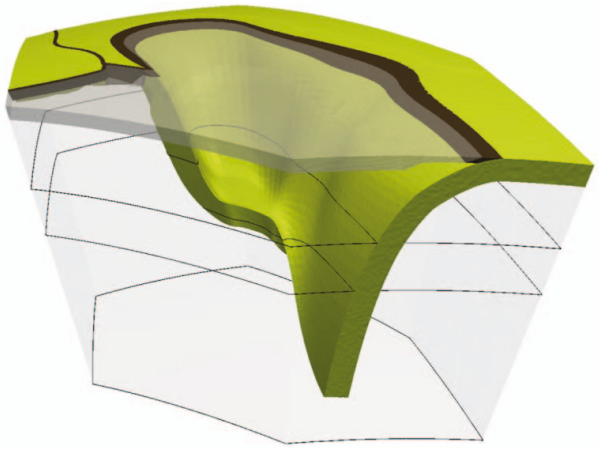

to which the behavior of the model is found to be rather sensitive. Additionally, we propose that a mantle flow component is required in order to maintain the northern slab limb in the case that it has detached from the surface lithosphere. In the absence of flow-induced resistance, our results suggests that further convergent motion can effect a transition towards large-scale slab detachment progressing southward if there is little buoyant support at the d660 phase transition.

References

Spakman, W., and R. Hall (2010), Surface deformation and slab–mantle interaction during banda arc subduction rollback, Nature Geoscience, 3 (8), 562–566.

Towards 3D seismo-thermo-mechanical models of the subduction thrust

Casper Pranger[1], Ylona van Dinther[1], Taras Gerya[1], Fabio Corbi[2,3], Francesca Funiciello[3]

[1] *Institute of Geophysics, ETH Zürich, Soneggstrasse 5, CH-8092 Zürich, Switzerland*
[2] *Earthquake and Volcano Physics, GFZ Potsdam, Telegrafenberg, 14473 Potsdam, Germany*
[3] *LET - Laboratory of Experimental Tectonics, Univ. "Roma Tre", L.S.L. Murialdo 1, 00146 Rome, Italy*
e-mail: *casper.pranger@erdw.ethz.ch*
session: *(Seismo-) Tectonics*

The recent development of numerical seismo-thermo-mechanical (STM) models bridges the gap between geodynamic and seismic timescales and thereby links long-term deformation and subduction dynamics to short-term seismogenesis (e. g., van Dinther et al., 2013, 2014). Complementing dynamic rupture models of a priori defined fault planes, this approach allows for spontaneous emergence of rupture paths, both on and off the megathrust, through slow tectonic loading, rate-dependent friction, and visco-elastic relaxation.

In twin papers (Corbi et al., 2013; Van Dinther et al., 2013), the STM technique has been robustly validated with laboratory models of a deforming visco-elastic gelatine wedge (Figure 1 a). In these laboratory models, the gelatine wedge is fixed at the backstop while being dragged in the down-dip direction at the base. A seismogenic zone is formed on this base by locally introducing a gelatine-sandpaper interface with strainrate-weakening characteristics, which is superseded in the up-dip and down-dip limits by a gelatine-plastic strainrate-strengthening interface. In a 2D center-line vertical section of the gelatine wedge, particles are observed moving away from the trench during co-seismic time intervals (cf. Figure 2 a), while during the seismic event they surge towards the trench (cf. Figure 2 b).

While the center-line sampling of the semi-2D laboratory setup (constant along-strike) should

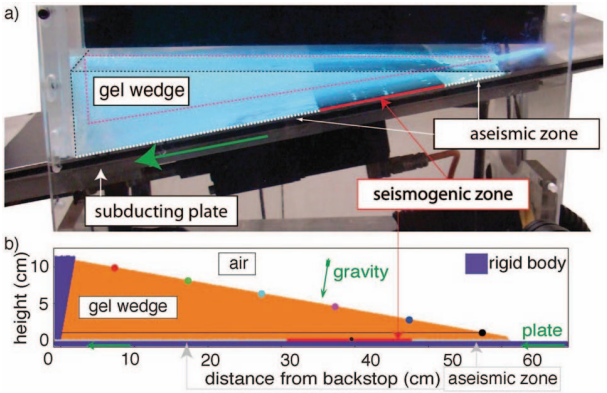

Fig. 1.: a) Laboratory setup. A visco-elastic gel wedge is dragged in the down-dip direction by a subducting plate, but is prevented from transportation by the backstop (left). b) Numerical replica of the laboratory setup, slightly rotated to allow for easier implementation. Note that the body force component is rotated accordingly.

inhibit the detrimental effects of the strike-normal boundaries, it is now clear from top-view surface particle motion measurements that 3D phenomena are substantial (Corbi and Funiciello, pers. comm.): many seismic events nucleate close to the lateral side-walls and pass through the center-line section only transiently, which may lead to an underestimation of slip area, slip magnitude, and seismic moment magnitude.

While the center-line sampling of the semi-2D laboratory setup (constant along-strike) should inhibit the detrimental effects of the strike-normal

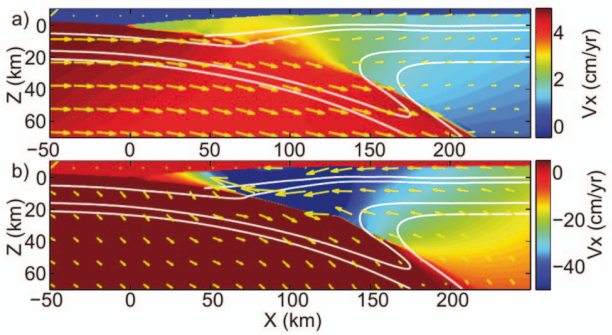

Fig. 2.: a) Locking, and b) seismic release in a numerical STM model of self-consistent subduction (van Dinther et al., 2014).

boundaries, it is now clear from top-view surface particle motion measurements that 3D phenomena are substantial (Corbi and Funiciello, pers. comm.): many seismic events nucleate close to the lateral side-walls and pass through the centerline section only transiently, which may lead to an underestimation of slip area, slip magnitude, and seismic moment magnitude.

By incorporating the existing STM functionality and elasticity into the 3-dimensional finite difference code I3ELVIS (Zhu et al., 2009), we will be able to perform a more exhaustive validation test against results obtained in the laboratory. In the future, a new generation of 3D STM models will allow us to investigate the full spatio-temporal source parameter distribution of on- and off-megathrust events in (real-Earth) subduction zones.

References

Corbi, F., F. Funiciello, M. Moroni, Y. van Dinther, P. M. Mai, L. A. Dalguer, and C. Faccenna (2013), The seismic cycle at subduction thrusts: 1. Insights from laboratory models, J. Geophys. Res. Solid Earth, 118, 1483-1501, doi:10.1029/2012JB009481.

van Dinther, Y., T. V. Gerya, L. A. Dalguer, F. Corbi, F. Funiciello, and P. M. Mai (2013), The seismic cycle at subduction thrusts: 2. Dynamic implications of geodynamic simulations validated with laboratory models, J. Geophys. Res. Solid Earth, 118, 1502-1525, doi:10.1029/2012JB009479

van Dinther, Y., T. V. Gerya, L. A. Dalguer, P. M. Mai, G. Morra, and D. Giardini (2014), The seismic cycle at subduction thrusts: insights from seismo-thermo-mechanical models, J. Geophys. Res.: Solid Earth, doi:10.1029/2013JB010380.

Zhu, G., T. V. Gerya, D. A. Yuen, S. Honda, T. Yoshida, and J. A. Connolly (2009). Three-dimensional dynamics of hydrous thermal-chemical plumes in oceanic subduction zones. Geochemistry, Geophysics, Geosystems, 10(11).

Smart or Beautiful? Accretionary wedge evolution seen as a competition between minimum work and critical taper

Tasca Santimano[1], Matthias Rosenau[1], Onno Oncken[1]

[1] *Deutsches GeoForschungsZentrum GFZ Potsdam, Germany*
e-mail: *tsanti@gfz-potsdam.de*
session: *(Seismo-) Tectonics*

Introduction

Accretionary wedge evolution has been described by two theories: The Critical taper theory (CTT, Davis et. al., 1983) and the minimum work concept (MWC, Masek & Duncan, 1998). CTT is based on force balance and predicts the ideal ("beautiful") shape (critical taper, CT) of an accretionary wedge system and its tectonic regime (extensive, compressive, stable). However, it does not specify which structures are formed and reactivated to reach the preferred geometry during accretionary wedge growth. The latter can be predicted by MWC which states that deformation is accommodated in a energetically "smart" way by faults that allow to minimize total (frictional plus gravitational) work. In this study we test the applicability and interplay of both concepts to accretionary wedge growth by analysing the evolution of a homogeneous sand wedge. We describe geometry changes and the work done through accretion cycles and hypothesize that there is a competition between minimizing work and reaching the critical taper that controls the evolution of accretionary wedges.

Experimental setup and analysis methods

The experimental setup consists of a sandbox that creates a typical plane strain compressional sand (friction coefficient ~ 0.7) wedge with a low friction basal detachment (glass beads, friction coefficient ~ 0.45) by pulling the sand layer against a rigid backwall. The evolution of the wedge is recorded from the side using CCD (charge coupled device) cameras whose sequential images are analysed by means of the Particle Image Velocimetry (PIV). This allows for a time-series collection of the incremental geometries and internal displacement fields (velocity) of the entire wedge. The topographic peak (crest) and the tip of the wedge were assigned active wedge height and length (H, L), are used for calculating the wedge slope ($\arctan(\frac{H}{L})$). The vertical component (D_y) of the resulting vector field (i. e. uplift against gravity g) and the horizontal component (D_x, basal displacement against basal friction μ) are used to calculate the gravitational (W_g) and frictional (W_f) work done by the wedge with weight W, respectively ($W_g = WD_y$ and $W_f = WD_x\mu$). Observed geometrical evolution and work history has finally been compared to analytical solutions of a self-similarly growing and critically tapered wedge.

Observations and analytical results

Accretion cyclicity

The wedge evolves in a typical cyclic manner of accretion resulting in saw-tooth like growth curves in height, length and slope (Fig. 1 A, 1 B). An accretionary cycle involves the localization of strain to form a new set of conjugated thrust and back thrust. While the backthrust is quickly abandoned, displacement along the forethrust continues until the end of the accretionary cycle

when a new fault is formed. The wedge allows for both frontal accretion and sporadic deep underthrusting and basal accretion due to smearing of the ramp and shallow detachment by entrained glass beads. Long underthrust episodes are always followed by a short frontal accretion cycles resulting in a bimodal periodicity of accretion.

Geometric evolution

After a short initiation phase the wedge develops towards a stable wedge taper ($\sim 10°$) with systematic fluctuations associated with accretionary cycles (Fig. 1 A). Wedge length and height grow according to a power law again with fluctuations associated with accretionary cycles (Fig. 1 B). Longterm trends fit well to the analytical predictions of self-similar wedge growth. Importantly geometrical predictions are met at the onset of an accretionary cycle. During accretion, wedge geometry evolves away from the predictions by shortening and uplift towards higher slopes, i. e. into the stable (or locally even extensional) CT regime.

Work done

Work analysis shows (Fig. 1 C) that gravitational work is significantly lower than frictional work. This is because vertical displacement is generally less than horizontal displacement of the wedge. On a long time scale, frictional work increases as the wedge grows and the basal detachment area increases, however gravitational work reaches an upper bound because uplift ceases naturally as the wedge grows. Total work increases consistently as the wedge grows. Longterm trends fit at first order scale to the analytical predictions of a self-similar wedge growth. Looking at shorter timescales, total work is minimized and closest to the theoretical predictions at the end of the accretion cycle. At the onset of a new accretion cycle, gravitational work is minimized but increases subsequently as the active thrust ramp penetrates deeper into the wedge (i. e. uplifts successively larger volumes). Frictional work, in contrast, is maximized at the onset of a new accretion cycle and subsequently minimized because the length of the shallow flat increases at the cost of the deep flat of the thrust as the active thrust ramp penetrates into the wedge.

Discussion, Conclusions & Implications

The analysis above shows that sand wedges might be both smart and beautiful but not at the same time: The preferred CT geometry is met only at the beginning of a new accretion cycle while work is minimized at the end of an accretionary cycle. Compared to a self-similarly growing wedge which can be viewed as an ideal, always smart and always beautiful wedge growing by infinitesimal basal accretion of diffuse deformation, real accretionary wedges obviously switch between states consistent with CTT and MWC. Underthrusting appears to be the energetically preferred path of accreting material but leads to shortening and uplift of the wedge. Shortening and uplift steepens the wedge and therefore causes its departure from the critical state. The latter can only be re-established by forming a new, energetically unfavorable frontal thrust ahead of the wedge tip lowering the taper.

Fig. 1 D is a synoptic plot of the geometric and energetic performance of the wedge. The ideal (smart and beautiful) state is at the origin of this plot where predicted and observed slope and work are the same. Obviously, accretionary cycles cannot reach the ideal state easily but rather circles between energetically vs. geometrically optimized states at progressively decreasing distance from the origin. When comparing observed values to the predicted values of work and slope done by the wedge respectively, the deviation of the observed values from the predicted value becomes minimized immediately before and after thrust formation, respectively. It follows that accretionary wedges are described in rare instances (around the formation of a new thrust) by either CTT or MWC. Instead, most wedge stages reflect the competition of reaching criticality and minimum work, i. e. are a mixture between a geo-

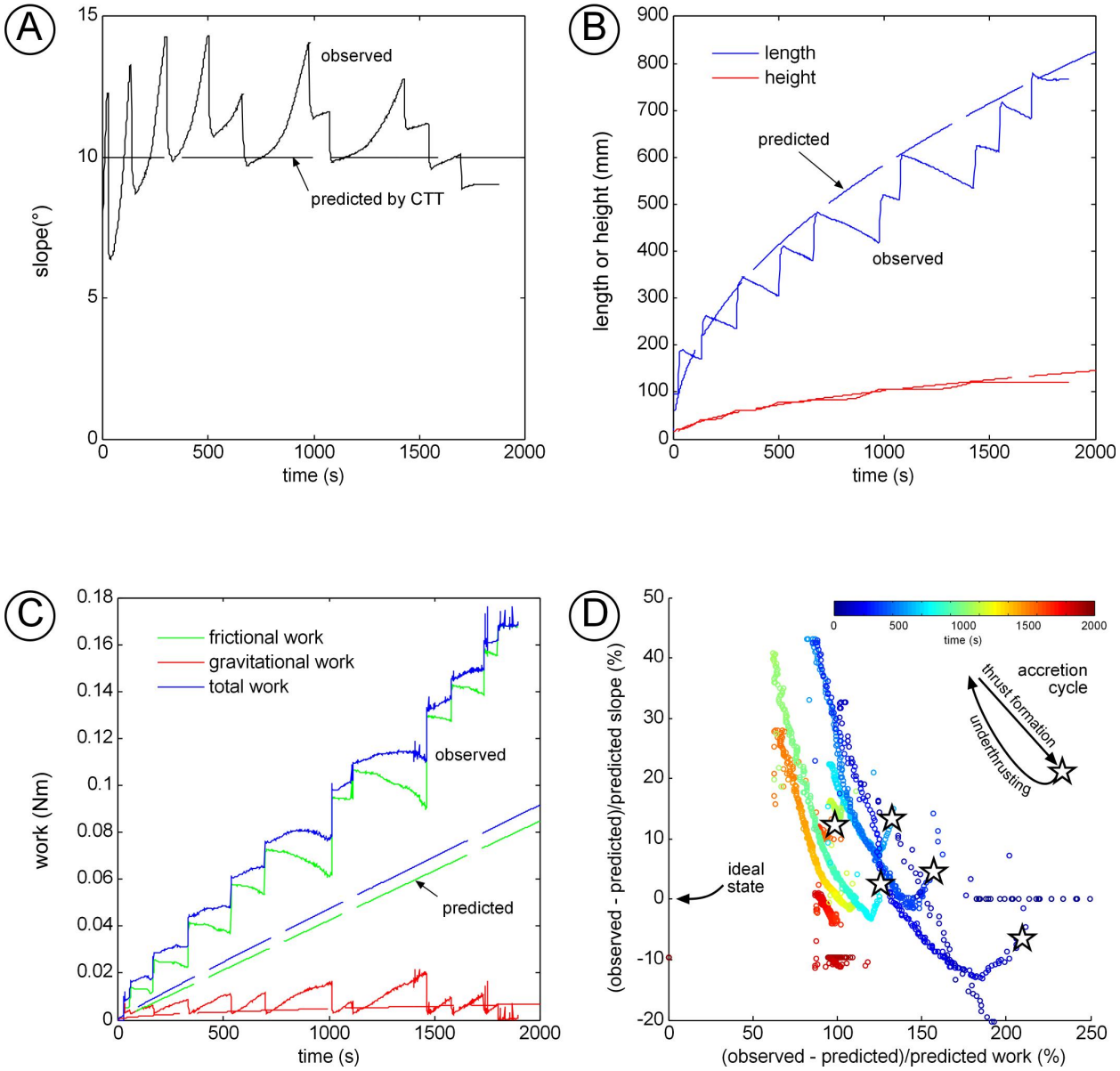

Fig. 1.: Geometrical wedge evolution and work done: (A) slope vs. time, (B) height and length vs. time, (C) work vs. time. Analytical solutions from self-similar wedge growth indicated by stippled trends, (D) Synoptic plot of wedge performance: Normalized deviation of observed slope values from the predicted slope values (%) vs. normalized deviation of observed work values from the predicted work values (%).

metrically versus an energetically preferred state. The analysis implies that inferences on wedge mechanics from natural observations based on CTT and MWC should be drawn only during the formation of a new frontal thrust. Only very mature wedges composed of several tens of accreation cycles might be able to reach a state where both geometry and work are optimized through the accretionary cycle (i. e. the origin in Fig. 1 D).

References

Davis, D., Suppe, J., Dahlen, F.A., 1983: Mechanics of Fold-and-Thrust Belts and Accretionary Wedges. Journal of Geophysical Research 88, 1153-1172.

Masek, J.G., Duncan, C.C., 1998: Minimum-work mountain building. Journal of Geophysical Research, 103,907-917.

CHANDRAYAAN-1 data infers tectonic activity on the south pole of the moon

Priyadarshini Singh, Saumitra Mukherjee

School of Environmental Sciences, Jawaharlal Nehru University, New Delhi – India
e-mail: *ps.sesjnu@gmail.com*
session: *(Seismo-) Tectonics*

Introduction

Morphological characteristics of the moon were studied using data strips from the miniature synthetic aperture radar (Mini-SAR) payload onboard CHANDRAYAAN-1 mission. Fault lines and rocky avalanches developed post dislocation along such fault zones within the South Polar Region have been identified in this study. Also, the identified features show morphological similarity to the features seen on terrestrial surfaces. Mini-SAR imaging radar onboard CHANDRAYAAN-1 mission was the first mono-static lunar orbiting synthetic aperture radar (SAR). It conveniently reveals various crater features in completely or partially shadowed regions of the lunar poles on the surface as well as the lunar regolith [Mohan et al., 2011; Spudis et al., 2009]. Previous studies investigating lunar tectonic activity have used optical data primarily to study lunar tectonics. However, active remote sensing using microwave data has helped in studying the lunar topography in order to demarcate unique features otherwise not visible from simple optical data due to the ability of microwaves to reveal images of shadowed regions as well as penetrating the surface regolith [Mohan et al., 2011]. Optical images from Wide Angle Camera onboard the Lunar Reconnaissance Orbiter Camera (LROC) have also been used alongside the SAR data to pinpoint regions falling within shadowed parts of the lunar south pole. It is being reported that the lunar surface morphology is largely governed by these tectonic perturbations. Further it has been found out that cosmic rays and solar wind flux variability coupled with the interior tectonic activity and meteorite impact has given the tectonic activity of the moon. This finding is supported by the manifestation of tectonic activities on the moon in the form of faults and related dislocations. Present work confirms that partially and completely shadowed crater interiors present in the Polar Regions contain unique features indicative of tectonic activity. The study therefore focuses on the identification of these features indicating the presence of faults/lineaments/fractures on the lunar topography.

Study area and methodology

The study area falls within the south polar region of the moon lying within Cabeus B crater. Cabeus B is an impact crater centered at 82°18′ S and 54°12′ W with a diameter of ~61 km. Stokes parameters (S_0, S_1, S_2 and S_3) and degree of polarization (m) were derived for each pixel using ENVI software to generate $m - \chi$ decomposition images (Raney et al., 2007). Stokes Parameters (S_0, S_1, S_2 and S_3), degree of polarization (m) and $m - \chi$ scattering contributions were calculated for each pixel on ENVI software using the following band math equations. Each pixel in an image strip consisted of 16 bytes data in four channels of 4 bytes each as $|\mathrm{LH}|_2$, $|\mathrm{LV}|_2$, Real $(\mathrm{LH} \cdot \mathrm{LV}^*)$ and Imaginary $(\mathrm{LH} \cdot \mathrm{LV}^*)$ [Mohan et

al., 2011].

$$S = \begin{bmatrix} S_0 &= \langle |E_{\mathrm{LH}}|^2 + |E_{\mathrm{LV}}|^2 \rangle \\ S_1 &= \langle |E_{\mathrm{LH}}|^2 - |E_{\mathrm{LV}}|^2 \rangle \\ S_2 &= 2\Re e \langle E_{\mathrm{LH}} E_{\mathrm{LV}}^* \rangle \\ S_3 &= -2\Im m \langle E_{\mathrm{LH}} E_{\mathrm{LV}}^* \rangle \end{bmatrix} \quad (1)$$

where E_{LH} and E_{LV} are the electric fields for the horizontal and vertical linear polarizations received respectively, and the averages are time or spatial averages and * represents the conjugate of the complex number.

Reference [3] equations were used to calculate the degree of polarization (m). Reference [4] and [5] were used to calculate the degree of circularity (χ) and $m - \chi$ scattering contributions for each pixel on ENVI software. The equations used are as follows:

$$m = \frac{\sqrt{S_1^2 + S_2^2 + S_3^2}}{S_0} \quad (2)$$

$$B = \sqrt{\frac{S_0 m \left(1 - \sin\left(2\chi\right)\right)}{2}} \quad (3)$$

$$G = \sqrt{S_0 \left(1 - m\right)} \quad (4)$$

$$R = \sqrt{\frac{S_0 m \left(1 + \sin\left(2\chi\right)\right)}{2}} \quad (5)$$

Here blue (B) indicates single-bounce (Bragg) backscattering, green (G) represents the randomly polarized constituent or volume scattering and red (R) corresponds to double-bounce scattering.

Results and Discussion

Cabeus B is a relatively large impact crater having several small impact craters on its floor. After applying $m - \chi$ decomposition technique to the mini-SAR data, a distinct fault line was observed traversing the floor of the northern wall of the crater and reaching till the southern end before it disappears beneath a debris avalanche lying on the southeastern wall. Both the debris avalanche and the fault line are not visible on optical wide angle camera image. Alternately, these features can be distinctly seen on the $m - \chi$ decomposition image. The neighboring areas lying beyond the rim of Cabeus B also have extensions of the inferred fault lines traversing regions lying within and extending up to neighboring craters around Cabeus B.

The debris avalanche lying at the visible southern end of the identified fault line can be seen on the optical image as a faint structure. On $m - \chi$ decomposition image, however, this feature can be seen distinctly covered with green pixels due to volume scattering. It extends from the tip of the south eastern inner wall of the crater and end at the floor of the crater. The fault line disappears beneath this debris avalanche. There is a possibility that the formation of the debris avalanche has taken place due to dislocation and seismic shaking along the identified fault line.

References

[1] S. Mohan, A. Das and M. Chakraborty, "Studies of polarimetric properties of lunar surface using Mini-SAR data," Current Science, vol. 101, no. 2, pp. 159-164, 2011.

[2] P. Spudis, S. Nozette, B. Bussey, K. Raney, H. Winters, C.L. Lichtenberg, W. Marinelli, J.C. Crusan and M.M. Gates, "MiniSAR: an imaging radar experiment for Chandrayaan-1 mission to the Moon", Current Science, vol. 96, no. 4, pp. 533-539, February 2009.

[3] R.K. Raney, "Hybrid-polarity SAR architecture", IEEE Trans. Geosci and. Remote Sensing, vol. 45, no. 11, pp. 3397-3404, November 2007.

[4] R.K. Raney, J.T.S. Cahill, G.W. Patterson, and D.B.J. Bussey, "The m-chi decomposition of hybrid dual-polarimetric radar data", IEEE International IGARSS, pp. 5093-5096, 2012.

[5] R. K. Raney, J.T.S. Cahill, G. W. Patterson, D. Benjamin, J. Bussey and the Mini-RF Team, "Characterization of lunar craters using m–χ decompositions of mini-RF radar data", LPSC, Abstract no. 2380, 2012.

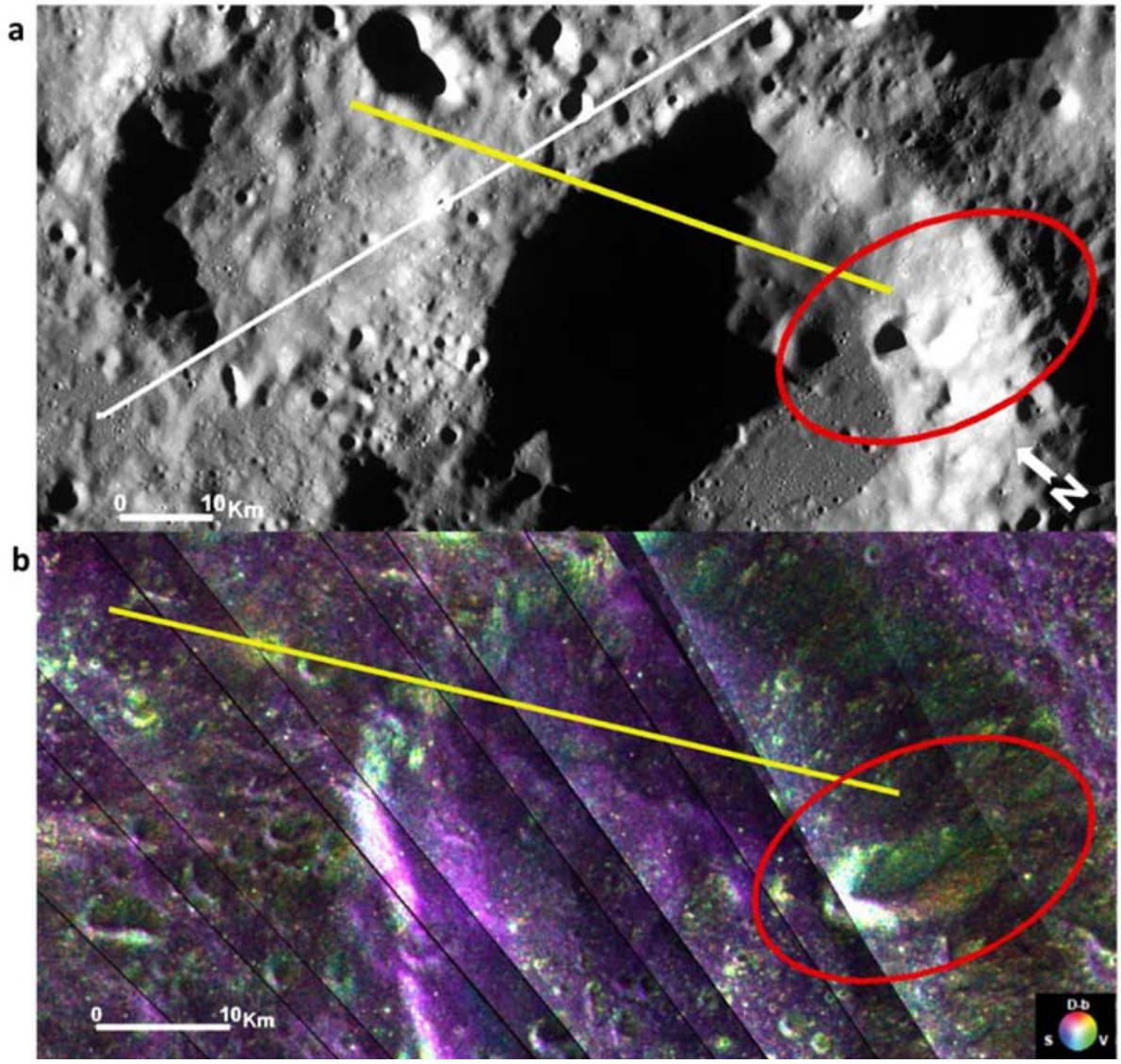

Fig. 1.: Fault lines and debris avalanche within Cabeus B (centered at $82°18'$ S and $54°12'$ W). **a.)** Wide Angle Camera image of Cabeus B crater and surrounding region with the inferred fault lines and the debris avalanche marked with red ellipse. **b.)** $m - \chi$ decomposition image of the region in a.); fault line invisible in optical image can be seen lying below the length of the yellow line; the debris avalanche marked with red ellipse visible clearly with green pixels from volume scattering showing the rough surface due to the debris.

The concepts of complex network advance understanding of earthquake science

Norikazu Suzuki

College of Science and Technology, Nihon University, Chiba, 274-8501, Japan
e-mail: *suzu@phys.ge.cst.nihon-u.ac.jp*
session: *(Seismo-) Tectonics*

Seismicity is governed by yet unknown dynamics of the earth crust as a complex system. Although seismology has a long tradition, only a few universal laws have been discovered. The celebrated examples are the Omori law (Omori 1894) for the temporal pattern of aftershocks and the Gutenberg-Richter law (Gutenberg and Richter 1949) for the scaling relation between frequency and magnitude. Although there are some discussions about the theoretical bases of these laws, it seems fair to say that essentially they still remain empirical. The situation shows how understanding physics of earthquakes is far from maturity. And, there may be much to be explored even at the empirical level. This in turn suggests a possibility that approach from the viewpoint of science of complexity may shed new light on seismicity.

In the recent investigations (Abe and Suzuki 2003, 2005a), we have analyzed the spatiotemporal properties of seismicity from the viewpoint of nonextensive statistical mechanics. Nonextensive statistical mechanics is constructed based on the Tsallis entropy (Tsallis 1988) and generalizes Boltzmann-Gibbs statistical mechanics in order to treat complex systems. We have found that both the spatial distance and time interval between two successive earthquakes are well described by the q-exponential distributions, which are characteristics of nonextensive statistical mechanics and maximize the Tsallis entropy under appropriate constraints. The fact that two successive earthquakes obey such definite statistical laws implies that successive events are indivisibly correlated, no matter how large their spatial distance is. In fact, there is a report (Steeples and Steeples 1996), which shows that an earthquake can be induced by a foregoing earthquake more than 1000 km away. Furthermore, it is known that, after the big earthquake M=9.0 in Japan three years ago, the seismic wave traveled the whole surface of the earth at least 5 times. This seismic wave actually triggered many subsequent earthquakes in Japan, China, Canada, Mexico and U.S.A. (Peng et al. 2013). This means that the seismic correlation length may be enormously large, indicating a strong similarity to phase transition phenomena and making it inappropriate to put spatial windows in analysis of seismicity, in general. Thus, we are naturally led to a conclusion that the earth crust always stays in a critical state.

Now, in contemporary science, the concept of complex networks is receiving much attention. The research in this direction was initiated by the works of Watts and Strogatz (1998) on small-world networks and of Barabási and Albert, (1999) on scale-free networks. A main purpose of this research area is to understand the topological and dynamical properties appearing in the network structure behind various complex systems, such as collaboration of actors, citation pattern of scientific papers, metabolic networks, social networks, WorldWideWeb, electrical power grids, and so on. Common features among these are that they are scale-free networks with power-law connectivity distributions and are small-world ones characterized by large values of the cluster-

ing coefficient as well as small values of the characteristic path length. In particular, the model proposed by Barabási and Albert (1999), which assumes network growth combined with the so-called preferential attachment rule, is known to generate scale-free networks.

As mentioned above, two successive events obey the definite statistical laws. It indicates that successive events are indivisibly correlated each other. This motivates us to describe seismicity by making use of a network, in which vertices and edges represent events and their correlations, respectively. In this way, novel aspects of seismicity as a complex phenomenon are expected to be revealed.

In this talk, we discuss a novel method of describing complexity of seismicity, which has recently been introduced in the literature (Abe and Suzuki 2004 a, 2006 a). The seismic data are mapped to growing random networks. Vertices and edges of such networks correspond to coarse-grained events and event-event correlations, respectively. Yet unknown microscopic dynamics governing event-event correlations and fault-fault interactions is replaced by these edges. Global physical properties of seismicity can then be explored by examining its geometric (e. g., topological etc.), statistical and dynamical properties.

Firstly, we show that the earthquake network is scale free (Abe and Suzuki 2004 a, 2006 a), being characterized by the power-law connectivity distribution (Figure 1) . We give a physical interpretation to this result based on network growth with the preferential attachment rule (Barabási and Albert 1999) together with the Gutenberg-Richter law (Gutenberg and Richter 1949).

Secondly, we study the small-world structure of the earthquake network reduced to an undirected simple network (Abe and Suzuki 2004 b, 2006 a). The value of the clustering coefficient is found to be much larger than that of the classical random network. In addition, the average path length is very small.

Thirdly, we show that the earthquake network possesses hierarchical organization (Abe and Suzuki 2006 b). We interpret this fact in terms of vertex fittness and vertex deactivation by the process of stress release at faults.

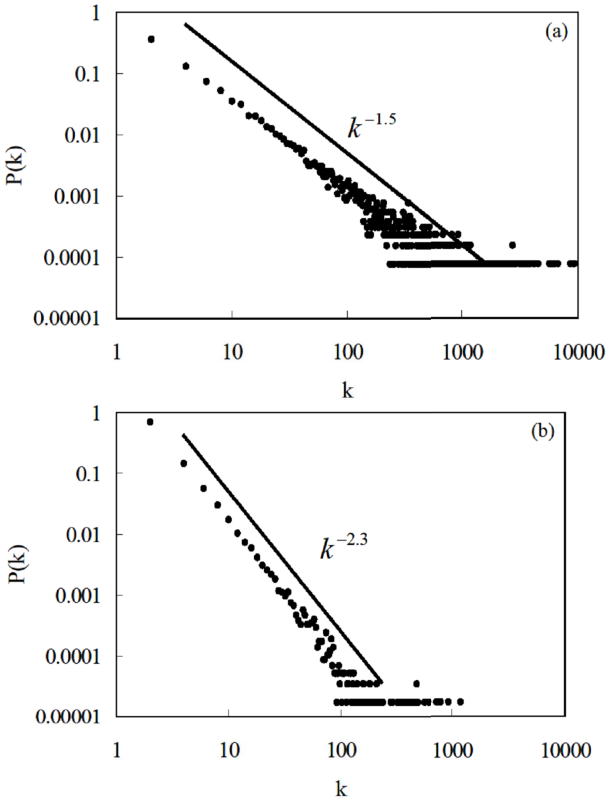

Fig. 1.: The log-log plots of the connectivity distributions of the earthquake networks P(k) in (a) California and (b) Japan.

Fourthly, we find that the earthquake network has the property of assortative mixing (Abe and Suzuki 2006 b). This point is an essential difference of the earthquake network from the Internet that has disassortative mixing.

Finally, we report the discovery of a scale-invariant law of the period distribution in the directed earthquake network (Abe and Suzuki 2005 b), which indicates that after how many earthquakes an earthquake returns to the initial location. This result manifests a fundamental difficulty in statistically estimating the value of period.

Combined with other dynamical properties (Suzuki 2012, Abe and Suzuki 2007, 2009 a, 2009 b, 2009 c, 2012 a, 2012 b), the present results imply that yet unknown mechanism governing seismicity may be so-called glassy dynamics (Abe and Suzuki 2004 c, 2012 c) on a growing complex

network. These observations have obvious importance for constructing and improving physical models of seismicity such as the ones exhibiting self-organized criticality.

References

Abe, S., Suzuki, N. (2003).: Law for the distance between successive earthquakes. J. Geophys. Res. 108, B2, 2113-2117.

Abe, S., Suzuki, N. (2004a): Scale-free network of earthquake. Europhys. Lett., 65, 581-586.

Abe, S., Suzuki, N. (2004b): Small-world structure of earthquake network. Physica A 337, 357-362.

Abe, S., Suzuki, N. (2004c): Aging and scaling of earthquake aftershocks. Physica A 332, 533-538.

Abe, S., Suzuki, N. (2005a): Scale-free statistics of time interval between successive earthquakes. Physica A 350, 588-596.

Abe, S., Suzuki, N. (2005b): Scale-invariant statistics of period in directed earthquake network. Eur. Phys. J. B, 44, 115-117.

Abe, S., Suzuki, N. (2006a): Complex-network description of seismicity. Nonlin. Processes Geophys., 13, 145-150.

Abe, S., Suzuki, N. (2006b): Complex earthquake networks: Hierarchical organization and assortative mixing. Phys. Rev. E, 74, 026113 p1-p5.

Abe, S., Suzuki, N. (2007): Dynamical evolution of clustering in complex network of earthquake. Eur. Phys. J. B, 59, 93-97.

Abe, S., Suzuki, N. (2009a): Earthquake networks, complex. in Encyclopedia of Complexity and Systems Science, Springer, New York, 2530-2538.

Abe, S., Suzuki, N. (2009b): Determination of the scale of coarse graining in earthquake networks. EPL, 87, 48008 p1-p5.

Abe, S., Suzuki, N. (2009c): Violation of the scaling relation and non-markovian nature of earthquake aftershocks. Physica A, 388, 1917-1920.

Abe, S., Suzuki, N. (2012a): Universal law for waiting internal time in seismicity and its implication to earthquake network. EPL, 97, 49002 p1-p5.

Abe, S., Suzuki, N. (2012b): Dynamical evolution of the community structure of complex earthquake network. EPL, 99, 39001-p1-p4.

Abe, S., Suzuki, N. (2012c): Aftershocks in modern perspectives: Complex earthquake network, aging, and non-Markovianity, Acta Geophysica, 60, 547-561.

Barabási, A-L., Albert, R. (1999): Emergence of scaling in random networks, Science. 286, 509-512.

Gutenberg, B., Richter, C.F. (1949): Seismicity of the earth and associated phenomena. Princeton University Press, Princeton.

Omori, F. (1894), On the aftershocks of earthquakes, J. Coll. Sci. Imp. Univ. Tokyo, 7, 111– 216.

Peng, F., Gonzalez-Huizar, H., Chao, K., Aiken, C., Moreno, B., Armstrong, G. (2013): Tectonic Tremor beneath Cuba Triggered by the Mw 8.8 Maule and Mw 9.0 Tohoku-Oki Earthquakes, Bull. Seismol. Soc.Am. 103 595-600.

Steeples, D.W., and Steeples, D.D. (1996): Far-field aftershocks of the 1906 earthquake, Bull. Seismol. Soc. Am. 86, 4, 921-924.

Suzuki, N. (2012): Complex network of earthquakes: Universal law for waiting internal time in seismicity. in Proceedings of 8th International Conference on Signal Image Technology and Internet Based systems (IEEE Computer Society), 707-709.

Tsallis, C. (1988), Possible generalization of Boltzmann-Gibbs statistics, J. Stat. Phys., 52, 479– 487.

Watts, D. J., Strogatz, S. H. (1998): Collective dynamics of 'small-world' networks. Nature, 393, 440-442.

Hypothesis of geodynamic processes in the lithosphere under catastrophic earthquake Tohoku-Oki

V. N. Tatarinov, A. I. Kagan, T. A. Tatarinova

Geophysical Center of Russian Academy of Sciences, 117296, Moscow, Molodezhnaya 3
e-mail: *victat@wdcb.ru*
session: *(Seismo-) Tectonics*

Earthquake Tohoku-Oki, 11.03.2011 happened near the island of Honshu, has attracted attention not only for its energy capacity and catastrophic consequences of tsunami and the destruction of three nuclear reactors, "Fukushima-1", but also a unique experimental data on the co-seismic and post-seismic vertical and horizontal displacements of the Earth's crust in the area of the Japanese archipelago, which were received on geodynamic network GEONET (GNSS Earth Observation Network System).

The new facts gave rise to the construction of various geodynamic models of the region [1-3]. Almost all of them are based on postulates plate-tectonics under which earthquakes occurring in this region is the result of military pressure on the Eurasian continental plate (EP), the subducting Pacific plate under it (PP).

In inherently discussion tectonic "fixists" and "mobilists" victory on the side of the second, because still supported by a majority of geodynamic models of seismicity of the region, based on the primacy of force action PP. However, there are a number of fundamental contradictions that do not explain or do not notice.

In this connection, based on the analysis and synthesis of evidence on the kinematics of the upper lithosphere during and after the earthquake Tohoku-Oki as the subject for discussion Alternative hypotheses about the sources of power such catastrophic earthquakes occurring in the area of Japanese islands.

GPS-observations confirmed facts displacement of the upper part of the lithosphere caused by earthquakes in the eastern direction during earthquakes with magnitude M $>$ 7.5 [4-6] , suggest that over the past 100-120 years, the Japanese archipelago has shifted in the direction of the oceanic plate at a distance 10 m to 14 m. If we take the maximum speed of horizontal movements PP westboundfor 100 – 120 years it should integrally displaced approximately 10 m. Thus, the horizontal displacement of the oceanic plate in a westerly direction and reverse "rollback" edge of the Eurasian plate to the east by earthquakes in the mentioned period are comparable with each other.

Analysis of the available experimental data on seismicity, structure and deformation of the lithosphere, and the results of modeling and reconstruction stress on parameters of the earthquake led to the following conclusions.

1. Seismicity:
    - Japan Earthquake type occur at depths of up to 700 km, while the deeper the earthquake, the more the area in which it is felt;
    - Post-seismic motion capture vast territory, so at Tohoku-Oki earthquake displacement were recorded on a third of the Amur plate, the transverse dimensions of up to 1000 km, indicating that the deep nature of the source;
    - Development of the earthquake stepwise character and a huge area (not linear fracture) total rupture plane – about 200 km to 400 km. The type of

motion in the outbreak of catastrophic earthquakes - thrust with thrust;

- Location of earthquake foci almost to the border of the asthenosphere (700 km) in the marginal part of the continental plate, allows you to "seditious" assumption about the prevalence in the area to the specified depth of the horizontal components of stress. And just below this limit, the rocks are in hydrostatic stress state. At the edge of the oceanic plate boundary transition in hydrostatic condition is probably much higher and is determined Moho discontinuity, about 10 km. This assumption of asymmetric stress state plots pairing the continental and oceanic plates form the basis of the hypothesis of the power source of catastrophic earthquakes in the area.

2. Features of the structure of the lithosphere
   - According to the seismic tomography across the Pacific border land registered relatively more resilient species (up to 5 %), the incident angle of 50° – 60°, the power of which is 5 – 7 times greater than the thickness of the oceanic crust. In the upper mantle of the North American plate in the core is firmer deeper part (depth interval - 200 km to 600 km), and the inactive part of the board - only the upper part to a depth of 400 km. In tectonically active zone of continental plates at a depth of an extensive area of intense (elastic) rocks. As suggesting she may be considered as a potential energy source that initiates the destruction of the environment on the outskirts of the lithosphere plates.

3. Postseismic horizontal and vertical movement
   - Nature of post-seismic motions according to the following GPS-observations. Vertical movement: the eastern part falls, rises west (maximum positive movement in the area of focus to 3 m). Horizontal movement: directed toward the hearth (maximum displacements up to 24 m);
   - There is an approximate equality of the absolute values of the displacement of the Pacific plate and the "reverse recoil" at the edge of the Eurasian plate earthquakes over the past 100 a to 200 a;
   - No significant positive vertical movements edge of the Eurasian plate in the face of pressure on her Pacific plate in between earthquakes.

4. Reconstruction of stress on the earthquake source
   - Oceanic trench is a boundary separating two domains of the geodynamic regime: horizontal compression (to the west of the trough) and stretching (east);
   - The orientation of the principal compressive stress varies from west to east from 45° to 0° and −90° for the deep-sea trench [7]. Thus for gutter earthquake situation corresponds horizontal extension.

A hypothesis on the origin of power sources geodynamic Japan earthquake type which, without explaining the reasons for internal model (as is usually done), repelled from the actual material (Fig.1).

1. Elastic energy accumulation occurs in the deep parts of the continental plates where the maximum stresses exist, as rocks retain their elastic properties. This depth can be evaluated by the maximum depth of earthquakes - 700-600 km. Indirectly, this confirms the earthquake that occurred May 24, 2013 in the Okhotsk Sea at a depth of 600 km of M = 7.7.

2. Causes of the excess energy can be different and require separate consideration. We can only say that there is an asymmetrical

distribution of the ratio of the horizontal and vertical components of the stress tensor when a layer at a depth of horizontal stresses is growing at a faster rate than vertical. This leads to the creation of efforts upwards at an angle of 45° – 55° depths of the continental plate, and not by the PP, as it has traditionally been considered.

3. This force effect leads to the formation of zones of increased stress or denser rocks (set according to seismic tomography). When exceeding some threshold voltages failure occurs at the boundary of the medium plates in the form of reverse faults and displacement of large blocks in the upper crust in the direction of least resistance. According reconstruction earthquake focal that the main axis of the compressive stress change their orientation [7] is approximately 90° in the oceanic region for the gutter plate.

4. On the eastern border of the continental plate uplift occurs with dextral shear component. In this part of the plate "leans" on the western part of the ocean, making it subhorizontal tensile stress. Such destruction occurs at intervals of about once every 40 a in the seismic gap. Continental plate like a crocodile "devours" the oceans, causing it to sink down the edge portion. This may explain a series of faults and grabens lying in a gutter part of the oceanic plate.

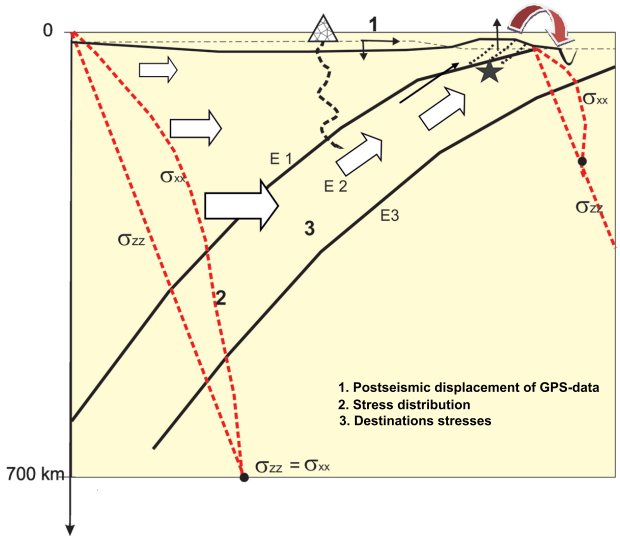

Fig. 1.: Geodynamic model of the development process in the earthquake Tohoku-Oki. 1 - Earth's surface before earthquake, 2 - after the earthquake. The dotted line shows the diagrams of the vertical and horizontal stresses in the continental plate and the oceanic. Elastic module E2 » E1> E3, where the indices 1 - rocks of the continental plate, 2 - zone of elastic rocks seismic tomography data, 3 - upper mantle rocks.

References

1. Shestakov N., Takahashi H., Ohzono M. and other. Analysis of the far-field crustal displacements caused by the 2011 Great Tohoku earthquake inferred from continuous GPS observations. Tectonophysics. 524–525 (2012) 76–86.

2. Mark Simons, Sarah E. Minson, A. Sladen and other. The 2011 Magnitude 9.0 Tohoku-Oki Earthquake: Mosaicking the Megathrust from Seconds to Centuries. Science. Vol.332. 2011.

3. Tong P., Zhao D. and Yang D. Tomography of the 2011 Iwaki earthquake (M 7.0) and Fukushima nuclear power plant area. Solid Earth, 3, 43–51, 2012.

4. http://earthquake.usgs.gov/earthquakes/eqarchives/year/m

5. The Geospatial Information Authority of Japan (GSI). http://www.gsi.go.jp.

6. Paul Segall. GPS applications for geodynamics and earthquake studies. Annu. Rev. Earth Planet. Sci. 1997. 25:301–36.

7. Rebetsky Y.L., Polec A.Y. Stress state of the lithosphere before the catastrophic earthquake in Japan Tohoku. 11.03.2011. Tectonic seminar. Report of December 17, 2013.http://omts.ifz.ru/17_12_2013.html.

Seismo-thermo-mechanical modeling of subduction zone seismicity

Ylona van Dinther[1], Taras Gerya[1], Luis A. Dalguer[2], P. Martin Mai[3]

[1]*Institute of Geophysics, ETH Zurich, Switzerland*
[2]*Swiss Seismological Service, ETH Zurich, Switzerland, now at SwissNuclear,* [3]*Division of Physical Sciences and Engineering, KAUST, Saudi Arabia*
e-mail: *ylona.vandinther@erdw.ethz.ch*
session: *(Seismo-) Tectonics*

Introduction

Recent megathrust earthquakes, e. g., the 2011 M 9.0 Tohoku and the 2004 M 9.2 Sumatra events, illustrated both their disastrous human and economic impact and our limited physical understanding of their spatial occurrence. To be able to better assess earthquake hazard, it is necessary to improve our physical understanding of what drives these events and what makes them more or less catastrophic. One increasingly important tool to improve our understanding is numerical modeling. However, there was no numerical subduction model that a) includes the three key ingredients of seismic cycle modeling in subduction zones -rate dependent friction, slow tectonic loading, and visco-elastic stress relaxation of medium and mantle- (Wang, 2007), b) allows for the spontaneous propagation of ruptures along naturally emerging paths, also outside the megathrust interface, nor c) links long-term subduction dynamics and relating deformation to the short-term seismogenesis. To improve long-term seismic hazard assessment by overcoming the restricted direct observations in time and space, we developed such a seismo-thermo-mechanical (STM) model. The validation and application of such a physically consistent seismo-thermo-mechanical approach is the objective of this study.

Methodology

This 2D continuum-mechanics based model uses an Eulerian-Lagrangian finite difference framework with similar on- and off-fault physics. We implicitly solve the conservation of mass, momentum, and energy for an incompressible medium with a visco-elasto-plastic rheology. Brittle failure is mimicked through Drucker-Prager plasticity. Rapid slip transients are generated through a local, invariant implementation of strongly rate-dependent friction. The validation of this approach is accomplished through a comparison with a laboratory seismic cycle model (Corbi et al., 2013; van Dinther et al., 2013a).

Results for a more realistic setup resembling Southern Chile

A more realistic geometry and physical setup of the Southern Chilean margin showed that results also agree with a range of seismological, geodetic, and geological observations, albeit at lower coseismic speeds (van Dinther et al., 2013b). The strength of a physically consistent approach is highlighted by the qualitative and, after coseismic slip correction, also quantitative agreement of interseismic and coseismic surface displacements with static GPS displacements (Figure 1). These GPS data were recorded before and during the 2010 M8.8 Maule earthquake and a spatial agreement was obtained without a single data

fitting iteration. These results, moreover, highlight the presence of a second-order flexural bulge within the overriding plate, at distances more than 200 km from the trench. A more detailed study of this phenomenon also revealed a similar bulge following the 1960 Valdivia, 1964 Alaska, and 2011 Tohoku earthquakes. The physical mechanisms governing such a bulge remain obscured, but ongoing study aims to identify these.

This study suggests several interesting implications. Slip deficit is observed to vary from one cycle to the next. On the long-term about 5 % of cyclic deformation is permanently stored within the wedge.

We also observe a self-consistent downdip transition zone arising between 350 °C and 450 °C due to the temperature-dependence of viscosity (and a quartzite flow law). Consequent interseismic locking in relation to a fore-arc Moho limits hypocenter locations to temperatures below 350 °C. Stress relaxation due to ductile shearing limits ruptures from propagating beyond 450 °C. These thermal limits correspond to estimates from thermal modeling and laboratory experiments.

Finally, our modeling results suggest that megathrust should be weak to sustain subduction along the megathrust. To generate events with a recurrence intervals and displacements typical for megathrust earthquakes, pore fluid pressures are suggested to be in the range of 75 % to 99 % of that of solid pressures.

Off-megathrust events

Finally, we exploit the main advantage of this innovative approach; the spontaneous unstable rupturing of off-megathrust events (van Dinther et al., 2014). Shallow off-megathrust subduction events are important in terms of hazard assessment and coseismic energy budget. Their role and spatiotemporal occurrence, however, remain poorly understood.

The characteristics of simulated normal events within the outerrise and splay and normal antithetic events within the wedge (Figure 2a-d) resemble seismic and seismological observations in terms of location, geometry, and timing. Their occurrence agrees reasonably well with both long-term analytical predictions based on dynamic Coulomb wedge theory and short-term quasi-static stress changes resulting from the typically triggering megathrust event. The impact of off-megathrust faulting on the megathrust cycle is distinct, as more both shallower and slower megathrust events arise due to occasional off-megathrust triggering and increased updip locking. This also enhances tsunami hazards, which are amplified due to the steeply dipping fault planes of especially outerrise events (Figure 2e – g).

Conclusions

Despite 3D and temporal limitations, these seismo-thermo-mechanical model results captured a wide range of natural observations and dynamic features. This demonstrates the potential of these physically-consistent models and opens a world of interdisciplinary research between geodynamics and seismology. This can relate to the generation and characteristics of megathrust earthquakes and beyond.

References

Corbi, F., Funiciello, F., Moroni, M., van Dinther, Y., Mai, P.M., Dalguer, L.A., and Faccenna, C. (2013). The seismic cycle at subduction thrusts: 1. insights from laboratory models, JGR, 118(4), 1483-1501, doi:10.1029/2012JB009481.

van Dinther, Y., Gerya, T., Dalguer, L., Corbi, F., Funiciello, F., and Mai, P. (2013). The seismic cycle at subduction thrusts: 2. Dynamic implications of geodynamic simulations validated with laboratory models, JGR. Solid Earth, 118(4), 1502–1525, doi:10.1029/2012JB009479.

van Dinther, Y., Gerya, T.V., Dalguer, L.A., Mai, P.M., Morra, G., and Giardini, D. (2013). The seismic cycle at subduction thrusts: insights

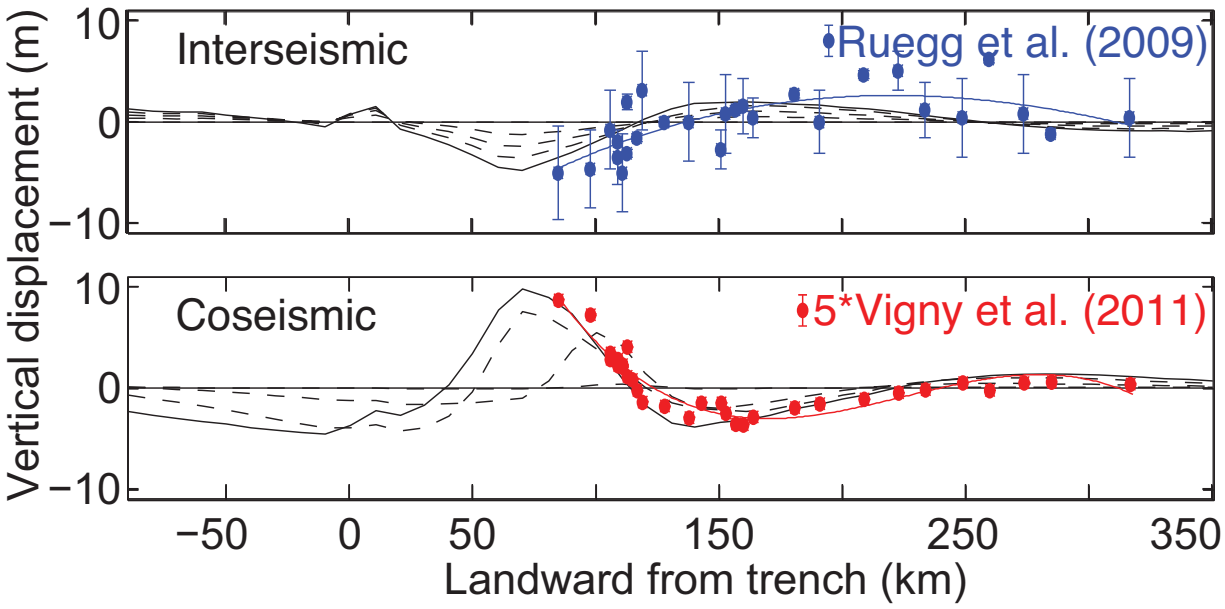

Fig. 1.: Vertical displacements agree spatially with interseismic and coseismic GPS data.

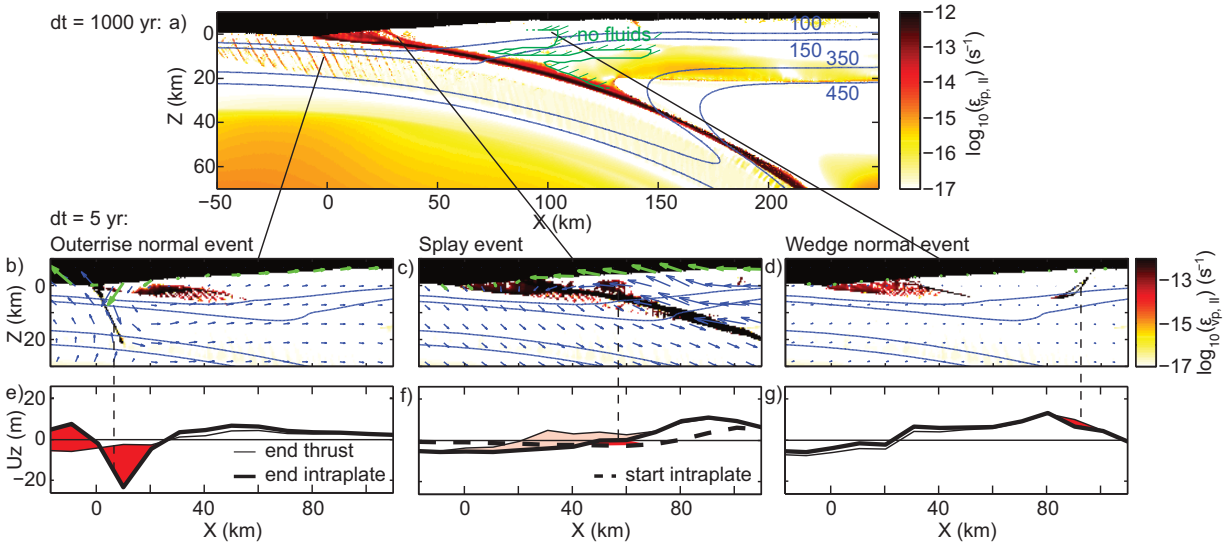

Fig. 2.: a) Long-term off-megathrust variability, b-d) spatiotemporal zooms of each off-megathrust event type, and e-g) accumulated vertical surface displacements w.r.t. the triggering megathrust event.

from seismo-thermo-mechanical models, JGR, 118, 6183-6202, doi:10.1002/2013JB010380.

van Dinther, Y., Mai, P.M., Dalguer, L.A., and Gerya, T.V. (2014). Modeling the seismic cycle in subduction zones: the role and spatiotemporal occurrence of off-megathrust events, GRL, 41 (4), 1194-1201, doi:10.1002/2013GL058886.

Ruegg, J. C., A. Rudlo, C. Vigny, R. Madariaga, J. B. De Chabalier, J. Campos, E. Kausel, S. Barrientos, and D. Dimitrov (2009), Interseismic strain accumulation measured by GPS in the seismic gap between Constitucion and Concepcion in Chile, PEPI, 175.

Vigny, C., et al. (2011), The 2010 Mw 8.8 Maule Megathrust Earthquake of Central Chile, Monitored by GPS, Science, 332 (6036), 1417-1421.

Wang, K. (2007), Elastic and Viscoelastic Models of Crustal Deformation in Subduction Earthquake Cycles, in The Seismogenic Zone of Subduction Thrust Faults, edited by T. Dixon and J. Moore, pp. 540-575, Columbia University Press, New York.

Thermal Expressions of Stick-slip and Creeping Subduction Megathrusts

Kelin Wang[1], Xiang Gao[2]

[1]*Pacific Geoscience Centre, Geological Survey of Canada, Natural Resources Canada, 9860 West Saanich Road, Sidney, British Columbia, V8L 4B2, Canada*
[2]*Key Laboratory of Marine Geology & Environment, Institute of Oceanology, Chinese Academy of Sciences, No. 7 Nanhai Road, Qingdao 266071, China*
e-mail: *kwang@nrcan.gc.ca*
session: *(Seismo-) Tectonics*

The strength of subduction faults and its variations in seismic slip are important to long-term geological deformation as well as earthquake cycles deformation. It is widely assumed that highly seismogenic megathrusts, that is, those that primarily exhibit stick-slip behavior and produce great earthquakes, are stronger than those that creep. Interseismically locked faults are thus described as being "strongly coupled". However, the opposite is also proposed on the basis of the recognition that very rugged subducting seafloor promotes megathrust creep (Wang and Bilek, 2012, 2014). In these rough faults, resistance to creep due to geometrical irregularities is expected to be larger than the failure stress of stick-slip faults. We investigate this paradox by modeling thermal energy dissipated from subduction faults using two-dimensional finite element models constrained by surface heat flow observations.

We first consider two end-member cases (Fig. 1). Japan Trench is a highly seismogenic subduction zone. The subducting seafloor is rather smooth in the area of the 2011 M 9 Tohoku earthquake. Northern Hikurangi is in sharp contrast with Japan Trench. Most of the megathrust is creeping at the subduction rate (100 % creeping ratio), and the subducting seafloor is extremely rugged, featuring a number of subducting seamounts. At both subduction zones, heat flow data provide adequate model constraints.

The model results show that the thermally defined frictional strength of the subduction faults is extremely low, with $\mu' \approx 0.025$ for Japan and 0.13 for Hikurangi (Fig. 1). In comparison, the effective friction of rocks based on the Byerlee's law and at hydrostatic pore fluid pressure is about 0.4. More important is the significant difference between the two subduction zones. The difference is much larger than can be explained by uncertainties, because the highest μ'-value (0.06) marginally acceptable in Japan is still lower than the lowest value marginally acceptable in Hikurangi (0.08) (Fig. 1).

One reason for a lower μ' in Japan is that it primarily represents coseismic fault strength (Fig. 2). As is widely observed in laboratory experiments (Di Toro et al., 2011), faults weaken typically by a factor of three to five when their slip accelerates to seismic rates of $1\,\mathrm{m\,s^{-1}}$, regardless of their frictional behavior at lower rates. In real faults such dynamic weakening may cause complete stress drop in limited areas, but it cannot massively happen, as evidenced by the very small average stress drops in great earthquakes. The Tohoku earthquake exhibits a greater average stress drop than other great earthquakes, but the value is still only about 4 MPa to 7 MPa, although the peak value in a small part of the rupture area might be as high as 40 MPa (Kumagai et al., 2012). At 20 km depth, roughly in the middle of the depth range of the Tokoku rupture,

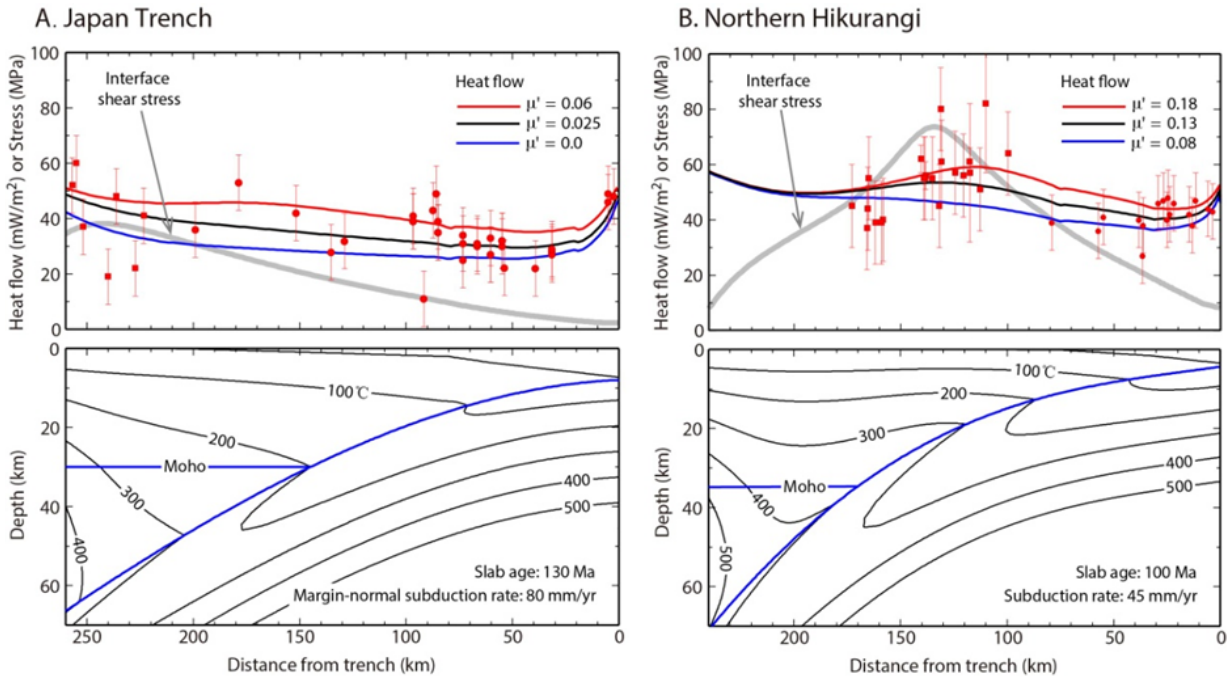

Fig. 1.: Heat dissipation models for Japan Trench and northern Hikurangi. For each subduction zone, top panel shows observed (symbols) and model-predicted (thin lines) surface heat flows and model interface shear stress (thick gray line). Circles and squares indicate marine and land heat flow measurements, respectively (supplementary online text). Bottom panel shows model subsurface temperatures (black contours) and plate interface geometry (blue line).

σ_n (approximated by the weight of the overlying rock column) is about 500 MPa, so that a 5 MPa static stress drop only requires a 0.01 decrease in μ'. In other words, a factor of 1/3 decrease in μ', e. g., from 0.035 to 0.025, is adequate to explain the Japan Trench results. The seemingly small decrease in fault stress is sufficient to reverse the stress state of the upper plate in the rupture area from margin-normal compression to tension (Wang and Suyehiro, 1999), a change that indeed happened as a result of the Tohoku earthquake (Hasegawa et al., 2012).

Therefore, despite the remarkable weakness of subduction faults, the average stress drop in great earthquakes is just a fraction of the average fault strength, albeit a significant fraction. Dramatic dynamic weakening in parts of the fault must be accompanied by much less weakening or even strengthening (negative stress drop) in other parts, such that the average stress drop of the entire rupture zone is much less. An important implication is that the amount of frictional heat is several times the combination of the energy radiated as seismic waves and consumed in permanently deforming rocks around the rupture (Fig. 2). Since the difference in μ' between the two subduction zones cannot be fully explained by dynamic weakening, it must reflect a difference in static fault strength. From observations and theoretical reasoning (Wang and Bilek, 2014), extreme ruggedness of the subducting seafloor such as at northern Hikurangi gives rise to heterogeneous stress and structural environments that promote creep and small earthquakes. But unlike creeping along a smooth fault facilitated by weak gouge, as reported for the creeping segment of the San Andreas fault and shown in Fig. 2 as "weak creep", rough faults creep by breaking and wearing geometrical irregularities in a broad zone of complex internal structure. The integrated resistance to creep is expected to be relatively high, shown in Fig. 2 as "strong creep". Our results in-

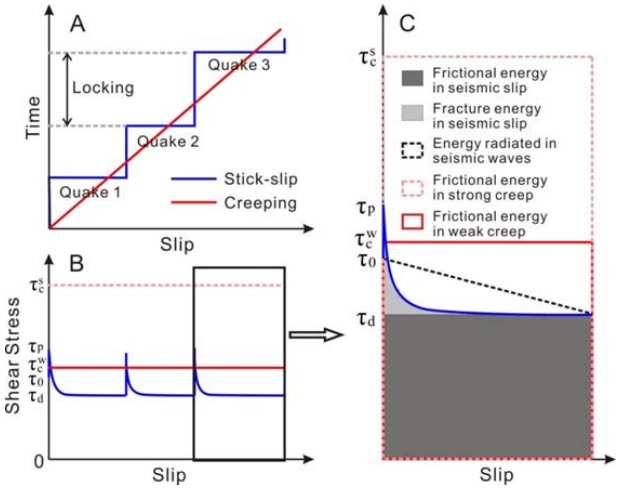

Fig. 2.: Schematic illustration of fault stress and frictional heating for stick-slip and creeping faults. (A) Fault slip history. (B) Fault stress. For stick-slip fault, τ_0 is pre-earthquake stress, τ_p is peak stress, and τ_d is stress during seismic slip (Abercombi and Rice, 2005; Kanamori et al., 2006). τ_c^w and τ_c^s are yield stresses of smooth/weak and rough/strong creeping faults, respectively. (C) A blown-up portion of (B) showing partitioning of energy in seismic slip for stick-slip faults, in comparison with energy dissipated by strong and weak creeping faults.

dicate that the creeping megathrust at northern Hikurangi is indeed stronger than the stick-slip, but much smoother, megathrust at Japan Trench.

We have pursued a global study. Only nine subduction zones including the above two presently have adequate heat flow observations to constrain frictional heating. The results are summarized in Fig. 3 in terms of fault strength results as a function of Mmax, the largest and clearly documented interplate earthquake at each margin. We have added Costa Rica to list. Here we exclude possible tsunami earthquakes, because they occur at a very shallow depth and do not represent the general slip mode of the megathrust. The M_{max} values are meant to provide a crude proxy of seismic slip over the long term. For subduction zones with M_{max} 8.2 to 9.5 (Nankai through Chile in Fig. 3), there is little doubt that fault motion is primarily by stick-slip. For three of the other four subduction zones, although M_{max} may not be an ideal representation of long-term slip behavior, the present locking/creeping state of the megathrust is constrained by modern geodetic measurements. They show significant creep, with northern Hikurangi having the most active creep (~100 % of subduction rate).

Our results suggest a tendency of decreasing μ' with increasing M_{max} or, approximately, less creep. All the highly seismogenic subduction zones in this suite feature rather smooth subducting seafloor, because the igneous crust is devoid of large seamounts or fracture zones, such as Japan Trench and Kamchatka, and/or because large amounts of sediments have evened the bathymetric relief, such as Cascadia and South-Central Chile. The three subduction zones geodetically seen to undergo significant creep all have rugged subducting seafloor. Evidently, it is the weaker but smoother megathrusts that are able to generate great earthquakes. The general correlation between subducting seafloor ruggedness, creeping, and greater heat dissipation, if further verified by future observations, offers a new perspective in assessing earthquake and tsunami hazards for risk mitigation.

References

Abercombie, R. E., J. R. Rice, Geophys. J. Int. 162, 406–424 (2005).

Di Toro, G., et al., Nature 471, 494–498 (2011).

Hasegawa, A., et al., Earth Planet. Sci. Lett. 355-356, 231–243 (2012).

Kanamori, H., L. Rivera, in The missing sinks: Slip localization in faults, damage zones, and the seismic energy budget, Geophys. Monogr. 170, Abercrombie, R., Ed. (America Geophysical Union, Washington DC, 2006), pp. 3–13.

Kumagai, H., N. Pulido, E. Fukuyama, S. Aoi, S., Earth Planets Space 64, 64 –654 (2012).

Wang, K., S. L. Bilek, Tectonophys. 610, 1–24 (2014).

Wang, K., S. L. Bilek, Geology 39, 819–822 (2011).

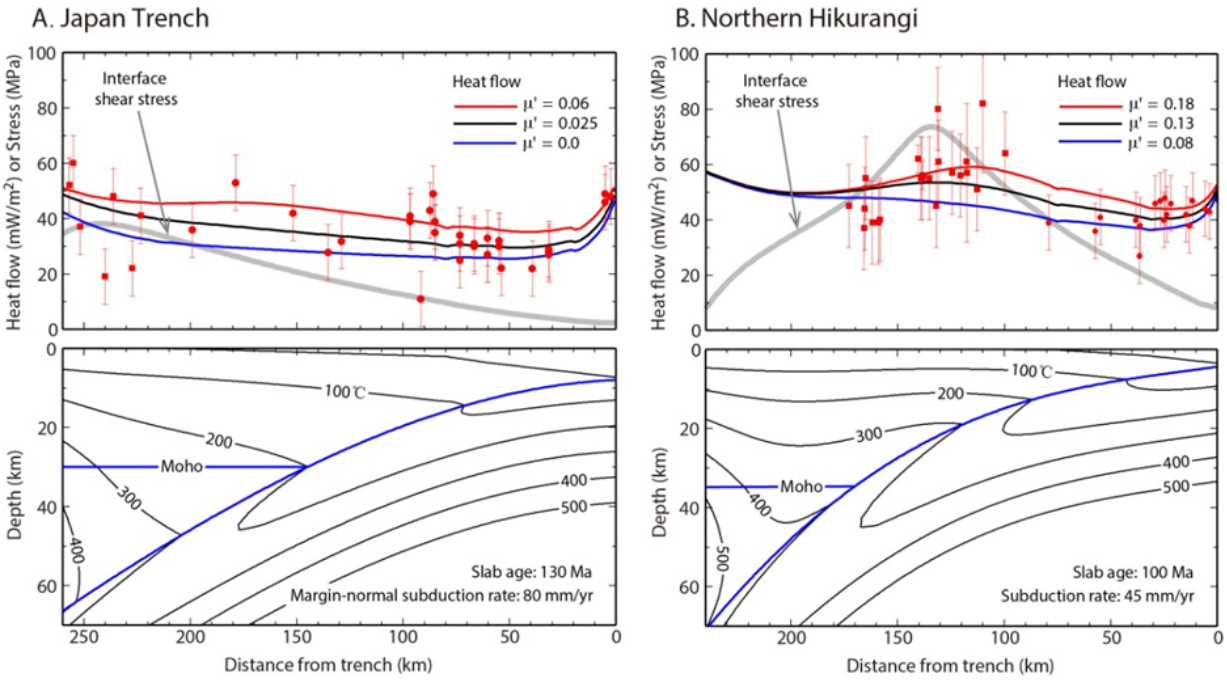

Fig. 3.: Apparent friction of megathrust vs. maximum size of clearly documented interplate earthquakes: 1 – northern Hikurangi, 2 – northern Manila, 3 – Costa Rica, 4 – Kermadec, 5 – Nankai, 6 – Kamchatka, 7 – northern Cascadia, 8 –Japan Trench, 9 – Sumatra, and 10 – south-central Chile (table S 2). The Costa Rica value is an average of previously published results.

Wang, K., K. Suyehiro, Geophys. Res. Lett. 26, 2307–2310 (1999).

GFZ
Helmholtz Centre
POTSDAM

GeoMod2014

Modelling in Geosciences

Programme & Extended Abstracts

31 August - 5 September 2014

Editors:
Kirsten Elger
Øystein Thordén Haug
Malte Ritter

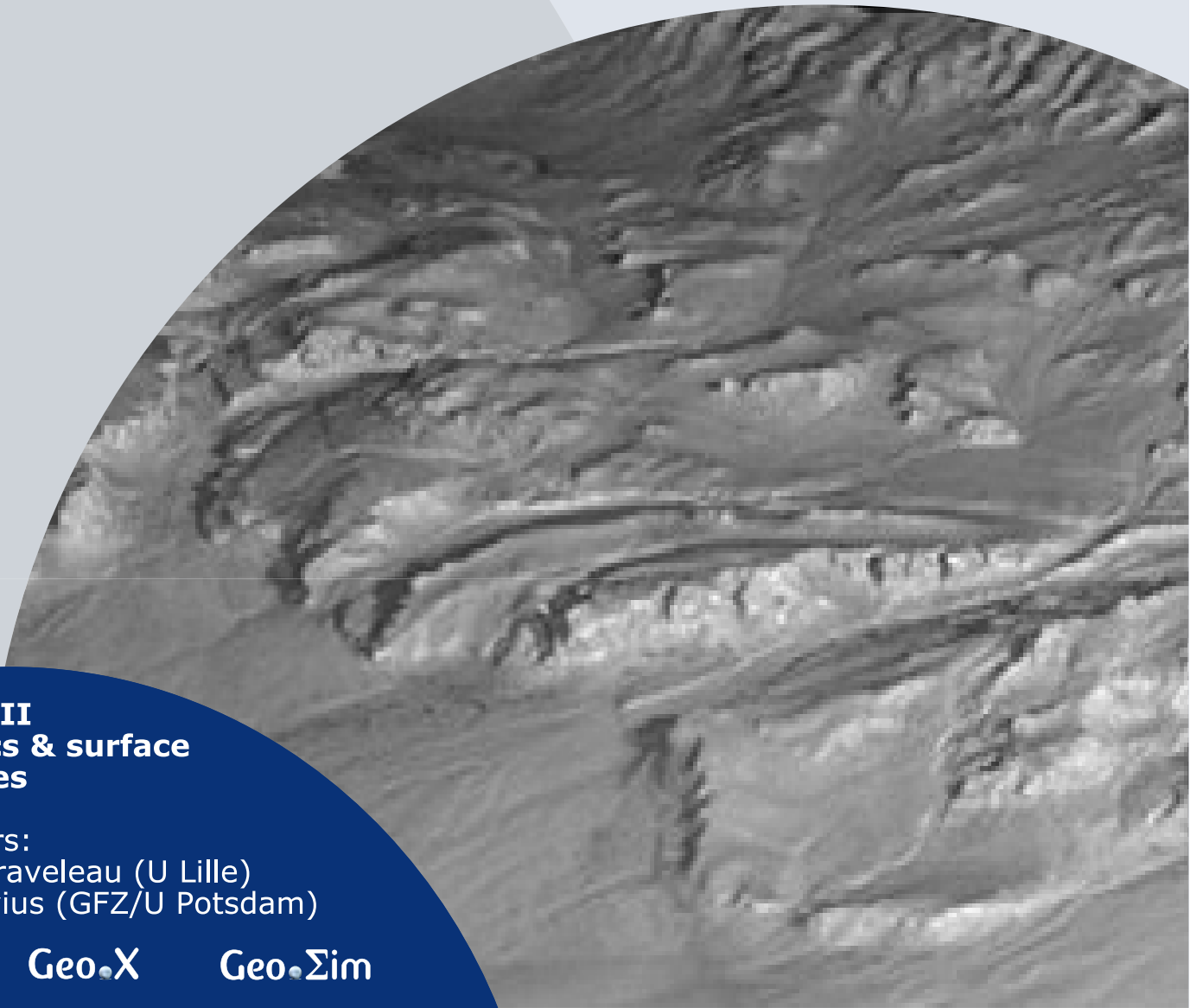

Session II
Tectonics & surface processes

Conveners:
Fabien Graveleau (U Lille)
Niels Hovius (GFZ/U Potsdam)

DFG Geo.X Geo.Sim

Session II.

Tectonics and Surface Processes

Session Description: Tectonics and Surface Processes

Conveners: Fabien Graveleau (U Lille), Niels Hovius (GFZ/U Potsdam)

Interactions between tectonics and surface processes are a primary control on the dynamics of topography, deformation of the lithosphere and the evolution of sedimentary basins. Due to this link, landforms contain information about tectonic processes, basins about the development of surrounding topography, and lithospheric structures about the history of Earth's surface. To read this information, and to resolve with it processes that happen elsewhere in this coupled system is an outstanding challenge in the Geosciences. Different approaches must come together to address this challenge. Geomorphic, geological, sedimentological and geophysical observations can describe past or present manifestations of the system, but such observations do not necessarily resolve the nature of the processes that link between tectonics and surface processes, and their characteristic scales. Numerical and analogue modelling can fill this gap with simplifications and abstractions of the essential physics of the system, yielding predictions that can be tested against the geological reality. To this session, we warmly welcome works that develop both approaches, as well as innovative contributions addressing technical and theoretical challenges in modelling of the interactions between tectonics and surface processes.

Neotectonic evolution of the El Salvador Fault Zone. Insights from 4D analogue experiments.

J. Alonso-Henar[1,2], G. Schreurs[3], J.J. Martínez-Díaz[1,4], J.A. Álvarez-Gómez[5]

[1]*Department of Geodynamics, Faculty of Geology, Universidad Complutense Madrid. Spain*
[2]*CEI Campus Moncloa, UCM-UPM, Madrid, Spain.*
[3]*Institute of Geological Sciences, University of Bern, Bern, Switzerland*
[4]*Instituto de Geociencias IGEO (UCM,CSIC), Madrid, Spain*
[5]*GNS Science, New Zeland*
e-mail: *jahenar@geo.ucm.es*
session: *Tectonics and Surface Processes*

Introduction

The El Salvador Fault Zone (ESFZ) is an active, c. 150 km long and 20 km wide segmented, dextral strike-slip fault zone within the El Salvador Volcanic Arc striking N90° -100° E (figure 1) (Martinez-Diaz et al., 2004). Although several studies have investigated the surface expression of the ESFZ, little is known about its structure at depth and its kinematic evolution. Structural field data and remote sensing images reveal a trenchward migration of the volcanic arc. Some evidences suggest that not all structures within the ESFZ can be explained with the current tectonic context, but require a phase of extension or an extensional component of deformation at some stage in the evolution of the ESFZ. Such extension and migration of the volcanic arc could be related to a subduction roll-back of the Cocos Plate beneath the Chortis Block in Mio-Pliocene times.

We carried out 4D analogue model experiments to test whether or not an early extensional phase is required to form the present-day fstructure of the ESFZ. We have carried out different experiments combining transtensional, strike-slip and extensional settings in different ways and with different geometries of a weak zone related to the current position of the volcanic arc (table 1 and figure 1 B). The deformation was imaged with X-ray computed tomopgraphy. All the experimental process has been carried out in the Experimental Tectonic Laboratory of the Institute of Geological Sciences of the University of Bern and in the CT Scan room of the Institute of Forensic Medicine of the University of Bern. Some of the experiments were analyzed with a X ray Scan Tomography as a non-destructive way that allows us to see the 3D structure during the evolution of the experiment (Colleta et al., 1991).

Results

The results of the models that better mimics the geometry of ESFZ are the models 443 and 448 (figures 2 and 3). Both models include an extensional phase that create several independent grabens along the discontinuous weak zone. During a second deformation phase (simple shear in model 443 and transtension in model 448), all the grabens are connected and inter-graben areas with more diffuse deformation appear. In the experiment 443, the stages 2 and 3 in the Figure 2 are the closest to the geometry of ESFZ In the experiment 448, the stage 2 also reproduce geometries similar to ESFZ.

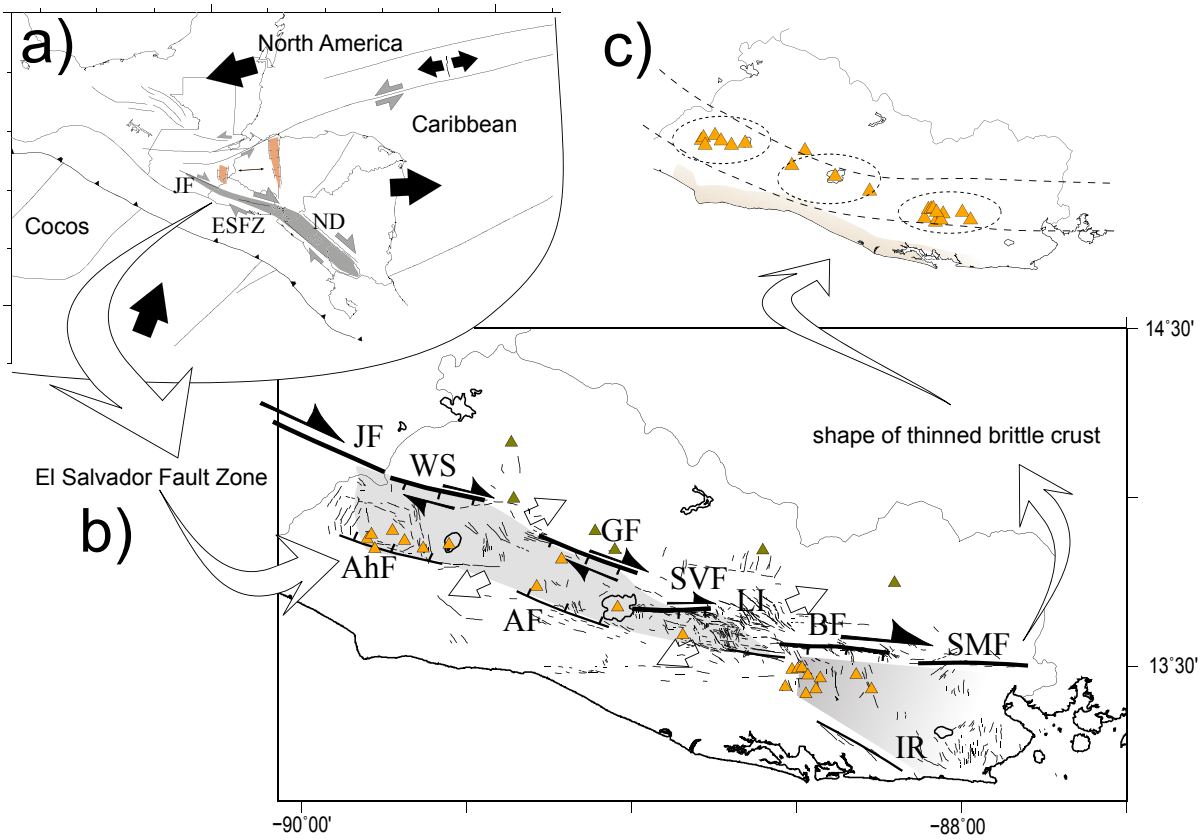

Fig. 1.: A: Tectonic setting of northern Central America. Orange triangles show the positions of volcanoes in the Central America Volcanic Arc. Abbreviations are: PF: Polochic Fault; MF Motagua Fault; JF: Jalpatagua Fault; ESFZ: El Salvador Fault Zone; HE: Hess Scarp. B: Synoptic sketch of the geometry of the continuous and discontinuous weak zone used in the experimental procedure. C: Main structures of the El Salvador Fault Zone. Green triangles are Miocene Volcanoes, orange triangles are Pleistocene Volcanoes. Upper right corner: JF: Jalpatagua Fault; WS: Western segment; AhF: Ahuachapan Fault; GF: Guaycume Fault; AF: Apaneca Fault; SVF: San Vicente Fault; LI: Lempa Intersegment Zone; BF: Berlin Fault; SMF: San Miguel Fault; IR: Intipucá Range. Faults from Canora et al., 2010 and 2012.

Discussion and conclusions

Our experiments suggest that a two-phase tectonic evolution explain better the ESFZ structure: an early pure extensional phase linked to a segmented volcanic arc is necessary to form the main structures of the ESFZ and can explain the shallow geometry of the fault zone. This extensional phase is followed by a strike-slip dominated regime, which results in inter-segment areas with local transtension and segments with almost pure strike-slip motion. The previous extensional phase could be related with a subduction roll-back of the Cocos Plate beneath the Chortís Block. This roll-back could heat in a non-homogeneous way the upper crust. Large magma chambers along the volcanic arc control the formation of grabens along the CAVA crossing El Salvador. Once the roll-back ceased, the structures generated during the first phase where reactived as strike-slip faults. Between the main strike slip faults intersegment zones would be developed with distributed deformation and local transtension areas. Pull-apart basins and releasing bends would also be created (figures 2 and 3).

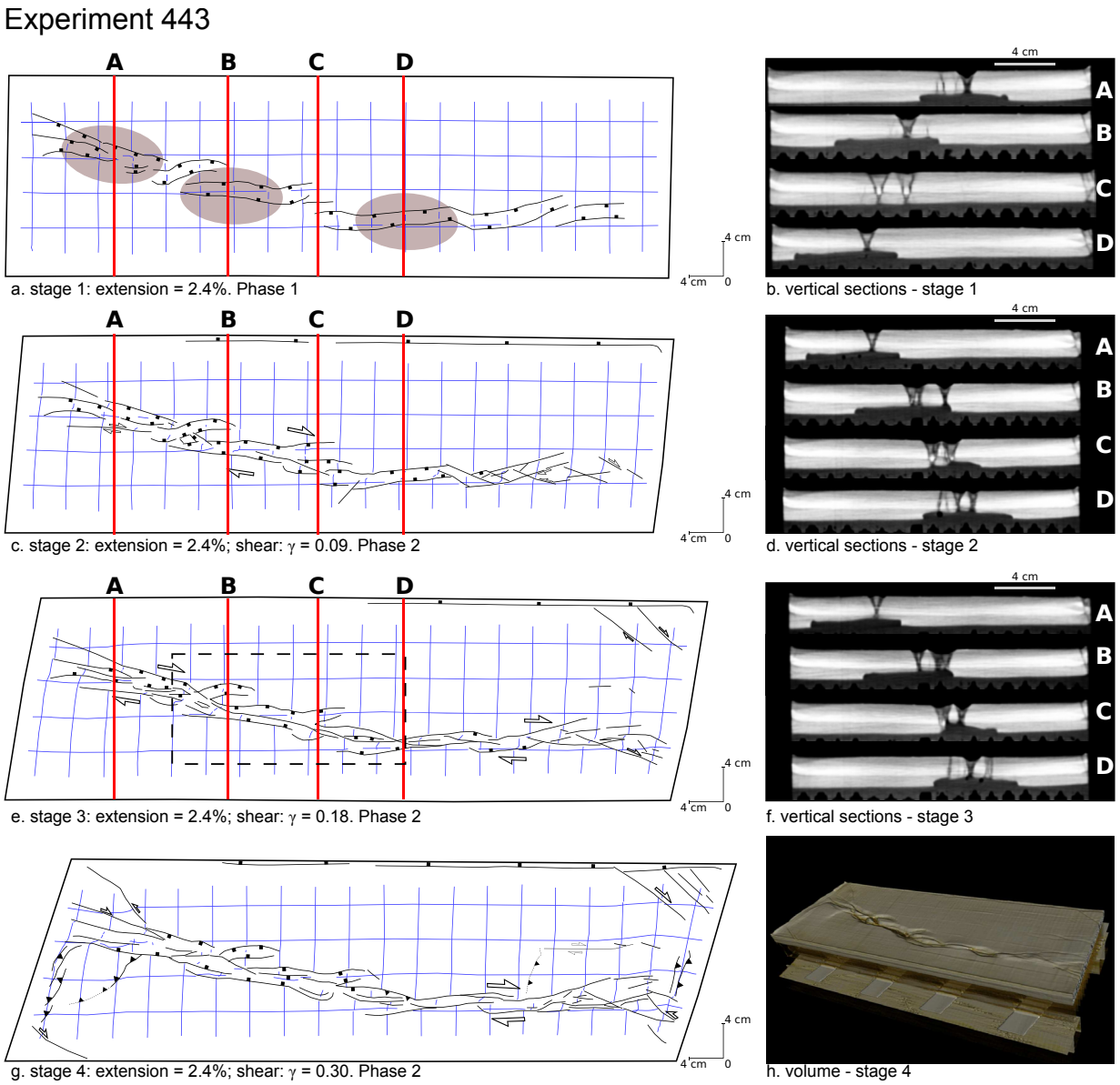

Fig. 2.: Experiment 443, extension followed by pure strike-slip, running over a discontinuous weak zone. Vertical sections and volume from the CT Scan.

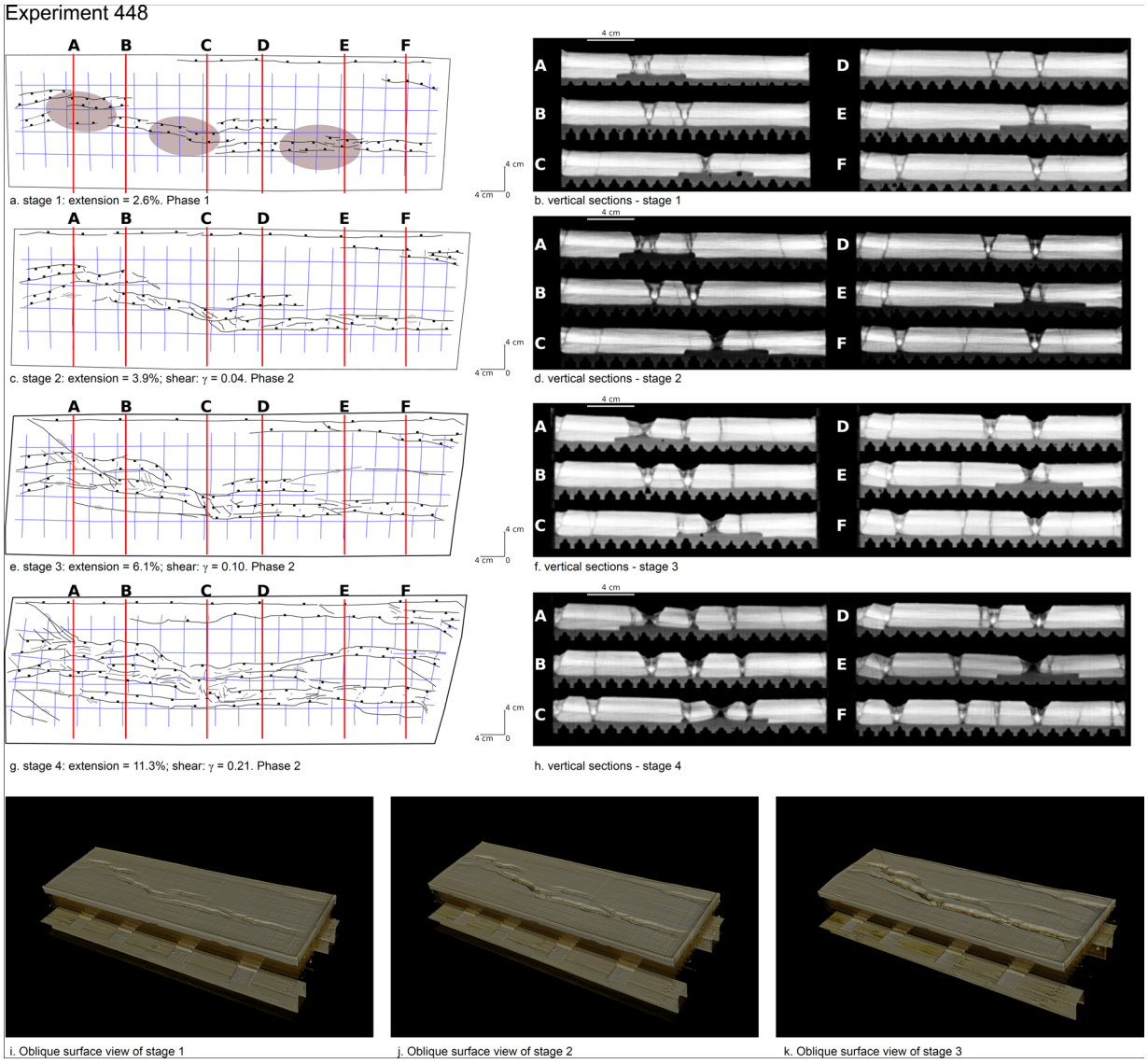

Fig. 3.: Experiment 448, Extension followed by transtension running over a discontinuous weak zone. Vertical sections and volumes from the CT Scan.

Tab. 1.

Exp. No.	Kind of weak zone	Kind of kinematic	Original dimensions (mm)	Extension (mm)	Shear (mm)	Ductile layer thickness (cm)	Brittle layer thickness (cm)	Max. Shear strain
435	Continuous	Strike-slip	230 × 786	0	80	0.5	2.5 or 2	0.35
438	Discontinuous	Strike-slip	230 × 786	0	80	0.5	2.5 or 2	0.35
443	Discontinuous	Extension + Strike-slip	230 × 786	5,5	70	0.5	2.5 or 2	0.3
444	Continuous	Extension + Strike-slip	230 × 786	8	51	0.5	2.5 or 2	0.21
445	Discontinuous	Transtension	230 × 786	22	54	0.5	2.5 or 2	0.21
446	Continuous	Transtension	230 × 786	22	54	0.5	2.5 or 2	0.21
447	Continuous	Extension + Transtension	23 × 80	28	49	0.5	2.5 or 2	0.19
448	Discontinuous	Extension + Transtension	23 × 80	26	49	0.5	2.5 or 2	0.19

References

Canora, C., Martínez-Díaz, J.J., Villamor, P., Berryman, K., Álvarez-Gómez, J.A., Pullinger, C., Capote, R., 2010. Geological and seismological analysis of the Mw 6.6 13th February 2001 El Salvador earthquake: Evidence for surface rupture and implications for seismic hazard. Bulletin of the Seismological Society of America 100 (6), 2873- 2890.

Canora, C., Villamor, P., Martínez-Díaz, J.J., Berryman, K., Álvarez-Gómez, J.A., Capote, R., Hernández, W., 2012. Paleoseismic analisys of the San Vicente segment of the El Salvador Fault Zone, El Salvador, Central America. Geologica Acta 10, 103-123.

Colleta, B. , Bale, P., Ballard, J.F., Letouzey, J., And Pinedo, R., 1991. Cumputed X-ray tomography analysis of sandbox models: Examples of thin-skined thrust systems: Geology, v. 19, p. 1063-1067.

Martinez-Diaz, J., Alvarez-Gomez, J., Benito, B., and Hernandez, D., 2004. Triggering of destructive earthquakes in el salvador. Geology 32(1), 65-68.

Schreurs, G., 2003. Fault development and interaction in distributed strike-slip shear zones: an experimental approach. In: Storti, F., Holdsworth, R.E., Salvini, F. (Eds.), Intraplate Strike-slip Deformation Belts. Geological Society, London, Special Publications 210, 35–52.

Restraining and releasing bands along a sinistral strike-slip shear zone: A physical modeling approach

Blanco, A.[1], Alves da Silva, F.C.[2]

[1]*Programa de Pós-Graduação em Geodinâmica e Geofísica (PPGG), Universidade Federal do Rio Grande do Norte – UFRN*
[2]*Departamento de Geologia - Universidade Federal do Rio Grande do Norte – UFRN*
e-mail: *ablanco@sapo.pt*
session: *Tectonics and Surface Processes*

Introduction

Modeling has become a powerful tool to reproduce geological structures in diverse tectonic environments. Strike-slip faults and associated pull-apart basin modeling appear in many papers in the literature. In this work, we modeled a sinistral strike-slip fault and associated releasing and restraining bends, and explore the nucleation and development of thrusts, normal fault, as well as their relationship with the principal deformation zone represented by strike-slip fault.

Modeling methods

In the experiments described here, we used only quartz sand from dunes. Narrow layer of artificially painted sand was intercalated into natural color sand pack as markers of the deformation (total pack width is 3cm). The sand box dimensions were 50×35×20 cm (l × w × h), with three fixed walls and a mobile one (figure 1). The motor-controlled speed of the mobile wall was 0,42 mm/s. The velocity discontinuity, in the bottom of the box, is represented by a paperboard, attached to the moving wall, which geometry stimulates the development of contractional and extensional sites at the edges of a transcurrent segment (anticlockwise displaced) (figure 1).

The experiments, reproduced several times, were registered both by conventional photos and by PIV (Particle Image Velocimetry). Distension was about 6 cm and the final stage cut in slices, each of which with 0,5 cm, enabling the analysis of the structures in the subsurface. An arbitrary North was created only to facilitate the reference of the formed structures. The strike of the transcurrent fault was settled north-south.

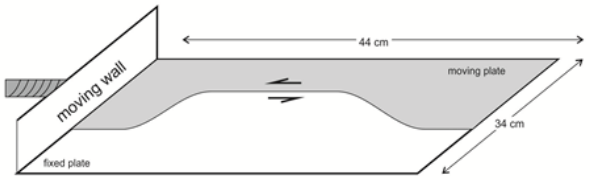

Fig. 1.: Line drawing of the basal portion of the sand box illustrating the geometry of the velocity discontinuity.

Models results

Three distinct sites of deformation were developed in the models involving normal, reverse and strike-slip faults. In the south, the contraction induced the nucleation of oblique NE-SW trending reverse faults characteristic of restraining bends (figure 2a). The southward propagation of the transcurrent segment led to the development of NW-SE back thrusts. In surface, this region marks a topographic high in the top of which some small extensional structures could form. In subsurface a positive flower geometry is recorded (figure 2b).

The northern extremity of the model shows

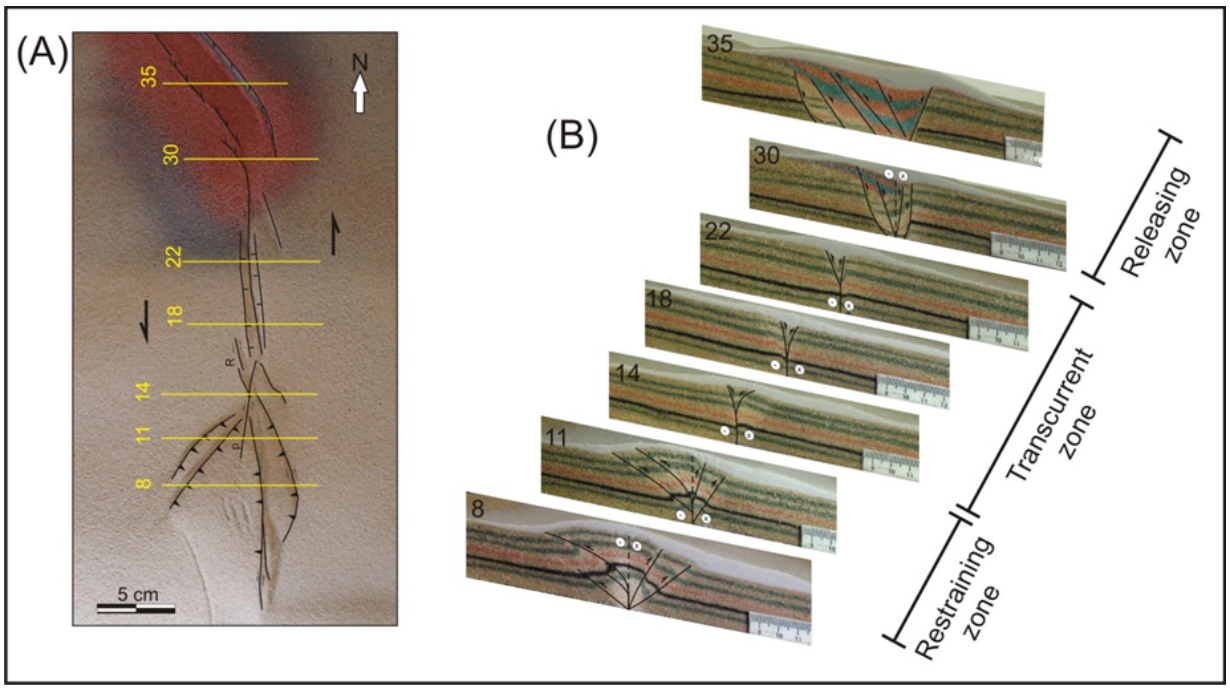

Fig. 2.: (A) Surface of the experiment at its final stage of deformation (displacement of 6 cm). The main structures are drawn and the sections locations are marked; (B) Interpreted sections displaying the geometry of the structures in subsurface. Notice the positive flower (pop-up like structure) formed in the restraining bend and the basin developed at the releasing bend.

NW-SE trending normal faults that originated an oblique basin characteristic of releasing bends (figure 2a). The sections 30 and 35 (figure 2b, see location in figure 2a) reveal a steep dipping master fault in the eastern and several less inclined antithetic faults in the western side. At least in the SE extremity of the basin, in the interface between normal faults and the strike-slip segment, a negative flower like-structure was developed (figure 2b, section 30). During the deformation, the north board fault became inactive while a sequence of antithetic faults progressively developed toward SE consequently widening the basin. Figure 3 shows the strain and the geometry of the basin on surface. In figure 3a, we verify that the progress of the strike-slip fault into the basin led to the development of a new normal fault to the SE and the earlier formed one became inactive.

The sinistral strike-slip fault is better marked in the central part of the model, connecting the restraining and releasing bends. In the very early stage of its development, R shears nucleated along with Y shear. The initial stage of these structures is not visible at naked eye, so it was recorded by PIV (figure 4a). In the restraining bend, one R segment became important prior the development of the reverse faults (figure 4b). With the ongoing deformation, the strike-slip segment along with the NE-SW trending thrust became dominant and R segment turns into NW-SE trending back thrust (figures 4c, d). Then in the restraining bend, a positive flower developed, as shown in figure 2b (sections 8 and 11).

Final remarks

The experiments showed the nucleation of R and Y shear very early (0,5cm of displacement) in the strike-slip fault. There is an important interaction between the transcurrent segment and the restraining and releasing bend's faults. In the restraining site, the transcurrent fault develops in between forward and backward thrusts (these

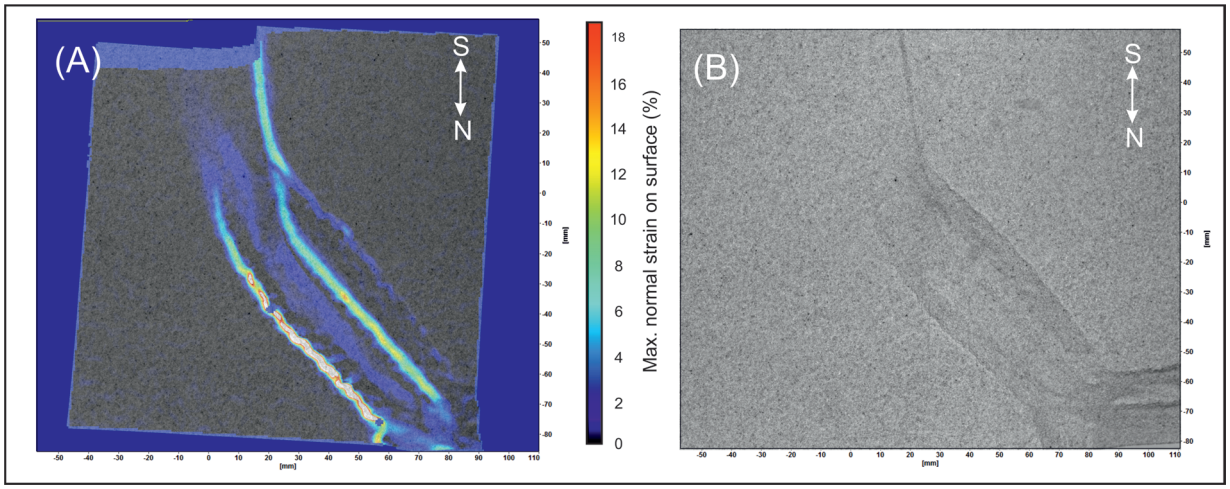

Fig. 3.: (A) PIV picture showing the maximal strain in surface. Note a small segment of strike-slip fault connected with a normal fault approximately in the middle of the basin. The board fault attenuated once deformation progress southward. (B) Conventional photo depicting the basin geometry. In the SE extremity, sand collapsed into the basin covering part of the faults.

later nucleated initially as R shear), forming positive flower. When advancing into the oblique basin, in the realizing bend, the interaction with normal faults led to negative flower formation. At surface, restraining and releasing area are marked by positive and negative topography, respectively (figure 5).

During the experiments, the movement along the strike-slip fault was intended to be pure transcurrence, but once only one plate moved relative to the other, the 0,2 mm thick paperboard used as velocity discontinuity provoked a slight opening along the strike-slip, resulting in a transtensional component.

Acknowledgements

Blanco A. thanks the Brazilian ANP (Agência Nacional do Petróleo) for his PhD scholarship. The Laboratório de Modelagem Estrutural da UFRN is sponsored by Rede de Geotectônica of CENPES/PETROBRAS.

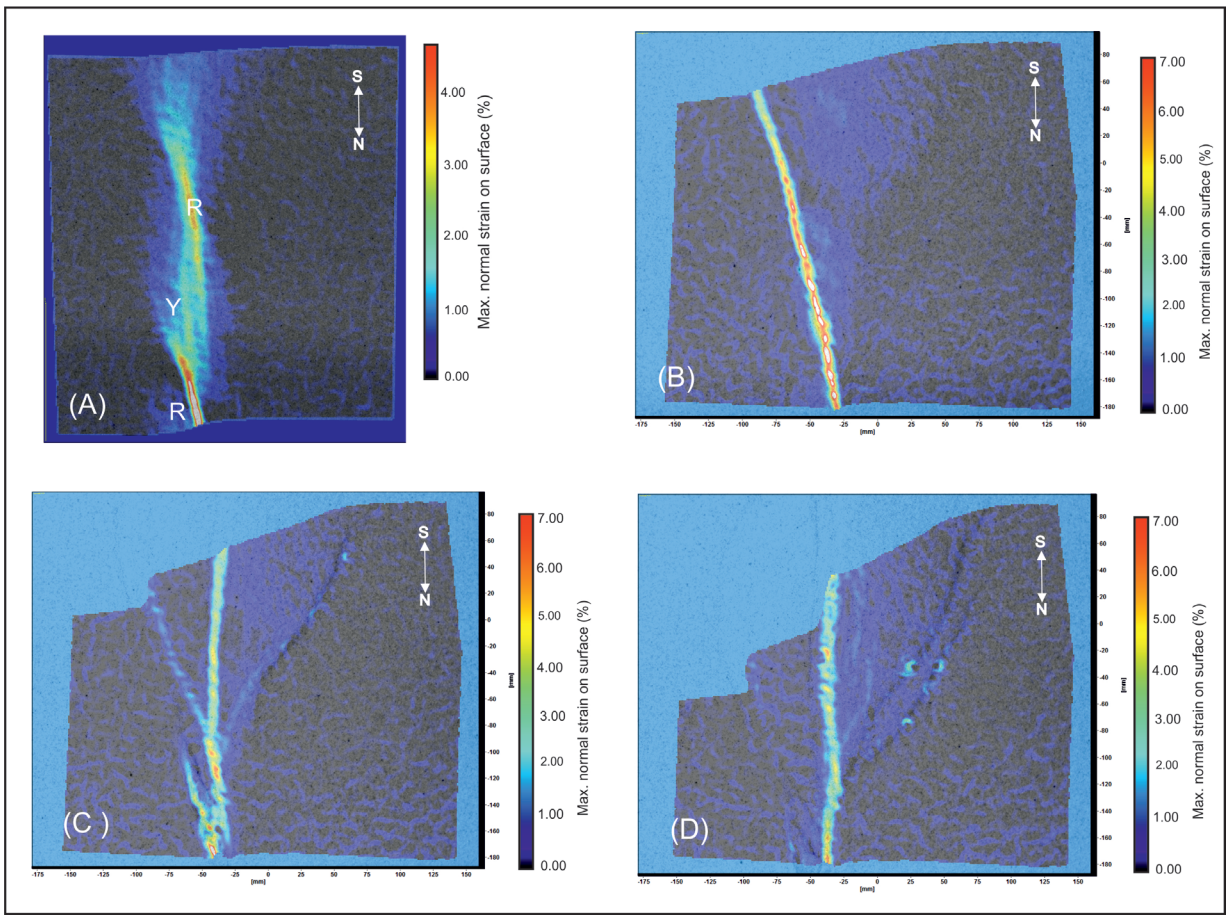

Fig. 4.: PIV picture depicting the maximal strain on surface. (A) Earlier stage of deformation with the development of R and Y shear; (B) R shear in the restraining bend; (C) (D) development of the strike-slip segment in between thrusts and back-thrusts faults

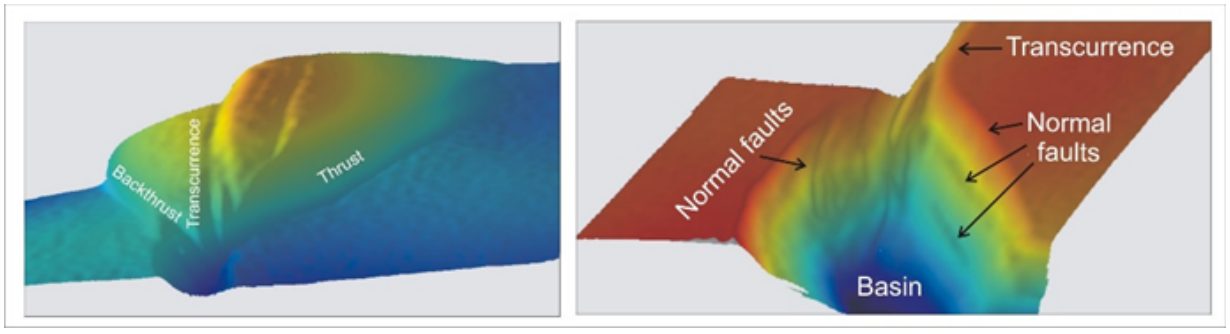

Fig. 5.: 3D model of the restraining and releasing beds, respectively.

Numerical basin modelling of a salt rim syncline: insights into rim syncline evolution and salt diapirism

Christian Brandes[1], Jutta Winsemann[1]

[1]*Institut für Geologie, Leibniz Universität Hannover, Callinstraße, 30167 Hannover, Germany*
e-mail: *brandes@geowi.uni-hannover.de*
session: *Tectonics and Surface Processes*

Salt rim synclines are directly linked to salt diapirs and their sedimentary filling is the key for understanding the temporal and spatial evolution of the respective diapir. Furthermore, the development of rim synclines is a driving mechanism for down-building. The load of the adjacent rim syncline causes lateral salt flow from the source layer into the diapir.

This study deals with rim syncline and salt wall development in northern Germany. With up to 300 salt structures, the North German Basin is a perfect natural laboratory for studying salt-dominated basins. The analysed rim syncline is called Schöningen rim syncline and developed along the flank of the Helmstedt-Staßfurt salt wall in northern Germany. The entire salt wall is 70 km long and trends NW-SE. Including the rim synclines on both sides, the complete structure is 6 to 10 km wide.

Basis for the study are exploration wells that were drilled by the Braunschweigische Kohlen-Bergwerke (BKB, now E.ON Kraftwerke GmbH) over five decades. Altogether, 357 wells were used to construct a 3D subsurface model. The subsurface modeling was performed with the software package GOCAD®and the model covers an area of 32 km^2. The basin modelling part of this study was carried out with the software PetroMod®2D, which was developed by the Schlumberger Aachen Technology Center (AaTC), IES GmbH, Germany. PetroModâ is a software that simulates and analyses the burial history and temperature evolution of a sedimentary basin. It is a dynamic forward simulation based on the finite element method.

The Schöningen rim syncline is 8 km long and 3 km wide. The basin-fill is up to 366 m thick and characterized by 13 more or less continuous lignite seams with thicknesses between 0.1 and 30 m. The coal-bearing succession is subdivided into the early Eocene Lower Seam Group (LSG) and the Middle Eocene Upper Seam Group (USG). The clastic units in the syncline include seven depositional stages: (1) tidally influenced fluvial estuarine channel deposits; (2) mixed tide- and wave- dominated estuarine deposits; (3) prograding wave dominate delta deposits; (4) transgressive shoreline deposits; (5) braided fluvial channel deposits; (6) estuarine deposits; and (7) prograding tide-dominated channel deposits. The succession defines four 3rd order sequences and several higher order sequences that are possibly related to Milankovitch cycles (Osman et al., 2013).

Based on the well data, the basin-fill architecture of the rim syncline was reconstructed in 3D. The basin axis runs parallel to the trend of the salt wall. Several cross-sections perpendicular to the basin axis indicate that the basin-fill has a very pronounced lenticular shape. This shape varies from more symmetric in the NW to clearly asymmetric in the SE, where the steeply dipping beds are close to the salt wall and more gently dipping units are found along the opposite side of the basin margin. The 3D model displays that the basin-fill of the rim syncline consists of a vertical stack of concave packages, where younger units cover a smaller area than the older ones. The depositional units show a lateral migration towards the NNE.

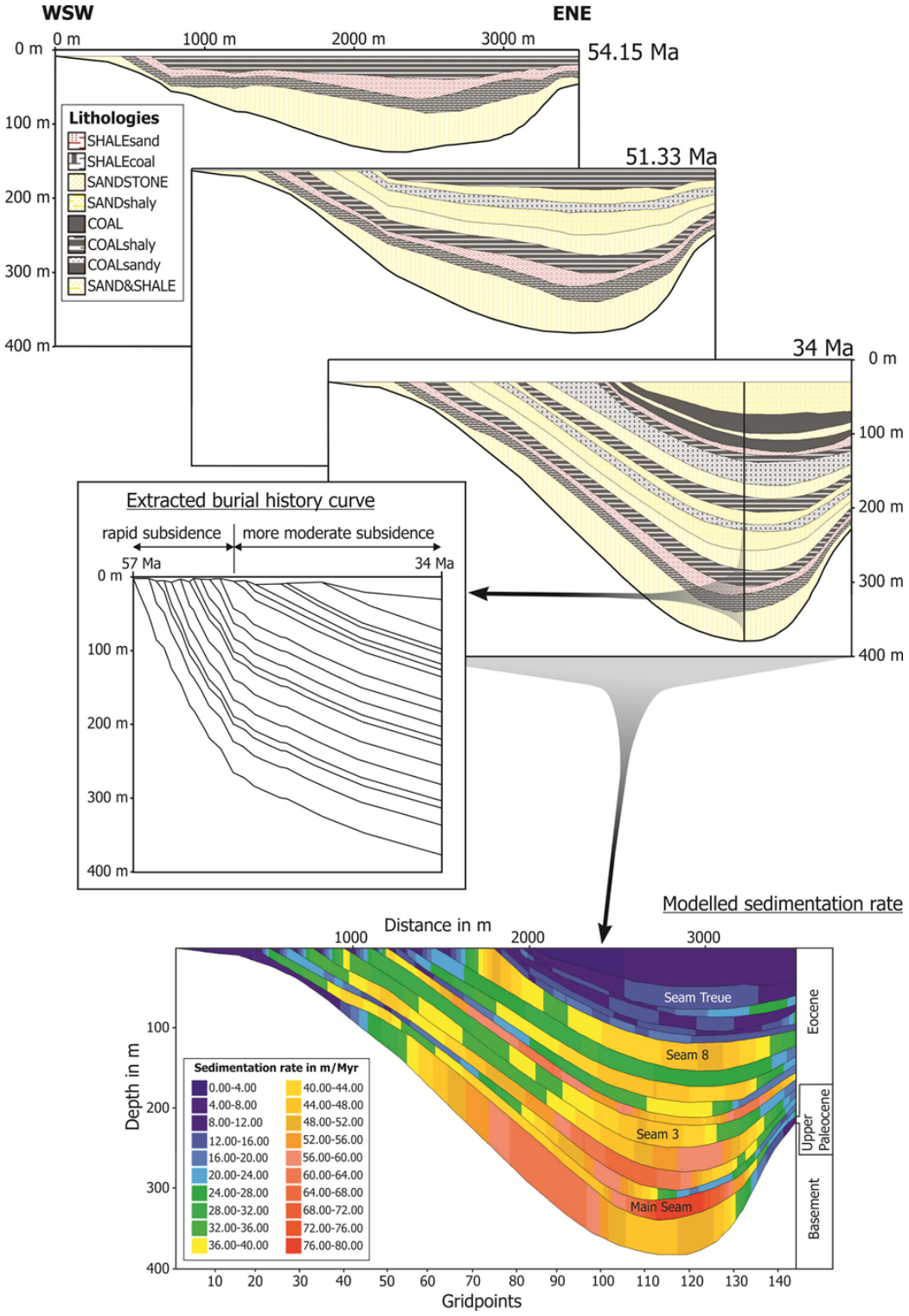

Fig. 1.: Basin modelling results. The simulation shows the progressive migration of the depocentre of the rim syncline towards the salt wall. From the 2D simulation, a burial history curve was extracted, which shows an initial rapid subsidence between 57 and 50 Ma and a more moderate subsidence from 50 to 34 Ma. The highest sedimentation rate of 76 to 80 m/Myr occurred during the deposition of the main seam. During the formation of the Upper Seam Group, the rates were significantly lower with values between 20 to 12 m/Myr (modified after Brandes et al., 2012).

For the basin simulation, a cross-section was extracted from the static 3D subsurface model. This cross-section trends ENE-WSW, is 3.5 km long and runs perpendicular to the basin axis. It is a very suitable cross-section for the basin simulation because there are 16 wells located on the section, which provide lithology and age control. The finite element grid that is used for the 2D simulation has rectangular cells defined by vertical grid lines and horizontal event lines. The horizontal event lines are time lines derived from the geological cross-section. The vertical grid lines are placed at an equal distance along the section to generate a mesh. During the simulation, the finite element grid is fixed to the basin-fill and subsides with the depositional units. The modeling workflow with PetroMod®has been described in detail by Poelchau et al. (1997). The first step for basin simulations is the construction of a conceptual model. This was done on the basis of the 2D cross-section derived from the 3D subsurface model. The geometry of the basin-fill was transferred to PetroMod®and the depositional history of the basin was divided into distinct layers. Absolute ages and lithologies were assigned to each layer. The lithology controls the behaviour during compaction. The lithology for each depositional layer was derived from the wells. Each lithology is characterized by several physical parameters. Based on the well data, we chose the appropriate lithology for the simulation. The water depth is determined based on fossils, facies and lithology. The conceptual model for the 2D simulation consists of 18 layers, which have been defined on the basis of well data and are characterized by a standardized lithology as provided by the program. The geometry of the individual layers is derived from the 3D subsurface model. For the simulation, a finite element mesh was used with 144 vertical grid lines.

The simulation shows that the present-day asymmetry of the basin-fill, which is characteristic for the southern part of the Schöningen rim syncline, was already developed in the early phases of basin evolution. The maximum subsidence is concentrated close to the salt wall. In addition, the modeling results show a progressive migration of the depocentre of the rim syncline towards the salt wall (Brandes et al., 2012). A similar migration of the depocentre towards the salt wall was observed based on isopach maps derived from the 3D subsurface model. Though the isopach maps are not decompacted they show the same depocentre evolution as the basin simulation. We therefore assume that most of the thickness variations visualized on the isopach maps, represent the subsidence pattern and are not compaction effects.

From the 2D simulations, a geohistory curve was extracted that shows initial rapid subsidence between 57 and 50 Ma and a more moderate subsidence from 50 to 34 Ma. The subsidence of the basin can therefore be subdivided into two distinct phases.

The sedimentation rates were highest in the area of the basin axis. A clear decrease in sedimentation rates through time can be observed. In the early phase of basin evolution, the sedimentation rates were high, with values of 60 – 80 m/Myr during the formation of the Main Seam and Seams 1 and 2. Subsequently, the sedimentation rates decreased to 32 – 56 m/Myr during the formation of Seams 3 to 9. In the final stage of basin evolution, the sedimentation rates were much lower with values of 2 – 20 m/Myr.

The southeastern part of the Schöningen rim syncline has an asymmetric geometry with the deepest part of the basin close to the flank of the diapir. In contrast, the northwestern part, is more symmetric. The geometry of the rim syncline seems to be a function of the diapir morphology. This may be coupled to the well known fact that sediments close to a diapir margin tend to be sheared by the rising diapir (Stewart, 2006), an effect which is probably enhanced where the diapir becomes broader and the related rim syncline is more asymmetric.

The fill of the Schöningen rim syncline consists of a vertical stack of concave depositional units, where the younger units cover a smaller area than the older ones. This implies that the area where deposition took place became constantly smaller over time. It is very likely related to a decrease in subsidence and the migration of the depocentre.

The 2D basin simulation shows the progressive migration of the depocentre towards the flank of the diapir.

The geohistory curve of a rim syncline may reflect salt migration from the source layer into the salt wall. The geohistory curve derived from our basin simulation shows initial rapid subsidence between 57 and 50 Ma and more moderate subsidence from 50 to 34 Ma. It implies that initial salt-withdrawal was rapid but later decreased probably due to depletion of the source layer. Though a salt weld is not developed, this points to a certain depletion of the source layer. Even without the development of a salt weld, the salt flow into the diapir can be significantly reduced. Hudec and Jackson (2007) described that halving the thickness of the salt layer will slow down the flow by a factor of 8. This would explain why the rise of the Helmstedt-Staßfurt salt wall stopped, though there is still salt in the source layer. The highest subsidence rate for the Schöningen rim syncline is 76 - 80 m/Myr during the early phase of basin formation.

Isopach maps derived from the 3D subsurface model indicate that the depocentre evolution is complex and did not take place in a uniform fashion. There is not a simple migration of the depocentre towards the flank of the diapir as the 2D section implies. Depocentres also shifted laterally, parallel to the basin axis. The shifting of the depocentres might be a consequence of non-uniform salt-withdrawal from the source layer and give a first hint of along-strike variations in salt movement.

References

Brandes, C., Pollok, L., Schmidt, C., Wilde, V. and Winsemann, J. (2012) Basin modelling of a lignite-bearing salt rim syncline: insights into rim syncline evolution and salt diapirism in NW Germany. Basin Research, 24, 699-716.

Hudec, M.R. & Jackson, M.P.A. (2007) Terra infirma: Understanding salt tectonics. Earth Science Reviews, 82, 1-28.

Osman, A., Pollok, L., Brandes, C., Winsemann, J. (2013) Sequence stratigraphy of a Paleogene coal-bearing rim syncline: interplay of salt dynamics and sea-level changes, Schöningen, Germany. Basin Reseach, 25, 675-708.

Poelchau, H.S., Baker, D.R., Hantschel, T., Horsfield, B. & Wygrala, B. (1997) Basin simulation and the design of the conceptual model. In: Petroleum and basin evolution (Ed. by D.H. Welte, B. Horsfield & D.R. Baker), pp. 3-70, Springer Verlag.

Stewart, S. (2006) Implications of passive salt diapir kinematics for reservoir segmentation by radial and concentric faults. Marine and Petroleum Geology, 23, 843-853.

Modelling Syntectonic Sedimentation in a Extensional Faults System

Ana Carmona[1], Roger Clavera-Gispert[1], Oscar Gratacós[1], Stuart Hardy[1,2], Josep Anton Muñoz de la Fuente[1]

[1] *GEOMODELS Research Institute, Departament de Geodinàmica i Geofìsica, Universitat de Barcelona, Barcelona, Catalonia, Spain*
[2] *Icrea, Institució Catalana de Recerca i Estudis Avançats, Catalonia, Spain*
e-mail: *anacarmona@ub.edu*
session: *Tectonics and Surface Processes*

Introduction

Relay ramps and transfer fault zones are typical in extensional environments. These structures play a significant role in sediment dispersal as they control the sedimentary pathways. Unlike for subaerial settings, the impact of subaqueous relay ramps on sediment dispersal, clastic sedimentation or carbonate deposits evolution, is less studied. In these subaqueous cases, numerical approximations could be a good approach to understand the syntectonic sedimentation.

Considering this, a numerical model is used to study the sedimentary infill in an extensional basin and specifically related to a relay ramp system. The main aim of this contribution is to show the potential of the syntectonic sedimentation program to analyse these extensional systems. In this contribution, initial results are presented together with an analysis of the treated configuration.

The program

The program uses a novel approach that combines a discrete element model (DEM) (Finch et al., 2004; Hardy and Finch, 2006) and a process based sedimentary model, the SIMAFADIM-CLASTIC program (Gratacós et al., 2009), to link both processes, deformation and sedimentation, in a single model (Carmona et al., 2010). It provides information in many useful different ways, no just the resulting topography to combine sedimentation plus deformation, it also gives detailed information about the deposition and facies distribution as well as the evolution of this new strata with the deformation, therefore the resulting structure. It also allows the study of the evolution of the deformation into the pre and syntectonic materials, so the affection of these new material in the evolving structure.

The program can simulate different extensional environments, e.g., movement of one or two faults (overlapped -relay ramp- or not) in different scales (since cm to km). For one particular configuration it allows playing with different parameters, as positions and movement rates of the faults, and the overlap distance and separation distance in the case of a two faults system (figure 1). The sedimentary model also allows different boundary conditions, as the number of clastic sediments, the sedimentation and transportation parameters that characterize each sediment type (density, settle rate, critical velocity for deposition), the inflowing water and sediment source points and the proportion for each sediment type.

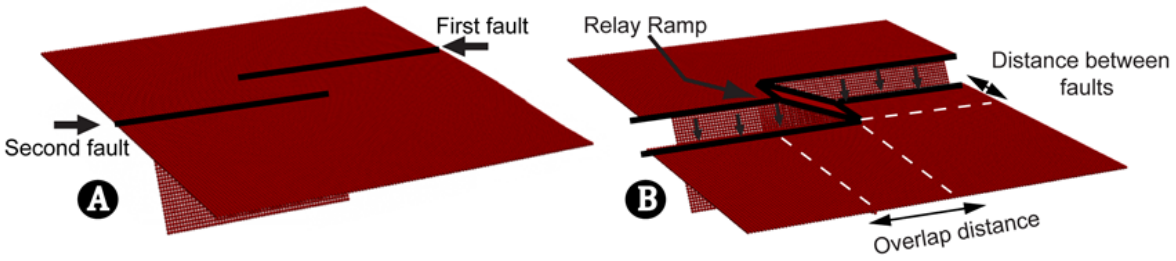

Fig. 1.: Boundary box base of the DE model for the two overlapped extensional faults configuration at the beginning of the simulation (A) and in the final stage (B).

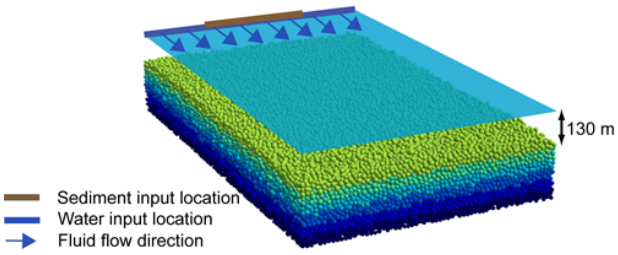

Fig. 2.: Initial and boundary conditions for the sedimentation model.

Initial configuration

In this example, the DEM assemblage has a size of 2,000 m × 1,500 m × 300 m and consists of 111,132 spheres of four different radii: 12.5, 11.25, and 10.0, 8.75 m. Two faults are defined in the DE boundaries (figure 1) with an overlap distance of 500 m and distance between the two faults of 375 m. Total displacement along the faults plane is 200 m. Simulated time is 3,060 years.

A finite element mesh of 300 nodes for the Simsafadim-Clastic program is located above the assemblage surface. An initial bathymetry of 130 m is defined in the basin. Sealevel is constant during the evolution of the model, so changes in bathymetry will be consequence of sedimentation and deformation. Two clastic sediments are defined in the model. The inflowing water and sediment points are defined as is shown in figure 2.

First preliminary results and discussion

To analyse the evolution of the model figure 3 shows four representative time steps of the DEM. It can be appreciated the displacement of the faults (FD) and the new sediments added by the sedimentary model. In each time step, it is worthy to note an asymmetric deposition pattern for the syntectonic sediment due to the fault configuration. It can also be observed how sedimentation migrates basinwards and it takes place mainly in the region where subsidence is more relevant since more accommodation space is available.

To have a look to the final results the model has been divided in seven cross-sections, four longitudinal and three transversal (figure 4). The pretectonic materials have been represented in blue just to have a better view of the new deposited materials. Analysing the sytectonic sediments, growth strata can be observed in both relay ramp and basinward directions (see longitudinal and transversal sections in figure 4).

Syntectonic sediments shows different geometries into the basin related to the fault position and its influence over the accommodation space. In the overlapping area (figure 4 B) the pretectonic surface slope is lower than the surrounding parts (figures 4 A and 4 C) with only one fault and consequently a steeper pretectonic surface slope. So the thickness of the new materials over the overlap area increases slower basinward than in the rest of the model, where the deformation area is smaller and the jump between the footwall

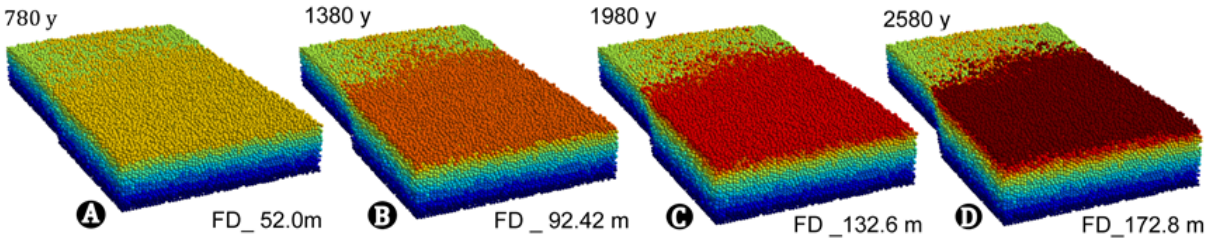

Fig. 3.: Evolution of the DE element model represented by four different time steps. In yellow and reddish colours are represented the new DE added by the sedimentation model.

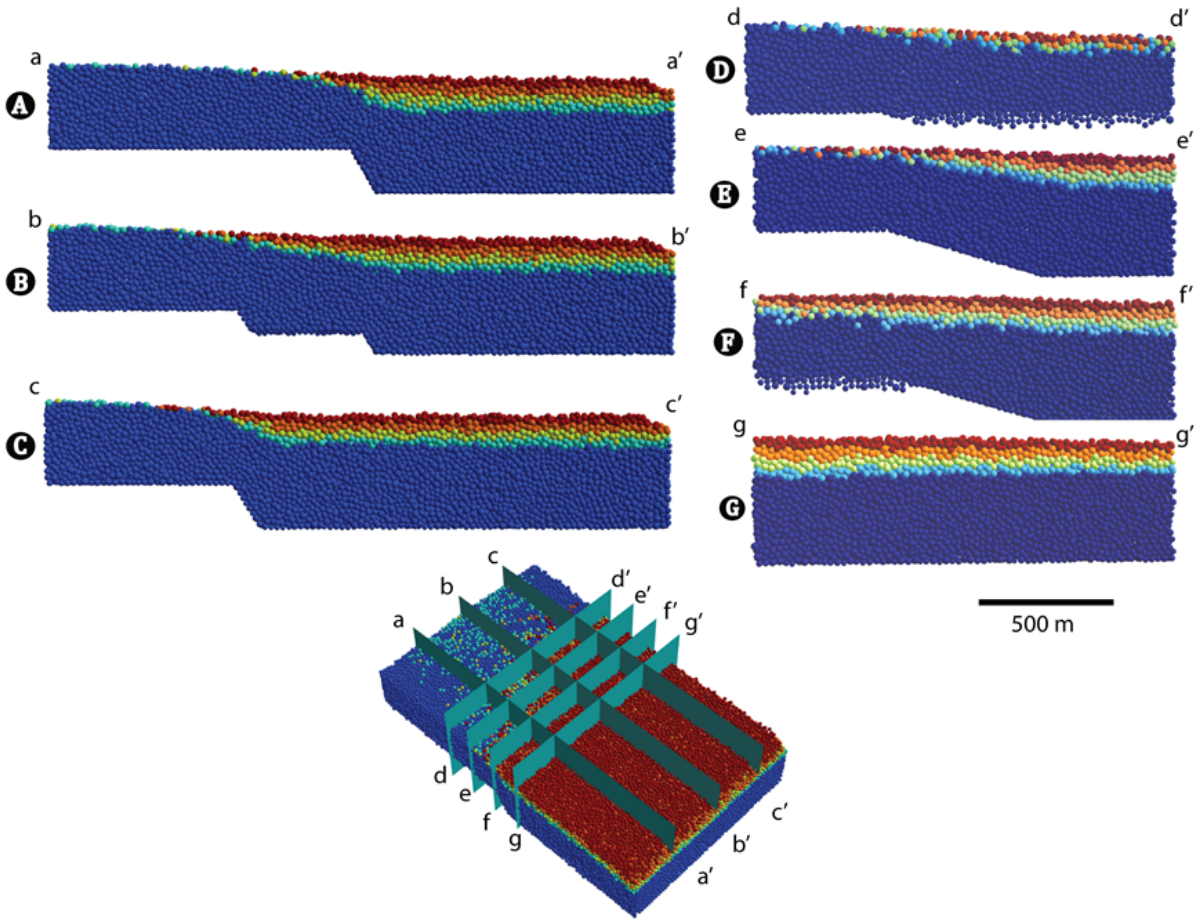

Fig. 4.: Cross-sections of the final stage of the DE model, three transversal, A, B and C; and four longitudinal D, E, F and G. The pretectonic materials are represented in deep blue for a better visualization of the syntectonic materials.

and the hangingwall areas is steeper.

In figure 5, there are represented the evolution of the fluid flow and the thickness of each clastic sediment type in the same four time steps. Regarding to the fluid flow, an asymmetric values and a velocity increase over the time can be appreciated.

Looking to the sedimentation of both materials we can observe again the asymmetric pattern of deposition due to the position of the two faults. Coarse materials settle in the whole basin, proximal and distal areas, obviously taken more relevance in distal parts where more accommodation space is created. As the model moves forward the deposition of the coarse material is concentrated just in the distal area.

On the other hand, fine material sedimentation just takes place in distal regions where the fluid flow is lower and allows its deposition. The sedimentation of the fine materials is prograding basin forward and its thickness decreases in each time step.

Also, we can appreciate that, for both materials, sedimentation is slightly higher in the subsidence area near the second fault. This is probably due to the fact that the bypass, i.e., regions where fluid flow values do not allow significant deposition, is wider in the region that precedes the second fault, so that the amount of sediment in suspension that arrive to this subsidence area is higher.

Conclusions

The results show that the program is a good tool to analyse the change of sedimentation patterns with the evolution of the deformation.

The example presented showed that the evolution of the sedimentation is consistent with the position and movement of the two faults.

Future work should analyse the same initial configuration used in this example but with different boundary conditions, in order to better understand subaquatic extensional systems with relay ramps

References

Carmona A, Clavera-Gispert R, Gratacós O, Hardy S (2010) Modelling syntectonic sedimentation: Combining a discrete element model of tectonic deformation and a process-based sedimentary model in 3D. Mathematical Geosciences 42(5): 519–534

Finch E and Hardy S, Gawthorpe R (2004) Discrete element modelling of extensional fault propagation folding above rigid basement fault blocks. Basin research 16: 489-506

Gratacós O, Bitzer K, Cabrera L, Roca E (2009) Simsafadim-clastic: A new approach to mathematical 3d forward simulation modelling for terrigenous and carbonate marine sedimentation. Geologica Acta 7(3): 311–322

Hardy S, Finch E (2006) Discrete element modelling of the influence of cover strength on basement involved fault-propagation folding. Tectonophysics 415:225–238

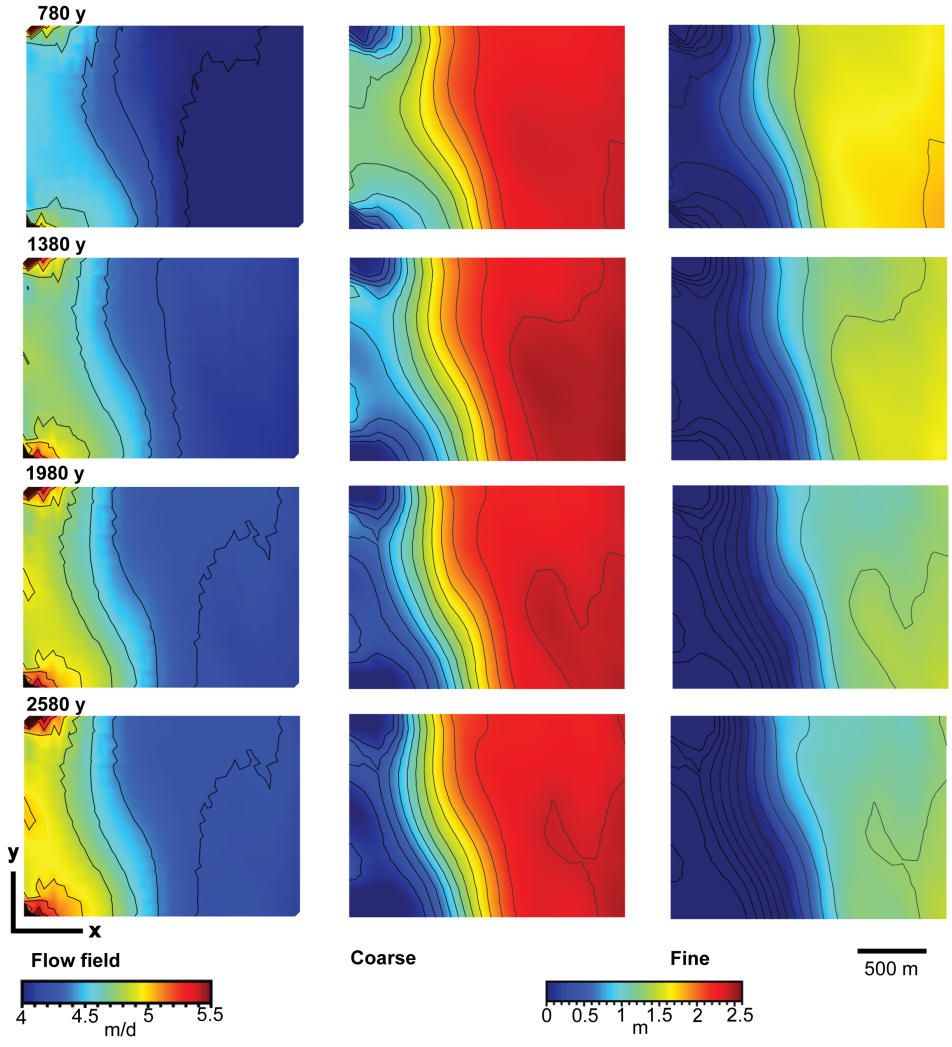

Fig. 5.: Evolution of the fluid flow (m/y), and deposition (in m) of each material, coarse and finer in four different time steps

Process-Based Forward Numerical Modelling SIMSAFADIM-CLASTIC: The Vilomara Composite Sequence case (Eocene, Ebro basin, NE Iberian Peninsula).

Roger Clavera-Gispert[1,2], Oscar Gratacós[1,3], Miguel López-Blanco[1,4], Raimon Tolosana-Delgado[5]

[1]*Institut de recerca Geomodels. Universitat de Barcelona. Spain*
[2]*Abteilung Geologie. Universität Bayreuth, Germany*
[3]*Dept. Geodinàmica i Geofísica. Universitat de Barcelona. Spain*
[4]*Dept. Estratigrafia i Paleontologia. Universitat de Barcelona. Spain*
[5]*Dept. of Modelling and Valuation, Helmholtz Institute Freiberg for Resource Technology. Germany*
e-mail: *roger@clavera.cat*
session: *Tectonics and Surface Processes*

Abstract: SIMSAFADIM-CLASTIC is a 3D process-based forward numerical model that simulates the stratigraphic infill and evolution of marine sedimentary basins (Bitzer and Salas, 2001, 2002; Gratacós et al., 2009a, 2009b; Carmona et al., 2010; Clavera et al., 2013). The program is designed to model processes of transport and sedimentation for clastic terrigenous and clastic carbonate sediments. The program, also include the interaction between carbonate producing organisms and clastic sediments in suspension. Considering that, the objective of the program is to model and to represent the spatial and temporal interplay of the generated sedimentary bodies, obtaining realistic depositional architectures in order to reproduce the 3D sediment distribution and the complex heterogeneity present in the sedimentary record.

The model for siliciclastic transport and sedimentation is based on a potential fluid flow. This fluid flow model can establish the general trend of the flow system to determine the sediment transport in the basin over a geological time scale at basin scale (hundred meters to kilometres) with an acceptable computational time. Regarding to the sediment transport, the fluid flow model can determine the movement of solid particles in suspension due to fluid movement processes that include advection, diffusion, and dispersion.

The carbonate production model is based in the generalized equation of Lotka-Volterra ecological modelling. The program takes into account the influence of environmental factors to model the carbonate producing organisms associations (water depth, nutrients, clastic sediment concentration is suspension, fluid flow velocity and bottom slope), and the interaction among them (predation, prey, mutualism, competition...).

Other processes are modelled to generate (or reduce) accommodation space in the marine basin, including sea level variations, compaction, and isostasy.

In order to show the application and possibilities of the code, the Vilomara Composite Sequence (VCS) of Sant Llorenç del Munt (SLM) fan delta complex (Ebro basin, NE Iberian Peninsula) is modelled.

The Bartonian/Priabonian SLM clastic wedge is located on the south-eastern margin of the Ebro foreland basin, adjacent to the Catalan Coastal Ranges. López-Blanco et al. (2000a, 2000b), and Gómez-Paccard et al. (2012) provide an analysis of the tectonosedimentary, tectonogeomorphic and paleoclimatic setting of the Sant Llorenç del

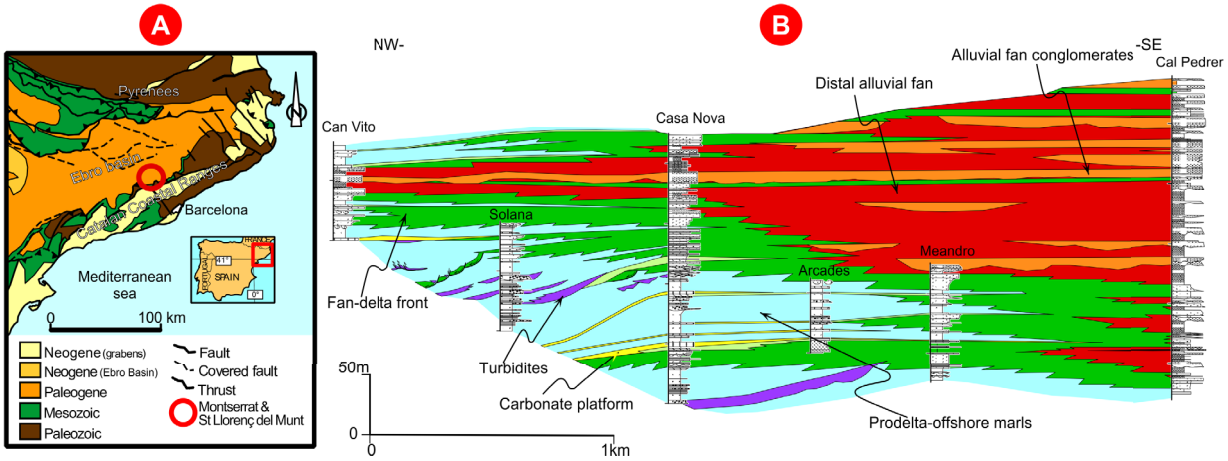

Fig. 1.: Geological and geographic situation of the studied area (A) and the correlation panel of six stratigraphic logs in the western part of Sant Llorenç del Munt system (B) (From López-Blanco et al., 2000b).

Munt complex, as well as an estimate of the rates of geological processes controlling the fan-delta development.

VCS was deposited during the regressive composite sequence set of the transgressive–regressive megasequence of Milany described by the SLM fan-delta complex, and comprises an alternation of detrital sediments interbedded with subordinate carbonate platform deposits. The facies associations in the VCS are from proximal to distal: proximal alluvial fan, distal alluvial fan, fan-delta front, carbonate platform, and fan-delta slope and prodelta.

The VCS is structured into a lower transgressive sequence set (TSS) and an upper regressive sequence set (RSS). This transgressive-regressive trend is built from the piling of seven repetitive, metre-scale transgressive–regressive high-frequency fundamental sequences (Fig.1). These sequences are bounded by maximum regressive surfaces, which correspond to the time of regressive- to-transgressive turnaround of the shoreline, located at the first indication of upward deepening following a regression. These sequences are made up of a transgressive systems tract (TST), overlain by a regressive systems tract (RST), separated by a maximum flooding surface (MFS). They record fluctuations in detrital input, most probably related to a combination of allocyclic (periodic to episodic, relative sea-level changes, tectonic pulses and Milankovitch climatic oscillations) and autocyclic factors (variations in the organization of distributary channels). TSTs develop during periods of low terrigenous input and/or increasing accommodation; RSTs are a response to episodes of high terrigenous input and/or decreasing accommodation space.

Taking into account these previous geological settings, the observed depositional architecture has been interpreted as controlled by fluctuations in the sediment supply rate and changes in accommodation space. The models obtained using SIMSAFADIM-CLASTIC can help us to discuss which of both parameters, fluctuations in the sediment supply rate and/or changes in accommodation space, has great influence on the geometry and on facies distribution.

To show this and considering the observed field data, 3 different configurations have been done considering the variation of key parameters (Fig.2): sediment supply and sea level. Configuration A (Fig.2A) models the influence of variation in sea level, for this reason it varies the sea level as shown in Fig.2 and sediment supply is constant; Configuration B (Fig.2B) models the influence of sediment supply, and this configuration varies sediment supply as shown in Fig.2B and sea level rises linearly (to minimize the affection of it generating the necessary space); and configuration C (Fig.2C) combines sea level and sediment supply

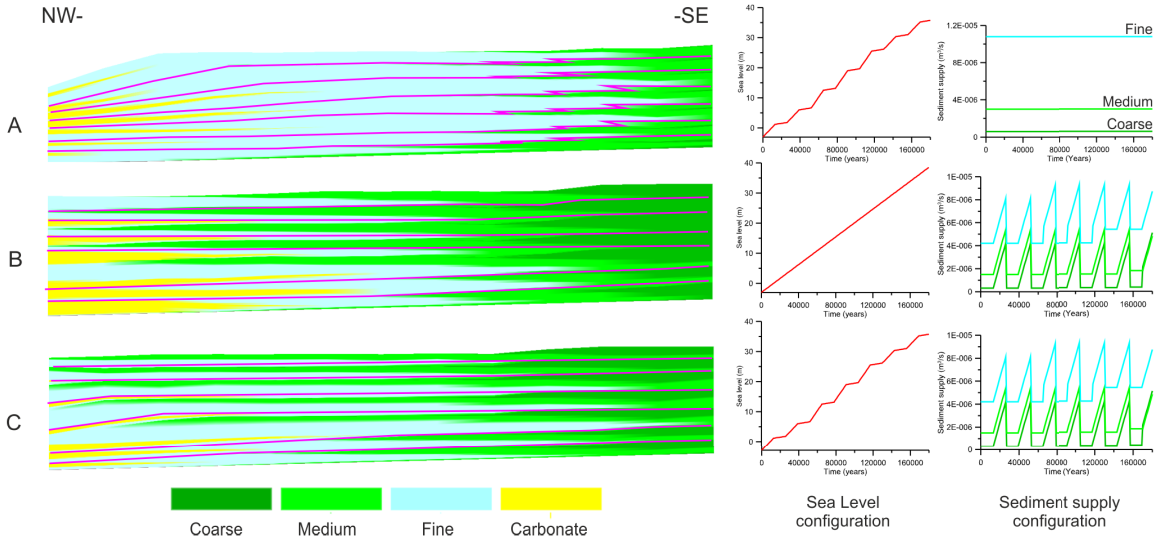

Fig. 2.: Cross-sections and related sea level and sediment supply in each configuration in function of the main affecting parameter defined: A. sea level. B. sediment supply. C. sea level and sediment supply (see text for more explanations).

variations as shown in Fig.3C.

The results for the Configuration A show the carbonate sediments trends to join in the distal part of the basin, and the coarse sediments from fan-delta front does not prograde to the centre of the basin and are located in most proximal part in the SE. This model does not show the internal Transgressive –regressive trend of the VCS.

The Configuration B results show tabular geometry of the sedimentary bodies, the carbonate sediments have been growth from the central part of the basin to the distal parts with a great thickness. The coarse and medium sediments from fan-delta front prograde inside de basin. This configuration shows the internal Transgressive -regressive trend of the VCS.

The Configuration C results show a sigmoidal geometry; the carbonate development is less thick than Configuration B and growth from central part of the basin till distal parts in NW. The coarse and medium sediments of fan-delta front prograde from proximal parts in SE to central part of the basin. This configuration shows the internal Transgressive –regressive trend of the VCS.

From these configurations, Configuration C is the most accurate model and shows a better correlation with the data observed in the field than others configurations, concluding that both, sea level and sediment supply play an important role in the architecture of the depositional system. Even so, Configuration A shows more distant results from observed data; while Configuration B shows better sediment distribution compared with field data, concluding that the sediment supply affects more than accommodation space in the body geometry and sediment distribution.

References

Bitzer, K., Salas, R. (2001) Geologic Modeling and Simulation - Sedimentary Systems, 1 edn., chap. Simulating carbonate and mixed carbonate-clastic sedimentation using predator-prey models, pp. 169-204. Kluwer Academic.

Bitzer, K., Salas, R. (2002) Simsafadim: Three-dimensional simulation stratigraphic architecture and facies distribution modelling of carbonate sediments. Computers and Geosciences 28(10), 1177- 1192.

Carmona, A., Clavera-Gispert, R., Gratacós, O., Hardy, S. (2010) Modelling syntectonic sedimentation: Combining a discrete element

model of tectonic deformation and a process-based sedimentary model in 3d. Mathematical Geosciences 42(5), 519-534.

Clavera-Gispert, R., Carmona, A., Gratacós, O., Tolosana-Delgado, R. (2012) Incorporating nutrients as a limiting factor in carbonate modelling. Palaeogeography, Palaeoclimatology, Palaeoecology 329-330, 150-157.

Gómez-Paccard, M., López-Blanco, M., Costa, E., Garcés, M., Beamud, E., Larrasoaña, J.C. (2012)Tectonic and climatic controls on the sequential arrangement o fan alluvial fan/fan-delta complex (Monserrat, Eocene, Ebro Basin, NE Spain). Basin research, 24, 437-455.

Gratacós, O., Bitzer, K., Cabrera, L., Roca, E. (2009a) Simsafadim- clastic: A new approach to mathematical 3d forward simulation modelling for terrigenous and carbonate marine sedimentation. Geologica Acta 7(3), 311-322.

Gratacós, O., Bitzer, K., J.L.Casamor, Cabrera, L., Calafat, A., Canals, M., Roca, E. (2009b) Simulating transport and deposition of clastic sediments in an elongate basin using the simsafadim-clastic program: The camarasa artificial lake case study (ne spain). Sedimentary Geology 222(1-2), 16-26.

López-Blanco, M., Marzo, M., Piña, J. (2000a) Transgressive-regressive sequence hierarchy of foreland, fan delta clastic wedges (Montserrat and Sant Llorenç del Munt, Middle Eocene, Ebro basin, Spain) Sedimentary Geology, 138 (1-4). pp 41-69.

López-Blanco, M., Marzo, M., Burbank, D., Vergés, J., Roca, E., Anadón, P.,Piña, J. (2000b) Tectonic and climatic controls on the development of foreland fan deltas: Montserrat and Sant Llorenç del Munt systems (Middle Eocene, Ebro basin, NE Spain) Sedimentary Geology, 138 (1-4). pp 17-39.

The balance between uplift and fluvial erosion over a single seismic cycle – an example from Taiwan

Kristen Cook[1], Fabien Graveleau[2], Jens Turowski[1], Niels Hovius[1], John Suppe[3]

[1]*Helmholtz Zentrum Potsdam, GFZ Section 5.1, Potsdam, Germany*
[2]*Géosystèmes, Université Lille 1, CNRS UMR 8217, Villeneuve d'Ascq*
[3]*Department of Geosciences, National Taiwan University, Taipei*
e-mail: *kristenlcook@gmail.com*
session: *Tectonics and Surface Processes*

The relationship between tectonic and geomorphic processes is important for understanding how topography evolves, and how the landscape reflects tectonic and climatic signatures. We present a case study of the relationship between uplift and erosion on the scale of a single seismic cycle, in which we can observe the creation of substantial coseismic topography and its subsequent removal by fluvial erosion. In Sept. 1999, the Mw 7.6 Chi-Chi earthquake struck western Taiwan. At the northern end of the rupture zone, in the Daan River valley, the earthquake activated the Dongshi Anticline, resulting in up to 13 m of uplift due to coseismic folding. Where the Daan River crosses the anticline, the river responded to the coseismic uplift by very rapidly cutting into the uplifted topography, and by 2009 the river had carved a narrow bedrock gorge extending the width of the anticline. In the current stage of erosion, the river has ceased cutting down, and is now eroding laterally. Although widening within the gorge is relatively slow, the river is cutting back the upstream boundary of the anticline at a rate of about 15 m/yr. At this rate, the river will remove the uplifted topography and returned to its pre-uplift morphology in about 50 years. The post-1999 erosion rates in the Daan River are several orders of magnitude faster than background rates, and represent a transient phase of erosion in response to the disequilibrium created by coseismic uplift. In this case, the river is able to respond to the coseismic uplift of the Dongshi anticline solely through this transient response, and without long term changes in the river's morphology. This example highlights the potential importance of short-lived signals of uplift and erosion in the relationship between tectonics and landscape morphology.

Joint analog modeling of marine and terrestial geological processes: state of the art and new developments

S. Dominguez[1]

[1] *University of Montpellier 2, CNRS, UMR 5243 Geosciences, Place E. Bataillon, F-34095 Montpellier, France*
e-mail: *stephane.dominguez@gm.univ-montp2.fr*
session: *Tectonics and Surface Processes*

In Geosciences, an invisible frontier separates marine geologists and geophysicists from their "terrestrial" colleagues. In other words, most of geologists are specialized on dry or wet geological context and often lack of an integrating view linking land and sea observation. Consequently, the interactions and couplings between these two domains, where intense material fluxes and geomorphological processes concentrate, remain relatively unstudied. This is also the case for the analog modeling approach that generally focus exclusively either on terrestrial processes like mountain building, river dynamics, watershed evolution or on marine ones like marine sedimentation processes, submarine landslides, turbidite currents dynamics. Up to now, very few experimental works have investigated the interactions that exist between land and submarine geological processes at the scale of a whole active or passive margin.

Compared for instance to active foreland settings, several first order additional key parameters must be taken into consideration (Figure 1), like eustatic changes of sea level, sea bottom tectonic deformation, underwater sediment transport controlled by current dynamics, biogenic hemipelagic sediment production and also fluid pressure driven processes (mud diapirism, hydrofracturation,...).

Some of them have been investigated using analog modeling. One should notice that the state of the art can be quickly summarized since there is apparently a limited amount of published works available in the literature. Among those, several workers have developed original experimental setups, modeling self-channelized gravity currents to study the formation of submarine fans and canyons (e.g. Muto and Steel 2001; Métivier et al., 2005; Lajeunesse et al., 2010). Others have modeled experimentally passive margin sedimentation, particularly to study delta stratigraphy architecture (e.g. Van Heijst et al. 2001b; Kim and Paola, 2007; I. Fardiansyah & A. Budiman, GPRG) with convincing results when compared to their natural counterparts imaged by seismic profiling (Figure 2). Most of these experimental works, however, simulate land sediment input to the sea using a simple pipe providing a water+sand mixture flow which does not allow to reproduce feedback process, that is the influence of marine sedimentation on landscape morphology dynamics. S. Y. J. Lai and H. Capart (Hydraulic and Ocean Engineering National Cheng Kung University) have been among the firsts to perform geomorphic experiments coupling landscape and submarine erosion/sedimentation processes (Figure 2). Their results show striking analogies between model and nature in terms of aerial and submarine morphologies.

Why such type of experiments are still relatively scarce ? The fact is that analog modeling faces several limitations related to the use of fresh and salty water to erode landscape morphology and to simulate the sea which inevitably induced scaling distortions (Paola, 2009). Finding an appropriate analog material rheology to model both

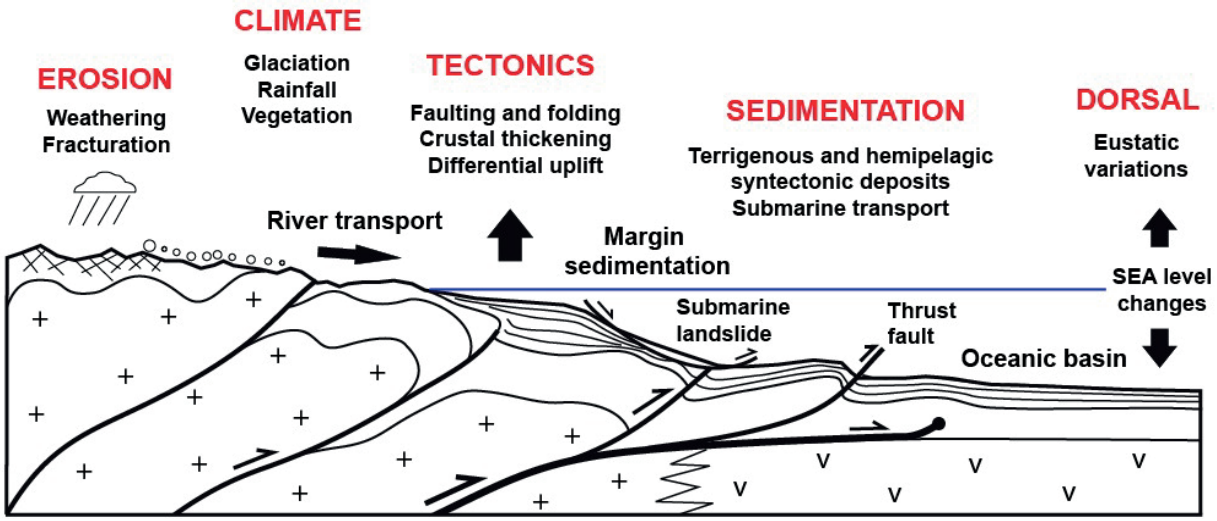

Fig. 1.: Geodynamic context and main interactions between active geological, climatic, terrestrial and marine processes

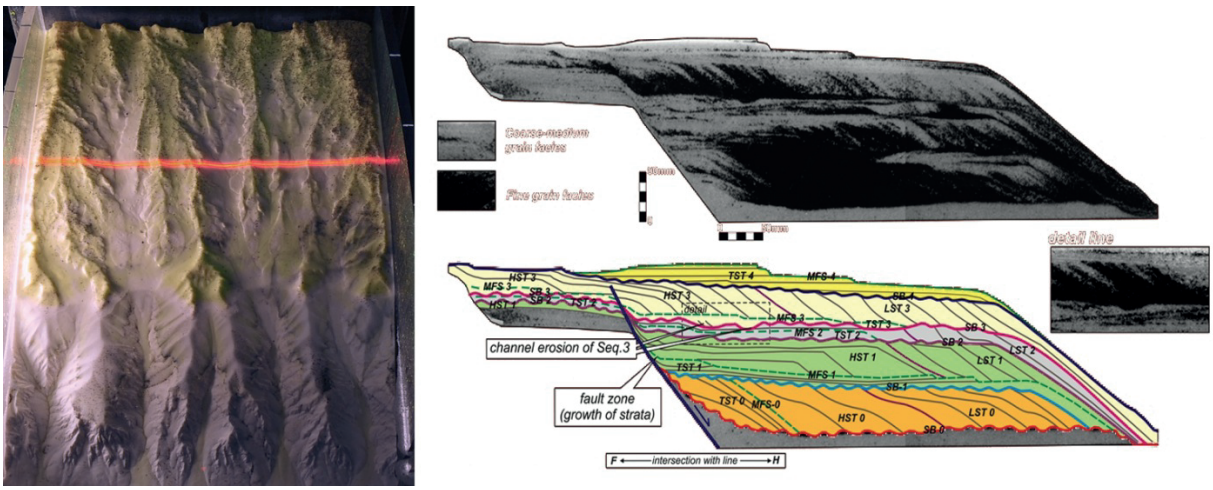

Fig. 2.: Left) geomorphic experiment coupling landscape and submarine erosion/sedimentation processes performed by S. Y. J. Lai and H. Capart (Hydraulic and Ocean Engineering National Cheng Kung University, Taiwan). Right) geomorphic experiment dedicated to study interactions between margin sedimentation /active faulting/sea level changes performed by I. Fardiansyah & A. Budiman (GPRG, Indonesia).

landscape and seascape morphogenetic processes is also another difficulty to overcome, especially when tectonic deformation must be also taken into account.

To illustrate the scientific issues and the potential of modeling coupled sea-land geological processes, I will present some recent technical developments and preliminary results dealing with the tectonic inversion of the Algerian passive margin (Figure 3) and an ongoing project to study tectonic and morphogenetic sea-land processes on the Eastern coast of Taiwan. The Algerian margin is a tectonized passive margin that undergoes active compression since at least Late Quaternary. As a result, its submarine morphology and terrestrial reliefs suffered huge changes in the last 2 millions years including coastal emersion, margin shortening and steepening. The Eastern coast of Taiwan is one of the most tectonically active region in the world. Here, the collision

between the Luzon volcanic arc, carried by the Philippine Sea Plate, and the continental margin of the Eurasian plate induces the formation of a high mountain range (4000m) that literally emerge from the sea at a very high speed. It is, then, another appropriate natural laboratory to study the couplings between submarine and terrestrial geological processes.

These two natural examples and corresponding experimental models will be used to demonstrate that analog modeling is potentially a relevant tool to investigate such complex geodynamic contexts which cannot be studied yet numerically in 3D with the same degree of detail. The final objective of this presentation will be to outline the interest of developing new experimental projects, scientific collaborations and improving technics to enlarge the field of investigation of analog modeling.

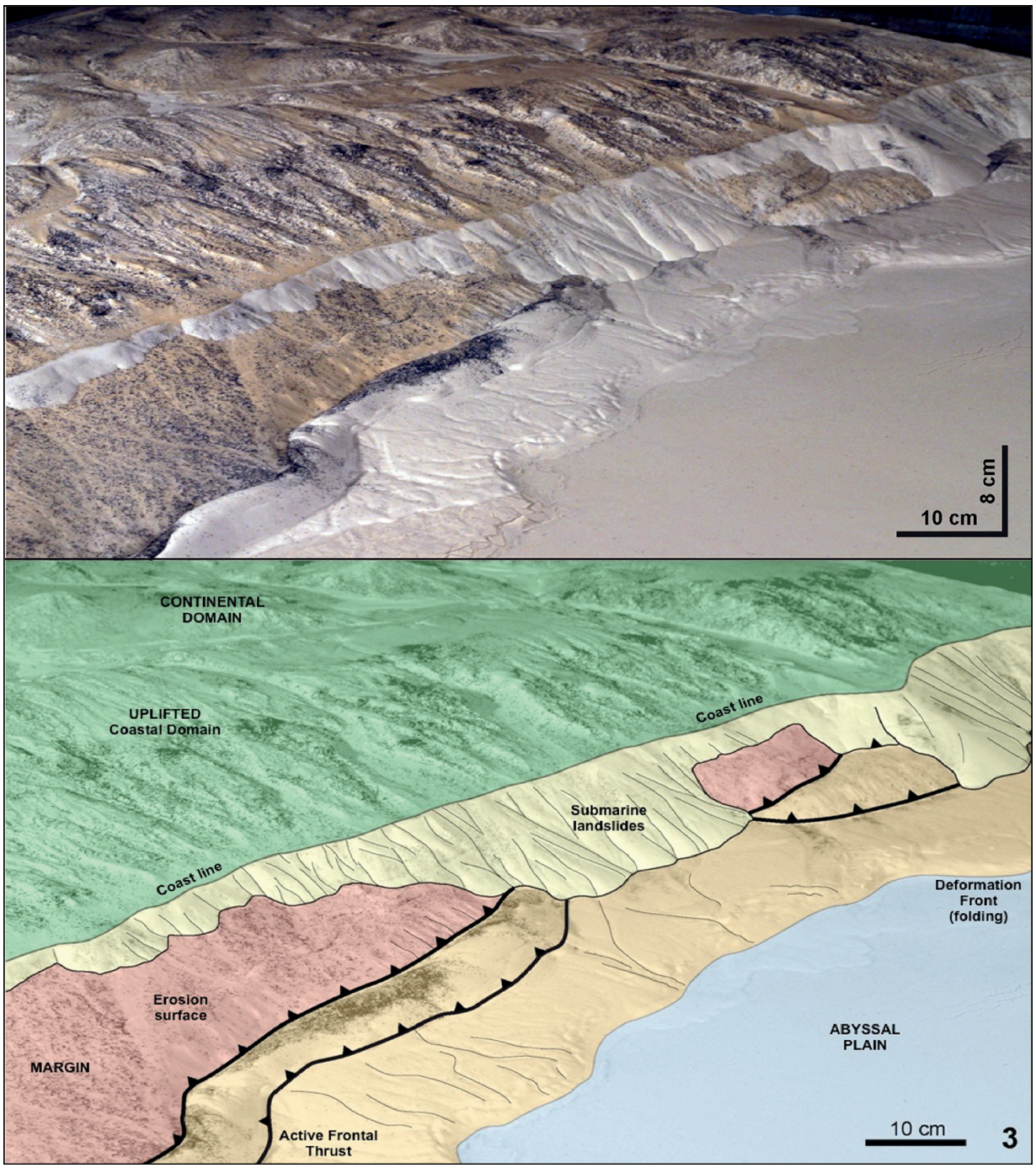

Fig. 3.: Example of the final stage (water has been removed) of a morphotectonic analog experiment simulating the Plio-Quaternary morpho-tectonic evolution of the Algerian margin. Hemipelagic (and pelagic) sedimentation was not simulated, only terrigenous sedimentation (sediments transported from land to the ocean by rivers) were modeled

Fold growth rates in 3D buckle folds

Marcel Frehner[1]

[1] *Geological Institute, ETH Zurich, Switzerland*
e-mail: *marcel.frehner@erdw.ethz.ch*
session: *Tectonics and Surface Processes*

Summary: Geological folds are inherently 3D structures; therefore they also grow in three dimensions. Here, fold growth in all three dimensions is quantified by numerically simulating upright single-layer folds in 3D Newtonian media. Horizontal uniaxial shortening leads to a buckling instability, which grows from a point-like initial perturbation in all three dimensions by fold amplification (vertical), fold elongation (parallel to fold axis), and sequential fold growth (parallel to shortening direction) The two lateral directions exhibit similar averaged growth rates leading to bulk fold structures with aspect ratios close to 1. However, fold elongation is continuous with increasing bulk shortening, while sequential fold growth exhibits jumps whenever a new sequential fold appears. Compared to the two lateral growth directions, fold amplification exhibits a slightly higher growth rate.

Introduction

Geological folds are important natural features for structural geologists. In the field, the orientation and geometry of small-scale folds in the three-dimensional (3D) space helps identify larger-scale structures not visible in one single outcrop. Fold structures also provide an essential basis for tectonic interpretations, for example for estimating tectonic shortening directions. Equally important, the wavelength, the arclength, and the overall geometry of a fold are functions of the rheological parameters of a folded rock layer and its surrounding matrix. Therefore, analyzing the shape of a fold can reveal information about the rheological properties of the involved rocks (Huddleston and Treagus, 2010).

The fold shape that can be observed in the field is a result of the fold growth history. Therefore, it is essential to not only describe the fold shape but also to understand the process of fold growth. Geological folds are inherently 3D structures; hence their growth also needs to be studied in 3D.

Definitions of 3D fold growth

To avoid confusion, the following terminology for fold growth in 3D is used here, using the coordinate system defined in Figure 1:

- Fold amplification (growth in z-direction) describes the growth from a fold shape with low limb-dip angle to a shape with larger limb-dip angle.
- Fold elongation (growth in y-direction) is parallel to the fold axis and describes the growth from a dome-shaped (3D) structure to a more cylindrical fold (2D).
- Sequential fold growth (growth in x-direction) is parallel to the shortening direction and describes the growth of additional folds adjacent to the initial isolated fold. The initial fold is termed 0th sequential fold; later grown folds are numbered consecutively.

Here, lateral fold growth is used as an umbrella term for both fold elongation and sequential fold growth.

Aim of this study

Existing studies do not quantify all three growth directions at once. Analytical solutions for 3D

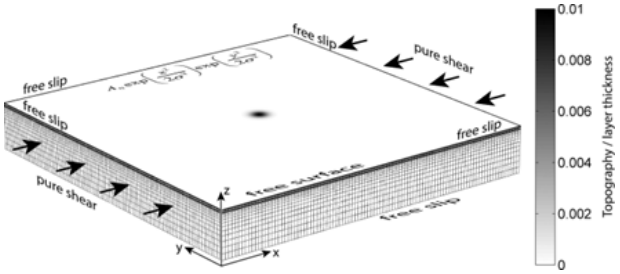

Fig. 1.: Initial numerical model grid, boundary conditions, and coordinate system for studying 3D fold growth. Gray values on the top interface represent the initial topography (equation given in the figure), normalized by the thickness of the top layer. Arrows indicate the pure-shear shortening boundary condition.

folding (e.g., Fletcher, 1991) neglect the two lateral growth rates because a periodic initial perturbation is assumed. The few numerical 3D folding studies (e.g., Schmid et al., 2008) do not quantify fold growth, but rather investigate one specific 3D phenomenon (e.g., linkage). The aim of the presented study is to numerically simulate simplified test cases of 3D folding and to quantify fold growth in all three dimensions to better understand the first-order relationships between the different growth directions.

Model and Methods

3D buckle folding is assumed to be a slow flow process governed by Newtonian rheology. The self-developed finite-element (FE) code solving the corresponding continuum mechanics equations is a 3D version of the code tested and used in Frehner and Schmalholz (2006) and Frehner (2011). The model (Figure 1) consists of a higher-viscosity layer (thickness H_L=1) on top of a lower-viscosity layer (thickness H_M»H_L) with viscosity ratio R. The model has a free surface and is compressed horizontally in x-direction with a constant shortening strain rate, D_{xx}<0. This corresponds, for example, to pure-shear analog models with lubricated base and side walls or to fold belts, where flow parallel to the fold axes is prohibited.

To allow a mechanical folding instability to develop, a point-like initial perturbation is added to the bottom and top interfaces of the upper layer corresponding to a two-dimensional Gaussian (equation given in Figure 1; A_0=0.01). The effective initial wavelength of the Gaussian is defined as

$$\lambda_0^{eff} = 2 \times FWHM = 2 \times \sqrt{8ln(2)\sigma} \qquad (1)$$

The full width at half maximum (FWHM) corresponds to the circle diameter in the x-y-plane, within which the initial perturbation is larger than $A_0/2$ (i.e., half maximum).

During the FE-simulations, the bulk amplitudes (or extent) of the fold structure in all three coordinate directions are calculated based on the folded upper surface of the model:

- Amplitude in z-direction:

$$A_z = z\Big|_{x=0,y=0} - z_{ref} \qquad (2)$$

- Amplitude in y-direction:

$$A_y = max(y) \text{ where } z\Big|_{x=0} - z_{ref} = \frac{A_0}{2} \qquad (3)$$

- Amplitude in x-direction:

$$A_x = max(x) \text{ where } z\Big|_{y=0} - z_{ref} = \frac{A_0}{2} \qquad (4)$$

The reference topography, z_{ref}, is the average of the upper model surface. In Figure 2, A_z corresponds to the color in the model center and A_y and A_x correspond to half the extent of the central contour line in y-direction and to half the maximal extent of all contour lines in x-direction, respectively.

Exponential growth is assumed in all three directions. Taking into account the shortening and extension directions, the exponential bulk amplitude evolution laws are (t is time):

- Exponential growth in z-direction:

$$A_z = A_z\Big|_{t=0} exp[-(q_z+1)D_{xx}t] \qquad (5)$$

- Exponential growth in y-direction:

$$A_y = A_y\Big|_{t=0} exp[-q_y D_{xx}t] \qquad (6)$$

- Exponential growth in x-direction:

$$A_x = A_x\Big|_{t=0} exp[-(q_x - 1)D_{xx}t] \qquad (7)$$

Equations (2)–(7) are valid for the fold structure as a whole (bulk values). Similarly, amplitudes can be calculated for each individual sequential syn- and antiform. The amplitudes in z- and y-direction of the initial (or 0^{th} sequential) fold are equal to the bulk amplitudes.

Results and Interpretations

As an example, the simulation with viscosity ratio R=100 and initial perturbation σ=6 (Figure 1) is shown and discussed below.

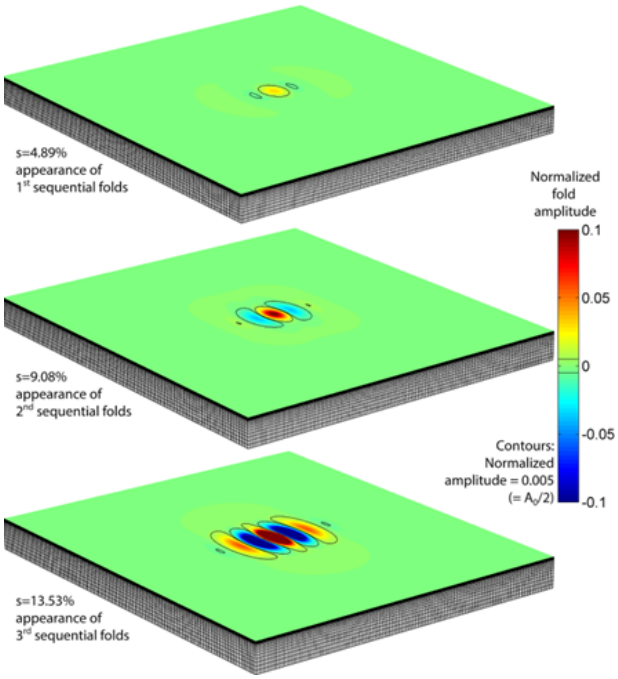

Fig. 2.: Snapshots of a typical FE-simulation showing the evolution of the 3D fold structure with increasing background shortening, s. The fold amplitude (z-direction) is normalized by the thickness of the top layer; black lines are contour lines of the normalized fold amplitude equal to half the initial value (0.005). The maximum extent in x- and y-direction of these contour lines is used to calculate the fold amplitude in x- and y-direction (Equations (5) and (4)). Parameters for this simulation are: R=100 and σ=6.

Fold shape evolution and individual folds

Figure 2 shows snapshots of the evolving fold structure with increasing background shortening ($s = 1^{\smile} exp(D_{xx}t)$). The fold grows in all three dimensions. Fold amplification (z-direction) is evident from the increasing topography (indicated by colors); fold elongation (y-direction) is evident from the elongation of the $A_0/2$ topographic contour line in the model center; sequential fold growth (x-direction) is evident from the sequential appearance of new $A_0/2$ topographic contour lines.

The initial isolated fold starts with normalized amplitudes, aspect ratio, and amplitude ratios all equal to 1 (Figure 3), which represents the initial condition of the simulation. Both the z- and y-amplitudes of the individual folds increase with increasing shortening. At the same time, growth in x-direction of the individual folds is limited to an x-amplitude of around 1 (Figure 3a) showing that the fold structure as a whole grows in x-direction by sequential folding, and not by the growth of one individual anti- or synform. The combination of the two lateral growths leads to an increasing aspect ratio of the initial isolated fold (Figure 3b). New sequential folds appear already with an elevated aspect ratio and continue elongating with further shortening (see also Figure 2). Generally, fold amplitude ratios with the z-amplitude as the denominator (Figure 3c) decrease with increasing shortening, indicating that fold growth in z-direction exhibits a higher rate than the two lateral directions.

Bulk fold amplitudes and growth rates in 3D

Figure 3 also shows the data for the bulk fold structure (thick lines). The bulk amplitudes in z- and y-direction are equal to the amplitudes of the initial isolated fold and increases continuously with increasing shortening. Growth of the fold structure in x-direction (Figure 3a) is marked by sudden jumps every time a new sequential fold appears. Despite these jumps, the average amplitude in x-direction is of the same order as

in y-direction leading to an almost constant bulk fold aspect ratio of around 1 (Figure 3b). Such equal growth in both lateral directions also occurs when using different parameter combinations and seems to be a universal feature of 3D fold growth. However, these two lateral growths exhibit a lower rate compared to fold amplification (growth in z-direction) leading to fold amplitude ratios clearly below 1 (Figure 3c). This is also the case for the other tested parameter combinations.

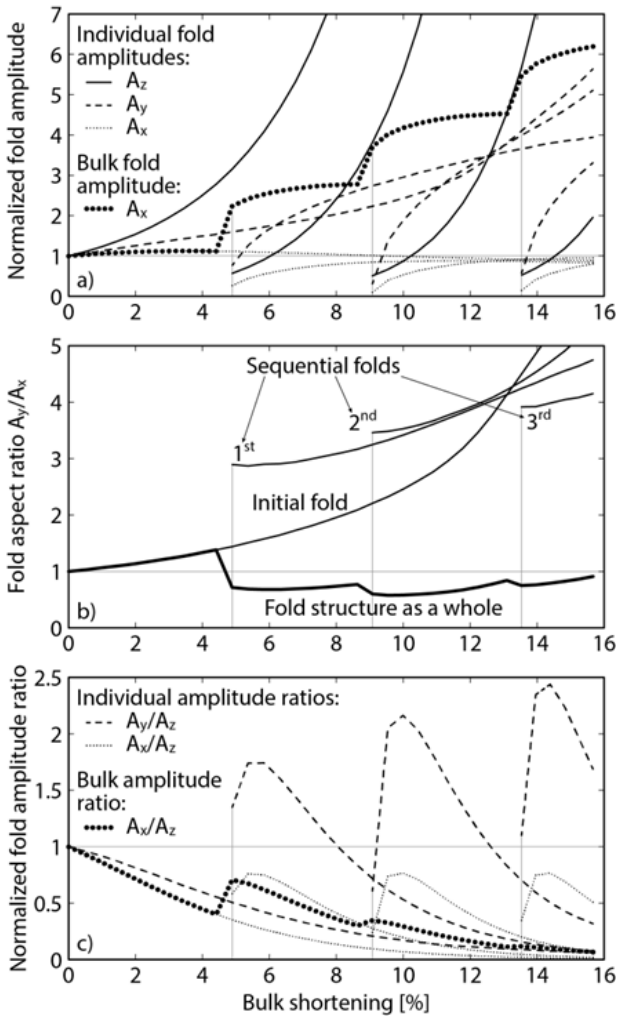

Fig. 3.: Fold amplitude (a), fold aspect ratio in the x-y-plane (b), and fold amplitude ratio (c) with increasing shortening for the individual sequential folds (individual anti- and synforms; thin lines) and the bulk fold structure (thick lines) for the same simulation as in Figure 2. The bulk fold amplitudes in z- and y-direction are equal to the individual fold amplitudes of the initial fold. All values are normalized by the initial amplitude in each corresponding direction. b) and c) are derived from a). Vertical gray lines indicate the first appearance of sequential folds.

Applying Equations (5)–(7) to the amplitude data in Figure 3a, the fold growth rates in all three directions can be calculated (Figure 4). The fold amplification rate (z-direction) increases slightly (from ∼19–25) with increasing shortening (Figure 4a), while the fold elongation rate (y-direction) stays roughly constant at a value of around 10. The sequential fold growth rate (x-direction) exhibits sharp jumps when new sequential folds appear. In the long term, both lateral fold growth rates are similar, represented by a lateral growth rate ratio close to 1 (Figure 4b), and about half of the fold amplification rate (growth rate ratio around 0.5; Figure 4b). This general relationship between the different fold growth rates also occurs for all other tested parameter combinations.

Discussion

Recently, interest in the lateral growth and linkage process of natural folds has been renewed by the oil- and gas-industry because it can lead to compartmentalization of structurally controlled reservoirs within an anticline. Previous studies only considered fold elongation to explain the linkage process (Bretis et al., 2011; Grasemann and Schmalholz, 2012), without including the second lateral growth direction (sequential fold growth). However, this study demonstrates that both lateral growth directions are equally important. In case two initially isolated fold structures grow in all three directions, the initial fold of one structure (0^{th} sequential fold) may well link with the 1^{st} sequential fold of the second structure. Grasemann and Schmalholz (2012) termed this scenario *no linkage*, yet it is equally important for understanding linked bulk fold structures and the term *1st order linkage* is proposed here. Accordingly, Grasemann and Schmalholz (2012)'s *linear linkage* and *oblique linkage* scenarios (linkage of two initial folds) are categorized as *0th*

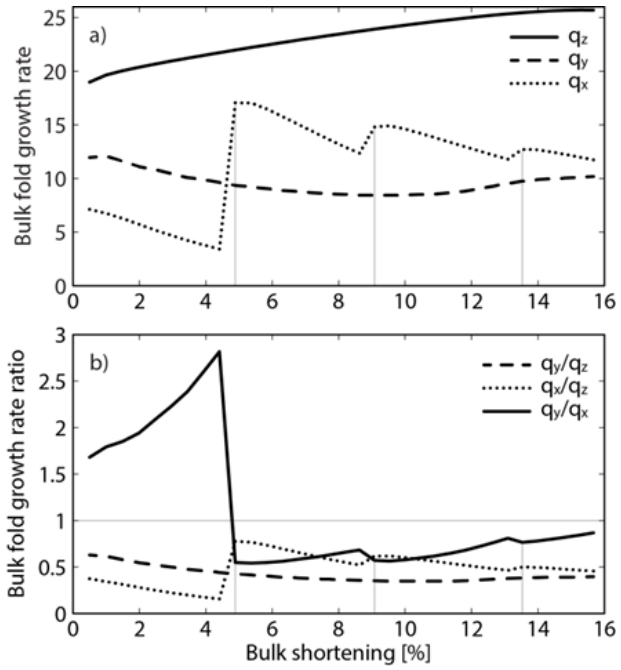

Fig. 4.: Fold growth rates (a) and ratio between fold growth rates (b) for the bulk fold structure with increasing shortening for the same simulation as in Figure 2 and 4. (a) is derived by applying Equations (6)–(8) to data shown in Figure 3a. (b) is derived from (a). Vertical gray lines indicate the first appearance of sequential folds.

order linkage.

The numerical simulations represent simplified test cases in that they only comprise a two-layer system, linear viscous (Newtonian) rheology, and no erosion at the upper surface. Therefore, the modeled geometries may not be translated one-to-one to natural fold structures. However, the aim of these simulations is to demonstrate first-order phenomena of 3D fold growth. The general result of almost equal fold growth rates in both lateral directions (fold elongation and sequential fold growth) and slightly larger fold growth rate in vertical direction (fold amplification) is expected to still hold in more realistic modeling scenarios or natural situations.

Conclusions

Numerical 3D folding simulations using a range of parameter combinations demonstrated that a fold structure grows in the two lateral directions with similar rates while the fold amplification rate is slightly higher. Such growth behavior results in fold structures that hardly change their bulk aspect ratio with increasing shortening. If a fold structure originates from an isolated perturbation (e.g., diapir) its aspect ratio remains roughly 1:1; if a fold structure originates from a line perturbation (e.g., fault) its aspect ratio remains large. However, large-aspect ratio fold structures can also be formed by linkage of two or more individual fold structures. Thereby, higher-order linkage (linkage between sequential folds of different order) is equally important as 0^{th} order linkage because of the equal fold growth rates in the two lateral directions.

Acknowledgements

Discussions with Neil Mancktelow and Naiara Fernandez are greatly acknowledged. This work has been supported by the ETH Zurich, Switzerland.

References

Bretis, B., Bartl, N. and Grasemann, B., 2011. Lateral fold growth and linkage in the Zagros fold and thrust belt (Kurdistan, NE Iraq). Basin Research, 23, 615–630.

Fletcher, R.C., 1991. Three-dimensional folding of an embedded viscous layer in pure shear. Journal of Structural Geology, 13, 87–96.

Frehner, M., 2011. The neutral lines in buckle folds. Journal of Structural Geology, 33, 1501–1508.

Frehner, M. and Schmalholz, S.M., 2006. Numerical simulations of parasitic folding in multilayers. Journal of Structural Geology, 28, 1647–1657.

Grasemann, B. and Schmalholz, S.M., 2012. Lateral fold growth and fold linkage. Geology, 40, 1039–1042.

Hudleston, P.J. and Treagus, S.H., 2010. Information from folds: A review. Journal of Structural Geology, 32, 2042–2071.

Schmid, D.W., Dabrowski, M. and Krotkiewski, M., 2008. Evolution of large amplitude 3D fold patterns: A FEM study. Physics of the Earth and Planetary Interiors, 171, 400–408.

Furrow-and-ridge morphology on rockglaciers explained by gravity-driven buckle folding: A case study from the Murtèl rockglacier (Switzerland)

Marcel Frehner[1], Isabelle Gärtner-Roer[2], Anna H.M. Ling[1,2]

[1] *Geological Institute, ETH Zurich, Switzerland*
[2] *Department of Geography, University of Zurich, Switzerland*
e-mail: *marcel.frehner@erdw.ethz.ch*
session: *Tectonics and Surface Processes*

Summary: Our study promotes buckle folding as the dominant process for the formation of furrow-and-ridge morphology on rockglaciers. Applying analytical buckle folding expressions to a high-resolution digital elevation model of the Murtèl rockglacier allows us to estimate the viscosity ratio between the higher-viscous active layer and its almost pure ice substratum. Using these constraints in a dynamic finite-element model of viscous rockglacier flow reproduces all key natural observations of the furrow-and-ridge morphology.

Introduction

Rockglaciers often feature a prominent furrow-and-ridge morphology, for which the Murtèl rockglacier in Switzerland (Figure 1) is a spectacular example. Previous studies suggesting that a longitudinal compressive flow in the lower part of a rockglacier is responsible for these structures are based on qualitative descriptions and remained speculative.

Buckle folding is the mechanical response of a layered viscous material to shortening if the mechanical contrast between the layers is significant. The resulting buckle folds are common structures in rocks and are well-studied in field outcrops, experimentally, numerically, and mathematically.

We propose that gravity-driven buckle folding is also the main responsible process for the formation of the transverse furrow-and-ridge morphology on rockglaciers. In this cross-disciplinary study we use the buckle folding theory, which is well-established in the field of structural geology, and apply it to the field of rockglacier geomorphology.

Data and Methods

For building a representative model we require two key ingredients: accurate geometrical information and information on the material behavior (i.e., rheology). Both ingredients are elucidated below in two subchapters

Geometrical Information

We analyze the surface topography using a 1 m-resolution digital elevation model (DEM) based on low-altitude aerial photographs. The three-dimensional (3D) furrow-and-ridge morphology is evident when considering the 200 m-diameter differential elevation (diffDEM; Figure 1C). The average wavelength of the furrow-and-ridge structure is around 20 m; the average amplitude is around 2 m.

Borehole deformation measurements (Arenson et al., 2002) demonstrate that the lower part of the Murtèl rockglacier is immobile and detached from the upper 30 m by a discrete shear zone. Borehole image logs and integrated interpretations of geoelectric, seismic, and georadar data

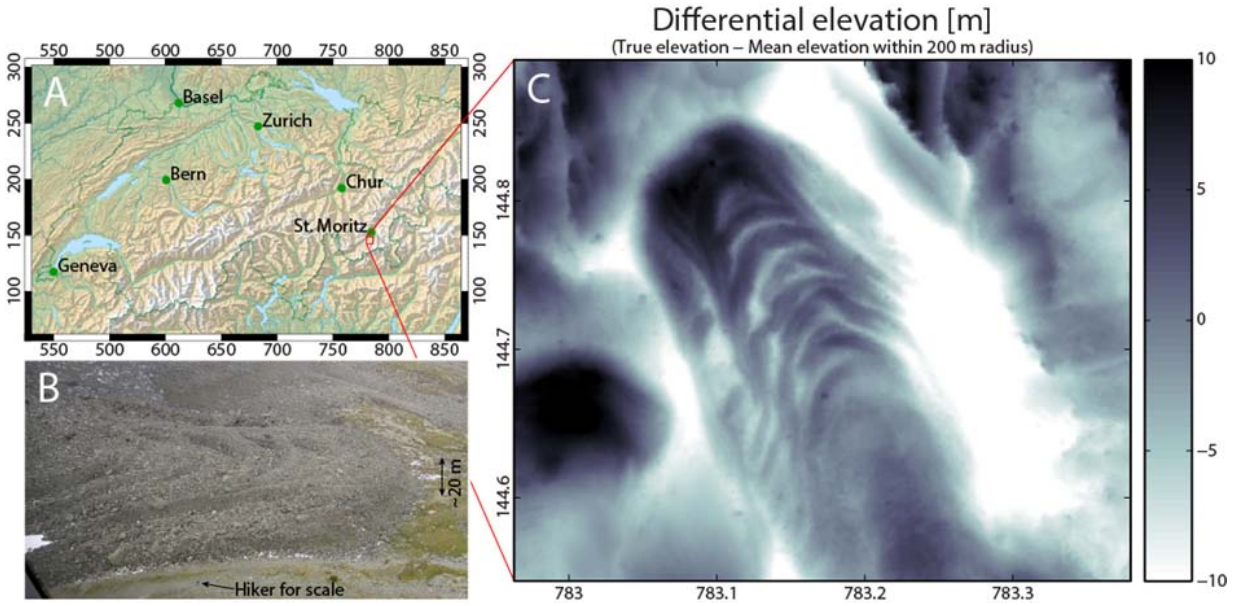

Fig. 1.: Location (A; source Swiss Federal Office of Topography) and surface structure (B, C) of the Murtèl rockglacier in Switzerland. The differential elevation is calculated as the true elevation minus the mean elevation within a 200 m diameter circle. The employed 1 m-resolution DEM is based on photogrammetry. Coordinates in Swiss coordinate system CH1903.

(Maurer and Hauck, 2007) suggest that the upper part is relatively homogeneous and consists of almost pure ice. The top-most active layer is 3–5 m thick and is a mixture of ice and rock fragments with sizes from sand to boulders (Figure 1B), which freezes and unfreezes during the course of a year. Kääb et al. (1998) speculated that the thickness of the active layer below ridges is larger than below furrows.

Based on this geometrical information we approximate the Murtèl rockglacier as a two-layer system consisting of a lower 27 m thick layer and an upper 3–5 m thick layer. Both layers are assumed to obey a viscous flow law, the upper exhibiting a higher viscosity because of its rock fragment content. We consider the part below 30 m not important for the formation of furrows and ridges and we neglect it.

Rheological information

Borehole deformation experiments (Arenson et al., 2002) demonstrate that the shear zone at 30 m depth accommodates 60% of the total deformation. The parabolic flow profiles above the shear zone can be approximated using a viscous flow law. For the active layer it is not possible to determine the power-law exponent, first because it is a complex mixture of ice and rock fragments and second because the borehole data is too sparse in this layer. Hence, we treat both layers as Newtonian (linear viscous) materials. This assumption has the advantage that the modeled deformation does not depend on strain rate and on absolute viscosity values, but only on the viscosity ratio.

To determine the viscosity ratio, R, we assume that the furrow-and-ridge morphology is a result of viscous buckle folding. The Fold Geometry Toolbox (FGT; Adamuszek et al., 2011) automatically analyzes the geometry of a folded layer and applies various buckle folding theories to determine the viscosity ratio between the folded layer and its surrounding. We feed the FGT with longitudinal sections of the furrow-and-ridge geometry derived from the diffDEM (Figure 1C). We vary the thickness of the active layer (3–5 m; Figure 2A) according to its uncertainty and also use a non-constant thickness (Kääb et al.,

1998). The FGT yields viscosity ratios of R=9–21 depending on the input model (Figure 2B).

Numerical Finite-Element Modeling

Based on the above geometrical and rheological analysis we designed a finite-element (FE) model (Figure 3B) to simulate rockglacier flow under the effect of gravity. The model solves the governing force balance and rheological (Newtonian) equations in 2D (details in Frehner, 2011; Frehner et al., 2012). For the Murtèl rockglacier the 2D approximation is justified because of its straight tongue-like geometry and unidirectional flow field (Kääb et al., 1998). The initial model surface is randomly disturbed (Figure 3A), representing natural irregularities of rock fragments and boulders, but also allowing the mechanical buckling instability to initialize.

Results

Figure 3C and 4A show the initial model state. Because we only consider the viscosity ratio, calculated stresses cannot be taken as absolute stress levels. The active layer exhibits layer-parallel compression towards the rockglacier toe, which is also reflected by the orientation of the most compressive stress parallel to the layer. Immediately below the active layer, compression is much smaller but still layer-parallel. These discontinuous stresses across the layer interface drive the buckling instability.

For further analysis we focus on the rockglacier toe (Figure 4), where active buckling takes place. The modeled buckle folds develop self-consistently with a wavelength of around 20 m. Around 150 m from the rockglacier front, compression in the active layer is largest; hence buckle folds develop the fastest. Further towards the front, buckle folds still develop, but at a lower rate. This is directly comparable to the Murtèl rockglacier (Figure 1C). The amplitudes in Figure 4C of about 2 m are comparable to the present-day amplitudes on the Murtèl rockglacier; hence, Figure 4C represents today's situation while Figure 4B represents an earlier situation.

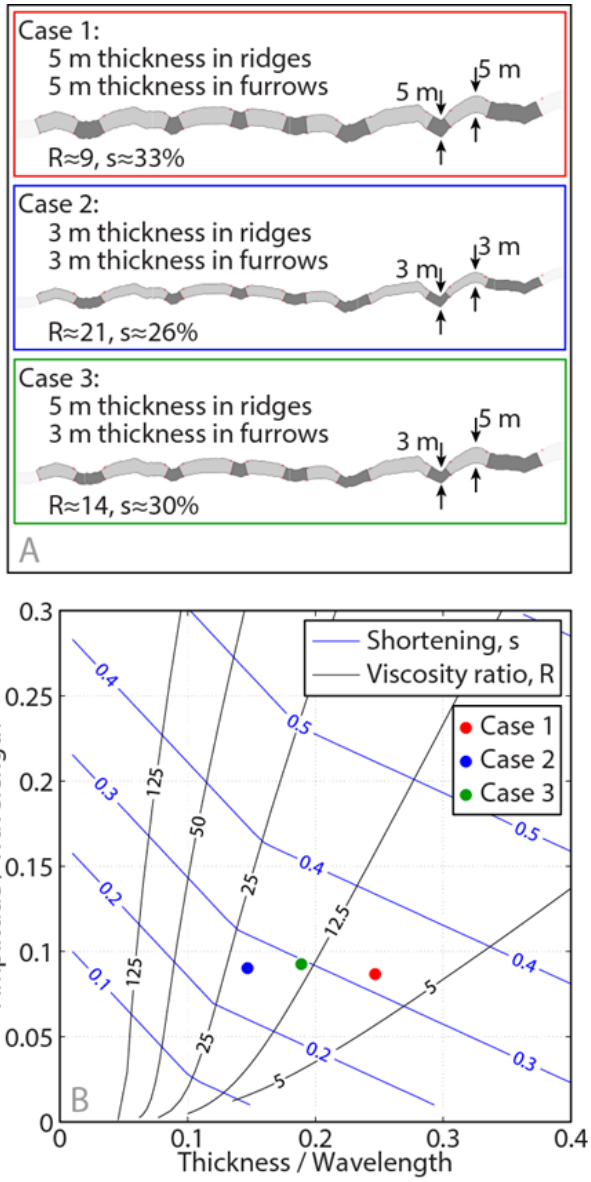

Fig. 2.: Geometrical and rheological information of the Murtèl rockglacier (modified screenshots from the FGT). A: Different input models using different layer thicknesses of the active layer. Gray shades: furrows and ridges as identified by the FGT. B: Resulting fold amplitude-to-wavelength and thickness-to-wavelength ratios with overlain shortening and viscosity ratio contour lines.

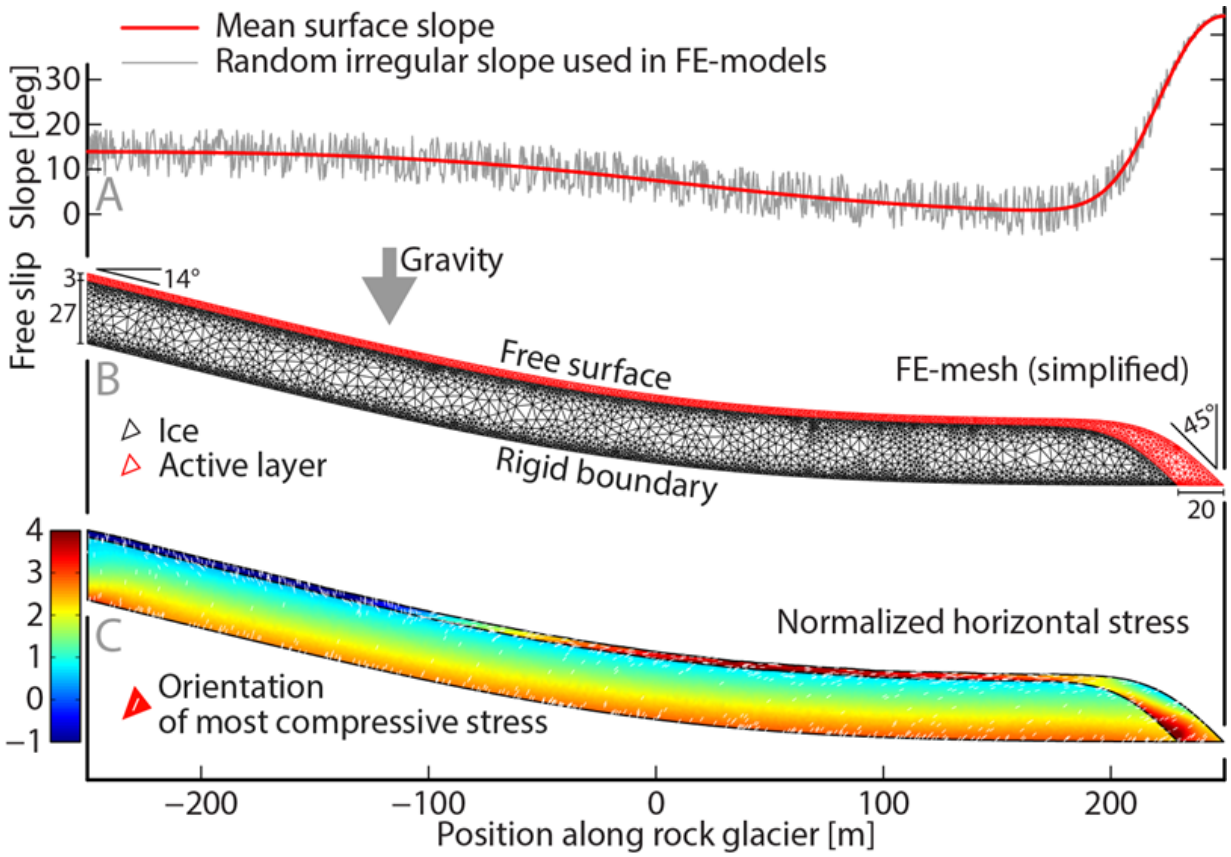

Fig. 3.: Initial and boundary conditions of the FE model, which is inspired by the Murtèl rockglacier. The numerical mesh (B) is simplified because the real mesh is too dense to be depicted. C shows the initial normalized horizontal stress (positive = compression) and the orientation of the most compressive stress as white lines.

Figure 4D shows the modeled borehole deformation (colored lines) from the surface down to 5 m above the fixed model bottom. The deformation of all boreholes and for both time intervals exhibits the typical parabolic shape, confirming the viscous flow profile within the rockglacier. The developing buckle folds disturb this otherwise smooth deformation profile in the active layer. Naturally, data measured on the Murtèl rockglacier (gray lines) show more variations. However, on average the deformation profiles are also parabolic and disturbed in the active layer. Hence, the modeled borehole deformation profiles can be directly compared to the real data.

Discussion

Because we do not accurately describe the shear zone, our FE simulation only accounts for 40% of the total deformation. Borehole deformation data and photogrammetric and terrestrial geodetic surveys yield surface velocities of the Murtèl rockglacier of 5 (Kääb et al., 1998) to 6 cm a–1 (Arenson et al., 2002; Müller et al., 2014). With 40% of this surface velocity, 625–950 years are necessary to reach the modeled surface displacement of 15–19 m (Figure 4D). While the natural 3D deformation (compared to the 2D model) may not significantly alter the deformation geometry, it does affect the rate of deformation. The curved furrows and ridges (Figure 1C) indicate a viscous flow pattern also in map-view resembling an open-channel flow. We estimate the velocity re-

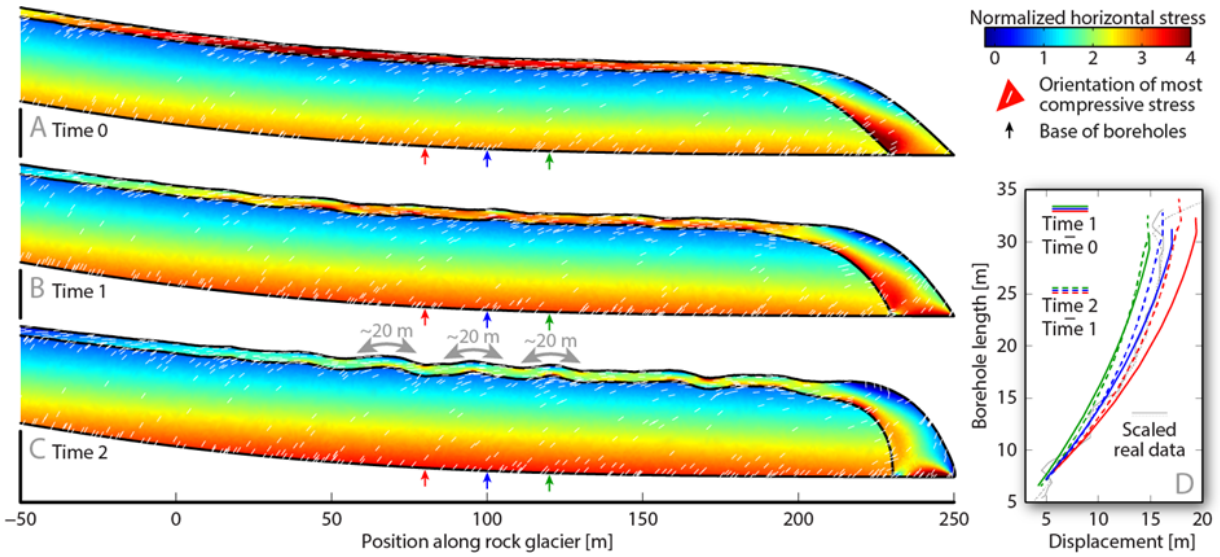

Fig. 4.: Snapshots at three different times (Times 0–2) of the rockglacier toe. D shows the modeled borehole deformation between Times 0 and 1 and between Times 1 and 2 at locations indicated in A–C. The two gray lines correspond to the borehole deformation data of Arenson et al. (2002) measured on the Murtèl rockglacier in a similar location.

duction in such a 3D flow to about 35% compared to our modeled 2D flow. Hence, the estimated time to develop the furrows and ridges extends to 960–1460 years. Time 1 in Figure 4 corresponds to 480–730 years and Time 2 corresponds to 960–1460 years after the initial state (Time 0).

Conclusions

Using the Murtèl rockglacier as an example, we promote gravity-driven viscous buckle folding as the dominant process explaining the furrow-and-ridge morphology characteristic for many rockglaciers. Buckle folding requires two main ingredients: mechanical layering and layer-parallel compression. In rockglaciers, the first is due to a layered ratio between ice and rock fragments. The second is due to the convex curvature of a rockglacier towards it toe. The associated slow-down leads to a compressive flow where curvature is largest. Our dynamical gravity-driven FE-model explains several first-order features of the Murtèl rockglacier: the amplitudes and wavelengths of the furrow-and-ridge morphology, the location of the largest-amplitude structures, and the parabolic flow profiles measured in boreholes. We estimate the time necessary to develop a furrow-and-ridge morphology as observed on the Murtèl rockglacier to be less than 1500 years.

References

Adamuszek, M., Schmid, D.W, and Dabrowski, M., 2011: Fold geometry toolbox – automated determination of fold shape, shortening, and material properties, Journal of Structural Geology, 33, 1406–1416.

Arenson, L., Hoelzle, M., and Springman, S., 2002: Borehole deformation measurements and internal structure of some rock glaciers in Switzerland, Permafrost and Periglacial Processes, 13, 117–135.

Frehner, M., 2011: The neutral lines in buckle folds, Journal of Structural Geology, 33, 1501–1508.

Frehner, M., Reif, D., and Grasemann, B., 2012: Mechanical versus kinematical shortening reconstructions of the Zagros High Folded Zone

(Kurdistan Region of Iraq), Tectonics, 31, TC3002.

Kääb, A., Gudmundsson, G.H., and Hoelzle, M., 1998: Surface deformation of creeping mountain permafrost. Photogrammetric investigations on rock glacier Murtèl, Swiss Alps, Collection Nordicana, 55, 531–537.

Maurer, H. and Hauck, C., 2007: Instruments and methods geophysical imaging of alpine rock glaciers, Journal of Glaciology, 53, 110–120.

Müller, J., Gärtner-Roer, I., Kenner, R., Thee, P., and Marche, D. 2014: Sediment storage and transfer on a periglacial mountain slope (Corvatsch, Switzerland), Geomorphology, in press.

Structural evolution and structural style of South Eastern Kohat deciphered through 3D geoseismic model using MOVE software, Shakardarra area, KP Pakistan

Humaad Ghani[1], Hamid Hussain[1], Muhammad Zafar[1], Irum Khan[1], Aamir Malik[2], Muhammad Abid[1], Ehtisham Javed[1]

[1] *Department of Earth & Environmental Science, Bahria University Islamabad*
[2] *Landmark Resources (LMKR),Jinnah Avenue, Blue area, Islamabad*
e-mail: *humaad.ghani@bahria.edu.pk, hammadtanoli@gmail.com*
session: *Tectonics and Surface Processes*

Abstract: Geologically Shakardarra is evolved through multiple episodes of deformation. In the current research structural evolution of south eastern Kohat is shown through 3D geoseismic model. It is prepared by integrating surface structural geological data and subsurface seismic reflection data. At surface doubly plunging anticlines and synclines are evolved on evaporites as detachment folds truncated by thrust faults along their limbs. In subsurface stratigraphic packages are marked on seismic sections based on regional stratigraphic studies and dominant reflections. The seismic data shows the thrust faults emanates from basal detachment located at sedimentary crystalline interface cutting up section to surface or lose their displacement to splay or back thrusts. At surface Shakardarra fault, Tolabangi fault, Chorlaki fault and axial trend of fold changes their strike from EW to NS which narrates that thrust and axial trend of folds are rotated along vertical axis by influence of Kalabagh strike slip fault. The current research suggests that Shakardarra is sequentially evolved in three episodes of deformation. In the first phase detachment folds developed on Eocene evaporites which are truncated by thrust faults emanating from basal detachment in second phase. In the third phase early formed folds and faults are rotated along vertical axis by the influence of Kalabagh fault.

Keywords: Structural Evolution, Detachment, Thrusting

Introduction

The Kohat Fold and Thrust Belt (KFTB) also known as Kohat Pleatue is an integral part of Himalayan Fold and Thrust System located in the Sub Himalayas. The KFTB extends from Main Boundary Thrust (MBT) in the north (Sarwar et al., 1979, Yeats et al., 1984, Coward et al., 1985) to Surghar range in the south (Ahmed et al., 1999). It is separated from its eastern counterpart Potwar Fold and Thrust Belt (PFTB) by Indus River and its western boundary is marked by Kurram Fault (Kazmi and Rana 1982). The KFTB and PFTB in their evolution are genetically related to Himalayan induced deformation (Ahmed, 1995 Ali, 1995 McDougal &Hussain, 1991 Abbasi and McElroy, 1991) in general and transpressional tectonics (Pivnik & Sercombe.,1994) in particular. However, Structural complexity is more pronounced in KFTB and the difference in structural style is attributed to the nature of decollment at base and secondary levels and role of strike slip faulting (Ahmed, 1995 Ahmed 2003 Ali, 1995 Dougal &Hussain, 1991 Abbasi and McElroy, 1991 Pivnik & Sercombe, Chen and Khan, 2010 Khan et al, 2012). Shakardarra is present at boundary of KFTB and PFTB with

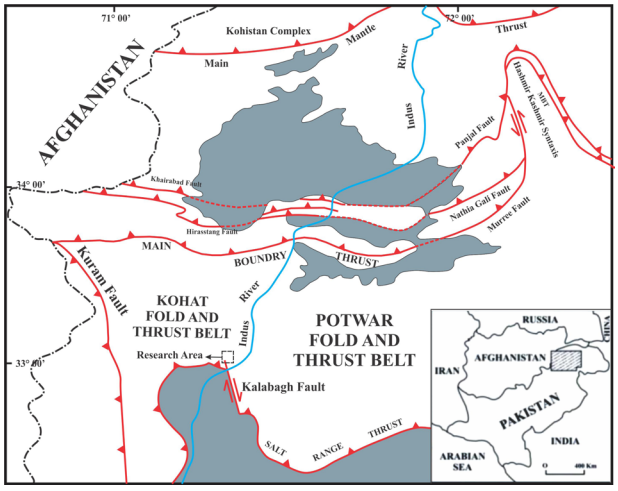

Fig. 1.: stratigraphic column of the study area

active Kalabagh strike slip present in south of it (figure 1). In the north of Shakardarra east-west trending structures change their orientation to north –south. The previous models (Abbasi., 1991, McDougall and Hussain., 1991) showed the lateral ramp in the subsurface causing the surface structures to change their orientation across it. Recent published work of (Khan et al 2012) on the nature and kinematics of Kalabagh fault shows its active nature and its presence as a lateral ramp in the northern part (Figure 1). The previous models developed had not taken the role of strike slip faulting in the deformational history as its presence in the near vicinity with still active nature cannot be avoided. The exposed structures at Shakardarra don't comply completely to the concept of lateral ramp. As the west vergence of thrust at the Hukni and continuation of these structures in north of Shakardarra with east-west trend are raising questions about the sole presence of lateral ramps in subsurface effecting the structures above.

Aim and Objectives

The aim of research is to understand structural evolution of the area in relation to fold and thrust kinematics and role of active strike slip faulting in reshaping the structures at surface and subsurface. The objectives are to prepare a 3 dimensional geoseismic model of the area to understand the genetic relationship between structures at surface and subsurface.

Methodology

Revised geological mapping of area at RF 1:50,000 by integrating published maps and field data. Seismic reflection data of 865-NK-02,05,08,11,15 are used for interpretation of subsurface structures, stratigraphy and depth to basement. Deformed geoseismic cross section are prepared by integrating surface geological, and seismic data in 2D move. 3D model is prepared in 3D move by integrating 2d cross sections, generating surfaces, ramps and fault planes to show the 3D structural geometries at surface and subsurface.

Stratigraphy and Tectonics

Kohat plateau is comprised of Eocene and younger sedimentary rocks and is located in the west of Potwar fold and Thrust belt. There are evaporates in the southern part of the plateau. In the northern region there are several thrust faults, synclinal folds and overturned folds. Low angle thrust faults are folded which are forming klippen. Evaporate sequence is missing or reduced in the northern part. Panobashales are present in the cores. There is E-W trending folds and reverse faults which are north and south dipping in the kohat plateau zone. Most of the faults are fault propagation folds. The Eocene sequence present in the Kohat plateau is very thick that is 300-500m. There are evaporates sequence in the central part of the Kohat plateau. The structures in the Shakardarra have an E-W orientation but it abruptly change direction E-W to N-S. Hukni fault which is a large thrust fault present in this area. (Figure 2)

Structural Geology

The structural geology of the research area is comprised of outcropping thrust faults and folds.

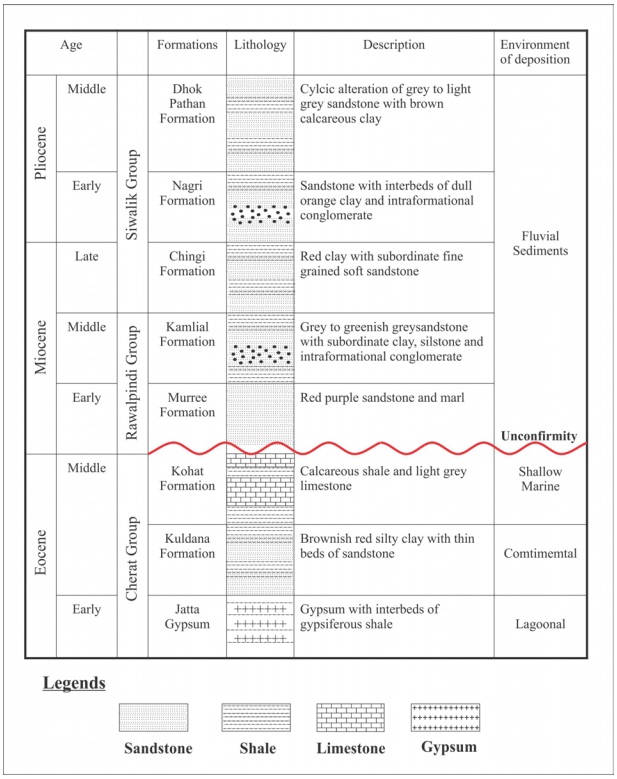

Fig. 2.: Tectonic map of northern Pakistan Showing major structural boundaries. The box shows the location of the project area

The general trend of the structures in the area is ENE-WNW. Fault bounded doubly plunging anticlines and broader synclines are present at the surface. Revised geological map of the area is prepared at 1:50,000 by integrating published geological map (Meissner,1974), and field orientation data (figure 3).

Seismic Interpretation

Seismic data is interpreted by solving velocity windows panels to obtain the average velocity. Time and depth of stratigraphic packages is calculated using these velocities.Eocene, Paleocene, Jurassic, Triassic and Permian Tops reflectors were marked. Basement was marked on 10 km by its presence as a prominent reflector on seismic lines. (Figure 4) It is also evident from previous research work ((Ahmed, 1995 Ahmed 2003 Ali, 1995 Dougal&Hussain, 1991 Abbasi and McElroy, 1991). Some outcropping faults are correlated to seismic shot point locations.

Cross sections

The cross sections are prepared manually by interpolation the surface geological data (contacts and orientations) and subsurface depth domain data of reflectors. The manually prepared reflectors are redrawn on 2D move software to maintain the accuracy for thickness of each horizon. Cross sections are later imported to Move for 3D model generation.

Section AB and CD

Both sections are north south orientated 17.5 km and 18.5 km in length.In north of section AB and CD, Nari banda fault (NRF), Bargazi banda fault (BBF) and Shakardarra fault (SF) are the thrust faults emanates from basal detachment to surface. Bab-e- Shakardarra fault (BSF) and two splay faults emanates at shallow depth in north and south of Shakaradarra fault. Eocene rocks are thrusted over younger rocks by these two thrust faults. In south of SF an open anticlinal and synclinal structure is transected by complex network of faults. In subsurface north facing thrust had uplifted the stratigraphic section toward north at deeper level. Tolabanghi khel fault and Chorlaki fault originates as south facing faults from north facing thrust at deeper level transects the limbs of folds. Triangular zones are formed at depth in between the opposite facing thrusts.

Section EF, GH, IJ & KL

Sections EF, GH and IJ are 27.1, 29.4 and 32.5 long orientated in NE-SW direction. Sections EF, GH, IJ are oriented oblique to the strikes of exposed structures, however section EF is east west oriented perpendicular to the strikes of structures. NRF is present in the EF section thrusting Eocene rocks over the Kamlial formation. SF is present in all sections thrusting Eocene rocks over the Kamlial and Nagri formations. NRF and SF

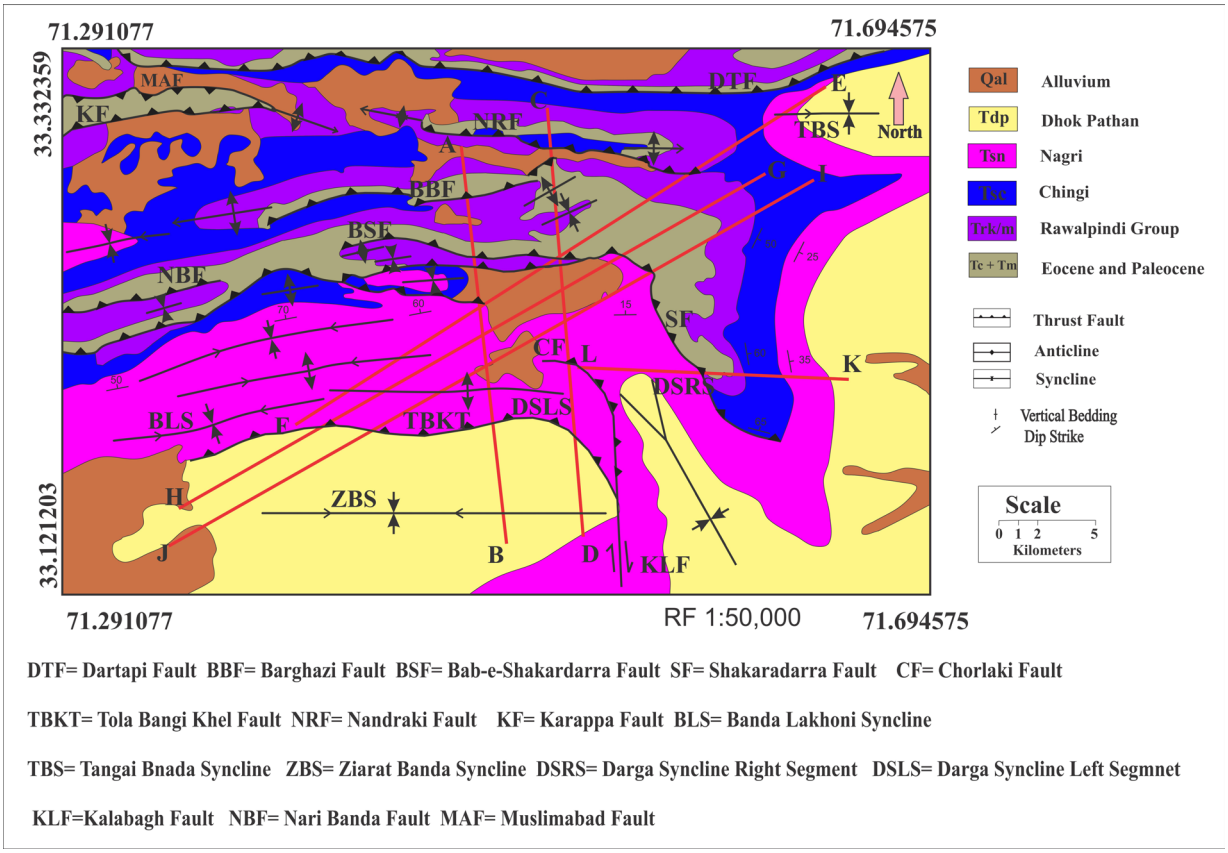

Fig. 3.: Tectonic map of northern Pakistan Showing major structural boundaries. The box shows the location of the project area

are cutting up section from basal detachments to surface. Tolabangi Khel fault in the sections GH and IJ is thrusting Nagri formation in the hanging wall over the Dhok Pathan formation in the foot wall. In subsurface Pop-up and triangle zones are present. In section KL steeply dipping Chorlaki fault (CF) is present with less stratigraphic throw. (Figure 5)

Discussion

Geologically Shakardarra is comprised of complex deformational structures, developed and modified by multiple deformational events. The structural models of area show the distribution of structures in 3 dimensional at surface and subsurface. Area is occupied by tight anticlinal structures in north and broader synclinal structures in south.The presence of Eocene Jatta gypsum in the core of anticlinal structures indicates that folds are formed as result of detachment folding on Eocene evaporites. The truncation of folds at limbs by faults narrates that faults are emplaced later in the deformational history of area than folds. The trends of folds axial traces and strikes of faults are ENE to WSW which indicates there development genetically linked to Himalayan induced deformation. The cross sections show that these faults are developed from basal detachment located at sedimentary crystalline interface. The cross section shows that back thrust are originated from fore-thrust at much shallower depths to achieve critical taper for initiation of fore thrust in south of it In the central portion of area south dipping blind thrust had uplifted the stratigraphic sequence northward in subsurface. TBKF and CF originate from these blind back thrusts cut up section to the surface. The faulting in the

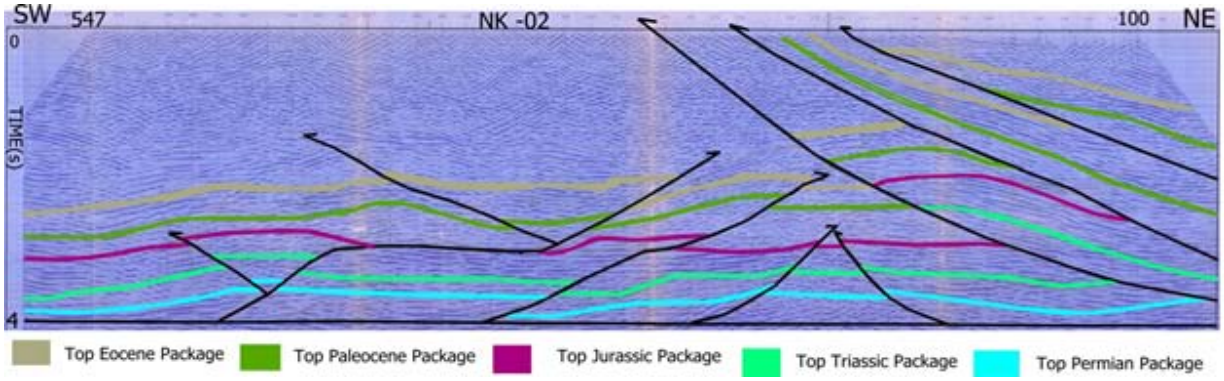

Fig. 4.: Interpreted Seismic Section 865-Nk-02

[!t]

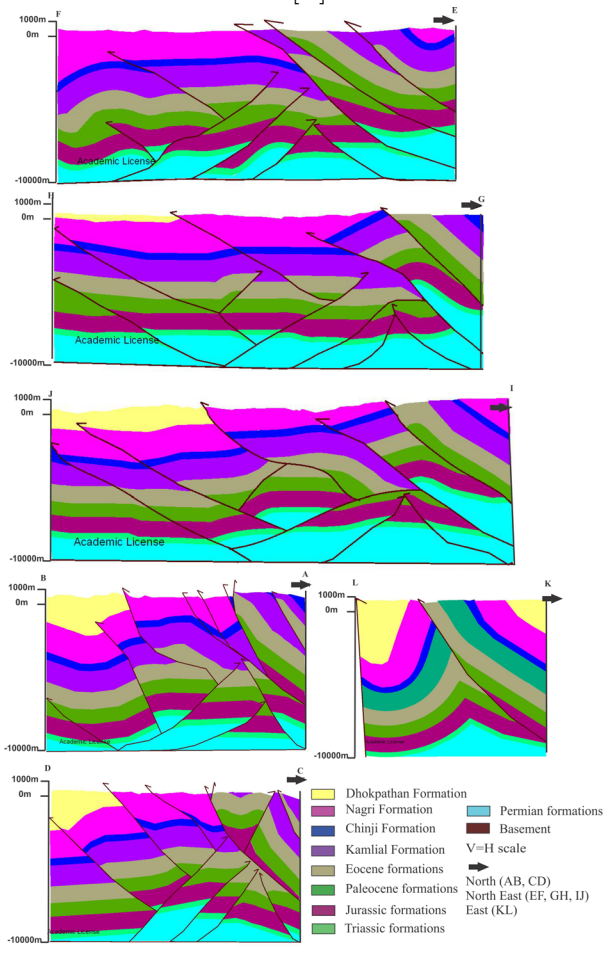

Fig. 5.: Geological Cross sections showing surface and subsurface geometries

central formation of study area is developed to achieve the critical taper for initiation of Surghar range frontal thrust in south of shakardarra. The structural geology of area in central portion is comprised of pop-up and triangle zone geometries in subsurface. The reservoirs formations of Jurassic age are structurally uplifted and transected by these faults forming the structures favorable for exploration of hydrocarbon. The change in orientation of Shakardarra fault, Tola bangi khail fault and Chorlaki fault from E-W to N-S in the eastern portion of area is strongly influenced by right lateral movement of Kalabagh fault present in south east of this area. Dominant flexure/bends in the strikes of Surghar range thrust in west of Kalabagh fault and Shakardarra fault in east represents that the early formed thrusts are rotated along the vertical axis of rotation related to kalabagh strike slip fault. The deformation related to Kalabagh strike slip fault had changed the orientation and dips of Nagri formation to vertical near the rotated fault plane of Chorlaki fault and Tola bangi khail fault. The research suggests that area is evolved sequentially in three episodes of deformation. In first phase of deformation folding is developed on Eocene evaporate horizons as detachment folds. In second phase of deformation thrusting from basal detachment had truncated the folded structures and elevated the whole stratigraphic sequence. In third phase of deformation early formed thrust faults are rotated from EW to NS by the influence of Kalabagh strike slip fault. (Figure 6)

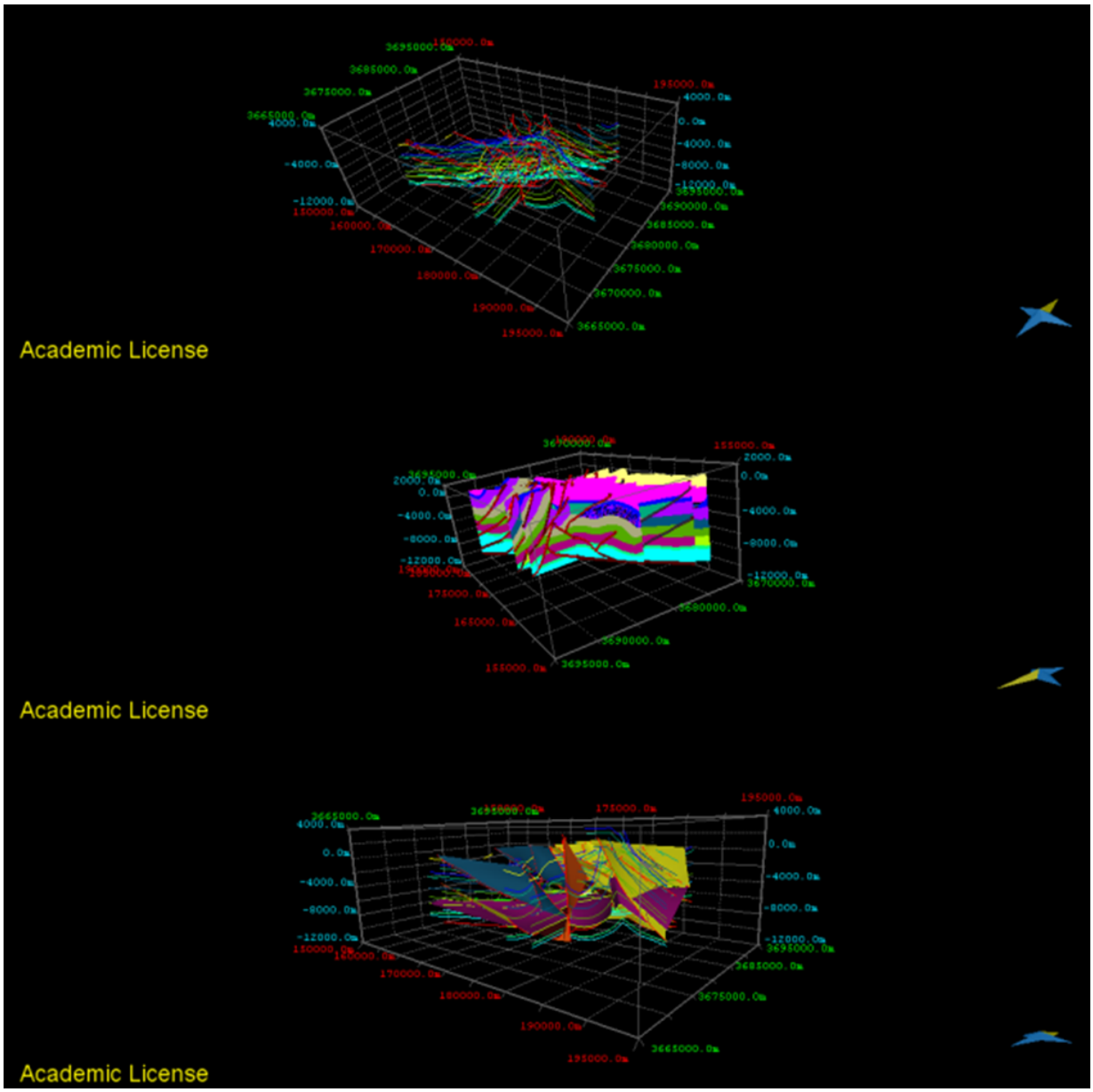

Fig. 6.: 3d models showing complete fault pattern and integration of 2d into 3d

Conclusions

The current research had concluded following points

1. Two distinctive detachment horizons are present in the subsurface at sedimentary crystalline interface and Eocene evaporates sequence.
2. The general trend of faults and folds is ENE-WSW which shows their genetic link to Himalayan induced deformation.
3. The truncations of fold limbs by faults indicate that faults are emplaced later in deformational history of area than folds.
4. The back thrusts in the area are developed to achieve the critical taper for initiation of fore thrust towards south.
5. The change in strikes of shakardarra fault, surghar range thrust, Tola bangikhel fault and chorlaki fault indicates that these early formed thrust are rotated along vertical axis by the influence of Kalabagh strike slip fault.
6. The area is evolved sequentially in three episodes of deformation, detachment folding followed by thrusting superimposed by strikeslip faulting.

References

Abbasi, I.A., and McElroy, R., 1991. Thrust kinematics in the Kohat Plateau, Trans Indus Range, and Pakistan J. Of Struct. Geol, Vol. 13, No. 3, p.319-327.

Ahmad, D., 1995. Tectonic analysis of Southern Kohat plateau, N.W.F.P., Unpublished M Phil thesis, NCEG, University of Peshawar.

Ahmed, S., 2003. A comparative study of structural styles in Kohat plateau, NW Himalayans, NWFP, Pakistan. PH.D thesis, NCEG, University of Peshawar.

Ahmed, S., Ali, F., Sayab, M., Ahmed, I., Hamidullah, S., 1999. Structural geometry of the Himalyan frontal Thrust zone: Surghar range, Pakistan. Geological Bulletin, University of Peshawar 32, 13-23

Ali, F., (1995). Imprints of transpressional deformation on southern Kohat Plateau, Karak area, NW Himalayas, NWFP, Pakistan. Geol. Bull. Univ. Peshawar, Vol.33, pp.87-95

Chen, L., Khan , S.D., 2010. InSAR observations of the strike slip faults in the NW Himalyan frontal Thrust system. Geosphere 6, 731-736.

Coward, M.p., Butler, R.W.H., 1985. Thrust Tectonic and the deep structure of the Pakistan Himalayan. Geology, 13:417-420

Khan, A. A., 1999. Structure and tectonic setup of the area, south and southwest of Kohat, N.W.F.P., Pakistan. Unpublished M.Phil thesis, NCE in Geology, University of Peshawar.92p.

Mc Dougal, J.W., and Hussain, A., 1991. Fold and thrust propagation in the western Himalaya based on a balanced cross section of the Surghar range and Kohat plateau, Pakistan. American association petroleum Geologists, bulletin, 75. 463-478.

Meissner, C. R., Master, J.M., Rashid, M.A. and Hussain M., 1974. Stratigraphy of Kohat quadrangle, Pakistan. United States Geological Survey professional paper, 716 D.

Pivnik, D.A., and Wells, N.A., 1996. The translation from Tethys to the Himalaya as recorded in Northwest Pakistan, Geological Society of America Bulletin, v.108, p.1295- 1311.

Sarwar, G and Dejong, K.A., 1979. Arcs, oroclines, syntaxes- the curvatures of Mountain Belts in Pakistan.

Yeats, R.S and Lawrence, R.d., 1984. Tectonics of the Himalayan thrust belt in northern Pakistan.

Lithospheric scale analogue models of the southern Gulf of California oblique rift

Diego Gracia-Marroquín[1], Rodrigo Portillo-Pineda[2], Mariano Cerca[3], Giacomo Corti[4]

[1]*Posgrado en Ciencias de la Tierra, Centro de Geociencias, Universidad Nacional Autónoma de México, Blvd. Juriquilla, 3001, 76230, Juriquilla, Querétaro, México*
[2]*PEMEX Exploración y Producción, Activo de Exploración de Cuencas del Sureste, Coordinación de Modelado Geológico Regional, Edificio Administrativo, primer piso ala poniente, Región Marina Sureste, Calle 33, 90, Colonia Burócratas, Ciudad del Carmen, Campeche C. P. 24179*
[3]*Laboratorio de Mecánica de Geosistemas, Centro de Geociencias, Universidad Nacional Autónoma de México, Blvd. Juriquilla, 3001, 76230, Juriquilla, Querétaro, México*
[4]*Consiglio Nazionale delle Ricerche (CNR), Istituto di Geoscienze e Georisorse, U.O. Firenze, Via G. La Pira, 4, 50121 Florence, Italy*
e-mail: *diegograciam@geociencias.unam.mx*
session: *Tectonics and Surface Processes*

Introduction

The rift of Gulf of California represents an exceptional case of oblique rifting where incipient seafloor spreading is occurring (Lizarralde et al., 2007; Sutherland et al., 2012). This rift is characterized by a dextral movement which has an angle of ∼20° between the transform zone in the center of the Gulf of California and the Baja California peninsula (Stock & Hodges, 1989; Fletcher et al., 2007). Analogue models reproducing oblique rifting, which is characterized by a relative displacement between two tectonic blocks with an angle with respect to the rift axis of less than 90° (Agostini et al., 2009; Autin et al., 2010), have found that, among other factors, the obliquity might be a consequence of the presence of a pre-existing oblique lithospheric weakness zone both in the crust and in the mantle. The influence of pre-existence weak zone is believed to help to localize the deformation causing rifting.

In order to investigate some aspects of the evolution of deformation of the GoC oblique rifting a series of astenospheric-scale analogue models were carried out. The experiments consider a central zone of weakened rheology. The objectives of this study are to analyze the geometry of fault patterns in the southern Gulf, to reproduce the deformation between Baja California (Baja) and Sierra Madre Occidental (SMO) blocks (figure 1), and finally to remark some similarities between model and the southern part of the Baja California rift.

Experimental Setup

The models were built at the Laboratorio de Modelado Analógico, Centro de Geociencias, UNAM. The suitability of cold lithosphere physical models for studying rifting has previously been tested by Autin et al. (2010). In our experiments, the model lithosphere consist of four layers: a) upper brittle crust, composed by a mixture of hollow and dense glass microspheres; b) lower ductile crust, made by mixing silicone, corundum sand, and plasticine (100:30:10); c) lithosphere mantle, composed by a mixture of silicone, dry quartz sand, and plasticine (80:100:25) and, d) the astenosphere, made by glycerin and gypsum. The materials flow curves and density were properly scaled with respect to natural values. The model lithosphere floats on the astenosphere,

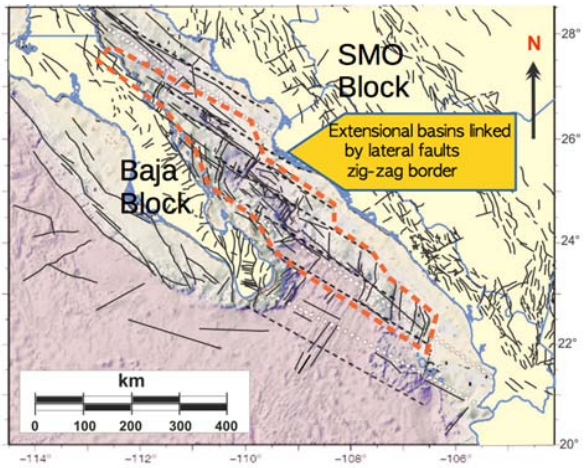

Fig. 1.: Geometry of fault patterns in the southern Gulf of California. The zone located in the central part of the GoC has a "zig-zag" geometry defined by normal and lateral faults, these features might have an influence on the faults observed in the edge of the Baja California and Sierra Madre blocks localizing deformation and forming border faults.

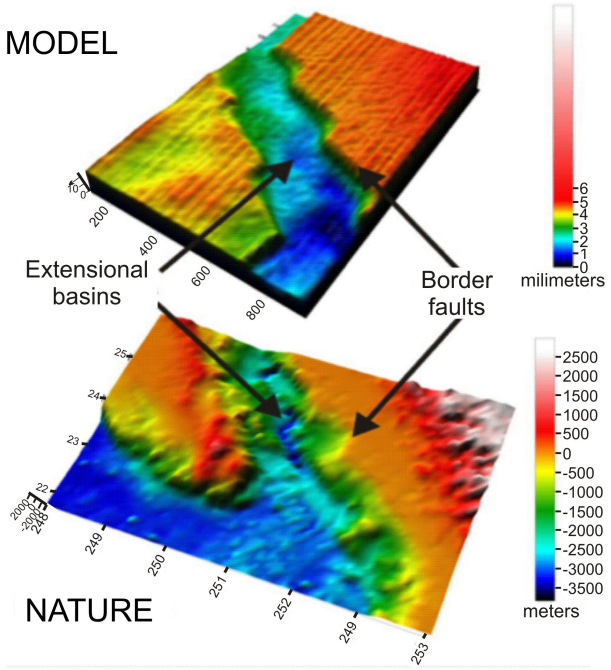

Fig. 2.: Digital elevations models of the experiment and the southern GoC.

which is a high density and high viscosity material. A weakness zone was built as a band in the middle of the model that corresponds to the position of the Gulf of California, reducing the viscous resistance of the lower crust and the lithosphere mantle by adding oleic acid (10%) to the mixtures.

The low resistance band divided the model into a fixed block (Mexico mainland) and a mobile block (Baja California) and they were built in a plexiglass box with dimensions 40x40 cm^2. The angle of the weak zone with respect to the direction of displacement was about 20°, corresponding to the angle among the proposed displacement of the Baja California Block with respect to the mean rift axis (e. g., Fletcher et al., 2007). Deformation of the experiments surface was recorded by plain view images and its digital topography was obtained by using the Zebra software.

Results

The model reproduces the general topographic features of the Gulf of California narrow rifting including the "zig-zag" geometry of the border faults and the individual extensional basins along the rift axis (Figure 2). In the analogue models it is not possible to reproduce the continental rupture and adding of material and thus is pertinent only for the pre-rupture Miocene to Pliocene (∼12 to 3 Ma) history of the rift. However, we consider that the geometry of the transform system in the gulf is a consequence of the progressive previous history and it does not alter the border faults geometry and the discussion about the location and migrations of the depocenters sustains. Our model focus in reproducing the geometry of the rift and does not consider the causes of such geometry. However, it has been suggested that the Gulf of California narrow rift evolution is the continuation of a long history (more than 30 Ma) of widespread extension in the western North American plate (Ferrari et al., 2013). A probable cause of the "zig-zag" geometry of the border faults and the presence of a weaker lithosphere localizing deformation is the rift segmentation that occurred in previous extension episodes (Axen, 1995). The conclusion is that the initial geometry of the bor-

der faults has an important influence leading to the geometry of the transform system after the continental rupture.

In Figure 3 we present the evolution of three topographic profiles with an orientation perpendicular to the experimental rift axis to visualize differences in the evolution of the rifting with extension. In the three cases, the model reproduces the observation of a westward migration of the extensional basins activity (Aragon-Arreola and Martin-Barajas, 2007).

The width of the extension zone confined within the weaker band is prescribed by the model set up but there are significative variations in the depocenter depths along the rift axis. Greater asymmetry is observed at the northern part of the model. Extension localizes initially at the SMO block and progressively migrates to be closer to the Baja block. Modeling reproduces suitably the migration of depocenters.

References

Agostini, A., Corti, G., Zeoli, A., Mulugeta, G., 2009, Evolution, pattern and partitioning of deformation during oblique continental rifting: Inferences from lithospheric-scale centrifuge models: Geochemistry Geophysics Geosystems, v. 10, Q11015, doi:10.1029 /2009GC002676.

Aragón-Arreola, M., Martín-Barajas A., 2007, Westward migration of extension in the northern Gulf of California: Geology, v. 35(6), p. 571–574. Autin, J., Bellahsen, N., Husson, L., Beslier, M. O., Leroy, S., d'Acremont, E., 2010, Analogue models of oblique rifting in a cold lithosphere: Tectonics, 29, TC6016, doi:10.1029/2010TC002671.

Axen, G., 1995, Extensional segmentation of the Main Gulf Escarpment, Mexico and United States: Geology, v. 23, p. 515–518.

Ferrari, L., López-Martínez, M., Orozco-Esquivel, T., Bryan, S. E, Duque-Trujillo, J., Lonsdale, P.F., 2013, Late Oligocene to middle Miocene rifting and syn-extensional magmatism in the southwestern Sierra Madre Occidental, Mexico: the beginning of the Gulf of California rift: Geosphere, v. 9, n. 5, p. 1161-1200

Fletcher, J. M., Grove, M., Kimbtrough, D., Lovera, O., Gehirels, G., 2007, Ridge-trench interactions and the Neogene tectonic evolution of the Magdalena shelf and southern Gulf of California: Insights from detrital zircon U-Pb ages from the Magdalena fan and adjacent areas: Geological Society of America Bulletin, v. 119, p.1313–1336.

Lizarralde, D., Axen, G. J., Brown, H., E., Fletcher, J. M., Gonzales-Fernandez, A., Harding. A., J., Holbrook, W, S., Kent, G, M., Paramo, P., Sutherland, F., Umhoefer, P, J., 2007, Variation in styles of rifting in the Gulf of California: Nature, v. 448, p. 466-469.

Stock, J. M., & Hodges, K. V., 1989, Pre-Pliocene extension around the Gulf of California and the transfer of Baja California to the Pacific Plate: Tectonics, v. 8, p. 99–115.

Sutherland, F. H., Kent, G. M., Harding, A. J., Umhoefer P. J., Driscoll, N. W., Lizarralde, D., Fletcher J. M., Axen G. J., Holbrook, W. S., González-Fernández A., Lonsdale P., 2012, Middle Miocene to early Pliocene oblique extension in the southern Gulf of California: Geosphere 2012;8;752-770 doi: 10.1130/GES00770.1

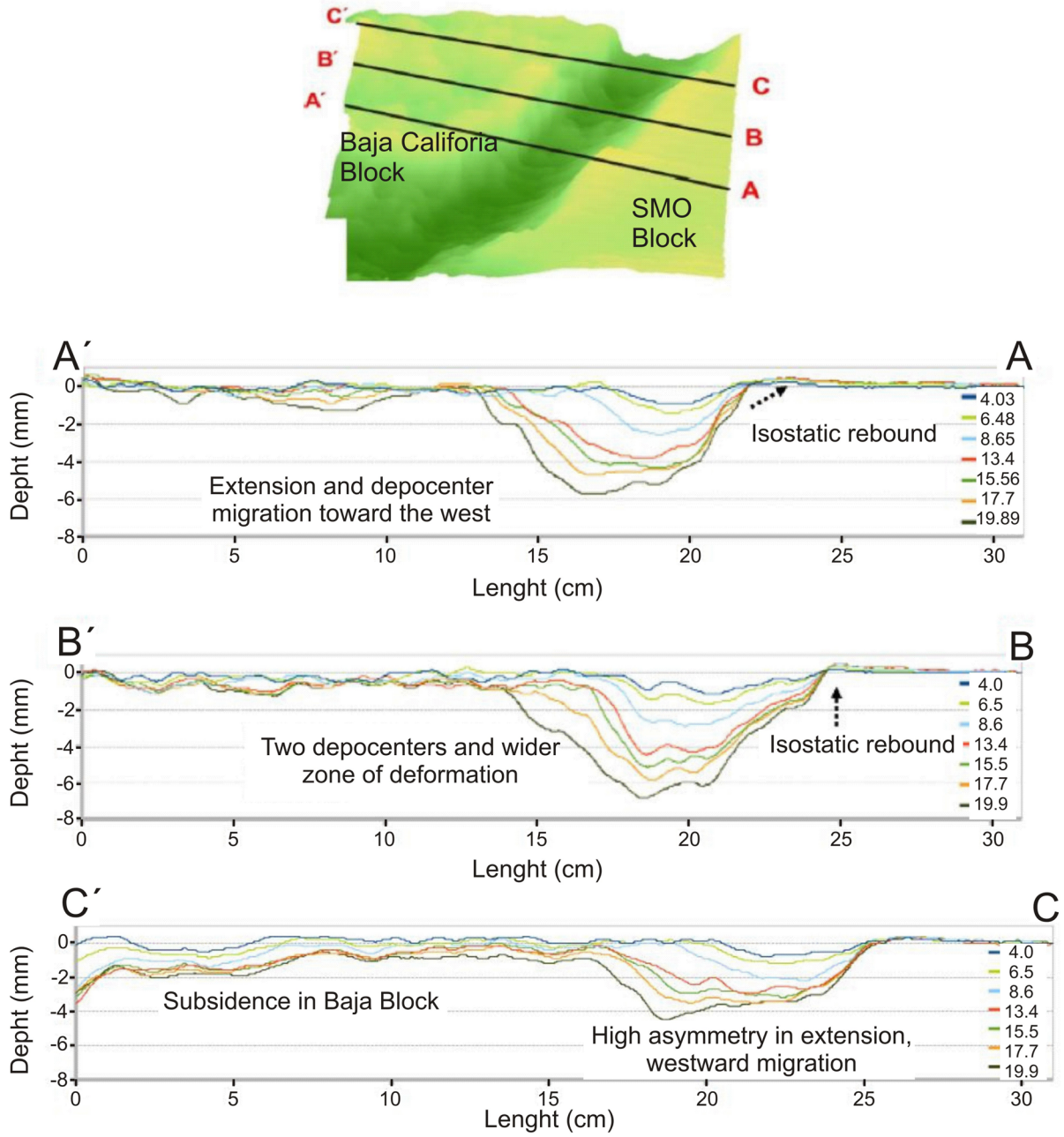

Fig. 3.: Topographic sections of the model showing the differences in depocenter evolution along the rift axis. In the three cases presented the depocenter migrates westward with differences in the symmetry of the rift. The depocenter locates closet to the moving block.

The negative inversion of thrust faults and related basin geometries: insight from analogue modelling experiments

Fabien Graveleau[1], Olivier Averbuch[1], Bruno Vendeville[1], Aimie Quinion[1], Mustapha Ouzgaït[1]

[1] *Université Lille 1, CNRS UMR 8217, Géosystèmes, Avenue Paul Langevin, F59655 Villeneuve d'Ascq, France*
e-mail: *Fabien.Graveleau@univ-lille1.fr*
session: *Tectonics and Surface Processes*

The extensional reactivation of thrusts (i.e. the negative tectonic inversion process) has often been suggested as a major deformational mechanism in post-orogenic sedimentary basins and rifted margins. The recognition of this negative tectonic inversion process is generally based on combined structural features including the collapse of major thrust-related structural relief, the collapse of the backlimb of thrust-related folds, the development of post-orogenic syn-rift deposits upon the crest of previously developed ramp-related anticlines and the general parallelism of extensional and compressional structures in map view. The direct relationships between normal faults and the underlying thrusts are however rarely exposed due to the general burial of these structures below a sedimentary cover controlled by the tectonic subsidence. Seismic profiles across post-orogenic basins generally does not allow providing, at depth, a precise image of such relationships due to the overall structural complexity.

To give further insight into this mechanism, and provide a guide for structural and seismic interpretation at depth in basins controlled by the extensional reactivation of basement thrust faults, a set of analogue modelling experiments have been conducted. Modelling of the negative tectonic inversion process has been rarely considered conversely to the positive inversion that has been the object of numerous studies. Basically, our models involve a brittle, cohesionless, dry, porous 3 cm-thick sand unit overlying a basal 1 cm-thick silicone layer designed to localize the basal décollement of the deformed structures. All models, initially 110 cm long and 49 cm large, were built above a flat, horizontal, rigid base. The entire model was first subjected to a phase of shortening by moving progressively at a constant speed (0.5 cm/hour) the left-hand wall until a value of about 39% bulk shortening was reached (87 hours of shortening). An orogenic wedge formed against the moving wall, then propagated progressively rightward by formation of new forethrusts and by bulk thickening of the wedge itself. At the end of compression episode, a post-tectonic sand layer was deposited to bury completely the structural relief and generate a horizontal datum for the next extensional phase Experiments were then tilted hinterlandward to simulate a flexural response of the lithosphere to orogenic loading. For the extensional phase of the experiment, two different basal slopes were tested (2.5° and 5°) to investigate the influence of internal thrust dips on the extensional dynamics. Models were extended by moving backwards the mobile sidewall at a speed of 1 cm/hour. As extension proceeded, the horizontal post-compression datum subsided locally along fault-bounded grabens that were incrementally filled-up with sand layers simulating the syn-rift deposits. At the end of each experiment, models were cut along equidistant vertical cross-sections and integrated as a 3D structural model using Move®. geomodelling software (Mid-

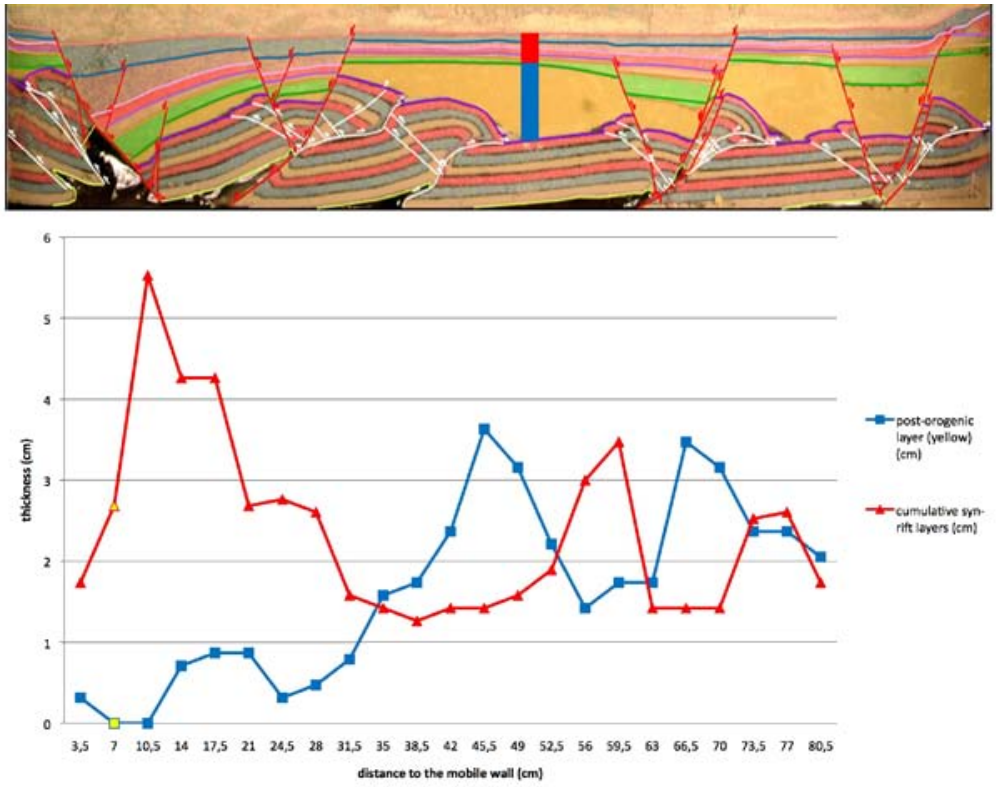

Fig. 1.: Cross-sections across the centre of the models illustrating the relationships between the basin geometry, the normal faults and the underlying thrust structures.

land Valley Ltd). Some representative sections were restored at the main steps of the basin development to provide a progressive view of the structural evolution of the basin.

Results of modelling experiments (Fig. 1) give a new insight into the geometries and kinematics of the negative tectonic inversion process, and allow further discussion on the main parameters controlling the reactivation of basement thrusts during a subsequent extension. They particularly emphasize the characteristic geometric and kinematic features of post-orogenic basin development, and especially, argue for the ramps of fore- and backthrusts to localize at depth respectively the master normal faults controlling depocenters and some antithetic secondary faults accommodating the adjustment of the hangingwall over the basal thrust surface.

Experimental modelling of deformation-erosion-sedimentation interactions in compressional, extensional and strike-slip settings

Fabien Graveleau[1,5], Vincent Strak[2], Stéphane Dominguez[3,5], Jacques Malavieille[3,5], Marina Chatton[3], Isabelle Manighetti[4], Carole Petit[4]

[1] *Université Lille 1, CNRS UMR 8217, Géosystèmes, Avenue Paul Langevin, F59655 Villeneuve d'Ascq, France*
[2] *School of Geosciences, Monash University, Melbourne, Victoria, Australia*
[3] *Université Montpellier 2 – CNRS UMR 5243, Géosciences Montpellier, CC 60, Place Eugène Bataillon, F34095 Montpellier, France*
[4] *Université de Nice Sophia-Antipolis, CNRS UMR 7329, Géoazur, Observatoire de la Côte d'Azur, La Darse, BP 48, 06235 Villefranche-sur-mer, France*
[5] *International Associated Laboratory ADEPT, CNRS- NSC, France-Taiwan*
e-mail: *Fabien.Graveleau@univ-lille1.fr*
session: *Tectonics and Surface Processes*

Tectonically controlled landforms develop morphologic features that provide useful markers to investigate rates of tectonic deformation and mechanisms of relief growth. In this work, we review results of morphotectonic experiments obtained with an innovative approach combining tectonic deformation and surface processes, coupled with accurate measurement techniques. This allows for a qualitative and quantitative analysis of landscape evolution associated with active deformation achieved through compressional, extensional and strike-slip tectonic settings (Fig. 1).

Major results indicate first that experimental morphologies evolve significantly at a short time scale (several seconds to tens of minutes, which scales about to 1 – 500 kyr), suggesting that morphogenetic processes have a short time response to tectonic and climatic forcing. For compressional settings, the formation of alluvial terraces above an active thrust is controlled by regular incision of the main channel through the uplifting hanging wall and by avulsion of deposits on fan-like bodies. Deformation of terraces well records the growth of the structure. For extensional settings, the dynamics of hanging-wall sedimentary filling controls the position of the base level, which in turn controls footwall erosion. Two phases of relief evolution are recognized: the first is a phase of relief growth and the second is a phase of upstream propagation of topographic equilibrium reached primarily in the sedimentary basin. During the phase of relief growth, the formation of triangular facets occurs by degradation of the fault scarp and their geometry (height) becomes stationary during the phase of topographic equilibrium propagation. For strike-slip settings, the complex geometry of the wrench zone, composed of several interacting fault segments, enhances the interactions with the drainage network. Consequently, numerous morphologic markers form continuously, but their lifetime is generally short due to erosion. A significant amount of distributed deformation is also observed along the fault zone. Locally, less than a quarter of the far field displacement can be measured using fault offsets, leading to a systematic underestimation of the real fault slip rate.

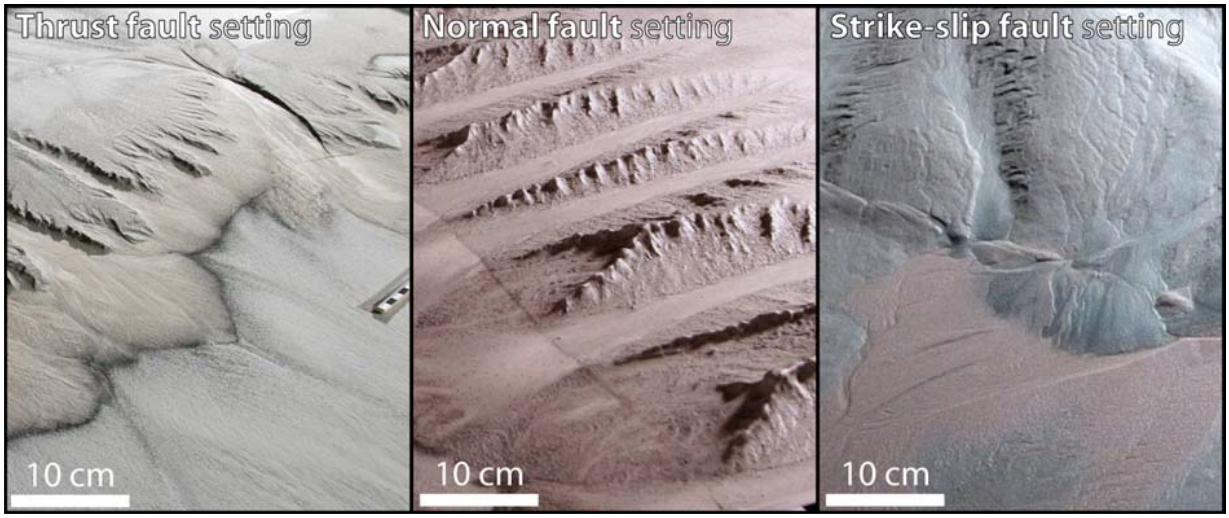

Fig. 1.: Experimental modelling results of landscape dynamics along an active A) thrust fault, B) normal fault, and C) Strike-slip fault. Note the modelling of morphotectonic markers such as fault scarps, faceted spurs, alluvial terraces, restraining bends and pressure ridges.

The experimental approach coupling deformation mechanisms and erosion-transport-sedimentation processes is well adapted to study the morphologic evolution of diverse tectonically controlled landforms.

Linking lithosphere deformation and sedimentary basin formation over multiple scales

Ritske .S. Huismans[1]

[1]*Department of Earth Science, University of Bergen, Allégaten 41, N-5007 Bergen, Norway*
e-mail: *ritske.huismans@geo.uib.no*
session: *Tectonics and Surface Processes*

Here we focus on the relationships between tectonic deformation and sedimentary basin formation. Resolving the interaction and feedback between tectonic crust-lithosphere scale deformation and surface processes through erosion of elevated areas and formation of sedimentary basins over multiple scales has been a long-standing challenge. While forward process based models have been successful at showing that a feedback is expected between tectonic deformation and redistribution of mass at the earth's surface by erosion, transport, and deposition, demonstrating this coupling for natural systems has been an even greater challenge and is strongly debated. Observational constraints on crust-lithosphere deformation and surface processes are typically collected at highly varying spatial and temporal scales, while forward process based models are typically run at either very large lithosphere-mantle scale, or at the scale of the sedimentary basin making it difficult to investigate and explore the detailed interaction and feedback between these systems. Here I will report on recent advances in forward modelling linking crust-lithosphere deformation with surface processes over a large range of scales resolving tectonic plate scale deformation and sedimentary basin formation at stratigraphic scales. The forward numerical models indicate a linkage and interaction between the structural style of thick-skinned large-scale mountain belt and rift-passive margin formation, erosion-transport-deposition processes operating at the surface, and the thin-skinned deformation occurring in the associated sedimentary basins.

3D Analogue Modelling of the Effect of Fan Sedimentation on Accretionary Wedge Dynamics – the Magdalena Fan case, South Caribbean Margin, Colombia

Karen Leever[1], Elisabeth Johansen[2]

[1] *Deutsches GeoForschungsZentrum GFZ Potsdam, Germany*
[2] *Department of Petroleum Engineering, University of Stavanger, Norway*
e-mail: *karen.leever@gfz-potsdam.de*
session: *Tectonics and Surface Processes*

Introduction

Surface processes are well known to influence deformation in mountain belts and accretionary wedges. Erosion and sedimentation influence vertical motions (exhumation) and wedge geometry (number of faults and total strain accumulated on them) by redistribution of material. Critical taper theory has been successful in explaining the interaction between tectonics and surface processes in brittle wedges.

In terms of this interaction, the Magdalena Fan on the active South Caribbean margin in Colombia is a feature of particular interest. The Caribbean plate has subducted beneath north western South America since at least Eocene times and as a result, a long and wide accretionary prism has developed. One of the world's most sediment rich rivers, the Magdalena River has deposited its sediments on top of this accretionary wedge since the Middle Miocene. The resulting Magdalena Fan is a very prominent feature in the bathymetry of the continental slope. Thrusts in the wedge curve into the fan on both sides, creating a convex-outward shape in map view. Moreover, while thrusts are easily recognized on seismic sections in the wedge, no deformation is obvious on seismic sections inside the fan.

In previous studies, the curvature of the accretionary wedge has been explained both as a primary feature, due to curvature of the margin, and as a secondary feature, caused by loading by the Magdalena Fan. In this study, we test the latter hypothesis and investigate the role of strong syn-tectonic sedimentation from a point source. Could localized sedimentation lead to curvature of the accretionary wedge? How is deformation partitioned between the accretionary wedge and the fan and, in particular, how and where is deformation accommodated inside the fan? We address these questions by means of coupled 3D analogue modelling, in which we vary the sediment flux from a point source while tectonic accretion occurs at a constant rate.

Modeling strategy and setup

In a series of 3D scaled analogue models (1:10^5), we varied the sediment flux S while the tectonic accretion rate A was kept constant (Table 1), resulting in different S/A ratios.

We used a box of 80cm wide and 100cm length, with a high friction conveyor belt at the base, glass side walls and a vertical back wall. A 2cm thick layer of quartz sand was sieved onto the conveyor belt, representing the sediments on the incoming plate. An initial sand wedge was sieved against the back wall. Syn-tectonic sedimentation at different rates was achieved by pouring glass beads through a funnel connected to a gutter suspended above the deforming wedge in the middle of the back wall at regular time intervals (Table 1). Total shortening was 40cm.

Model	Model ID	Tot. displ. (mm)	Sedimentation rate	S (mm^3/s)	H (mm)	V (mm/s)	A (mm^3/s)	S/A
A	3D_50_4c	400	10 ml / 20 s	500	20	0.25	1000	1/2
B1	3D_50_4d	400	20 ml / 20 s	1000	20	0.25	1000	1
B2	3D_50_3e	500	20 ml / 10 s	2000	20	0.5	2000	1
C	3D_50_4b	400	40 ml / 20 s	2000	20	0.25	1000	2
D	3D_50_4e	400	90 ml / 20 s	4500	20	0.25	1000	4.5
–	3D_50_4a	400	45 ml / 20 s	2250	10	0.25	500	4.5

Tab. 1.: Model parameters. S is sediment flux; H thickness of the incoming layer, V displacement rate of conveyor belt. Tectonic accretion rate A was calculated by integrating the cross sectional material flux H*V over a domain of 20 cm width.

Materials were chosen such that the angle of repose of the sediment (given by its coefficient of internal friction) is similar to the slope angle of the critically tapered wedge (a function of basal and internal friction). Thus we used quartz sand ≤ 0.3 mm ($\mu = 0.75$) for the deforming sediment on the incoming plate and glass beads of 0.2-0.3 mm ($\mu = 0.5$) mixed with 10%vol colored sand for the fan sediment. The high friction base leads to $\mu b = \mu$ in the deforming wedge.

The experiments were monitored at short time intervals with high resolution digital cameras. At the end of each experiment, the model was covered and moisturized and cross sections were sliced at 2-5cm intervals.

Preliminary results

1. Loading by fan sediments forces the frontal thrust forward, such that it breaks the surface in front of (around) the fan (Figure 1).

2. Different modes of fault formation and slip partitioning occur depending on the sediment flux (Figure 1):
   - for low S/A ratios (S/A = 0.5), the new frontal thrust forms as a single fault along the wedge and curved around the fan;
   - in the intermediate case (S/A = 1) there is a small delay between the formation of a new thrust in front of the wedge (initially curving into the fan) and the one around the fan;
   - high S/A ratios (S/A >= 1) lead to prolonged lifetime of faults (and thus fewer faults) below the fan: underthrusting continues below the fan even as a new fault is formed in front of the wedge. This phenomenon may be enhanced by the lubricating effect of the (low friction) fan sediments. The newly formed faults in front of the wedge do not run straight but curve into the fan.

3. The structural evolution of the wedge proves to be sensitive also to the position of the sediment load (Figure 2): sediments deposited in a more distal /frontal position (prograding system, model B2) lead to duplex formation and associated uplift in the rear of the wedge below the fan and prolonged activity of the faults below the fan. For an aggrading or retrograding system a higher sediment flux (S/A ratio) is required to obtain the same effect (model B1, C)

4. Tectonics in return influences sedimentation: hanging wall uplift leads to backward tilt of fan, restricting sedimentation to the hanging wall of the active fault for some time and

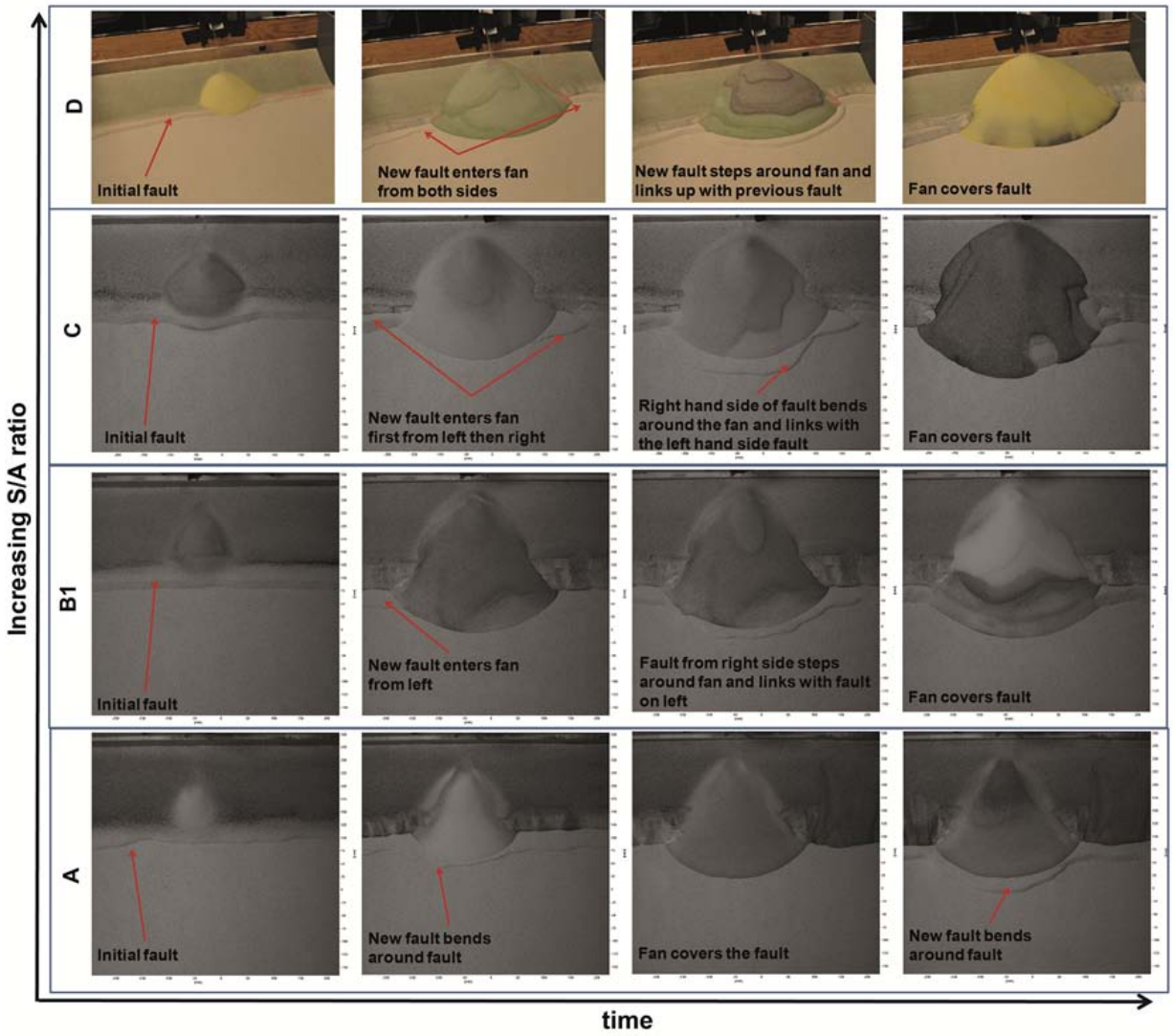

Fig. 1.: Differences in structural evolution in Model A-D (top view) as a function of increasing S/A ratio (Table 1). Horizontal time axis shows increase of time, but not the same time for the different models.

leading to locally higher sedimentation rates (Figure 1D, 2D). Aggradation and progradation are thus tectonically controlled in our subaerial models.

5. Fan sediments are strongly deformed by fault-bend folding in front of the active thrusts, but undeformed on the tectonically inactive part of the wedge (upper slope, Figure 2).

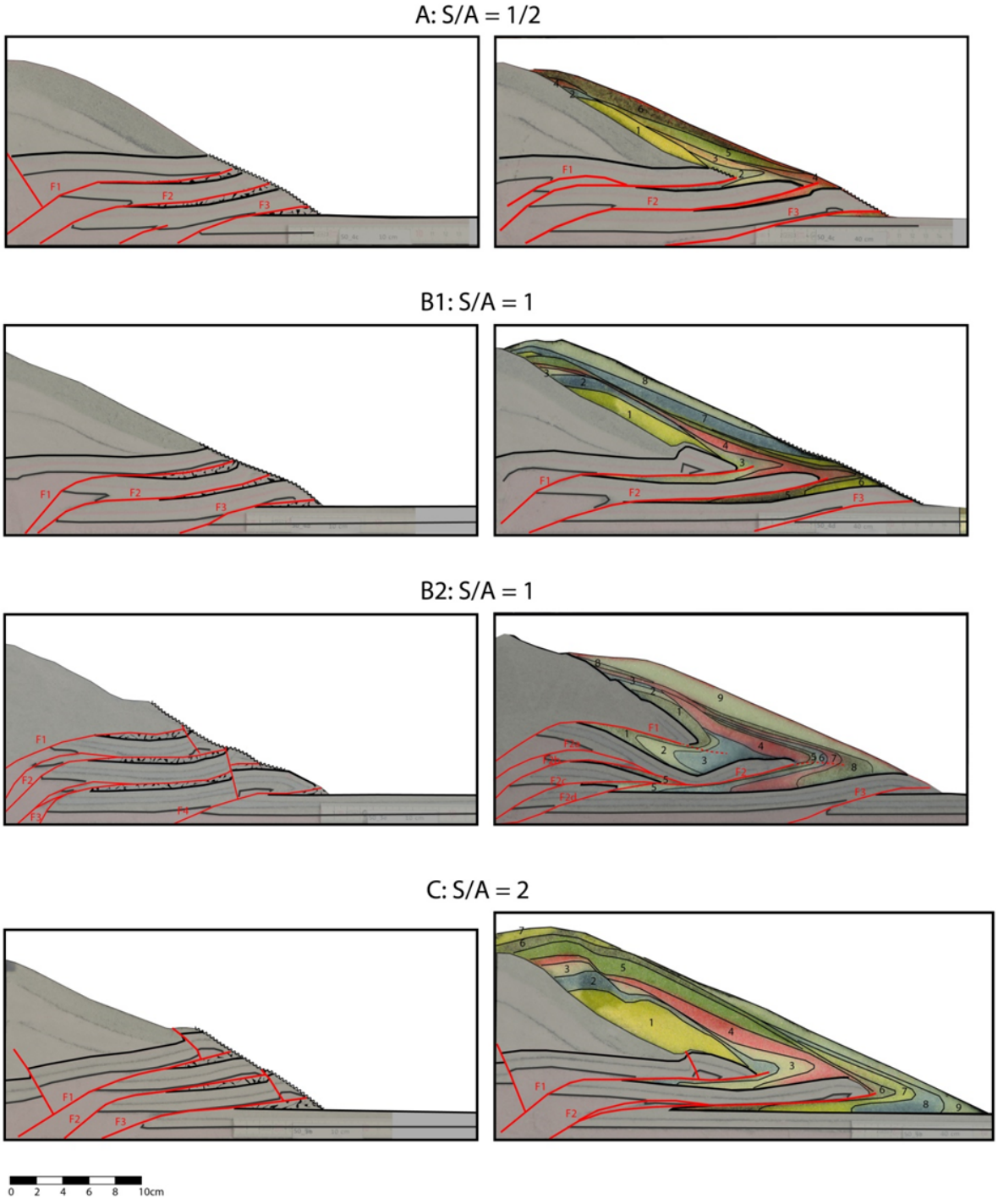

Fig. 2.: Cross sections at the end of the model run for four models with different S/A ratios. Left panels: outside the fan (10 cm from side wall), right panels: in the middle of the fan (40cm from side wall). The fan sediments are distinctly deformed by fault propagation folding. For high S/A ratios (B2, C), fewer thrusts with larger displacement have developed inside the fan than outside..

From continental rifting to seafloor spreading: Insight from 3D thermo-mechanical modeling

Jie Liao[1], Taras Gerya[1]

[1] *Geophysical Fluid Dynamics, Institute of Geophysics, ETH Zurich, Sonneggstrasse 5, CH-8092, Zurich, Switzerland*
e-mail: *jie.liao@erdw.ethz.ch*
session: *Tectonics and Surface Processes*

Introduction

The continuous process from continental rifting to seafloor spreading is a key step in Wilson's cycle (Wilson, 1966), but the complete process is hardly simulated. Continental rifting history influences oceanic spreading. Understanding the inheritance of continental rifting in seafloor spreading is crucial to study the incipient oceanic ridge evolution and remains a big challenge (Lister et al., 1986; Ebinger and Casey, 2001; Nielsen and Hopper, 2004; Taylor et al., 1999, 2009; Gerya, 2012). Compared to the continental rifting process, which has been widely studied by numerical and analogue modelings, few studies have been done on the complete rifting-spreading process due to several diffculties. One is that the long extension process requires large strain to reach the final steady state of seafloor spreading from the initial intact continental lithosphere, and it includes many complex geodynamic processes, such as magma formation, hydrothermal circulation, and crystalization (Gerya, 2010, 2013). Another diffculty is that oceanic spreading in nature is a 3D problem, as large heterogeneities are present along oceanic ridges. Ultra-slow spreading ridges are mostly oblique to spreading directions and consist of alternating magmatic-amagmatic segments (Dick et al., 2003). Symmetric and asymmetric accretion is alternatively distributed along slow spreading ridges (Escartin et al., 2008). Overlapping and transform faults are two common ways that oceanic segments interact (Gerya, 2012) (and reference therein). These 3D features of oceanic ridge require 3D models. Furthermore, the lack of natural observations make the rifting-spreading transition enigmatic. Unlike the widely distributed examples of continental rift and oceanic ridge, very few natural examples record the rifting-spreading transition informations, and some good examples are theWoodlark Basin in the southwestern Pacific ocean (Taylor et al., 1999, 2009), the Laptev Sea margin in the Arctic ocean (Franke D., 2001; Engen O., 2003) and the Red Sea-Gulf of Aden system (d'Acremont et al., 2010; Ligi et al., 2012; Brune and Autin, 2013).

The early-stage formed rift can be a template for the future rift development and continental breakup. However, numerous heterogeneities are generated during continental rifting, and rift propagation may divert from the initial rift trend (the trend of the pre-existing weakness), such as people proposed for the Main Ethiopian Rift (Keranen and Klemperer, 2008). To what extend does rifting history influence continental breakup and seafloor spreading is hardly constrained. Moreover, the importance of rifting history on continental breakup and seafloor spreading is addressed by the formation of transform faults. One possible formation of transform faults which is widely proposed is related with the inheritance of pre-existing weakness. Transform faults my initiate and develop along pre-existing fracture zones that perpendicular to oceanic ridges, such as the long transform fault in the equatorial Atlantic ridge between South America and Africa

(Wilson, 1965). The correspondence between the passive margins and the transform faults in the Gulf of Aden also suggests the possibility of inheritance of pre-existing weakness in transform faults formation (d'Acremont et al., 2010).

In this study, we aim to investigate the inheritance of continental rifting on incipient seafloor spreading by modeling the complete rifting-spreading process, with particular attention paid on the two accretion modes (symmetric and asymmetric accretion). The Initial rheological structure of continental lithosphere and the geometry of a pre-existing weak zone are the two key parameters that we study.

Modeling results

We investigate the effect of rheological coupling and decoupling on continental rifting and seafloor spreading using 3D numerical models (Fig. 1a). Two different rheological coupling structures in terms of the absence/presence of a strong lower crust are used in our models, named decoupled (DCP) rheology (i.e. weak lower crust) and coupled (CP) rheology (i.e. strong lower crust) (Fig. 1b). Two different idealized model setups in terms of the geometry of the weak zone are employed, named 2D-like and 3D-like setups (Figs. 1c and 1d). Our preliminary modeling results show that the asymmetric accretion involved with active detachments is favored by DCP models, while CP models most likely generate symmetric accretion. Initiation, development and termination of detachment faults, and curved geometry of oceanic detachment faults are discussed.

2D-like model setup

2D-like model setups (Fig. 1c) are used in this section. The decoupled (DCP) models generate numerous heterogeneities along the continental rifting direction which lead to significant 3D features, and promote asymmetric oceanic accretion (Figs. 2a and 2b). Deformation is more distributed (for instance the widespread molten asthenosphere), and longer extension time is required for the models to reach the steady state of seafloor spreading. Breakup of the lithospheric mantle occurs earlier than that of the crust. The volume of magma chamber is pressure and temperature dependent. Large magma chamber is generated in the DCP models (Fig. 2e), such as in Model 1. Growth rate of the oceanic crust becomes constant once the seafloor spreading reaches the steady state (Fig. 2f). The coupled (CP) models (with a strong lower crust) generate a roughly straight oceanic ridge developing from a straight continental rift (Figs. 2c and 2d), promoting symmetric oceanic accretion. A small amount of mantle rock is exhumed along the ocean-continental transition zones. In a relatively short time period, both models reach steady state of seafloor spreading, and the oceanic ridges are featured by symmetric accretion. Oceanic detachments are not formed in the CP models.

3D-like model setup

3D-like model setups (Fig. 1d) are used in this section. Instead of extending throughout the whole model box, the crustal or mantle weak zone has a length of 24.5 km along z direction (perpendicular to extension). Similar like the results with 2D-like setups, DCP models promote asymmetric oceanic accretion, while CP models favor symmetric accretion (Fig. 3). In the DCP models, seafloor spreading develops in a propagation way, and curved oceanic ridges form. The oceanic ridges are featured by asymmetric accretion involving active oceanic detachment faults which are established in the late continental rifting stage. The CP models generate relatively straight and symmetric oceanic ridges in a short time period. Molten asthenosphere occurs in a small area beneath the oceanic ridge, and a pair of narrow conjugate passive margins is formed. Along the passive margins, exhumed lithospheric mantle is observed, since high angle normal faults are rotated to low angle detachment faults.

Detachment fault formation

Two types of detachment fault termed continental and oceanic detachment fault are generated in

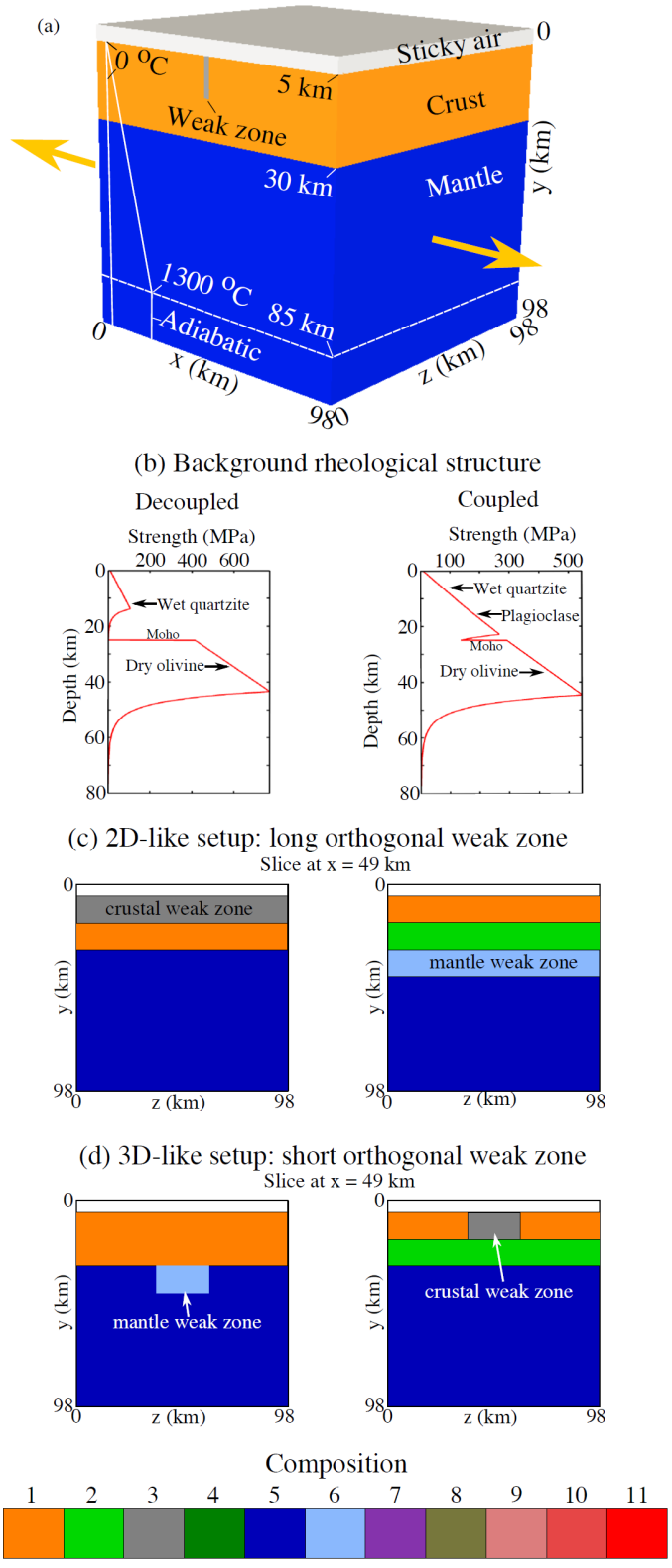

Fig. 1.: Initial model configuration. (a) An example setup of 3D model (corresponds to decoupled rheology with a 2D-like weak zone). (b) Two different rheological structures of the background (without the influence of weak zone) are used in this study, named decoupled and coupled rheology. Coupled rheology is implemented by imposing a strong lower crust. (c) 2D-like model setups for decoupled (left panel) and coupled (right panel) rheology. The slices are taken along y-z plane at x = 49 km. (d) 3D-like model setups for decoupled (left panel) and coupled (right panel) rheology. Normal extension velocity is prescribed on the whole left and right surfaces (half extension rate is 1.5 cm/yr). Based on mass conservation, the constant normal velocities on the top and bottom surfaces are calculated and prescribed (Gerya, 2013). The front and back surfaces are free slip. A free surface condition for the crustal surface is approximated by adding the sticky air layer on the top.

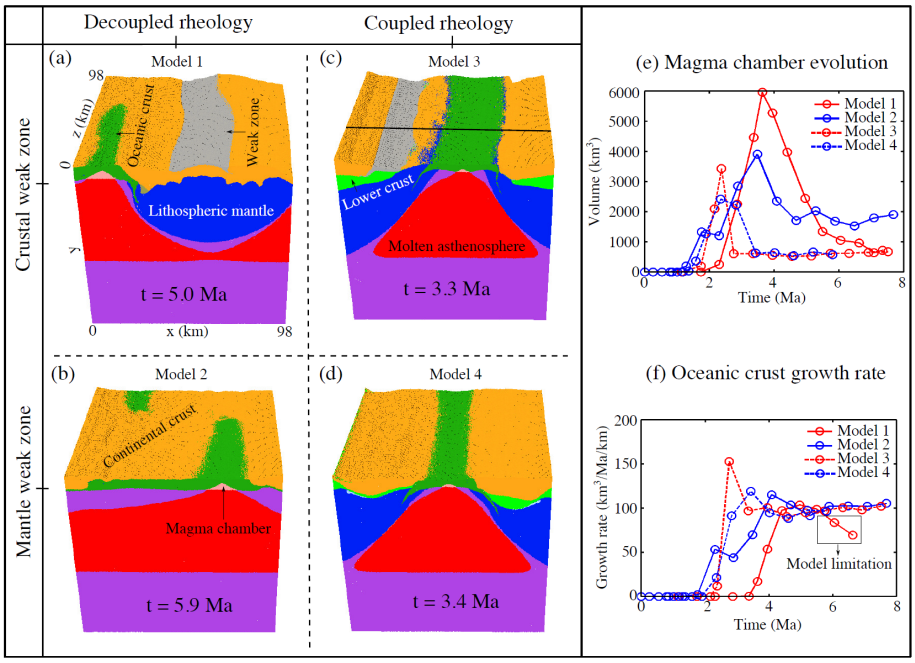

Fig. 2.: Comparison of modeling results with 2D-like setups. Rheological coupling/decoupling and weak zone location are varied in different models. Color shows composition (a-d), also see Fig. 1 for the colormap. (e) Dynamic evolution of magma chamber volume and (f) growth rate of oceanic crust are compared for each model. The black line in c shows the location of slices used in the Figs. 4 and 5. Note that the decoupled rheology promotes asymmetric accretion, while the symmetric accretion is favored by coupled rheology

the CP and DCP models, respectively. In the CP models, the continental detachment faults are generated through fast rotation of the high angle normal faults (Fig. 4). Due to the localized lithospheric extension and thinning, one branch of the major conjugate faults is rotated to low angle by the fast upwelling asthenosphere. Macleod et al. (2009) demonstrated that core complex detachment faults initiate from high angle ($60° \pm 10°$) normal faults and rapidly rotate to low angles ($\sim 30°$). The detachment faults initiated and developed in the continental rifting stage gradually become inactive in the late rifting and early spreading stages. This may caused by the rapid asthenosphere upwelling and intense magmatism which cut off the detachment faults and accommodate extension space (Lister et al., 1986; Ebinger and Casey, 2001; Macleod et al., 2009).

In contrast, in the DCP models, the oceanic detachments establish during the late continental rifting and early seafloor spreading (Fig. 5), accompanied by oceanic crust growth. Following the location of the initial weak zone, two conjugate normal faults form along the magma walls in the late rifting stage (t=3.4 Ma in Fig. 5a). One branch of the conjugate normal faults gradually develops into a detachment fault (t=4.6 Ma in Fig. 5a), as strain weakening and shear heating amplify perturbations along the normal faults and break up the symmetry. From the middle to the edges along z direction, the formation time of the detachment fault delays (t=6.4 Ma in Fig. 5a). Therefore, similar like the oceanic ridge propagation, the detachment fault forms first in a certain location and then propagates to two directions along the ridge. As a consequence, a curved geometry of the detachment fault forms on a map view (Fig. 5b). This 3D curved geometry of detachment faults can be in comparable with natural observations (left panel in Fig. 5d). Thus, our modeling results may provide a possible dynamic formation of curved detachment faults formation.

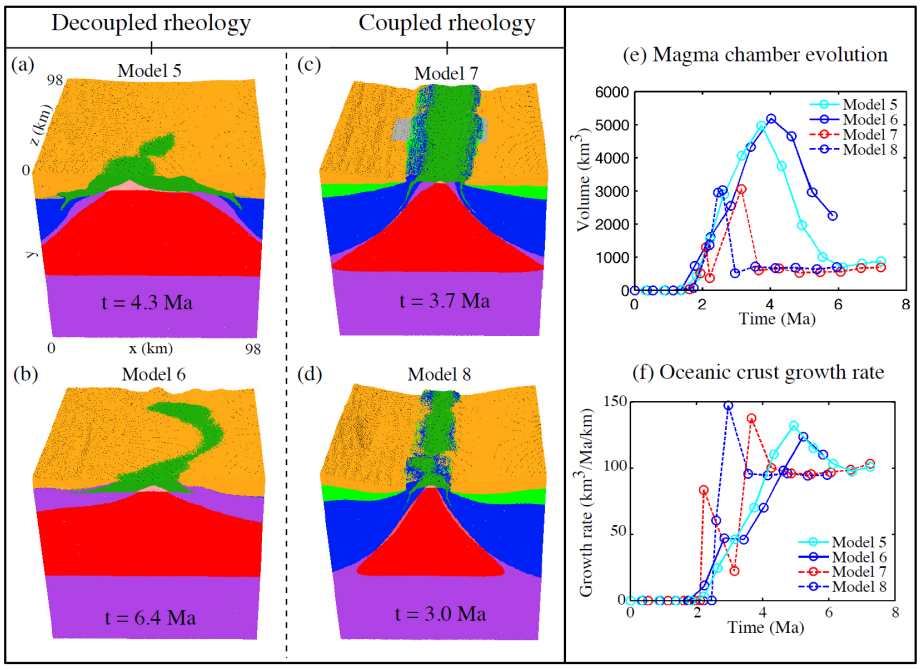

Fig. 3.: Comparison of modeling results with decoupled and coupled rheologies using 3D-like setups. (a-d) Comparison of composition (see Figs. 1 and 2 for the color notation). (e) Dynamic evolution of magma chamber volume and (f) growth rate of oceanic crust are compared for each model. Model 7 has a crustal weak zone, and Model 8 has a mantle weak zone, both of which are seating in the middle of the model domain. Note that the decoupled rheology promotes asymmetric accretion, while the symmetric accretion is favored by coupled rheology.

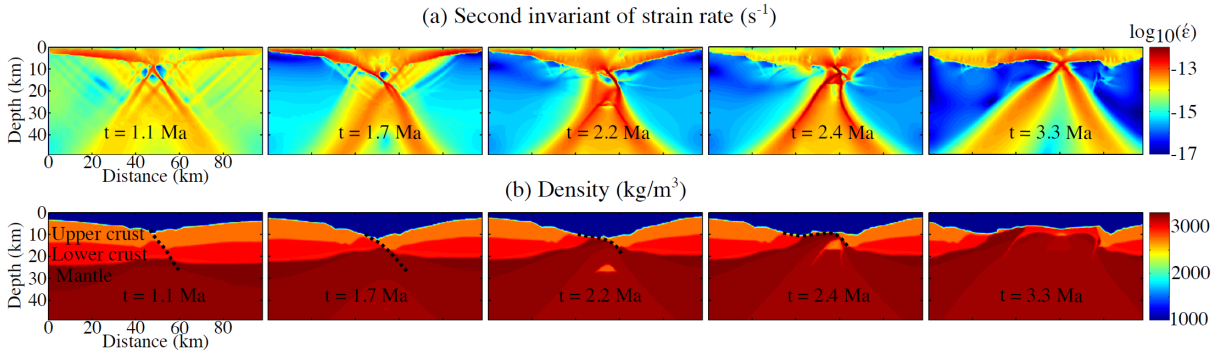

Fig. 4.: Evolution of the continental detachment fault generated in Model 3. Location of the slices is shown in Fig. 2c by the black line (z = 38 km). (a) Second invariant of strain rate and (b) density show the rotation of the high angle normal fault (black dotted line).

In the life cycle of OCCs (Macleod et al., 2009), detachment faults are terminated by intense magma that delivered to the footwall. This feature is observed in our modeling results (Figs. 4 and 5). Suffcient magma cuts through the detachment fault (compare the snapshot at t=6.4 Ma to the one at t=5.8 Ma in Fig. 5c), changing the accretion pattern from asymmetric to symmetric. And as a consequence, abandoned axial volcanic ridge (AVR) is generated on the conjugate plate (the hanging wall, Figs. 5b-5c, t = 6.4 Ma). The formation of abandoned AVR is evidenced by the natural example on the MAR at 5°S (Reston et al., 2002), where the extinct axial volcanic ridge and abandoned detachment faults are observed on the conjugate plate (Fig. 5d). The reconstruction (Fig. 5d) based on the bathymetry data (matching the fault scarps on the two flanks of the active ridge) indicates that the two core complexes (numbered 1 and 2 in the Fig. 5d) used to belong together. Thus, the abandonment of AVR may occur together with the abandonment of detachment faults.

Conclusion

Based on our modeling results, oceanic spreading has a strong dependence on continental rifting which is influenced by the initial rheological coupling/decoupling of continental lithosphere. Rheological coupling/decoupling generates two types of incipient oceanic ridge development: (1) coupled lithospheric rheology promotes symmetric oceanic accretion, while (2) decoupled lithospheric rheology favors the formation of asymmetric oceanic accretion involving development of active detachment faults. In the models with coupled rheology, lithospheric scale shear zones are generated and lithosphere thins rapidly. Decoupled models extend in a depth-dependent way. Two types of detachment fault establish in terms of their formation time. Continental detachment faults establish in the models with coupled rheology and mainly develop during rifting stage. Intense magmatism terminates the continental detachment faults in the late rifting stage. Oceanic detachment faults form in the oceanic crust, dominating ridge accretion asymmetrically. Magmatism can also terminates oceanic detachment faults, switching oceanic accretion from asymmetric to symmetric. Curved oceanic detachment faults can be simulated with 3D models.

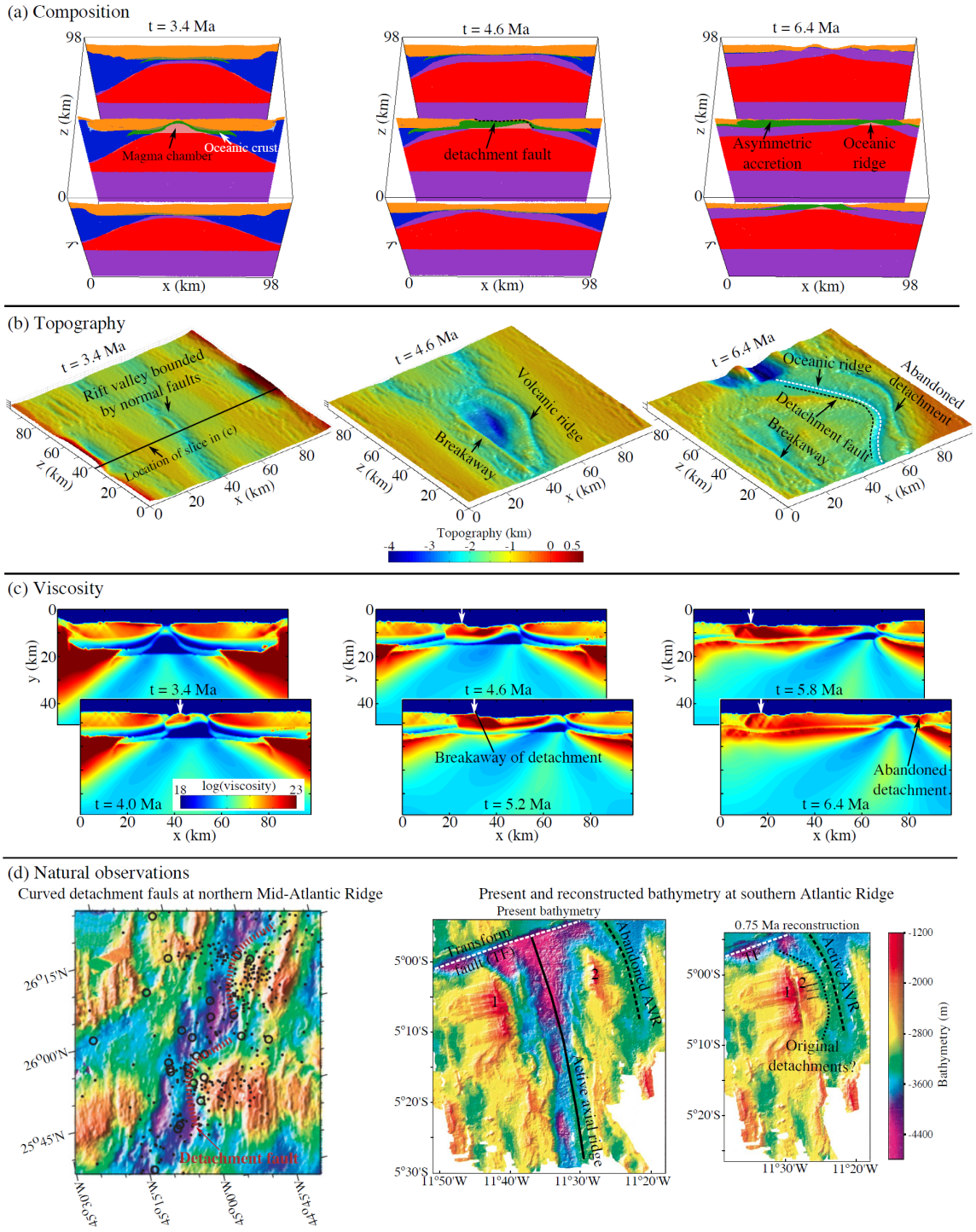

Fig. 5.: Evolution of the detachment fault generated in Model 6 and comparison with natural examples. (a) Composition, (b) topography and (c) viscosity snapshots of model results are shown for different times. The black line (z = 38 km) in (b) shows the location of viscosity slices in (c). White arrows in viscosity slices (c) show the positions of detachment breakaway. (d) Natural examples of curved detachment faults at northern Mid-Atlantic Ridge (modified after Escartin et al. (2008)) and ridge abandonment at 5°S Atlantic ridge (modified after Reston et al. (2002)).

References

Afonso, J.C., Ranalli, G., 2004. Crustal and mantle strengths in continental lithosphere: is the jelly sandwich model obsolete? Tectonophysics 394, 221–232. doi:10.1016/j.tecto.2004.08.006.

Allken, V., Huismans, R.S., 2012. Factors controlling the mode of rift interaction in brittle-ductile coupled systems: A 3d numerical study. Geochem. Geophys. Geosyst. 13, 1–18. doi:10.1029/2012GC004077.

Allken, V., Huismans, R.S., Thieulot, C., 2011. Three-dimensional numerical modeling of upper crustal extensional system. J. Geophys. Res. 116, 1–15. doi:10.1029/2011JB008319.

Armitage, J.J., Collier, J.S., Minshull, T.A., 2010. The importance of rift history for volcanic margin formation. Nature 465, 913–917. doi:10.1038/nature09063.

Brace, W.F., Kohlstedt, D.L., 1980. Limits on lithospheric stress imposed by laboratory experiment. J. Geophys. Res. 85, 6248–6252.

Brune, S., Autin, J.a., 2013. The rift to break-up evolution of the gulf of aden: Insights from 3d numerical lithospheric-scale modelling. Tectonophysics 607, 65–79. doi:10.1016/j.tecto.2013.06.029.

Brune, S., Popov, A.A., Sobolev, S.V., 2012. Modeling suggests that oblique extension facilitates rifting and continental break-up. J. Geophys. Res. 117, 1–16. doi:10.1029/2011JB008860.

Buck, W.R., 2006. The role of magma in the development of the afro-arabian rift system. Geological Society, London, Special Publications 259, 43–54. doi:10.1144/GSL.SP.2006.259.01.05.

Buck, W.R., Lavier, L.L., Pollakov, A.N.B., 2005. Models of faulting at mid-ocean ridges. Nature 434, 719–723. doi:10.1038/nature03358.

Burgmann, R., Dresen, G., 2008. Rheology of the lower crust and upper mantle: Evidence from rock mechanics, geodesy, and field observations. Annu. Rev. Earth Planet. Sci. 36, 531–567. doi:10.1146/annurev.earth.36.031207.124326.

Burov, E.B., 2010. The equivalent elastic thickness (te), seismicity and the long-term rheology of continental lithosphere: Time to burn-out "crème brûlée"? insights from large-scale geodynamic modeling. Tectonophysics 484, 4–26. doi:10.1016/j.tecto.2009.06.013.

Burov, E.B., Watts, A.B., 2006. The long-term strength of continental lithosphere: "jelly sandwich" or "crème brûlée"? GSA Today 16.

Byerlee, J., 1978. Friction of rocks. Pure Applied Geophysics 116, 615–626.

Chemenda, A., Deverchere, J., Calais, E., 2002. Three-dimensional laboratory modelling of rifting: Application to the baikal rift, russia. Tectonophysics 356, 253–273.

Choi, E., Lavier, L., Gurnis, M., 2008. Thermomechanics of mid-ocean ridge segmentation. Phys. Earth Planet. Inter. 171, 374–386. doi:10.1016/j.pepi.2008.08.010.

Corti, G., Van Wijk, J.W., Cloetingh, S., Morley, K., 2007. Tectonic inheritance and continental rift architecture: Numerical and analogue models of the east african rift system. Tectonics 26, 1–13. doi:10.1029/2006TC002086.

d'Acremont, E., Leroy, S., Maia, M., Gente, P., Autin, J., 2010. Volcanism, jump and propagation on the sheba ridge, eastern gulf of aden: segmentation evolution and implications for oceanic accretion processes. Geophys. J. Int. 180, 535–551. doi:10.1111/j.1365-246X.2009.04448.x.

Dick, H.J.B., Lin, J., Schouten, H., 2003. An ultraslow-spreading class of ocean ridge. Nature 426, 405–412.

Dunbar, J.A., Sawyer, D.S., 1988. Continental rifting at pre-existing lithospheric weaknesses. Nature 333, 450–452.

Ebinger, C.J., Casey, M., 2001. Continental breakup in magmatic provinces: An ethiopian example. Geology 29, 527–530.

Engen O., Eldholm O., B.H., 2003. The arctic plate boundary. J. Geophys. Res. 108, 2075–2092. doi:10.1029/2002JB001809.

Escartin, J., Smith, D.K., Cann, J., Schouten, H., Langmuir, C.H., Escrig, S., 2008. Central role of detachment faults in accretion of slow-spreading oceanic lithosphere. Nature 455, 792–794. doi:10.1038/nature07333.

Franke D., Hinz K., O.O., 2001. The laptev sea rift. Mar. Pet. Geol. 18, 1083–1127.

Gerya, T., 2010. Dynamics instability produces transform faults at mid-ocean ridges. Science 329, 1047–1050. doi:10.1126/science.1191349.

Gerya, T., 2012. Origin and models of oceanic transform faults. Tectonophysics 522-523, 34–54. doi:10.1016/j.tecto.2011.07.006.

Gerya, T.V., 2013. Three-dimensional thermomechanical modeling of oceanic spreading initiation and evolution. Phys. Earth Planet. Inter. 214, 35–52. doi:10.1016/j.pepi.2012.10.007.

Gregg, P.M., Behn, M.D., Lin, J., Grove, T.L., 2009. Melt generation, crystallization, and extraction beneath segmented oceanic transform faults. J. Geophys. Res. 114, 1–16. doi:10.1029/2008JB006100.

Huismans, R., Beaumont, C., 2011. Depth-dependent extension, two-stage breakup and cratonic underplating at rifted margins. Nature 473, 74–79.

Jackson, J., 2002. Strength of the continental lithosphere: Time to abandon the jelly sandwich? GSA Today 12, 4–10. doi:10.1130/1052-5173(2002)012¡0004:SoTCIT¿2.0.Co;2.

Keranen, K., Klemperer, S.L., 2008. Discontinuous and diachronous evolution of the main ethiopian rift: Implications for development of continental rifts. Earth Planet. Sci. Lett. 265, 96–111.

Ligi, M., Bonatti, E., Bortoluzzi, G., Cipriani, A., Cocchi, L., Tontini, F.C., 2012. Birth of an ocean in the red sea: Initial pangs. Geochem. Geophys. Geosyst. 13, 1–29. doi:10.1029/2012GC004155.

Lister, G.S., Etheridge, M.A., Symonds, P.A., 1986. Detachment faulting and the evolution of passive continental margins. Geology 14, 246–250. doi:10.1130/0091-7613(1986)14¡246:DFATEO¿2.0.CO;2.

Macleod, C.J., C., S.R., Murton, B.J., Casey, J.F., Mallows, C., Unsworth, S.C., Achenbach, K.L., Harris, M., 2009. Life cycle of oceanic core complexes. Earth Planet. Sci. Lett. 287, 333–344. doi:10.1016/j.epsl.2009.08.016.

Maggi, A., Jackson, J.A., Priestley, K., Baker, C., 2000. A re-assessment of focal depth distributions in southern iran, the tien shan and northern india: do earthquakes really occur in the continental mantle? Geophys. J. Int. 143, 629–661.

Nielsen, T.K., Hopper, J.R., 2004. From rift to drift: Mantle melting during continental breakup. Geochem. Geophys. Geosyst. 5, 1–24. doi:10.1029/2003GC000662.

Nyblade, A.A., Brazier, R.A., 2002. Precambrian lithospheric controls on the development of the east african rift system. Geology 30, 755–758.

Puthe, C., Gerya, T., 2014. Dependence of mid-ocean ridge morphology on spreading rate in numerical 3-d models. Gondwana Res. 25, 270–283. doi:10.1016/j.gr.2013.04.005.

Reston, T.J., Weinrebe, W., Grevemeyer, I., Flueh, E.R., Mitchell, N.C., Kirstein, L., Kopp, C., Kopp, H., participant of Meteror 47/2, 2002. A rifted inside corner massif on the mid-atlantic ridge at 5s. Earth Planet. Sci. Lett. 200, 255–269.

Smith, D.K., Cann, J.R., Escartin, J., 2006. Widespread active detachment faulting and core complex formation near 138 n on the mid-atlantic ridge. Nature 442. doi:10.1038/nature04950.

Taylor, B., Goodliffe, A.M., Martinez, F., 1999. How continents break up: Insights from papua new guinea. J. Geophys. Res. 104, 7497–7512.

Taylor, B., Goodliffe, A.M., Martinez, F., 2009. Initiation of tranform faults at rifted continental margins. C, R. Geoscience , 341.

Tucholke, B.E., Behn, M.D., Buck, W.R., Lin, J., 2008. Role of melt supply in oceanic detachment faulting and formation of megamullions. Geology 36, 455–458. doi:10.1130/G24639A.1.

Van Wijk, J., 2005. Role of weak zone orientation in continental lithosphere extension. Geophys. Res. Lett. 32, 1–4. doi:10.1029/2004GL022192.

Van Wijk, J.W., Blackman, D.K., 2005. Dynamics of continental rift propagation: the end-menber modes. Earth Planet. Sci. Lett. 229, 247–258.

Wilson, J.T., 1965. A new class of faults and their bearing on continental drift. Nature 207, 343–347.

Wilson, J.T., 1966. Did the atlantic close and then re-open? Nature 211, 676–681.

Wood, C.A., 1983. Continental rift jumps. Tectonophysics 94, 529–540.

Yamasaki, T., Gernigon, L., 2010. Redistribution of the lithosphere deformation by the emplacement of underplated mafic bodies: implications for microcontinent formation. Journal of the Geological Society, London 167, 961–971. doi:10.1144/0016-76492010-027. 5

Dynamic Modelling of Accretionary Prisms and Stratigraphy of Forearc basins

Utsav Mannu[1], Kosuke Ueda[1], Sean D. Willett[1], Taras Gerya[2], Michael Strasser[1]

[1] *Geological Institute, ETH Zürich, 8092 Zürich, Switzerland*
[2] *Institute of Geophysics, ETH Zürich, 8092 Zürich, Switzerland*
e-mail: *utsav.mannu@erdw.ethz.ch*
session: *Tectonics and Surface Processes*

Introduction

Subduction zones are often accompanied by a landward accumulation of sediments scraped off the subducting oceanic plate into the accretionary prism. Accretionary prisms are considered analogous to wedges of snow or soil in front of a moving rigid indenter and deform to attain a critical taper (Davis et al., 1983; Dahlen, 1984). However, contemporary analogue and theoretical models for accretionary prisms (Wang and Hu, 2006) and inferences from high-resolution seismic imaging (Park et al., 2002; Bangs et al., 2004; Moore et al. 2007) have lead to a change in our understanding of wedge dynamics. External factors such as sedimentation on the wedge top have the potential to stabilize the wedge and to reduce the extent of internal deformation (Storti and McClay, 1995). Amount and spatial variability of sedimentation (Simpson, 2010) can lead to different wedge architectures. As sedimentation rates can change in time and space, the overall feedback provided by sedimentation to wedge dynamics and vice-versa becomes important in understanding the evolution of accretionary wedges. We investigate the effects of sedimentation with a dynamic 2D thermo mechanical model incorporating surface processes, strain weakening and sediment subduction. The model includes high-resolution particle tracking of sediment layers in order to visualize the developing stratigraphy of the wedge-top basins. Stratigraphic features such as unconformities are easily observable in the model. Wedge top basin stratigraphy revealed by high-resolution seismic acquisitions and borehole data has proved to be an invaluable repository of past tectonic movements within accretionary prisms (Beaudry and Moore, 1985; Strasser et al. 2009). Numerical modeling presents an opportunity to test interpretations of seismic records for dynamic consistency. In this study, we present a new numerical model for: a) the architecture of the wedge; and b) the stratigraphy of wedge-top basins to understand the physics of wedge evolution.

Method

We use a modified version of the thermo-mechanical code I2VIS (Gerya and Yuen, 2003, 2007). It is based on the conservative fully staggered finite difference scheme with visco-brittle/plastic rheology, and a non-diffusive marker- in-cell technique. The modelling domain spans *3500 km* × *200 km* (Figure 1) on an irregular grid of 1284 x 300 nodes. The initial model setup mimics very broad features of a passive margin. Subduction initiation is achieved by the initial geometry and a prescribed weak zone (light blue in Figure 1). The weak zone also ensures decoupling between oceanic and continental crust during subduction initiation. The lower boundary of the model is permeable with an infinity-like external slip condition ensuring a free slip condition at an external prescribed boundary (Δz_{ext} = 2000 km). The adjoining 10 km

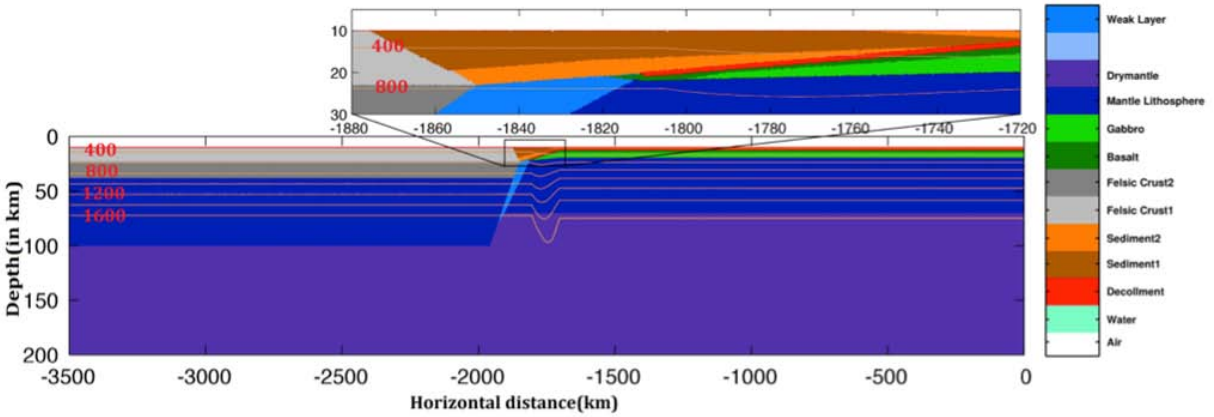

Fig. 1.: Initial model setup. The oceanic crust is overlain by two types of rheologically identical sediments (light and deep brown), for 2.5 km and another 1 km of weak layer prescribed to become the décollement (red). The oceanic crust is 7 km thick and consists of 2 km of basaltic (deep green) and another 5 km of gabbroic rocks (light green). The continental crust is 28 km thick having two equally thick layers for upper (light grey) and lower crust (dark grey) that differ in density and rheology.

zone is allocated maximum viscosity of 10^{19} Pa s to minimize the mechanical interactions along this boundary (Gorczyk et al., 2007a). A free slip condition is imposed on all other boundaries. The convergence velocity is implemented by imparting horizontal velocities to the distal oceanic and continental plates.

The basin isochronal surfaces are tracked by addition of a line of Lagrangian markers in time along the upper surface of the model, which subsequently are buried, transported, and deformed according to the velocity field generated in the model (Figure 2). The sedimentation is implemented in two ways: (i) focused deposition of sediments in the basin (i.e. simulating ponding geometries resulting presumably by gravity flows (e.g. turbidites) into closed basins, and (ii) continuous draping along the submerged wedge surface thus simulating hemi-pelagic sedimentation.

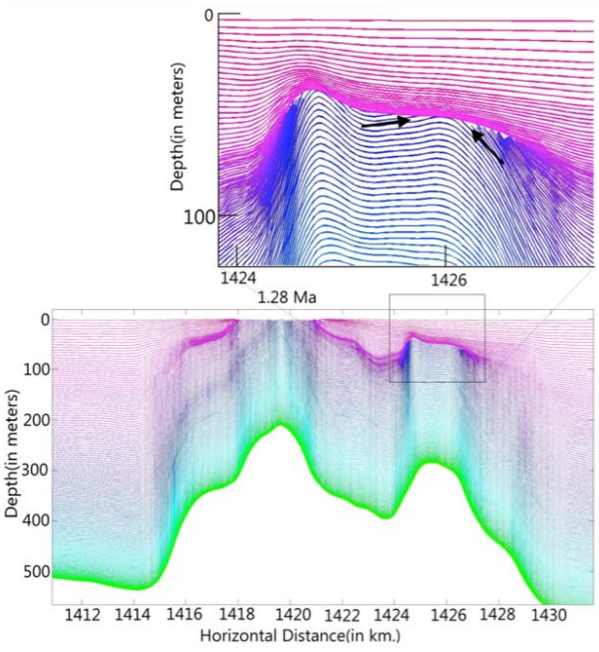

Fig. 2.: A typical result for basin stratigraphy illustrating an unconformity in the forearc basin (marked with black arrows). The unconformity illustrates the erosional surface during the subsequent thrust faults. The color from green to purple signifies the time when the marker line was placed on the surface, green being the oldest and purple youngest.

Preliminary Results

A reference model is illustrated in Figure 3 after 13.4 Myr of model run. Based on the observations of time frames from the reference model, a retro-forearc basin forms that remains passive for most

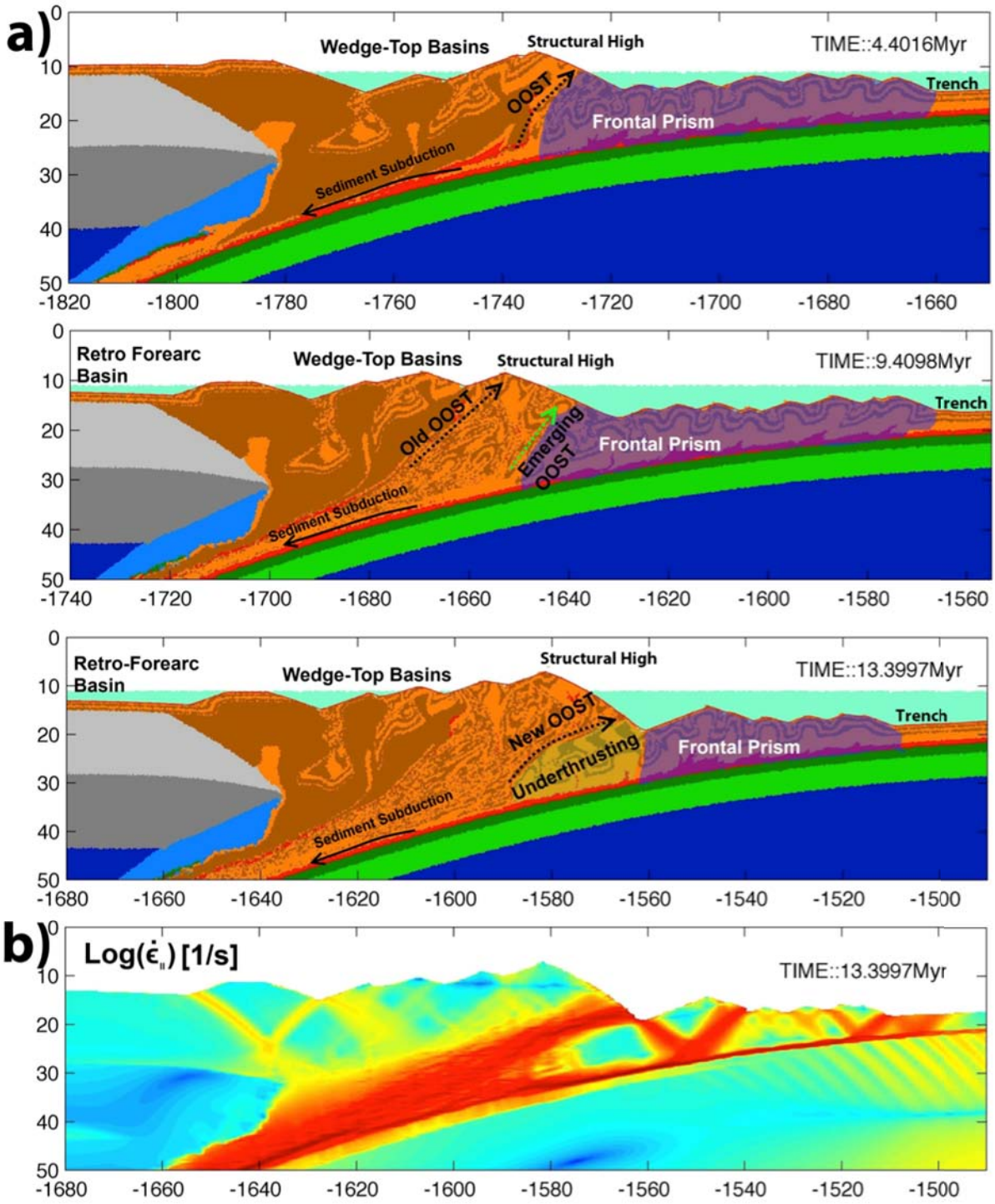

Fig. 3.: Accretionary prism formed in reference model with internal angle of friction for décollement $\tan(\phi_D) = 0.08$ and internal angle of friction for sediments $\tan(\phi) = 0.4$. The convergence velocity is 5cm/yr, distributed between the continental and oceanic plates in a ratio of 1:2. There is no sedimentation or strain weakening in this model. a) Plot of material types at ∼4.4Myr, ∼9.4 Myr and 13.4My. b) Plot of second invariant of strain rate tensor at ∼13.4Myr.

part of the model run. Other smaller wedge-top basins are formed on the top of the wedge, which is separated from the frontal prism by a structural high. The structural high is uplifted due to displacement along an Out-Of-Sequence Thrust (OOST) and subsequent back accretion. Figure 3 illustrates that episodic OOSTs form prior to back accretion of the frontal prism, and keeps on stepping forward with time. A deep slope basin is formed at the transition between the frontal prism and the uplifted part of the prism due to back accretion. This uplifted part of the prism is relatively stable and undergoes little deformation with time hence is referred to as the stable wedge. When a new OOST emerges, it rapidly overthrusts the frontal prism and slope basin. This causes the uplift of the material lying between the old OOST and the emerging one. Sediment subduction occurs throughout the model evolution. The volume of sediment subduction decreases around 5 Ma; thereafter, it fluctuates within a fixed range. The frontal prism undergoes perpetual in-sequence thrusting, accreting material off the trench. However, the effective length of the frontal prism decreases after initiation of back-accretion. When that the back-accretion halts, there is a rapid increase in frontal prism length. Based on various model run we observe amount of back-accretion is controlled by the strength of the décollement and of the sediments.

Discussion & Outlook

Building upon the work illustrated here, the study will present various coupled wedge- and sedimentation scenarios to discuss effects of spatio-temporal variation in sedimentation on wedge dynamics and vice versa. Preliminary results indicate that deformation style variations correlate with sedimentation regime along a trench to forearc basin transect. The synthetic stratigraphy of forearc basin and slope basin resulting from the newly developed isochronal surface tracking approach (Figure 2) illustrates distinct stratigraphic features including unconformities and truncation in the basin. The study will explore and discuss these generic stratigraphic signatures with respect to different structural and mechanical evolution paths of the accretionary prism.

References

Bangs, N. L., Shipley, T. H., Gulick, S. P., Moore, G. F., Kuromoto, S., & Nakamura, Y. (2004). Evolution of the Nankai Trough décollement from the trench into the seismogenic zone: Inferences from three-dimensional seismic reflection imaging. Geology, 32(4), 273-276.

Beaudry, D., & Moore, G. F. (1985). Seismic stratigraphy and Cenozoic evolution of West Sumatra forearc basin. AAPG Bulletin, 69(5), 742-759.

Dahlen, F. A. (1984). Noncohesive critical Coulomb wedges: An exact solution. Journal of Geophysical Research: Solid Earth (1978–2012), 89(B12), 10125-10133.

Davis, D., Suppe, J., & Dahlen, F. A. (1983). Mechanics of fold-and-thrust belts and accretionary wedges. Journal of Geophysical Research: Solid Earth (1978–2012), 88(B2), 1153-1172.

Gerya, T. V., & Yuen, D. A. (2007). Robust characteristics method for modelling multiphase visco-elasto-plastic thermo-mechanical problems. Physics of the Earth and Planetary Interiors, 163(1), 83-105.

Gerya, Taras V., and David A. Yuen. "Characteristics-based marker-in-cell method with conservative finite-differences schemes for modeling geological flows with strongly variable transport properties." Physics of the Earth and Planetary Interiors 140.4 (2003): 293-318.

Gorczyk, W., Willner, A.P., Gerya, T.V., Connolly, J.A.D., Burg, J.P. (2007): Physical controls of magmatic productivity at Pacific-type convergent margins: new insights from numerical modeling. Phys. Earth Planet. In., 163, 209–232

Moore, G. F., Bangs, N. L., Taira, A., Kuramoto, S., Pangborn, E., & Tobin, H. J. (2007). Three-dimensional splay fault geometry and implications for tsunami generation. Science, 318(5853), 1128-1131.

Park, J. O., Tsuru, T., Kodaira, S., Cummins, P. R., & Kaneda, Y. (2002). Splay fault branching along the Nankai subduction zone. Science, 297(5584), 1157-1160.

Simpson, G. D. (2010). Formation of accretionary prisms influenced by sediment subduction and supplied by sediments from adjacent continents. Geology, 38(2), 131-134.

Storti, F., & McClay, K. (1995). Influence of syntectonic sedimentation on thrust wedges in analogue models. Geology, 23(11), 999-1002.

Strasser, M., Moore, G. F., Kimura, G., Kitamura, Y., Kopf, A. J., Lallemant, S., ... & Zhao, X. (2009). Origin and evolution of a splay fault in the Nankai accretionary wedge. Nature Geoscience, 2(9), 648-652.

Wang, K., & Hu, Y. (2006). Accretionary prisms in subduction earthquake cycles: The theory of dynamic Coulomb wedge. Journal of Geophysical Research: Solid Earth (1978–2012), 111(B6).

Evolution of topography of post-Devonian Scandinavia: Effects and rates of erosion

Sergei Medvedev[1], Ebbe H. Hartz[1,2]

[1] *Centre for Earth Evolution and Dynamics, Oslo University, Norway*
[2] *Det norske oljeselskap, Oslo, Norway*
e-mail: *sergei.medvedev@fys.uio.no*
session: *Tectonics and Surface Processes*

Abstract The mechanisms and timing of regional uplift in Scandinavia remain enigmatic given that the region has been relatively tectonically inactive after the NE Atlantic breakup. In this study we combine analysis of the vertical motions of the region caused by the (dominantly) glacial erosion during the Quaternary with AFT analysis of rocks from the area. Using numerical models we first quantify how glacial erosion reshapes the topography. Glacial erosion carved out the fjords and valleys to a depth of 2 km below the palaeo-surfaces. This erosional event represents a major local weight loss and results in a up to 0.8 km uplift of rocks and up to 0.5 km rise of local topography. These estimates only marginally depend on the effective elastic thickness of the lithosphere and thus are robust. We show then that there is no correlation between sample altitude and published AFT data, but that there is a correlation between AFT age and the depth below our constructed pre-glacial summit surface. This correlation demonstrates the robustness of the numerical erosional model, quantifies average erosion rates during Carboniferous-Cretaceous at < 0.01 mm/yr, and outlines the regions of western Scandinavia (Lofoten and Bergen areas and Møre-Trøndelag fault complex) with atypical Mesozoic-Cenozoic evolution probably related to late restructuring.

Numerical model of Quaternary erosion

We use a simple quantitative approach by numerically filling the eroded places with crustal material and calculating the additional load. The resultant modelled surface is thus an approximation of the pre-erosional topography and is not tied to a specific time. This allows us to estimate the elastic response and potential vertical movements of surface topography backward in time (Figs. 1D-F). The numerical model utilizes Matlab-based numerical suite ProShell (Medvedev et al., 2008; Medvedev et al., 2013).

Figures 1 and 2 present results of the numerical model

Combined analysis of AFT data and erosional model

We assign the amount of exhumation calculated in the erosional model (Figs. 1,2) to all of the AFT data points (Hendriks et al., 2007; Ksienzyk et al., 2014). This way we assume that the modelled pre-glacial topography (1B) was the dominant shape of the topography during post-Devonian evolution of Scandinavia and thus the age of rocks is constant on such surfaces.We also introduced the general trend between exhumation and AFT ages (Fig 3.)

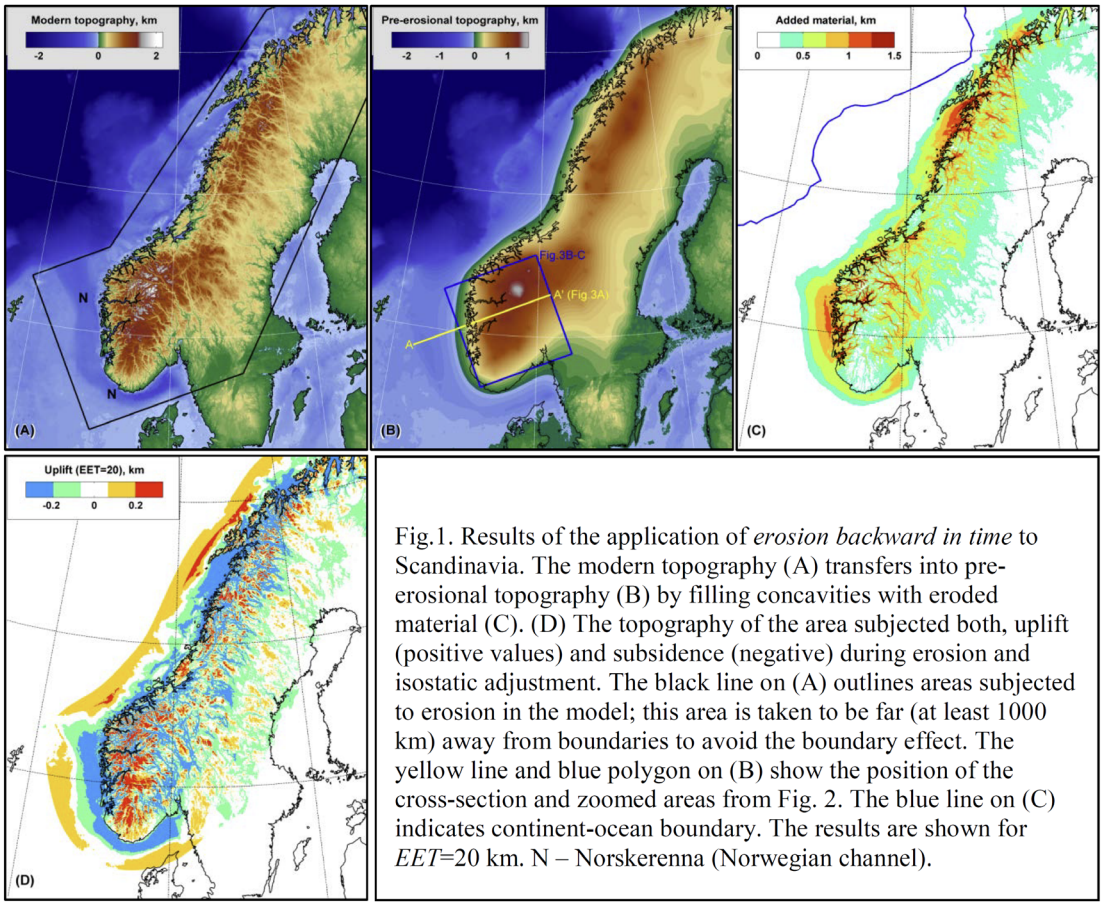

Fig.1. Results of the application of *erosion backward in time* to Scandinavia. The modern topography (A) transfers into pre-erosional topography (B) by filling concavities with eroded material (C). (D) The topography of the area subjected both, uplift (positive values) and subsidence (negative) during erosion and isostatic adjustment. The black line on (A) outlines areas subjected to erosion in the model; this area is taken to be far (at least 1000 km) away from boundaries to avoid the boundary effect. The yellow line and blue polygon on (B) show the position of the cross-section and zoomed areas from Fig. 2. The blue line on (C) indicates continent-ocean boundary. The results are shown for *EET*=20 km. N – Norskerenna (Norwegian channel).

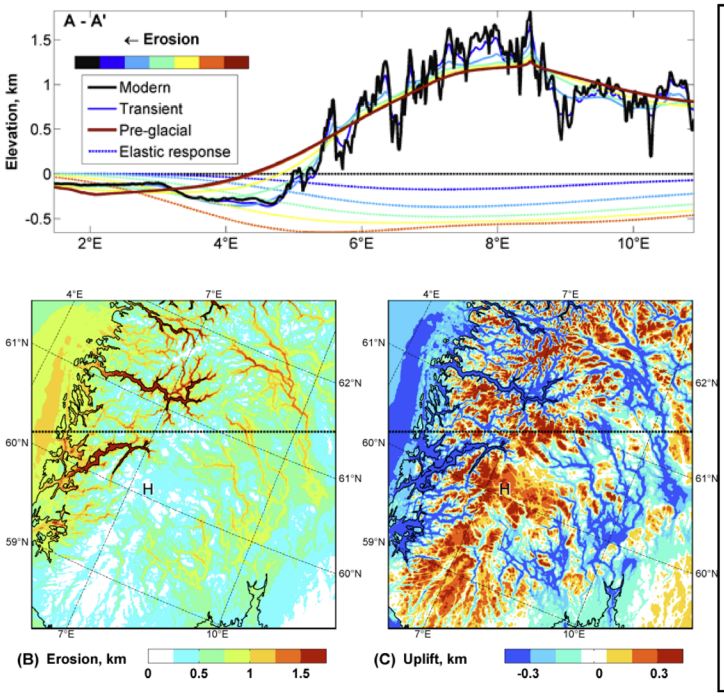

Fig. 2(A) Evolution of topography and the elastic response for profile A-A' Modern topography and modeled transient and pre-glacial topography displayed using colors that correspond to the degree of erosional evolution. The elastic response is 0 at modern time and increases in absolute value with increase of the weight of less eroded upper surface in the *backward-in-time* erosional model. Of note is the summit around 8 ºE which was uplifted by more than 0.4 km. (B) The amount of erosion and (C) erosion-driven elevation changes predicted by the model within a blue box from Fig. 1B. The results are shown for *EET*=20 km H – Hardangervidda (average elevation 1.0-1.1 km)

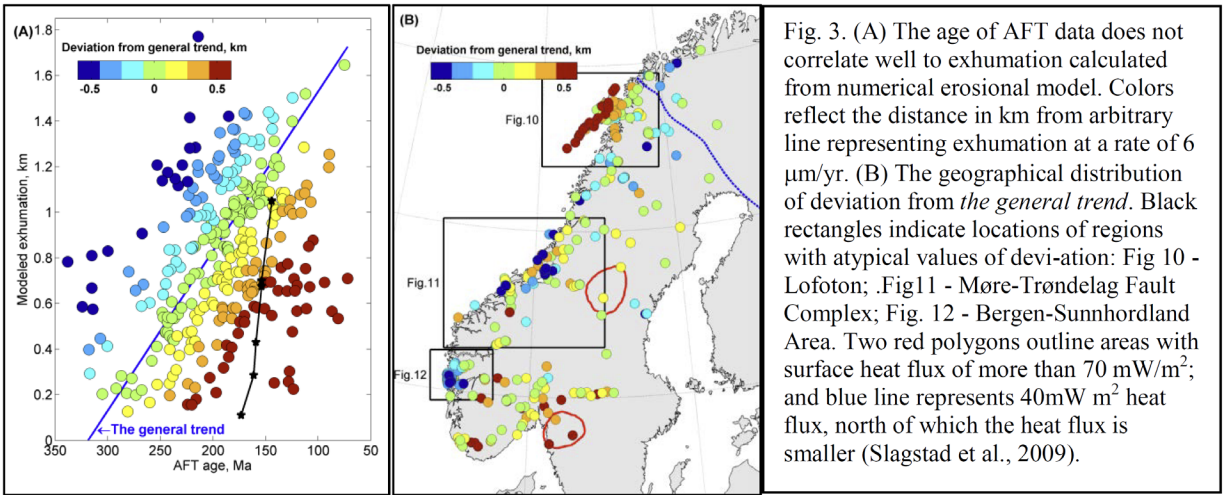

Fig. 3. (A) The age of AFT data does not correlate well to exhumation calculated from numerical erosional model. Colors reflect the distance in km from arbitrary line representing exhumation at a rate of 6 μm/yr. (B) The geographical distribution of deviation from *the general trend*. Black rectangles indicate locations of regions with atypical values of devi-ation: Fig 10 - Lofoton; .Fig11 - Møre-Trøndelag Fault Complex; Fig. 12 - Bergen-Sunnhordland Area. Two red polygons outline areas with surface heat flux of more than 70 mW/m^2; and blue line represents 40mW m^2 heat flux, north of which the heat flux is smaller (Slagstad et al., 2009).

Analysis of the distributions show:

1. The MTFC does not fit to our initial assumption of no tectonic activity. The Lofoton area has erosion of greater scale than one which can be explained by our simple erosional model. The Bergen-Sunnhordland area exhibits relative vertical motion postdating the AFT ages. Thus, we should exclude these areas from consideration.

2. Shallower closure conditions in the South correlate with higher surface heat flux measured in present day conditions and with heat from the Oslo plume during Late Paleozoic (Torsvik et al., 2008). Thus, we introduce an iteratively derived coefficient of 40 m per degree of latitude correction. This approximately corresponds to the 400 m difference in a closure depth over the entire domain, to a maximum of 4 °C/km difference in geothermal gradients.

Conclusions

The combined analysis of erosion model and AFT ages allows us to conclude:

1. The erosion model is robust and reasonable as a first order regional approximation for the reconstruction of pre-glacial topography of Scandinavia.

2. The vertical motion of topography due to glacial carving is a significant contributor to uplift of the Scandinavian mountains (up to 0.4-0.5 km). This result is almost independent from uncertain parameters such as EET.

3. The average thickness of the material eroded during active glacial carving is 430 m. This would correspond to an erosion rate of 0.1 mm/yr (if the glacial carving was active 4.3 My). Locally, however, the rate may exceed 1 mm/yr as a consequence of the localized nature of glacial erosion.

4. The erosion rate during the Mesozoic is less than 1 km per 100 My which corresponds to a rate of <0.01 mm/yr. This rate is low and thus topographic variations of Scandinavia were limited.

5. Our simple model allows the identification of anomalous regions within Scandinavia (non-standard evolution or active tectonic): Lofoton, Bergen-Sunnhordland area, and the Møre-Trøndelag fault complex.

References

Hendriks, B., Andriessen, P., Huigen, Y., Leighton, C., Redfield, T., Murrell, G., Gallagher, K., Nielsen, S.B., 2007. A fission track

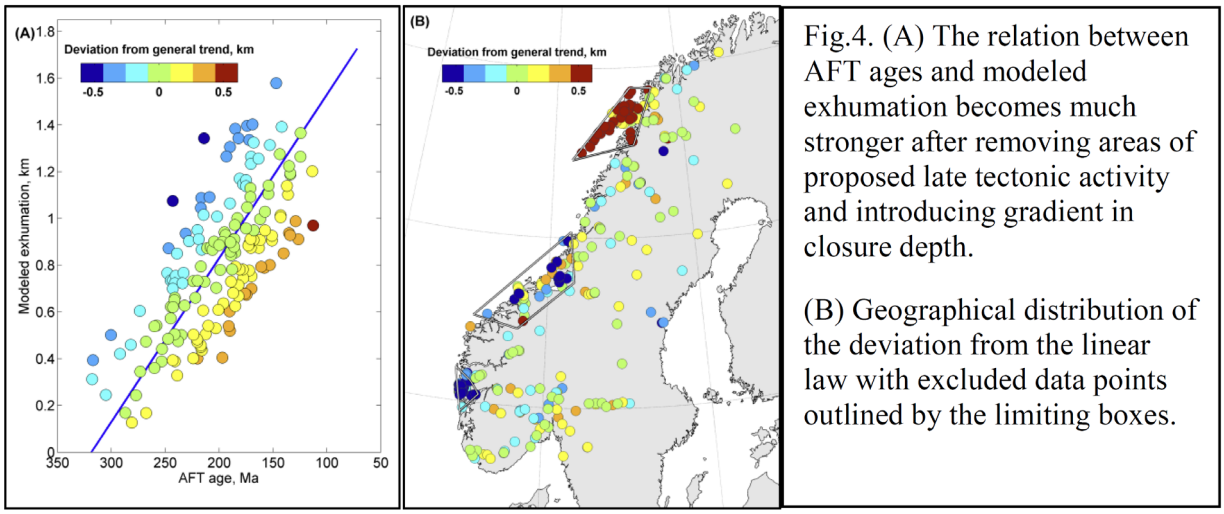

Fig.4. (A) The relation between AFT ages and modeled exhumation becomes much stronger after removing areas of proposed late tectonic activity and introducing gradient in closure depth.

(B) Geographical distribution of the deviation from the linear law with excluded data points outlined by the limiting boxes.

data compilation for Fennoscandia. Norw J Geol 87(1-2), 143-155.

Ksienzyk, A.K., Dunkl, I., Jacobs, D., Fossen, H., Kohlmann, F., 2014. From orogen to passive margin: constraints from fission track and (U–Th)/He analyses on Mesozoic uplift and fault reactivation in SW Norway Geological Society, London, Special Publications 390, 689-702.

Medvedev, S., Hartz, E.H., Podladchikov, Y.Y., 2008. Vertical motions of the fjord regions of central East Greenland: Impact of glacial erosion, deposition, and isostasy. Geology 36(7), 539-542.

Medvedev, S., Souche, A., Hartz, E.H., 2013. Influence of ice sheet and glacial erosion on passive margins of Greenland. Geomorphology 193, 34-46.

Slagstad, T., Balling, N., Elvebakk, H., Midttomme, K., Olesen, O., Olsen, L., Pascal, C., 2009. Heat-flow measurements in Late Palaeoproterozoic to Permian geological provinces in south and central Norway and a new heat-flow map of Fennoscandia and the Norwegian-Greenland Sea. Tectonophysics 473(3-4), 341-361.

Torsvik, T.H., Smethurst, M.A., Burke, K., Steinberger, B., 2008. Long term stability in deep mantle structure: Evidence from the similar to 300 Ma Skagerrak-Centered Large Igneous Province (the SCLIP). Earth Planet. Sci. Lett. 267(3-4), 444-452.

Numerical modeling of main inverted structures in the Western Barents Sea.

Muhammad Armaghan Faisal Miraj[1], Christophe Pascal[1], Roy H. Gabrielsen[2], Jan Inge Faleide[2]

[1]*Institut für Geologie, Mineralogie und Geophysik, Ruhr-Universität Bochum, Bochum, Germany.*
[2]*Department of Geoscience, University of Oslo, Norway*
e-mail: *Muhammad.FaisalMiraj@ruhr-uni-bochum.de*
session: *Tectonics and Surface Processes*

Introduction

A number of fault complexes in the western Barents Sea, preciously formed in response to different Paleozoic to Cenozoic tectonic events, were inverted between Late Triassic to Miocene. Tectonic inversion is evidenced by reactivation of normal faults. The aim of the study is to investigate by numerical modelling the origin of stresses responsible for the different inversion events. A secondary goal is to simulate slip on major faults as a result of tectonic inversion of the western Barents Sea. To these aims, we use a finite-element numerical code Code-Aster (Jean 2013) to simulate stresses and displacements in the study area and plan to use the SORTAN analytical method (Pascal 2004) to predict the sense of slip along major fault planes.

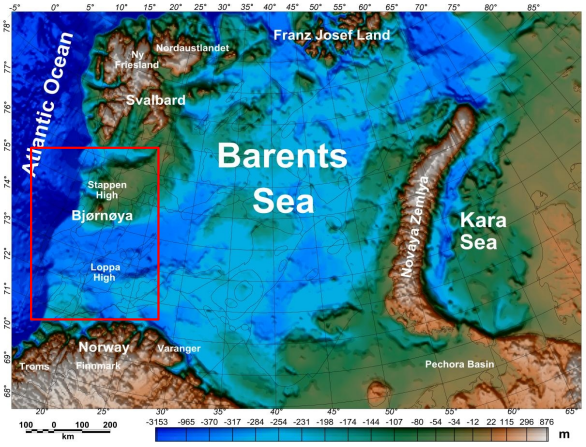

Fig. 1.: Regional setting and location of the study area (Modified from Barrère et al., 2009)

Geological setting

The study area is part of the western Barents Sea and extends from 15 - 25° E and 70 - 74° N (Figure 1 & 2). A lot of research work has already been done in the Barents Sea (Gabrielsen et al., 1990; Doré 1991; Ritzmann and Faleide, 2007; Tsikalas et al., 2012; Gernigon et al. 2014).

The major tectonic phases responsible for the development of the geological framework of the western Barents Sea includes the collision of Baltica and Laurentia in mid-Paleozoic time followed by Mesozoic rifting events and Cenozoic breakup (Gabrielsen et al., 1990; The first main tectonic event, the Timanian Orogeny, resulted in a fold-and-thrust belt along the northeastern passive margin of Baltica and the southwestern Barents Sea during (Ediacarian) times (Roberts and Olovyanishnikov, 2004; Gernigon et al. 2014). The Caledonian Orogeny resulted in the closure of the Iapetus Ocean due to the convergence of the Laurentian and Baltic plates at $\sim$ 400 Ma (Roberts, 2003).

The Late Mesozoic-Cenozoic tectonic evolution of the southwestern Barents Sea is influenced by several stages of extension and transtension. In Early Triassic, the western Barents Sea was af-

fected by rifting and this rift phase is also recorded in many parts of the Arctic and North Atlantic regions (Tsikalas et al., 2012 and Gernigon et al. 2014). Middle-Late Triassic was the postrift thermal subsidence time in the North Atlantic and Arctic basins (Gernigon et al. 2014) but in contrast, the Barents shelf area experienced the initiation of progressive uplift of the northern, eastern, and southern Barents Sea regions (Worsley et al., 2008).

The Middle Jurassic to Early Cretaceous Atlantic rifting affected the western margin of the Barents Sea Shelf (Faleide et al., 2008). These continuous rifting phases during the Jurassic are responsible for the development of major deep basins in the western Barents Sea (Gernigon et al. 2014). In the Late Cretaceous to Paleocene times strike-slip movements took place in the western Barents Sea which resulted in to the formation of pull-apart basins (Faleide et al., 1996).

During and after the Early Tertiary rifting and breakup of the northern North Atlantic, the western margin of the Barents Sea was subject to tectonic inversion, apparently involving elements of shortening in NE-SW and NW-SE directions (Leever et al., 2008). Several mechanisms responsible for the inversion have been suggested, including secondary effects of the uplift of Iceland and local transpression associated with the geometry and configuration of the plate boundary itself.

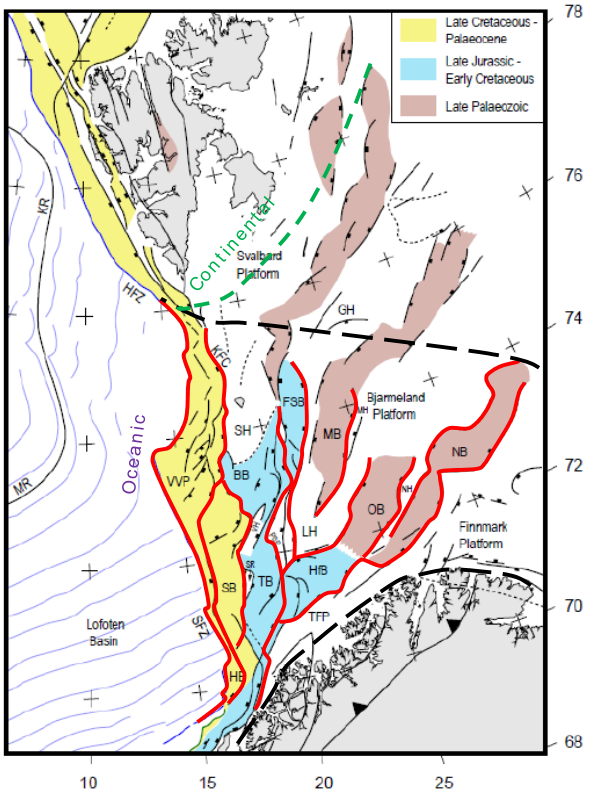

Fig. 2.: Major structural elements of the western Barents Sea and bordering areas (after Gabrielsen et al., 2010).

Numerical tools and modelling approaches

The numerical tools used for this study are Finite-Element Method Code-Aster & Salome Meca to simulate the stresses and displacement in the study area and the SORTAN to predict the sense of potential slip along the major fault planes.

CODE_ASTER

Code-Aster is a Finite Element Analysis code used for the study of the mechanical behavior of different structures. It can handle mechanical, thermal and associated phenomena in all sort of analysis. The code is capable to solve the problems related to all type of linear and non-linear statics e.g. 3D, 2D, beams, pipes, multi fibers, discrets, shells and plates etc. It produces a set of result files after given the appropriate data files set but without any colorful post processing images.

SALOME is open-source software that provides a generic platform for pre- and post-Processing for numerical simulation and is the integration of the Code-Aster solver in Salome platform. In figure 3 the deformation energy of a rock volume is minimized, assuming displacement constraints on some parts. Rocks follow linear elasticity and displacement constraints are used to input geological constraints. Finally finite element meshes are used to discretize the equations and Code-Aster is used to perform computations.

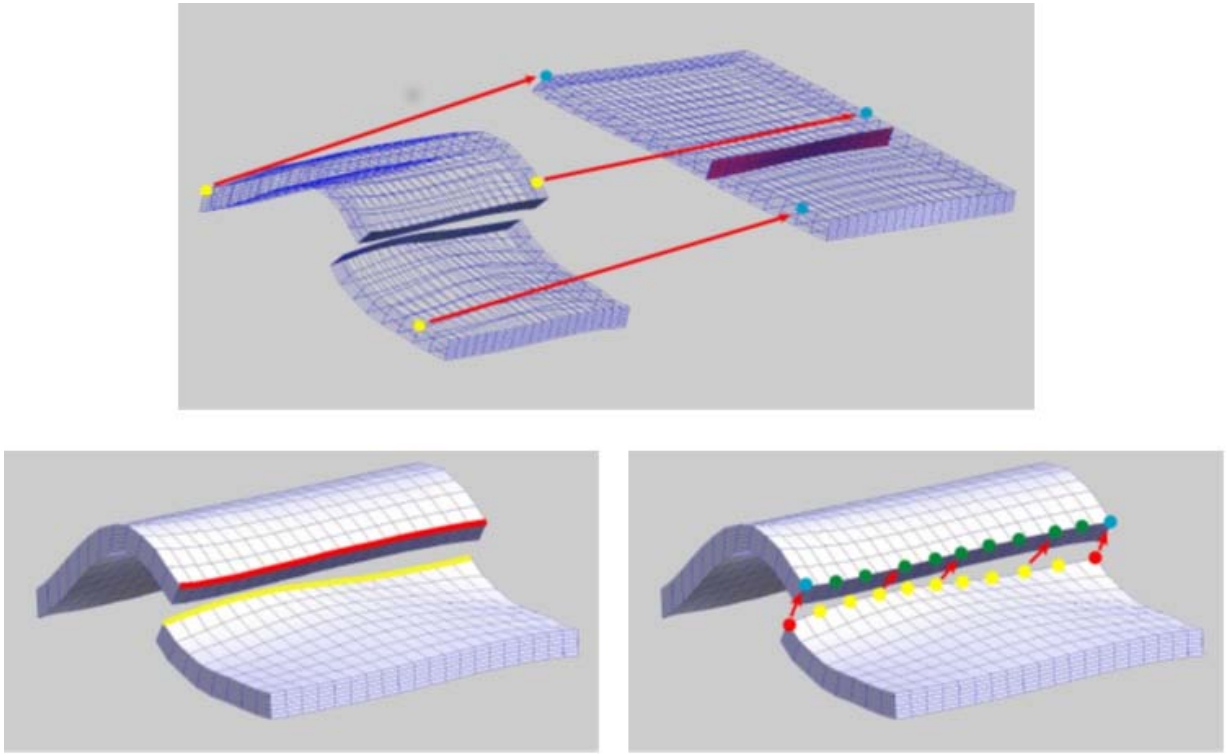

Fig. 3.: Expected results of the research showing inverted fault closure (after Rudkiewicz et al., 2009)

The SORTAN Method

SORTAN is used to calculate the sense of slip which is induced by stresses along fault planes (Pascal 2004). The method is based on the "Wallace-Bott" assumptions: that the slip on fault surfaces occurs parallel to the applied shear stress, faults are planar, blocks are rigid along the fault surfaces neither stress perturbations nor block rotations occur and applied stress state is stable for all tectonic events.

The input numerical parameters required for SORTAN are the azimuth θ and the shape ratio ϕ to describe the applied stress state and dip direction d and the dip angle p to describe the geometry of the fault.

Different fault complexes according to their respective ages of activation and reactivation have been selected (Figure 2). The selection of these fault systems is based on their orientations, structural style (basement involved, hard/soft-linked, salt influence, etc.), timings and evolution with respect to local and regional tectonic events.

References

Barrère, C., J. Ebbing, and L. Gernigon (2009), Offshore prolongation of Caledonian structures and basement characterization in the western Barents Sea from geophysical modelling, Tectonophysics, 470(1–2), 71–88.

Christophe Pascal and Roy H. Gabrielsen (2001) Numerical modeling of Cenozoic stress patterns mid-Norwegian margin and the northern North Sea. Tectonics, Vol. 20, No. 4, Pages 585-599.

Doré, A. G. (1991), The structural foundation and evolution of Mesozoic seaways between Europe and the Arctic, Palaeogeogr. Palaeoclimatol. Palaeoecol., 87(1–4), 441–492.

Faleide, J. I., A. Solheim, A. Fiedler, B. O. Hjelstuen, E. S. Andersen, and K. Vanneste (1996), Late Cenozoic evolution of the western Barents Sea-Svalbard continental margin: Impact of glaciations on basin evolution, data and models from the Norwegian margin and adjacent

areas, Global Planet. Change, 12, 53–74.

Gabrielsen, R.H., Jensen, L.N., Kalheim, J.E. and Riss, F., 1990. Structural Elements of the Norwegian Continental Shelf–Part 1: The Barents Sea Region Norwegian Petroleum Directorate Bulletin, 6, 47.

Gernigon, L., M. Brönner, D. Roberts, O. Olesen, A. Nasuti, and T. Yamasaki (2014), Crustal and basin evolution of the southwestern Barents Sea: From Caledonian orogeny to continental breakup, Tectonics, 33, doi:10.1002 / 2013TC003439.

Jean-Pierre Aubry 2013. Beginning with Code_Aster, A practical introduction to finite element method using Code_Aster Gmsh and Salom. Version 1.1.1 LAL 1.3, GNU FDL 1.3 et CC By-SA 3.0e.

Pascal, C., 2004. SORTAN: a UNIX program for calculation and graphical presentation of fault slip as induced by stresses. Computers & Geosciences 30 (2004) 259–265 pp. 163–195, Geol. Soc., London.

Exploratory analog modeling of the effects of a morpho-rheological obstacle across a wrench fault system: the example of the Gloria Fault – Tore Madeira Rise intersection in NE Atlantic

F. M. Rosas[1,2], J. Almeida[2], F. Barata[2], B. Carvalho[2], P. Terrinha[3], J. Duarte[4], C. Kullberg[2], R. Tomás[2]

[1]*Instituto Dom Luiz, Campo Grande, Ed. C1, Piso 2, 1749-016 Lisboa, Portugal*
[2]*Universidade de Lisboa, Faculdade de Ciências, Departamento de Geologia, Campo Grande, Ed. C6, Piso 4, 1749-016 Lisboa, Portugal*
[3]*Instituto Português do Mar e da Atmosfera, 1749-077 Lisbon, Portugal*
[4]*School of Geosciences, Monash University, Melbourne, VIC 3800, Australia*
e-mail: *frosas@fc.ul.pt*
session: *Tectonics and Surface Processes*

Tectonic setting

Recent tectonic mapping of the intersection between the Gloria Fault (GF) and the Tore Madeira Rise (TMR) in NE Atlantic (Fig. 1A) revealed a newly unveiled pattern of conspicuous morphotectonic features (Fig. 1B). In the present work we use analog modeling to preview the type of structural pattern expected from such an interference, testing different assumptions regarding the geometry and rheology of the main features at stake.

The GF is a major active (dextral strike-slip) fault corresponding to the eastwards continuation of the Atlantic transform fault that marks the Eurasia-Africa (Nubia) plate boundary in NE Atlantic, also known as the Azores-Gibraltar Fracture Zone (AGFZ, e.g., Jiménez-Munt et al., 2001). A dominant overall right-lateral strike-slip kinematics has been ascribed to the GF, confirmed namely by historical and instrumental seismicity data including high magnitude earthquakes (e.g. M=7.1 and M=8.4 of 08/05/1939 and 25/11/1941 respectively, implying surface ruptures of the order of 250-300 km, Buforn et al., 1988) with complying focal mechanisms attesting the present day active tectonic nature of this fault.

The TMR is a ∼1000km long NE-SW elongated submarine ridge, extending between the Madeira archipelago (to the southeast) and the submarine Tore seamount (to the northwest), which age and origin remain debatable and yet not fully understand. Nevertheless, numerous diachronic manifestations of volcanism have been reported by several authors, comprising ages ranging from late Cretaceous to middle-late Miocene to Present day (Geldmacher et al., 2006; Grange et al., 2010). Wide-angle refraction studies suggest a rheological structure in compliance with thickened oceanic crust in isostatic equilibrium, formed as a result of a possible phase of anomalous high accretion in the Mid-Atlantic Ridge (Peirce and Barton, 1991).

The key area targeted for modelling in the present work (Fig. 1) corresponds to the site of intersection and tectono-magmatic interference between these two major features. Our primary motivation was the newly obtained morphotectonic mapping of this area (outlined in Fig. 1B), which prompted the need to better understand the apparent control exerted by the revealed specific tectonic setting and the spatial-

time distribution of the volcanic manifestations in the area.

Analogue modeling and discussion of preliminary results

The main question addressed by the preformed scaled analog modeling was to preview the type of structural pattern (fault distribution and morphological variation) that is expected to be developed as the result of the intersection of a right-lateral strike-slip fault (accounting for the Gloria Fault system), and a morpho-rheological anomaly (accounting for the TMR). In our models it is assumed that this TMR anomaly corresponds to a softer crustal domain (e.g. with a mean viscosity closer to the one generally ascribed to the asthenosphere), and that the GF strike-slip propagates across such an anomaly from a brittle (crustal oceanic) medium.

We used the Perspex apparatus and the experimental initial configuration depicted in figure 2, using sand as a Coulomb-Mohr brittle analogous of the (oceanic) upper crustal behavior, and a scaled mixture of silicone putty (PDMS) and Wolframite powder to mimic the mechanical behavior hypothetically assumed for the TMR.

Top view photographs of the accommodation to successive wrenching increments are shown in figure 3. The main results reveal a monoclinic-like symmetry in the distribution of the main compressive and extensional structures (thrusts or graben-like/pull apart basins, respectively), which is broadly comparable to what happens in the natural example. Although a detailed geometrical correspondence is not always observed, a mechanical similitude concerning the bulk kinematics (and dynamics) at stake is possible to envisage. This is essentially manifested by the observation that the sites of silicone vertical extrusion, accounting for the volcanic highs and plugs in the natural example, are consistently coincident with the areas of intersection/confluence between the main faults and the main rheological boundaries.

Future work

Ongoing further upgrade of the experiments comprises varying the geometric and rheological configuration, considering: a) a more realistic angle of intersection ($\sim 115^{\circ}$) between the GF and the TMR; b) performing an experiment (strictly for benchmark comparative purposes) in which the considered TMR anomaly corresponds merely to a morphological anomaly, i.e. without any viscosity contrast; c) considering the existence of smaller rheological anomalies (working as localized seeds) aligned on top of the basement (GF) fault trace, embedded in the brittle medium represented by the sand.

Acknowledgements

This work was sponsored by the Fundação para a Ciência e a Tecnologia (FCT) through project MODELINK EXPL/GEO-GEO/0714/2013.

References

Buforn, E., Udias, A., and Colombas, M.A., 1988. Seismicity, source mechanisms and tectonics of the Azores-Gibraltar plate boundary. Tectonophys, 152(1-2), 89-118.

Geldmacher, J., Hoernle, K., Klugel, A., Bogaard, P. Wombacher, F., and Berning, B., 2006. Origin and geochemical evolution of the Madeira-Tore Rise (eastern North Atlantic). Journal of Geophysical Research 111, B09206, doi: 10.1029/2005JB003931.

Grange, M., Scharer, U., Merle, R., Girardeau, J. and Cornen, G., 2010. Plume Lithosphere Interaction during Migration of Cretaceous Alkaline Magmatism in SW Portugal: Evidence from U-Pb Ages and Pb-Sr-Hf Isotopes, 51(5), 1143-1170.

Jiménez-Munt, I., M. Fernandez, M. Torne, and Bird, P., 2001. The transition from linear to diffuse plate boundary in the Azores-Gibraltar region: Results from a thin-sheet model, Earth Planet. Sci. Lett., 192, 175– 189.

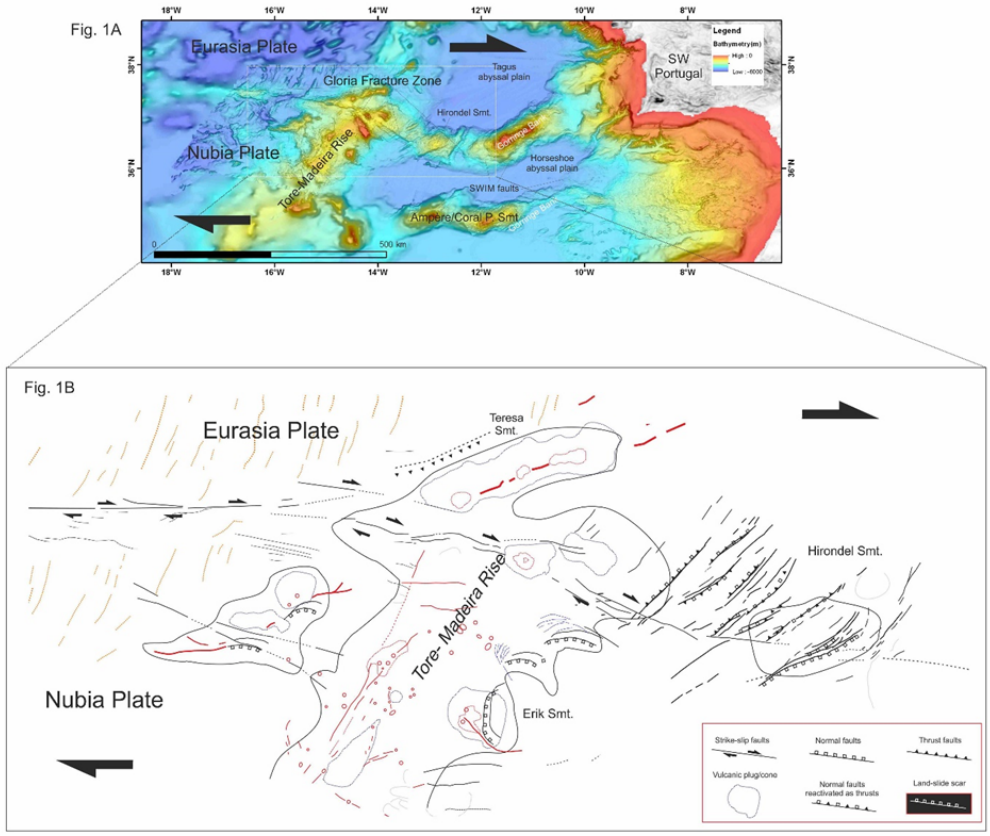

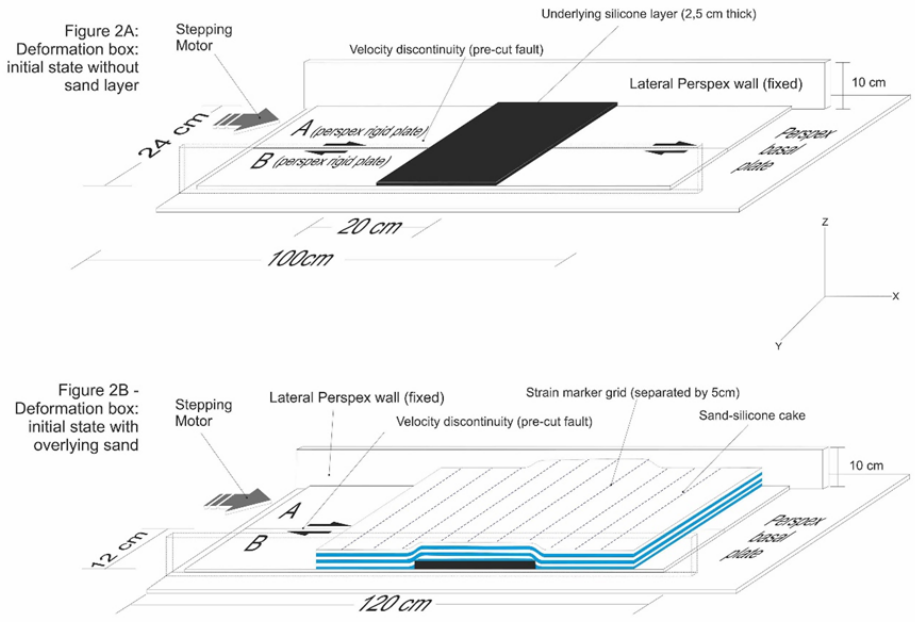

Fig. 1.: (top) A) General morpho-tectonic map of the study area; B) Detailed tectonic map (structural outline) of the key area targeted in the carried out modeling. **Fig. 2:** (bottom) Used Perspex deformation apparatus and experimental initial stage.

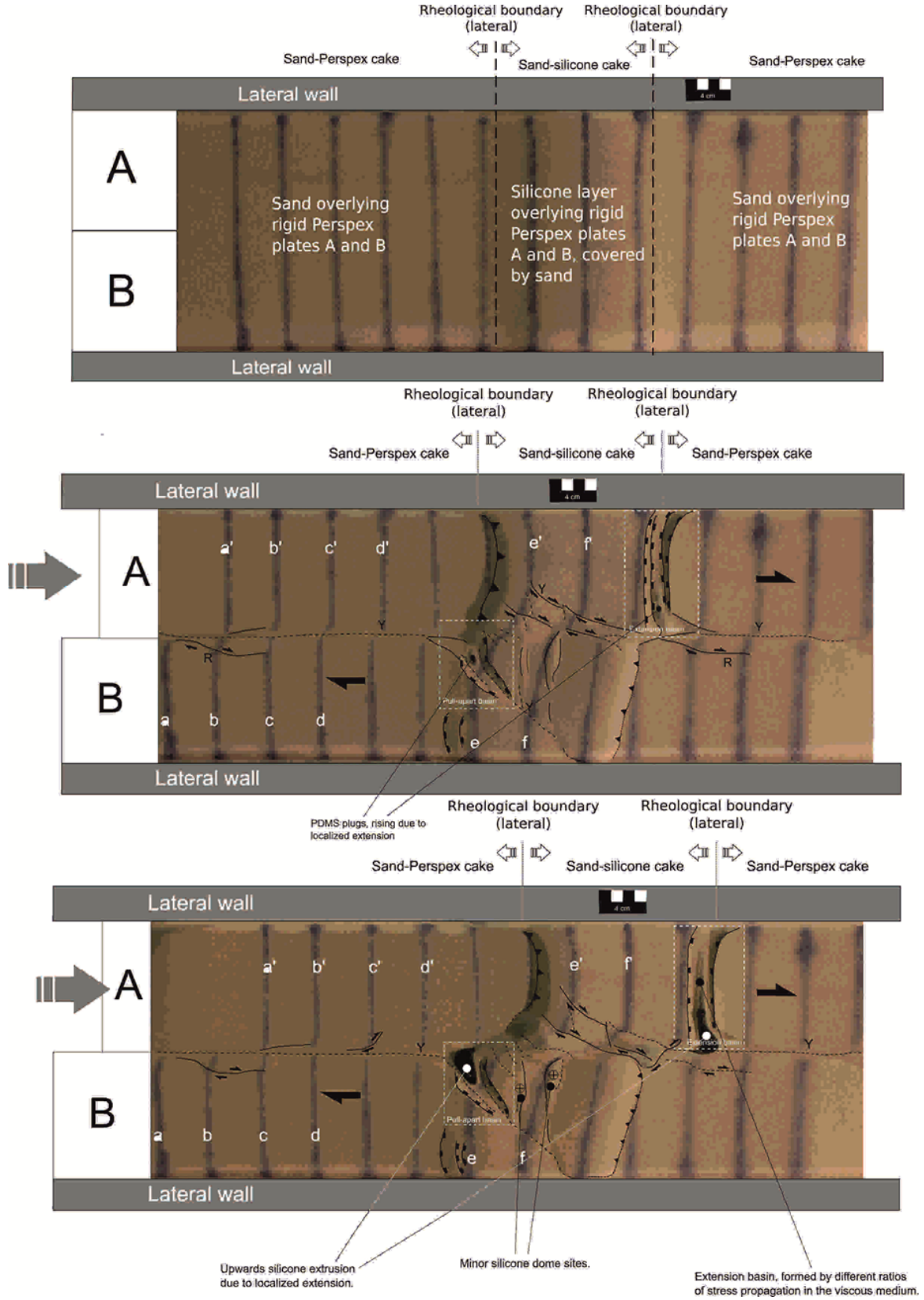

Fig. 3.: Experimental results for different incremental stages of deformation

Peirce, C., and Barton, P.J., 1991. Crustal structure of the Madeira-Tore rise, eastern North Atlantic - results of a DOBS wide-angle and normal incidence seismic experiment in the Josephine Seamount region, Geophys. J. Int., 106(2), 357-378.

DANSER: an open source surface evolution code beyond coupling with tectonic models

Sarah Schroeder[1], Richard Gloaguen[2], Jens Tympel[1], Andrey Babeyko[1], Stephan V. Sobolev[1]

[1] *GFZ Potsdam, Germany*
[2] *Bergakademie Freiberg, Germany*
e-mail: *sarah.schroeder@gfz-potsdam.de*
session: *Tectonics and Surface Processes*

Summary

We introduce the open source 2D Surface Evolution Code DANSER (Detachment limited lateral Abrasion Nonlinear diffusion Surface Evolution Routine). The code is intended to be coupled to any lithospheric scale (thermo-)mechanical code, and also to be applied to real Digital Elevation Models (DEM). Selected examples with analytically imposed uplift demonstrate that the code is able to simulate river capturing, induced by fault-bounded block rotations. In presented work, we highlight challenges and advances of the coupling to (thermo-)mechanical codes.

Introduction

First coupled lithospheric scale (thermo-)mechanical and Surface Evolution Models (SEM) were developed in the nineties (Beaumont et al., 1992, Willett, 1999). 2D thermo-mechanical codes were coupled with 1D (Willett, 1999) or 2D (Beaumont et al., 1992) surface evolution. Nevertheless, 3D (thermo-)mechanical codes are required to study more complex processes like continental collision. Since the influence of surface erosion on tectonics is not well understood, a coupled model of 2D surface evolution and 3D lithospheric scale (thermo-)mechanics (e.g. CASQUS, Kurfeß and Heidbach, 2009) could illuminate this topic.

DeLong et al. (2007) makes first attempts to adapt SEM to DEM. He applies the bifurcation method (Freeman, 1991; Pelletier, 2004) with different erosion parameters to a simulated plane. Further, he compares landslide threshold slope, drainage densitiy, relief and other topographic characteristics of the resulting topographies to a DEM of a field site in southern California. Accordingly, he chooses the input parameters of the best fit model as scaling values. The mentioned scaling parameters are used for surface evolution studies on the DEM.

It is of major importance for the scaling that the SEM is able to simulate flexible river networks. The bifurcation method makes this possible for small slopes (e.g. fans), but is not able to reflect this behaviour for steeper ones. E.g. in the Pamir orogen, the valley of the main river Panj is much broader than the stream. Nevertheless, the Panj laterally abrades the whole valley.

Simulations of river capturing events are widely studied. Approaches range from simple incision models (Garcia-Castellanos, 2002) without channel initiation function (Willgoose et al., 1991; O'Callagan and Marc, 1984) to finite-element models that compute the location of the drainage divide between every two neighbouring nodes (Castelltort et al., 2012). The challenge for every modeler is to find a balance between simple and fast algorithms on one hand, yet include complicated algorithms that capture processes that reflect the observations on the other hand.

Computational algorithm

DANSER is a Surface Evolution Code (SEC) that becomes open source available by the end of the year. It is designed for coupling with any lithospheric scale (thermo-)mechanical code. Furthermore, it can be applied to Digital Elevation Models (DEM).

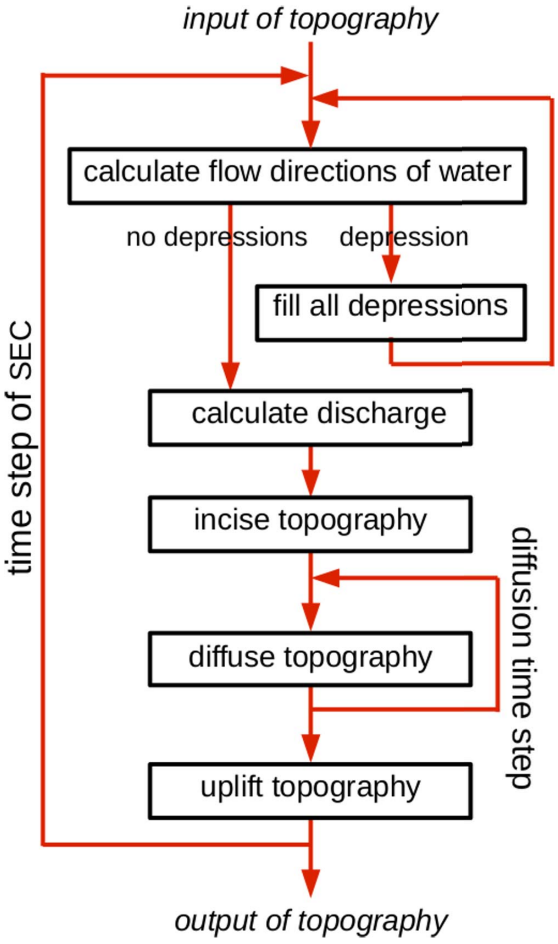

Fig. 1.: Flowchart of the 2D surface evolution algorithm DANSER. The red arrow on the left symbolizes the surface evolution time steps, the short one on the right the diffusion steps. The algorithm performs the filling cycle (arrow in the upper right corner) maximal once, if it is needed.

The routine follows the concept of the cellular automaton (Beaumont et al., 1992), implemented on a regular Eulerian grid. Fig.1 presents a flowchart of the routine. It comprises the D8 algorithm (O'Callaghan and Marc, 1984) for computation of flow directions and a new and fast filling algorithm (Planchon and Darboux, 2001), to get rid of topographic depressions. The new accumulation routine for water discharges works without time consuming sorting algorithm. It is a slightly transformed and faster version of O'Callaghan and Marks (1984) drainage accumulation algorithm. The supply limited incision code is based on the accepted stream power law. It includes a new algorithm to spread the water discharge over several cells, dependent on the distance, the height difference and the water discharge. This method leads to lateral abrasive rivers and may substitute the bifurcation method. Furthermore, we extend Beaumont's implementation (Beaumont et al., 1992) of the diffusion equation to nonlinear diffusion. We decouple incision from diffusion with the benefit of a simpler calibration and a reduction of filling.

The code automatically adjusts incision and diffusion time steps in order to stabilize the algorithms. Since one incision time step, including computation of flow directions and water discharges, is more time consuming than the computation of a diffusion step, we refine each incision step into multiple diffusion steps.

Special features, including the new lateral abrasion routine and the immediate removal of diffused material from the river bed, can be switched on and off in order to adapt DANSER to given challenges.

Coupling to lithospheric scale (thermo-)mechanical codes

To execute one time step of a tectonic code consumes remarkably more time than running a step of a SEC. Beside that fact, a SEM, especially riverbed incision, needs a finer resolution than a tectonic model to reflect surface processes sufficiently. As a consequence, a refinement of time steps and resolution should be implemented in a modern SEC, made for coupling to any tectonic code.

Fig. 2 presents the coupling of DANSER to tectonic codes. Before the initial tectonic time step,

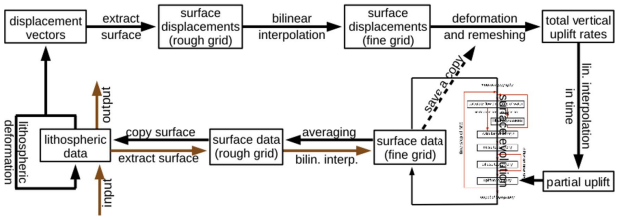

Fig. 2.: Coupling of DANSER to any tectonic code. Boxes indicate diverse data matrices and arrows illustrate methods of data computation. The dashed arrows symbolize data storage for the next time step. The brown arrows mark methods that are just performed in the first tectonic step.

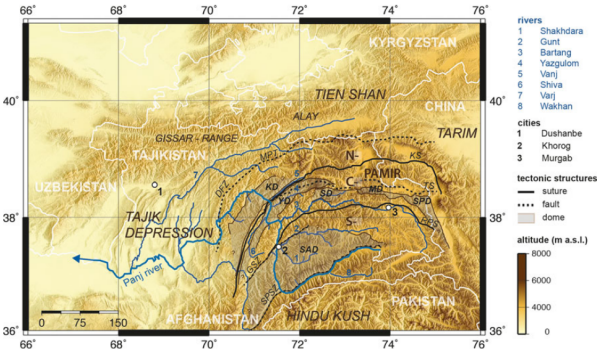

Fig. 3.: Topographic map of the Pamir orogen. Rivers are drawn in blue and faults in black. (Fuchs et al., 2013)

the surface elevations are extracted and bilinearly interpolated to a finer resolution. This fine resolution grid with elevation data gets stored for the first surface evolution time step. In every following tectonic step, three dimensional displacement vectors pass the surface deformation data from the tectonic code to the SEC. These vectors serve, interpolated to the fine resolution surface grid, for evaluation of the uplift rates. DANSER continues with alternating uplift and erosion in finer time steps. Subsequently, the resulting fine resolution elevation data get stored in a static array for the next time step. Finally, averaged to the deformed tectonic mesh, the elevation data modify the surface coordinates of the underlying model. Accordingly, the tectonic code performs the next time step.

Application 1: River capturing in the Pamir

The highly active Pamir orogen is penetrated by sub-parallel faults. The main rivers of the Pamir flow from east to west, following the fault system (fig. 3). They join the river Panj, that abruptly turns at 71.5° longitude from east-west direction to the north. An old river bed in direction to south-west can be observed at the sudden turn. It is unknown, how strong such a fault system influences a river network. Might the Panj river have changed its direction due to a river capturing event, induced by a recently forming fault?

This numerical study aims to clarify if and how a system of faults may influence the development of a river network. We simulate the effect of varying angles between riverbed and faults on river flow direction, and study for which configuration a deflection of the river is possible. We also compare the influence of uplift and high erodibility zones on the deviation of the river networks.

We simulate an inclined plane with white noise and five faults, arranged from east to west. The direction of inclination defines the main flow direction of the arising rivers. We study fault-bounded block rotations that are modelled as regions of increased erodibility and analytically imposed uplift. Fig. 4 shows a river capturing event, enabled by the new lateral abrasion routine.

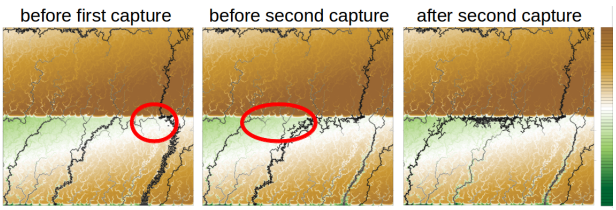

Fig. 4.: Simulation of a river capturing event. Three time steps illustrate the rapidity of two capturing events in a row. Colours illustrate the topographic relief (brown: high, green: low). The main streams are marked in black.

Application 2: Coupling to Slim3D

SLIM3D is a three-dimensional lithospheric-scale thermo-mechanical C++ based code (Popov and Sobolev, 2008). It allows modelling of lithospheric deformation with an elasto-visco-plastic rheology with diffusion, dislocation, Peierls creep mechanisms and Mohr–Coulomb plasticity. The code incorporates an arbitrary Lagrangian Eulerian formulation with free surface and Winkler boundary conditions.

We couple DANSER to Slim3D and present a coupled model of plateau growth. Challenges and advantages of the coupling method are discussed.

References

Beaumont, C., Fullsack, P., Hamilton, J. (1992), Erosional control of active compressional orogens, in McClay, K. R., ed, Thrust tectonics: New York, chapman and Hall, 1-18

Castelltort, S., Goren, L. , Willett, S. D., Champagnac, J. D., Herman, F. and Braun, J. (2012), River drainage patterns in the New Zealand Alps primarily controlled by plate tectonic strain, Nature Geosciences, 5, 744-748

DeLong, S. B., Pelletier, J. D., Arnold, L. (2007), Bedrock landscape development modeling: Calibration using field study, geochronology, and digital elevation model analysis, GSA Bulletin, 119, 157–173, doi: 10.1130/B25866.1

Freeman, T. G. (1991), Calculating catchment area with divergent flow based on a regular grid, Computers and Geosciences, 17, 413-422

Fuchs, M. C., Gloaguen, R., Pohl, E. (2013), Tectonic and climatic forcing on the Panj river system during the Quaternary, Int J Earth Sci, doi: 10.1007/s00531-013-0916-2

Garcia-Castellanos, D. (2002), Interplay between lithospheric flexure and river transport in foreland basins, Basin Research, 14, 89-104

O'Callagan, j. F. and Mark, D. M. (1984), The Extraction of Drainage Networks from Digital Elevation Data, Computer vision, graphics, and image processing, 28, 323-344

Pelletier, J. D. (2004), Persistent drainage migration in a numerical landscape evolution model, Geophysical Research Letters, 31, L20501, doi:10.1029/2004GL020802

Planchon, O. and Darboux, F. (2001), A fast, simple and versatile algorithm to fill the depressions of digital elevation models, Catena, 46, 159–176

Popov A. A. and Sobolev, S. V. (2008), SLIM3D: A tool for three-dimensional thermomechanical modeling of lithospheric deformation with elasto-visco-plastic rheology, Physics of the Earth and Planetary Interiors, 171, 55–75

Willett, S. D. (1999), Orogeny and orography: The effects of erosion on a structure of mountain belts, Journal of Geophysical Research, 104, 28,957-28,981

Willgoose, G, Bras, R. L. and Rodriguez-Iturbe, I. (1991), A Coupled Channel Network Growth and Hillslope Evolution Model, Water Resources Research, 27, 1671-1684

Kinematic reconstruction of the hastings block, southern New England Orogen, Australia

Yan, Jie[1], Lennox, Paul[1], Kelly, Bryce F.J.[1], Offler, Robin[2]

[1]*School of BEES, The University of New South Wales, Sydney 2052, NSW, Australia*
[2]*New South Wales Institute of Frontiers Geoscience, University of Newcastle, NSW 2308*
e-mail: *z3371716@student.unsw.edu.au*
session: *Tectonics and Surface Processes*

This research project uses 3D geological modeling software to build a 3D structural surface model of the Permo-Carboniferous rocks in the northern Hastings Block (NHB) [1] (Figure 1). The model is being built using comprehensive strike and dip structural data and a digital elevation model. It is designed to unravel a comprehensively mapped, complexly folded, extensively faulted geological sequence where there are no well-log data. It is believed that this new workflow will be widely applicable in the oil, gas, mining, and groundwater sectors.

Several tectonic models have been proposed to explain the structural and tectonic development of the Hastings Block which is outboard of similar Carboniferous fore-arc basin sequences in the Tamworth Belt, Australia. Mechanisms of development include emplacement either by faulting with or without rotation [2,3], or rotation during folding of the southern section of the Tamworth Belt [4,5,6]. The new 3D model will enable testing of the validity of these existing tectonic models. It will assist in constraining the relative timing of fault development, testing fault emplacement of the block, and verification of the number and orientation of folding events in the NHB.

The NHB is dominated by an open, $\sim$ 40 x 30 km NW-trending dome with the dominant fold axis plunging gently northwest [1]. It has been extensively faulted and possibly rotated after some fault developments (Figure 2). Construction of the 3D model fault-block by fault-block (Figures 3, 4 and 5) has highlighted shortcomings with the existing geological map of the NHB [7]. These include the variability in the orientation of bedding within some fault blocks, between adjacent fault blocks, and around significant sections of the dome. This is clearly illustrated in the Birdwood Fault Block (Figure 5), a fault-bounded block of Devonian-Carboniferous sequences on the SW limb of the dome that contains sequences facing northwest. In contrast, the surrounding rock sequences face northeast (Leitch E.C. pers.comm.) or possibly southwest [7] suggesting at least 90° rotation during emplacement.

Resolution of these challenges requires the reappraisal of the simple dome model for the NHB. Each fault in the NHB is being analyzed systematically to determine the duration of faulting, apparent sense of movement, and the relationship to other faults and the folds (Figure 2). The fault history plays an important role in building backward and forward models. Comparison between the cross-sections constructed from the 3D model (Figure 4) and those from the existing fieldwork provide better constraints on the validity of the 3D model.

References

[1] Lennox P.G., Roberts J. & Offler R., 1999, Structural analysis of the Hastings Terrane. In Flood, P.G. ed. New England Orogen, Eastern Australia: Regional Geology, Tectonics and Metallogenesis 115-124.

[2] Cawood P. A. & Leitch E. C., 1985, Accretion and dispersal tectonics of the southern New England Fold Belt, eastern Australia, Tectonostratigraphic Terranes of the Circum-Pacific Region, 1, 481-492.

[3] Schmidt P.W., Aubourg C., Lennox P.G. & Roberts J., 1994, Palaeomagnetism and tectonic rotation of the Hastings Terrane, eastern Australia, Australian Journal of Earth Sciences, 41, 547-560.

[4] Cawood P. A., Pisarevsky S. A and Leitch E. C., 2011a, Unraveling the New England orocline, east Gondwana accretionary margin, Tectonics, 30, TC5002, doi:10.1029/2011TC002864.

[5] Rosenbaum G., Li P. and Rubatto D., 2012, The contorted New England Orogen (eastern Australia): new evidence from U–Pb geochronology of early Permian granitoids, Tectonics, 31, http://dx.doi.org/10.1029/2011tc002960 (TC1006).

[6] Korsch R. J. & Harrington H. J., 1987, Oroclinal bending, fragmentation and deformation of terranes in the New England Orogen, eastern Australia, Terrane Accretion and Orogenic Belts, American Geophysical Union Geodynamic Series, 19, 129-140.

[7] Roberts J.R., Leitch E.C., Lennox P.G. & Offler R., 1995, Devonian - Carboniferous Stratigraphy of the Southern Hastings Block, eastern Australia, Australian Journal of Earth Sciences 42, 609-634.

[8] Glen R.A., Roberts, J., 2012, Formation of oroclines in the New England Orogen, Eastern Australia, J. Virtual Explor, 43 (Paper 3), http://dx.doi.org/10.3809/jvirtex.2012.00305.

[9] Crowell J.C., 1984, Notes to accompany lectures on tectonics, sedimentation and structural analysis of basins, Petroleum Exploration Society of Australia, 138-142.

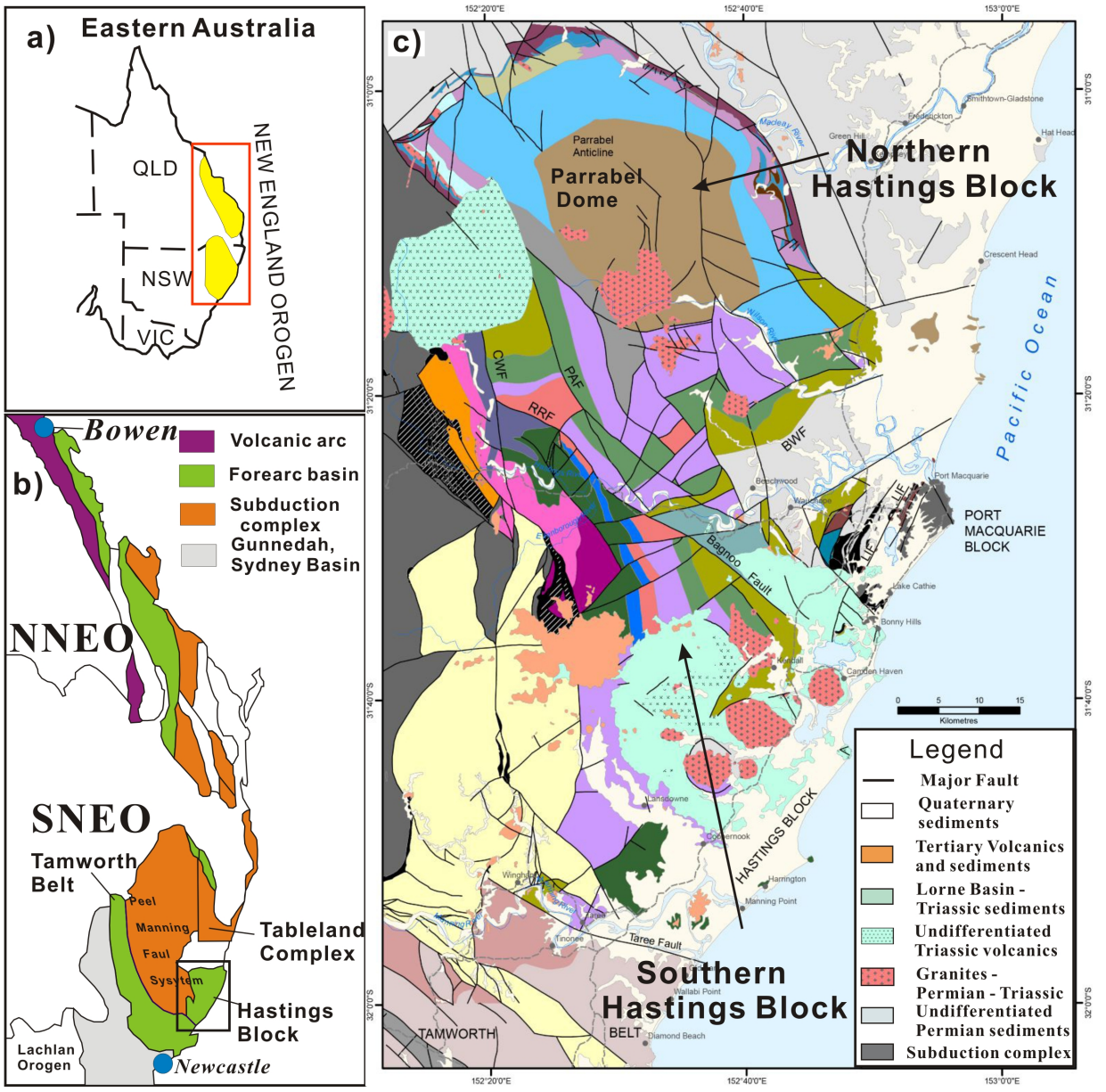

Fig. 1.: Location and tectonic setting of the Hastings Block (from Cawood et al. 2011 and Glen et al. 2012): (a) within eastern Australia, (b) within the southern New England Orogen. (c) major tectonic units and faults within and adjacent to the Hastings Block. (NNEO – Northern New England Orogen; SNEO - Southern New England Orogen).

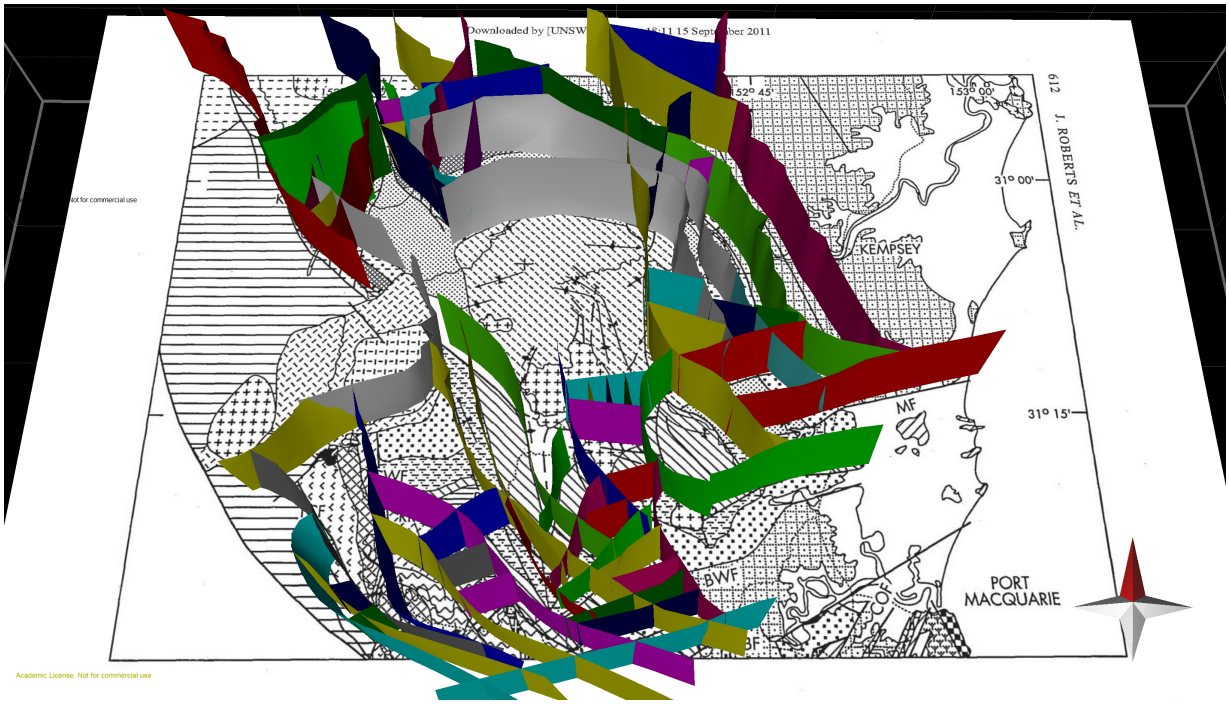

Fig. 2.: The preliminary 3D fault network model for the northern Hastings Block. This model was constructed using Leapfrog (www.leapfrog3d.com) and 3D MOVE (www.mve.com). At present all fault surfaces are vertical. The inclination of the fault surfaces will be adjusted to be consistent with both the geological information available from field studies and the literature, and the need to balance geological processes over the region.

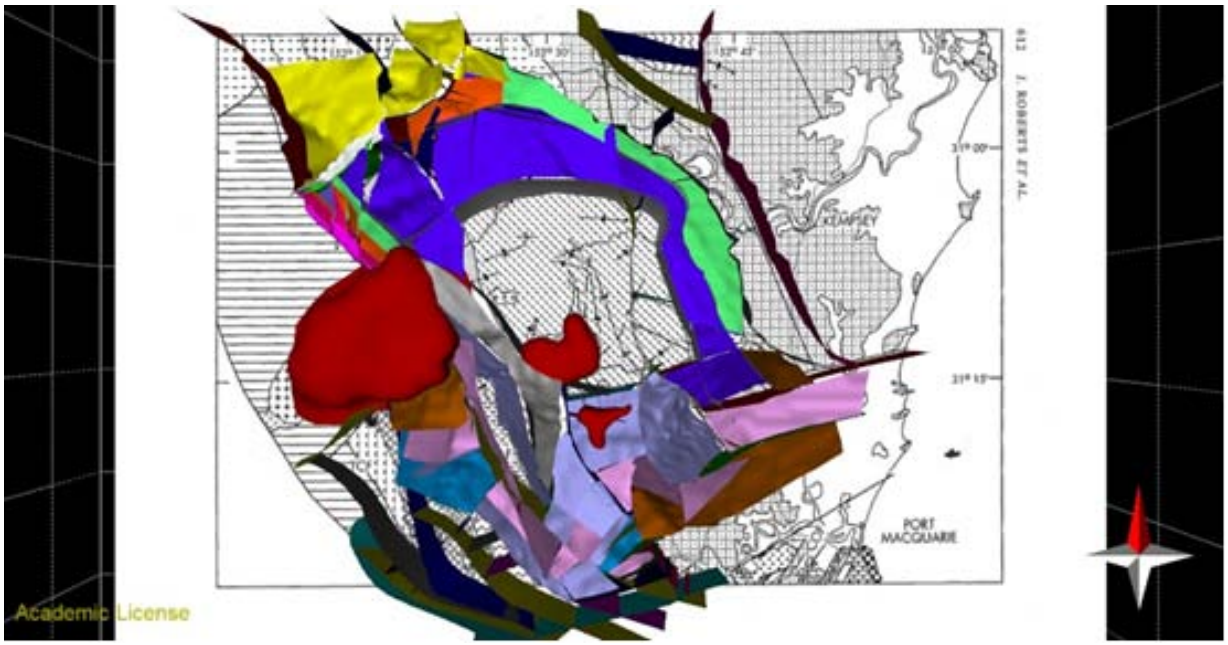

Fig. 3.: The 3D geological model of the northern Hastings Block showing selected geological horizons. Horizons are being constructed within each individual fault-block using a combination of field mapping data and the consideration of the requirements of balanced geological sections.

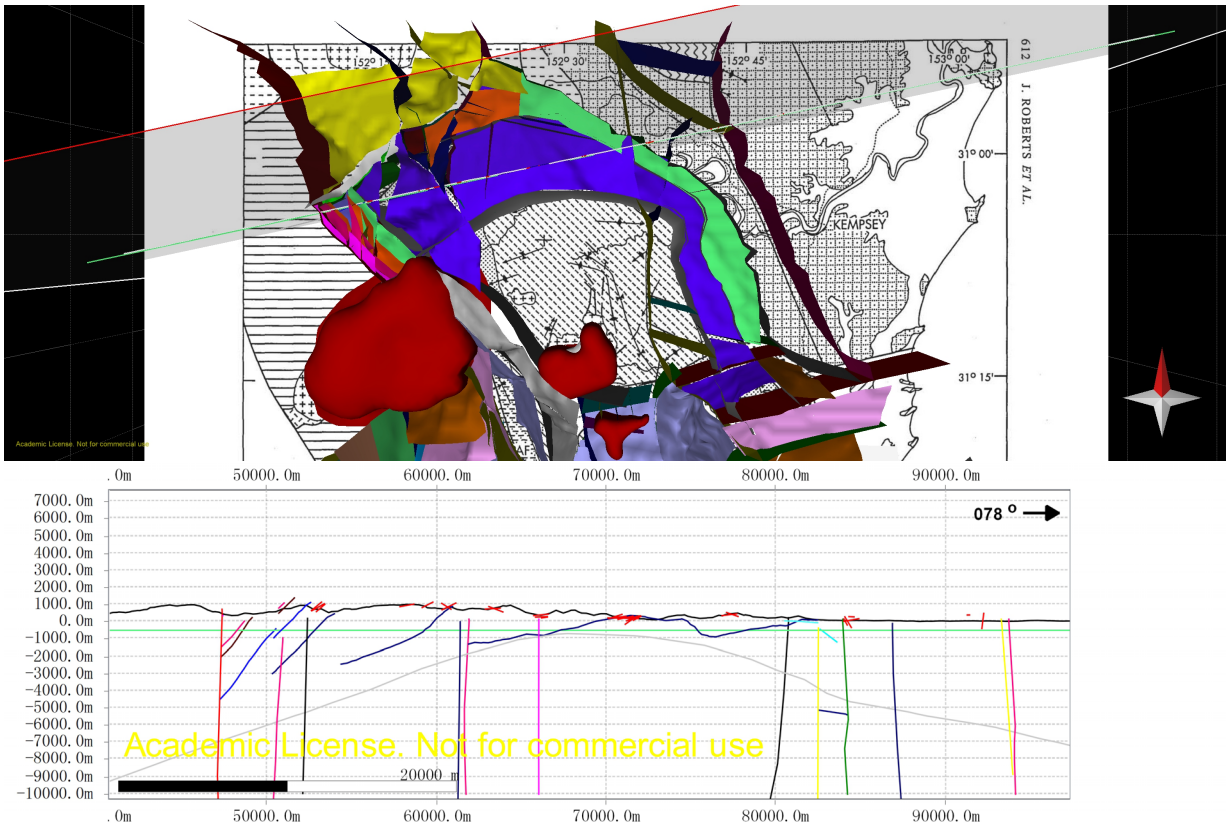

Fig. 4.: A preliminary cross-section extracted from the 3D geological model across the northern section of the Parrabel Dome. Such cross-sections highlight inconsistencies with the present fault and horizon interpretation. Through iterative interpretations, the goal is to develop a 3D geological model that is consistent with the field mapping data and known geological processes that occurred in the area.

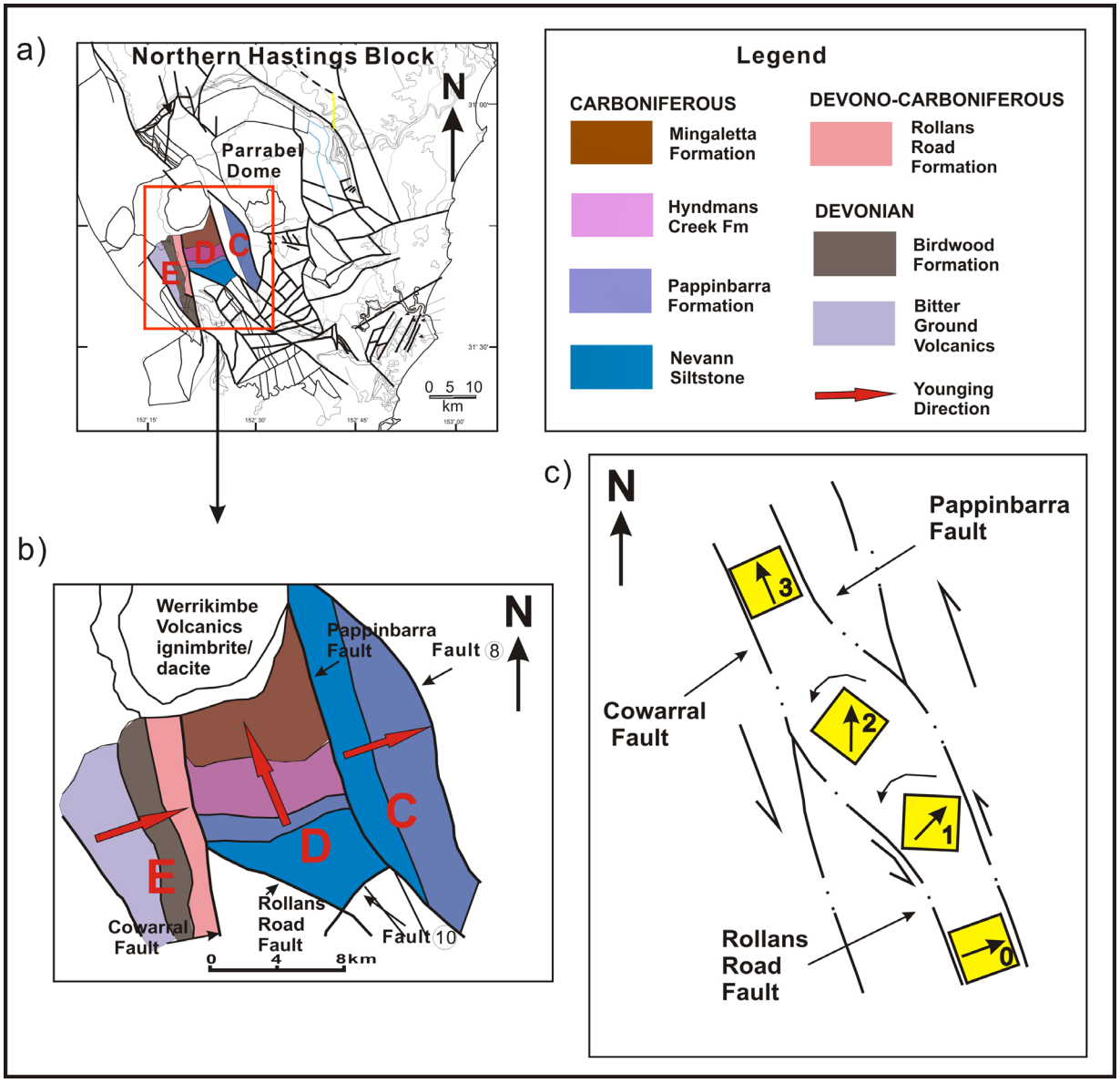

Fig. 5.: Location of the Birdwood Fault Block (Fault block D): (a) within Northern Hastings Block, (b) the surrounding rock sequences face east or west. (c) a possible model to explain how the Birdwood Fault Block experienced at least 90o rotation during it's emplacement (Adapted from Crowell, 1984).

Stability of over-pressured cohesive and frictional materials based on Sequential Limit Analysis

Xiaoping Yuan[1], Yves M. Leroy[1], Bertrand Maillot[3], Yves Guéguen[1]

[1]*Laboratoire de Géologie, CNRS, École Normale Supérieure, Paris, France*
[2]*now at Total, CSTJF, Pau, France*
[3]*Laboratoire Géosciences et Environnement Cergy, Université de Cergy-Pontoise, France*
e-mail: *xyuan@geologie.ens.fr*
session: *Tectonics and Surface Processes*

Summary

The gravitational collapse mechanism in over-pressured cohesive and frictional materials of arbitray topography and resting on an inclined weak décollement is examined by analytical means. The dominant mechanism consists in finding the length of the active décollement and the dips of the normal-fault and of the conjugate shear-plane composing the emerging half-graben, and the dips of the ramp and of the shear-plane bounding the frontal hanging-wall. The predictions of the maximum strength theorem (MST), part of the kinematic approach of limit analysis, not only match exactly the theoretical solutions, but generalises them in several aspects: failure geometry, composed of cohesive material, arbitrary topography and pre-existing faults. We show in particular that the MST predicts the failure geometry of the body triggerred by fluid over-pressure in a physical experiment. The evolution of the materials on the décollement is predicted with a two step method called sequential limit analysis. The first step is based on the above dominant mechanism. The second step leads to a modification of the geometry due to extensional fault-bend folds and compressional fold-thrust belts. The evolution simulation captures the main features of gravitational collapse of the sandbox analogue experiment.

Introduction

The geodynamics context of interest here is mainly extensional zones, motivated by the following examples : seismic reflection profiles documented many extensional wedges associated with normal-faults, such as the Brazos Ridge fault, offshore Texas [Xiao and Suppe, 1992; Withjack et al., 1995] and sequences of normal-faults in the convergent margin off Antofagasta [Delouis et al., 1998; von Huene and Ranero, 2003; Sallarés and Ranero, 2005]. The more complex Niger Delta shows the link between the extensional province on the shelf and the contraction in the toe-thrust systems in the deep water [Corredor et al., 2005; Kostenko et al., 2008]. Instabilities of compression/extension were also reproduced in the laboratory with sandbox analogue experiments [Mourgues et al., 2009; Lacoste et al., 2012].

The objective of this work is to propose a simple method to analyze the gravitational deformation occurring in over-pressured cohesive and frictional wedges extending the stability conditions presented by Lacoste et al., [2012] to an arbitrary-sloped topography, and cohesive materials. The kinematic approach of limit analysis, also called the maximum strength theorem (MST) [Maillot and Leroy, 2006], for compressional deformation [Cubas et al., 2008] and for the onset of gravitational instability in over-pressured materials [Yuan et al., 2014] is extended for that purpose.

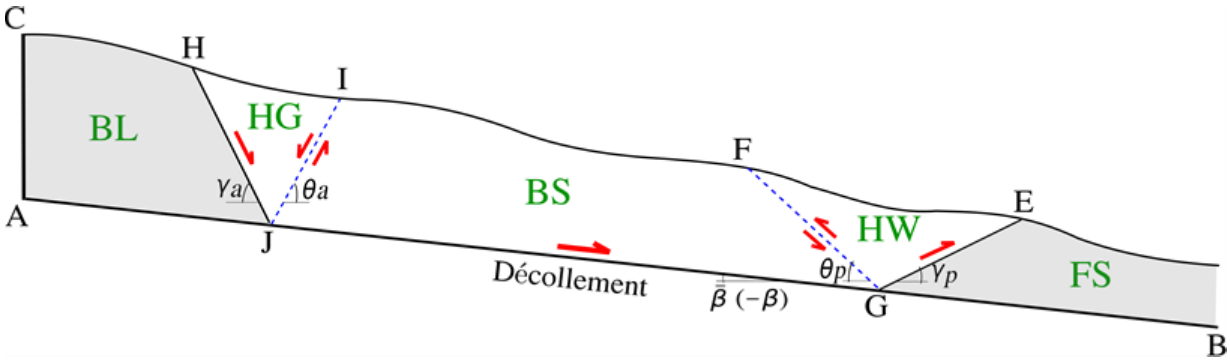

Fig. 1.: The prototype of gravitational instability composed of half-graben (HG), back-stop (BS) and hanging-wall (HW).

Prototype and of the collapse mechanism

The geometry of our prototype and of the collapse mechanism is presented in Figure 1. It consists of a slope of arbitrary topography resting on a décollement inclined (AB) at an angle β. The mode consists of the gravitational collapse by the action of two normal faults bounding a half-graben (HG) and two reverse faults composing a frontal hang-wall (HW), rooting on the décollement and completed by the seaward sliding of a back-stop (BS), the transition part of the materials. Materials within the HG are sliding on the normal-fault (JH dipping at γa) and part of the material is flushed through the conjugate shear plane (JI, dipping at θa). This flux has for consequence the push of the BS part of the slope seaward, as in Figure 1, parallel to the décollement. The HW bounded by a ramp GE dipping at γp and shear-plane GF dipping at θp is formed by the seaward movement of the BS.

Application of the maximum strength theorem (MST) requires now to maximise the difference between external effective power and maximum resisting power for the proposed velocity field in terms of the dips γa, θa, γp and θp and the length LJG. If that maximum difference power is negative, the system is stable, otherwise there is a quasi static or a dynamic instability and the optimum five parameters (γa, θa, γp, θp, LJG) define the dominant collapse mechanism.

Onset validation

It is now proposed to apply the collapse mechanism accounting for the slope parallel model. The arbitrary topography is simplified to be a straight line parallel to the décollement, e.g. $\alpha = \beta$ (Figure 2a), and h is the thickness between the topography and the décollement. The collapse length [LJG/h]c is compared with the theoretical collapse length from (9) in Lacoste et al. [2012]. The comparison of the MST (symbols) and theoretical results (curves) are presented in Figure 2b for two sets of décollement overpressure ratio λD = 0.6, 0.8 with the décollement friction angle ϕD = 10$\circ$ and bulk λB = λhydro = 0.5. They are coinciding with each other very well. The comparison is extended in Figure 2c which presents the optimum dips of active and passive faults according the two theories, keeping the décollement pressure ratio constant λD = 0.8. The theoretical dips (γac, θac, γpc, θpc) are provided by the method of the geometrical construction of Mohr's circles [Lehner, 1986] for the active and passive Rankine stress state. The two sets of predictions coincide exactly. Note that the sum of active faults $\gamma ac + \theta ac = 50\circ (= \pi/2 - \phi B)$ and passive dips γpc + θpc = 120$\circ$ ($= \pi/2 + \phi$B).

The dips of active faults are also validated by applying the MST to the sand-box experiment of Mourgues and Cobbold [2003] for the increase of décollement fluid ratio. The experimental set-up consists of rectangular glass box in which sand packs were built with a length 40 cm and the

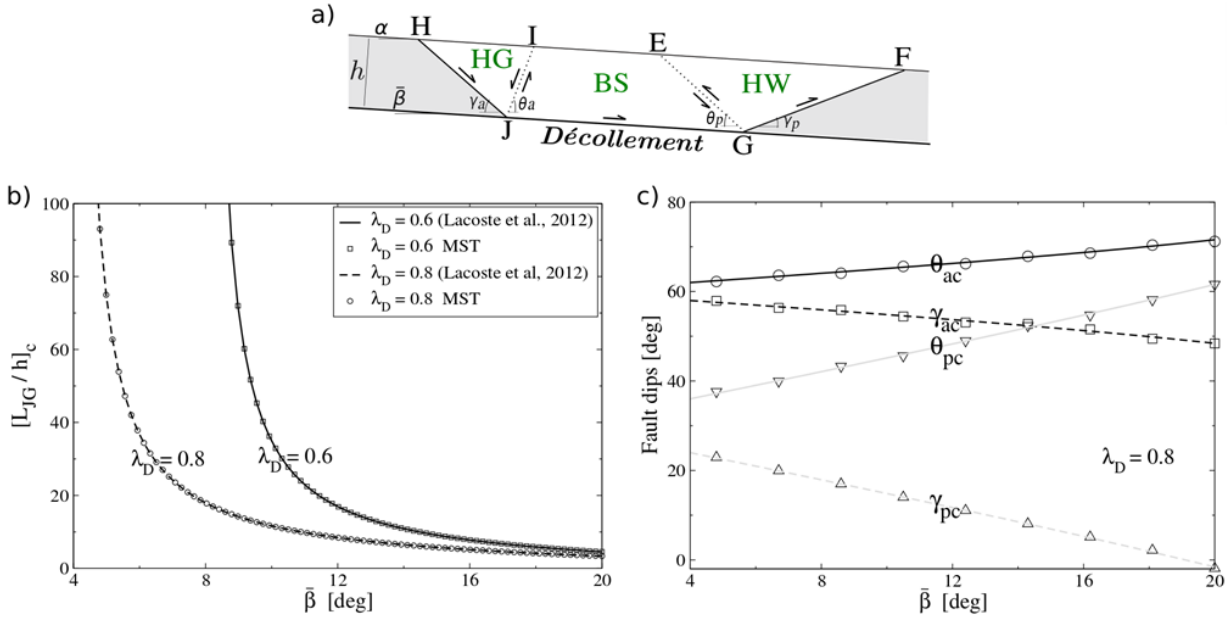

Fig. 2.: a) Illustration of the slope parallel model ($\alpha = \beta$). The validation for the collapse length ([LJG/h]c) and fault dips (γac, θac, γpc, θpc) keeping the bulk pressure ratio constant λB = 0.5 and décollement friction angle ϕD = 10∘. b). Collapse length [LJG/h]c as the function of décollement dip β. c). The dips of faults as the function of décollement dip β for the active and passive failure. The symbols are the predictions of maximum strength theorem and the curves are the theoretical results [Lacoste et al., 2012].

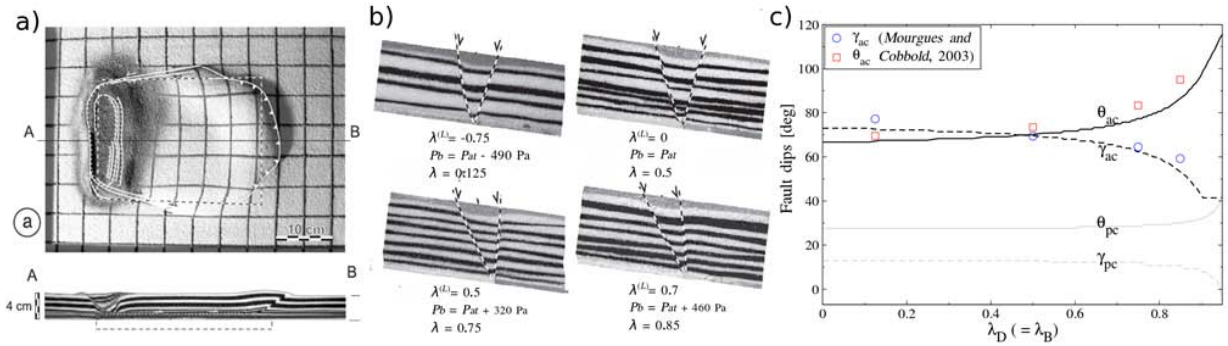

Fig. 3.: a) Gravitational collapse as a result of fluid overpressure from analogue experiments [Mourgues and Cobbold, 2003]. The extensional faults form by different air pressure, modified after Mourgues and Cobbold [2003], b). The comparison of extensional fault dips (γac, θac) from experiments and predictions from MST as function of fluid ratio, c).

height 4 cm, yielding a surface slope $\alpha = \beta = 6.7$∘. It rests on one overlapping sieve. Beneath the sieve was a pressure chamber, which acted as a reservoir for compressed air and provided a uniform air pressure (Pb) at the base of the model. Air flowed through the sand in a direction perpendicular to the slope, and the air pressures in upper chamber is Pup (atmospheric pressure Pat in this experiment). The uniform air pressure through the sand body in the experiment produced identical pressure ratios in the décollement and into the wedge : λB = λD [Mourgues and Cobbold, 2003; Lacoste et al., 2012; Pons and Mourgues, 2012]. The sand density ρs (1700 kg/m^3), the internal friction coefficient $\mu = 1.18$ (ϕB = 50∘) and the bulk cohesion (12 - 72 Pa)

are provided by the authors. We assume the cohesion CD = 0 Pa and the décollement friction can be any value (e.g. ϕD = 10$\circ$ in this analysis) since the active fault dips of interest are independent on this value. The experimental results and predictions from MST are presented in Figure 3c where the dips of faults are as function of fluid ratio λD (= λB). The experimental results show that the normal-fault dip γac (circle symbols) decreases and the shear-plane dip θac (square symbols) increases with the increases of fluid ratios. The theoretical results (γac, θac, black curves) present the same trend with the results of experiment. We conclude that the series of four experiments is well described by the MST despite the lack of passive fault dips γpc, θpc from the experiments for the comparison.

Evolution

The complete evolution is analyzed in Figure 4 which presents four stages revealing the processes of development. The material rests on a décollement with an initial topography slope $\alpha = \beta =$ 5$\circ$. The décollement fluid overpressure is applied in the red dashed box (Figure 4). The density of saturated material ρ = 2000 kg/m^3 (hydrostatic pressure ratio λhydro = 0.5), décollement ratio λD = 0.9 and bulk ratio λB = 0.7. The décollement friction angle ϕD = 10$\circ$ and material friction angle ϕB = 30$\circ$. The materials and interfaces are assumed cohesionless. The frontal part become thick by a series of three folds increasing in amplitude downdip, and the back region is thinned by a series of normal faulting. The deformation captures the main features of gravitational collapse of the analogue experiment in Figure 3a. The simulation was carried out until stability was reached, i.e., when the external effective power became less than the maximum resisting power The present approach does not allow us to determine the power of acceleration, and therefore we have no time scale to follow the evolution of a gravitational collapse. Comparison to more general methods accounting for inertia effect will be necessary to evaluate the adequacy of our quasi-static solutions.

Conclusion

The work proposes a mechanical analysis for extensional province and compressional toe inspired by the extensional fault-bend folds and compressional fold-thrust belts, respectively. This mechanism generalise in several aspects : fluid pressure, composed of cohesive material, arbitrary topography and failure geometry of the materials. We validate it by comparing with theoretical solutions and experimental results for the onset of failure. The evolution simulation captures the basic features of sandbox analogue experiments. Beyond the direct applications presented here, there are some perspectives the development of sequential limit analysis in other settings such as the sedimentation influence in Niger Delta [Corredor et al., 2005; Kostenko et al., 2008], the fluid ratio change with sedimentation, the effect of listric normal fault, and the weakening of pre-existing faults.

References

Cubas, N., Y. M. Leroy, and B. Maillot (2008), Prediction of thrusting sequences in accretionary wedges, Journal of Geophysical Research, 113 (B12), 1–21.

Delouis, B., H. Philip, L. Dorbath, and A. Cisternas (1998), Recent crustal deformation in the antofagasta region (northern chile) and the subduction process, Geophysical Journal International, 132, 302–338.

Lacoste, A., B. C. Vendeville, R. Mourgues, L. Loncke, and M. Lebacq (2012), Gravitational instabilities triggered byfluid overpressure and downslope incision insights from analytical and analogue modelling, Journal of StructuralGeology, 42 (0), 151 – 162.

Lehner, F. K. (1986), Comments on "Noncohesive Critical Coulomb Wedges: An Exact Solution by F. A. Dahlen, Journal of Geophysical Research, 91 (B1), 793–796.

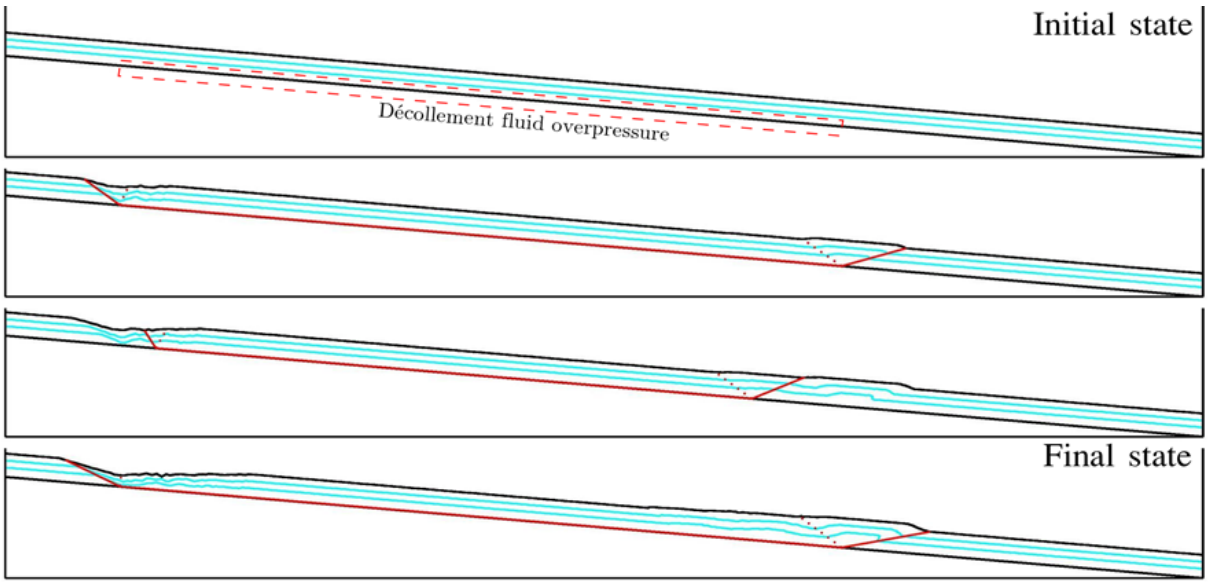

Fig. 4.: The complete evolution of the gravitational collapse triggered by an applied fluid over-pressure along the décollement (red dashed box). In the final state the material is stable for the applied over-pressure. Red lines show the current dominant mechanism. Blue lines representing the internal deformation are passive markers.

Maillot, B., and Y. M. Leroy (2006), Kink-fold onset and development based on the maximum strength theorem, Journal of the Mechanics and Physics of Solids, 54 (10), 2030–2059. Mourgues, R., and P. Cobbold (2003), Some tectonic consequences of fluid overpressures and seepage forces as demonstrated by sandbox modelling, Tectonophysics, 376, 75–97.

Mourgues, R., E. Lecomte, B. Vendeville, and S. Raillard (2009), An experimental investigation of gravity-driven shale tectonics in progradational delta, Tectonophysics, 474, 643–656.

Pons, A., and R. Mourgues (2012), Deformation and stability of over-pressured wedges: Insight from sandbox models, Journal of Geophysical Research, 117 (B09404), doi:10.1029/2012JB009379.

Sallarés, V., and C. R. Ranero (2005), Structure and tectonics of the erosional convergent margin off antofagasta, north chile (23 degrees 30' s), Journal of Geophysical Research, 110 (B06101), doi:10.1029/2004JB003418.

von Huene, R., and C. R. Ranero (2003), Subduction erosion and basal friction along the sediment-starved convergent margin off antofagasta, chile, Journal of Geophysical Research, 108 (B2), doi:10.1029/2001JB001569.

Withjack, M. O., Q. T. Islam, and P. R. Lapointe (1995), Normal faults and their hanging-wall deformation – an experimental study, AAPG Bulletin, 79 (1), 1–18.

Xiao, H.-B., F. A. Dahlen, and J. Suppe (1991), Mechanics of extensional wedges, Journal of Geophysical Research, 96 (B6), 301–318.

Yuan, X. P., Y. M. Leroy, and B. Maillot (2014), Tectonic and gravity extensional collapses in over-pressured cohesiveand frictional wedges, to prepare.

4D Transfer Zone Modeling in Continental Rifts

Frank Zwaan, Guido Schreurs

University of Bern, Switzerland
e-mail: *frank.zwaan@geo.unibe.ch*
session: *Tectonics and Surface Processes*

Introduction

Inherited structures in the Earth's crust are generally considered to represent weak zones along which deformation will focus during subsequent tectonic phases. In extensional settings, such as the Cenozoic European Rift System, the East African Rift System and many others (fig. 1), faulting initiated along such structures. However, to develop a full-scale rift system, these initial faults have to connect, which is usually achieved through transfer zones. Those transfer zones themselves might also follow the course of an inherited structural grain, as is the case in for example the Rhine-Bresse Transfer Zone (Ustaszewski et al., 2005).

The development of transfer zone structures has been investigated by means of analogue modeling. However, most of these studies focus on the oceanic domain and the well-known transfer faults associated with mid-oceanic ridges (eg. Serra & Nelson, 1988; Mauduit & Dauteuil, 1996; Dauteuil et al., 2002; Amibilia et al., 2005). Other studies do focus on the continental domain, but only in the shallow crust (Acocella et al., 1999; Ustaszewski et al., 2005). Basile & Brun (1999) do consider the whole (brittle/ductile) continental crust, but only in a pull-apart setting. All studies mentioned above have in common that they apply a rigid base plate to force localized deformation in overlying sand, clay and/or silicon layers.

The models from Acocella et al. (1999) are taken as a starting point to investigate the influence of inherited crustal weakness geometries on the development of transfer zones in continental rift systems. The model series described here improves upon the previous models by 1) considering the complete continental crust and 2) by the application of a method that creates a more natural, distributed type of deformation than the rigid base plate set-up.

Model Set-up & Methods of Analysis

The machine used for the experiments consisted of two long rigid walls between which a series of 78 cm long, 5 cm high plexiglass and foam bars were tightly stacked to fill the 25 cm wide initial gap (fig. 2A). By moving the walls apart using computer-controlled motors, the decompressing foam expands and fills the extra space. This system allows a uniform extensional deformation at the base of any overlying model materials. In addition, one of the base plates can move laterally, which allows strike-slip and transtensional set-ups. A rubber wall confined the short sides of the models, to ensure uniform extension and to minimize border effects.

To model the ductile lower continental crust, a 1 cm thick layer of PDMS (RGB-0910) silicone putty was placed on the foam/plexiglass base. For the brittle upper crust, a 2 cm thick cover of fine quartz sand was sieved on top of the PDMS, intercalated with thin layers of dark corundum sand to visualize displacement in sections. For further material characteristics, see Buiter et al., (2006) and Panien et al., (2006). The 3 cm of sand and silicone represents a 30 km thick crust. To create pre-existing weak zone, lines of silicone

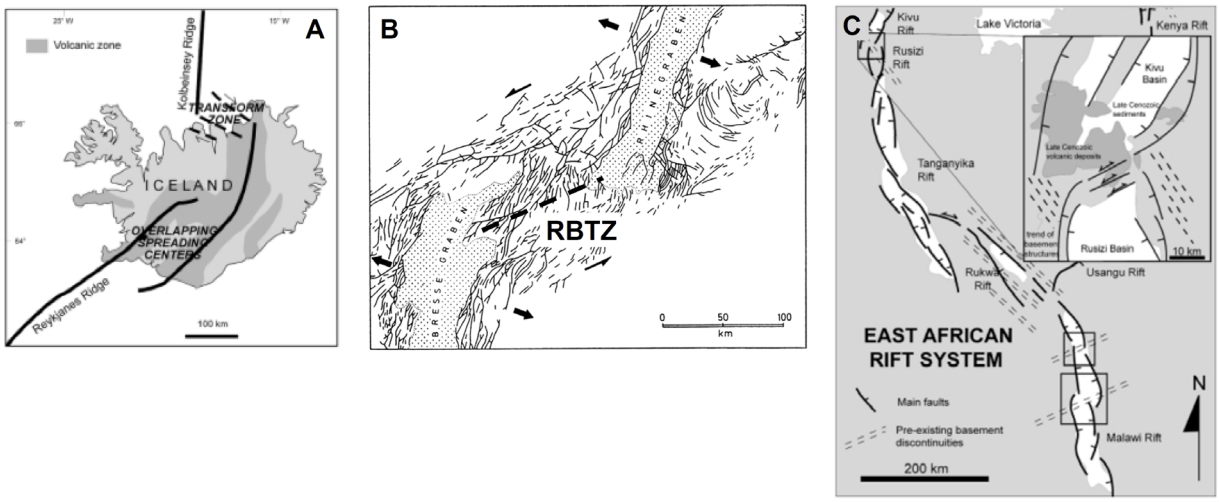

Fig. 1.: Examples of transfer zones in extensional settings: A) Iceland and the Mid Atlantic Ridge, (modified after Acocella et al., 1999); B) The Rhine-Bresse Transfer Zone (RBTZ), which is part of the Cenozoic European Rift System, between the Rhine and Bresse Grabens, eastern France (modified after Illies, 1977); C) The East African Rift System (modified after Acocella et al., 1999).

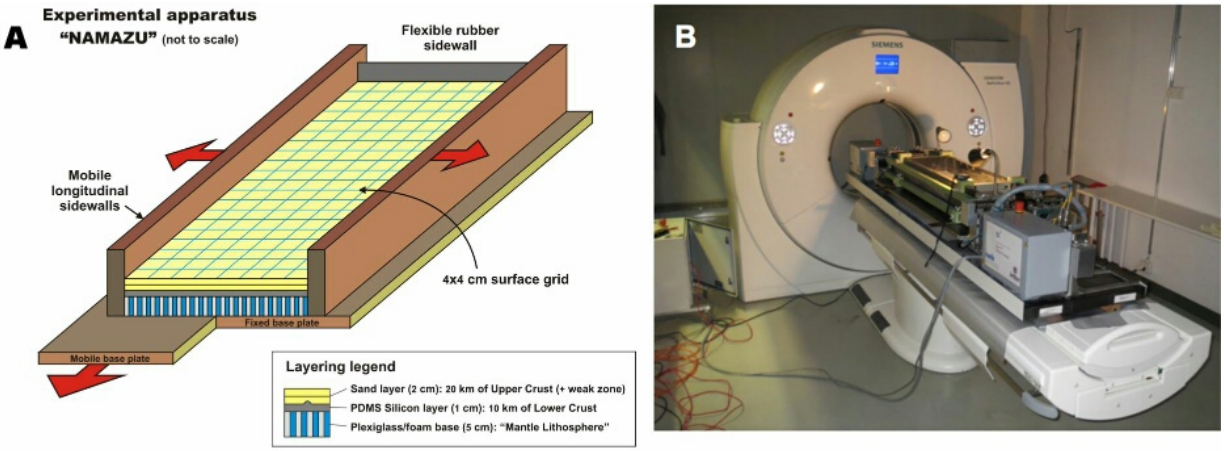

Fig. 2.: A) Model set-up, using a foam and plexiglas base, which allows distributed deformation. Image modified after Schreurs & Colletta (1998); B) CT-scanner installation with the sandbox machine during a model run.

(5x5 mm in diameter) were laid down on top of the basal silicone layer. The extension velocities were in the order of 0.6 cm/h, or ca. 10 mm/y in nature, using the scaling formulas from Corti et al., (2003) and data from Bürgmann & Dresen (2008).

Top view photographs were taken in order to follow the surface evolution. Additional cross-sections were made to observe the final structures at the end of each model run. Furthermore, several models were run in a CT-scanner to reveal the evolution of internal structures while the model was running (fig. 2B).

Results & Discussion

A series of 7 models was completed and interpreted (fig. 4). A first order observation is that the localization of deformation along the longitudinal weak zones worked well, all models developed distinct rift structures. However, several models did not produce linkage between both rift zones, which is an important difference with the results from previous studies. Only in model Tz1, the

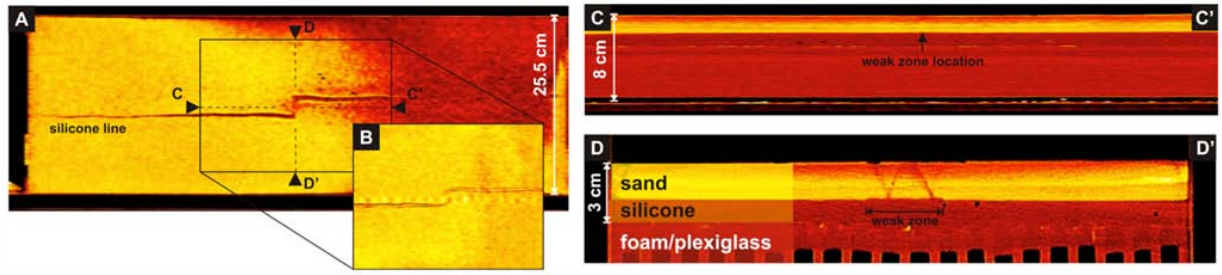

Fig. 3.: CT Sections trough model Tz7 after 60 minutes, showing the lack of deformation along the weak zone between both rift arms. A) Horizontal section at weak zone level, showing the weak zone geometry (compare with fig. 4); B) Horizontal section ca. 5 mm higher than slice A, indicating fault activity (darker lines) along the longitudinal weak zones, but no faulting occurs along the connecting weak zone. The same is evident in sections C-C' and D-D': normal faults are clearly present (D), but the weak zone in between is not active at all (C). For locations of these sections, see A.

45° oriented weak zone was clearly activated. Although the curved rift in model Tz6 seems to follow the weak zone, it actually cuts trough it. In addition, the successful linkage in models Tz5 and Tz7 was not the result of weak zone activation (see the CT imaging in fig. 3), but was most likely due to the close proximity of both rift arms; in the other models the rifts are just too far apart to join. This outcome can be explained by the lack of cohesion in sand (Van Mechelen, 2004): the sand layer is not strong enough to act as a rigid whole. This view is supported by a later experiment in which wet sand was applied and transfer zones did activate.

The models without linkage show propagation of the rift structures along strike of the longitudinal weak zones, but they also show a slightly curving towards the center of the model (model Tz4 did not yet, but shows the same early evolution as model Tz3). These structures are somewhat similar to the overlapping spreading centers in SW Iceland (fig. 1A), although Iceland is situated in an oceanic setting while the models were meant to represent a continental system. In contrast, models Tz5 and Tz7 did develop a linked transfer zone and seem to be quite similar (although a 31° oblique extension was applied to model Tz7). The results are roughly comparable to the structures in the Rhine-Bresse Transfer Zone (fig. 1B): two parallel deep graben structures connected by a less subsided oblique fault zone.

Model Tz6 shows some interesting results; both rift arms have developed in a completely different fashion with respect to each other and with respect to those in the other models of this series. The upper graben (a) has a more normal fault character with little oblique features and propagated furthest. This propagation was oriented perpendicular to the (31° oblique) direction of extension and created corresponding normal faulting. The lower graben (b) on the other hand has developed more oblique features, which are perpendicular to the extension direction. Its propagation shows a strong curve, which might have been influenced by the weak zone. But CT imaging shows that the structure cuts right trough the weak zone; the latter did not activate significantly.

Conclusions and future modeling

The results of this first series of transfer zone models have lead to the following conclusions:

1. The presence of high angle (at least $> 45°$) pre-existing weak zone does not define the occurrence of linkage between two graben structures, although this is probably due to the low cohesion of sand;

2. In contrast, the distance between both rift arms determines the occurrence of linkage here;

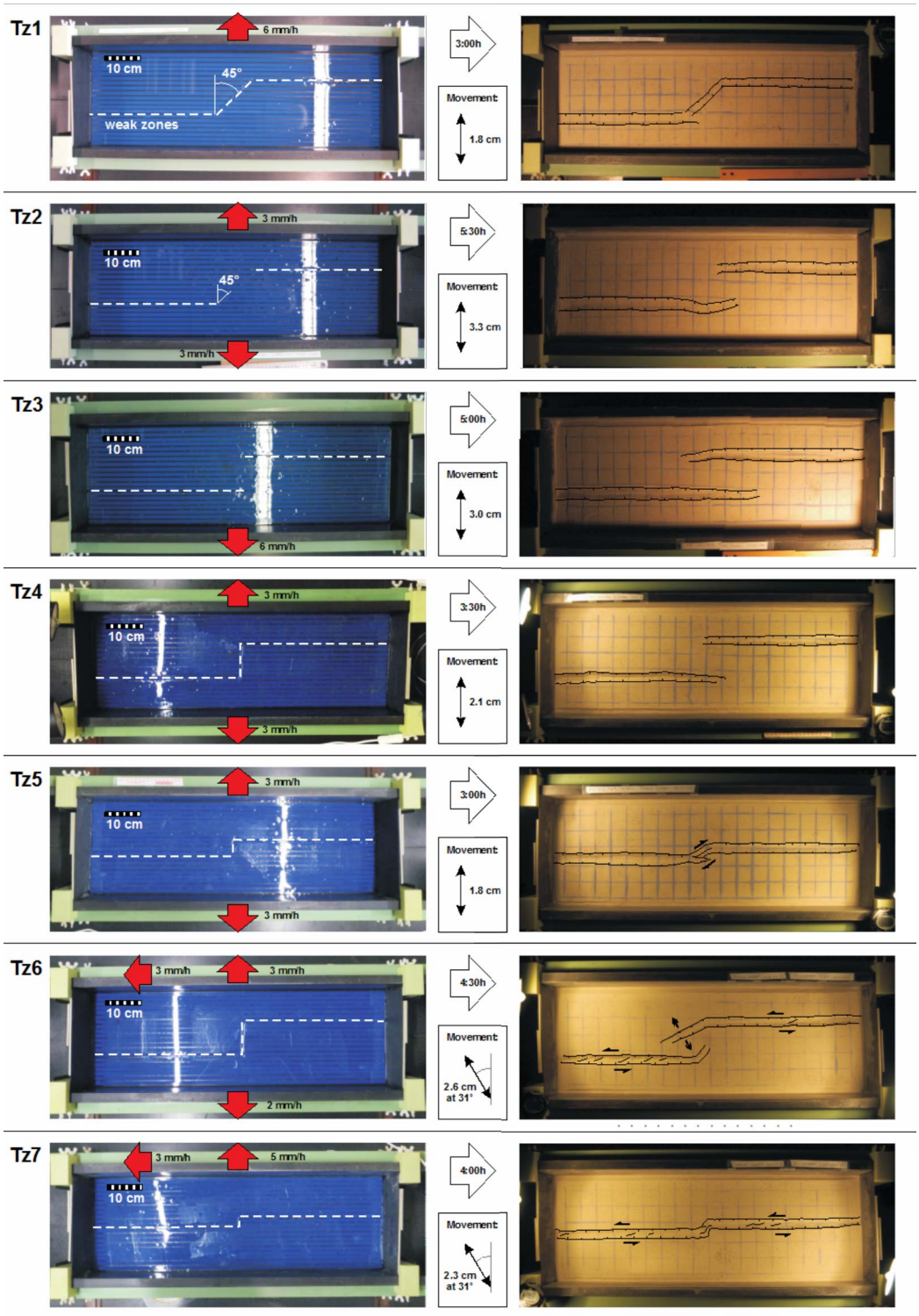

Fig. 4.: Left: Top views of the model set-up showing the weak zone geometry (white dotted lines) and the deformation vectors (red arrows, indicating the extensional deformation and for the transtensional models Tz6 and Tz7, the additional strike-slip components); Right: the resulting surface structures. NB: all models did produce half-graben structures along the longitudinal sidewalls, but these boundary effects were considered not to have a major influence on the structures in the center of the model.

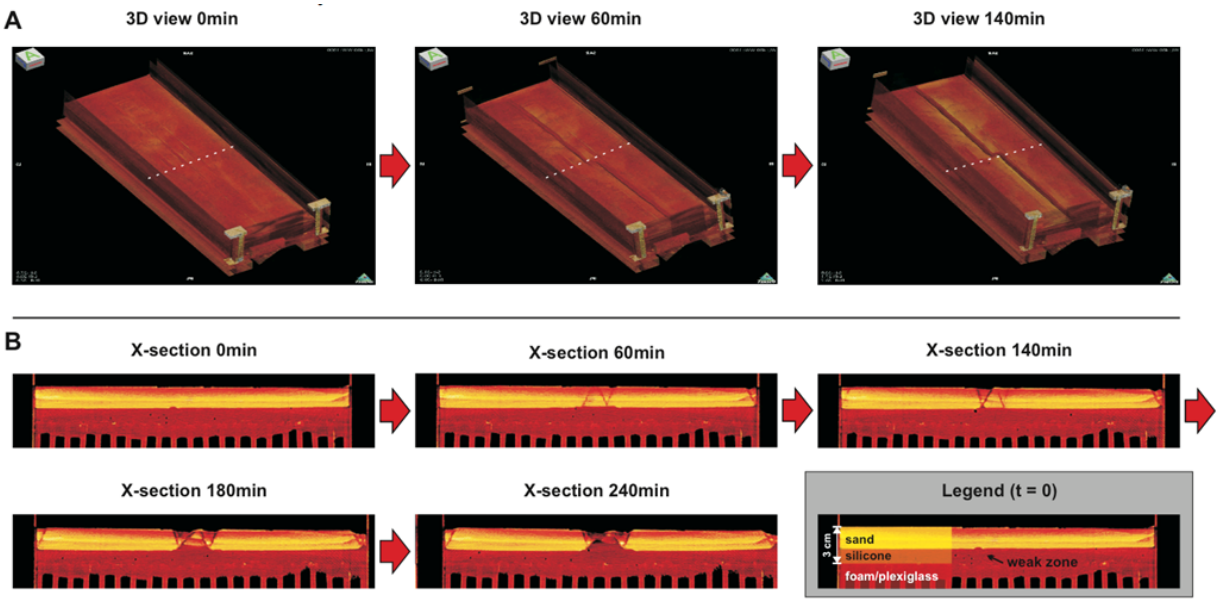

Fig. 5.: Application potential of CT data. A) 3D views of model Tz7, showing the initial model and the deformation after 60 minutes and 140 minutes; B) Cross-sections at the center of model Tz7 (for section locations, see dotted lines in A), showing the progressive deformation through time.

3. Oblique extensional deformation creates rather different structures with respect to orthogonal rifting;

4. Some models resemble natural examples (Iceland, Rhine-Bresse Transfer Zone).

It is however clear that more research is needed to fully describe the system. The top view photos of all models have to be examined in more detail and the available CT data from models Tz4-Tz7 has to be thoroughly analyzed. Also digital image correlation techniques could be applied, especially since the CT data allow motion tracing in 3D. These results should then be compared to those from previous modeling studies and with natural examples.

This model series was part of a PhD project start-up, and partially aimed to test the potential of the newly adjusted sandbox machine in Bern. Future work within this project will mostly focus on transtensional settings: different plate geometries and the modeling of natural examples of oblique extension: e.g. the Norwegian margin, the Knipovich Rigde near Svalbard and the Mid-Atlantic Ridge around Iceland. Also, collaboration with colleagues from the numerical domain will be arranged, to fully combine and exploit the possibilities of both sides of the modeling spectrum.

References

Acocella, V., Faccenna, C., Funiciello, R., Rossetti, F. (1999) Sand-box modelling of basement-controlled transfer zones in extensional domains. Terra Nova, Vol. 11, No. 4, pp 149-156

Amilibia, A., McClay, K. R., Sabat, F., Munoz, J.A., Roca, E. (2005) Analogue Modelling of Inverted Oblique Rift Systems. Geologica Acta, Vol. 3, No. 3, pp 251-271

Basile, C., Brun, J.-P. (1999) Transtensional faulting patterns ranging from pull-apart basins to transform continental margins: an experimental investigation. Journal of Structural Geology, Vol. 21, pp 23-37

Buiter, S. J. H., Babeyko, A. YU., Ellis, S., Gerya, T. V., Kaus, B. J. P., Kellner, A., Schreurs, G., Yamada, Y. (2006) The numerical sandbox: comparison of model results for a shortening and an extension experiment. In: Buiter, S. J. H., Schreurs, G. (eds.) Analogue and Numerical Modelling of Crustal-Scale Processes. Geological Society, London, Special Publications, Vol. 253, pp 29-64

Bürgmann, R., Dresen, G. (2008) Rheology of the Lower Crust and Upper Mantle: Evidence from Rock Mechanics, Geodesy and Field Observations. Annual Review of Earth and Planetary Sciences, Vol. 36, pp 531-567

Corti, G., Bonini, M., Conticelli, S., Innocenti, F., Manetti, P., Sokoutis, D. (2003) Analogue modeling of continental extension: a review focused on the relations between the patterns of deformation and the presence of magma. Earth-Science Reviews, Vol. 63, pp 169-247

Dauteuil, O., Bourgeois, O., Maudit, T. (2002) Lithosphere strength controls oceanic transfer zone structure: insights from analogue models. Geophysical Journal International, Vol. 150, pp 706-714

Illies, J. H. (1977) Ancient and recent rifting in the Rhinegraben. In: Frost, R. T. C., Dikkers, A. J. (eds., 1977) Fault tectonics in N.W. Europe. Geologie en Mijnbouw, Vol. 56, pp 329-350

Mauduit, T., Dauteuil, O. (1996) Small-scale models of oceanic transform zones. Journal of Geophysical Research, Vol. 101, No B9, pp 20,196-20,209

Panien, M., Buiter, S. J. H., Schreurs, G., Pfiffner, O. A. (2006) Inversion of a symmetric basin: insights from a comparison between analogue and numerical experiments. In: Buiter, S. J. H., Schreurs, G. (eds.) Analogue and Numerical Modelling of Crustal-Scale Processes. Geological Society, London, Special Publications, Vol. 253, pp 2253-2270

Schreurs, C., Colletta, B. (1998) Analogue modeling of faulting zones of continental tanstension and transpression. In: Holdsworth, R. E., Strachan, R. A., Dewey, J. F. (eds.) Continental Transpressional and Transtensional Tectonics. Geological Society, London, Special Publications

Serra, S., Nelson, R. A. (1988) Clay modeling of rift asymmetry and associated structures. Tectonophysics, Vol. 153, pp 307-312

Ustaszewski, K., Schumacher, M.E., Schmid, S M., Nieuwland, D. (2005) Fault reactivation in brittle-viscous wrench systems-dynamically scaled analogue models and application to the Rhine-Bresse transfer zone. Quaternary Science Reviews, Vol. 24, pp 365-382

Van Mechelen, J. L. M. (2004) Strength of moist sand controlled by surface tension for tectonic analogue modeling. Tectonophysics, Vol. 384, pp 275-284

GFZ
Helmholtz Centre
POTSDAM

GeoMod 2014

Modelling in Geosciences

Programme & Extended Abstracts

31 August - 5 September 2014

Editors:
Kirsten Elger
Øystein Thordén Haug
Malte Ritter

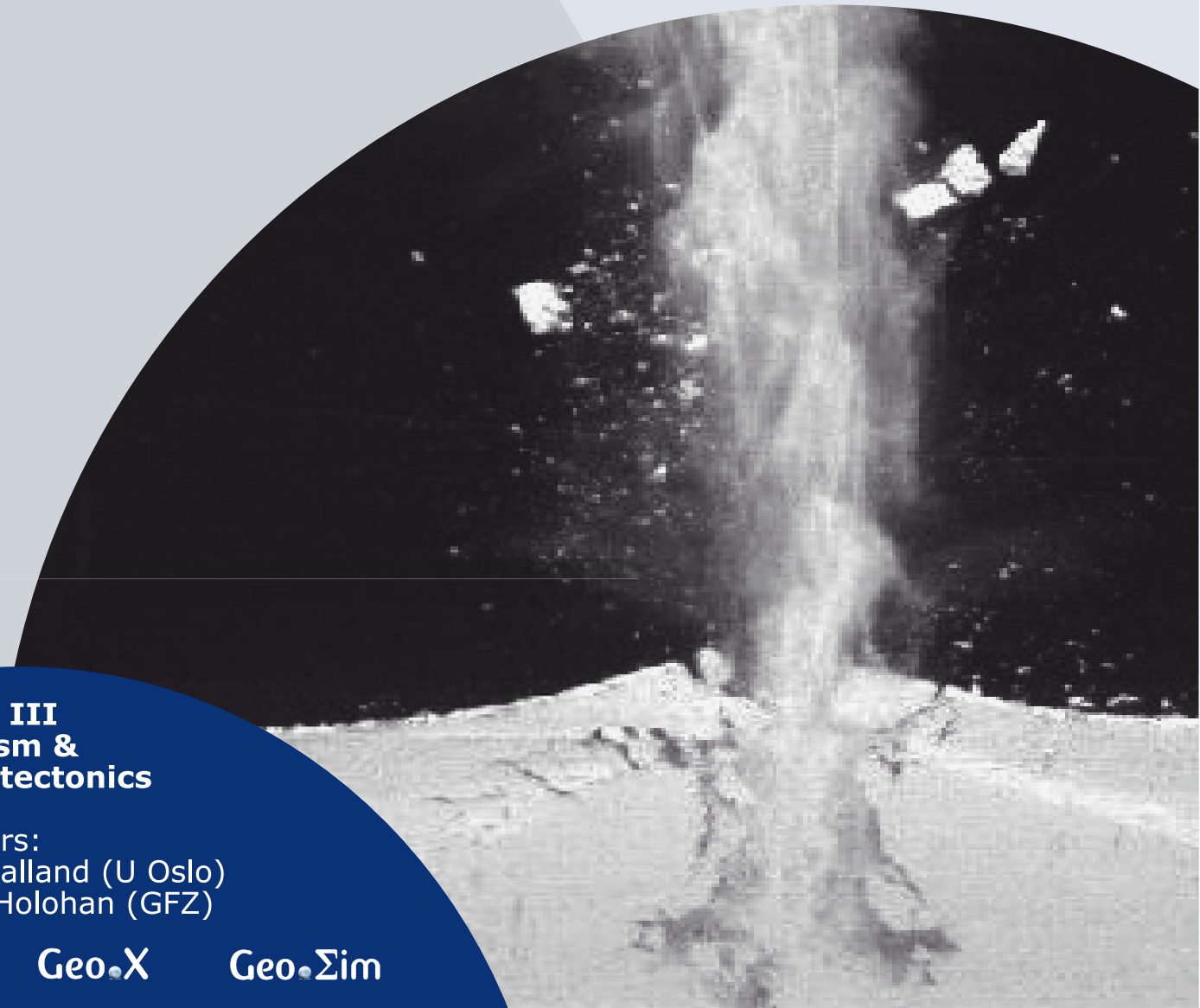

Session III
Volcanism & volcanotectonics

Conveners:
Olivier Galland (U Oslo)
Eoghan Holohan (GFZ)

DFG GeoX GeoSim

Session III.

Volcanism and Volcanotectonics

Session Description: Volcanism and Volcanotectonics

Conveners: Olivier Galland (U Oslo), Eoghan Holohan (GFZ)

Volcanic plumbing systems evolve through the interaction of numerous processes governing the ascent, emplacement, and eruption of magma. A full physical understanding of sub-volcanic and volcanic processes faces stimulating challenges. For instance (1) magma transport through the Earth's crust is not only governed by the mechanical behaviour of the magma or of the host rock, but also by the complex interplay between them. In addition, (2) magma eruption is governed by the complex rheology of the magma and multiphase flows involving gas, liquid and solid phases, with sometimes moving conduit walls. Advanced and quantitative experimental, numerical, and theoretical modelling techniques are thus crucial to unravel these challenging and exciting processes. The Volcanotectonic and Volcanic Processes Session of this GeoMod 2014 international meeting aims to bring together laboratory, numerical and theoretical modellers studying the complex processes governing the mechanics of magma/ host rock systems, and volcanic eruptions.

Solidification effects on sill formation: an experimental approach

L. Chanceaux [1], T. Menand[1,2,3]

[1] *Université Blaise Pascal, Laboratoire Magmas et Volcans, F-63000 Clermont-Ferrand, France 3*
[2] *CNRS, UMR 6524, LMV, Clermont-Ferrand, France 4*
[3] *IRD, R 163, LMV, Clermont-Ferrand, France*
e-mail: *l.chanceaux@opgc.univ-bpclermont.fr*
session: *Volcanism and Volcanotectonics*

The effects of solidification on the formation of sills are studied and quantified with scaled analogue laboratory experiments. Sills represent a major mechanism for constructing continental Earth's crust because these intrusions can amalgamate and form magma reservoirs and plutons. As a result, numerous field, laboratory and numerical studies have investigated the conditions that lead to sill emplacement. However, all previous studies have neglected the potential effect magma solidification could have on sill formation.

The experiments presented here (fig. 1) involved the injection of hot vegetable oil (a magma analogue) which solidified during its propagation as a dyke in a colder and layered solid of gelatine (a host rock analogue), and were correctly scaled geometrically, kinematically, dynamically, and thermally. The gelatine solid had two layers of different stiffness, to create a priori favourable conditions to form sills (Kavanagh et al, 2006). The injection temperature T_i and the injection flux Q were systematically varied between experiments.

To analyse the experiments, we follow the experimental analysis of Taisne and Tait (2011) and define two dimensionless parameters. One describes the thermal conditions of the experiments (dimensionless temperature θ) and the other describes their dynamical conditions (dimensionless flux ϕ). The dimensionless temperature θ is defined as:

$$\frac{(T_\mathrm{s} - T_\mathrm{g})}{(T_\mathrm{i} - T_\mathrm{g})} \tag{1}$$

where T_s is the solidification temperature of vegetable oil, $T_\mathrm{s} = 31°\mathrm{C}$ (Galland et al., 2006); T_g is the gelatine temperature during the injection, typically between 5 and 7°C; T_i is the injection temperature of the vegetable oil. The dimensionless flux ϕ is defined as the ratio between the heat advected by vegetable oil and the heat lost by conduction in the gelatine. During each experiment, a feeder dyke formed first, which, provided an adequate rigidity contrast at the interface, may subsequently form a sill. The dimensionless flux ϕ was thus defined for this feeder dyke (Taisne and Tait, 2011):

$$\frac{3Q\Delta\rho g}{(2E\kappa)} \tag{2}$$

where Q is the flux of injection; $\Delta\rho$ is the difference of density between the gelatine and the vegetable oil; E is the Young's modulus of the lower layer; κ is its thermal diffusivity (assumed to be identical to that of water); and g is the gravitational acceleration.

T_s and T_g were essentially the same for all experiments so θ varied only with T_i the injection temperature. Likewise, $\Delta\rho$, g, κ were all kept constant. Consequently, ϕ varied with the injection flux Q and the Young's modulus E_{low} of the lower layer. θ and ϕ were maintained constant during an experiment (T_i, E_{low} and Q constant),

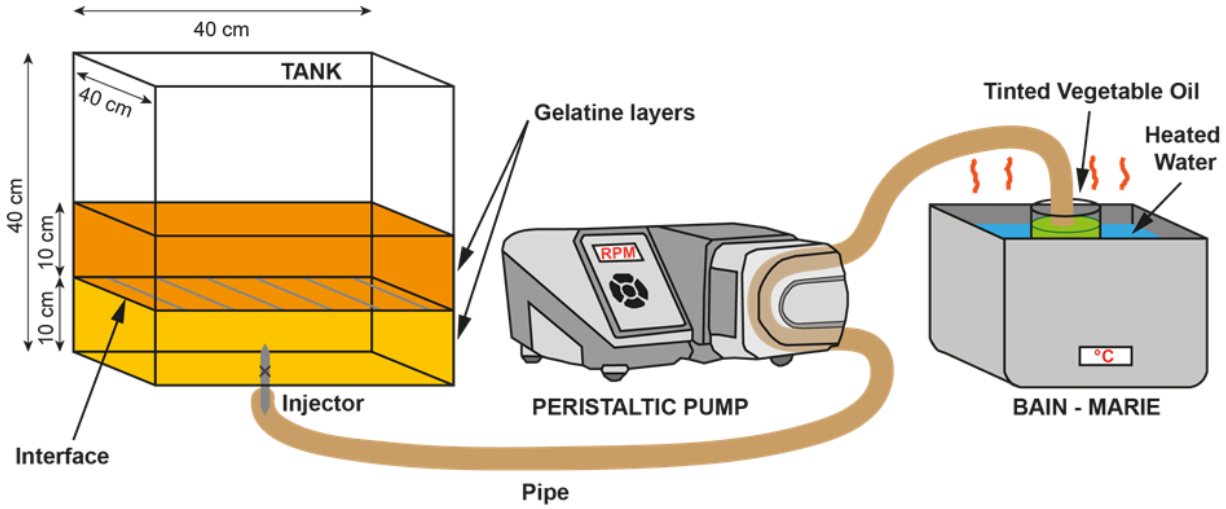

Fig. 1.: Experimental apparatus. The gelatine solid has two layers of different stiffness, to create a priori favourable conditions to form sills. Vegetable oil is heated with a bain-marie and injected at a constant rate with a peristaltic pump in the layered gelatine solid.

Tab. 1.: Behaviour of the dimensionless temperature θ and dimensionless flux ϕ.

$\theta \to 1$	$T_\mathrm{i} \to T_\mathrm{s}$	solidification operates rapidly
$\theta \to 0$	$T_\mathrm{i} \gg T_\mathrm{s}$	almost no solidification
$\phi \to 0$	low Q values	solidification operates rapidly
$\phi \gg 1$	high Q values	almost no solidification

and were varied systematically between experiments to quantify their respective influence of the formation of sills. θ varies between 0 and 1 and ϕ varies between 0 and ∞. Table 1 summarises the behaviour of θ and ϕ. The experiments were carried out under dimensionless conditions (temperature θ and flux ϕ) identical to those present in nature.

Several types of intrusions (fig. 2) were observed: dykes stopping at the interface, dykes passing through the interface and sills. These different shapes demonstrate that contrary to isothermal experiments (no temperature effect able to block sill formation), a rigidity contrast between two layers is not a sufficient condition to create a sill.

The results of the fifteen experiments performed, that is crossing dykes (low solidification effects), sills (moderate solidification effects), blocked dykes (high solidification effects), and cases when fluid could not intrude the gelatine (extreme solidification effects), are all summarized on a graph showing the dimensionless temperature θ, which describes the experimental thermal conditions, as a function of the dimensionless flux ϕ, which describes their dynamical conditions (fig. 3). Solidification effects increase as $\theta \to 1$ and $\phi \to 0$. Four areas are clearly identified:

- When the dimensionless temperature is relatively high and the dimensionless flux is very low ($\theta \approx 0.75$ to 0.95 and $\phi < 6$), there is no propagation (fig. 3, stars). Solidification effects are so important that vegetable oil freezes and solidifies in the tube and no intrusion is observed;

- When the dimensionless temperature is high and for larger dimensionless fluxes ($\theta \approx 0.7$ to 0.95 and $\phi < 15$), dykes are blocked at the interface between the two gelatine layers (fig. 3, squares). Solidification effects are important and the dyke partially solidifies

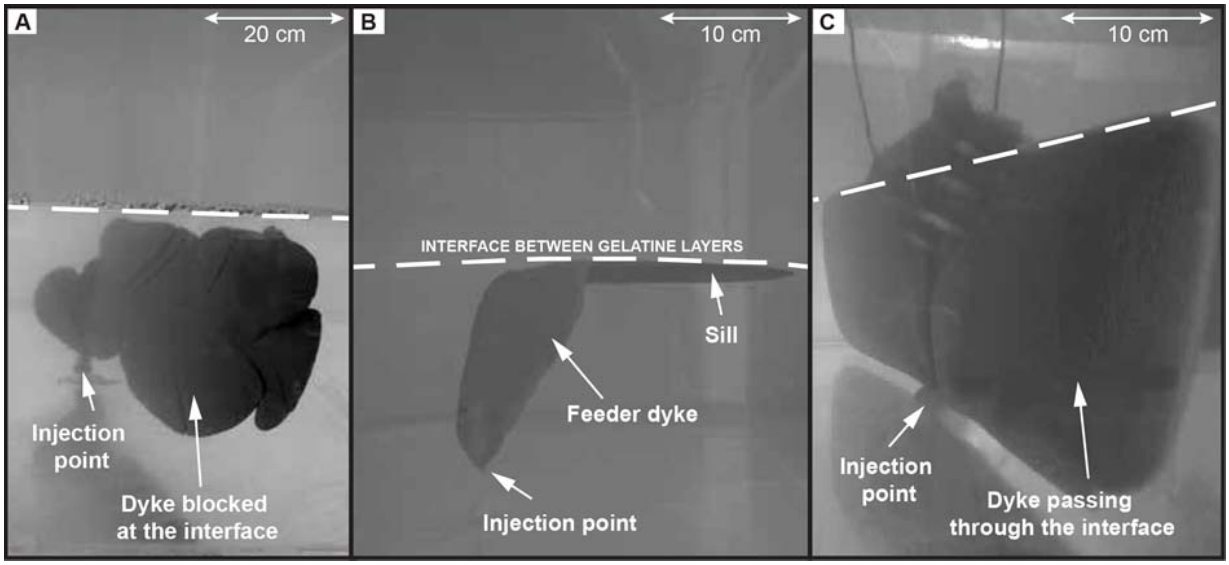

Fig. 2.: Experimental intrusions. (A) Experimental dyke blocked at the interface, three-quarter view. (B) Experimental sill, side view. (C) Experimental dyke passing through the interface, three-quarter view. The dyke takes a triangular shape above the interface.

at its walls during its propagation and development. Solidification at the upper tip of the dyke blocks its propagation, and prevent its piercing of the interface and subsequent propagation in the upper stiffer layer or its spreading along the interface as a sill;

- When the dimensionless temperature has intermediate values ($\theta \approx 0.60$ to 0.90 and $\phi < 16$), sills are created (fig. 3, disks). Solidification effects are smaller. Consequently, the feeder dyke propagates as a sill by spreading at the interface between the two layers;

- Finally, when the dimensionless temperature is low ($\theta \approx$0.6 to 0.7 and $\phi > 2$), dykes passing through the interface are created (fig. 3, triangles). Dykes do not create sills but instead pierce directly the interface to propagate in the upper layer, easily fracturing the gelatine presumably because of their high temperature: higher input of hot vegetable oil at the tip of the feeder dyke leads to lower solidification effects and presumably easier fracturation; the injection flux seemed to have less of an effect. However, solidification along the walls of the dyke seem to prevent the fluid from intruding the interface between the gelatine layers.

Thus, solidification effects restrict sill formation at an interface with a favourable rigidity contrast (upper layer stiffer than the lower one). Sill formation occurs only for a restricted and specific range of dimensionless temperatures θ and fluxes ϕ: $\theta_{\min} \leq \theta \leq \theta_{\max}$, where (c) $\theta_{\min} = 0.0039\phi + 0.61$ and (b) $\theta_{\max} = 0.019\phi + 0.68$ (fig. 3). The thermal conditions (θ) depend on injection temperature T_{i}, and dynamical conditions (ϕ) depend on injection flux Q and rigidity contrast of the intruded solid. Therefore, in our experiments, sill formation along an interface depends on three critical parameters: the injection temperature T_{i}, the injection flux Q, and the rigidity of the solid below this interface.

These experiments demonstrate that contrary to isothermal experiments where cooling could not affect sill formation, the presence of an interface that would be a priori mechanically favourable is not a sufficient condition for sill formation; solidification effects restrict sill formation. The results are consistent with field observations and provide a means to explain why some dykes form sills when others do not under seemingly similar

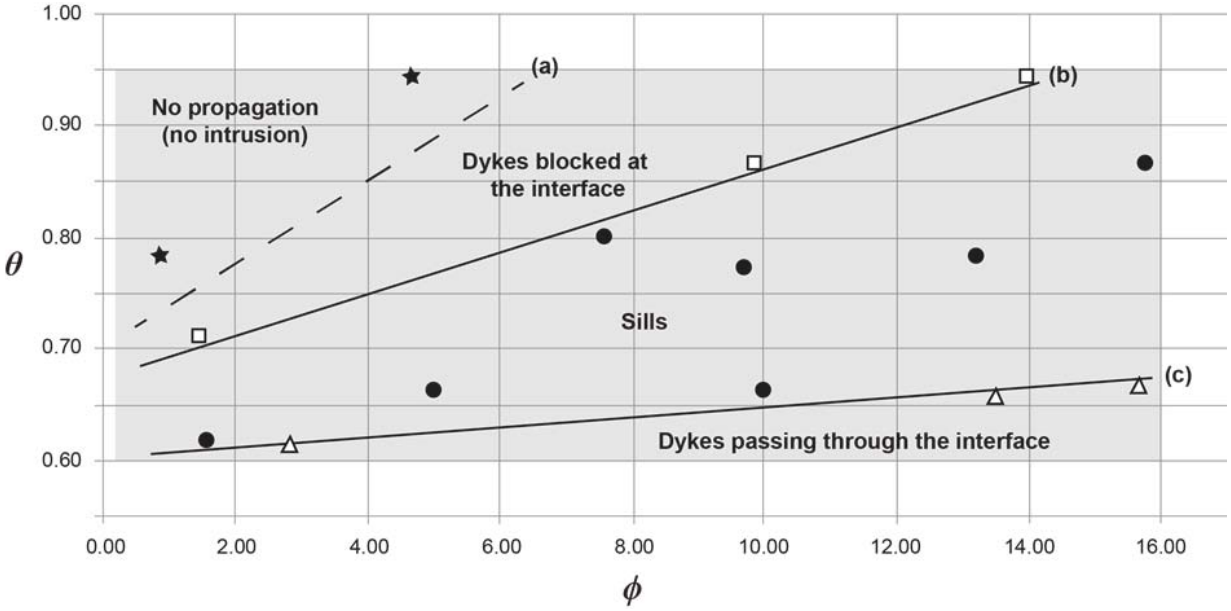

Fig. 3.: Dimensionless temperature θ as a function of dimensionless flux ϕ. Gray area shows natural ranges of values for θ and ϕ. Stars represent experiments where no propagation occurred; squares are dykes blocked at the interface; disks are sills; triangles are dykes passing through the interface. Lines (a), (b) and (c) delimit the areas for each type of intrusions. The dashed line (a) is only qualitative whereas the continuous lines (b) and (c) can be determined reliably. See text for details.

Fig. 4.: Sill with its feeder dyke in the Henry Mountains, Utah, USA, modified from Menand (2011). The view is from the East. The sill, its feeder dyke (both outlined by dashed white lines) and the intruded layered sandstone (continuous white lines) have all been rotated almost $90°$. The feeder dyke crosses several similar interfaces before spreading as a sill.

geological conditions (Fig. 4).

References

Chanceaux, L., & Menand, T. (2014). Solidification effects on sill formation: An experimental approach. Earth and Planetary Science Letters, 403, 79-88.

Galland, O., Cobbold, P. R., Hallot, E., de Bremond D'Ars, J., & Delavaud, G. (2006). Use of vegetable oil and silica powder for scale modelling of magmatic intrusion in a deforming brittle crust. Earth and Planetary Science Letters, 243(3), 786-804. doi:10.1016/j.epsl.2006.01.014

Kavanagh, J. L., Menand, T., & Sparks, R. S. J. (2006). An experimental investigation of sill formation and propagation in layered elastic media. Earth and Planetary Science Letters, 245(3), 799-813. doi:10.1016/j.epsl.2006.03.025

Menand, T. (2011). Physical controls and depth of emplacement of igneous bodies: A review. Tectonophysics, 500(1), 11-19. doi:10.1016/j.tecto.2009.10.016

Taisne, B. and Tait, S., 2011. Effect of solidification on a propagating dike. Journal of Geophysical Research 116 (B1), B01206. doi:10.1029/2009JB007058

The origin of circumferential fissures: insights from analog models

F. Corbi[1], E. Rivalta[1], V. Pinel[2], F. Maccaferri[1], V. Acocella[3]

[1] *GFZ German Centre for Geosciences, Section 2.1, Telegrafenberg, 14473 Potsdam, Germany.*
[2] *ISTerre, Université de Savoie, IRD, CNRS, Campus Scientifique, Le Bourget du Lac F73376, France.*
[3] *Dipartimento di Scienze, University 'Roma Tre', L.S.L. Murialdo, 1, 00146, Rome, Italy.*
e-mail: *fabio.corbi@gfz-potsdam.de*
session: *Volcanism and Volcanotectonics*

At caldera volcanoes eruptive fissures may align with the regional stress field, radiate along the flanks, or circumscribe the caldera [e.g., Acocella, 2007]. The circumferential fissures are often associated with ring faults and only in few cases they appear independent of the existing faults. The origin of the latter is debated [e.g., Chadwick and Dieterich 1995]. Using analog models we find that the stress perturbation due to caldera unloading affects dike dynamics and the resulting eruptive pattern. Air (magma analog) is injected within a cylindrical Plexiglas®. container filled with stiff gelatin (volcano analog) with caldera morphology. The injected air forms a buoyancy driven fracture (dike analog) that, depending on the competition between buoyancy and external forcing, steers outward. We observe analog dikes that arrest at depth, erupt in the caldera region, or in the summit plateau. The summit eruptions form arcuate fissures that develop tangentially to the volcanic edifice as circumferential fissures do in nature. Our gelatin models demonstrate that caldera unloading represents a mechanism responsible for the origin of the circumferential eruptive fissures.

References

Acocella, V. Understanding caldera structure and development: An overview of analogue models compared to natural calderas. Earth-Science Rev. 85, 125–160 (2007).

Chadwick, W. W. & Dieterich, J. H. Mechanical modeling of circumferential and radial dike intrusion on Galapagos volcanoes. J. Volcanol. Geotherm. Res. 66, 37–52 (1995).

Megatsunami generation from caldera subsidence

Max Gallagher, Ben Kennedy[1], Christopher Gomez, Tim Davies

[1] *University of Canterbury*
e-mail: *ben.kennedy@canterbury.ac.nz*
session: *Volcanism and Volcanotectonics*

Mega-tsunamis potentially have devastating global consequences. We use the term mega-tsunami to describe proximal tsunami waves greater than 100m in height. Despite extensive research into fault- and landslide-generated mega-tsunamis, and an ongoing debate about tsunamis generated by explosions and pyroclastic flows, very little is known about the potential of a subsiding caldera to generate a tsunami. Field investigations of historic medium sized caldera-forming events have identified tsunami deposits at runup heights of 10-30m, although numerical modelling has struggled to separate the causative mechanisms of submarine pyroclastic flows, landslides and caldera subsidence. Past efforts to replicate tsunamis generated by caldera subsidence have been dominantly through numerical modelling (e.g. Novikova et al., 2011). To date, only one analogue methodology has been investigated (Gray and Monaghan, 2003). Gray and Monaghan's (2003) analogue model focused on caldera subsidence, where the initial caldera floor is above sea level and the process producing waves in the modelling is most similar to a dam-break flood. As many the majority of potential tsunamis producing calderas are already partially of fully submerged, we focus our modelling on submerged calderas.

Here, we use an analogue model of a submerged subsiding piston to isolate and parameterise the caldera subsidence conditions required to generate a waves (Figure 1).

Our results show that water pours into the space created by the subsiding piston to produce a central dome of water. Waves then radially propagate away from this dome as a series of rings (Figure 1). Wave heights are measured close to the experimental caldera via video analysis of a buoy. Dimensional analysis of our analogue experiment shows that the key parameters are the velocity of subsidence (V_s), the amount of subsidence (S), water depth (D_w). We explored parameter space relevant to scaled submerged calderas. Our wave height data can thus be explained by plotting $V_s^2/\mathrm{g}D_w$ against S/D_w (Figure 2).

Some wave height variation is created in our results by the complex interaction between waves as they leave the caldera. The number and style of waves are affected by the competition between the flow rate into the subsiding caldera and the volumetric rate that space is created by the subsiding caldera and whether waves are created during or after subsidence. Each experiment creates multiple waves that radiate from the centre of the caldera at varying rates and can add and subtract affecting the wave height. Here we focus our results on the largest waves and dominant trends. These data show that larger waves are generated in shallower water and by faster subsidence rates, while the amount of subsidence becomes increasingly important at faster subsidence velocities (Figure 2). The nondimensional parameters allow us to compare our results to natural calderas. We focus our discussion on the formation of mega-tsunamis.

The results show that even large diameter calderas need to subside rapidly to generate mega-tsunamis. The following conditions are necessary for natural calderas to generate mega-tsunamis-subsidence rates $>$ 10m/s, $>$ 3km diameter calderas, $>$100 m subsidence, and water depth

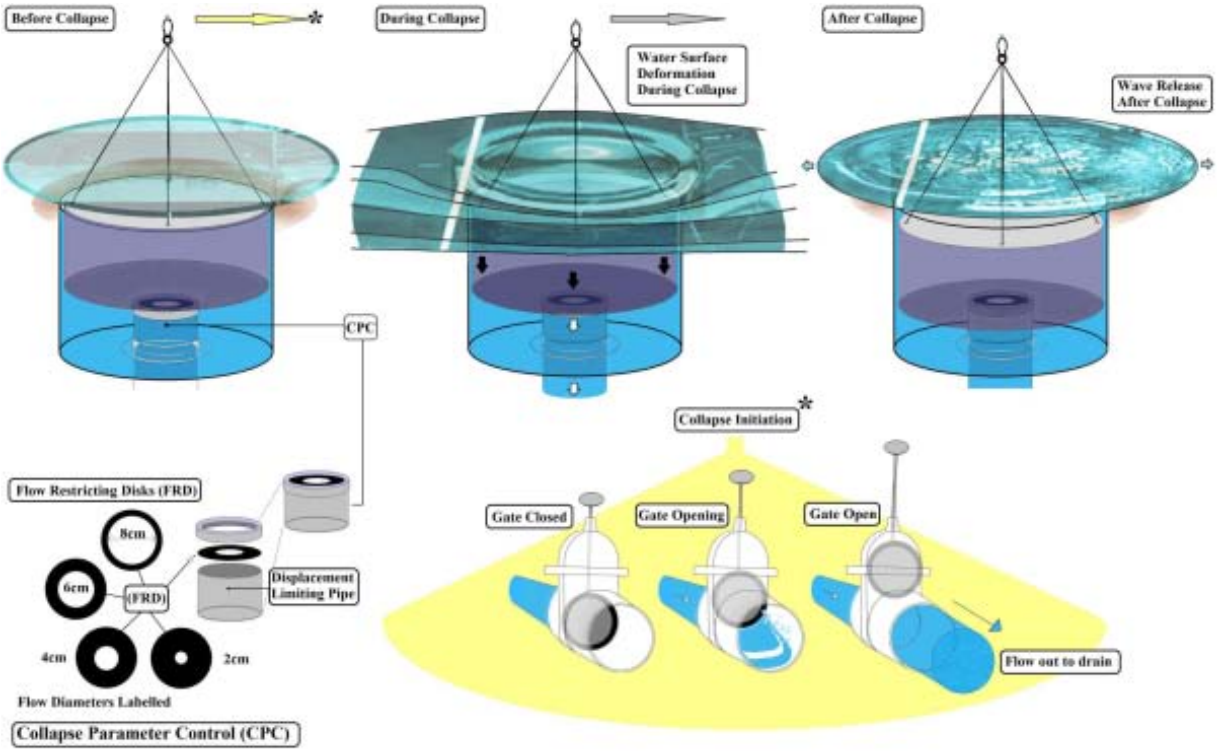

Fig. 1.: Experimental apparatus.

<1000m. These conditions show that near source mega-tsunamis could be generated by many caldera forming events e.g. Krakatoa caldera, Indonesia, Santorini caldera, Greece, Campi Flegrei caldera, Italy, Kikai caldera, Japan, Rabaul caldera, Papua New Guinea. Historic events at Santorini and Krakatoa produced waves with only 10-30m run up on coastlines indicating that these waves either rapidly decreased in height away from source or subsidence rates at these calderas were <10m/s. Unfortunately, the scale of our study prevents extrapolation of wave heights to medial and distal locations and at present subsidence rates at natural calderas are poorly constrained by limited observation. The global effects of caldera generated mega-tsunamis emphasizes the need for numerical modelling to study the propagation of caldera subsidence generated tsunamis and encourages innovative new techniques to estimate subsidence rate during large caldera forming events.

References

Gray, J. P., and J. J. Monaghan, 2003, Caldera collapse and the generation of waves: Geochemistry Geophysics Geosystems, v. 4, p. 1525-2027.

Novikova, T., G. A. Papadopoulos, and F. W. McCoy, 2011, Modelling of tsunami generated by the giant Late Bronze Age eruption of Thera, South Aegean Sea, Greece: Geophysical Journal International, v. 186, p. 665-680.

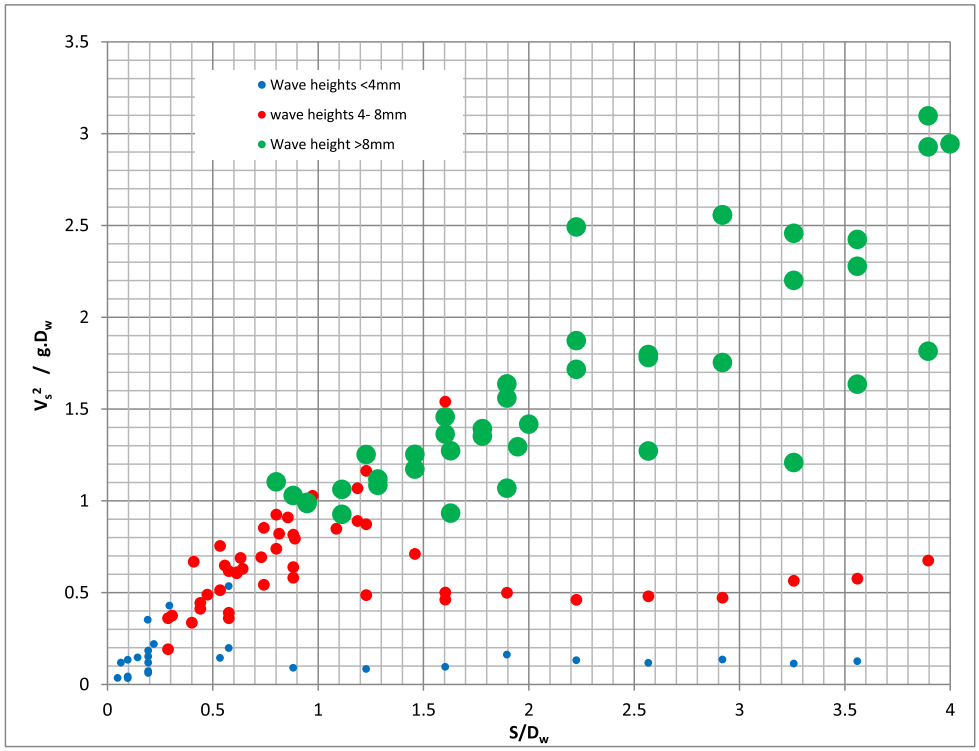

Fig. 2.: Wave height results plotted against critical dimensional parameters.

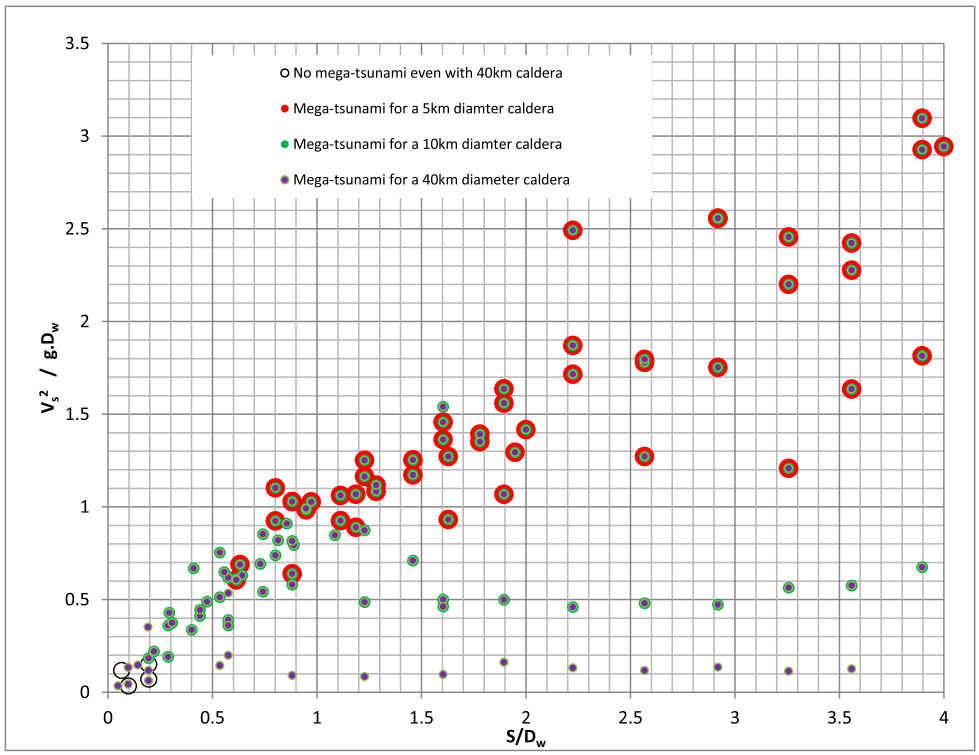

Fig. 3.: By varying the length scale of our experiments, we indicate the different conditions that submerged calderas of 5km, 10km and 40km in diameter can form mega-tsunamis.

Toward a unified dynamic model for dikes and cone sheets in volcanic systems

Olivier Galland[1], Steffi Burchardt[2], Erwan Hallot[3], Régis Mourgues[4], Cédric Bulois[4]

[1]*Physics of Geological Processes (PGP), University of Oslo, Norway*
[2]*Department of Earth Sciences, Uppsala University*
[3]*Géosciences Rennes, University of Rennes1, France*
[4]*L.P.G.N, Université du Maine, France*
e-mail: *olivier.galland@fys.uio.no*
session: *Volcanism and Volcanotectonics*

Swarms of hundreds to thousands of igneous sheet intrusions represent the main magma pathways through the Earth's brittle crust. Field observations in extinct and exhumed volcanic areas worldwide have identified different geometries of sheet intrusions, among which (i) vertical dikes [e.g., Pollard, 1987; Rubin, 1995], (ii) inclined cone sheets [Burchardt et al., 2011], and (iii) horizontal sills [e.g. Burchardt, 2008; Galland et al., 2009] represent the main types (Figure 1). The spatial association and the close temporal relations between cone sheets and dikes led Walker [1992] to propose that they may be fed by a common source. The following key question, however, remains unsolved: what are the physical parameters that lead either to vertical dikes or cone sheets in volcanic systems, and particularly those fed from the same source?

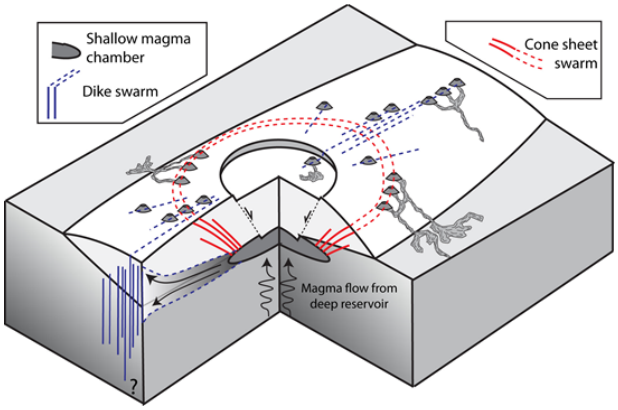

Fig. 1.: a) Schematic drawing of the characteristic structure of volcano plumbing systems [Galland et al., in revision]. A shallow magma reservoir may feed different conduits, such as dikes (blue) or cone sheets (red). Some of the dikes and cone sheets may result in eruptive fissures.

Here we present scaled laboratory experiments that reproduced dike and cone sheet intrusion geometries under controlled conditions. The model rock is crystalline silica flour. Its average grain size is $\sim$15 μm. The flour fails according to a Mohr-Coulomb criterion, and we measured its cohesion (C) and friction coefficient (μ) at 369 $\pm$ 44 Pa and 0.81 $\pm$ 0.06, respectively [Galland et al., 2009]. The model rock is a vegetable oil. It is solid at room temperature but melts from $\sim$31°C. The viscosity of the oil is poorly temperature-dependant [Galland et al., 2006]; we injected it at $\sim$50°C, temperature at which its viscosity is $\eta \sim 2 \cdot 10^{-2}$ Pa s and density is 890 kg m^{-3}.

The experimental apparatus used in this study is a modified version of that of Galland et al. [2009], Galland [2012] and Galland et al. [in revision]. The models laid in a 40 cm wide square box filled with a layer of compacted silica flour of variable thickness and controlled density of 1050 kg m^{-3} (Figure 2). A pump injected the oil at constant and controlled flow rate through a circular inlet of variable diameter (d) into the model, and the oil intruded directly into the silica flour. After the experiments, the oil solidified and the intrusion was excavated to observe its shape.

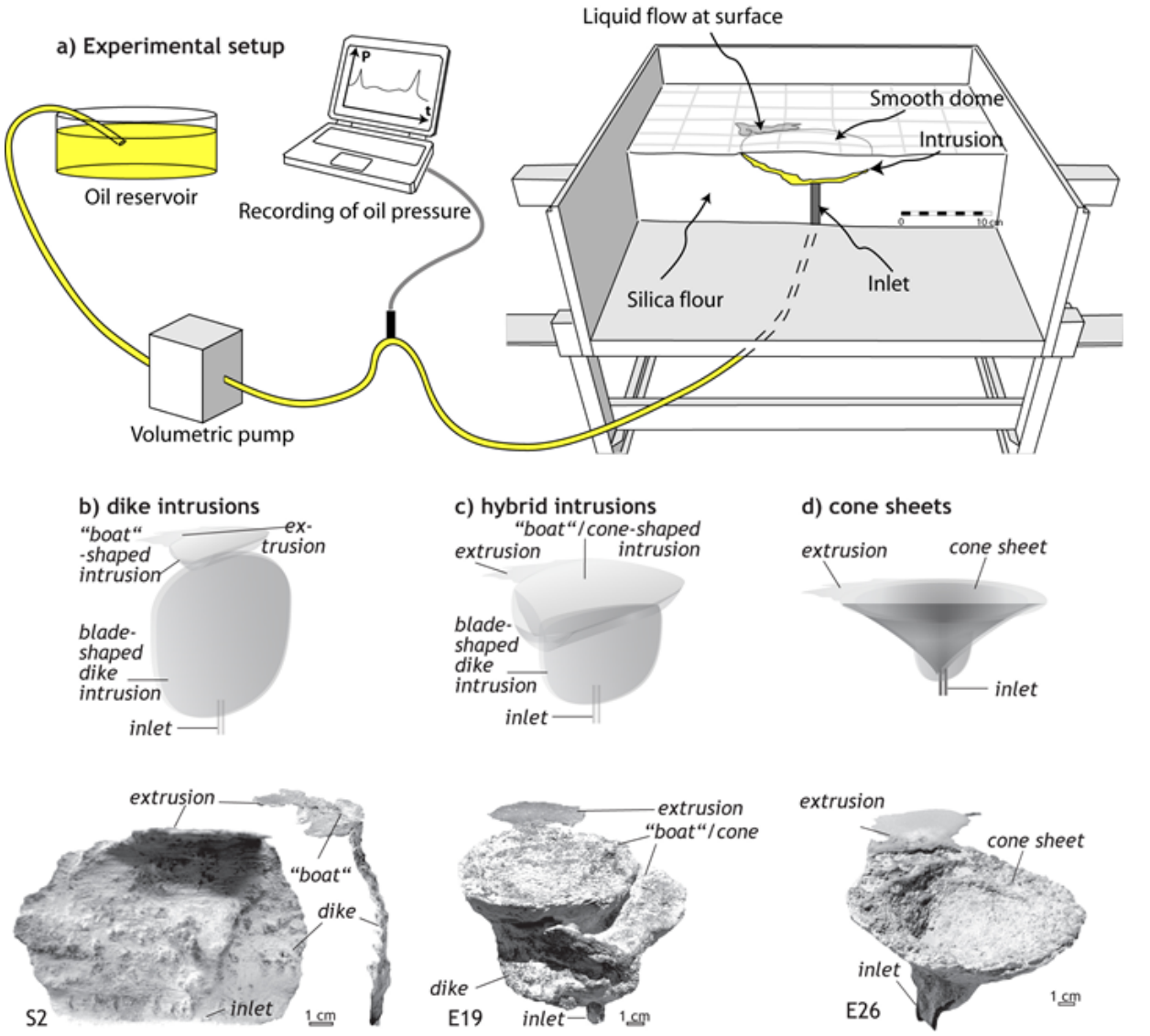

Fig. 2.: a) Drawing of the experimental apparatus used in this study [modified after Galland et al., 2009; Galland, 2012]. b) Schematic drawing (top) and photograph (bottom) of a typical dike produced during the experiments and excavated from the host-powder after solidification of the oil [Galland et al., in revision]. The dike initiated from the inlet at the bottom and fed an elongated v-shaped, or "boat"-shaped, sheet intrusion to the very top. c) and d) Schematic drawings (top) and photographs (bottom) of typical excavated hybrid and cone sheet intrusions, respectively.

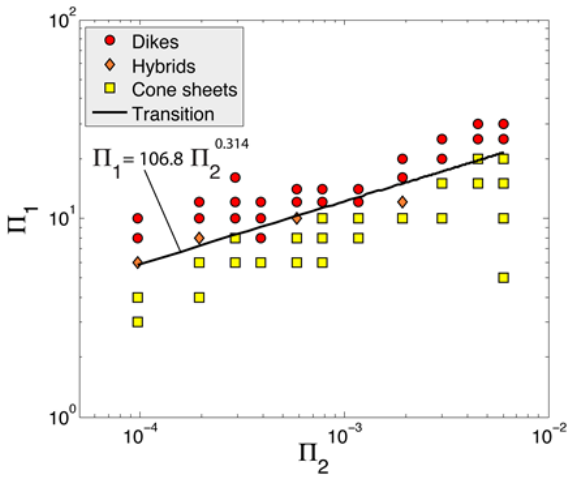

Fig. 3.: Log-log dimensionless phase diagram distinguishing the intrusion shapes obtained in the 52 experiments of this study: dikes (red circles), hybrid intrusions (orange lozenges), and cone sheets (yellow squares) [Galland et al., in revision]. Π_1=h/d and Π_2=vη/Cd. The dikes and cone sheet experiments plot in two distinct fields, separated by a line, expressed by the power law $\Pi_1 = 106.8 \cdot \Pi_2^{0.314}$.

We present the results of 52 experiments, in which we varied independently three controlled parameters: the depth of the injection inlet (h) below the free surface, the diameter of the injection inlet (d), and the oil injection velocity (v). The experiments produced two basic sheet intrusion morphologies that compare to natural dikes and cone sheets, as well as a transitional type of intrusion referred to as hybrid intrusions (Figure 2b, c, d).

We performed a dimensional analysis of the studied system and identified two dimensionless parameters that account for the coupling between the host rock and the magma source: a geometric dimensionless ratios (Π_1=h/d), which describes the geometry of the magma source, and a dynamics dimensionless ratio (Π_2=vη/Cd), which compares the local viscous stresses in the flowing magma to the host-rock strength. Plotting our experiments against these two numbers results in a phase diagram evidencing a dike and a cone-sheet field, separated by a sharp transition that fits a power law (Figure 3). This result shows that dikes and cone sheets correspond to two distinct physical regimes of magma emplacement in the Earth's crust. Cone sheets preferentially form when their source is shallow relative to their size, when the magma influx (or viscosity) is large, or when the host rock is weak. In addition, both dikes and cone sheets may form from the same source, the shift from one regime to the other being then controlled by magma dynamics, i.e. different values of Π_2.

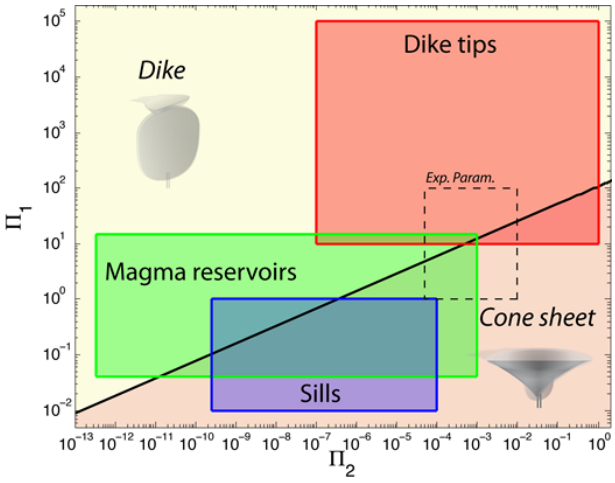

Fig. 4.: Graph comparing the experimental results of this study (dashed line box) to characteristic geological values of Π_1 and Π_2 [Galland et al., in revision]. The dike-to-cone sheet transition is extrapolated from experimental phase diagram of Figure 3. Geological boxes correspond to dike tips (red), magma reservoirs in volcanoes (green) and shallow sills in sedimentary basins (blue).

In order to test the relevance of our empirical law highlighted in Figure 3, we extrapolate it over the geological ranges of Π_1 and Π_2, and compare it with magmatic feeders of dikes and cone sheets of different scales and shapes. In Figure 4, we consider three main types of magmatic feeders leading to dikes and/or cone sheets: (i) magmatic reservoirs in central volcanoes, which feed both dikes and cone sheets (Figure 1a); (ii) sills in sedimentary basins dominantly leading to the formation of sub-circular inward-dipping inclined sheets; (iii) dike tips, considered as local moving magma sources, which dominantly propagate as dikes or sometimes split into V-shaped, boat-

shaped or cup-shaped intrusions. The excellent match between our experimental results and geological data from various magmatic feeding systems suggest that our empirical dike-to-cone sheet power law transition can be extrapolated to a wide range of magmatic settings. This indicates that our experimental models capture general magma emplacement mechanisms, reconciling existing specific models of distinct magmatic feeding systems.

References

Burchardt (2008), New insights into the mechanics of sill emplacement provided by field observations of the Njardvik Sill, Northeast Iceland, J. Volcanol. Geotherm. Res., 173(3-4).

Burchardt et al. (2011), Three-dimensional geometry of concentric intrusive sheet swarms in the Geitafell and the Dyrföll volcanoes, eastern Iceland, G3, 12(7).

Galland (2012), Experimental modelling of ground deformation associated with shallow magma intrusions, Earth Planet. Sci. Lett., 317-318(0).

Galland et al. (2009), Experimental modelling of shallow magma emplacement: Application to saucer-shaped intrusions, Earth Planet. Sci. Lett., 277(3-4).

Galland et al. (2006), Use of vegetable oil and silica powder for scale modelling of magmatic intrusion in a deforming brittle crust, Earth Planet. Sci. Lett., 243.

Galland et al. (in revision), Toward a unified model for dykes versus cone sheets in volcanic systems, J. Geophys. Res.

Pollard (1987), Elementary fracture mechanics applied to the structural interpretation of dikes, edited by H. C. Halls and W. F. Fahrig, Geological Association of Canada Special Paper.

Rubin (1995), Propagation of magma-filled cracks, Annu. Rev. Earth Planet. Sci., 23.

Walker (1992), "Coherent intrusion complexes" in large basaltic volcanoes – a new structural model, J. Volcanol. Geotherm. Res., 50(1-2).

Morphology and dynamics of explosive vents through cohesive rock formations

Olivier Galland[1], Galen Gisler[1], Øystein Thordén Haug[1,2]

[1] *Physics of Geological Processes, University of Oslo, Norway*
[2] *GFZ German Research Center for Geosciences, Holmholz Center Potsdam, Potsdam, Germany*
e-mail: *olivier.galland@fys.uio.no*
session: *Volcanism and Volcanotectonics*

Shallow explosive volcanic processes, such as kimberlite volcanism, phreatomagmatic and phreatic activity, produce volcanic vents exhibiting a wide variety of morphologies, including vertical pipes and V-shaped vents. So far, most studies on explosive eruption dynamics have focused on the processes within existing magmatic conduits, i.e. magma degassing and fragmentation, assuming that the walls were infinitely rigid [Melnik et al., 2005, Starostin et al., 2005, Dellino et al., 2007]. Hence, these studies were not suitable for unraveling the formation of explosive vents.

In this study we report on experimental and numerical models designed to capture a range of morphologies in an eruptive system. Using dimensional analysis, we identified key governing dimensionless parameters, in particular the gravitational stress-to-fluid pressure ratio ($\Pi_2 = P/\rho gh$), and the fluid pressure-to-host rock strength ratio ($\Pi_3 = P/C$). We used combined experimental and numerical models together to test the effects of these parameters.

The experiments build on the experiments by Haug et al. [2013] and were used to test the effect of Π_2 on vent morphology and dynamics. Two distinct morphologies were observed in the experiments: vertical pipes (Figure 1a) and diagonal fractures (Figure 1b). A phase diagram demonstrates a separation between morphologies, with vertical structures occurring at high values of Π_2, and diagonal ones at low values of Π_2 (Figure 1c).

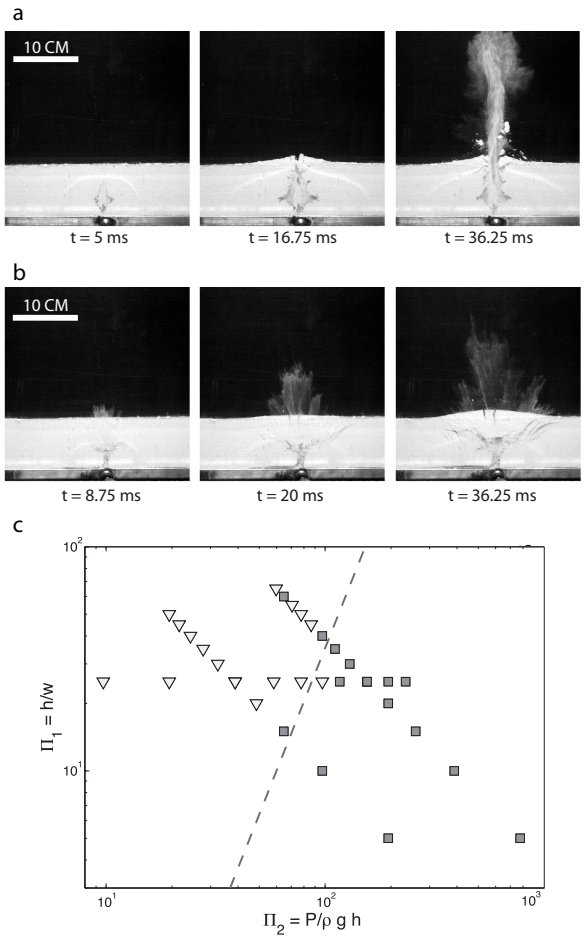

Fig. 1.: (a) Snapshots of experiments with relative high pressure compared to thickness: the air carve straight through the layer. (b) Experiment with relatively low pressure compared to the thickness of the layer: diagonal fractures propagate towards the surface. (c) Phase diagram showing that the two morphologies are determined by Π_1 and Π_2

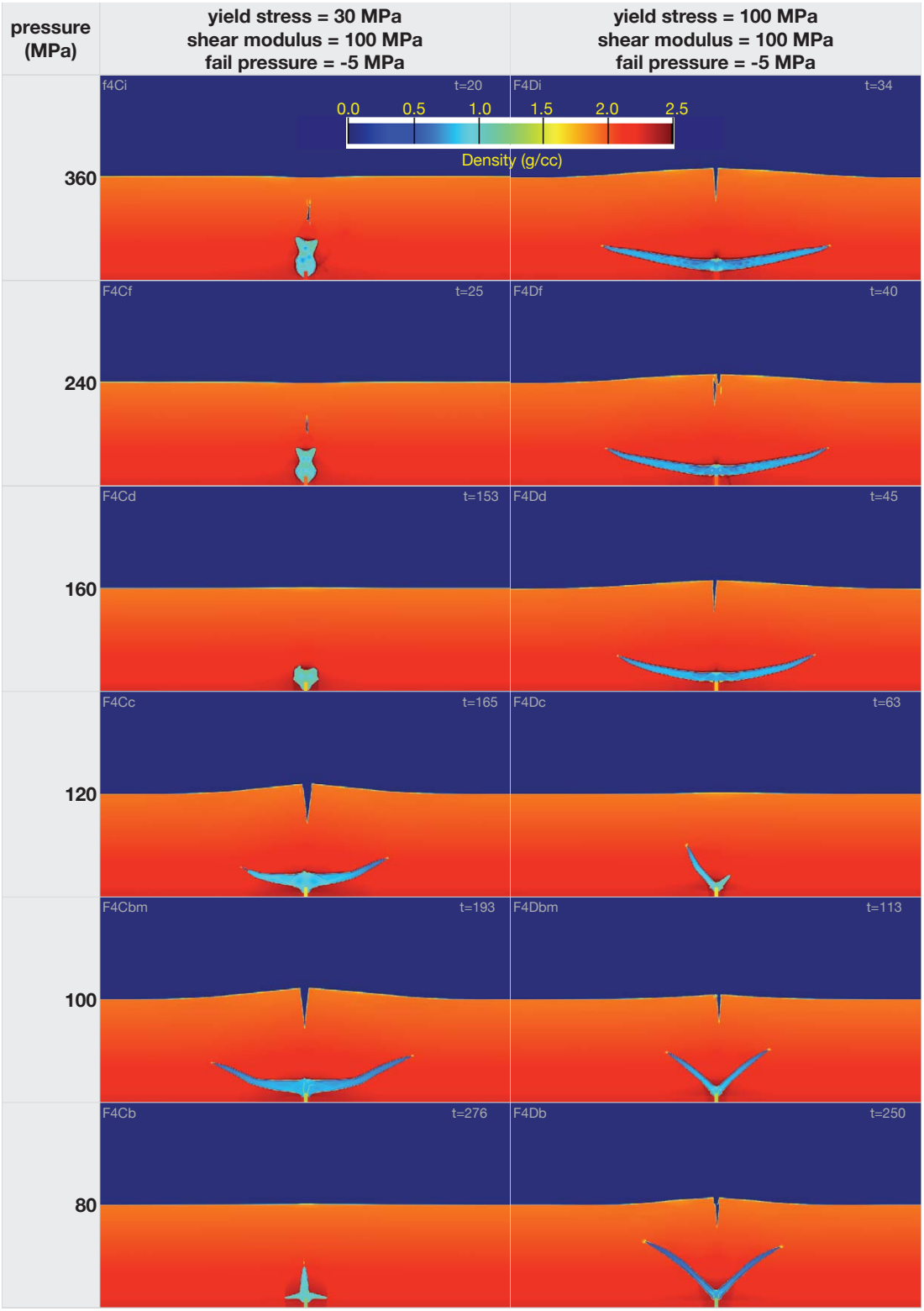

Fig. 2.: Phase diagram showing snapshots of numerical simulations. It is observed that for high value of Π_3 vertical pipes, for low values of Π_3 diagonal pipes and for intermediate Π_3 horizontal sills are produced.

The numerical simulations were used to test the effect of Π_3 on vent morphology and dynamics. In the numerical models we see three distinct morphologies: vertical pipes are produced at high values of Π_3, diagonal pipes at low values of Π_3, while horizontal sills are produced for intermediate values of Π_3 (Figure 2).

The distribution of stress (Figure 3) reveal that vertical pipes form by plasticity-dominated yielding for high-energy systems (high Π_2 and Π_3), whereas diagonal and horizontal vents dominantly form by fracturing for lower-energy systems (low Π_2 and Π_3).

Although our models are 2-dimensional, they suggest that circular pipes result from plastic yielding of the host rock in a high-energy regime, whereas V-shaped volcanic vents result from fracturing of the host rock in lower-energy systems.

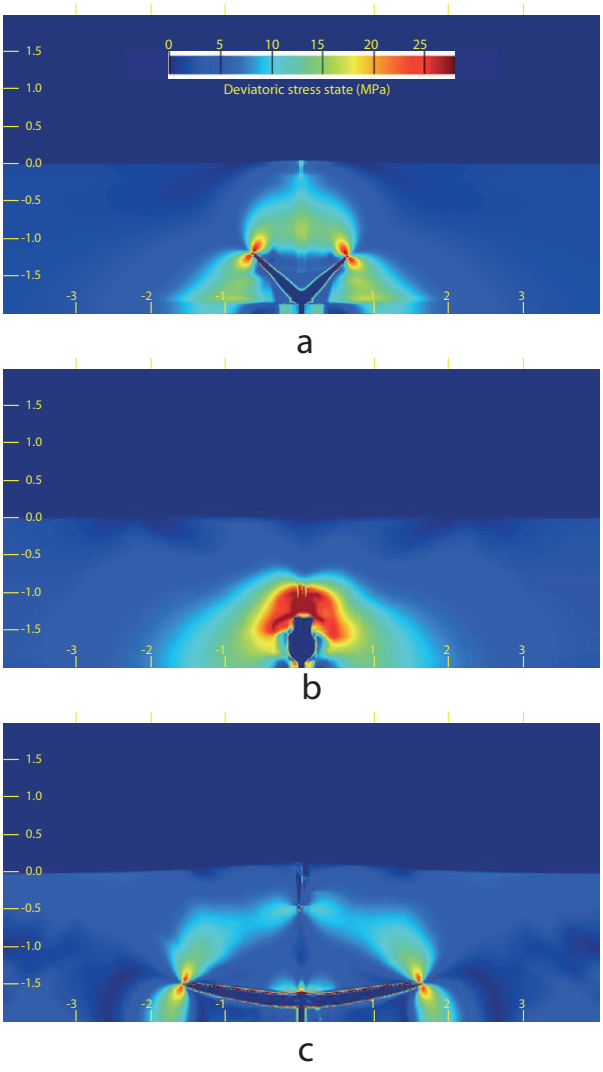

Fig. 3.: Snapshots of the deviatoric stress for the three morphologies observed in the numerical simulations. The diagonal fractures, as well as the horizontal sills have a distribution of stress compatible with elastic fracturing. The vertical pipes, however, display distributed stress around the propagating fracture, suggesting a plastic yielding.

References

P. Dellino, B. Zimanowski, R. Büttner, Luigi La Volpe, D. Mele, and R. Sulpizio. Large-scale experiments on the mechanics of pyroclastic flows: Design, engineering, and first results. Journal of Geophysical Research: Solid Earth (1978-2012), 112(B4), 2007.

Ø. T. Haug, O. Galland, and G. Gisler. Experimental modelling of fragmentation applied to volcanic explosions. Earth and Planetary Science Letters, 384:188-197, 2013.

O Melnik, A.A. Barmin, and R. S. J. Sparks. Dynamics of magma flow inside volcanic conduits with bubble overpressure buildup and gas loss through permeable magma. Journal of Volcanology and Geothermal Research, 143 (1):53-68, 2005.

A. B. Starostin, A. A. Barmin, and OE Melnik. A transient model for explosive and phreatomagmatic eruptions. Journal of volcanology and geothermal research, 143(1):133-151, 2005.

Temporal changes in mantle wedge geometry and magma generation processes in the Central Andes: towards linking petrological data to thermomechanical models

Rosanne Heistek[1], Melanie Brandmeier[1], Heye Freymuth[1,2], Gerhard Wörner[1]

[1]*Institut für Geowissenschaften, Universität Göttingen, Goldschmidtstr. 1, 38077 Göttingen, Deutschland.*
[2]*Dept. Earth Sciences, Univ. Bristol, Uk*
e-mail: *rheiste@gwdg.de*
session: *Volcanism and Volcanotectonics*

Temporal and spatial patterns of Neogene ignimbrite magmatism in the Central Andes were analyzed using GIS and geostatistical modeling. We compiled a comprehensive ignimbrite database using available literature, satellite imagery and geochemical data. 203 individual ignimbrite sheets were digitized in GIS, for which geochemical, isotopic (partly), and geochronological data are available from literature sources and own data (`http://www.arcgis.com/home/item.html?id=47038ddc0628473f9f0ce67aa2eff8be`). Based on this analysis, we estimate composition, volumes and sources of erupted ignimbrite magmas through space and time for five segments of the Central Andes.

The total erupted ignimbrite magma volume is estimated to be about 31,000 km^3 for the past 30 Ma, with the highest average eruption rates (r^m) for the northern Puna segment (3.4 km^3 Ma^{-1} km $(arc)^{-1}$), followed by 0.7 km^3 Ma^{-1} km $(arc)^{-1}$ for the Altiplano. For Southern Peru, r^m is smaller (0.5 $km^3 Ma^{-1} km$ $(arc)^{-1}$), which might be due to the lack of knowledge about intra-caldera volumes. Furthermore there is a clear N-S "younging" of ignimbrite pulses. Major pulses of high magma eruption rate occurred at 19-24 Ma (e.g. Oxaya, Nazca Group), 13-14 Ma (e.g. Huaylillas ignimbrites), 6-10 Ma (Altiplano and Puna ignimbrites, e.g. Vilama ignimbrite) and 3-6 Ma (e.g. Atana, Los Frailes, Toconao). In contrast, small volume young ignimbrites from 0-3 Ma (e.g. Lauca-Perez, Purico) do not show the spatio-temporal pattern of eruptions that are documented for the large- volume ignimbrite flare-ups.

Compositional and Sr-O isotopic data indicate that ignimbrite magmas are more crustally derived in younger flare-ups in the Southern Central Andes (up to 50 % crustal melts) compared to older ignimbrites in the north (only up to 20 % crustal melts). This suggests that thermal conditions, juvenile magma production in the mantle, thickness, and/or composition of the crust must have been different along the Central Andes at the time when ignimbrite flare up magmas formed.

The amount of juvenile magmas that entered the crust and the degree and volume of partial melting within the crust can thus in principle be constrained in time and space by these data. Such data are essential in order to understand the thermal evolution of the Andean crust in space and time.

The Miocene large-volume, plateau forming ignimbrites always overly a pronounced unconformity and occur after a time with no magmatism. They are followed, however, by andesitic arc magmatism characterized during the Late Miocene by low angle, large-volume ($\sim$2.2 km^3 per lava flow) volcanic shields with long single lava flows up to 20 km. These shields are succeeded by younger and more evolved steeply-sided strato-cones that characterize much of the CVZ active volcanic

front for Pliocene-Quaternary times. Andesites in such young stratovolcanoes (∼0.7 km^3 per lava flow) are often characterized by amphibole phenocrysts.

In principle, the transition between these andesite regimes could be due to:

1. a change in the mantle melting regime from decompression (hot and dry?) to flux melting (wet and lower T?),

2. different rates in magma production and effusion, and

3. different P-T-regimes of magma evolution within the crust as is shown by the depletion in HREE and Y from Miocene to Pleistocene volcanic rock caused by a residual garnet after crustal assimilation in a thickened crust.

To understand the shift from andesite shields to stratovolcanoes we studied Miocene to modern Central Andean volcanic rocks that represent different ages but are similar in petrography and composition in order to test differences in processes of magma generation. Based on a survey of ∼1300 chemical analyses of lava samples (`http://andes.gzg.geo.uni-goettingen.de/`) we selected three representative sample types: (1) most mafic samples (50-55 % SiO_2), (2) intermediate andesites representing 63 % of the data (55-60 % SiO_2), and (3) felsic samples (60-65 % SiO_2), all of which were identified before as important end-member magma type in the Central Andes. Using a range of geothermometers, hygrometers and MELTS modelling we show that the P-T parameters at the time of eruption, for a given composition, remained surprisingly constant trough time and throughout the Central Andes (e.g. 975 °C to 985 °C for 2-px thermometry). Moreover, the depth of the last (phenocryst) crystallization of Miocene to Present magmas took place between 9 and 3.5 km throughout Andean history. These observations clearly indicate that estimated temperatures only reflect the late crystallization history at shallow levels and that any distinct regimes of magma formation in the mantle wedge that may have existed are entirely dampened out during the passage through the crust. Density, viscosity and degassing of andesite magmas control the latest stages of ascent and crystallization and these parameters are independent of crustal conditions, subduction geometry and mantle wedge conditions. Therefore, the thickened upper crust not only serves as a chemical filter for mantle wedge magmas but also controls (and synchronizes) P-T conditions of crystallization as recorded in erupted products.

Deep evolution at the level of the magma sources and lower crust, where assimilation and magmatic differentiation takes place, is thus completely decoupled from the shallow processes of late crystallization. Therefore only the rate of effusion, and by implication, magma production and upper crustal stress regime remain as primary factors that may have influenced differences between Miocene and Recent magmatic products.

Since the sequence of distinct magmatic regimes (plateau-ignimbrites, shield andesites and evolved stratovolcanoes) is diachronous during the past 26 Ma of Andean evolution with ages getting younger from N to S. This suggests control by "deeper" processes guided by the geometry of the slab and the thermal evolution of the upper plate during Andean orogeny. As patterns, timing of events, subduction parameters and magma production rates in the mantle wedge change regionally and temporally during ongoing thickening of the Central Andean crust, the upper plate reacts at any given location individually to these changes according to its present thermal state, crustal composition, magmatic history and tectonic stress conditions at that time and space.

We propose that large-volume ignimbrite eruptions occurred in the wake of subduction of the Juan-Fernandez ridge that passed below the Central Andes from N to S during the past 25 Ma. This event resulted in compression, uplift, low angle subduction (flat slab) and fluid release in a first stage, followed by massive inflow and melting of asthenospheric mantle after the passing of the ridge when the slab again steepened rapidly. This in turn caused massive melting within the crust

aided by advective heat transport shortly after slab steepening. Differences in chemical and isotopic composition of the large-volume ignimbrites are related to changes in crustal thickness, and its "preconditioning" during the Anden orogeny over time.

The change in effusion rate during the Miocene to Pliocene/Quarternary may be the only parameter that relates to changing angles and/or convergence rates of the slab. Since only convergence rates changed during the last 26 Ma (Sérbier and Solar, 1991), this parameter likely controls magmatic activity (Cagnoicle et al., 2007). In southern Peru, Miocene voluminous magmatic activity correlates with high convergence rates, both decreasing in the last 10 Ma (Sébrier and Soler, 1991).

Previous model predictions for arc magmatism (Sobolev et al., 2006) follows from the comparison between the evolution of tectonic shortening and the evolution of the mantle temperature beneath the magmatic arc. Processing the delamination material throught the asthenospheric wedge by corner flow results in an increasing shortening rate. Simultaneously, the temperature of the asthenospheric wedge beneath the magmatic arc decreases, which in turn should lead to reduced magmatic activity. However, apart from the Puna (Kay and Kay, 1993) and Northern Altiplano (Back and Zandt., 2002; Yuan et al., 2002)) no evidence exists for mantle lithosphere delamination in the Central Andes. Therefore a new model based on our volumes, eruption rates, petrological constraints and the movement of the Juan Fernández ridge should give a better understanding of the controlling factors of arc magmatism.

References

Back SL, Zandt G (2002) The nature of orogenic crust in the Central Andes. J Geophys Res 107:n doi 10.1029/2000JB000124

Cagnioncle AM, Parmentier EM, Elkins-Tanton LT (2007) Effect of solid flow above a subducting slab on water distribution and melting at convergent plate boundaries. J Geophys Res 112: B09402

de Silva, S., Gosnold, W.D. (2007) Episodic construction of batholiths: Insights from the spatiotemporal development of an ignimbrite flare-up. J. Volcanol. Geotherm. Res. 167: 320–335.

Kay RW, Kay SM (1993) delamination and delamination magmatism. Tectonophysics 219:177 - 189

Sébrier, M., Solar, P. 1991. Tectonics and magmatism in the Peruvian Andes from late Oligocene time to the Present. Geological Society of America 265, 259–278.

Sobolev SV, Babeyko AY, Koulakov I, Oncken O (2006) Mechanism of the Andean orogeny: insight from numerical modeling. In: Oncken O, Chong G, Franz G, Giese P, Götze H-J, Ramos VA, Strecker MR, Wigger P (eds) The Andes – active subduction orogeny. Frontiers in Earth Science Series, Vol 1. Springer-Verlag, Berlin Heidelberg New York, pp 513–536, this volume

Yáñez, G., Cembrano, J., Pardo, M., Ranero, C., Selles, D., 2002. The Challenger–Juan Fernández– Maipo major tectonic transition of the Nazca–Andean subduction system at 33–34 S: geodynamic evidence and implications. Journal of South American Earth Sciences 15, 23-38.

Yáñez, G.A., Ranero, C.R., Huene, R., Díaz, J., 2001. Magnetic anomaly interpretation across the southern central Andes (32–34 S): The role of the Juan Fernández Ridge in the late Tertiary evolution of the margin. Journal of Geophysical Research: Solid Earth (1978–2012) 106, 6325-6345.

Use of the Distinct Element Method in Volcano-tectonic Modeling

E.P. Holohan[1,2], H. Sudhaus[1], M.P.J. Schöpfer[2,3], T.R. Walter[1], J.J. Walsh[2]

[1] *German Research Centre for Geosciences (GFZ-Potsdam), Sektion 2.1 – Physics of Earthquakes and Volcanoes, Helmholtzstrasse 7, 14467 Potsdam, Germany.*
[2] *Fault Analysis Group, UCD School of Geological Sciences, University College Dublin, Ireland.*
[3] *Department for Geodynamics and Sedimentology, University of Vienna, Althanstrasse 14, Vienna, Austria.*
e-mail: *holohan@gfz-potsdam.de*
session: *Volcanism and Volcanotectonics*

Introduction

Certain volcano-tectonic processes, such as caldera collapse, flank spreading or sector collapse, involve large discontinuous (i.e. fault- or fracture-related) strains of rock masses. Analogue models can readily reproduce such deformation, but their exact scaling to natural systems is often uncertain. Numerical models scale more accurately, but the continuum-based approaches typically used to date have an inherent difficulty in simulating fracture or fault system development. Moreover, since continuum-based analytical solutions are routinely used to model geodetic data from actively-deforming volcanoes, the effects of fracturing (particularly in the sub-surface) on deduced finite deformation sources may be underestimated and misinterpreted.

Distinct Element Method (DEM) models

The DEM simulates the finite displacements and rotations of discrete particles[1]. In the 2D DEM code PFC2D[2], the particles are rigid discs (Fig. 1). The particles interact with each other and with rigid boundary walls through a contact law based on linear force-displacement and Coulomb friction. Other contact laws are also possible. Beam-like elastic bonds ('parallel bonds') can be added to hold the particles together. The bonds transmit both forces and moment, and they break if their tensile or shear strength is exceeded. As broken bonds accumulate within a particle assembly, they link together and promote further strain localisation, such that large-displacement fracture systems may ultimately develop. Consequently, the DEM material undergoes a transition from quasi-continuum behaviour to discontinuum behaviour, and so bridges past analogue and numerical approaches.

An important feature of the DEM is that material properties are defined and varied at the bond and particle scale. Bulk material properties (elasticity, strength, friction) emerge from the larger-scale interaction of particles and bonds based on the micro-scale properties. Bulk properties must therefore be calibrated by means of simulated rock deformation tests (Fig. 2). For the caldera collapse model shown here, the bulk material properties lie within the ranges characteristic of natural rock masses on a large (c. 100 m) scale [3].

Application to Pit-crater and Caldera subsidence

One suitable use of DEM models in volcano-tectonic modelling is for the simulation of the structural development of pit crater or caldera

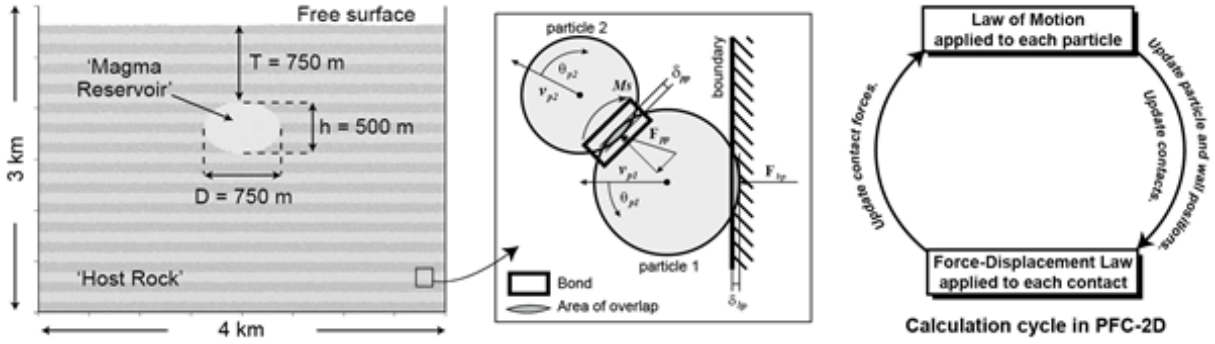

Fig. 1.: Overview of DEM as implemented in PFC-2D and applied to model caldera collapse. Left: Pre-depletion view of a collapse caldera model. Shaded light grey are non-bonded, low friction (0.01) particles that make up the simulated magma reservoir. Around this are bonded, higher-friction (0.5) particles that make up the simulated host rock. Note that the layers here are passive markers and do not represent any material heterogeneity. The boundary wall conditions are free-slip. Centre: Close up of particle-bond-boundary relations used in PFC-2D calculations. M = moment, F = force, v = particle velocity, θ = angular rotation, δ = particle-particle or particle-boundary overlap. Right: Schematic of PFC calculation cycle.

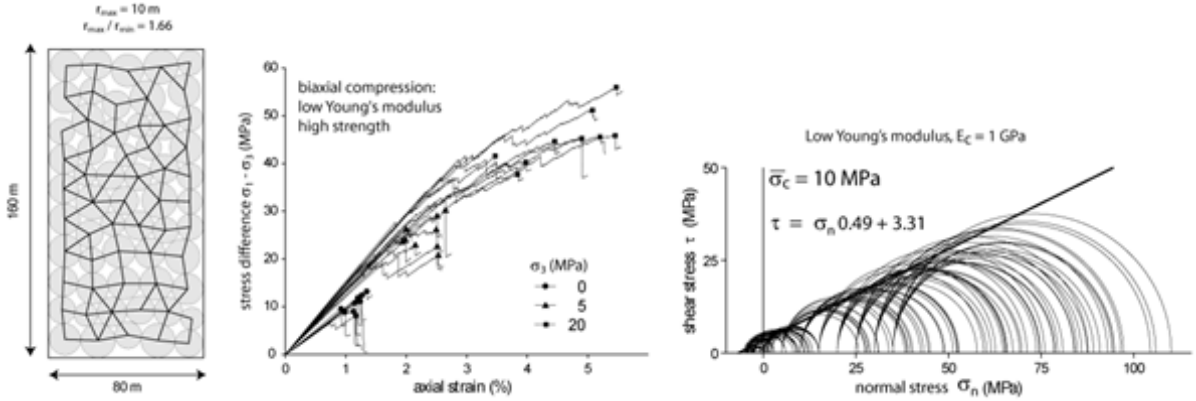

Fig. 2.: Illustration of the process for bulk property calibration in DEM models (modified from [3]). Left: Sample of the model assemblage in Figure 1 to be subjected to biaxial compression and tension tests. Centre: Stress-strain plot for biaxial compression tests at various confining pressures, each with 10 realisations (i.e. different particle arrangements). Symbols on stress-strain curves denote peak strengths at differing confining pressures (σ_3). Most of these curves' post-peak extents were removed for clarity. The pre-failure slopes of these curves indicate a confining-pressure-dependent Young's modulus of 1 – 1.4 GPa. Right: A linear Mohr-Coulomb failure envelope fitted to the biaxial compression test results. The envelope indicates a bulk material cohesion of 3.31 MPa and a friction coefficient of 0.49 for this sample (sample has particle contact modulus of 1 GPa and bond strength of 10 MPa).

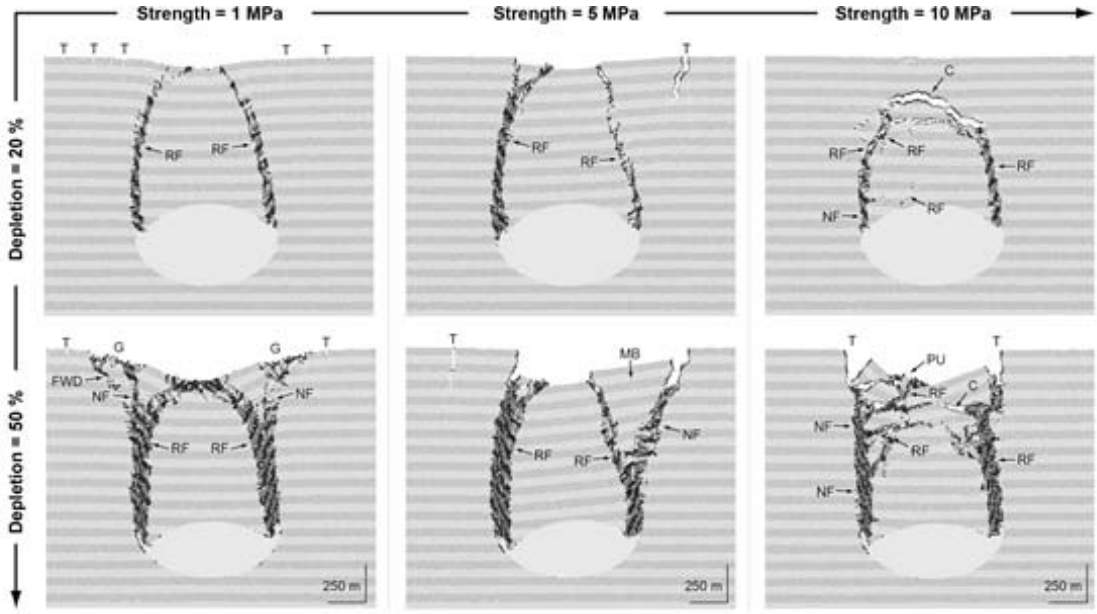

Fig. 3.: Structural development in DEM models of pit crater or caldera collapse (modified from [3]). Shown here are three models that differ only in host-rock strength (unconfined compressive strength). Each model is shown at reservoir area depletions of 20% and 50%. Strain localisation is shown by shading those particles around which the maximum finite shear strain exceeds 0.75. Structures are annotated as follows: T= tensile fracture (crevasse), RF = reverse fault, NF = normal fault, G = graben, FWD = footwall detachment, MB = marginal bench, C = cavity, PU = pop-up structure. For this geometry of the reservoir roof, low to intermediate strength models show a single central block collapse style, with near surface sagging at the lowest strength. In contrast, high strength models show a collapse style comprising the upward-migrating detachment of multiple blocks (resulting in opening and closure of ephemeral cavities) before finally forming a depression at surface.

subsidence [3, 4]. Here we illustrate the effects of host-rock strength on this development with models for which the initial model state shown above (Fig. 1). Magma withdrawal in these models is simulated by incrementally reducing the area of each reservoir particle. Resultant gravity-driven failure and fault-controlled subsidence of the overlying reservoir roof is explicitly replicated (Fig. 3).

The DEM models reproduce the main structural features seen in both analogue models and nature (cf. [3]). These include reverse faults that are steeply outward-inclined from the crater centre, as well as more peripheral near-surface tensile fractures and inward-dipping normal faults. Moreover, the DEM also reproduces strength related effect on the collapse style, such as coherent collapse with sagging at low strength and non-coherent collapse with cavity formation at high strength.

Such DEM models can also be used to examine how sub-surface fracturing may affect analytically-inferred source models for deformation at active volcanoes. By reproducing surface displacements observed at active volcanoes, such continuum-based analytical models are typically used to constrain the characteristics of the deformation source(s), e.g. magma bodies, responsible for the surface changes (cf. [5]).

Here we similarly 'blindly' fit surface displacements arising in DEM models of magma reservoir deflation to those from an analytical solution (Fig. 4), as for natural cases, but in which the extent and nature of sub-surface fracturing are known. To approximate the 2D conditions of the DEM simulation, our analytical source model comprises two intersecting rectangular dislocation planes [6] that are fixed to be perpendicular

to the 2D plane of interest and, in that direction, are extremely long relative to the model scale. In the absence of fracturing, the orientation and location of the optimum analytical source model are consistent with those of the DEM reservoir. Where significant fracturing occurs, however, the optimum analytical source may become strongly tilted and be sited in the roof above the reservoir. In such fracture-influenced cases in nature, analytical source models may hence underestimate the true reservoir depth.

Wider Application of DEM in Volcano-tectonics, Limitations and Future Directions

Other recent applications of the DEM in volcano-tectonics include simulations of volcano-spreading[7], volcano flank collapse[8], and sill intrusion[9]. That all applications published thus far have been 2D studies reflects one of the main limitations of the DEM: its computational intensity. This necessitates a trade-off between model size, particle resolution, and computing time, which particularly impacts simulations at length-scales typical for many volcano-tectonic processes.

Advances in computing power are nonetheless reducing DEM computing times, such that high-resolution 3D-DEM modelling is now an increasingly viable approach for volcano-tectonic studies. These developments open the door for the closest yet integration of volcano-tectonic models with geodetic and seismic observations.

Acknowledgements

Research grants awarded to EPH by the Irish Research Council and Marie Curie Actions.

References

[1] Cundall and Strack

[2] Potyondy, D.O. & Cundall, P.A., (2004), Int. J. Rock Mech. Mining Sci., 41: 1329–1364.

[3] Holohan, E.P. et al., (2011), J. of Geophys. Res., 116: B07202.

[4] Hardy, S., (2008), Geology, 36: 927-930.

[5] Dzurisin, D., (2007), Volcano Deformation, Springer Verlag.

[6] Okada Y., (1992), Bull. Seismol. Soc. Am. 82: 1018-1040

[7] Morgan, J. & McGovern, P. (2005), J. of Geophys. Res., 110: B05402.

[8] Thompson et al., (2010), J. Volcanol. Geotherm. Res. 192: 191-200

[9] Malthe-Sørensen et al., Geol. Soc. Spec. Pub. 234: 215-227.

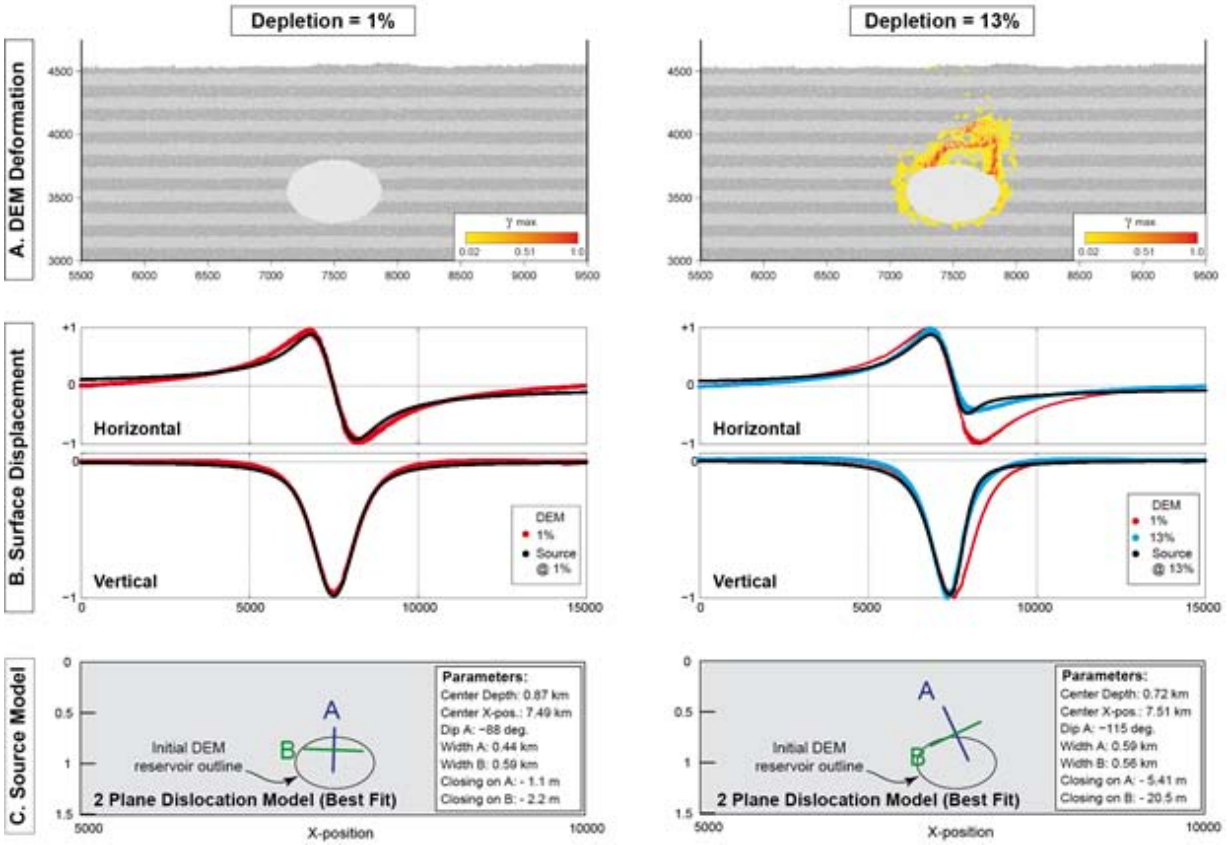

Fig. 4.: 2D-DEM model displacements and 'blindly-fitted' analytical finite sources. (A) Close-up images of deformation in a model set-up as in Figure 1, but with a height of 5 km and width of 15 km. Deformation is visualised as the maximum finite shear strain around each particle (see colour scale). The low-strain yellow areas correspond closely to areas of bond breakage. (B) Normalised horizontal and vertical components of surface displacement in the 2D-DEM model. Note the asymmetry in the displacement profiles at 13% depletion. This reflects the typically asymmetrical development of the sub-surface fracturing. (C) Optimum analytical finite deformation sources inferred for the 2D-DEM surface displacement data at each stage of depletion. The source models tested here comprise two rectangular dislocation planes[6] that are fixed to be mutually perpendicular, but all other parameters are otherwise free. To approximate the 2D conditions of the DEM models, the dislocation planes are infinitely long in the direction normal to the plane of observation. Note the changes in shape, orientation and depth of the inferred deformation source at 13% depletion. These reflect the combination of magma chamber depletion and host rock deformation.

Three-Dimensional Analysis of dike/fault interaction at Mono Basin (California) using the Finite Element Method

D. La Marra[1], M. Battaglia[2]

[1]*Dept of Sciences, Roma Tre University*
[2]*Dept of Earth Sciences, Sapienza - University of Rome*
e-mail: *daniele.lamarra@uniroma3.it*
session: *Volcanism and Volcanotectonics*

Mono Basin, Inyo Dike and the Hartley Springs Fault

Mono Basin is a northward trending graben situated east of the Sierra Nevada, extending from the northern edge of Long Valley Caldera to Body Hills, north of Mono Lake (Bursik and Sieh, 1989). The Mono-Inyo volcanic chain forms a northward trending line of volcanic vents extending within the Mono Basin (Figure 1). Several studies indicate that the youngest eruptions in the Mono-Inyo chain occurred, most likely around ∼1350 A.D. (Bailey, 1989). The existence of a dike at shallow depth between vents was confirmed by the drilling program along the trend of the Inyo Domes (Fink, 1985). Stratigraphic data suggest that a series of strong earthquakes (M ∼5.5–6.5) occurred during the North Mono-Inyo eruption sequence of ∼1350 A.D. Several geomorphologic data suggest that more than 0.5 m of mean slip occurred along the Hartley Springs Fault in numerous events at the time of the ∼1350 A.D. eruption. The spatial and temporal immediate proximity between earthquakes on the Hartley Springs Fault and Inyo Dike intrusions suggest a possible relationship between seismic events and eruptions (Bursik et al., 2003).

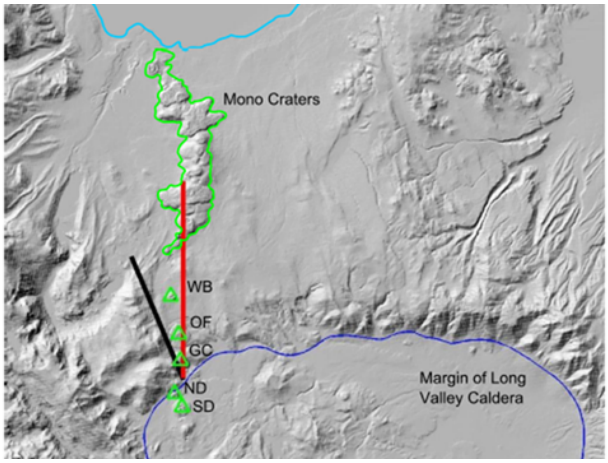

Fig. 1.: The Mono Basin area: the Inyo Dike (red line), trending approximately N-S, intercepts the Hartley Springs Fault (black line), extending from the northern rim of Long Valley caldera to the June Lake.

Three-dimensional Finite Element Method model

We use the Finite Element Method to develop a three-dimensional model of the Mono Basin and investigate the feedback mechanism between dike intrusion and slip along the Hartley Springs fault. The three-dimensional geodynamic model is implemented using the Structural Mechanics module of COMSOL Multiphysics (www.comsol.com). The crust is modeled as an elastic medium (500 km of width and length, 200 km depth), divided in cylindrical sub-domains with increasing radii to achieve a gradual refining of the mesh toward the center of the domain (Figure 2A). The medium is not homogenous: a representation of the mechanical heterogeneities in the region is obtained by combining a 40-km-long density profile across the Mono Basin (after McDonell et al., 2013; Figure 2B) with a P-waves velocity profile

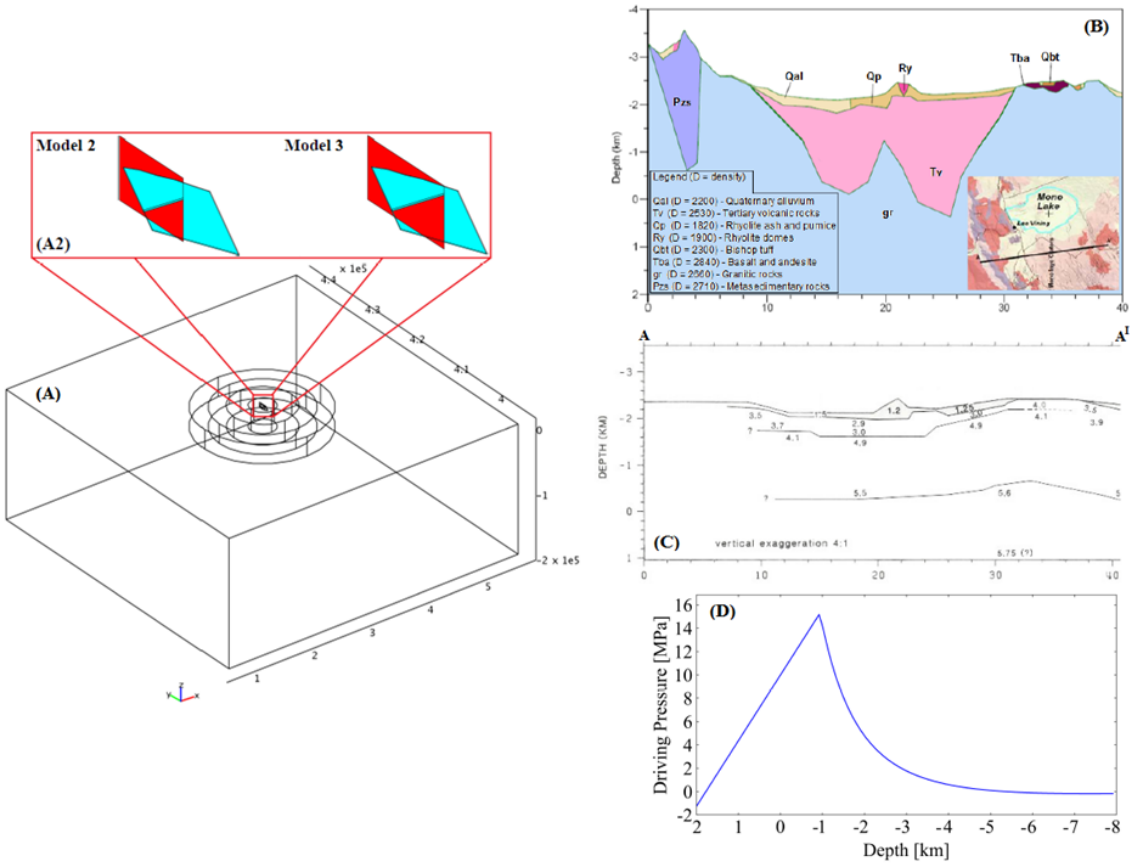

Fig. 2.: 3D geodynamic model: (A) geometry; (A2) geometry of the Inyo Dike (red surface) and the Hartley Springs Fault (light-blue surface) for the dike 10 km-length (Model 2) and 12 km-length (Model 3); (B) 40-km-long density data profile across the Mono Basin (after McDonell et al., 2013); (C) seismic profile velocities (after Hill et al., 1985) along the profile A-A' used in the models; (D) driving pressure applied as tensile component to the vertical sides of the dike (after Reches and Fink, 1988).

with depth (Hill et al., 1985; Figure 2C). To include the topography in our model (Figure 3), we used the Moving Mesh ALE module. The module allows us to insert an external vector function that assigns to each point on the surface of the model a value of altitude (topography). Using the elevation data from the Digital Elevation Model (DEM), the module distorts the mesh in the z-direction simulating the topographic relief that cover Mono Basin, Long Valley Caldera and part of the Sierra Nevada. The georeferenced topography has been exported as a CAD data file and imported to be used in the next steps of modeling.

We simulate the Hartley Springs Fault (HSF) and the Inyo Dike (ID) as mechanical discontinuities. Following Bursik et al. (2003), we approximate the HSF by a sub-vertical plane 9.5 km-long, 10 km-deep from the surface and with a 60° dip. The top edge of the fault cuts and follows the free surface to represent a relisting escarpment (Figure 4B). The Inyo Dike is simulated by a rectangular cavity 10 m-wide, and 7 km-deep with the top of the dike between 300 and 500 meters below the surface. We used the normal driving pressure values extrapolated from the model of Reches and Fink (1988) to model the opening of the Inyo dike (Figure 2D).

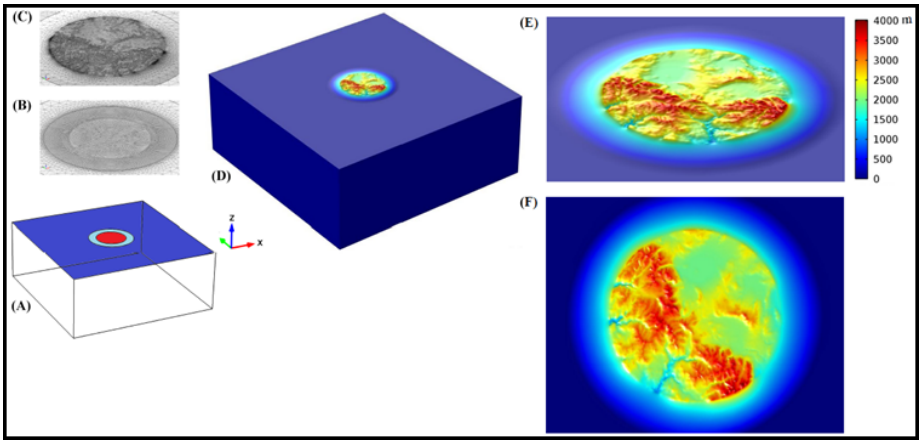

Fig. 3.: 3D FEM model with topography using the Digital Elevation Model: (A) flat domain where, on the red surface the deformed mesh is applied in order to build the topography; the light blue surface is left free to deform in order to accommodate the connection with the topography; the blue surface is kept fixed at the sea level; (B-C) mesh of red surface pre- and post-deformation; (D) domain with topography; (E-F) highlight of the topography of Mono-Basin/Long Valley Caldera.

Case (1): Inyo dike intrusion triggers earthquakes along the Hartley Springs Fault

We analyze the distribution of the Coulomb stress change (ΔCFS) along the fault plane (simulated as a passive receiver fault) for different length of the opening fracture (Model 1: dike 4, 6, 8, 10, 12, 14 km-long from the center of Mono Craters; Figure 4). In particular, we compute the percentage of fault area encouraged to slip normally and right laterally because of the dike intrusion for ΔCFS$>$ 0, 0.1, 1, 5, 10 bar (Figure 4A). We use an effective friction coefficient of 0.5 (e.g., Bursik et al., 2003). Positive Coulomb stress changes $>$ 1 bar are considered to be significant to trigger earthquakes (Walter et al., 2005). The ΔCFS changes $>$ 1 bar imply that the fault is encouraged to slip only when the dike is approaching the fault. When the dike is near the south tip of the Hartley Springs Fault, normal and right lateral slips are more difficult to initiate. Since earthquakes can be triggered by ΔCFS as small as 0.1 bar (Walter et al., 2005 and reference therein), our first numerical experiments investigate seismic triggering for values of ΔCFS $>$ 0.1 bar. In this case, when the dike is 10 km-long, close to the location of the Obsidian Dome, about 46 % of the fault plane may slip with a release of energy equal to an earthquake of magnitude 6.0, consistent with observed geological data. When the dike is 12 km-long, with its southern tip close to Glass Creek, about 42 % of the fault may slip with the possibility to trigger an earthquake of magnitude 6.0.

Case (2): slip along the Hartley Springs fault facilitates the opening of the Inyo dike

The Hartley Springs Fault is simulated (in Model 2-3, Figure 2 A2) creating "master-slave" contact pairs between subdomains to take into account the ratio of contacts and stress transfer between the planes. We move only the part of the fault that may slip (ΔCFS $>$ 0.1 bar; Figure 4B).

We run numerical experiments both for a 10 km long dike for a slip along the HSF equivalent to an earthquake of magnitude 6.0 (Model 2), and a dike 12 km-long for a slip along the HSF equivalent to an earthquake of magnitude 6.0 (Model 3). The numerical results show that when the dike is near Obsidian Flow (dike 10 km-long), a slip along the fault can increase the

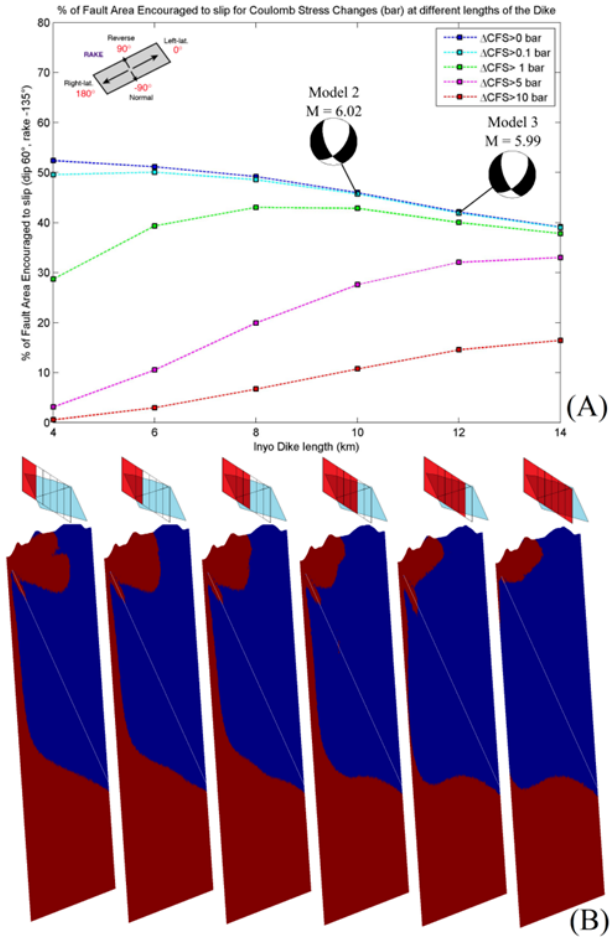

Fig. 4.: Analysis of Coulomb stress changes: percentage of fault area encouraged from a dike intrusion for different lengths of the dike; (B) distribution of Coulomb stress changes (ΔCFS $>$ 0.1 bar) on the fault plane for different lengths of the dike (red for slip encouraged; blue for slip discouraged).

maximum tensile stress in correspondence of the Obsidian Flow and Glass Creek domes (Figure 5 A,C). When the dike is near Glass Creek (dike 12 km-long) a slip along the fault can increase the maximum tensile stress nearby this dome (Figure 5 B,D).

Conclusions

The quasi-static analysis of the Coulomb stress change indicates that the opening of the Inyo Dike could enable right-lateral and oblique-slip motions along the Hartley Springs Fault. In particular, slip along the fault is facilitated when the dike is approaching the fault near Obsidian Flow dome. However, the opening of the dike does not promote slip along the fault when it reaches the south tip of the Hartley Springs Fault. The analysis of stress changes along the dike surface indicates that slip along the HSF could increase the local maximum tensile stresses facilitating the opening of the Inyo dike. Furthermore, the increase in tensile stress at the top of the dike indicates local conditions promoting the propagation of the dike toward the surface, especially near the southern tip of the fault, close to the Obsidian Flow and Glass Creek Flow domes.

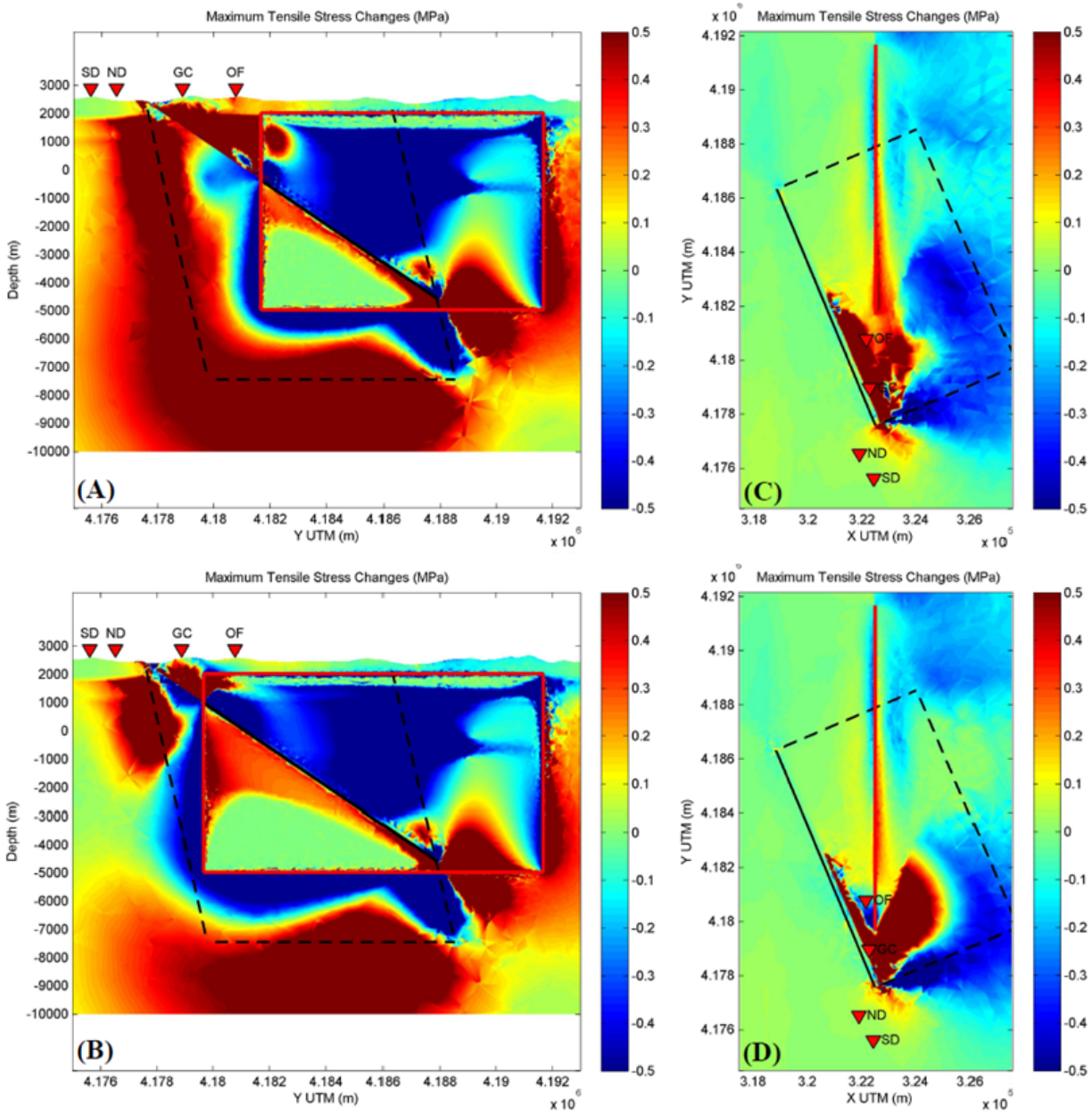

Fig. 5.: Maximum Tensile stress changes (MPa) triggered by earthquakes along Hartley Springs Fault: slice parallel to the dike (YZ plane) for Model 2 (A) with a dike 10 km long and Model 3 (B) with a dike 12 km long; slice on the top of dike (XY plane) for Model 2 (C) and Model 3 (D); red triangles indicates the position of the craters (OF = Obsidian Flow; GC = Glass Creek Flow; ND = North Deadman Dome; SD = South Deadman Flow); solid black line indicate the superficial trace of the Harley Springs Fault, dashed black line indicate the deep position of the fault; solid red line indicate the trace of the Inyo Dike.

Modeling of Cooling History for the Jurassic Composite Granitic Plutons in the Central Nanling Region, South China: Implications for the Mineralization Process and Tectonic Evolution

Huan LI[1], Koichiro WATANABE [1], Kotaro YONEZU[1]

[1] *Department of Earth Resources Engineering, Faculty of Engineering, Kyushu University, Fukuoka 819-0395, Japan*
e-mail: *li-huan@mine.kyushu-u.ac.jp*
session: *Volcanism and Volcanotectonics*

Introduction

The southern part of China (South China) is an excellent natural laboratory for studying intra-continental geological processes. The intra-continental magmatism in the South China is characterized by huge volumes of Phanerozoic granitoids, which indicate a widespread, episodic crustal reworking.

The Nanling region in the central part of South China is a most unique and very important W, Sn, Mo, Bi, Pb, Zn, Cu, REE, and U metallogenic belt in the world (Chen et al., 2002; Hsieh et al., 2008; Fig.1a). It occupied more than 60% and about 20% of the world's total W and Sn reserves, respectively, formed within a short period which is known as the Early Yanshanian period (aged at 190–140 Ma, between the middle to late Jurassic periods) (Shu et al., 2011). The former explorers and researchers have investigated lots of representative granites and mineral deposits of this area, and gained abundant information. The Early Yanshanian magma activity is frequent and is characterized by multiple stages and multiple intrusions, resulting in lots of granite composite and related resources (Fig.1b). Although the mineralization is widely known to be associated with the Yanshanian intrusions, the genetic relationships with the granitic exhumation and cooling of the plutons remain poorly understood. Discrepancies among various U–Pb ages and younger age determinations based on Rb–Sr, Ar–Ar and K–Ar isotopic systems from granitoids of the Nanling region have raised questions about the timing of the most related mineralization of these rocks and the details of their cooling path. In this study, we systematically collected a wide variety of dating data of some Early Yanshanian granitic intrusions in the central Nanling region, and based on the different types of age results given by different minerals with different closure temperature, we try to rebuild the cooling history and calculate the exhumation process for each representative granite composite, and hopefully to give some insight to the granite related mineralization and the tectonic evolution in this area.

Data collection and cooling–exhumation calculations

In this study, published zircon U–Pb, whole rock Rb–Sr, and muscovite, biotite and K-feldspar K–Ar or Ar–Ar age data for the different intrusive stages of the respective granite composites in the central Nanling region were systematically collected. These age data was deliberately screened, and the unreliable data was removed. Here, we assumed that the closure temperature of zircon, Rb–Sr whole rock, muscovite, biotite and K-feldspar are 800°C, 600°C, 350°C, 300°C and 150°C, respectively.

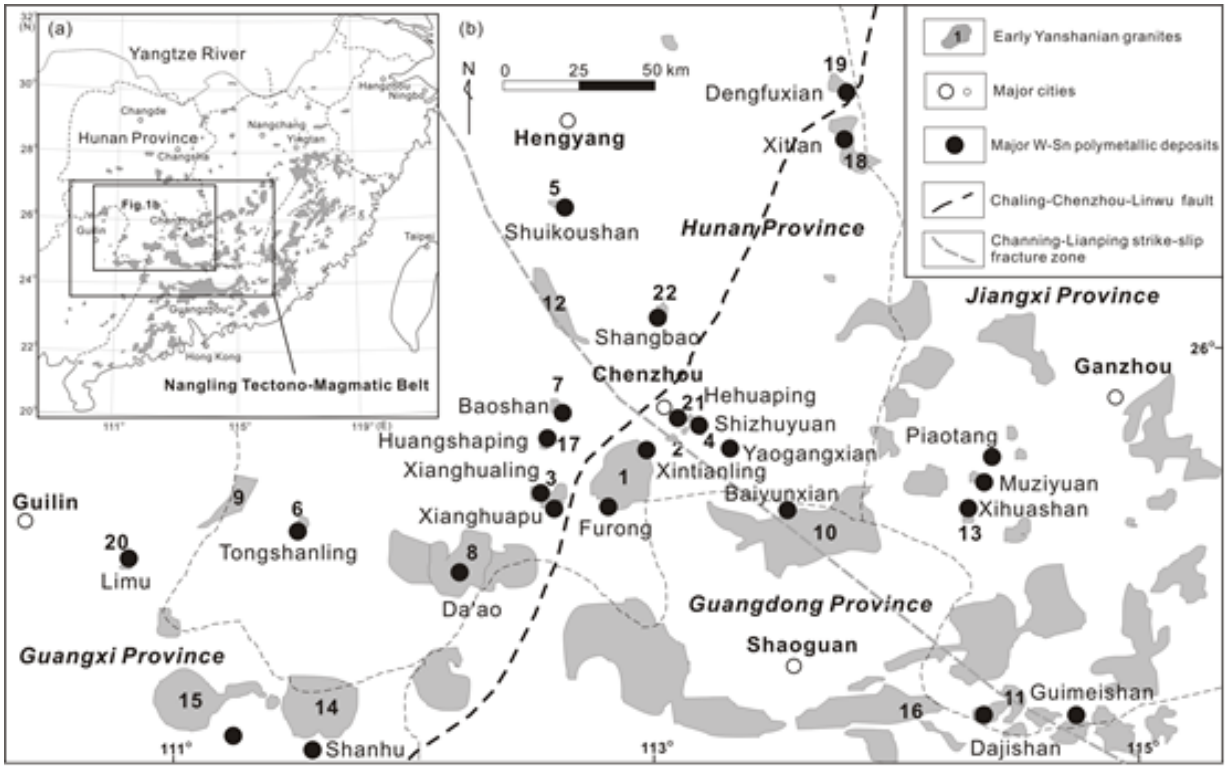

Fig. 1.: Distribution of Early Yanshanian granite composite and related ore deposits in (a) South China and (b) central Nanling region (modified from Yu, 2011). Granite composites: 1=Qitianling, 2=Qianlishan, 3=Xianghualing, 4=Yaogangxian, 5=Shuikoushan, 6=Tongshanling, 7=Baoshan, 8=Jinjiling, 9=Dupangling (eastern pluton), 10=Zhuguangshan, 11=Dajishan, 12=Dayishan, 13=Xihuashan, 14=Guposhan, 15=Huashan, 16=Guidong, 17=Huangshaping, 18=Xitian, 19=Dengfuxian, 20=Limu, 21=Wangxianling-Hehuaping, 22=Shangbao

Based on the above reliable age determinations and estimates of closure temperature, estimates have been done for the cooling rates of the composites in the Nanling Region. Fig. 2 shows a reconstruction of the cooling rates of these granite composites. Based on the modelling results we can conclude that the cooling paths of the first stages of these granites are steepest (e.g., BS1, ZGS1, and TSL1), indicating the fastest cooling processes. On the contrary, the cooling paths of the followed intrusive stages gradually become more flat, suggesting increasingly slower cooling history. For the purpose of computing the cooling path, we consider that the first stages of these composite cooled from 800°C to 300°C within a very short time span of 5 Ma. The followed subsequently second stages experienced a time span of 15 Ma from 800°C to 150°C. Collectively, the temperatures go down from 800°C to 150°C for the third stages may spend a time span of around 40 Ma, and 50 millions of years could be taken for the final stages of these granites to cool them down from 800°C to 300°C. The average cooling rates of the first stages are about 100°C Ma^{-1}, and the second, the third and the fourth are around 45°C Ma^{-1}, 15°C Ma^{-1}, and 10°C Ma^{-1}, respectively. In short, compared to the granites in other areas, the cooling rates of these granite composites in the central Nanling region are markedly fast, especially for the first two stages.

If we assume that the temperatures maintained by granitic intrusions are mainly affected by the geothermal gradients which are corresponded to different burial depths, we can calculate the uplift rates based on the cooling rates of the granites in the central Nanling region. We assume the geothermal gradient in the central Nanling region

was 50 °C km^{-1}. Accordingly, we calculate that the uplift rates of the first stages of the granite composites are the fastest, with the value of $\sim$ 2 mm y^{-1}, followed by 0.9, 0.3, and 0.2 mm y^{-1} for the rest stages, respectively. Active denudation and erosion was due to ongoing tectonic uplift of the area by thrusting and thickening of the crust.

Mineralization implications

The most famous peak episode of Mesozoic large-scale magmatism and associated ore formation in South China is 170–150 Ma. Mineralization of the 170–160 Ma age range is mostly of porphyry and skarn type (Cu–Au) and of granite-related vein type (Pb–Zn–Ag), while the 160–150 Ma age range is characterized by granite-related W–Sn polymetallic mineralization (Li et al., 2012). According to this study, the 170–160 Ma Cu–Pb–Zn mineralization was related to the earlier round quick ascended magmas, whereas the later 160–150 Ma W–Sn polymetallic mineralization was resulted from the slower cooling and ascending plutons.

Different ascent rates and evolutionary process of the magmas and intrusions caused the different mineralization related intrusions. If the intrusions ascend slowly, the crystal fractionation as well as upper crustal contamination and assimilation would have enough time to occur. W, Sn, Bi, Mo, As, and Sb become more enriched during fractionation compared to the base metals Zn, Pb, and Cu (Mustard et al., 2006). The rift-related rapid extension of the crust caused deep Cu source evoked and generated in a low-pressure environment, while the extreme crystal fractionation aided by high volatile activity, coupled with crustal contamination and assimilation under a relatively stable settings produced the W–Sn polymetallic mineralization in the central Nanling region.

Mantle plume-generated triple junction rifts: A new model

Intraplate lithospheric thickening events rather than the subduction of the Pacific plate was proposed for Nanling region (Shu et al., 2011). Based on the distribution of major W–Sn polymetallic deposits and deep faults in the central Nanling region and the calculations of the cooling and uplift rates, we proposed a new model for this region during the early Yanshanina period: mantle plume generated triple junction rifts (Fig. 3). This triple junction rift system was centered by the Qiantianling granite composite and composed of three major cross arms which extended to the NE, SW, and SE directions, respectively, and the extension length for each arm was more than 200 km. the NE and SW arms extended basically along the Chaling–Chenzhou–Linwu deep fault, while the SE arm mostly overlapped with the Channing–Lianping strike-slip fracture zone. The basic supports for this model come from the following two points: 1), the distribution of the granite associated deposits. Fig.1b shows that large scale deposits are concentrated and surrounded in the Qitianling area, and diverging to three different opposite directions which reach at the Denghuxian–Xitian deposit, the Shanhu deposit, and the Xihuashan–Dajishan deposit, respectively. In the Qitianling area where the mantle plume lies below, Cu, Pb, and Zn are also largely outputted besides W-Sn mineralization (Fig. 3). 2), the differences in the cooling and uplift rates. Most of the granite composites located in the Qitianling area have very quick cooling and uplift rates, especially for their first stage of their intrusive activities. On the contrary, far away from the center, granite composites such as the Guposhan, the Huashan, the Dajishan, and the Dengfuxian have much slower cooling and uplift rates. They may be formed by more highly evolved magma and have more discernable intrusive stages. In our model of mantle plume generated triple junction rifts system, the mantle plume started its activities at the beginning of the early Yanshanina period, causing large amount of

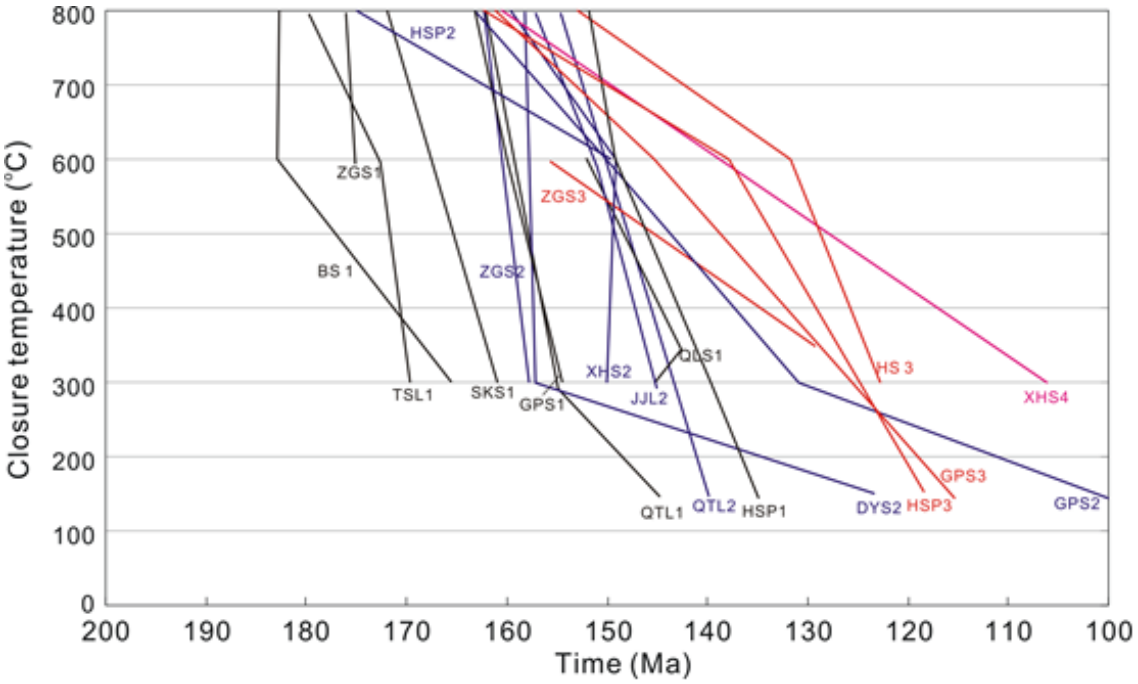

Fig. 2.: Cooling paths of some representative granite composite in the central Nanling region. Granite composites: BS = Baoshan, ZGS = Zhuguangshan, TSL = Tongshanling, SKS = Shuikoushan, GPS = Guposhan, QTL = Qitianling, QLS = Qianlishan, HSP = Huangshaping, XHS = Xihuashan, DYS = Dayishan, HS = Huashan. The figures followed by each granite composite represent the intrusive stage.

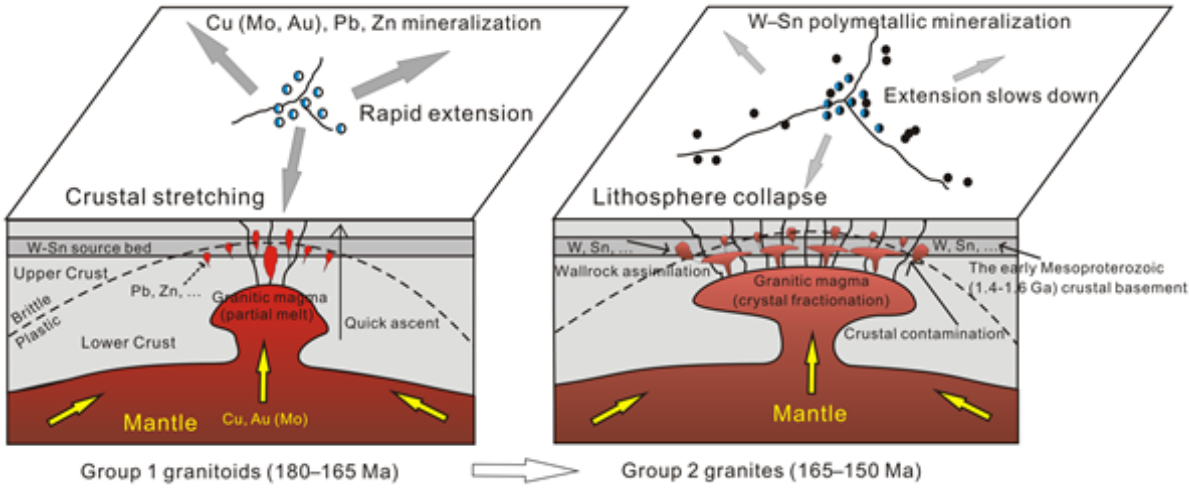

Fig. 3.: A model of mantle plume generated triple junction rifts for the central Nanling region during the 180–150 Ma period.

magma activities and resulting in the most of the earlier stages of the intrusions of the granite composites. During this period (180–165 Ma), triple junction rift activity was generated by the mantle plume and lasted effectively for a short period of time. The intrusions ascended very quickly and cooled down fast, and also brought some Cu, Pb and Zn base mental mineralization, forming

the major parts of the Baoshan, the Shuikoushan, the Huangshaping and the Shangbao deposits. After this period, the extension activity slowed down (165–150 Ma), and the following magmatisms have more time to extract more ore-forming elements from the upper crust by contamination and assimilation, resulting in the world-famous Nanling W–Sn mineralization belt (Fig. 3).

References

Chen, P.R., Hua, R.M., Zhang, B.T., Lu, J.J., and Fan, C.F., 2002. Early Yanshanian post-orogenic granitoids in the Nanling region–Petrological constraints and geodynamic settings. Science in China Series D: Earth Sciences, 45, 755–768.

Hsieh, P. S., Chen, C. H., Yang, H. J., and Lee, C.Y., 2008. Petrogenesis of the Nanling Mountains granites from South China: Constraints from systematic apatite geochemistry and whole-rock geochemical and Sr–Nd isotope compositions. Journal of Asian Earth Sciences, 33, 28–451.

Li, C.Y., Zhang, H., Wang, F.Y., Liu, J.Q., Sun, Y.L., Hao, X.L., Li, Y.L., and Sun, W.D., 2012. The formation of the Dabaoshan porphyry molybdenum deposit induced by slab rollback, Lithos, 150, 101–110.

Mustard, R., Ulrich,T., Kamenetsky, V. S., and Mernagh, T., 2006. Gold and metal enrichment in natural granitic melts during fractional crystallization. Geology, 34, 85–88.

Shu, X.J., Wang, X.L., Sun, T., Xu X.S., and Dai, M.N., 2011. Trace elements, U–Pb ages and Hf isotopes of zircons from Mesozoic granites in the western Nanling Range, South China: Implications for petrogenesis and W–Sn mineralization. Lithos, 127, 468–482.

Yu, C.W., 2011. The characteristic target-pattern regional ore zonality of the Nanling region, China (I). Geoscience Frontiers, 2, 147–156.

The gravitational unloading due to rift depression: A mechanism for the formation of off-rift volcanoes in (continental) rift zones

Francesco Maccaferri[1], Eleonora Rivalta[1], Derek Keir[2], Valerio Acocella[3]

[1] *GeoForschungsZentrum Potsdam, Section 2.1, Telegrafenberg, 14467, Potsdam, Germany*
[2] *National Oceanography Centre Southampton, University of Southampton, Southampton, SO14 3ZH, UK*
[3] *Dipartimento Scienze, University of Roma Tre, L. S.L. Murialdo, 1, 00146, Roma, Italy.*
e-mail: *francesco.maccaferri@gfz.potsdam.de*
session: *Volcanism and Volcanotectonics*

Introduction

Rift valleys are the surface expression of prolonged extension of the continents. During rift initiation, the lithosphere thins by ductile stretching and normal faulting, creating a rift valley [1]. The upwelling asthenosphere melts by adiabatic decompression, with the greatest degree of partial melting beneath the most thinned part of the crust [2,3]. Melt can accumulate at the brittle-ductile transition, in magmatic reservoirs centred on the rift axis. Crustal stretching and melt production underneath the rift axis, often result in the formation of volcanoes within the rift valley, as observed, for instance, in the North Volcanic Zone of Iceland. A not trivial but relatively common observation in continental rift zones, is the occurrence of off-rift volcanism [4,5,6]: which is the presence of volcanoes located out of the rift border faults, displaced up to tens of kilometres outside the rift valley (Fig. 1). Off-rift volcanoes and off-rift volcanic provences are generally aligned, parallel to the rift axis, and they are often associated with early rifting [4,5]. In the Red Sea Rift, ∼25 Ma-old rift-parallel dykes focus near the ∼30 Ma-old rift margins, while the youngest volcanoes focus along the ridge axis [7]. Even in far less magmatically active settings, such as the Baikal Rift (Siberia) or the Chaine des Puys (CdP) in the Cenozoic rift system of France, off-rift volcanism occurred after the onset of rifting. The mechanism driving magma from deep rift-centred magma reservoirs to feed off-rift volcanic systems is still debated.

Methodology

We used a numerical (boundary element) model to simulate the propagation of magmatic dykes [8,9,10] starting from a deep magmatic reservoir located at the base of the crust, and centred on the rift axis. Our model gives as output the expected location of volcanism at surface, as well as the path followed by dykes before getting arrested within the crust or arriving at surface.

A fundamental input for our model is the stress field within the crust, since dykes tend to orient perpendicular to the direction of the minimum compressive stress ($\sigma 3$). We model the stress field in the rift setting accounting for:

1. the lithostatic pressure;
2. the tectonic stress;
3. the mechanical effect due to the gravitational unloading (decompression) induced by the mass deficit at the rift valley.

The resulting stress field in the crust is the superposition of 1, 2 and 3. Where 1 is assumed

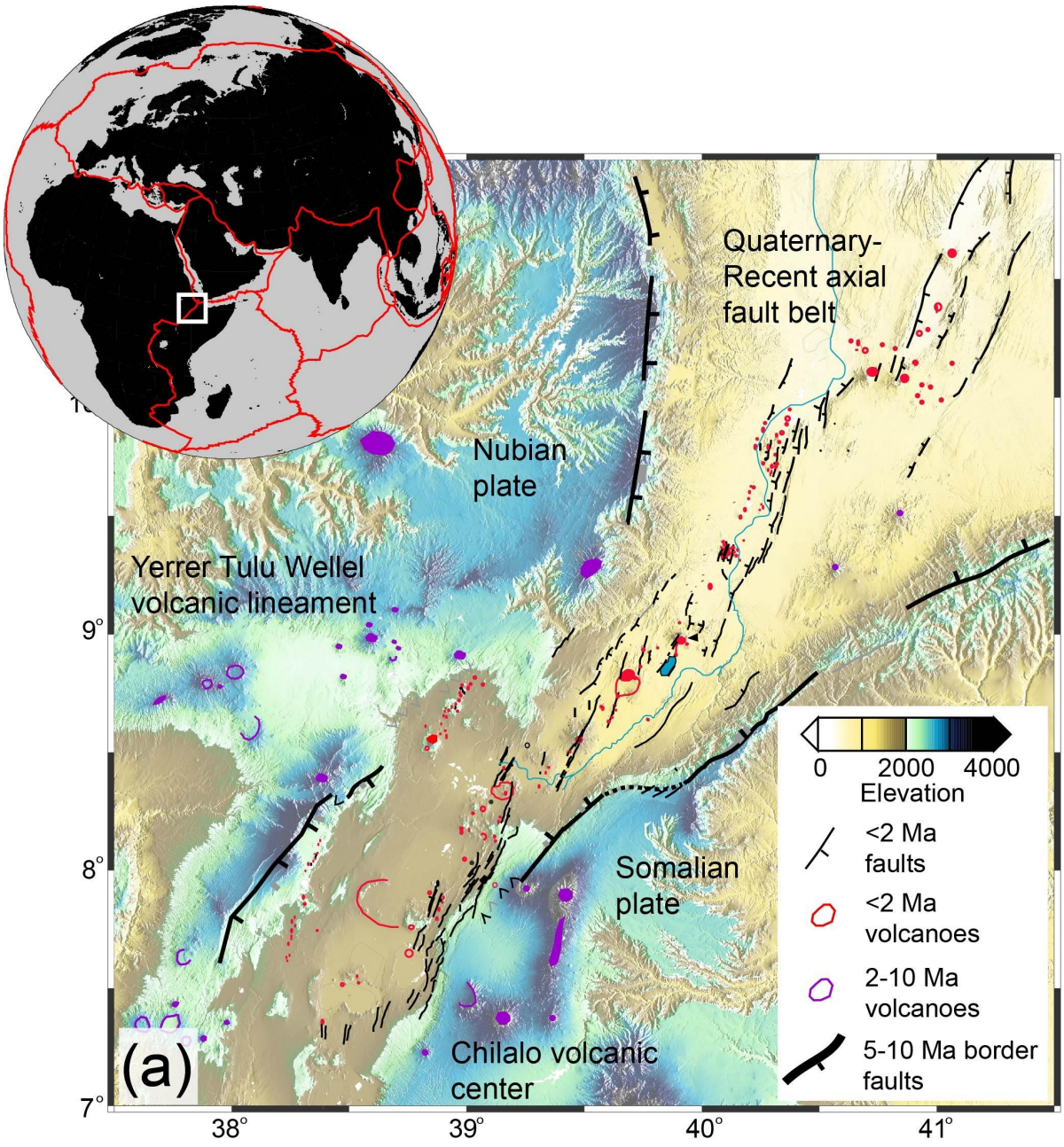

Fig. 1.: Topographic, structural and volcanic architecture of the Main Ethiopian Rift. Miocene border faults are thick black lines with direction of down throw indicated and the Quaternary-Recent faults within the rift are thin black lines. Early syn-rift volcanic edifices are purple and Quaternary-Recent volcanoes and cones are red. Note that the early syn-rift volcanism ranges from being just outboard of the Miocene border faults, to as far as 100 km from the rift valley. (Figure from [13])

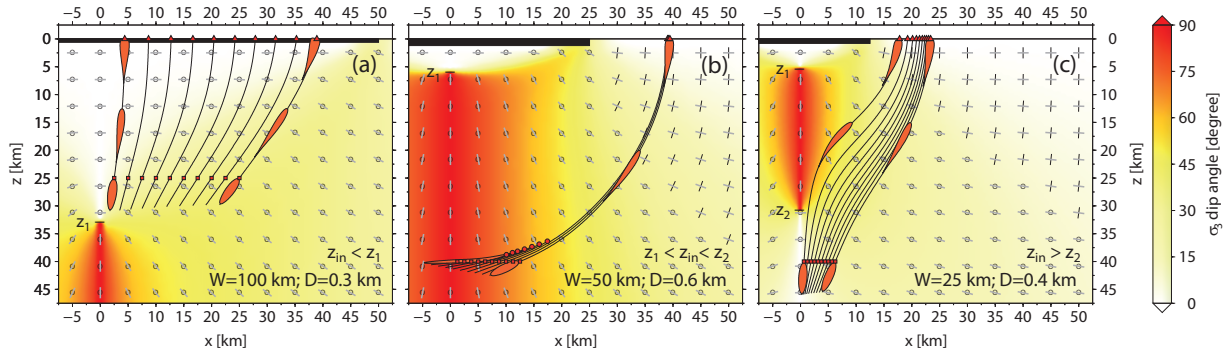

Fig. 2.: Dyke trajectories for scenarios A, B, and C. Red squares indicate the upper tip of the dyke at injection, red circles indicate that a dyke has been arrested as sill; red triangles indicate the position of the arrival at surface. Black and gray segments show the directions of $\sigma 1$ and $\sigma 3$ respectively (a circle indicates direction perpendicular to the page) for three nominal sets of graben width, W, and depth, D, (see insets). The dip angle of $\sigma 3$ is color-shaded: where sub-vertical (reddish color), a stress barrier to vertical ascent of dykes is acting. The stress barrier is expected to dissipate in a weak lower crust or mantle. (Figure from [13])

to be isotropic and therefore does not contribute to the orientation of the principal stress; 2 is the horizontal tension due to crustal stretching (assumed to be in the range of 5 to 10 MPa) and tend to favour the horizontal orientation of $\sigma 3$; 3 can be computed with the analytical formulas by [11].

Results

The contribution of gravitational unloading is the essential component in our study. When the gravitational unloading dominates over the tectonic stretching, $\sigma 3$ becomes vertical in a confined volume beneath the rift. This volume constitutes a sort of "stress barrier zone", in which stacked sills are favoured, and which deflects the ascending dykes to the rift sides. Sideways from the rift centre, $\sigma 3$ becomes first inward dipping and then horizontal (Fig. 2).

Depending on where the dykes nucleate relative to the stress barrier zone, three scenarios for their propagation and for the final surface distribution of magmatism occur:

A *If dykes start above the stress barrier* (or if the theoretical location of the stress barrier is deeper than the crustal thickness) in-rift volcanism occurs. Magma-filled dykes ascend subvertically, or propagate laterally within the rift parallel to the axis (Fig. 2a), and the dyke arrivals are spread within the graben.

B *If dykes start within the stress barrier* (or the stress barrier extends across the crust and extends until the brittle-ductile transition), our model predicts off-rift volcanism with sill formation. The injected magma at the base of the crust forms sub-horizontal magmatic sheets that, depending on their initial distance from the rift axis, get trapped as stacked sills above the ponding zone or escape to the side of the stress barrier, turning into subvertical dykes and eventually reaching the surface (Fig. 2b). For a given set of parameters, dykes emerge very tightly spaced at a distance from the rift axis equal to about 1 to 2 (and up to 3) graben half-widths.

C *If dyke starts underneath the stress barrier*, off-rift volcanism occurs without sill formation: vertical dykes are deflected towards the rift sides, with a more scattered arrival distribution at the surface (Fig 2c). This occurs with deep nucleation depths below shallow and narrow grabens, and is the least likely configuration for a reasonable range of values for graben depths and widths and crustal thickness.

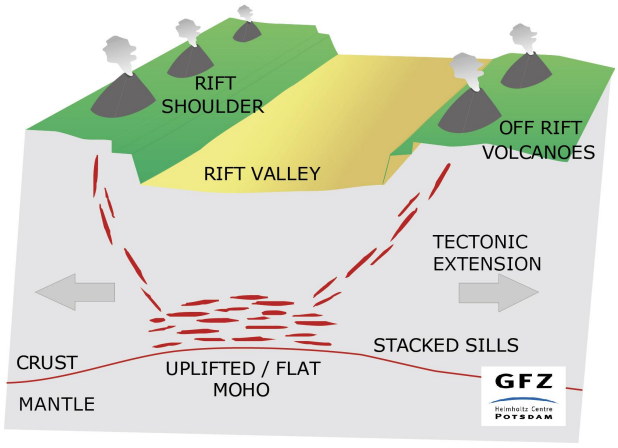

Fig. 3.: Summary cartoon illustrating the magma paths behind off-rift volcanism.

Conclusions

For deep grabens the upper limit of the stress barrier (z1) is shallow (z1∼10 km for a 100 km wide and 1 km deep graben) so that in-rift arrivals occur only for shallow nucleation depths. For a nucleation depth in the range of 30 - 40 km, which represent a reasonable estimate for the crustal thickness at the early stage of continental rifting, in-rift volcanism occurs only for wide (>100 km) and shallow (<0.6 km) rift depressions, or for graben depths which are too small to create a stress barrier (i.e. the tectonic stretching dominates over the gravitational unloading). A thinner crust thickness or the presence of shallower reservoirs, result in favouring "in-rift volcanism", as expected for the North Volcanic Zone of Iceland (NVZ) or for Quaternary volcanism in the MER.

According to our findings, the most likely configuration for the early stages of continental rifting is scenario B. This may result in the construction of large off-rift volcanoes aligned parallel to the rift. Also, for this scenario, our model predict that magmatic intrusion will get easily trapped as stacked sills underneath the rift axis, above the Moho (Fig. 2b and Fig. 3). Recent results from seismic tomography at Baikal rift suggest that a deep, rift centred reservoir, at Moho depths, formed by means of staked sills [12].

As the rift matures, the magma ponding zone near the base of the crust becomes progressively shallower due to crustal thinning and to sills piling one above the other and functioning as new, shallower reservoirs, driving the system towards the condition of case A and to a transition to in-rift volcanism.

References

1. McKenzie, D. Some remarks on the development of sedimentary basins. Earth Planet. Sci. Lett. 40, 25-32 (1978).

2. Lubimova, E. A. Heat flow patterns from Baikal and other rift zones. Tectonophysics 8, 457-467 (1969).

3. Bown, J. W. & White, R. S. Effect of finite extension rate on melt generation at rifted continental margins. J. Geophys. Res. 100, 18011-18029 (1995).

4. Ellis, M. & King, G. Structural control of flank volcanism in continental rifts. Science 254, 839-842 (1991).

5. Morton, W. H., Mitchell, J. G., Rex, D. C. & Mohr, P. Riftward younging of volcanic units in the Addis-Ababa region, Ethiopian rift valley. Nature 280, 284-288 (1979).

6. Kiselev, A. I. Volcanism of the Baikal rift zone. Tectonophysics 143, 235-244 (1987).

7. Bosworth, W., Huchon, P. & McClay, K. The Red Sea and Gulf of Aden Basins. J. African Earth Sci. 43, 334-378 (2005).

8. Dahm, T. Numerical simulations of the propagation path and the arrest of fluid-filled fractures in the Earth. Geophys. J. Int. 141, 623-638 (2000).

9. Maccaferri, F., Bonafede, M. & Rivalta, E. A numerical model of dike propagation in layered elastic media. Geophys. J. Int., vol. 180, pp. 1107-1123 (2010)

10. Maccaferri, F., Bonafede, M. & Rivalta, E. A quantitative study of the mechanisms governing dike propagation, dike arrest and sill formation. J. Volcanol. Geotherm. Res. 208, 39-50 (2011).

11. Davis, R. & Selvadurai, A. Elasticity and Geomechanics (Cambridge Univ. Press, Cambridge, 1996).

12. Thybo, H. & Nielsen, C. A. Magma-compensated crustal thinning in continental rift zones. Nature. 457, 873-876 (2009).

13. Maccaferri, F., Rivalta, E., Keir, D., Acocella, V., Off-rift volcanism in rift zones determined by crustal unloading Nature Geosci., vol 7, pp. 297-300, doi: 10.1038/ngeo2110.

The formation of terrace-bounding faults on Olympus Mons volcano, Mars

S. Musiol[1], B. Cailleau[2], E. P. Holohan[3], T. R. Walter[3], D. A. Williams[4], A. Dumke[1], S. van Gasselt[1]

[1]*Freie Universität Berlin Planetary Sciences and Remote Sensing*
[2]*Freie Universität Berlin, Institute of Geological Sciences, Geophysics, Berlin, Germany*
[3]*Helmholtz-Zentrum Potsdam, Deutsches Geoforschungszentrum, Sektion Erdbeben- und Vulkanphysik, Potsdam, Germany*
[4]*Arizona State University, School of Earth and Space Exploration, Planetary Geology Group, Tempe, AZ, USA*
e-mail: *stefanie.musiol@fu-berlin.de*
session: *Volcanism and Volcanotectonics*

Introduction and Background

Olympus Mons volcano is located in the northern hemisphere of Mars, west of the Tharsis volcanic province. It is a basaltic shield volcano with a height of 22 km, a diameter of 600 km, and an average flank slope of 5° (Plescia 2004). The main features of Olympus Mons include a summit caldera complex, upper- to mid-flank terraces, lower-flank radial scarps, and a basal circumferential scarp up to 9 km high with a slope of about 30°.

The morpho-structural map of Olympus Mons below (Fig. 1) shows radial scarps and mesas, as well as circumferential graben and troughs on the lower flanks that were previously interpreted as extensional features, probably due to volcanic spreading (e.g., Morris and Tanaka 1994, Borgia et al. 2000, McGovern and Morgan 2009). On the other hand, the terraces on the upper flanks were interpreted as compressional features due to lithospheric flexure (McGovern and Solomon 1993, Byrne et al. 2009, 2013). Lithospheric flexure is observed from a prominent trough around Olympus Mons that is filled by lava (Isherwood 2013).

Since the asthenospheric mantle behaves like a fluid on long timescales, the overlying elastic lithosphere bends due to volcanic loading. A flexural trough forms around the volcano and a bulge forms further outside the trough. This flexure leads to a lateral compression of the volcano and a lateral extension of the upper lithosphere peripheral to the volcano (e.g., Comer 1983, Watts 2001). Spreading affects the volcano when a basal layer or interface characterized by low friction decouples the volcano from the lithosphere, such that the volcano can slide over the lithosphere during flexure (e.g., Byrne et al. 2013).

The aim of our work is to understand terrace development over time, and the relation of terraces and flank instability to volcano growth, lithospheric flexure, and volcanic spreading (i.e. basal decoupling).

Finite Element Modeling

The deformation of a volcanic cone under Martian gravity was investigated with finite element models that take into account the combined effects of lithospheric flexure and volcanic spreading. The axisymmetric setup consists of three parts: an elastoplastic volcano and lithosphere overlying a viscoelastic asthenospheric mantle. Spreading was realized by means of a frictional interface

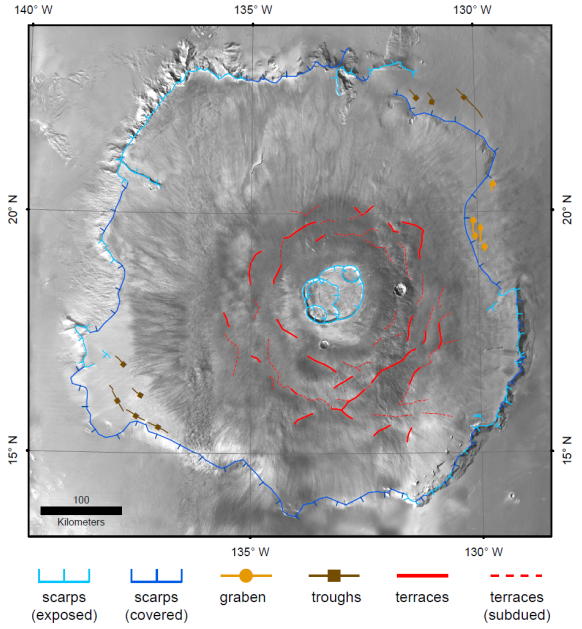

Fig. 1.: Mapping results. Structural mapping of Olympus Mons based on a High Resolution Stereo Camera (HRSC) slope map, and on Thermal Emission Imaging System (THEMIS) daytime data.

between volcano and lithosphere. The interface's coefficient of friction was varied between 0 and 0.6 and in addition, a welded contact was investigated. The cohesion of the volcano was varied between 6 and 60 MPa (basaltic rock mass vs. laboratory-measured basaltic sample, according to Schultz 1995).

We simulated two cases of loading: (1) an instantaneously-emplaced volcano and (2) an incrementally grown volcano. For the latter, the volcano was constructed by successively adding five parts of equal volume, and viscous relaxation of the asthenospheric mantle was allowed between the five loading steps. After emplacement of a volcano load, the lithosphere and asthenospheric mantle behave elastically in the beginning. As the asthenospheric mantle relaxes and becomes increasingly viscous, the volcano and lithosphere develop plastic deformation. Isostatic equilibrium of the load and mantle is reached after about 500,000 years. Further model details can be found in Musiol (2013).

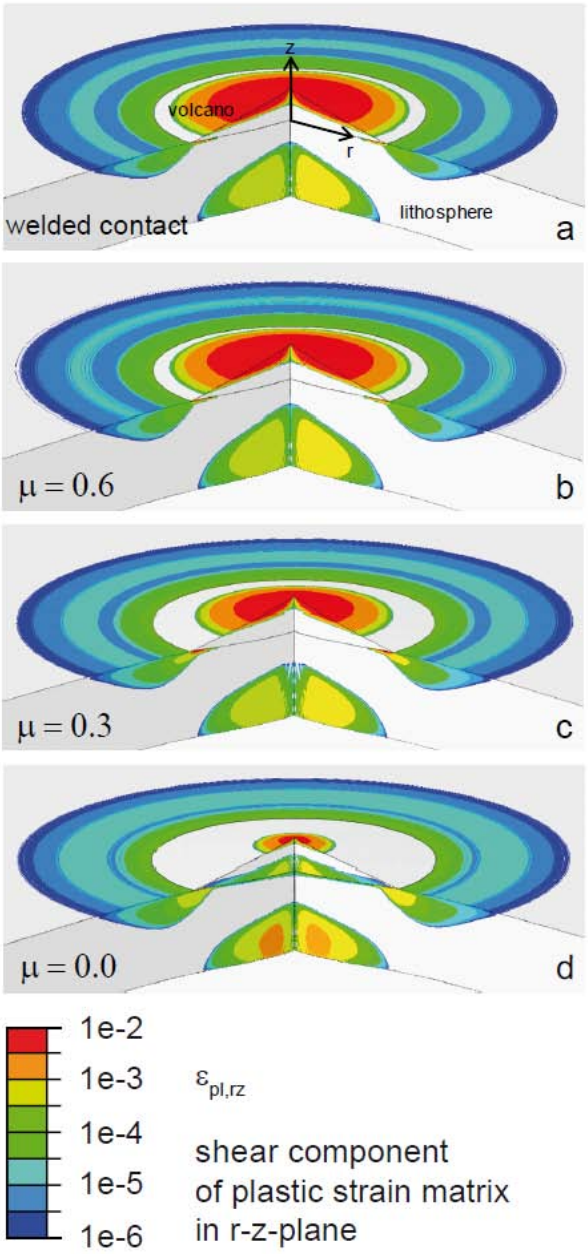

Fig. 2.: Plastic shear strains at the end of isostatic adjustment within models of instantaneous volcano emplacement and varying basal friction. Shown here are cut-away, vertically-exaggerated views of: a) a model with welded contact; b-d) models with decreasing coefficient of friction on the edifice-lithosphere interface. Note the migration of the zone of high plastic strain on the edifice flanks toward the summit with decreasing friction, and an increasingly large plastic strain zone at the interface of volcano and lithosphere.

Results

We show the model results for the instantaneous volcanic load as accumulated plastic shear strains in the axisymmetric plane (Fig. 2). Highest shear strain denotes potential faulting, which is observed on the volcano flanks and at the interface of volcano and lithosphere. With decreasing friction at the interface of volcano and lithosphere, the zone of plastic deformation on the flanks migrates toward the summit area and the zone of basal overthrusting increases. Terrace-bounding faults can be seen at high resolution and are compatible with radial compression leading to thrust faulting on the volcano flanks.

In the models with a growing load, and regardless of cohesion, the areas of observed faulting for the first increment are in agreement with the instantaneous model. As more layers are added, no further plastic straining of the volcano flanks is observed with high cohesion, but plastic strain zones corresponding to terrace-related faulting were produced on every incrementally-formed volcano surface with low cohesion.

Conclusions

Terrace-bounding faults on Olympus Mons upper flanks are explained with thrust faulting resulting from lithospheric flexure. The presence and expression of terrace-bounding faults depends on the coupling of volcano and lithosphere, on the time of volcano growth relative to mantle relaxation, and on the edifice cohesion.

References

Borgia, A., P. T. Delaney, and R. P. Denlinger (2000), Spreading volcanoes, Annu. Rev. Earth Pl. Sci., 28, 539-570.

Byrne, P. K., B. van Wyk de Vries, J. B. Murray, and V. R. Troll (2009), The geometry of volcano flank terraces on Mars, Earth Planet. Sci. Lett., 281, 1-13, doi:10.1016/j.epsl.2009.01.043.

Byrne, P. K., E. P. Holohan, M. Kervyn, B. van Wyk de Vries, V. R. Troll, and J. B. Murray (2013), A sagging-spreading continuum of large volcano structure, Geology, 2013090, doi: 10.1130/G33990.1.

Comer, R. P. (1983), Thick plate flexure, Geophys. J. R. astr. Soc., 72, 101-113.

Isherwood, R. J., L. M. Jozwiak, J. C. Jansen, J. C. Andrews-Hanna (2013), The volcanic history of Olympus Mons from paleotopography and flexural modeling, Earth and Planet. Sci. Lett., 363, 88-96, doi: 10.1016/j.epsl.2012.12.020.

McGovern, P. J., and J. K. Morgan (2009), Volcanic spreading and lateral variations in the structure of Olympus Mons, Mars, Geology, 37, 139-142.

McGovern, P. J., and S. C. Solomon (1993), State of stress, faulting, and eruption characteristics of large volcanoes on Mars, J. Geophys. Res., 98, 23,553-23,579, doi:10.1029/93JE03093.

Morris, E. C., and K. L. Tanaka (1994), Atlas of Mars: Olympus Mons Region, Geol. Inv. Series I-2327, U. S. Geological Survey, Denver.

Musiol, S. (2013), Geodynamics of the Volcanoes Hadriaca Patera and Olympus Mons on Mars, Ph.D. Thesis, Fachbereich Geowissenschaften, Freie Universität Berlin.

Plescia, J. B. (2004), Morphometric properties of Martian volcanoes, J. Geophys. Res., 109, E03003, doi:10.1029/2002JE002031.

Schultz, R. A. (1995), Limits on strength and deformation properties of jointed basaltic rock masses, Rock Mech. Rock Engng., 28, 1-15.

Watts, A. B. (2001), Isostasy and Flexure of the Lithosphere, 1st ed., 458 pp., Cambridge Univ. Press, Cambridge.

Surface deformation simulations of volcanic and tectonic processes in Iceland

Rikke Pedersen[1]

[1]*Nordic Volcanological Center, Institute of Earth Sciences, University of Iceland, Iceland.*
e-mail: *rikke@hi.is*
session: *Volcanism and Volcanotectonics*

Spatially and temporally dense observations of crustal deformation events is an important data source when trying through numerical modeling to obtain insight into geological processes working at depth, for instance by visualization of magma transport and emplacement beneath volcanic structures, as well as simulations of tectonic processes within plate boundary zones. Iceland is an excellent target for remote sensing of crustal deformation processes, especially for the use of interferometric combination of synthetic aperture radar images (InSAR). The Icelandic crust deform continuously due to a variety of volcanic and tectonic processes, and the relatively barren ground furthermore makes an ideal reflector for radar beams emitted from SAR satellites. Three recent Icelandic examples of crustal deformation events related to active plate spreading processes and subsurface magma movements, and the inferences numerical modeling facilitate, will here be demonstrated.

1

The Northern Volcanic Zone (NVZ) is an extensional rift segment, forming a sub-aerial exposure of a part of the mid-Atlantic ridge. The NVZ is bounded to the south by the Icelandic mantle plume, and to the north by the Tjörnes transform zone. The NVZ has typically been divided into five partly overlapping en-echelon fissure swarms, each with a central main volcanic production area. A complex interplay of a number of tectonic and magmatic processes in the NVZ has been revealed by a series of InSAR images: A) two shallow sources experiencing subsidence coincides with known crustal magma chambers at Askja and Krafla central volcanoes, B) elongated subsidence signals within the relatively narrow fissure swarms (15-20 km), inferred to be related to plate spreading, C) horizontal plate spreading distributed over a much wider zone (∼80-100 km), and finally D) a wide area of uplift which may reflect on processes near the crust mantle boundary. Construction of finite element method (FEM) models of the NVZ, have facilitated exploration of the role spatial variation of rheological properties may play, in modifying the style of regional and local surface deformation at this extensional plate boundary. The models indicate that the observed inter-rifting plate spreading deformation field is controlled by local rheological variations within the arrangement of fissure segments, and that a regional central ridge axes model does not apply. The best fitting crustal structure within the most active fissure swarms consists of a wedge of weak elastic material on top of a local visco-elastic ridge.

The Askja system is one of the five *en echelon* volcanic systems making up the NVZ. It consists of a fissure system elongated along the plate boundary and a central complex of at least three nested calderas. The smallest, most recent caldera formed over an extended period of up to 40 years following a highly explosive eruption in 1875. The volcano has been somewhat of a geodetic enigma for many years, as continuous subsidence has been observed by dry-tilt level-

ing there since 1983, and possibly been ongoing since 1973. Seismic studies around Askja have provided new information on possible magma pathways from deep crustal levels, to inferred storage zones in the upper crust. FEM models, simulating surface deformation locally at the Askja volcano, indicates that the tectonic setting with an established shallow magma chamber situated within a diverging plate boundary plays a major role in the continuous, long-term high subsidence rates observed at Askja for the past 30-40 years. In order to fully understand the cause and effect of the complicated volcano-tectonic setting additional advanced models integrating realistic rheological subsurface structures are needed.

2

Since Iceland was settled in the 9th century Hekla volcano has had 23 confirmed eruptions, varying considerably from highly explosive (VEI 5) to calm effusive (VEI 1). Hekla produces mainly andesitic melts, though products range from basaltic to rhyolitic. The silica content is directly correlated to the repose interval, providing a strong argument for the presence of a well-established magma chamber. Numerous geophysical studies have attempted to determine the depth and location of the Hekla magma chamber, but results are as many as the number of studies. Several other characteristics of Hekla volcano make it unique in a global context. The ridge shaped edifice is highly unusual, and the dual nature of the seismicity is not only unusual but also poorly understood. In inter-eruptive periods the volcano is practically aseismic, and the few micro-earthquakes that do occur appear to be related to a nearby transform-zone, whereas co-eruptive earthquakes are clearly connected to magmatic movements. No earthquakes occur below 4 km depth before eruption onset, but during eruptions most are located at 4-9 km depth.

Since InSAR imaging have been applied, a highly improved map of the Hekla surface deformation has been achieved. The spatial density of deformation measurements obtained by this technique revealed a rather complicated surface deformation pattern, which more than one process is thought to contribute to. A roughly circular area 20 km in diameter (centered at the summit) subsides continuously during inter-eruptive periods. The subsidence peaks on the most recent lava flows, primarily due to cooling and compaction of the erupted material, although subsidence is not confined to areas covered by recent lava flows. A subtle, but continuous, uplift signal ($\sim$5 mm/yr) circumscribes the region of local subsidence. This uplift region has a diameter of $\sim$40 km (centered on the summit).

A relatively simple model capable of predicting the observed deformation pattern combines a contracting shallow magma chamber (local subsidence of the edifice), a deeper chamber that is expanding (regional uplift), and finally thermal contraction of recent lava fields. However, this model is problematic, because no independent evidence for a shallow magma chamber exists. An alternative model is here presented, where the composite pattern of deformation is attributed to local thermal contraction of recent lava fields combined with gravitational loading of the volcano edifice and finally magma accumulation at a deep-seated magma chamber. Finite element models where a gravitational load on a 2D problem domain having an elastic upper crust, underlain by a viscoelastic mantle that hosts magma accumulation within a deep-seated magma chamber have been explored.

3

Eyjafjallajökull volcano is situated south of the intersection between the South Iceland Seismic Zone and the Eastern Volcanic Zone (EVZ). The area is characterized by significant topographic relief and a lower spreading rate than the EVZ. As opposed to tholeiitic products in the axial rift zone further north, volcanic products here belong to the alkaline or transitional suite, and the area is, based on the petrological difference as well as poorly developed extensional fractures, characterized as a volcanic flank zone. Eyjafjallajökull is

an icecap covered stratovolcano rising to an elevation of 1666 m.a.s.l.. The icecap covers an area in the summit region about 80 km2 in size, making interferometric measurements unattainable within this area throughout the year. The volcano is characterized by its quiet nature. Activity in the system is episodic, with only four eruptions in the last 1400 years. About a handful of earthquakes associated with the volcanic system had been detected prior to the 1990s. Earthquake swarms did, however, occur in 1994, 1996, 1999 and finally in 2009-2010 preceding the eruption in the spring of 2010 which caused an exceptional, unprecedented disruption to European air traffic. Ground deformation measurements through the 18 years of intermittent unrest have facilitated a coarse mapping of the volcano's current plumbing system, through inverse modeling.

The typical pattern of surface deformation observed prior to, spanning and following eruptions of Iceland's frequently active volcanoes, often referred to as "the volcanic cycle", relates to melt accumulation, drainage and renewed replenishment from an established crustal magma chamber, which can be reproduced by pressure changes within a simple Mogi point source. However, such a simple modeling approach cannot explain the complex behavior observed at the moderately active Eyjafjallajökull volcano. Homogeneous elastic half-space modeling of a complicated network of sill intrusions forming at more than 5 km depth explains the distinct behavior of the volcano. The temporal development of the intrusive complex over the 18 years of intermittent unrest will be demonstrated.

Overburden bulking in analogue models of depletion-induced collapse quantified with computed X-ray micro-tomography

S. Poppe[1], E. P. Holohan[2], E. Pauwels[3], V. Cnudde[3,4], M. Kervyn[1]

[1] *Department of Geography, Vrije Universiteit Brussel, Brussels, Belgium*
[2] *Helmholtz Centre Potsdam, German Research Center for Geosciences (GFZ), Section 2.1, Potsdam, Germany.*
[3] *UGCT, Department of Physics and Astronomy, Ghent University, Ghent, Belgium.*
[4] *UGCT, Department of Geology and Soil Science, Ghent University, Ghent, Belgium*
e-mail: *sam.poppe@vub.ac.be*
session: *Volcanism and Volcanotectonics*

Introduction

Closed, near-circular, topographic depressions are common features on Earth and other planets. These are termed sinkholes or dolines in karst rock regions, and pit-craters (diameter $<\sim$1 km) or calderas (diameter $>\sim$ 1 km) in volcanic regions. Past analytical, numerical and analogue models mainly explored collapse caldera structures by documenting 2D and 3D model surface deformation, and 2D model cross-sections (e.g. Martí et al. 1994; Roche et al. 2000; Holohan et al. 2011). Kinematic and dynamic aspects of caldera collapse are less well understood, though a necessity for the interpretation of recent monitoring data.

We present here a novel application of computed X-ray micro-tomography (μCT) in (volcano-) structural analogue modeling. In this study, we illustrate the methodology through models of volumetric depletion of a sub-surface body and consequent destabilisation and gravitational collapse of the overburden. We investigate two end-member models: 1. Near-continuous collapse into a depleting sub-surface body; and 2. Near-instantaneous collapse into a large sub-surface cavity. Our model results correspond to a natural length scale of $\sim<$ 2 km of the surface depression's diameter, hence applicable to sinkholes, pit-craters and 'small' calderas.

The X-ray micro-tomography methodology

Our analogue model set-up is similar to the 'sandbox' used in most analogue studies (e.g. Martí et al. 1994; Roche et al. 2000). Two dry well-sorted silica sand – plaster mixtures (SP-mix) with cohesions of $\sim$180 and $\sim$300 Pa simulated brittle rock in near-continuous and near-instantaneous experiments, respectively. Golden syrup (GS) with a viscosity of $\sim$50 Pa.s (22°C) served as a fluid analogue (i.e. rock salt, fluid magma; see Figure 1). Garnet sand was used to make passive marker layers, as the difference in elemental composition and density between silica and garnet sand ensured an easily detectable contrast in radiographs. Drainage was initiated by lowering an external GS reservoir below the model base. Geometric, dynamic and kinematic scaling of the simulations was ensured by dimensionless analysis (cf. Roche et al., 2000).

Time-lapse radiographs taken at 2.5-minute intervals documented ongoing model deformation. Vertical subsidence rates were calculated from vertical displacements of the garnet marker layers in the radiographs. Volumes of the sub-surface fluid reservoir, collapsing overburden column and surface depression were calculated from surface areas assuming an axi-symmetrical geometry. After de-

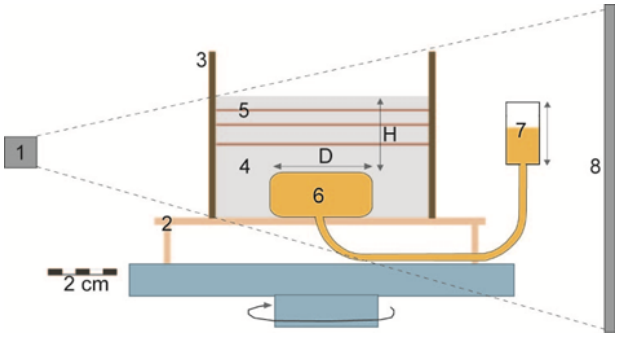

Fig. 1.: X-ray tomography set-up: 1. X-ray beam source; 2. Plastic stand with central outlet; 3. Plastic tube; 4. SP-mix; 5. Thin garnet sand marker layers; 6. GS analogue fluid body; 7. Silo containing GS, adaptable in elevation; 8. X-ray beam detector; H. Overburden height; D. Fluid body diameter.

formation, models were scanned with the μCT scanners of the UGCT (www.ugct.ugent.be; Masschaele et al. 2006). The spatial resolution was 80 - 111 μm, higher than in medical CT scanners. Data sets were reconstructed with the Octopus software. The Morpho+ and VGStudioMax software were used for 3D rendering of model volumes.

Results and Discussion

Near-instantaneous vs. near-continuous collapse

Two representative end-member models are depicted in Figure 2. Despite their much-reduced scale, our analogue models reproduced overall structural and morphological characteristics as modelled previously ((Fig. 2a-c); e.g. Martí et al., 1994; Roche et al., 2000; Geshi et al., 2012), and as observed or inferred from natural collapsed sinkholes, pit-craters and small calderas. Our highest-cohesion models reproduced sub-surface meta-stable cavities (Fig. 2d-e), which collapsed when triggered by mild tapping on the model (Fig. 2f). In these 'near-instantaneous' models, GS depletion had initially resulted in the coherent subsidence of a sub-surface block. Above this formed a convex-upward cavity, with its apex half-way in between initial reservoir level and the model surface. A 3D scan of a collapsed near-instantaneous model into a cavity demonstrates how the overall collapse structure resembles the near-continuous one, however the initial stratigraphy is highly disrupted on the small-scale (Figure 2f). Similar to rockslide avalanches (Glicken, 1996), this effect can be attributed to a rapid acceleration of the collapsing roof into the unconfined cavity.

Syn-collapse velocity and volume evolution

Patterns of vertical subsidence rate during depletion in models of near-continuous collapse demonstrate that, even within an apparently coherent column, spatially and temporally distinct slip events occur (cf. Ruch et al., 2012). The volumetric growth of the subsiding overburden occurred in our models through three processes: 1. Material was added as the collapse propagated upward and laterally within the overburden; 2. Material within the subsiding overburden underwent a volumetric expansion. This is seen as a decrease in the grey value of the subsiding overburden volume, (effective decrease of grain packing - cf. Panien et al., 2006); and 3. Material was added as debris from scarp failure of the surface depression once the collapse reached the surface. Differences between initial and final affected overburden column volumes in our models can be mainly attributed to the volumetric expansion of the brittle overburden within a collapse-bounding ring fault system. Such volumetric expansion of collapsing overburden is termed 'bulking', and has been reported in studies of mining collapse (e.g. Whittaker and Reddish, 1989), sinkhole formation (e.g. Andrejchuk and Klimchouk, 2002) and debris avalanches (Siebert, 1984).

Conclusion

This study illustrates a first use of computerized X-ray micro-tomography (μCT) to image and quantify the evolution of deformation in analogue models of overburden collapse induced by sub-surface fluid withdrawal. 3D μCT scans of

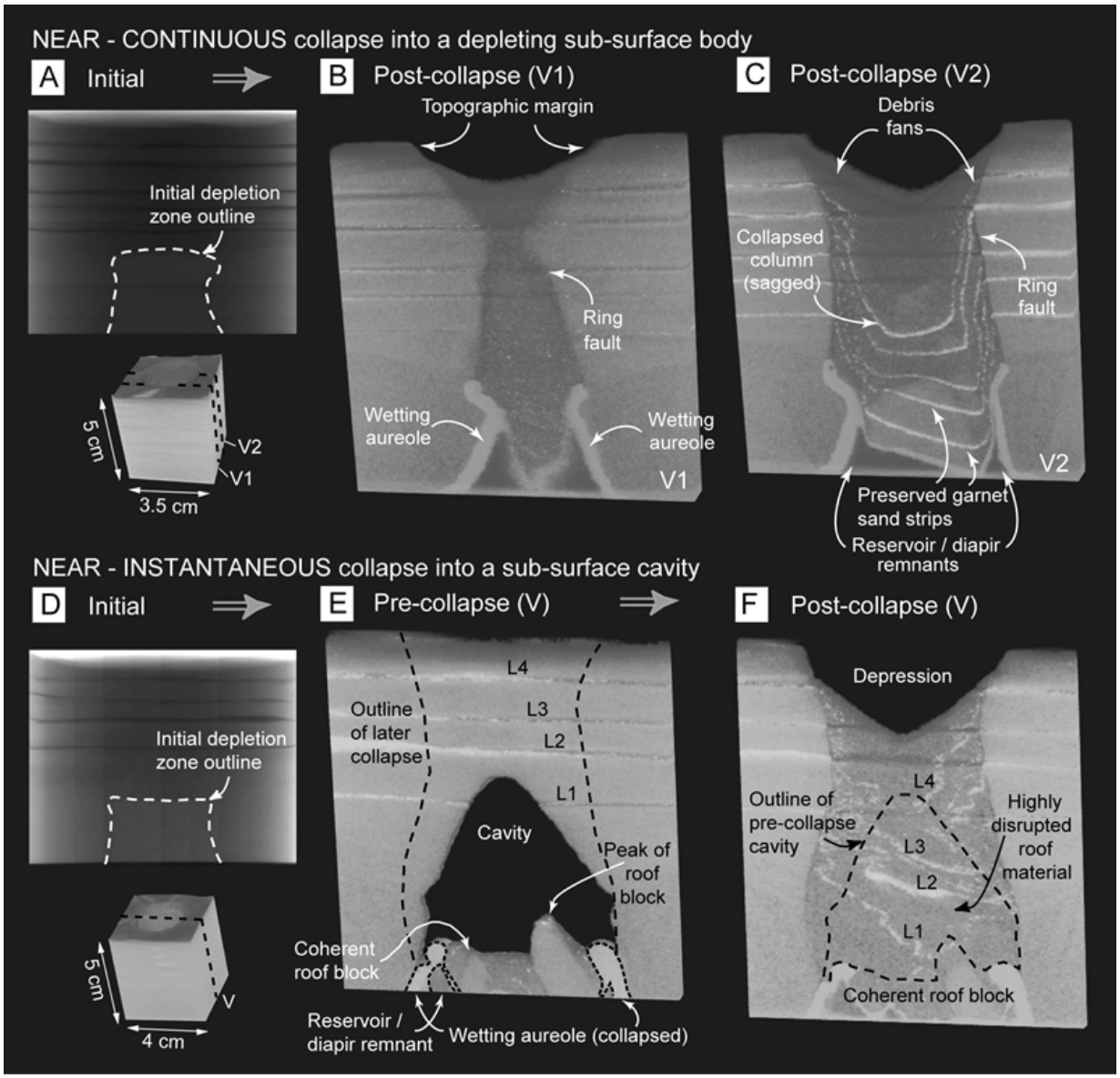

Fig. 2.: Representative models of (above) near-continuous collapse into a depleting sub-surface body and (below) near-instantaneous collapse into a sub-surface cavity: (A, D) Radiographs before depletion; (B, C) Vertical slices - V1 and V2, respectively, in part A - through a 3D scan of the near-continuously collapsed model. Note the differences in apparent ring fault geometry depending on position of cross section from the collapse center; (E, F) Vertical slices through 3D scans of the pre- and post-collapse stages of near-instantaneous collapse model. Note the greater small-scale disruption of the initial stratigraphy in (F) compared with that in (C).

models representing end-member styles of near-continuous collapse into a depleting sub-surface body versus near-instantaneous collapse into a large sub-surface cavity reveal that the final collapse structures are quite similar, except for a more pervasive small-scale disruption of the overburden in the latter case. Subsidence velocity patterns demonstrate subtle differential movements of discrete sections of overburden columns in 3D space, similar to previous results in 2D-space (Ruch et al., 2012). Lastly, a volumetric expansion of the collapsing overburden can be accounted for by a density reduction, i.e. 'bulking', of the brittle material. Further improvements of this μCT imaging methodology could lead to enhanced quantitative assessment of the geometry, kinematics and dynamics of volcano-tectonic processes, with the unique advantage of immediate comparison of modelling results to monitoring data in the field.

References

Andrejchuk, V. and Klimchouk, A., 2002. Int. J. Speleol., 31:1/4, 89-114.

Burchardt, S. and Walter, T.R., 2010, Bull. Volc., 72, 297-308.

Dahm, T., Heimann, S., and Bialowons, W., 2011, Nat. Haz., 58, 1111-1134.

Geshi, N., Shimano, T., Chiba, T. and Nakada, S., 2002, Bull. Volc., 64, 55-68.

Geshi, N., Acocella, V. and Ruch, J., 2012. Bull. Volc., 74, 1553-1567.

Glicken, H., 1996, U.S.G.S. Open File Report, 96-677, 90 pp.

Holohan, E.P., Schöpfer, M.P.J. and Walsh, J.J., 2011, J. Geophys. Res., 116.B07202, 23pp.

Kervyn, M., Boone, M.N., van Wyk de Vries, B., Lebas, E., Cnudde, V., Fontijn, K. and Jacobs, P., 2010, Geosph., 6(5), 482-498.

Martí, J., Ablay, G.J., Redshaw, L.T. and Sparks, R.S.J., 1994, J. Geol. Soc. Lond., 151, 919-929.

Masschaele, B.C., Cnudde, V., Dierick, M., Jacobs, P., Van Hoorebeke, L. and Vlassenbroeck, J., 2006, Nucl. Instr. & Meth. Phys. Res. Abstr., 580, 266-269.

Panien, M., Schreurs, G. and Pfiffner, A., 2006, J. Struct. Geol., 28, 1710-1724.

Roche, O., Druitt, T.H. and Merle, O., 2000, J. Geophys. Res., 105, 395-416.

Ruch, J., Acocella, V., Geshi, N., Nobile, A. and Corbi, F., 2012, J. Geophys. Res., 117, B07301.

Siebert, L., 1984. J. Volc. Geoth. Res., 22, 163-197.

Whittaker, B.N. and Reddish, D., 1989, Dev. Geotech. Engin., 56, Elsevier, 528 pp.

Mechanisms of entrainment of a granular substrate by pyroclastic density currents: insights from laboratory experiments and models, and implications for flow dynamics.

Olivier Roche[1], Yarko Niño[2]

[1]*Laboratoire Magmas et Volcans, Université Blaise Pascal-CNRS-IRD, Clermont-Ferrand, France.*
[2]*Department of Civil Engineering and Advanced Mining Technology Center, Universidad de Chile, Santiago, Chile.*
e-mail: *o.roche@opgc.univ-bpclermont.fr*
session: *Volcanism and Volcanotectonics*

Introduction

Pyroclastic density currents (PDCs) are gas-particle mixtures generated during volcanic eruptions by gravitational collapse of a lava dome or of an eruptive column, lateral explosion of a pressurized magma body, or during caldera collapse. They represent important natural hazards because they can propagate on distances of several kilometers from the eruptive vent, even on relatively horizontal topographies. Mitigation of hazards posed by PDCs, for instance through numerical simulations that can predict areas covered by the currents, requires a good knowledge of their fundamental physics.

Field studies of PDCs deposits have led volcanologists to propose two end-member emplacement mechanisms of the parent flows (Figure 1). A PDC is either a pyroclastic surge that is a fully turbulent dilute mixture with low particle volume fraction of ∼0.1-1% and bulk density of ∼1-10 kg/m^3, or consists of a pyroclastic flow that is a ground-hugging dense gas-particle mixture with a bulk density of ∼10^3 kg/m^3 and that is overridden by a turbulent ash cloud. Particle transport away from the eruptive vent is favored by turbulence in dilute PDCs or by long-lived high interstitial pore fluid pressure that reduces internal friction of the dense basal flow of PDCs. These two mechanisms have been proposed in particular for large ash-rich PDCs, whose accumulation form ignimbrites of volume up to several tens to hundreds of km^3. Such deposits often contain particles of size of several centimeters to decimeters captured from an underlying substrate by the parent currents. The substrate is commonly an earlier coarse-grained pyroclastic fall or flow deposit, the disaggregated surface of a debris avalanche or of a lava field, or a sedimentary fluvial conglomerate. In contrast, granular substrates such as fine-grained pyroclastic ash fall deposits are often not reworked by PDCs. These counter-intuitive observations serve as a base for the present study. Here we investigate the interaction mechanisms of PDCs with a granular substrate in order to discuss the mode of emplacement (dilute or dense) of the currents.

Dense gas-particle flow on a granular substrate

We carried out laboratory experiments to investigate the propagation of a dense PDC on a granular substrate. Experiments consisted on dam-break flows generated by sudden release of a granular material fluidized in a reservoir and that propagated on a horizontal granular layer of particles (Figure 2). The flow particles were fine glass

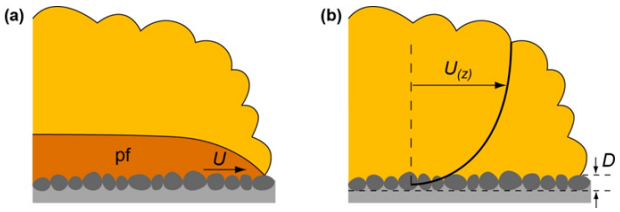

Fig. 1.: End-member pyroclastic density currents propagating on a granular substrate (not to scale). (a) Pyroclastic flow (pf) with front velocity U, overridden by a turbulent ash cloud. (b) Dilute turbulent current on a substrate of particles of mean size D, with mean velocity U(z) increasing upward.

beads of diameter d=80 μm that conferred a low material hydraulic permeability of $\sim 10-11$ m^2, which permitted slow diffusion of the interstitial pore fluid pressure generated before release and hence propagation in a fluid-like state at front velocity U$\sim$(gH)$^{1/2}$, with H the height of the initial reservoir height (Roche 2012). The flows were non turbulent, according to the terminology used for single-phase fluids. The granular substrate consisted of particles identical to those of the flows (d=80 μm) or were coarse glass or steal beads of size d=1500-1590 μm.

Experiments filmed at 1000 frames/s revealed different modes of interaction between the sliding head of the flow and the substrate (Figure 2). In case of a smooth substrate of fine particles, shear wake-like instabilities of height of $\sim$1 mm were generated. These structures stretched so much as the flow propagated that the final deposit revealed almost no evidence of entrainment. In contrast, flow particles penetrated into interstices between coarse beads forming a rough substrate. Most of the uppermost beads were first surrounded by the fines and entrained from the substrate, and then dragged very slowly (at $\sim$0.07U) at flow base. Many of the dragged beads were uplifted within the flow to a height up to $\sim$6-8 mm and were transported downstream. These beads finally settled at flow base and stopped motion, at the same time as the granular flow, at height up to $\sim$4-5 mm above the original top of the substrate.

Pore fluid pressure measurements at flow base revealed that the sliding head generated a relative underpressure (i.e. pressure less than atmospheric):

$$\Delta P = \gamma \rho U^2 \qquad (1)$$

where $\gamma \sim 0.06$ was an empirical constant in the experiments and $\rho \sim$1400 kg/m^3 was the bulk flow density. This caused an upward pressure gradient because (atmospheric) pore pressure within the substrate was almost unchanged. We made the hypothesis that this pressure gradient could cause uplift of the coarse substrate beads dragged slowly at flow base (this implies that the uplift mechanism was non operant in case of a smooth substrate whose particles were not entrained individually). Beads of volume V and density ρ_p could be uplifted at a critical pressure gradient $\Delta P_c = (\rho_p - \rho_{air})Vg/S$, where $S = \pi d^2/4$ was the effective area to which the upward force due to the pressure gradient was applied, so that $\Delta P_c = 2(\rho_p - \rho_{air})gd/3$. Experiments involving substrates of coarse glass or steal beads confirmed that onset of uplift did occur approximately at ΔP_c.

We used our experimental findings to infer the velocity of pyroclastic flows as a function of the characteristics of substrate-derived particles found in PDC deposits. Assuming that particles had the ideal shape of a parallelepiped and were uplifted with their short axis a vertical according to the condition of minimum energy, then $\Delta P_c = (\rho_p - \rho_{air})ga$, and from eq. 1,

$$U = \sqrt{\frac{(\rho_p - \rho_{air})ga}{\gamma \rho}} \qquad (2)$$

Results in figure 3 predict that the biggest blocks of typical size a$\sim$1-1.5 m and density $\rho_p \sim$2000-3000 kg/m^3 reported in literature can be entrained by dense PDCs of velocity of 25-30 m/s (assuming ρ 875-1400 kg/m^3 for fluidized dense pyroclastic flows, see Roche et al. 2013 for details). Comparison with natural data suggests that our model is robust. The 18 May 1980 eruption at Mount St Helens is a rare example where velocity of pyroclastic flows was measured from video analysis. Blocks of size a=0.25-0.35 m and

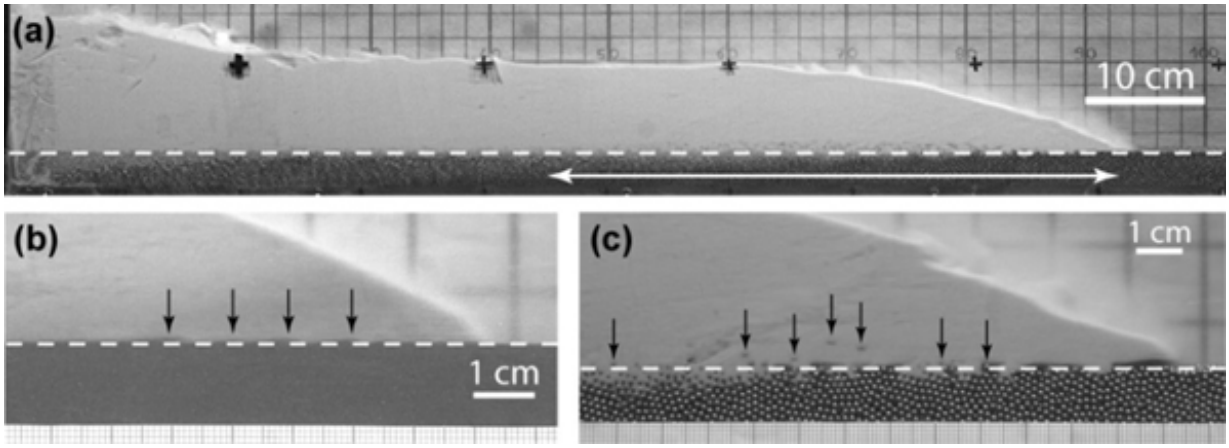

Fig. 2.: Experimental dam-break dense gas-particle flows on a granular substrate. (a) General view of a flow fluidized initially in the reservoir (left, not shown) and propagating at front velocity U=3.06 m/s. The double arrow shows the sliding head. (b) Flow on a smooth substrate of fine glass beads, with small instabilities at base (arrows). (c) Flow on a rough substrate of steal beads, with individual uplifted beads shown by arrows.

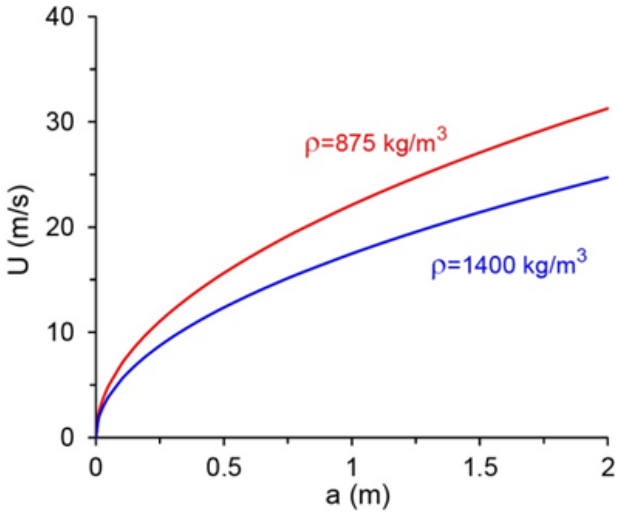

Fig. 3.: Front velocity of pyroclastic flows as a function of the size of substrate-derived particles of typical density ρ_p=2500 kg/m^3. ρ is the bulk flow density.

density ρ_p ~2600 kg/m^3 were captured by pyroclastic flows at ~5.6-7.2 km from the vent on gentle slope <4° (Brand et al. 2014). According to eq. 2, the corresponding velocity of the pyroclastic flows was ~10 m/s, in excellent agreement with field observations.

Dilute turbulent current on a granular substrate

The case of a dilute PDC on a substrate of particles is treated theoretically by considering a hydraulically rough, turbulent fluid flow with low particle concentration (Figure 1). The aim is to determine the current velocity at some height above the ground, where it can be measured in nature, and the corresponding velocity profile required for entrainment of substrate particles of mean size D. The velocity profile of the current is:

$$U_{(z)} = \frac{u_*}{\kappa} ln\Big(\frac{z}{z_0}\Big), \qquad (3)$$

where $U_{(z)}$ is the mean flow velocity at height z, u_* is the shear velocity, κ=0.4 is the von Karman constant, and z_0=D/30 is the hydrodynamic roughness (Garcia 1999). The ability of the current to entrain substrate particles through both traction and saltation depends on the dimensionless Shields number:

$$\theta = \frac{\rho u_*^2}{(\rho_p - \rho) g D}. \qquad (4)$$

The critical Shields number required to set particles in motion depends on the particle Reynolds number $Re_p = u_* D/\nu$, where ν is the gas

kinematic viscosity. Here we consider the dimensionless particle diameter $R_p = Re_p/\theta^{1/2} = [(\rho_p - \rho)gD^3/\rho]^{1/2}$ defined by Niño et al. (2003) because it is independent on u_*, which is unknown in the present case. For turbulent PDCs and substrate particles of typical size of 0.1-1 m and density of 2000-3000 kg/m^3, $R_p > 10^5$ (i.e. $Re_p > 10^4$), which means that we have to consider a range of critical Shields number θ_c=0.052-0.086 according to the extensive data compilation of Buffington and Montgomery (1997). This range reflects various arrangements and shapes of the substrate particles. Combining eqs. 3 and 4 permits to eliminate u_* and gives the critical velocity profile required to set in motion substrate particles of maximum size D,

$$U_{c(z)} = \frac{1}{\kappa}\sqrt{\frac{\theta_c(\rho_c - \rho)gD}{\rho}}ln\Big(\frac{z}{z_0}\Big) \qquad (5)$$

Results are presented in Figure 4 for a current of bulk density of 2 kg/m^3 (larger than that of atmosphere) or 10 kg/m^3 (maximum value given in literature) and considering typical substrate particle density ρ_p=2500 kg/m^3 and current thickness of ∼500 m. They show that even for relatively small blocks of size of 10 cm, the flow velocity at height of a few hundred meters above the ground required for entrainment is significantly higher than the maximum velocity U_{max}=100 m/s commonly accepted in literature for dilute PDCs. In fact, the size of substrate particles that can be entrained by dilute currents is of a few centimeters if U_{max}, for instance at height of 500 m typical of most currents, is assumed.

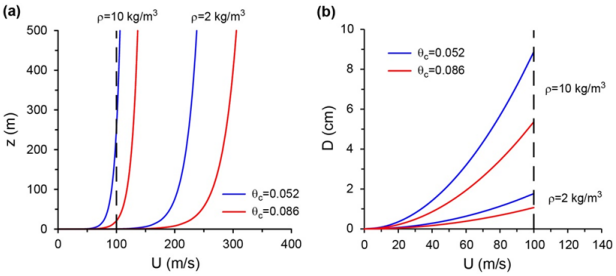

Fig. 4.: Conditions required for entrainment of substrate particles of density ρ_p=2500 kg/m^3 by a dilute PDC, for ranges of bulk flow densities (ρ) and critical Shields number (θ_c), with maximum velocity U_{max}=100 m/s indicated by a dashed line. (a) Critical current velocity as a function of height z for particles of size D=10 cm. (b) Size of entrained substrate particles as function of the critical current velocity at z=500 m.

Conclusion

Our study suggests that substrate-derived particles in PDC deposits can provide information on the dynamics of the parent currents. Dilute turbulent PDCs are able to entrain substrate particles of size of a few centimeters if a maximum current velocity of ∼100 m/s at height of a few hundred meters above the ground is considered. Therefore, we infer that blocks larger than ∼10 cm can be entrained by PDCs if these consist of a concentrated basal pyroclastic flow. According to our experiments, capture can occur through uplift caused by an upward pressure gradient at the flow-substrate interface once substrate particles are dragged individually at flow base. Considering the size and density of substrate particles found in PDC deposits, we infer front velocities up to ∼25-30 m/s for pyroclastic flows. In contrast, substrates of fine particles of size similar to that of the flow particles are not eroded because the flow slides on the smooth substrate and renders the uplift mechanism non operant.

References

Brand, B.D., Mackaman-Lofland, C., Pollock, N.M., Bendaña, S., Dawson, B., Wichgers, P. (2014). Dynamics of pyroclastic density currents: Conditions that promote substrate erosion and self-channelization - Mount St Helens, Washington (USA). J. Volcanol. Geotherm. Res. 276, 189-214.

Buffington, J.M., Montgomery, D.R. (1997). A systematic analysis of eight decades of incipient motion studies, with special reference to gravel-bedded rivers. Water Res. Res. 33, 1993-2029.

García, M. (1999). Sedimentation and erosion hydraulics, in: Mays, L.W. (Ed.), Hydraulic

Design Handbook, McGraw-Hill Professional, chapter 6. Niño, Y., García, M. (2003). Threshold for particle entrainment into suspension. Sedimentology 50, 247-263.

Roche, O. (2012). Depositional processes and gas pore pressure in pyroclastic flows: an experimental perspective. Bull. Volcanol. 74, 1807–1820.

Roche, O., Niño,Y., Mangeney, A., Brand, B., Pollock, N., Valentine, G.A. (2013). Dynamic pore-pressure variations induce substrate erosion by pyroclastic flows. Geology 41, 1107–1110.

Influence of crust type on the long-term deformation of a volcano: example from Mt. Etna (Italy)

Salvatore Scudero[1], Giorgio De Guidi[1], Sebastiano Imposa[1], Mimmo Palano[2]

[1] *University of Catania, Department of Biological, Geological and Environmental Sciences, Earth Science Section, Corso Italia 57, 95129, Catania, Italy*
[2] *Istituto Nazionale di Geofisica e Vulcanologia, Osservatorio Etneo - Sezione di Catania, Piazza Roma 2, 95123, Catania, Italy*
e-mail: *salvatore.scudero@gmail.com*
session: *Volcanism and Volcanotectonics*

Introduction

The volcanic areas experience the greatest deformation in term of velocity and spatiotemporal variability. Cyclic episodes of short-term inflation and deflation, registered during eruptions, are related to magma chambers or dykes migration. Long-term deformations are ascribable to intrusion of large subvolcanic bodies into the crust or even to sub-crustal processes like the rise of a mantle plume. Unfortunately, is not always possible to discriminate among all these processes because they superimpose in space and in time.

In this research, bringing the example of Mt. Etna volcano (Italy), we highlight the existence of a source of deformation not directly related to a volcanic process, but that is rather related to the nature of the crust hosting the volcanism.

The occurrence of "anorogenic" volcanism such Mt. Etna in the collisional context of the Central-Mediterranean area can sometimes appear anomalous (Lustrino et al. 2011), and is a part of why the tectonic origin of volcanism of Mt. Etna is still debated. Also debated is the nature of the crust on which Mt. Etna emplaced about 500 ka. Several authors suggest that this crustal block is not continental but it is rather a remnant of an old, weathered oceanic crust (Sapienza and Scribano 2000; Ciliberto et al. 2009; Manuella et al. 2013; Barreca 2014).

In this work we are able to accurately describe and model the altimetric distribution of a stratigraphic marker within the Etnean substratum and, taking into account the geological features of the area, we identify the different individual Quaternary deformation processes that have interacted.

Late quaternary deformation at Mt. Etna

A basin filled with more than 1000 m of pelagic sediments (dated at 1.2-0.6 Ma; Di Stefano and Branca 2002) lie south of Mt. Etna. The marine deposits are widespread below the entire volcanic edifice although they crop out only locally where they have not been covered by younger deposits and lava flows. They comprise 600 m of marly clays with rare, thin, sand levels evolving upwards in tens of meter of thicker yellow sands with intercalations of polygenic conglomerate. The transition between marly clays and sand is easy to detect in boreholes or geophysical surveys and represents a very useful stratigraphic marker. We detected this marker in 3056 borehole logs; the overall altitude range of the data is between -98 m below and 452 m above sea level.

Knowing the deposition depth and the age of the deposit we can estimate the vertical deformation rate for the marker. Moreover, considering the main tectonic features of the study area (Catalano et al. 2011), we are able to detect sources of deformation with different magnitude

(from 0.2 mm/y to 1.3 mm/y) and acting at different scale (local and regional). In detail we recognize:

1. homogeneous, regional uplift (from 0.3 mm/y to 0.5 mm/y) interpreted either as an isostatic response to the passive subduction of the detached Ionian slab (Wortel and Spackman 2000) or as an asthenospheric flow at the lateral edge accompanying the roll-back of the slab (Shellart 2010; Faccenna et al. 2011);

2. localized uplift coherent with the activity of two local thrust ramps;

3. differential uplift component linearly increasing northwards and not ascribable to the known features of the area.

Other morphological markers (Late-Pleistocene marine terraces and a submerged marine platform of 20 ka) are consistent with the last, so far unknown, source of deformation. Our study suggests that it acted in the same area, constantly over time, and with rates ranging from 0.16 mm/y to 0.75 mm/y (De Guidi et al., 2014). Considering its bell-like pattern and its almost axial position with the volcano, we propose a volcano-related origin for this uplift component.

Certainly very short-term deformations affect the volcanic edifice, (e.g. inflation and deflation), but, it is reasonable to suppose that over long periods these localized, cyclic deformations become negligible and, we require a greater, stable source of deformation to explain the pattern of surface doming.

Modelling

To model the doming we performed an analytical inversion of the whole buried sedimentary substrate of Mt. Etna. To minimize effects of erosion before the substrate was covered by lava flows we selected only the ridges of the paleovalleys, therefore avoiding the areas with greatest loss of material.

The estimated vertical component of the domical deformation was used as an input to constrain an isotropic half-space elastic inversion model, as is routinely done with GPS and InSAR ground-deformation data. Values of 30 GPa and 0.25 were assumed for the shear modulus and Poisson's ratio in the half-space, respectively. The value of the shear modulus chosen corresponds to a typical value of crustal rigidity commonly used in modeling which is found to be an average rigidity value for Mt. Etna (Chiarabba et al. 2000). The inversions were performed by using the genetic algorithm approach. Because of the data's distribution and the 1D nature of deformation data, to model the observed vertical ground deformation pattern we adopted the point source model (Mogi 1958), representing the simplest source used in volcano deformation modeling. In order to test biases due to our chosen starting parameters, we performed several inversions with different sets of model parameters. In all inversions, the algorithm converged rapidly to a similar solution. The best result indicates a pressure source located at a depth of 16.4 km b.s.l. beneath the upper western flank of the volcano with a volume change of $3.8 \cdot 10^6$ m^3/yr . This source is able to explain a large amount of the observed uplift and rates, reproducing well the wavelength of the deformation pattern (Fig. 1).

Although a viscoelastic rheology could be more appropriate to describe the medium at the mantle-crust transition, we retain a simple elastic rheology because i) the deformation's vertical component alone is insufficient to constrain the depth of the pressurized magma body using a viscoelastic rheology, because the main effect of viscous deformation is to reduce the contribution of the horizontal component of deformation with respect the vertical component as function of the viscosity, and ii) there is little known about the viscoelastic medium beneath Etna at depths greater than 10 km.

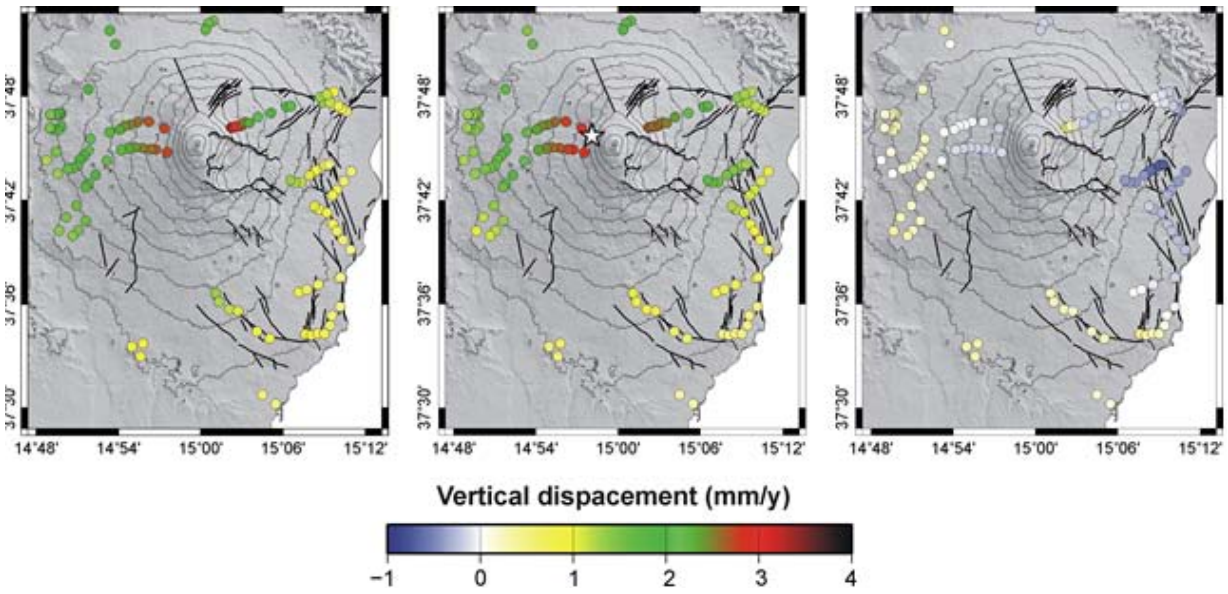

Fig. 1.: Observed deformation pattern of the buried sedimentary substrate (left), calculated deformation (centre) and residual differences between observed and calculated (right); the white star represent the projection of the source of deformation; black lines represent the faults.

Conclusions

Several authors suggest that the Hyblean crust (i.e. the crust under Mt. Etna) is a remnant of an old, weathered oceanic crust. It is also confirmed the existence of a Triassic hydrothermal fossil system which reactivation, connected with magmatic episodes, caused the diapiric emplacement of serpentinized clays at shallow level in the crust (Scribano et al. 2006; Manuella et al. 2012; Barreca 2014).

The process and the mechanism leading to the formation of serpentinites intrusions are consolidated in the literature (Fryer and Fryer 1987; Fryer 2002). The increase of volume that drives the diapiric uprise has been estimated to be ∼40% (Iyer et al. 2010) and the uplift rate ranging from mm to cm per year (Skelton and Jakobsson 2007). Giant diapirs up to 2 km in height have been recognized worldwide showing conical shapes at surface (Fryer et al. 1990; Fryer 2002; Schuiling 2011). Within this frame, the doming of Mt. Etna could result from a volcano-driven diapiric emplacement of a notable amount of hydrothermal material from the lower crust to the shallow levels. In various areas of this crustal block (onshore and offshore) there are geological and geophysical evidences of such intrusions (Catalano et al. 2000; Manuella et al. 2012). Minor evidences of this phenomenon are represented by superficial hydrothermal activity widespread all around the volcanic edifice. Moreover the contemporaneous beginning of the doming and of the volcanic activity at Mt. Etna (∼ 600 ky) strongly support this hypothesis.

Even agreeing with the mantle-plume origin of Mt. Etna as suggested by some authors (Tanguy et al. 1997; Clocchiatti et al. 1998; Montelli et al. 2003) a rising thermal anomaly would melt the lithospheric mantle rather than provoke its volumetric expansion causing, in the long term, the thinning of the overlying crust and not the crustal arching (Burov and Guillou-Frottier 2005; Sleep et al. 2006; Leng and Zhong 2010), therefore a mantle-related process is definitely excluded.

Volcanic doming with similar uplift patterns and magnitude is encountered in other volcanic districts (Acocella and Mulugeta 2001; Zhong and Watt 2002; Pim et al. 2008; Marturano et al. 2011), but the causative mechanism has sometimes been neglected. Therefore considering the nature of the crust is of fundamental import-

ance approaching the long.-term deformation of a volcano.

Acknowledgements

This work was supported by grants from V3 Project (DPC-INGV agreement).

References

Acocella V, Mulugeta G (2001) Surface deformation induced by pluton emplacement: the case of Amiata (Italy). Phys Chem Earth 26:355–362

Barreca G (2014). Geological and geophysical evidences for mud diapirism in south-eastern Sicily (Italy) and geodynamic implications. Journal of Geodynamics.

Burov E, Guillou-Frottier L (2005) The plume head–continental lithosphere interaction using a tectonically realistic formulation for the lithosphere. Geophysical Journal International 161(2): 469-490

Catalano R, Franchino A, Merlini S, Sulli A (2000) A crustal section from the Eastern Algerian basin to the Ionian ocean (Central Mediterranean).Mem Soc Geol It 55: 71-85.

Catalano S, Torrisi S, Tortorici G, Romagnoli G (2011) Active folding along a rift-flank: The Catania region case history (SE Sicily). J Geodyn 51:53-63

Chiarabba C, Amato A, Boschi E, Barberi F (2000) Recent seismicity and tomographic modeling of the Mount Etna plumbing system. J. Geophys. Res. 105: 10923-10938

Ciliberto E, Crisafulli C, Manuella FC, Samperi F, Scirè S, Scribano V, Viccaro M, Viscuso, E (2009) Aliphatic hydrocarbons in metasomatized gabbroic xenoliths from Hyblean diatremes (Sicily): Genesis in a serpentinite hydrothermal system. Chemical Geology 258(3): 258-268

Clocchiatti R, Schiano P, Ottolini l, Bottazzi P (1998) Earlier alkaline and transitional magmatic pulsation of Mt. Etna volcano. Earth Planet Sci Lett 163:399–407

De Guidi G, Imposa S, Scudero S, Palano M (2014). New evidence for Late Quaternary deformation of the substratum of Mt. Etna volcano (Sicily, Italy): clues indicate active crustal doming. Bull Volc 76(5): 816

Di Stefano A, Branca S (2002) Long-term uplift rate of the Etna volcano basement (southern Italy) based on biochronological data from Pleistocene sediments. T Nov 14:61-68

Faccenna C, Molin P, Orecchio B, Olivetti B, Bellier O, Funicello F, Minelli L, Piromallo C, Billi A (2011) Topography of the Calabria subduction zone (southern Italy): Clues for the origin of Mt. Etna. Tect 30:TC1003

Fryer P (2002) Recent studies of serpentinite occurrences in the oceans: Mantle-ocean interactions in the plate tectonic cycle. Chemie Der Erde-Geochemistry 62(4): 257-302.

Fryer P, Fryer GJ (1987) Origins of nonvolcanic seamounts in a forearc environment. Geophysical Monograph Series 43: 61-69

Fryer P, Saboda K L, Johnson LE, Mackay ME, Moore GF, Stoffers P (1990) Conical Seamount: SeaMARC II, Alvin submersible, and seismic reflection studies. In Proc. Ocean Drill. Program Sci. Results 125: 69-80

Iyer K, Rüpke LH, Morgan JP (2010) Feedbacks between mantle hydration and hydrothermal convection at ocean spreading centers. Earth and Planetary Science Letters 296: 34–44

Leng W, Zhong S (2010) Surface subsidence caused by mantle plumes and volcanic loading in large igneous provinces. Earth and Planetary Science Letters 291(1): 207-214

Lustrino M, Duggen S, Rosenberg CL (2011) The Central-Western Mediterranean: Anomalous igneous activity in an anomalous collisional tectonic setting. Earth Sci Rev 104:1–40

Manuella FC, Brancato A, Carbone S, Gresta S (2013) A crustal-upper mantle model for southeastern Sicily (Italy) from the integration of petrologic and geophysical data. Journal of Geodynamics 66: 92-102

Manuella FC, Carbone S, Barreca G (2012) Origin of saponite-rich clays in a fossil serpentinite-hosted hydrothermal system in the crustal basement of the Hyblean Plateau (Sicily, Italy). Clays and Clay Minerals 60(1): 18-31

Marturano A, Aiello G, Barra D (2011) Evidence for Late Pleistocene uplift at the Somma-Vesuvius apron near Pompeii. J Volcanol Geotherm Res 202:211-227

Mogi, K. (1958) Relation between the eruptions of various volcanoes and the deformations of the ground surfaces around them, Bull. Earthquake Res. Inst. Univ. Tokyo, 36, 99-134

Montelli R, Nolet G, Dahlen FA, Masters G, Engdahl ER, Hung SH (2004) Finite-frequency tomography reveals a variety of plumes in the mantle, Science 303:338-343

Pim J, Peirce C, Watts AB, Grevemeyer I, Krabbenhoeft A (2008) Crustal structure and origin of the Cape Verde Rise. Earth Planet Sci Lett 272:422-428

Sapienza G, Scribano V (2000) Distribution and representative whole-rock chemistry of deep-seated xenoliths from the Iblean Plateau, South-Eastern Sicily, Italy. Periodico di Mineralogia 69(2): 185-204

Schellart WP (2010) Mount Etna-Iblean volcanism caused by roll-back induced upper mantle upwelling around the Ionian slab edge: an alternative to the plume model. Geol 38/8:691–694

Scribano V, Sapienza G, Braga R, Morten L (2006) Gabbroic xenoliths in tuff-breccia pipes from the Hyblean Plateau: insights into the nature and composition of the lower crust underneath South-eastern Sicily, Italy.Mineralogy and Petrology 86(1-2): 63-88

Skelton A, Jakobsson M (2007) Could peridolite hydralion reactions have provided a contributory driving force for Cenozoic uplift and accelerated subsidence along the margins of the North Atlantic and Labrador Sea? Norvegian Journal of Geology, 87(1/2): 241 -248

Sleep NH (1990) Hotspots and mantle plumes: Some phenomenology. Journal of Geophysical Research: Solid Earth 95(B5): 6715-6736

Tanguy JC, Condomines M, Kieffer G (1997) Evolution of the Mount Etna magma: constraints on the present feeding system and eruptive mechanism. J Volcanol Geotherm Res. 75:221–250

Wortel MJR, Spakman W (2000) Subduction and slab detachment in the Mediterranean-Carpathian region. Science 290:1910-1917

Zhong S, Watt AB (2002) Constraints on the dynamics of mantle plumes from uplift of the Hawaiian Islands. Earth Planet Sci Lett 203:105-116

Analogue and numerical modeling of rifting events. Complementary tools to understand the rifting process.

Trippanera D.[1], La Marra D.[1], Acocella V.[1], Ruch J.[1], Rivalta E.[2]

[1]*Roma Tre University, Rome, Italy*
[2]*GFZ, Potsdam, Germany*
e-mail: *daniele.trippanera@uniroma3.it*
session: *Volcanism and Volcanotectonics*

Rifts are typical features of divergent plate boundaries that usually composed of normal faults, graben and eruptive fissures. The relative role played by magma and tectonics in controlling the geometry, kinematics and evolution of rifts are still unclear. Recent observations of rifting events clearly associated to dike injections along the divergent plate boundaries have highlighted the importance of magma in shaping rifts. Rifts are studied by means of the InSAR technique, by seismology and structural geology. However, geodetic and seismic data allow us to observe only an instant frame of the entire rifting process, in terms of geological times. Moreover, field observations along the rifts allow us to see only a static photograph taken in a certain time of the rift life, representing only the expression of the cumulative long (or short) time surface deformation.

To better observe and understand the entire rifting process from its beginning to its mature stage, we use analogue and numerical modeling. Since recent observations point out that dike injections are intimately related to the surface deformation during the rifting episodes, we decide to perform analogue and numerical models of multiple dike injections and to observe the surface deformation induced by them. The analogue experiments allow us to reproduce in laboratory the rift formation and evolution through time. The numerical models help us to better understand both the results of the analogue models and the natural process. Moreover, both types of model, allow us to investigate one by one the different parameters acting in the rifting process.

The main aims are to understand: 1) if dikes are able to generate all the long term surface deformation observed on the field along the rifts and 2) how the diking process can eventually affect the rift formation and its evolution. The starting point for the analogue models are the physical models performed by Mastin and Pollard, 1988. They intruded cardboard sheets inside a sleeve - able to dilate - consisting of two sheets of linoleum. We use the same concept of Mastin and Pollard, 1988 aiming to improve their models using new observation techniques and different materials. The setup consists of a rectangular glass box placed on a table and filled with crushed silica sand, the host rock analogue. Using this material, 1 cm on the model corresponds to ≈200m in nature. An intrusion apparatus is located in the box center, in which the dike analogues (0.5 mm thick iron plates) are intruded one by one. In this way, during the evolution of a single model the dike depth remains constant while the intrusion thickness increases progressively (from 0 up to 1 cm at maximum). In order to test the effect of the intrusion depth, different analogue models have been performed varying the sand thickness above the intrusion tip (from 1 cm to 8 cm). Two intrusion geometries have been also tested, in order to investigate the effect of the maximum dilation on the intrusion top: the final shape of the intrusion apparatus tip is flat in one case (rectangular shape) and sharp in the other

case (triangular shape). The surface deformation has been monitored by means of a laser scan with a sub-millimeter resolution (for vertical displacement) and the Particle Image Velocimetry (PIV) technique (for horizontal displacement). The results of the analogue models show that, intruding dikes, a depression with different geometry forms above the dike tip. The depression geometry and the relative fault kinematics vary according to depth and shape of the intrusion. For our numerical models we use the COMSOL Multiphysics software. We reproduce the same geometries of the analogue models (box included). In order to model the flat intrusion tip we use the boundary conditions that allow us to replicate the analytical solutions for constant-opening rectangular dislocations. To avoid artificially induced subsidence we set the top of the intrusion fixed along the vertical axis. Then, to numerically simulate the triangular intrusion shape we use a mathematical function imposing an opening that increases from the top to the bottom of the intrusion. One of the main aims of numerical models is to observe the pattern of the stress induced by the different intrusion geometries and to understand how these can affect the depression geometries (e.g. control on the fault trajectories by the maximum compressive stress change) and the fault kinematics (amount of stress induced at surface).

The results of the numerical models show that the intrusion geometry affects the pattern of the induced stress and the maximum compressive stress change trajectories. We also observe that for the same intrusion depths, the geometry of the intrusion tip affects the amount of surface deformation. These results are consistent with those obtained by means of analogue models.

Finally, in order to simulate the long term rifting cycle – based on the recent rifting events data and the natural basalt properties – we perform numerical models of dikes opening at different depths. We model dikes with an elliptical geometry (more similar to natural cases), applying a progressive dike dilations from 1 to 10 m. By means of these models we also aim to calculate the critical dike depth (D) / thickness (T) ratio beyond which it is possible to have surface fracturing induced by the dike injections.

Analogue and numerical models suggest that the geometry of the faults observed in the analogue models are compatible with some features observed along the eruptive fissure (e.g. Laki, Iceland) and the fissural areas of the magmatic systems and central volcanoes (Krafla, Reykjanes in Iceland; MER in Ethiopia; Hawaii). In addition, the surface displacement observed in the models is also consistent with the deformation pattern observed by means of analytical and geodetic data acquired during the recent rifting events (eg. Krafla, Dabbhau). Moreover, the geometry of the depression is strongly controlled by the D/T ratio parameter because of different stress distribution related to the different intrusion geometry. The D/T ratio together with the least litostatic load and the free surface effect near the surface also controls the possibility to have or not brittle failure at surface during dike injections.

These dataset allow us to suggest that diking is the primary way to form rifts along magmatic divergent plate boundaries and central volcanoes.

GFZ
Helmholtz Centre
POTSDAM

GeoMod2014

Modelling in Geosciences

Programme & Extended Abstracts

31 August - 5 September 2014

Editors:
Kirsten Elger
Øystein Thordén Haug
Malte Ritter

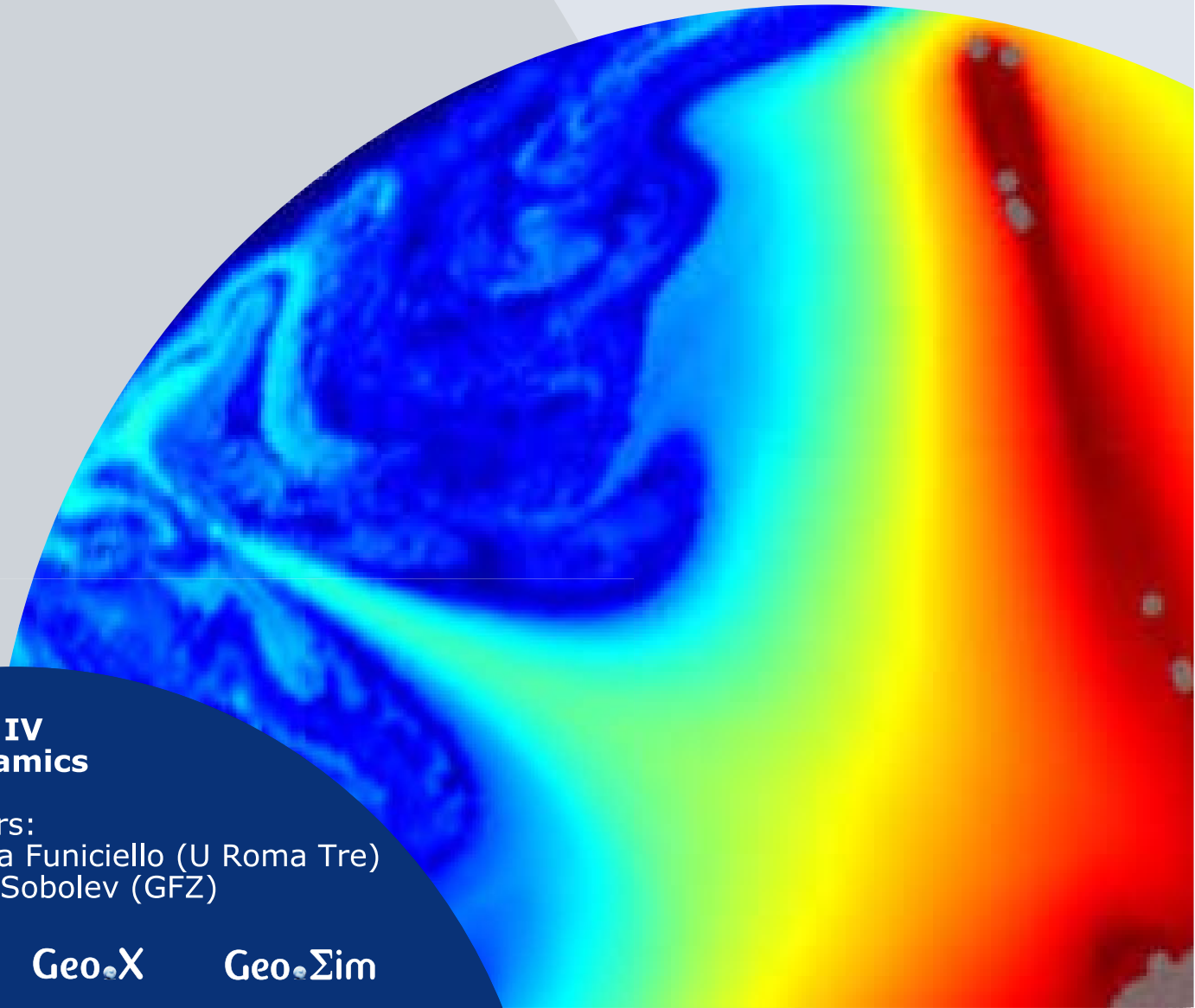

Session IV
Geodynamics

Conveners:
Francesca Funiciello (U Roma Tre)
Stephan Sobolev (GFZ)

DFG GeoX GeoSim

Session IV.

Geodynamics

Session Description: Geodynamics

Conveners: Francesca Funiciello (U Roma Tre), Stephan Sobolev (GFZ)

We are living in the time when initially observational-qualitative geology is rapidly turning into the quantitative-predictive science where numerical and analogue modelling are essential. Both these modelling techniques have their strong and weak sides and their combination is potentially very desirable, but is not often practiced. In this session we would like to focus at geodynamic problems where both modelling techniques could best cooperate. Those include, but are not limited to deformation of lithosphere, subduction, mantle convection and plumes. We invite contributions of numerical and analogue modellers in all these fields and particularly welcome joint numerical-analogue modelling approaches and ideas on efficient cross-technique collaboration.

Anomalous structure of the oceanic lithosphere in the North Atlantic and Arctic oceans: preliminary analysis based on bathymetry, gravity and crustal structure

O. Barantseva, I. M. Artemieva, H. Thybo, M. Herceg

IGN, University of Copenhagen, Denmark
e-mail: *olba@ign.ku.dk*
session: *Geodynamics*

We present preliminary analysis of the crustal and upper mantle structure of the oceanic lithosphere in the North Atlantic and Arctic oceans with the specific goals of establishing factors that control variations in crustal thickness, and recognizing upper mantle structure which, together with the crustal structure, controls the bathymetry.

In comparison to continents, oceanic crust and upper mantle is commonly believed to have a simple structure, and in young oceans (< 80 Ma) bathymetry usually follows the square-root-of-age law. However, this is not true for the Northern Atlantic, northwards from the Charlie Gibbs transform zone. Although the Northern Atlantic ocean started opening ca. 65 Ma, it has anomalously thick crust and anomalously shallow bathymetry that does not follow theoretical predictions. These anomalies may, in part, be controlled by mantle processes at around Iceland. Further north and into the Arctic ocean, spreading rate decreases rapidly, having effect on the structure of the oceanic lithosphere. In the Arctic Ocean the main geodynamic factor that controls the crustal and lithospheric development, is the presence of a unique system of ultraslow mid-ocean ridges.

Our analysis is based on modeling of gravity anomalies caused by subcrustal anomalous masses. The calculations are based on removing the gravitational effect of water, crust and the deep mantle from the observed gravity field. The bathymetry is based on the global NOAA database ETOPO1. For crustal correction we use a part of the global model CRUST1.0, and for comparison, a regional seismic model EUNAseis. Gravity data is derived from GOCE satellite data. As a result we aim at understanding the links between the deep lithosphere dynamics, ocean spreading, ocean floor bathymetry, heat flow and structure of the oceanic lithosphere in the region where classical models of evolution of the oceanic lithosphere appear to be unreasonable.

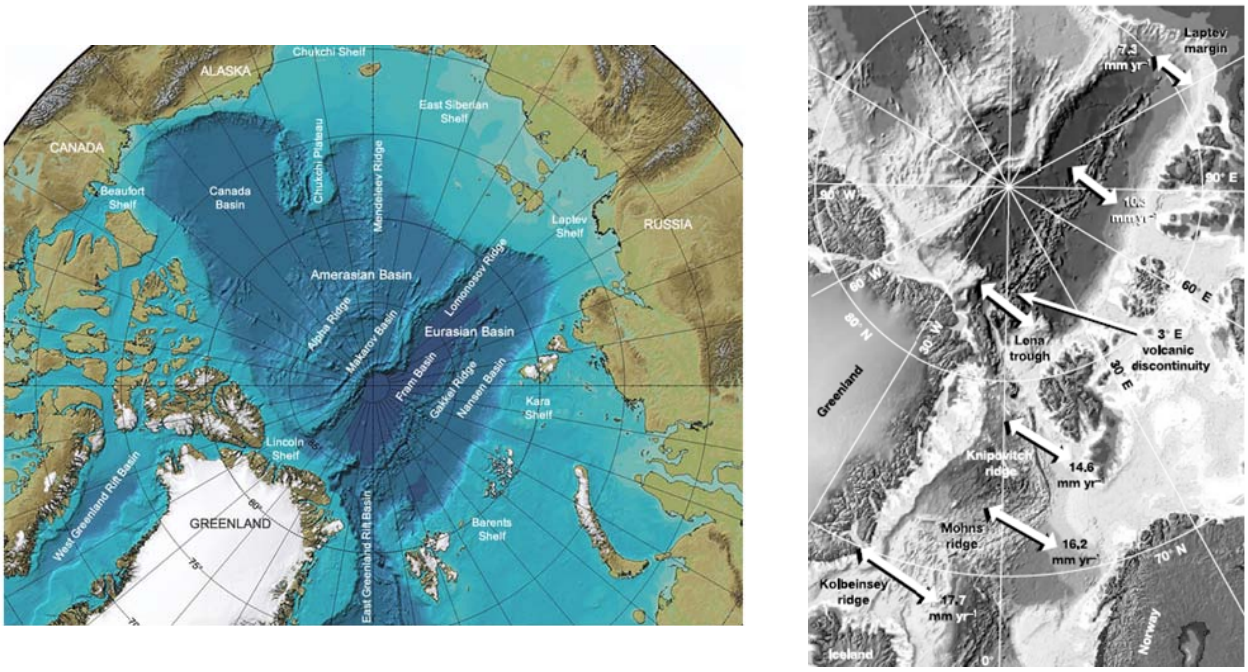

Fig. 1.: Simplified map of the area of study. North-Atlantic and Arctic transitional ridge system.

Constraining the rheology of the lithosphere through geodynamic inverse modelling

Tobias Baumann, Boris Kaus* Anton Popov

Institute of Geosciences, Center for Computational Sciences & VAMOS research center, Johannes-Gutenberg University, Mainz, Germany
**presenting author*
e-mail: *kaus@uni-mainz.de*
session: *Geodynamics*

Abstract

Understanding the physics of lithospheric deformation requires good constraints on lithospheric rheology and in particular on the effective viscosity. Typically, rheology is determined from laboratory experiments on small rock samples, which are extrapolated to geological conditions - an extrapolation over 10 orders of magnitude in deformation rates. Ideally, we thus need a new independent method that allows constraining the effective rheology of the lithosphere directly from geophysical data, which is the aim of this work.

Our method uses the fact that the geodynamically controlling parameters of lithospheric deformation are its effective viscosity and density structure. By appropriately parametrising the rheological structure of the lithosphere we perform instantaneous forward simulations of present-day lithospheric deformation scenarios with a finite element method to compute the gravity field as well as surface velocities. The forward modelling results can be compared with observations such as Bouguer anomalies and GPS-derived surface velocities. More precisely, we automatise the forward modelling procedure with a Markov-Chain Monte Carlo method, and in fact solve a joint geodynamic and gravity inverse problem. The resulting misfit can be illustrated as a function of rheological model parameters and a more detailed analysis allows constraining probabilistic parameter ranges.

Yet, the lithosphere has non-linear rheologies that can be plastic or temperature-dependent powerlaw creep depending on stresses. As the thermal structure of the lithosphere is in general poorly constrained, and only affects the dynamics of the lithosphere in an indirect manner, we developed a parameterised rheology that excludes a direct temperature dependency. To test the accuracy of this approximation we perform lithospheric-scale collision forward models that incorporate a temperature-dependent visco-plastic rheology to create synthetic surface observations. In a second step, we deploy these synthetic data sets to perform a joint inversion, using our simplified parameterized rheology. Results show that we can recover the rheology of the lithosphere reasonably well, provided that lithospheric layers contribute to the large-scale dynamics. In addition, we have applied the models to the India-Asia collision zone, and first results are consistent with the Tibetan plateau having a weak lower crust, but the Indian mantle lithosphere having large viscosities.

Acknowledgements

Funding was provided by the European Research Council under the European Community's Seventh Framework Program (FP7/2007-2013) / ERC Grant agreement #258830. Numerical computations have been performed on MOGON (ZDV Mainz computing center) and JUQUEEN (Jülich high-performance computing center).

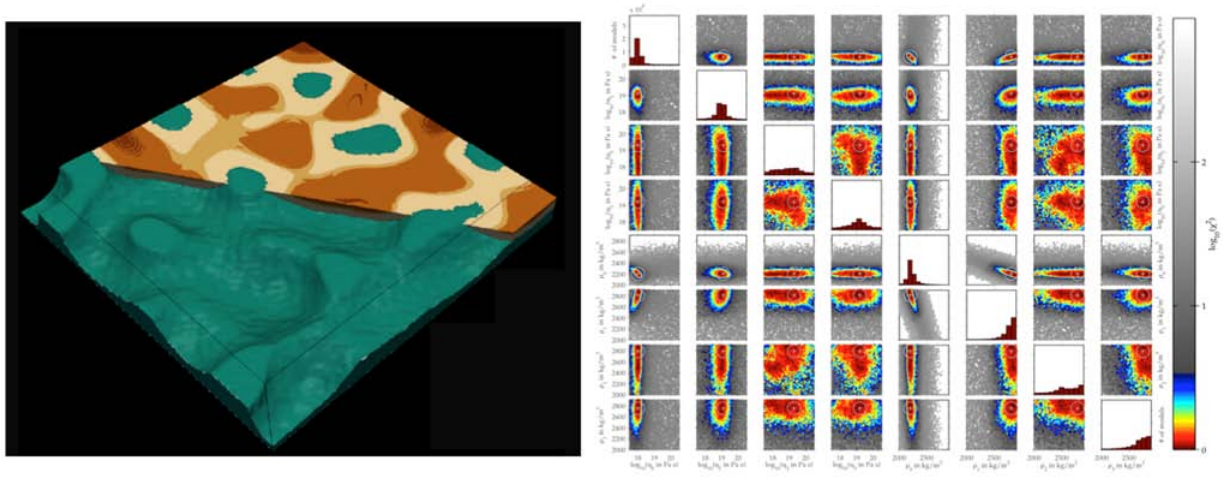

Fig. 1.: Left: 3D model of salt tectonics in the presence of sedimentation and erosion ("downbuilding"), of which we use one snapshot to define the geometry of our model. From this snapshot, we compute the gravity anomalies and the surface velocities, which forms our synthetic dataset. Right: In a next step, out inversion method runs many forward models in which density and viscosity of each of the layers is varied in an automatic fashion and the resulting model output is compared with the data which gives one misfit value per simulation (dots on these plots). Models that fit the data well have red colors. Results show that we can retrieve the true data (larger circles) very well, provided that the layers are not too thin (pictures taken from Baumann et al. 2014).

References

Baumann T., Kaus B., Popov A. (2014). Constraining effective rheology through parallel joint geodynamic inversion. Tectonophysics. DOI:10.1016/j.tecto.2014.04.037

A new model for the architecture of magma-poor rifted margins

Sascha Brune[1,2], Christian Heine[1], Marta Pérez-Gussinyé[3], Stephan V. Sobolev[2]

[1] *EarthByte Group, School of Geosciences, The University of Sydney, Australia*
[2] *Geodynamic Modelling Section, GFZ German Research Centre for Geosciences, Potsdam, Germany*
[3] *Royal Holloway College, University of London, UK*
e-mail: *sascha.brune@sydney.edu.au*
session: *Geodynamics*

Magma-poor rifted margins often exhibit highly extended continental crust with a thickness of less than 10 km. The width of these thin crustal regions varies from 70 km off Iberia (Whitmarsh et al., 2001) to 200 km in the Central South Atlantic segment (Contrucci et al., 2004). The respective conjugate margin, however, is often restricted to few tens of kilometres resulting in large scale crustal asymmetry (Hopper et al., 2004; Unternehr et al., 2010). Seismic observations as well as kinematic reconstruction of the Iberia/Newfoundland conjugates suggest that an array of ocean-ward younging sequential faults is responsible for the typical asymmetric architecture (Ranero and Perez-Gussinye, 2010). Up to now, no thermo-mechanically verified model exists that explains the existence of highly thinned crust, margin asymmetry, and sequential fault activity simultaneously.

Here, we use thermo-mechanical modelling (SLIM3D, Popov and Sobolev, 2008) to understand the spatio-temporal evolution of the Iberia/Newfoundland and the Brazil/Angola passive margins. Our finite element model involves an elasto-visco-plastic rheology formulation that allows for the self-consistent generation of faults and ductile shear zones as well as stress- and temperature-dependent viscosity. We constrain our experiments with detailed plate kinematic history of the pre-break up and early seafloor spreading phase, laboratory-based rheology, and melt fraction evaluation of mantle upwelling. Our results are consistent with observed fault patterns, crustal thickness, and basin stratigraphy.

We propose rift migration as a key process during magma-poor margin formation (for more detail, see Brune et al., 2014). Our numerical models show that steady-state rift migration is maintained by sequential faulting in the brittle crust and balanced by lower crustal flow (Fig. 1). Hence, the degree of rift migration is controlled by the lower crustal viscosity adjacent to the moving rift, whereas the viscosity of the lower crust is a function of lower crustal composition, initial thermal structure, intensity of strain softening and most importantly extension velocity. By demonstrating how rift velocity affects the final margin width, we explain the formation of highly thinned crust and the along-strike asymmetry variation of the Central South Atlantic segment (Fig. 2). The effect of initial lower crustal viscosity was most important to shape the Iberia-Newfoundland margins. Their structure is best described with an initially decoupled, moderately asymmetric fault phase that is followed by crust-mantle coupling, sequential faulting, and low degree rift migration. Rift migration may be also relevant for other highly thinned and asymmetric margin pairs such as Antarctica–India, the North-East Atlantic, the Southern South Atlantic segment and the East Australia/Lord Howe Rise conjugate.

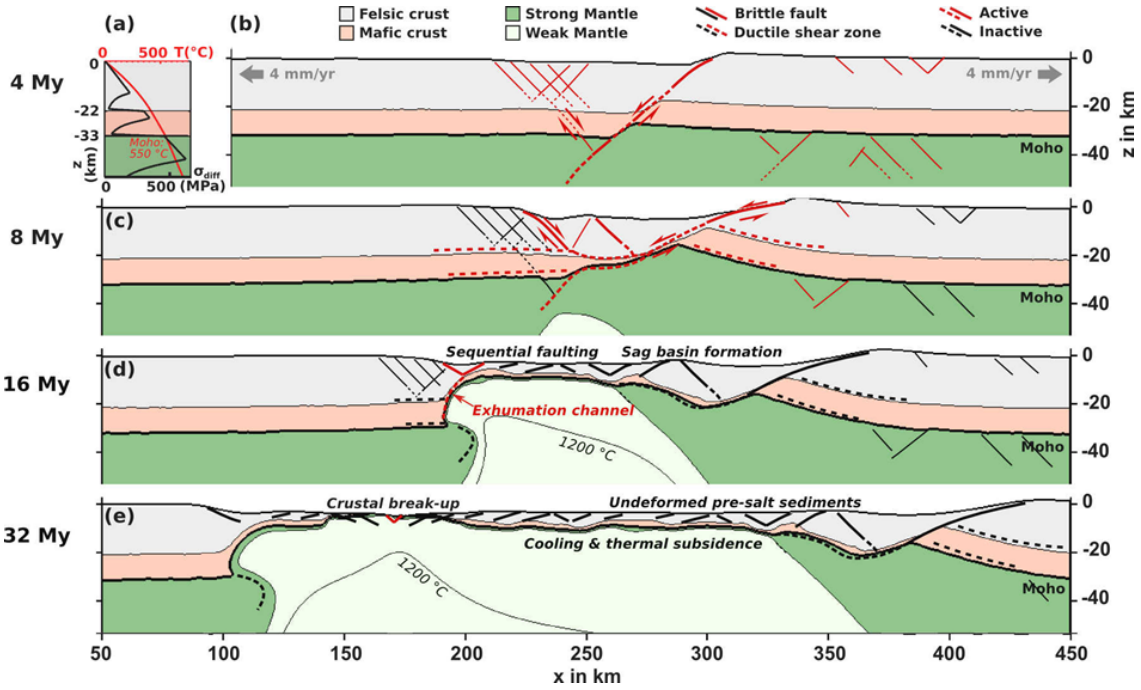

Fig. 1.: Active faults are shown in red, inactive faults in black. Brittle faults are indicated with solid lines, ductile shear zones with dashed lines. The wide margin is formed through rift migration and sequentially active faulting towards the future ocean. Hence, undisturbed pre-salt sediments pre-dating breakup are predicted by our model to be deposited in the landward part of the margin.

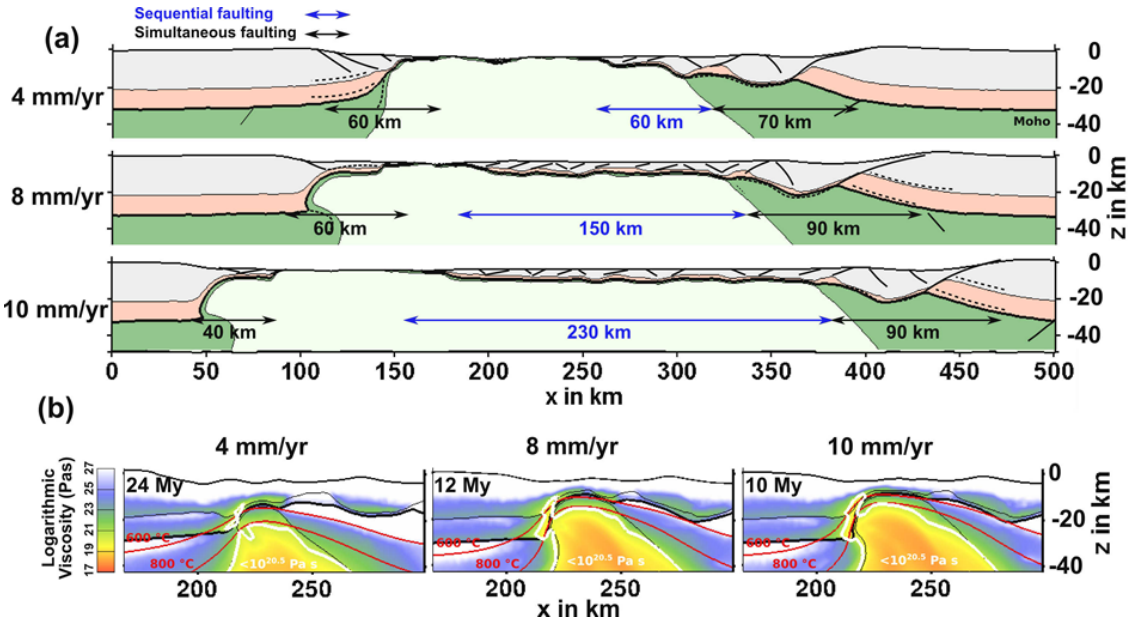

Fig. 2.: **(a)** Conjugate margin structure for 4, 8, and $10\,\mathrm{mm/a}$ full rift velocities. The width of simultaneously faulted areas is indicated by black arrows, while sequentially faulted domains are depicted by blue arrows. The width of the wide margin increases with rift velocity. The reason for this behaviour is shown in **(b)**: Higher velocities lead to advection of the isotherms to shallower depths. This heats the lower crust more efficiently forming a weaker and larger exhumation channel (see white iso-viscosity line that cuts into the lower crust).

References

Brune, S., Heine, C., Perez-Gussinye, M., Sobolev, S.V., 2014. Rift migration explains continental margin asymmetry and crustal hyperextension. Nature Communications (in press.) doi:10.1038/ncomms5014

Contrucci, I., Matias, L., Moulin, M., Geli, L., Klingelhofer, F., Nouze, H., Aslanian, D., Olivet, J.L., Rehault, J.P., Sibuet, J.C., 2004. Deep structure of the West African continental margin (Congo, Zaire, Angola), between 5 degrees S and 8 degrees S, from reflection/refraction seismics and gravity data. Geophys. J. Int. 158, 529–553.

Hopper, J.R., Funck, T., Tucholke, B.E., Larsen, H.C., Holbrook, W.S., Louden, K.E., Shillington, D., Lau, H., 2004. Continental breakup and the onset of ultraslow seafloor spreading off Flemish Cap on the Newfoundland rifted margin. Geology 32, 93–96. doi:10.1130/G19694.1

Popov, A.A., Sobolev, S.V., 2008. SLIM3D: A tool for three-dimensional thermo mechanical modeling of lithospheric deformation with elasto-visco-plastic rheology. Phys. Earth Planet. Inter. 171, 55–75. doi:10.1016/j.pepi.2008.03.007

Ranero, C.R., Perez-Gussinye, M., 2010. Sequential faulting explains the asymmetry and extension discrepancy of conjugate margins. Nature 468, 294–299. doi:10.1038/nature09520

Unternehr, P., Peron-Pinvidic, G., Manatschal, G., Sutra, E., 2010. Hyper-extended crust in the South Atlantic: in search of a model. Pet. Geosci. 16, 207–215. doi:10.1144/1354-079309-904

Whitmarsh, R.B., Manatschal, G., Minshull, T.A., 2001. Evolution of magma-poor continental margins from rifting to seafloor spreading. Nature 413, 150–154. doi:10.1038/35093085

Oblique extensional structures from initial deformation to breakup: Insights from numerical 3D lithospheric-scale experiments

Sascha Brune

EarthByte Group, School of Geosciences, The University of Sydney, Australia
Geodynamic Modelling Section, GFZ German Research Centre for Geosciences, Potsdam, Germany
e-mail: *sascha.brune@sydney.edu.au*
session: *Geodynamics*

Oblique extension takes place when the relative velocity of two diverging plates is at an angle to the zone of deformation. Brittle deformation is accommodated by complex normal fault systems that are controlled by reactivation of pre-rift structures, extension direction, erosion, sedimentation, melting and dyke dynamics. The relative impact of these processes on the observed fault pattern, however, is difficult to deduce from field-based studies alone. This study provides insight in crustal stress patterns and fault orientations by employing a laterally homogeneous, 3D rift setup with constant extension velocity and direction (Fig. 1). While previous analogue models elucidated the fault patterns of initial rift phases, the entire rift evolution from the beginning of extension to breakup has not be addressed so far. In order to validate the model, I explicitly compare its results to a set of analogue experiments that have been conducted on crustal scale (Clifton et al., 2000) and lithospheric scale (Agostini et al., 2009). Despite the simplicity of the setup, the presented rift models feature a large variety of fault orientations that are solely due to the three-dimensionality of oblique rift systems.

The presented numerical models cover all possible rift obliquities (i. e. rift-orthogonal extension, low obliquity, high obliquity, strike-slip deformation) by extending a previous study that focused on the moderately oblique Gulf of Aden Rift (Brune and Autin, 2013). Hence, model results are applicable to diverse oblique rifts that existed in the past or are active at present day, such as the presently active Main Ethiopian Rift (Corti, 2008), the Gulf of California Rift (Bennett and Oskin, 2014) the Equatorial Atlantic Rift (Heine and Brune, 2014), and the Antarctica/Australia Rift (Whittaker et al., 2007). Moreover, the model yields insight in oblique mid ocean ridges like the Reykjanes and Mohns Ridge (Dauteuil and Brun, 1993) and the South West Indian Ridge (Montési et al., 2011).

Rift evolution is computed using the finite element model SLIM3D that features realistic, elasto-visco-plastic rheology and a free surface. The modelled lithospheric segment involves crustal and mantle layers accounting for self-consistent necking of the lithosphere. Along-strike model sides use a periodic boundary condition that mimics an infinitely long rift zone. Despite recent advances, 3D numerical experiments still require relatively coarse resolution so that individual faults are poorly resolved. This issue is addressed by employing a simple post-processing method that uses the surface stress-tensor to evaluate stress regime (extensional, strike-slip, compressional) and preferred fault azimuth (Brune and Autin, 2013). The described method is applicable to any geodynamic model and easy to introduce.

The evolution of a moderately oblique rift system is illustrated in Fig. 2. Initial small-scale faults strike with an azimuth that exactly in the middle between the rift-parallel and the extension

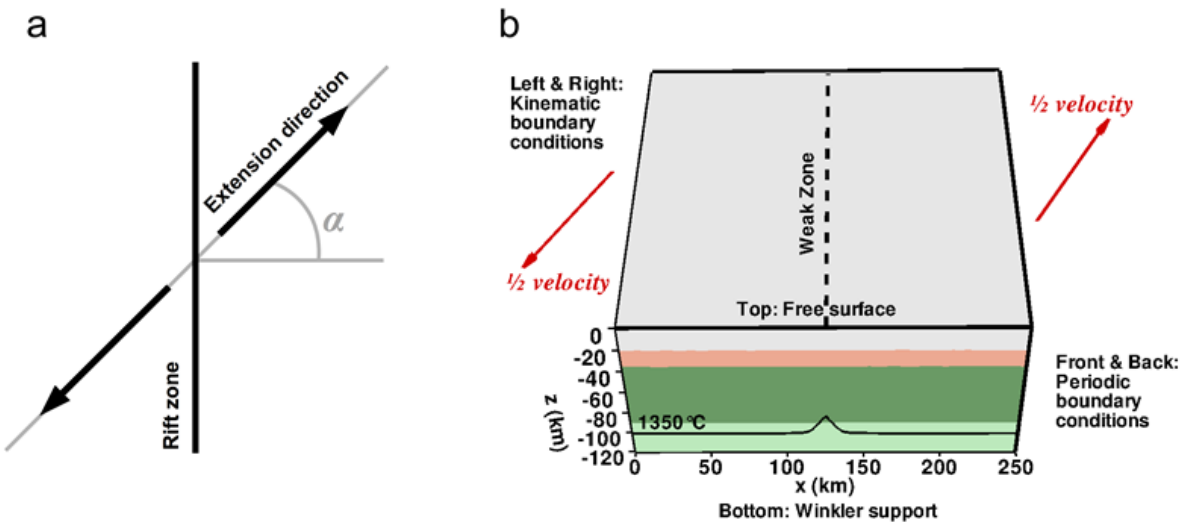

Fig. 1.: (a) Fundamental geometry of oblique extension. The angle of obliquity α is defined as the angular difference between extension velocity and rift normal. **(b)** The numerical model setup involves four layers: felsic crust (grey), mafic crust (red), strong mantle (olive), and weak mantle (light green). Extensional velocities are prescribed at the boundaries in x-direction.

orthogonal direction. This agrees with previous analogue experiments and theoretical considerations (Withjack and Jamison, 1986). The small-scale faults coalesce into an en-échelon system at 6 My. The phase of en-échelon deformation is accompanied with smoothly varying fault orientations that exceed the rift-parallel azimuth of 0° (Fig. 2c). At 11 My, pronounced rift-parallel faults emerge adjacent to the rift centre. This takes place at the end of the en-échelon deformation when strong lithospheric necking occurs below the central part of the rift. Simultaneously, a thin, strike-slip dominated area emerges in the rift centre indicating strain-partitioning. The latest stages of rifting show intermediate fault orientations while additional extension-orthogonal fault azimuths emerge during breakup.

While fault directions are often used to infer palaeo plate movements, this study shows that local changes in crustal stress field and fault orientation may arise intrinsically during rift maturation and may not require plate motion changes. These changes follow a characteristic temporal pattern that is linked to the maturity of the rift system. In natural rift systems this pattern might be modified by additional heterogeneities, erosion, sedimentation, melting and dyke dynamics.

References

Agostini, A., Corti, G., Zeoli, A., Mulugeta, G., 2009. Evolution, pattern, and partitioning of deformation during oblique continental rifting: Inferences from lithospheric-scale centrifuge models. Geochem. Geophys. Geosystems 10, Q11015. doi:10.1029/2009GC002676

Bennett, S.E.K., Oskin, M.E., 2014. Oblique rifting ruptures continents: Example from the Gulf of California shear zone. Geology G34904.1. doi:10.1130/G34904.1

Brune, S., Autin, J., 2013. The rift to break-up evolution of the Gulf of Aden: Insights from 3D numerical lithospheric-scale modelling. Tectonophysics 607, 65–79. doi:10.1016/j.tecto.2013.06.029

Clifton, A.E., Schlische, R.W., Withjack, M.O., Ackermann, R.V., 2000. Influence of rift obliquity on fault-population systematics: results of experimental clay models. J. Struct.

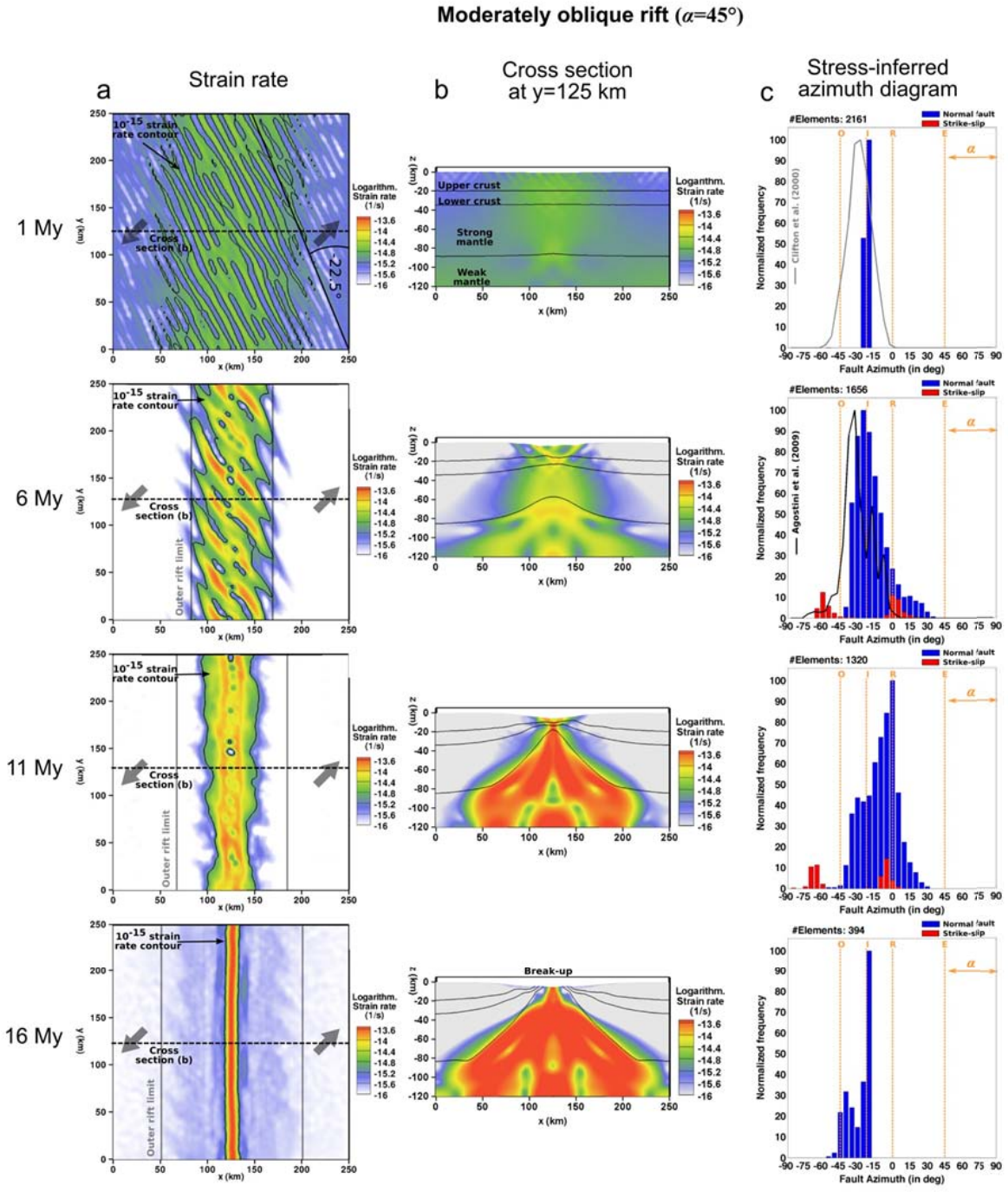

Fig. 2.: (a) The surface strain rate at 1 My shows small-scale shear zones that correspond excellent to the theoretically derived value ($-22.5°$, Withjack and Jamison, 1986). Further evolution involves rotating sigmoidal shear zones and basin-ward localization until crustal break-up is achieved. **(b)** Cross sections show the degree of lithospheric necking. **(c)** Azimuth diagram depicting the characteristic evolution of stress-inferred fault directions at the model surface. Abbreviated directions indicate the rift-parallel azimuth (R), intermediate fault orientation (I), extension-orthogonal direction (O), and the direction of extension (E). For comparison, fault distributions of analogue experiments by Clifton et al. (2000) and Agostini et al. (2009) are plotted at 1 My, and 6 My, respectively.

Geol. 22, 1491–1509. doi:10.1016/S0191-8141(00)00043-2

Corti, G., 2008. Control of rift obliquity on the evolution and segmentation of the main Ethiopian rift. Nat. Geosci. 1, 258–262. doi:10.1038/ngeo160

Dauteuil, O., Brun, J.P., 1993. Oblique Rifting in a Slow-Spreading Ridge. Nature 361, 145–148. doi:doi:10.1038/361145a0

Heine, C., Brune, S., 2014. Oblique rifting of the Equatorial Atlantic: Why there is no Saharan Atlantic Ocean. Geology 42(3), 211–214. doi:10.1130/G35082.1

Montési, L.G.J., Behn, M.D., Hebert, L.B., Lin, J., Barry, J.L., 2011. Controls on melt migration and extraction at the ultraslow Southwest Indian Ridge 10°–16°E. J. Geophys. Res. Solid Earth 116, B10102. doi:10.1029/2011JB008259

Whittaker, J.M., Müller, R.D., Leitchenkov, G., Stagg, H., Sdrolias, M., Gaina, C., Goncharov, A., 2007. Major Australian-Antarctic Plate Reorganization at Hawaiian-Emperor Bend Time. Science 318, 83 –86. doi:10.1126/science.1143769

Withjack, M.O., Jamison, W.R., 1986. Deformation produced by oblique rifting. Tectonophysics 126, 99–124. doi:10.1016/0040-1951(86)90222-2

Initial models of the influence of collision-phase inheritance on continental rifting

Susanne Buiter[1,2], Joya Tetreault[1], Reza Khabbaz Ghazian[3,1]

[1] *Geological Survey of Norway, Trondheim, Norway*
[2] *The Centre for Earth Evolution and Dynamics, University of Oslo, Norway*
[3] *Statoil ASA, Oslo, Norway*
e-mail: *susanne.buiter@ngu.no*
session: *Geodynamics*

Numerical experiments of continental rifting often start from laterally homogeneous crustal layers with an inserted prescribed inhomogeneity to trigger deformation. Some examples of the prescribed inhomogeneity are a thermal anomaly, a variation in Moho geometry, or an inherited weak region. This approach has the advantage of controlling the location of rifting and keeping the rift buffered from boundary effects of the model domain. Yet a review of present-day passive margins quickly reveals that most passive margins are built on former collision zones. This is perhaps not surprising as continents are long-lived and therefore have undergone several deformation phases, increasing the likelihood of a rift forming at or near a suture. But collision zones can also act as intrinsic rift-localizers for several reasons: rifting at a suture may be initiated by extensional collapse of the mountain chain, the thicker crustal root of orogens and their associated increase in heat producing elements makes orogens thermally weak, and inherited thrust faults form large-scale heterogeneities.

Here we use 2-D numerical experiments to explore the role of inherited crustal structures on continental rifting and passive margin formation by actually making inherited collision zones. We first examine a series of experiments in which we explicitly prescribe collisional structures, such as increased Moho depth and inherited thrust zones. Differences in extension duration (the time from rift initiation to break-up) and crustal shear zone patterns result from varying the prescribed collisional structures. Overall the experiments have relatively fast break-up and develop short crustal tapers. Our second series of experiments builds a Wilson Cycle of subduction, collision, and extension. Closure of a 60 Ma ocean leads to continental collision and slab break-off, followed by some tens of kilometres of slab eduction. We use this set-up to investigate how extension localizes on a former continental collision zone. We will present first results of the roles of post-collision thermal equilibration time, lower crustal rheology, and shear zone healing on the evolution of passive margins that develop on continental collision zones.

Modelling subsidence history of rift-type basins

Mauro Cacace[1], Magdalena Scheck-Wenderoth[1,2]

[1]*Helmholtz Centre Potsdam GFZ – German Research Centre for Geosciences, Potsdam, Germany*
[2]*RWTH Aachen University, Department of Geology, Geochemistry of Petroleum and Coal, Aachen, Germany*
e-mail: *cacace@gfz-potsdam.de*
session: *Geodynamics*

This contribution aims to revaluate the character and evolution of large-scale crustal post-rift subsidence of basins that formed and evolved within extensional tectonic settings. Continental margins and intra-continental basins have been conventionally explained in terms of time-dependent thermal contraction of a thermal anomaly formed at the time of basin initiation. A common feature of models based on generic principles is to predict a post-rift subsidence component decaying exponentially in time with a rate controlled by the thermal diffusivity of the mantle lithosphere only. It has being now recognized that additional thermal and mechanical processes may modify (retarding, reducing or enhancing) the overall thermal subsidence pattern. However, their impact on the resulting 3D basin evolution is still to be quantified yet. Such processes comprise regional compensation to time varying sediment loading and internal thermal stresses, non–linear lithosphere thickening due to coupling between 3D conductive mantle cooling and thermal blanketing by low conductive sediments, and accelerated subsidence in response to vertical advection of the mantle lithosphere in response of mechanical loading by sediments and eustatic sea level changes. Conventional models which are based on first-order principles and which do not consider these "low-order" thermo-mechanical interactions are likely to result inadequate to explain the subsidence history as observed in many of the world's continental margin and intra-continental sedimentary basins.

The aim of this contribution is to analyze quantitatively the post-rift evolution of basins formed under extensional tectonics by means of 3D numerical modelling taking into account the dynamic coupling between sedimentation, lithospheric flexure and thermal contraction on the distribution, both in time and space, of the basin subsidence. We present and describe a quantitative tool to assist studies on the evolution of rift-type basins by means of a 3D thermo-mechanical program to model sedimentary basins evolution comprising: (1) uniform or non-uniform lithospheric stretching and related initial subsidence; (2) time-varying thermal evolution and associated subsidence/uplift component; (3) time-dependent loading distributions (sedimentation and sea level changes) and resulting vertical deformation; and (4) thermal effects on the mechanical structure of the lithosphere in terms of EET variations both in time and space by means of different rheologies. Versatility of the program stems from its modular structure that enables to address a variety of lithospheric processes and to account for the coupling among those, see Figure 1.

Efforts have been made to integrate into a unified modelling platform up-to-date concepts of the thermo-mechanical behaviour of the lithosphere in response to internal and external forcing. Active sediment deposition is considered to occur in time in the overlying basin domain. The thermal state and evolution of the forming basin is fully coupled with the evolving thermal configuration of the deeper crustal and mantle lithosphere. The thermal evolution of the system is governed by 3D conduction considering the effects of thermal

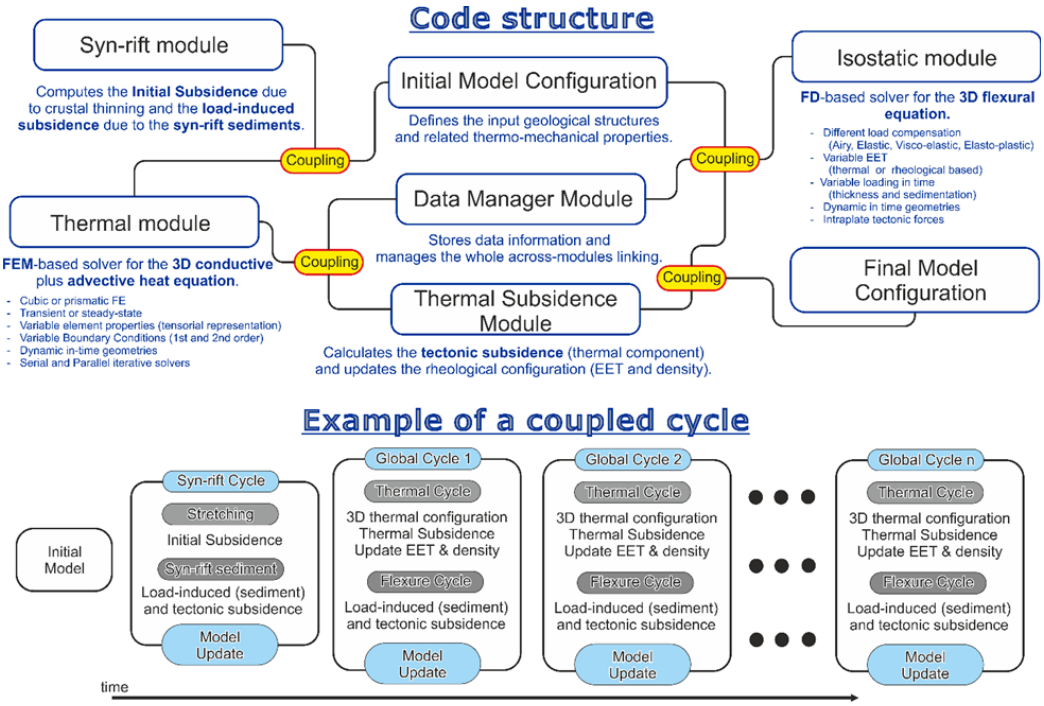

Fig. 1.: (Upper Figure) Schematic representation of the code structure illustrating the different modular components and combinations of across-modules coupling available. (Lower Figure) Example of a coupled cycle to model the subsidence evolution of a rift-type basin.

cooling as well as sediment loading and/or sea level changes. The lithosphere-asthenosphere boundary (LAB) is modelled as a thermal boundary whose location and geometry change in time in response to the computed thermal evolution. Lithospheric deformation occurs due to mechanical loading (sedimentation and sea-level changes) as well as time-dependent thermal stresses (bending moment and intraplate forces) due to a varying thermal configuration.

Applicability of the program to complex geological systems is ensured by accounting for variations through time and space of all rock properties, whether thermal or mechanical, as well as loading functions, sedimentation, thermal and intraplate stresses. Functional dependency of rock thermal properties on computed state variables (pressure and temperature) are considered. In this regard, the program enables not only to model the temporal evolution of a basin in a self-consistent way based and depending on the physics implemented, but it also offers enough flexibility to incorporate detailed information of the sedimentary succession and of the deeper crustal and mantle configuration as preserved at present. Therefore, data-based 3D lithosphere-scale geological model can be used to derive input parameters (lithosphere geometry and sediments thickness), while backward in time backstripping of these models can assist the forward modelling efforts by providing constraints on the configuration of the basin at the time of its initiation. The main advantages are (1) to determine how the rifting processes producing a 3D spatially variable stretching of the lithosphere, including syn-rift sediment deposition, might impact the post-rift evolution of the basin and the associated accumulation space for the sedimentary systems; and (2) to quantify the impact of the flexural behaviour of the lithosphere in response to both the post-rift thermal evolution (i. e. lithosphere cooling) and sedimentation history (i. e. gradual loading) on the post-break up vertical movement.

Strain localization during compression of a laterally heterogeneous lithosphere

Elisa Calignano[1], Dimitrios Sokoutis[1,2], Ernst Willingshofer[1]

[1]*Faculty of Geosciences, Department of Earth Sciences, Utrecht University, Budapestlaan 4, PO Box 80021, 3508 TA Utrecht, The Netherlands*
[2]*Department of Geosciences, University of Oslo, PO Box 1047 Blindern, N-0316 Oslo, Norway*
e-mail: *E.Calignano@uu.nl*
session: *Geodynamics*

Introduction

First order large scale stress fields, associated with active plate tectonic processes, interact with lateral heterogeneities in the lithosphere and generate strain redistribution [Zoback, 1992].

Continental lithosphere exhibits lateral variation in its mechanical properties, as evidenced from observations and supported by mechanical models [Audet and Bürgmann, 2011; Burov, 2011; Ranalli, 1997; Tesauro et al., 2012]. Lateral variation of strength in the lithosphere has been proven to be an important factor controlling the localization of deformation and far-field strain transmission [Sokoutis et al., 2005; Tommasi and Vauchez, 1997; Willingshofer et al., 2005; Ziegler et al., 1998]. Numerous modelling studies investigated the localization of deformation in compressional settings in case of lithospheric weak zones flanked by stronger domains. Such models have been successfully applied to examples of rift inversion [Brun and Nalpas, 1996; Cerca et al., 2004] or compression of weak orogenic wedges at plate boundaries [Willingshofer et al., 2005].

In this contribution, we focus on the strain redistribution resulting from the presence of a stronger rheological heterogeneity embedded in a weak lithosphere. To this purpose we use lithospheric scale analogue models. The experiments have been grouped in two sub-series characterized by different investigated parameters. First we investigated the role of varying convergence velocity and thickness of the upper brittle mantle when a strong lithospheric domain strikes perpendicular to the convergence direction. Both these parameters play an important role in the crust-mantle coupling. Subsequently we kept these two parameters constant and we varied the orientation of the rheological boundaries with respect to the convergence direction. In fact, reactivated lithosphere heterogeneities are often observed to strike oblique with respect to the main horizontal stress field.

Experimental set-up and modelling procedure

Figure 1 illustrates the set-up and different geometrical configurations for the presented experiments. Strength envelopes are representative for the very initial stage of deformation. All experiments consisted of three domains with different mechanical properties: two external blocks shared the same lithospheric stratification (reference lithosphere) and one central block where the increase in strength with respect to the reference lithosphere was achieved by increasing the brittle/ductile ratio in the crust.

The reference model lithosphere was defined by a four layers rheological stratification (brittle upper crust/ductile lower crust/brittle upper mantle/ductile upper mantle) representative for a stabilized lithosphere, characteristic for regions with low geothermal gradient [Afonso and Ranalli,

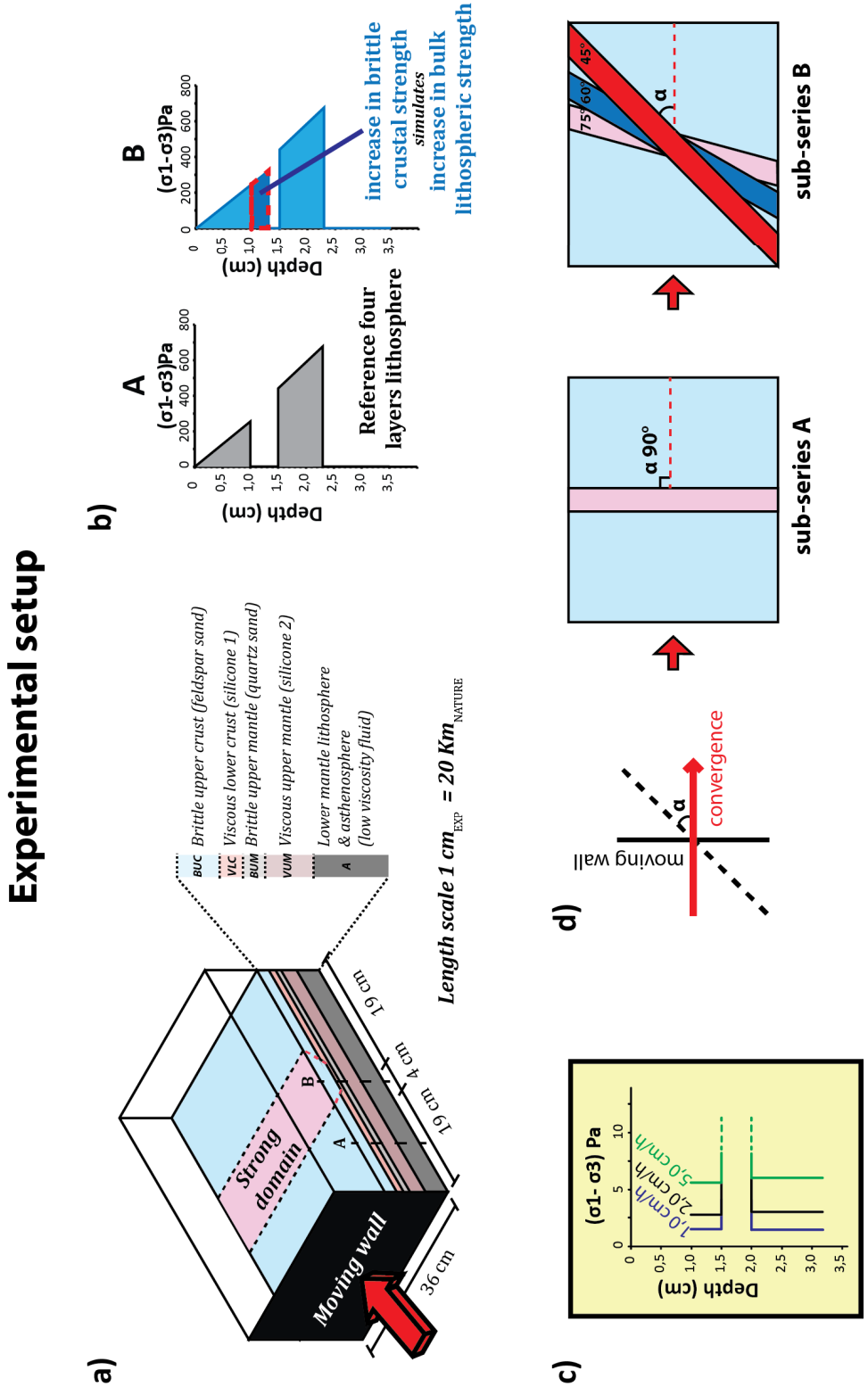

Fig. 1.: a) Sketch of the experimental set-up; **b)** representative strength profiles calculated for a convergence velocity of 1 cm/h; **c)** effect of different convergence velocities on the strength on the ductile layers and crust-mantle coupling; **d)** top view of the experiments: in sub-series A the strong domain has been kept parallel to the moving wall, while in sub-series B different obliquity angle have been tested.

2004] (Figure 1a).

The brittle crust and brittle upper mantle were simulated with dry feldspar and quartz sand respectively, while the lower crust and ductile lithospheric mantle were represented with silicone mixtures characterized by viscous non-Newtonian behaviour. The model lithosphere was resting on a high density and low viscosity fluid mixture representing the lower lithospheric mantle and asthenosphere. This facilitated the isostatic compensation. The density of the lithospheric mantle was lower than the asthenospheric fluid in all experiments, so that subduction was impeded.

The models were built inside a transparent Plexiglas box with dimensions 36 cm x 42 cm x 15 cm equipped with an internal moving wall. Experiments have been performed in normal gravity field. Deformation was monitored during the experiments with top view pictures and laser scanning at regular time intervals. At the end of each experiment the model was cut in cross sections parallel to the convergence direction in order to visualize the internal deformation at the latest experimental stage.

Preliminary Results

Experimental outcomes confirmed the role of lateral strength contrast in the lithosphere as an important factor controlling strain redistribution in compressional settings (Figure 2, 3).

In presence of a strong domain oriented perpendicular to the convergence direction deformation always localized along the rheological boundaries (Figure 2). Strain rate governed the geometry of the deep lithospheric structure. High convergence velocity resulted in asymmetry of the lithospheric root and main transport direction towards the moving wall (Experiment 1). A more symmetric deep lithospheric root characterized experiments with low convergence velocity (Experiment 2).

Brittle/ductile ratio in the lithospheric mantle determined the absence (low B/D) or presence (high B/D) of faults in the upper brittle mantle and the width of the area affected by upper crustal faults. Distributed deformation in the upper brittle crust characterized Experiment 3 where the increased brittle mantle thickness enhanced the decoupling along the ductile lower crust (Figure 2).

When the strong domain was oblique to the convergence direction, deformation resulted only partially localized along the rheological boundaries, due to the along-strike increase in distance from the moving wall (Figure 3 b). Two main thrust systems with different transport direction developed, connected by a complex transition zone (Figure 3 b).

The presented modelling results provide valuable insight for the strain localization in intraplate settings under various rheological and geometrical configurations and are applicable to natural areas.

References

Afonso, J. C., and G. Ranalli (2004), Crustal and mantle strengths in continental lithosphere: is the jelly sandwich model obsolete?, Tectonophysics, 394, 221–232, doi:10.1016/j.tecto.2004.08.006.

Audet, P., and R. Bürgmann (2011), Dominant role of tectonic inheritance in supercontinent cycles, Nat. Geosci., 4, 184–187, doi:10.1038/ngeo1080.

Brun, J.-P., and T. Nalpas (1996), Graben inversion in nature and experiments, Tectonics, 15, 677–687, doi:10.1029/95TC03853.

Burov, E. B. (2011), Rheology and strength of the lithosphere, Mar. Pet. Geol., 28, 1402–1443, doi:10.1016/j.marpetgeo.2011.05.008.

Cerca, M., L. Ferrari, M. Bonini, G. Corti, and P. Manetti (2004), The role of crustal heterogeneity in controlling vertical coupling during Laramide shortening and the development of the Caribbean-North America transform boundary in southern Mexico: insights from analogue models, Geol. Soc. Lond. Spec. Publ., 227, 117–139, doi:10.1144/GSL.SP.2004.227.01.07.

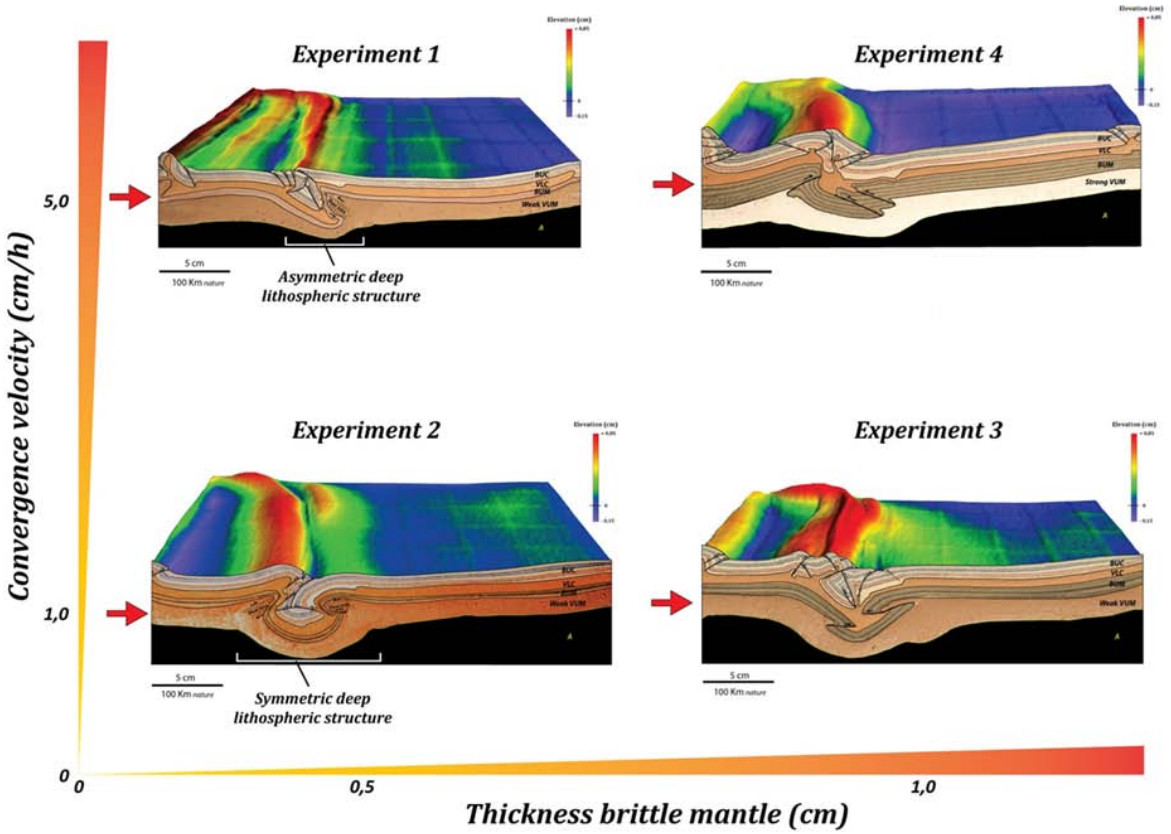

Fig. 2.: Experimental results for sub-series A. Representative cross sections and DEM (Digital Elevation Models) of the experiments' surface at 20 % bulk shortening for different convergence velocities and thickness of the brittle upper mantle.

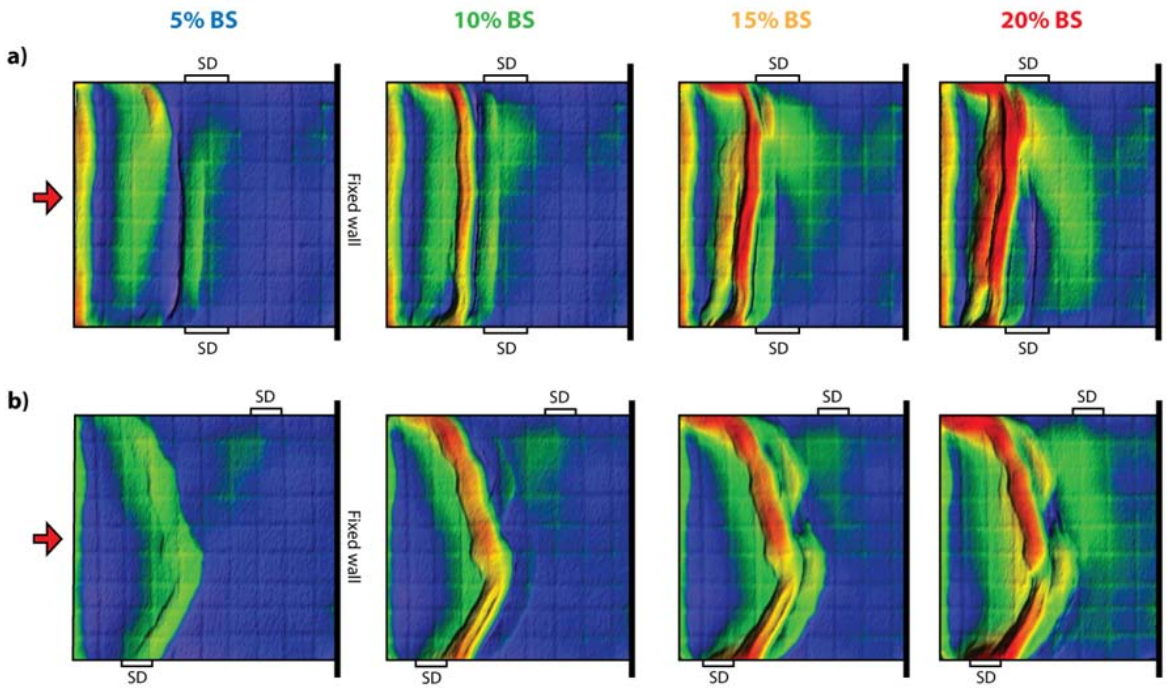

Fig. 3.: Comparison of experiments with different orientation of the strong domain. The evolution at subsequent bulk shortening (% BS) steps is shown with the help of DEMs. **a)** Experiment 3 (sub-series A): the strong domain (SD) strikes perpendicular to the convergence direction; **b)** Experiment 5 (sub-series B): the strong domain (SD) strikes at 60° to the convergence direction. Convergence velocity is $1\,\mathrm{cm\,h^{-1}}$ for both experiments.

Ranalli, G. (1997), Rheology of the lithosphere in space and time, Geol. Soc. Lond. Spec. Publ., 121, 19–37, doi:10.1144/GSL.SP.1997.121.01.02.

Sokoutis, D., J.-P. Burg, M. Bonini, G. Corti, and S. Cloetingh (2005), Lithospheric-scale structures from the perspective of analogue continental collision, Tectonophysics, 406, 1–15, doi:10.1016/j.tecto.2005.05.025.

Tesauro, M., M. K. Kaban, and S. A. P. L. Cloetingh (2012), Global strength and elastic thickness of the lithosphere, Glob. Planet. Change, 90–91, 51–57, doi:10.1016/j.gloplacha.2011.12.003.

Tommasi, A., and A. Vauchez (1997), Continental-scale rheological heterogeneities and complex intraplate tectono-metamorphic patterns: insights from a case-study and numerical models, Tectonophysics, 279, 327–350, doi:10.1016/S0040-1951(97)00117-0.

Willingshofer, E., D. Sokoutis, and J.-P. Burg (2005), Lithospheric-scale analogue modelling of collision zones with a pre-existing weak zone, Geol. Soc. Lond. Spec. Publ., 243, 277–294, doi:10.1144/GSL.SP.2005.243.01.18.

Ziegler, P. A., J.-D. van Wees, and S. Cloetingh (1998), Mechanical controls on collision-related compressional intraplate deformation, Tectonophysics, 300, 103–129, doi:10.1016/S0040-1951(98)00236-4.

Zoback, M. L. (1992), First- and second-order patterns of stress in the lithosphere: The World Stress Map Project, J. Geophys. Res. Solid Earth, 97, 11703–11728, doi:10.1029/92JB00132.

3-D numerical modeling of subduction evolution of the western Mediterranean region

M. V. Chertova[1], W. Spakman[1,2], A.P. van den Berg[1], T. Geenen[3], D.J.J. van Hinsbergen[1]

[1] *University of Utrecht, Utrecht, the Netherlands*
[2] *Centre of Earth Evolution and Dynamics (CEED), University of Oslo, 0316 Oslo, Norway*
[3] *SURFsara, Amsterdam, the Netherlands*
e-mail: *M.V.Chertova@uu.nl*
session: *Geodynamics*

This research is focused on various aspects of the evolution of the western Mediterranean region. This region underwent a long and complicated history of slab rollback and lithosphere tearing, for which the only direct observations come from its geological history and present day mantle structure inferred by tomographic data. Different tectonic reconstructions were proposed for this region based on these observations. Despite the general agreement on the initiation of subduction rollback around 35Ma and slab buoyancy being a major driving force leading to the present day slab under the Rif-Gibraltar-Betic (RGB) these reconstructions propose distinctly different initial configuration of the subduction zone, as well as temporal evolution of the region during 35 Ma to 0 Ma. We categorize all tectonic reconstructions into three different evolution scenarios and based on this in the first part of the research we investigated the evolution of the region employing 3D thermo-mechanical numerical modeling. The criteria to discriminate between these reconstructions are fits between observed and predicted slab and major subduction evolution temporal constraints, which are Mid-Miocene (16 Ma) thrusting of the Kabylides onto the African margin and a stalled subduction under the RGB arc since the Tortonian (~8 Ma).

The first scenario (S 1) proposes that subduction rollback started from a 300 km long trench to the southeast from Baleares. Initially rollback occurred southward with a rotation to westward, but changed its direction to westward after reaching the African margin (e. g. Rosenbaum et al. 2002; Spakman and Wortel 2004; van Hinsbergen et al. 2014). In the second scenario (S 2) a long trench from Gibraltar to Baleares is assumed with predominantly southward rollback (e. g. Gueguen et al. 1998; Faccenna et al. 2004). In the last, third scenario (S 3), it is proposed that subduction has started at the African margin with predominantly northwestward rollback (Verges and Fernandez 2012).

From these scenarios we configured three different initial buoyancy conditions in terms of initial geometry of subduction zone at 35Ma and optimize developed models by fitting the major morphological and temporal constraints varying the parameters for non-linear rheology implemented in our models and the geometrical settings within a range appropriate for each reconstruction scenario.

We obtained a good match between present-day mantle structure tomography (Spakman and Wortel 2004, Bezada et al. 2013) and predicted slab morphology for subduction models based on S 1 (Fig. 2). For S 3 we could simulate the curved slab structure under Betics in top 200 km, however, the deep part of the slab extends far to the south under the Africa, which is inconsistent with tomographic constraints. For the scenario S 2 we could not find a subduction model that reasonably fits the observed mantle structure under Gibraltar (Fig. 2).

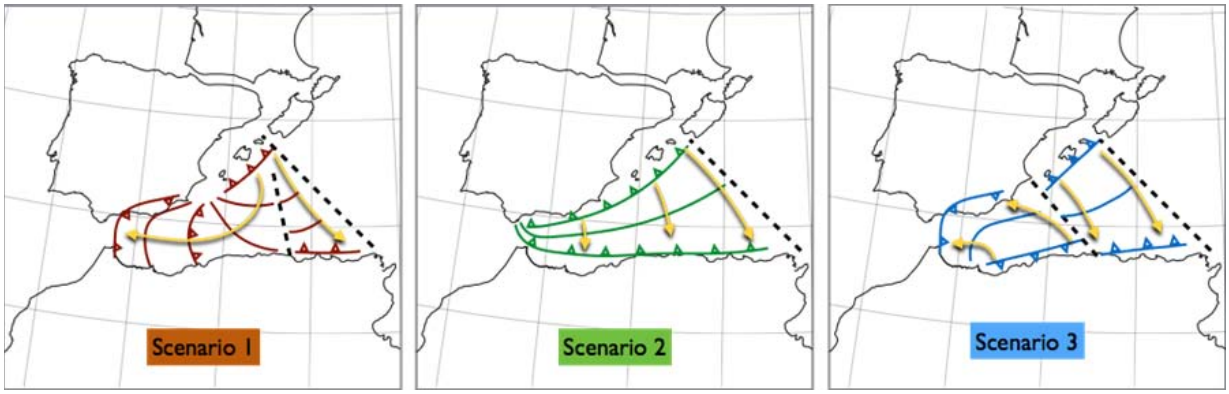

Fig. 1.: An illustration of rollback as portrayed in the three different reconstruction scenarios: scenario 1 (S 1), scenario 2 (S 2) and scenario 3 (S 3). Dashed lines represent proposed transform faults regions.

We concluded from our experiments that only models with the subduction evolution starting from a short NW-dipping subduction zone under Baleares at 35 Ma defining scenario S 1 can successfully predict trench rollback to the African margin of the RGB- and Kabylides slabs, westward tearing of the African margin and slab rotation by more than 180°, a dominant westward opening of the Algerian basin, and, finally a resulting slab under Gibraltar around 8 Ma.

This part of the research provides us with the favorable subduction framework for future investigations of the geological/tectonic evolution of the western Mediterranean region. Based on this we continued our research with investigation on the influence of absolute plate motions on the subduction evolution of this region. For a regional Earth subduction zone absolute plate motions might be an important factor controlling the subduction evolution and present-day stress field.

So far, instantaneous models of the western Mediterranean region as well as tectonic reconstructions only utilize relative plate motion reference frames with fixed Europe or Africa. However, only when considering the evolution of this region in an absolute plate motion frames for Africa and Iberia one can investigate the coupling between plate motion, mantle, and subduction. By using 3D thermo-mechanical modeling, we evaluate the impact of adopting four different absolute plate motion frames on subduction evolution of the western Mediterranean region during the last 35 Ma. The first one is determined from the global moving hotspot reference frame (GMHRF) of Doubrovine et al. (2012) and three are invented frames: a motion model with an African plate fixed to the mantle, a model with a fixed Iberian plate and a model in which Africa motion is twice that of GMHRF. We kept the same relative Africa-Iberia convergent motion in all motion frames.

The numerical experiments started from the same paleogeography, rheology and subduction settings conforming to subduction scenario S 1. The models demonstrated distinctly different 3-D subduction evolution showing a critical sensitivity of slab morphology evolution on absolute plate motions adopted. We achieved the best results in terms of fitting present day mantle structure and major temporal constraints with the model based on GMHRF (Fig. 3). The model with faster Africa demonstrated significant decrease in lithosphere tearing and associated rollback and resulted in slab stalling at the longitude of the eastern Betics. The African-fixed or Iberia-fixed reference frames led to a too early slab arrival at Gibraltar (Fig. 3). The model with Iberia fixed also resulted in a slab located to the north of the tomographically observed slab with continental lithosphere involved into subduction process during the final phase of the rollback (Fig. 3).

Our models demonstrated a strong correlation between the increase in northward Africa mo-

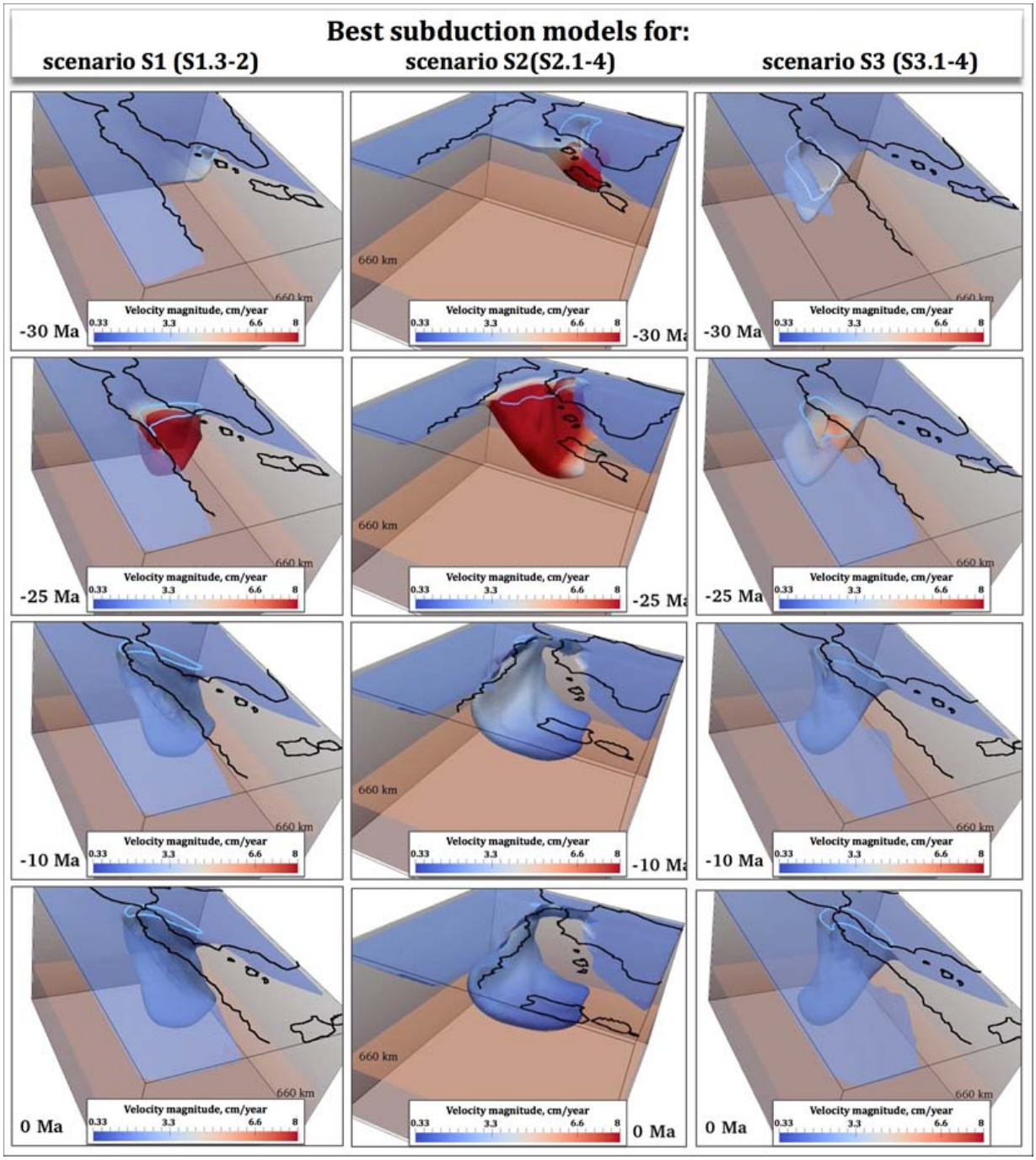

Fig. 2.: 3-D view on the evolution of the best model obtained for each reconstruction scenario. Left: model based on S 1, starting from a short trench at the Baleares margin, view from SE. Middle: model based on scenario S 2, starting from a long initial subduction zone and long slab, view from NE. Right: model based on scenario S 3, starting from a trench at the African margin, view from SE. Blue contours at the surface show the shape of the slab at depth of $200\,\mathrm{km}$.

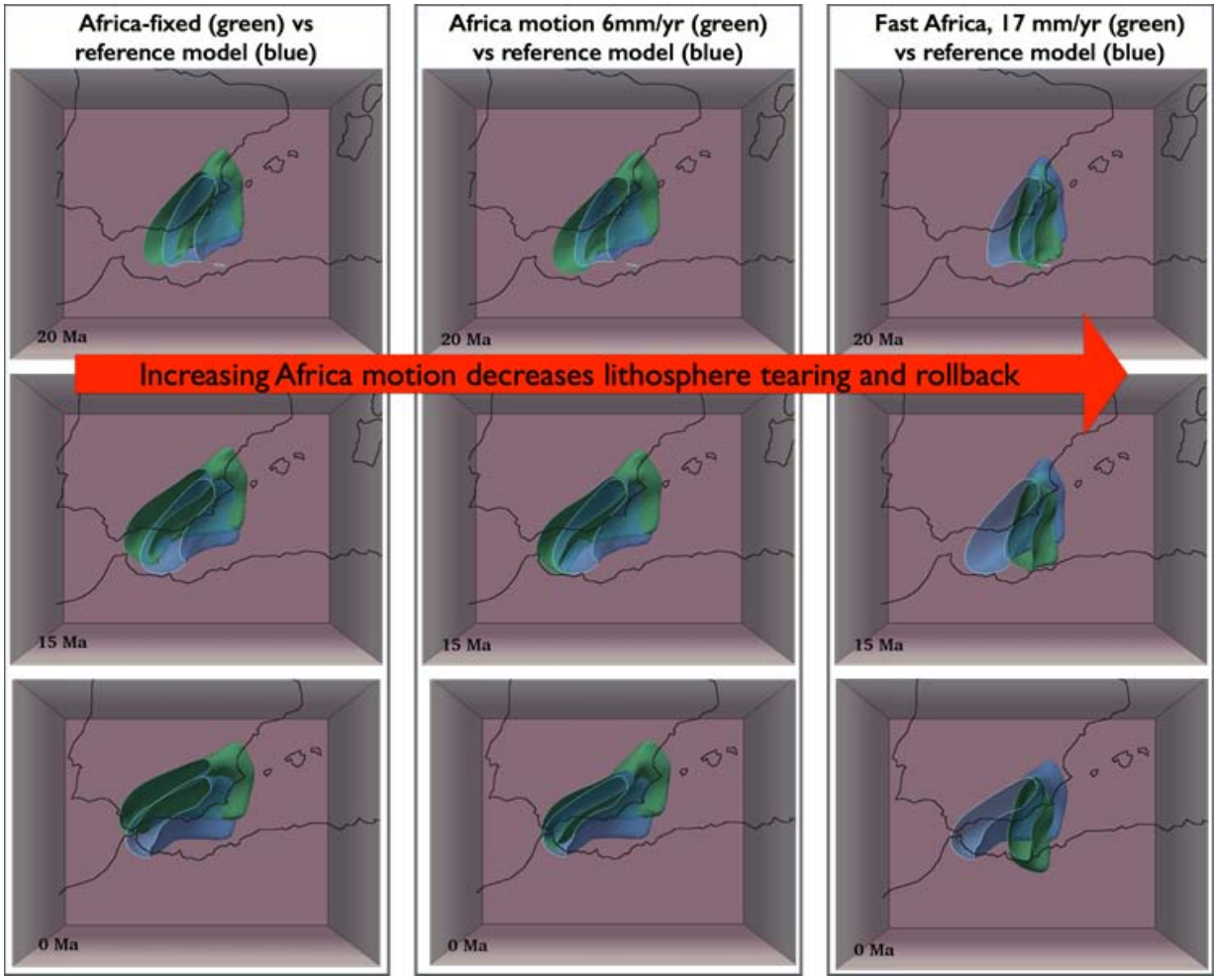

Fig. 3.: Slab morphology in the four subduction models at 20 Ma and 15 Ma. The reference model is shown in blue in all panels and belongs to a northward Africa motion of 8 mm/a. The first column shows the Africa-fixed model; the second column the Iberia-fixed model; the third column shows the model with two-times faster Africa. The 1400 K isotherm is shown from 200 km downward. The coastlines are shown in absolute plate motion frame of the reference model, i. e. GMHRF.

tion and a decrease in the speed of westward slab rollback along the African margin (Fig. 3). We relate this to an increased slab-mantle coupling and this provided new insight into propagation and dynamics of subduction transform edge propagator (STEP) faults as proposed by Govers and Wortel (2005). We conclude that absolute plate motions of the subducting and overriding plates can induce important dynamic slab-mantle couplings that may strongly affect subduction evolution. Furthermore, accurate absolute plate motion constraints are crucial for modeling subduction evolution and dynamics in natural settings and visa versa, modeling of natural subduction may provide novel constraints on absolute plate motions.

References

Bezada M.J., and E.D. Humphreys (2012), Contrasting rupture processes during the April 11, 2010 deep-focus earthquake beneath Granada, Spain, Earth and Planetary Science Letters, 353–354, 38-46, doi: 10.1016/j.epsl.2012.08.001.

Doubrovine, P. V., B. Steinberger, and T.H. Torsvik (2012), Absolute plate motions in a reference frame defined by moving hotspots in the Pacific, Atlantic and Indian oceans. Journal of Geophysical Research, 117, B09101, doi: 10.1029/2011JB009072.

Govers, R. and M.J.R. Wortel (2005), Lithosphere tearing at STEP faults: Response to edges of subduction zones, Earth and Planetary Science Letters, 236 (1-2), pp. 505-523.

Gueguen, E., C. Doglioni, and M. Fernandez (1998), On the post-25 Ma geodynamic evolution of the western Mediterranean, Tectonophysics, 298, 1–3, 259-269, doi: 10.1016/S0040-1951(98)00189-9.

Faccenna C., C. Piromallo, A. Crespo-Blanc, L. Jolivet, and F. Rossetti (2004), Lateral slab deformation and the origin of the western Mediterranean arcs. Tectonics;23:TC1012. doi:10.1029/2002TC001488.

Rosenbaum, G., G.S. Lister, and C. Duboz (2002), Reconstruction of the tectonic evolution of the western Mediterranean since the Oligocene. Journal of the Virtual Explorer, 8, 107–130.

van Hinsbergen, D.J.J., R.L.M. Vissers, and W. Spakman (2014), Origin and consequences of western Mediterranean subduction, rollback, and slab segmentation, Tectonics

Vergés, J., and M. Fernàndez (2012), Tethys–Atlantic interaction along the Iberia–Africa plate boundary: The Betic–Rif orogenic system, Tectonophysics, 579, 144-172, doi:10.1016/j.tecto.2012.08.032.

Spakman W., and M.J.R. Wortel (2004), A tomographic view on western Mediterranean geodynamics. In: Ziegler P., editor. The TRANSMED Atlas-The Mediterranean Region From Crust to Mantle. Berlin: Springer, pp. 31-52.

Surface manifestations of low-buoyancy mantle plumes: Insights from geodynamic modeling

Juliane Dannberg, Stephan V. Sobolev

German Research Centre for Geosciences Potsdam GFZ, Germany
e-mail: *dannberg@gfz-potsdam.de*
session: *Geodynamics*

According to widely accepted models, mantle plumes ascend from the lower mantle and cause massive melting when their heads reach the base of the lithosphere. Classical geodynamic models consider plumes as purely thermal and thus predict a flattening of the plume head to a disk-like structure and thin plume tails. However, there are seismic observations and paleo-topography data that are difficult to explain with this classical approach. In addition, geochemical data indicate that plumes have a different composition than the average mantle material and it has been suggested a long time ago that subducted oceanic crust could be recycled by mantle plumes (Hofmann & White, 1981).

While recent numerical models have considered a different chemistry (Sobolev et al., 2011, Ballmer et al., 2013) to explain complex plume shapes or zoning within plumes, they are either restricted to only a part of the plume evolution or use simplified material models. However, due to the high density of recycled oceanic crust, thermo-chemical plumes are expected to have much smaller buoyancy than thermal plumes. Therefore it is especially important to incorporate realistic material properties as they can influence the plume dynamics crucially, and determine if a plume reaches the lithosphere or remains in deeper parts of the mantle.

We perform numerical experiments in 3D spherical shell geometry to investigate the dynamics of the plume ascent, the interaction between plume- and plate-driven flow and the dynamics of melting in a plume head. For that purpose, we use the finite-element code ASPECT (Kronbichler et al., 2012), which allows for complex temperature-, pressure- and composition-dependent material properties. Moreover, our models incorporate phase transitions (including melting) with the accompanying rheological and density changes, Clapeyron slopes and latent heat effects for the peridotite and eclogite phase, mantle compressibility and a highly temperature- and depth-dependent viscosity.

We study under which conditions low-buoyancy plumes ascend through the whole mantle, their internal chemical zoning and the structures they form in the upper mantle. We then compare these results to observations of dynamic topography, geochemical trends and melting degrees of ocean island basalts, buoyancy fluxes and seismic tomography.

Modeling shows that high plume buoyancy results in plumes directly advancing to the base of the lithosphere, while plumes with slightly lower buoyancy pond in a depth of 300 km to 400 km and form pools or a second layer of hot material (Figure 1). These structures become asymmetric and finger-like channels begin to form when the plume gets entrained by a quickly moving overlying plate (Figure 2). Our models also suggest that thermo-chemical plumes ascend in the mantle much slower compared to thermal plumes and have thicker plume tails. The conversion of plume excess temperatures to anomalies in seismic velocity shows that thermo-chemical low-buoyancy plumes can explain a variety of features observed by seismic tomography much better than purely thermal plumes.

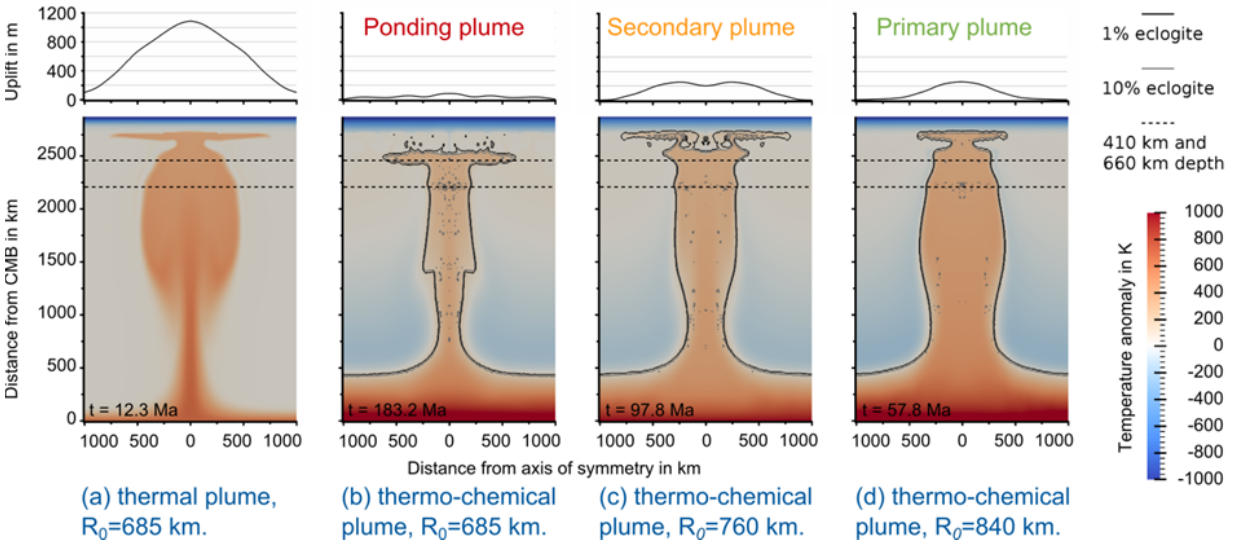

Fig. 1.: Snapshots of a thermal (a) and three thermo-chemical (b, c, d) plumes with different volumes, and the generated surface uplift. Colors represent excess temperature, the solid lines are isolines of chemical composition and dashed lines mark $410\,\mathrm{km}$ and $660\,\mathrm{km}$ depth. In dependence of their initial temperature and buoyancy flux thermo-chemical plumes show three different regimes: Primary plumes (d) ascend directly to the lithosphere, plumes with slightly lower buoyancy pond in $300\,\mathrm{km}$ to $400\,\mathrm{km}$ depth and generate smaller secondary plumes (c), and even lower buoyancy leads to plumes not reaching the lithosphere, but staying below $300\,\mathrm{km}$ depth. The surface uplift caused by a thermo-chemical plume is about an order of magnitude smaller than that of a purely thermal plume.

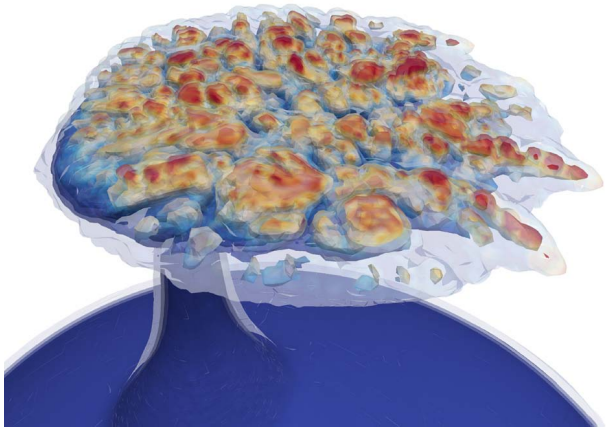

Fig. 2.: A thermo-chemical plume rising from the core-mantle boundary and getting entrained by an overlying, moving plate. The figure shows the isosurface of the chemical composition (fraction of recycled oceanic crust) and colors give an estimate of the melt fraction.

References

Hofmann, A.W, & White, W.M. (1981): Mantle plumes from ancient oceanic crust – Earth and Plaentary Science Letters, 57, 421-436.

Sobolev, S.V. et al. (2011): Linking mantle plumes, large igneous provinces and environmental catastrophes – Nature, 477, 312-316.

Kronbichler, M., Heister, T. & Bangerth, W. (2012): High accuracy mantle convection simulation through modern numerical methods – Geophysical Journal International, 191, 12–29.

Ballmer, M. D., G. Ito, Wolfe, C. J., and Solomon, S. C. (2013): Double layering of a thermochemichal plume in the upper mantle beneath Hawaii – Earth Planet. Science Lett., 376, 155-164.

Plumes to plate tectonics: insights from laboratory experiments

A. Davaille

Laboratoire FAST, CNRS/Université Paris-Sud, Bat. 502, Rue du Belvédère, 91405 Orsay, France
e-mail: *cdavaille@fast.u-psud.fr*
session: *Geodynamics*

Summary

Because laboratory experiments are crucial for exploring new physics and testing theories, they have long played a central role for understanding the physics that governs thermal convection and mantle dynamics. Mantle dynamics on geological time scales is dominated by "fluid" behavior, so that liquids around room temperature, and fluid mechanics techniques, can generally be used. With the development of computer power and lasers, it has become possible in the last years to measure the temperature, velocity, concentration and deformation fields in experimental tanks. Laboratory experiments can therefore also constitute important tools for benchmarking complex numerical codes. Moreover, the rheological characterization of complex fluids has made important progress. I shall review recent results on the dynamics and diversity of mantle plumes and lithospheric intrusions, and on the generation of asymmetric subduction and plate tectonics in the laboratory.

Plume signatures in a complex fluid: velocity, temperature, compositional fields

It is now possible to follow the ascent and growth of a starting plume through both its velocity and temperature fields (fig. 1). Key measurements are then the velocity of the stagnation point located on the top of the plume head V_A, and the velocity of the particles at this point $V_z(A)$. The former will give the same information as following dye (which underlines the maximum deformation) or following shadowgraph (which underlines the maximum temperature gradient), while $V_z(A)$ gives the same value as the uplift of the maximum vorticity centers. The latter constitutes the "true" plume head velocity. The difference $V_A - V_z(A)$ represents plume head growth by thermal diffusion, which remains quite small. We observe that the plume samples mostly the material coming from the thermal boundary layer above the heat source (fig. 1), in agreement with early numerical simulations (Farnetani and Richards, 1995).

When the bottom of the tank contains denser fluid (fig. 2 – left), the interplay of the compositional and thermal buoyancies produces complicated plume morphologies and histories which depend strongly on the buoyancy ratio B (Kumagai et al, 2008).

On the other hand, in a visco-elasto-plastic fluid (e. g. Carbopol), the morphology of plumes is very different from the mushroom-shape observed in newtonian fluids: a plug flow develops inside the plume thermal anomaly, producing a rising finger-shape with strong shear zones confined along its edges (fig. 2 – right)). And two conditions must now be fulfilled for an instability to develop and rise: 1) the Yield number Ψ_0 comparing the buoyancy-induced stress to the yield stress, should be greater than a critical value $\Psi_0 \approx 6$ (Davaille et al, 2013); and 2) the Bingham number B_i, comparing the yield stress to the viscous stresses, needs to be locally smaller

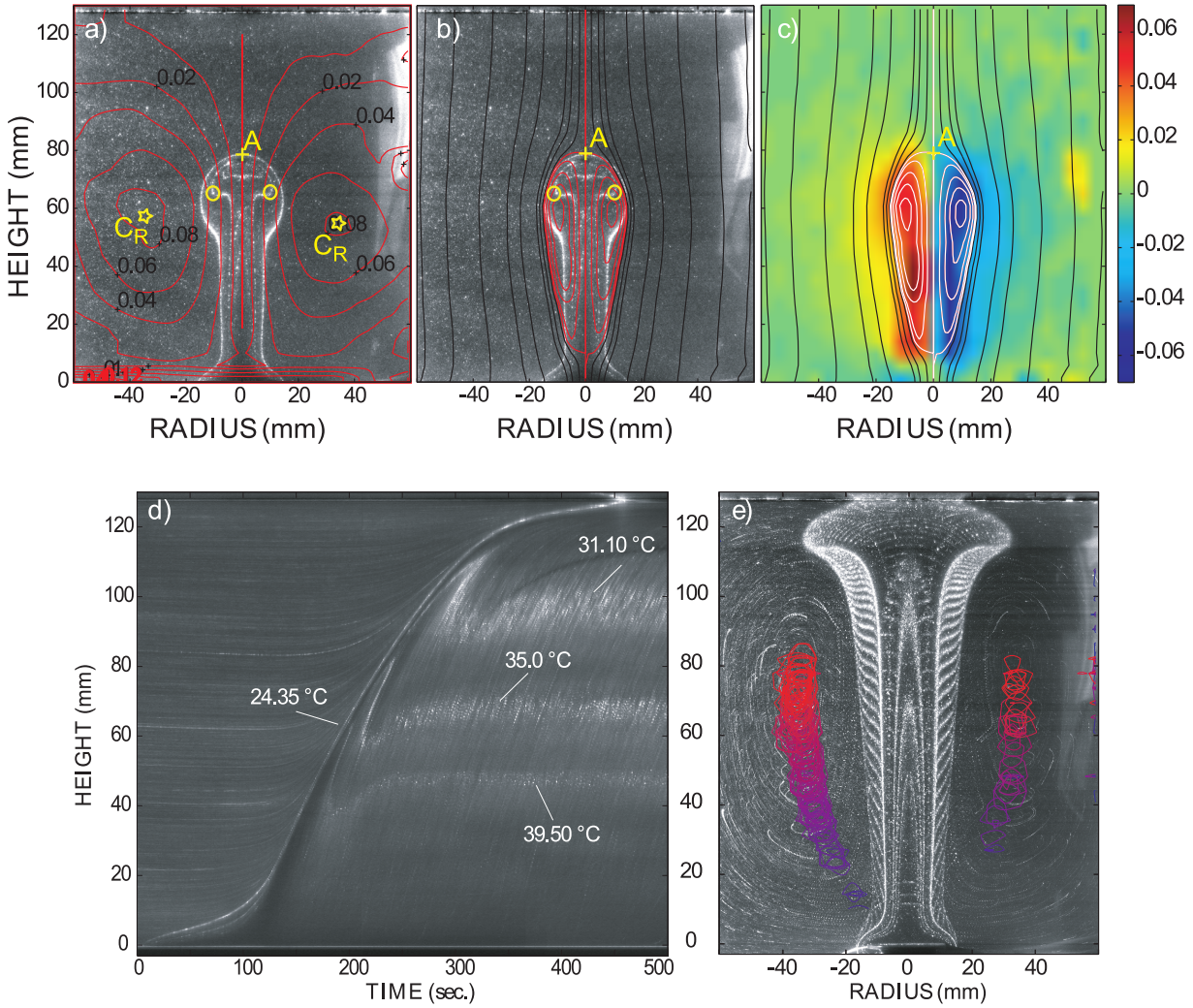

Fig. 1.: Thermal starting plume in sugar syrup ($\gamma = 47$). a) Streamlines in the laboratory reference frame on top of the plume image. The yellow cross represents the stagnation point A at the head top, the stars the rotation centers CR in the laboratory reference frame, and the yellow open circles point to the vorticity extrema. b) Streamlines in the "plume head" reference frame on top of the plume image, and c) on top of the vorticity field. d) Plume uplift through time followed through the image intensity along the plume vertical axis; the bright lines are the isotherms (labelled in white). e) Superposition of the plume images taken every 5 s between t = 100 and t = 500 s. The internal structure of the plume conduit, with its 5 isotherms, appears to be steady. The outer bright line underlines the steady growth of the plume head. The positions of the centers of rotation (corresponding to the position of the maximum values of the stream function) are represented in blue (early times) to red (late times) (adapted from Davaille et al., 2011a).

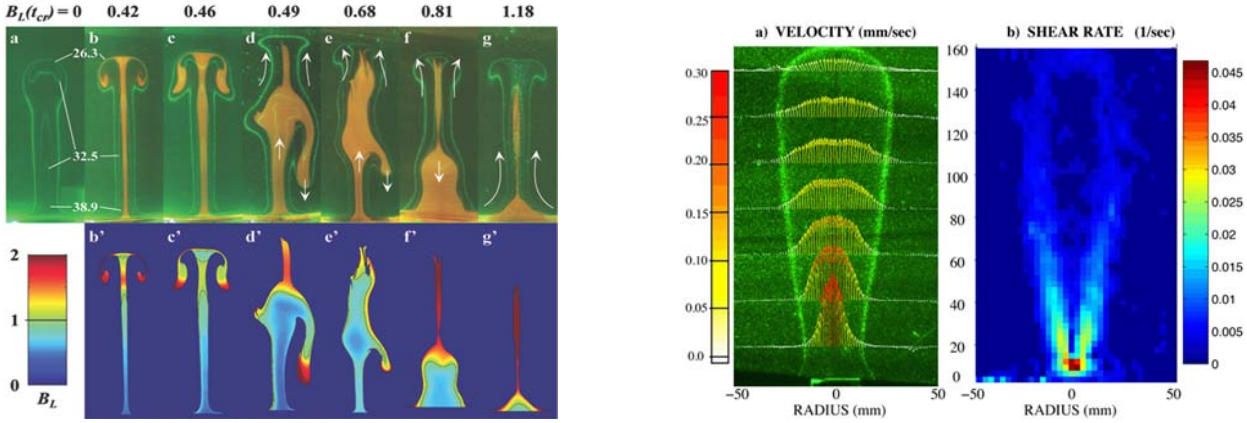

Fig. 2.: Left: Different morphologies as B increases. A thermochemical plume was generated on a flat heater with a constant power. Initially the orange denser material was in a thin layer at the bottom of the tank. The green lines are the isotherms. top) thermal and compositional fields. The white arrows indicate the fluid motions. bottom) local buoyancy ratio.(from Kumagai et al, 2008). Right : Thermal plume in a yield-stress and shear-thinning carbopol gel. a) Temper- ature (visualized by isotherms) and velocity structure. b) shear rate calculated from the velocity fields. Note how deformation is confined on the edges of the thermal finger. (from Davaille et al, 2013).

than 1. Moreover, the instability halts its ascent as soon as $\Psi_0 < \Psi_c$ or $Bi > 1$ (Massmeyer et al, 2013). The experimental finger-shaped plumes show strong similarities with diapiric intrusions in the Earth's lithosphere. A 10 km-diameter purely thermal anomaly could only be emplaced in a partially molten lithosphere (with $\sigma_0 \approx 100$ kPa), but the yield stress of the surrounding matrix could reach up to ~ 50 MPa if the instability also exhibits a chemical density anomaly.

Planetary dynamics: lessons from soft matter

On Earth, seismic tomography studies show that the subduction zones – and therefore the cold plates – distribution delimits two large cells in the mantle (the Pacific and the Indo-Atlantic "boxes"), each cell containing several hot instabilities (plumes). The existence of several scales of convection suggests that the Earth's mantle is in the "mobile lid" regime of convection in a strongly temperature-dependent viscosity (e. g. Solomatov, 1995; Androvandi et al, 2011). Given the mantle physical characteristics, this would imply that the effective viscosity of the lithosphere is not more than ~ 30 to 3000 times more viscous than the bulk mantle, in agreement with estimates using bathymetry and geoid constraints), regional models of subduction, or slab bending (Androvandi et al, 2011).

However, with an actual viscosity contrast across the lithosphere $\geq 10^7$, the Earth should be in the stagnant lid regime, i. e. a one-plate planet like for example Mars. So, if temperature-dependent viscosity is clearly a key ingredient for plate formation, this ingredient alone is not sufficient to generate Plate Tectonics convection. To make plate tectonics work, weakening and shear localization are also required. Moreover, the lithosphere can support over long time periods dormant weak zones (faults or rifts), which can be preferentially reactivated to become new plate boundaries. For years, experimentalists have been looking for an analogue fluid presenting the "right" kind of rheology to allow self-consistent, true plate tectonics. We are now using aqueous colloidal dispersions of nanoparticles, whose rheology depends strongly on the solid particle fraction ϕ_p and on the chemical activity a_χ, being Newtonian at low ϕ_p and low a_χ, and presenting yield stress, elasticity, and brittle

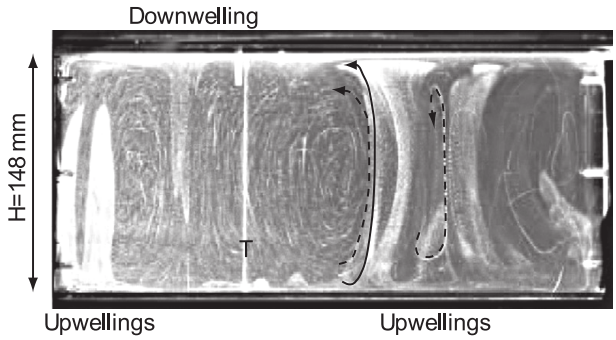

Fig. 3.: Experiment at high Rayleigh number and intermediate viscosity ratio (Rahot = 5.3x107; $\gamma = 142$). Snapshot of a vertical cross-section taken 8 cm from the front lateral wall. The bright lines are isotherms, except the clear straight line labelled 'T' at position x = 110 mm which is the thermocouple probe. Several hot plumes are seen while only one cold downwelling is observed. This situation resembles what is observed on Earth for example in the Pacific "box". (from Androvandi et al, 2011).

properties as ϕ_p or a_χ increase (Di Giuseppe et al, 2012). So by heating these fluids from below, as well as drying them (as an analogue to cooling) from above, several regimes can be observed whereas a visco-elasto-plastic skin forms at the surface and either stays there (convection under a stagnant lid), or breaks and sinks episodically in the fluid (episodic subduction, fig. 4 – left, Di Giuseppe and Davaille, 2010), or presents the continuous motion and renewal of surface plates (fig. 4 – right, Davaille et al, 2011b). The latter regime is close to the continuous plate tectonics observed on Earth, and subduction is always asymmetric.

References

Androvandi S., Davaille A., Limare A., Fouquier A. and Marais C. 2011. At least three scales of convection in a mantle with strongly temperature- dependent viscosity, Phys. Earth Planet. Int. 188, 132-141.

Davaille A., A. Limare, F. Touitou, I. Kumagai, J. Vatteville. 2011a. Anatomy of a laminar starting plume at high Prandtl number, Exp. Fluids, 50, 285-300.

A. Davaille, E. Di Giuseppe, S. Androvandi, M.-C. Renoult and F. Doumenc. 2011b. Convective regimes in "soft matter": implications for the dynamics of planetary interiors, EPSC-DPS 2011 Planetary Sciences, Nantes.

Davaille A., Gueslin B., Massmeyer A., Di Giuseppe E. 2013. Thermal in- stabilities in yield stress fluids: existence and morphology. J. Non-Newtonian Fluid Mech. 193, 144-153.

Di Giuseppe E., A. Davaille . 2010. Episodic Subduction arising from con- vection in a complex-rheology fluid: Insights from laboratory experiments, Geophysical Research Abstract 12, 07954.

Di Giuseppe, E., A. Davaille, E. Mittelstaedt, M. Franois. 2012. Rheo- logical and mechanical properties of silica colloids: from liquid Newtonian to brittle behavior, Rheologica Acta 51, 451-465.

Farnetani C.G., Richards M. A., 1995. Thermal entrainment and melting in mantle plumes, Earth Planet. Sci. Lett., 136, 251-267.

Kumagai I, Davaille A, Kurita K, Stutzmann E . 2008. Mantle plumes: Thin, fat, successful, or failing? Constraints to explain hot spot volcanism through time and space, Geophys. Res. Lett., 35, L16301.

Massmeyer A., E. Di Giuseppe, A. Davaille, T. Rolf, P.J. Tackley . 2013. Numerical simulation of thermal plumes in a Herschel-Bulkley fluid, J. Non- Newtonian Fluid Mech. 195, 32-45.

Solomatov S. 1995 Scaling of temperature- and stress-dependent viscosity convection. Phys. Fluids 7, 266-274.

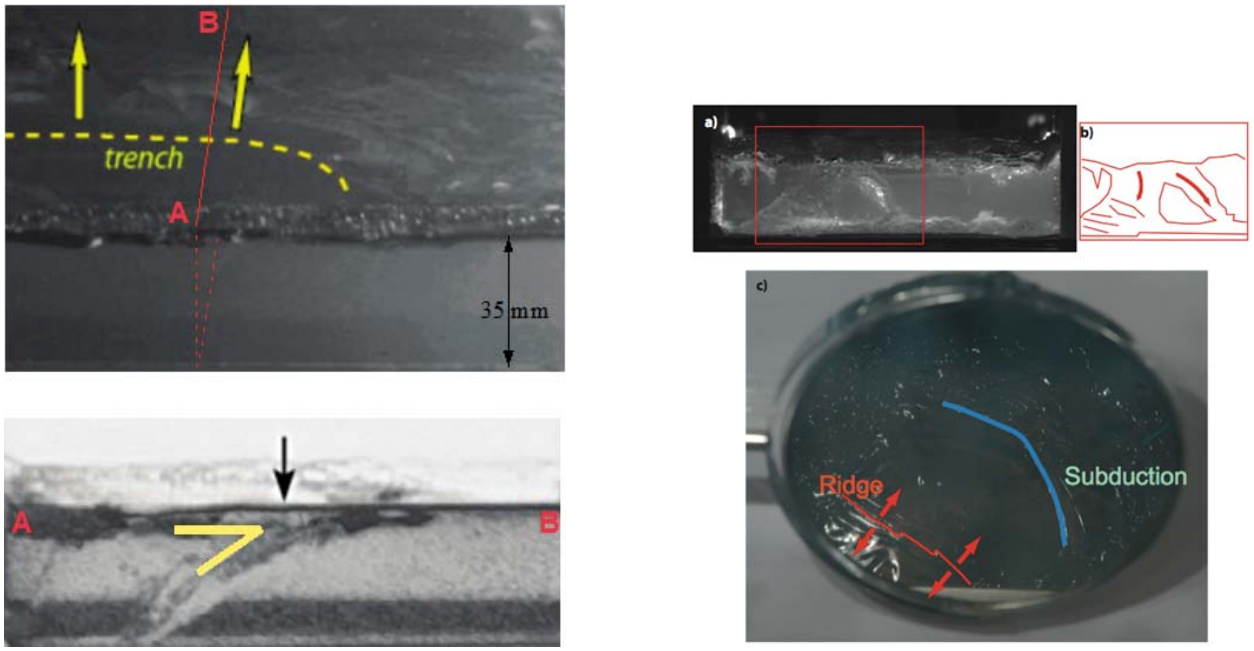

Fig. 4.: Left: Spontaneous asymmetric subduction in a layer of colloids dried from above at constant temperature and humidity. Top) view from above. The "trench" is outlined in yellow and the direction of trench rollback is indicated by the yellow arrows. Bottom) view from the side. The contrast has been enhanced to better see the subducting plate. The trench position is marked with a black arrow. (from Di Giuseppe & Davaille, 2010). Right : Convection in silica colloidal suspension: regime of continuous Plate Tectonics. a-b) View from the side. Two plates coming from the upper skin are subducting towards us. b) is the interpreted cartoon of the inset in a). The left subducting plate is folding and forming a pile on the tank bottom. c) View from the top: a spreading ridge is visible as well as a subduction zone.

Three dimensional laboratory models of subduction: plate interface, overriding plate deformation and energy dissipation

João C. Duarte, Zhihao Chen, Wouter P. Schellart, Alexander R. Cruden

School of Geosciences, Monash University, Melbourne, Australia
e-mail: *joao.duarte@monash.edu*
session: *Geodynamics*

Introduction

Subduction zones are major features on Earth and are believed to be one of the main drivers of plate tectonics and mantle convection. The subducted slabs are negatively buoyant and have the natural tendency to sink into the Earths' mantle, pulling their trailing plates at the surface. Slabs generally have a plane perpendicular component of movement that forces the trench at the surface to migrate (retreat or advance). In such cases, the overriding plate follows the subduction hinge, while remaining in physical contact with the subduction plate and deforming in the meantime.

Several works have used laboratory experiments to investigate a number of natural aspects of subduction (e. g. Kincaid & Olson 1987; Faccenna et al. 1996; Buttles & Olson 1998; Funiciello et al. 2003; Schellart 2004; Boutelier & Cruden 2008). In this work, we present three-dimensional fluid dynamic laboratory experiments of narrow subduction zones with an overriding plate and an interplate rheology. These results are based on and build on recent modelling studies on subduction zones with an overriding plate (Meyer and Schellart, 2013) as well as an interplate rheology (Duarte et al., 2013; Duarte et al., 2014).

Material and methods

In our subduction experiments we use a low viscosity glucose tank (Fig. 1) to simulate an upper mantle reservoir and a mixture of high viscosity silicone and fine iron powder to simulate the subducting plate (negatively buoyant) and overriding plate (neutrally buoyant). Mixtures of petrolatum and paraffin oil with an adjustable rheology are used to lubricate the subduction interface by applying them to the surface of the subducting plate. Our models are scaled using the Reynolds number and the Stokes velocity, insuring that geometry, kinematics, and dynamics (driving and resisting forces) are proportional to the natural example (see Duarte et al., 2013 for a detailed description of the scaling and modelling apparatus). No external velocity or force boundary conditions are applied in our models.

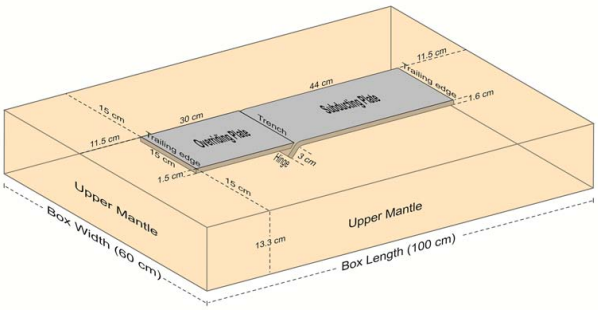

Fig. 1.: Model setup of our reference experiment

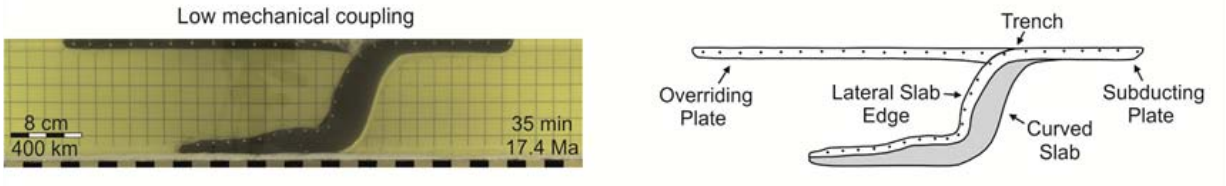

Fig. 2.: Example of a subduction experiment with both a subducting plate and an overriding plate, and an interplate rheology (adapted from Duarte et al., 2013).

Modelling results

The main results are: 1) The shear stresses at the subduction interface have a control on the plate velocity, with high shear stresses correlating with low velocities and vice-versa. Calculations of the interfacial shear force and comparison with natural subduction zones suggest that globally the interfacial shear stresses are low (<33 MPa); 2) In our models of narrow subduction zones the overriding plate always experiences overall extension, with an area of maximum (extensional) deformation localizing at a finite distance from the trench (~ 300 km), and with some shortening often occurring at the forearc. This implies that the extension is mainly driven by the toroidal component of the mantle return flow; 3) Only a small portion of the potential energy of the subducted slab is used to deform the overriding plate (less than 1 %). Considering that the energy dissipated in the slab and in the subduction zone hinge is also minor (less than 30 %), it implies that majority of the energy ($\leq$ 70 %) is dissipated in the ambient sub-lithospheric mantle. Furthermore, our models indicate that overriding plate deformation force is of comparable magnitude as the ridge push force (2×10^{12} N m^{-1} to 3×10^{12} N m^{-1}).

Final remarks

Even though our models of subduction incorporate some simplifications (isoviscous plates and sub-lithospheric mantle, isothermal conditions) the rigorous scaling procedure assures that they are robust at a first order approximation. We thus conclude that in nature the subduction zones interfaces are weak, in narrow subduction systems the overriding plate deformation is mainly controlled by the toroidal component of the mantle return flow and the energy dissipated in the overriding plate during such deformation is relatively low when compared to the potential energy release of the subducted slab.

Acknowledgements

The authors acknowledge financial support from a Discovery Grant DP110103387 from the Australian Research Council. Z.C. was supported by APA and IPRS scholarships.

References

Boutelier, D.A. & Cruden, A.R., 2008. Impact of regional mantle flow onsubducting plate geometry and interplate stress: insights from physical modelling, Geophys. J. Int., 174, 719–732.

Duarte, J.C., Schellart, W.P., Cruden, A.R., 2013. Three-dimensional dynamic laboratory models of subduction with an overriding plate and variable interplate rheology. Geophysical Journal International 195 (1), 47-66.

Duarte, J.C., Schellart, W.P., Cruden, A.R., 2014. Rheology of petrolatum - paraffin oil mixtures: applications to analogue modelling of geological processes. Journal of Structural Geology 63, 1-11.

Faccenna, C., Davy, P., Brun, J.-P., Funiciello, R., Giardini, D., Mattei, M. & Nalpas, T., 1996. The dynamics of back-arc extension: an experimental approach to the opening of

the Tyrrhenian Sea, Geophys. J. Int., 126, 781–795.

Funiciello, F., Faccenna, C., Giardini, D. & Regenauer-Lieb, K., 2003. Dynamics of retreating slabs: 2. Insights from three-dimensional laboratory experiments, J. geophys. Res.-Solid Earth, 108(B4) 2207, doi:10.1029/2001JB000896.

Meyer, C. & Schellart, W.P., 2013. Three-dimensional dynamic models of subducting plate-overriding plate-upper mantle interaction, J. geophys. Res.-Solid Earth, 118, 775–790.

Kincaid, C. & Olson, P., 1987. An experimental study of subduction and slab migration, J. geophys. Res., 92, 13 832–13 840.

Schellart, W.P., 2004. Kinematics of subduction and subduction induced flow in the upper mantle, J. geophys. Res., 109, B07401, doi:10.1029/2004JB002970.

Geometrical transitions of mantle plumes: an insight from numerical simulations

Urmi Dutta, Shamik Sarkar, Nibir Mandal

Department of Geological Sciences, Jadavpur University, Kolkata – 700032, India
e-mail: *urmidutta.geology@gmail.com*
session: *Geodynamics*

Thermo-mechanical instabilities occurs primarily at a seismically distinct zone called D" zone along the core–mantle boundary of the Earth's interior, triggering upwelling of hot and buoyant mantle materials in the form of thermal plumes. Understanding the mechanics of mantle plumes has raised renewed research interest in the last couple of decades, especially in the context of explaining the origin of large igneous provinces, i. e. the Deccan Traps and the Siberian Traps, and hotspots, i. e. the Iceland and Hawaiian Islands. A direction of plume research investigates the upwelling dynamics of plumes and the possible physical factors which may control this process. It has been demonstrated from physical and numerical experiments that the ascent behaviour of mantle plumes can be unsteady, leading to a complex evolutionary path through the mantle. Such an unsteady ascent is largely attributed to the time-dependent variations of plume-head geometry. The present study aims to explore the key physical parameters that may control the plume geometry, a question that still invokes controversies among the researchers.

We ran scaled model experiments by injecting a hot (~60 °C), buoyant viscous fluid (glycerine) into a relatively cold (30 °C) fluid (glycerine) medium. Experiments produced plumes with a bulbous head, which progressively increased in size during their ascent, and subsequently started to curl inwardly at their flanks, giving rise to a mushroom like shape (Figure 1a). On the other hand, the plume head continued to increase in size without any curling when the fluid was injected slowly. The latter condition produced plumes with a bulbous head (Figure 1b), as documented from many seismic tomography.

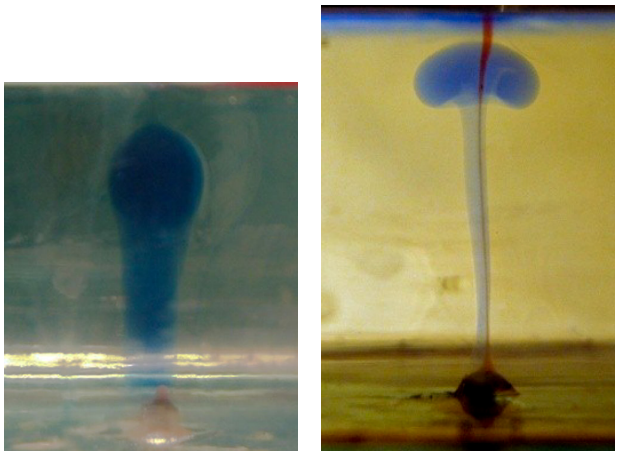

Fig. 1.: Different plume geometry from experiments: (a) Balloon-shaped, (b) Mushroom-shaped plumes.

For a quantitative analysis of these two principal two types: *bulbous-* and *mushroom-shaped* plumes, we performed numerical simulations employing the *Volume of fluid (VOF)* method for multiphase fluid flows. The VOF method applies the flow equations based on volume averaging and tracks the interfaces of two fluid phases using a phase indicator function γ (also denoted as color function or volume fraction). $\gamma = 1$ implies a phase, say Phase 1, whereas $\gamma = 0$ indicates another phase, say Phase 2. The interface between two phases can be tracked with $0 < \gamma < 1$. The VOF formulation assumes that the fluid phases taken for modeling remain in the immiscible state.

Non-dimensionalization of the different parameters in the governing equations is an important step while handling the fluid problems either theoretically or computationally. In our studies we have considered a fluid (*Phase 2*) of lower density (ρ_p), which is injected into a stagnant fluid (*Phase 1*) of higher density (ρ_p), as exercised in the laboratory experiments. Model simulations predict the development of plumes in two principal modes: i) *ballooning mode* and ii) *curling mode*, leading to the bulbous and mushroom-shaped geometry respectively. There can be a transition in the mode of plume ascent as a function of two independent physical variables: density contrast ($\Delta\rho = \frac{\rho_a}{\rho p}$, ρ_a and ρ_p are mantle and plume density respectively) and material influx rate (normalized in terms of Reynolds number $Re = \frac{\rho v d}{\mu}$ where v is the injection velocity and d is length of the cross-sectional area).

The ballooning mode (Figure 2) occurs in a condition of high $\Delta\rho$ ($\sim$1.2) and low Re ($\sim$6), which transforms into the curling mode (Figure 3) as the condition is reversed ($\Delta\rho = 1.1$ and $Re = 18$). We investigated the thermal structures of plumes from temperature profile across the plume head. The ballooning and curling types show contrasting temperature profiles (Figure 4). Ballooning type of plumes are characterized by steeper thermal gradients across their boundaries, as compared to that in the curling type. Secondly, the temperature remains laterally more uniform in case of ballooning. In the advanced stage the profile shows a temperature drop inside the head, which resulted possibly from a secondary convection process operating inside the plume head. The thermal front of a plume migrates laterally with time, and the rate of migration depends on the mode of ascent. The curling mode shows the thermal front migration at much faster rates, about ten times that for the ballooning mode (Figure 4).

Results from this fluid models has been employed to addresses a fundamental question why seismic images rarely detects the curling type of plume geometry, although it is widely reported from various model simulations. The maps of the temperature distribution in close proximity

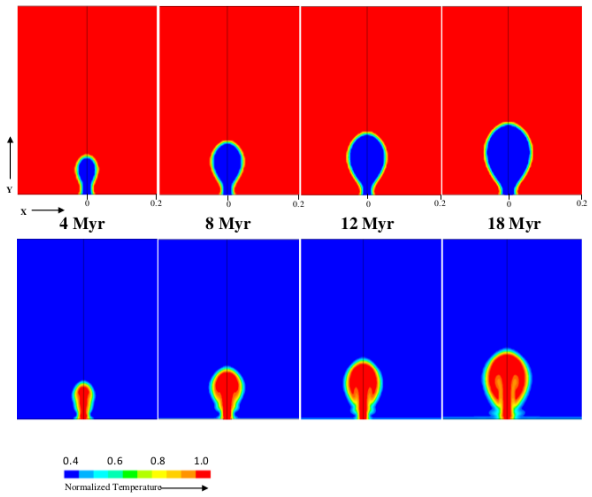

Fig. 2.: Progressive development of a plume in ballooning mode in VOF models. Mapping of the plume shapes by (a) phase and (b) thermal boundary are shown.

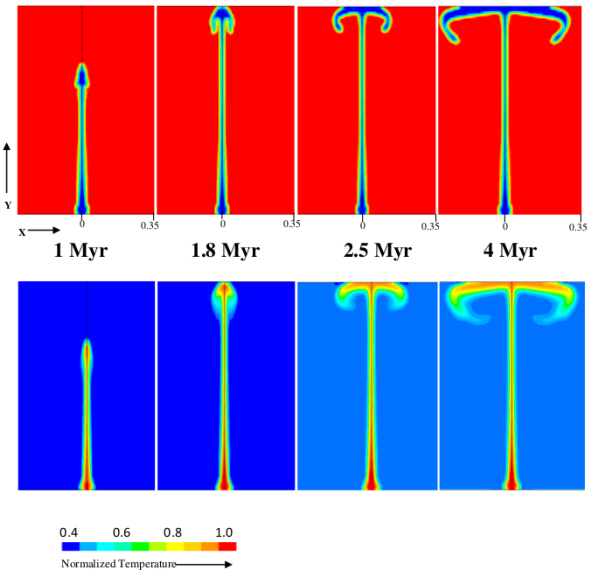

Fig. 3.: Development of plumes by curling mode in models with a low density contrast ($\Delta\rho = 1.1$) and a high influx rate ($Re \approx 20$). (a) Phase and (b) thermal structures.

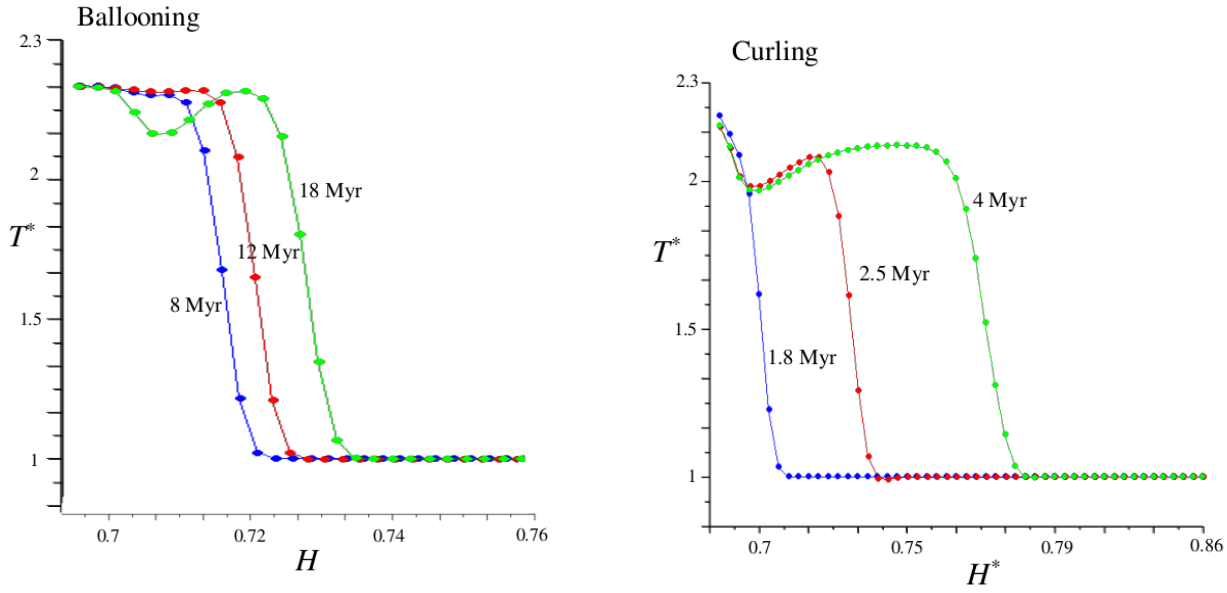

Fig. 4.: Temperature profile of plume head along a horizontal, central line passing through the head. Both temperature and horizontal distance have been shown by their values normalized with respect to the corresponding far-field temperatures and the horizontal model dimension, respectively.

to the plumes suggest that they differ considerably from plume phase boundary in case of the curling mode plume. The thermal structure always reveals a balloon-shaped geometry even if the phase boundary suggests a mushroom-shaped plume head. We infer that seismic tomography perhaps tracks the thermal boundary of plumes, rather than the mantle-plume phase boundary.

References

Dutta, U., Sarkar, S., Baruah, A.,Mandal, N., (2014). "Ascent modes of jets and plumes in a stationary fluid of contrasting viscosity". International Journal of Multiphase Flow, `http://dx.doi.org/10.1016/j.ijmultiphaseflow.2014.02.007`.

Dutta, U., Sarkar, S., Mandal, N., (2013). "Ballooning versus curling of mantle plumes: views from numerical models". Current Science. 104 (7), 893–903.

Thermo-mechanically coupled subduction with a free surface using ASPECT

Menno Fraters[1], Anne Glerum[1], Cedric Thieulot[1,2], Wim Spakman[1,2]

[1] *Utrecht University, Geosciences, Earth Sciences, Utrecht, Netherlands*
[2] *Centre of Earth Evolution and Dynamics, Oslo, Norway*
e-mail: *menno.fraters@outlook.com*
session: *Geodynamics*

ASPECT (Kronbichler et al., 2012), short for Advanced Solver for Problems in Earth's ConvecTion, is a new Finite Element code which was originally designed for thermally driven (mantle) convection. It has, among others, the following advantages and properties:

1. Modern numerial methods: linear and nonlinear solvers, stabilization of transport dominated processes;

2. adaptive mesh refinement;

3. Build from the ground up for parallelism (a high scalability on multiple processors);

4. Trivial to go from 2D to 3D

5. Build upon the well maintained and supported liberies deal.ii, Trilinos and p4est.

Here we present an application of ASPECT to modeling of fully thermo-mechanically coupled subduction. Our subduction model contains three different compositions: a crustal composition on top of both the subducting slab and the overriding plate, a mantle composition and a sticky air composition, which allows for simulating a free surface for modeling topography build-up. We implemented a visco-plastic rheology using frictional plasticity and a composite viscosity defined by diffusion and dislocation creep. The lithospheric mantle has the same composition as the mantle but has a higher viscosity because of a lower

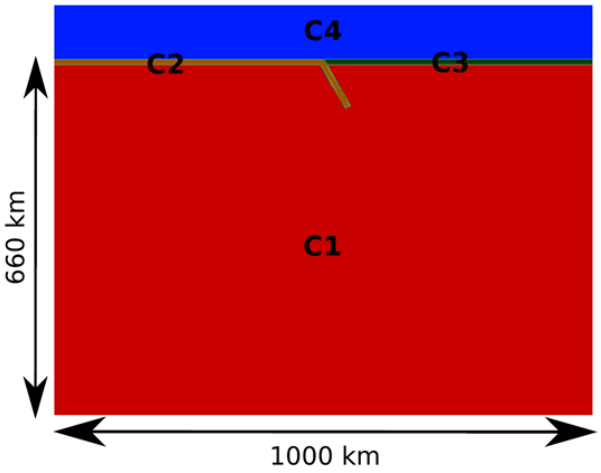

Fig. 1.: Model setup. C1 is mantle material, C2 and C3 are crust materials and C4 is a sticky air material.

temperature. The temperature field is implemented in ASPECT as follows: a linear temperature gradient for the lithosphere and an adiabatic geotherm for the sublithospheric mantle. Initial slab temperature is defined using the analytical solution of McKenzie (1970). The plates can be pushed from the sides of the model, and it is possible to define an additional independent mantle in/out flow through the boundaries.

We show that this model produces good results:

1. the free surface works in building reasonable topography;

2. the deformation is highly localized in the overriding and subducting plate in clear visible shear bands;

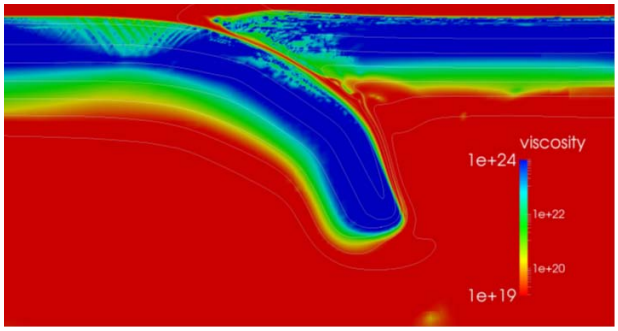

Fig. 2.: The viscosity field of the model described above after 1 myr where the plates are pushed from both sides.

3. a self-consistent evolution of the evolution of the subduction channel through the viscoplastic rheology;

4. transfer of crustal material from the subducting plate to the overriding plate;

5. Slab shape depending on mantle flow.

This setup is then used to investigate the western Mediterranean subduction and subsequent rollback. About 30Ma this rollback was initiated (Van Hindsbergen et al, 2014) and pulled Sardinia and Corsica from Iberia as a big block. We will show a preliminary set of models and results, highlighting the codes capabilities, such as the Adaptive Mesh Refinement, topography development, the influence of mantle flow on the subduction evolution, and the investigation into this blocklike behavior of Sardinia and Corsica.

References

Kronbichler, M., Heister, T., and Bangerth, W. (2012), High accuracy mantle convection simulation throughmodern numerical methods, Geophysical Journal International,191, 12-29, doi:10.1111/j.1365-246X.2012.05609.

McKenzie, D.P. (1970), Temperature and potential temperature beneath island arcs, Teconophysics, 10,357-366, doi:10.1016/0040-1951(70)90115-0.

Van Hinsbergen, D.J.J., Vissers, R.L.M. and Spakman, W. (2014), Origin and consequences of western Mediterranean subduction, rollback, and slab segmentation, Tectonics, doi:10.1002/2013TC003349

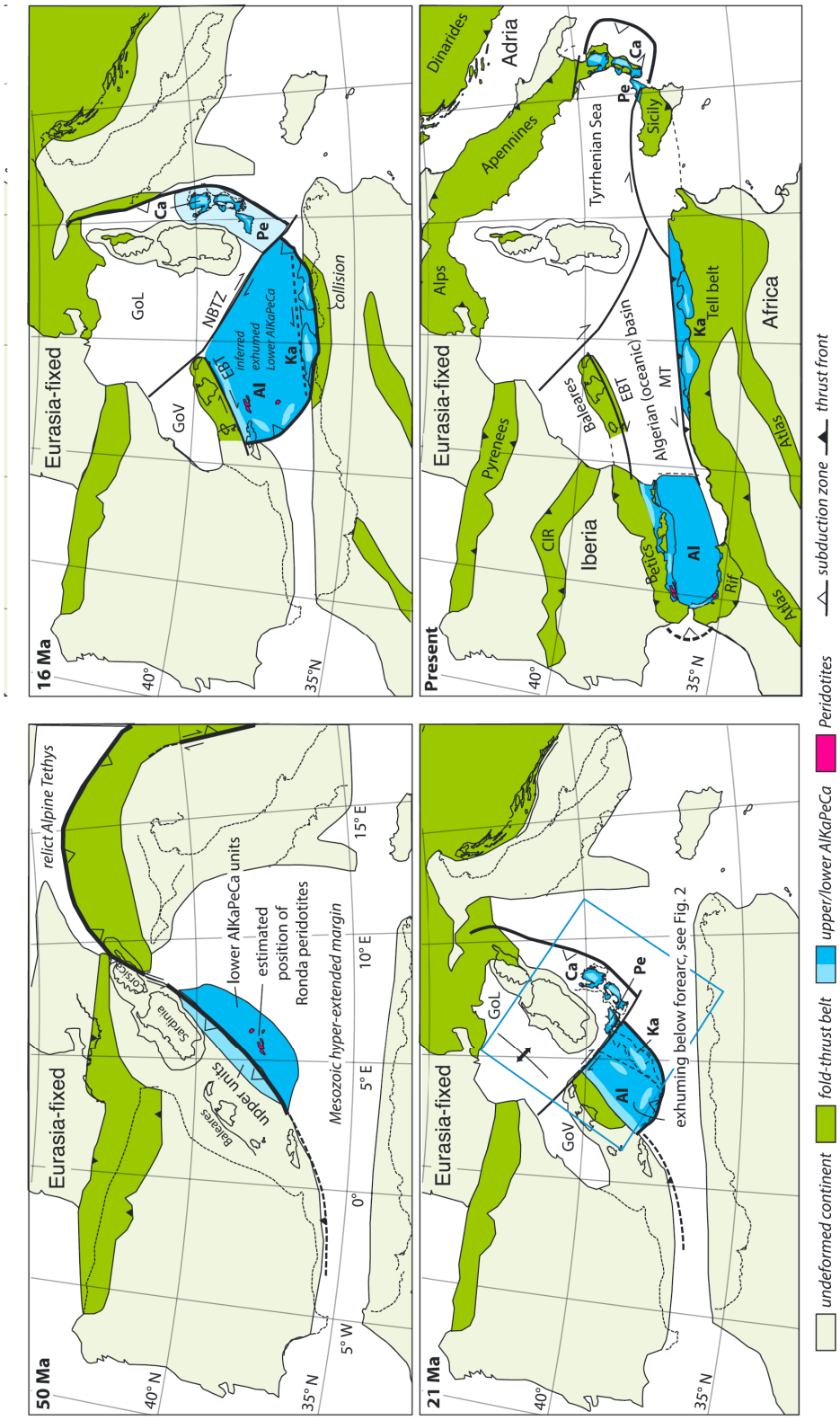

Fig. 3.: Western Mediteranian subduction and rollback history (Van Hindsbergen, 2014)

The Role of the Initial Condition in Numerical Models of the Present-day Mantle Flow Field

E. H. Fritzell, A. L. Aller, G. E. Shephard

CEED, Sem Sælands vei 24, Nedre Blindern, 0371 Oslo
e-mail: *evahfr@student.geo.uio.no*
session: *Geodynamics*

To perform any numerical model of convection in Earth's mantle, initial internal conditions (e. g., temperature and composition), boundary conditions (e. g., the velocity fields at the surface and the core-mantle boundary), and parameters such as the mantle viscosity profile must be imposed. Such conditions and parameters are crucial for simulating mantle convection, however, none are fully constrained, and assumptions on their values must be made. Using palaeomagnetically-derived tectonic plate motion velocities as time-dependent surface boundary conditions in numerical convection models, it is possible to simulate convective flow within Earth's mantle for periods encompassing several hundreds of Ma. Recent work has shown that such models can, to first-order, successfully reproduce the global present-day lower mantle velocity signature inferred from seismic tomography. For such models, assumptions must be made on the initial conditions and surface kinematics, along with a mantle viscosity profile. In this project, we will study the effect of the assumed initial condition on the resulting 3D flow field in simulations of mantle convection. We will investigate whether the assumption of an initial condition affects the present-day mantle dynamical structure on both local and global scales and aim to determine the time-dependence of the effect of initial conditions. We will investigate both isochemical (i. e., purely thermal) and thermochemical (thermal and compositional) modes of convection in Earth's mantle, and simulate convection over time periods of several hundreds of Ma. We will use the finite-element mantle convection code CitcomS in parallel with the interactive plate tectonic reconstruction software, Gplates, to simulate convection in Earth's mantle with palaeomagnetically-derived tectonic plate motion velocities as time-dependent surface boundary conditions. We will quantitatively and qualitatively compare predicted present-day mantle structure to inferences from alternative seismic tomography models and aim to determine the effect of initial conditions on numerical model results.

3-D computational modeling of the continental plate collision near South Island, New Zealand

Lev Karatun[1], Cedric Thieulot[2], Russel Pysklywec[1]

[1] *Department of Earth Sciences, University of Toronto*
[2] *University of Utrecht*
e-mail: *lev.karatun@mail.utoronto.ca*
session: *Geodynamics*

The orogenic zone at the South Island of New Zealand is of particular current interest in geodynamics/tectonics research as an active and young continental collision. These characteristics make the region amenable to studying the (enigmatic) nature of continental plate collisions using present-day geophysical/geological observables.

The fundamental nature of the lithospheric deformation, especially the deformation of the mantle lithosphere (sub-crustal lithosphere), at the South Island is unresolved. Two end-member behaviours have been proposed: mantle lithosphere may be accommodated by subduction-like underthrusting of one plate along a narrow shear zone (Beaumont et al., 1996); or it may be shortened by distributed thickening of a viscous mantle lithosphere root (Molnar et al., 1999; Stern et al., 2000). It may also be that lithosphere is deforming by a combination of these two, with a temporal transition from one to another (Pysklywec et al., 2002). An important feature of the South Island tectonics is the highly oblique nature of the plate collision: strike-slip motion ($\sim 4\,$cm/a) along the boundary exist at the same time with convergent motion ($\sim 1\,$cm/a). Moreover, the convergence velocity varies along the boundary owing to the proximity of the Euler pole of rotation. To the north, Hikurangi west-dipping subduction and to the south, Peysegur east-dipping subduction may also be modifying the collision in a type of subduction scissor (Pysklywec et al., 2010). However, previous studies on modelling the dynamics of the South Island collision have not included these important factors in the direction parallel to the plate boundary; instead considering this as a two-dimensional problem.

In the research we are conducting 3D geodynamical modelling to explore these tectonic questions for the collision. We are using a newly-developed code "Elefant" by Cedric Thieulot which has been designed for geodynamical simulations at crustal and lithospheric scales. It solves the Stokes and heat transport equations using finite element methods, relying on open-source solvers – MUMPS and SPLIB.

The code is very versatile and offers such features as:

- The so-called Arbitrary Lagrangian-Eulerian method (Donea et al., 2004) meaning that the grid deforms vertically allowing a free surface, but stays intact along the horizontal axes
- Lagrangian markers used to track the material displacements
- Velocity- and pressure-based boundary conditions allowing more realistic and flexible constraints for the models
- Diverse available rheologies – brittle, viscous and visco-plastic

Elefant has been thoroughly benchmarked and optimised for using on supercomputers; it scales well for 100+ cores. The NZ models are currently

being tested and running on the SciNet cluster – Canadas largest supercomputer.

The input parameters of the model is 4-layered structure with convergence occurring alongside with the strike-slip motions along the weak zone representing the Alpine fault. Here, I will show the first results of the work – general structures formed, material displacements, velocities, strain rate, and character of deformation from the forward computational modelling.

References

Beaumont, C., Kamp, P.J.J., Hamilton, J., and Fullsack, P., 1996, The continental collision zone, South Island, New Zealand: Comparison of geodynamical models and observations, Journal of Geophysical Research, 101, 3333–3359, doi: 10.1029/95JB02401.

Donea, J., Huerta, A., Ponthot, J., and Rodriguez-Ferran, A., 2004, Arbitrary Lagrangian-Eulerian Methods, Encyclopedia of Computational Mechanics, 1.

Molnar, P., et al., 1999, Continuous deformation versus faulting through the continental lithosphere of New Zealand, Science, 286, 516–519.

Pysklywec, R.N., Beaumont, C., and Fullsack, P., 2002, Lithospheric deformation during the early stages of continental collision: Numerical experiments and comparison with South Island, New Zealand, Journal of Geophysical Research, v. 107, p. 1–19, doi: 10.1029/2001JB000252.

Pysklywec, R. N., Ellis, S., Gorman, A. R., 2010, Three-dimensional mantle lithosphere deformation at collisional plate boundaries: A subduction scissor across the South Island of New Zealand, Earth and Planetary Science Letters, 289, 334-346.

Stern, T., Molnar, P., Okaya, D., Eberhart-Philips, D., 2000, Teleseismic p wave delays and modes of shortening the mantle lithosphere beneath South Island, New Zealand, Journal of Geophysical Research, 105 (8), 21615–21631.

Featuring lithosphere rheology in models of glacial isostatic adjustment

Volker Klemann[1], Magdala Tesauro[1], Zdenek Martinec[2,3], Ingo Sasgen[1]

[1] *German Research Centre for Geosciences, Germany*
[2] *Dublin Institute for advanced Studies, Ireland*
[3] *Charles University in Prague Chech Republic*
e-mail: *volkerk@gfz-potsdam.de*
session: *Geodynamics*

It is common to treat the lithosphere as a purely elastic plate parameterized by its flexural rigidity or effective elastic thickness if glacial isostatic adjustment processes are modeled. Furthermore, the viscous or viscoelastic mantle structure underlying the elastic plate is considered in a spherical, i. e. 1D symmetry. These assumptions downgrade the lithosphere to a thin plate where its rheological characteristics and structural features are neglected; but the assumptions are widely accepted as the horizontal extensions of the classical glacial loads in Scandinavia and North America are too large as to be sensitive to small-scale lateral variations of lithospheric strength. Likewise, the presently observed fading adjustment process due to the loading processes dating back several thousands of years is governed by the large-scale flow of mantle material.

To proof the validity of such an assumption, we apply the spectral finite element code VILMA which is based on Martinec (2000) where the field equations of a self-gravitating viscoelastic continuum are solved in the time domain and which allows for lateral variations in viscosity structure (Klemann et al., 2008) but also power-law rheology. On the two latter aspects we focus in this study where we investigate the influence of a rheologically constrained lithosphere with lateral variability in temperature and structure, which is based on Tesauro et al. (2012), on the response to glacial loading processes.

As a case example, we discuss the evolution of viscosity on a cross section that cuts the Laurentide ice sheet from its centre to the periphery and we apply a power-law rheology, where the effective viscosity is determined from the load induced stress field, σ, which is determined from the viscoelastic deformations of the earth:

$$\eta_{\text{eff}} = \frac{1}{A|\sigma|^{n-1}} \exp \frac{E}{RT} \qquad (1)$$

Here, A, E and n are material dependent quantities following from the considered earth structure and the temperature, T , follows from the considered thermal state of the lithosphere.

For reference, Fig. 1 shows the effective viscosity for a homogeneous shear-stress state of 1 MPa and 10 MPa, respectively, on this cross section. The increase of viscosity with radius is mainly due to the temperature decrease. Lateral heterogeneity reflects structural features of the lithosphere. Qualitatively, one can expect that the effective viscosity is lowest during the termination phase when the fast ice retreat induces largest changes in the stress state and, so, enhances the sub-lithospheric material transport.

This is shown in Fig. 2, where the viscosity in the mantle lithosphere drops by more than one magnitude during the termination phase and increases afterwards again.

Furthermore, we extend this study to more recent and smaller scale processes like the Little Ice Age and present time loading processes in tectonically active regions like Southern Patagonia, Antarctic Peninsula or Alaska.

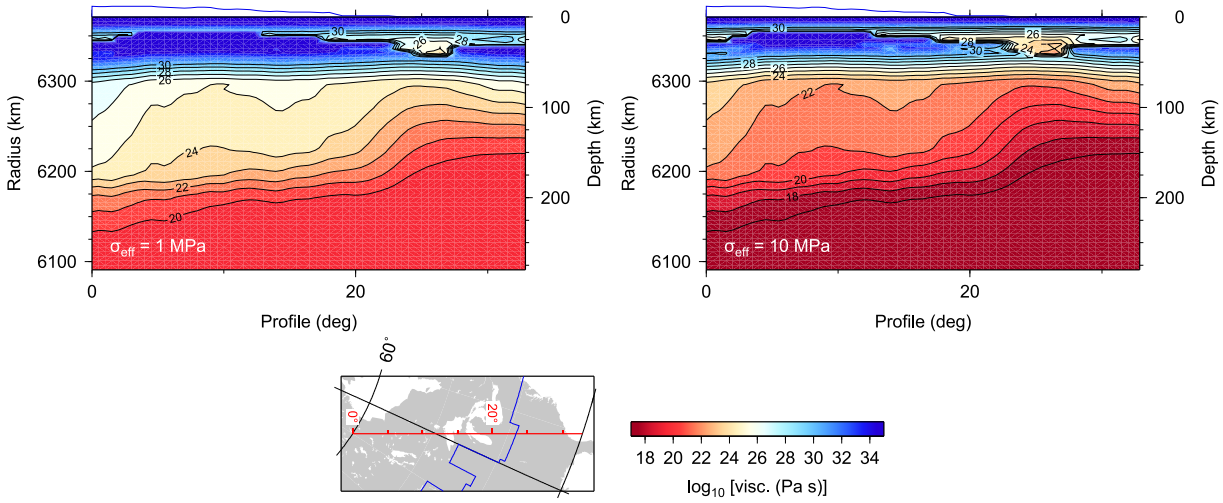

Fig. 1.: Effective viscosity for homogeneous stress state of $1\,\mathrm{MPa}$ and $10\,\mathrm{MPa}$. For orientation, the extension of the Laurentide ice sheet is shown at the top of each plot in blue. The map below shows the chosen profile from west of Hudson Bay towards Florida in red and the maximum extension of the adopted ice-sheet model again in blue.

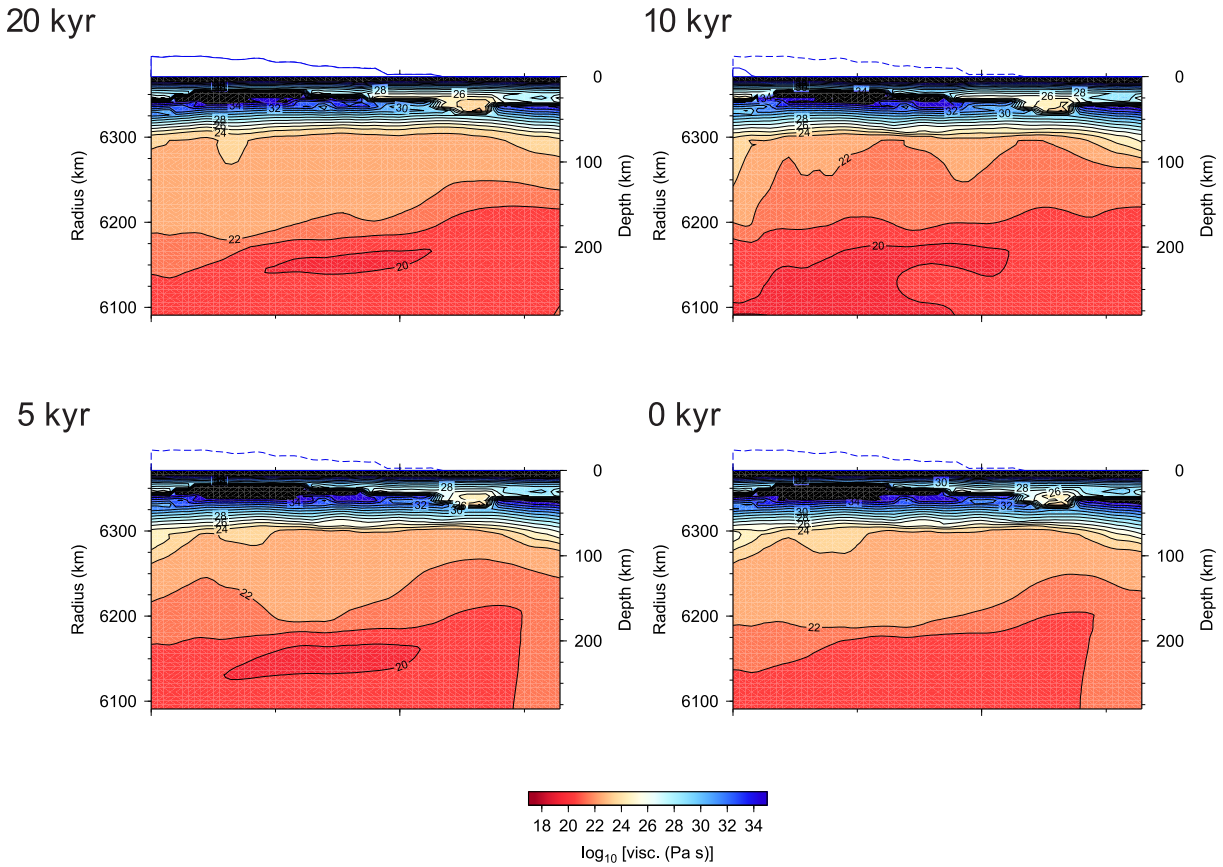

Fig. 2.: Effective viscosity at 20, 10, 5 and 0 ka before present day. Blue line at top shows the current extension of the ice sheet and the dashed line shows the extension at last glacial maximum.

References

Klemann, V., Martinec, Z. & Ivins, E. R. (2008). Glacial isostasy and plate motions, J. Geodyn., 46, 95–103, doi:10.1016/j.jog.2008.04.005.

Martinec, Z. (2000). Spectral–finite element approach for three-dimensional viscoelastic relaxation in a spherical earth, Geophys. J. Int., 142, 117–141, doi:10.1046/j.1365-246x.2000.00138.x.

Tesauro, M., Audet, P., Kaban, M. K., Bürgmann, R. & Cloetingh, S. (2012). The effective elastic thickness of the continental lithosphere: Comparison between rheological and inverse approaches, Geochem. Geophys. Geosyst., 13, 18, doi:10.1029/2012GC004162.

The 3D density and temperature distribution in an intracratonic basin setting: The Barents Sea and Kara Sea region

Peter Klitzke[1,2], Jan Inge Faleide[3], Judith Sippel[1], Magdalena Scheck-Wenderoth[1,2]

[1] *Helmholtz Centre Potsdam, GFZ German Center for Geosciences, Potsdam, Germany*
[2] *RHTW Aachen, Aachen, Germany*
[3] *Department of Geosciences, University of Oslo, Oslo, Norway*
e-mail: *klitzke@gfz-potsdam.de*
session: *Geodynamics*

Introduction

The Barents Sea and Kara Sea region as part of the European Arctic shelf is located in an intracratonical setting between the Proterozoic East-European Craton in the south and young Cenozoic passive margins in the north and the west. The region amalgamated during three major orogenies from latest Precambrian to late Paleozoic times (Breivik et al., 2002; Cocks and Torsvik, 2005; Gee et al., 2006; Gudlaugsson et al., 1998; Otto and Bailey, 1995; Puchkov, 2009; Ritzmann and Faleide, 2007; Roberts and Siedlecka, 2002) and subsequently, underwent multiple phases of locally varying subsidence (Breivik et al., 1998; Clark et al., 2013; Faleide et al., 1993; Gudlaugsson et al., 1998; Henriksen et al., 2011; Johansen, 1992). The present-day architecture of the sedimentary cover indicates different underlying crustal and lithospheric terranes and the influence of locally diverse causative geological processes. We assess how the density and temperature varies in response to the heterogeneous composition of the crystalline crust and the deeper lithosphere.

Therefore, a 3D structural model was developed resolving the sedimentary configuration, the crystalline crust and the lithospheric mantle. The sedimentary part is composed of four megasequences boundaries (pre-mid-Permian, mid-Jurassic, mid-Cretaceous and earliest Eocene. The geometries of the final 3D-structural model are well constrained as they are consistent with interpreted seismic refraction and reflection data, geological maps and previously published 3D-models.

The thickness distribution of each sedimentary megasequence varies strongly across the shelf indicating locally different development of the corresponding basins. The southwestern Barents Sea is characterized by narrow and elongated megasequence thickness maxima. Thereby, the distribution of sediment maxima indicates that the locus of major subsidence shifted towards the present-day continent-ocean boundary, thereby forming a fan-shaped basin system. The East Barents Sea Basin and the South Kara Sea Basin reveals a thick mid-Permian to mid-Jurassic megasequence indicating major subsidence back then. The overlying thinner sedimentary megasequences reveal that subsidence continued to early Cenozoic times in these two basins.

While the crystalline crust is thinned beneath regions where preserved sediments are thickest, the lithosphere-asthenosphere boundary (LAB) does not show any clear correlation with the sedimentary megasequences nor with the subsedimentary crust. Instead, the LAB as the base of the structural model, reveals a step-wise deepening structure towards the east. Thereby, levels of similar depths exhibit a clear correlation with the outline of sub-sedimentary crustal terranes

as defined by Marello et al. (2013).

The shallow LAB beneath the western Barents Sea (−60 km to −105 km) coincides with Caledonian Basement (southwest) and the Barentsia crustal block (northwest). Thereby, the local LAB depth configuration does not allow a clear differentiation of these two terranes. Late Cenozoic volcanism in the NW Barents Sea may have overprinted structural imprints of a Barentsia block. The eastern Barents Sea is underlain by LAB depths of about −150 km which widely correlates with the Timanian basement (Marello et al., 2013). The west coast of Novaya Zemlya exhibits the transition to the Uralian domain as observable by a major thickening of the lithosphere.

To extend the structural analysis in particular towards the composition of the subsiding crystalline crust we performed 3D gravity modelling. Therefore, the sedimentary units were assigned lithology-dependent matrix densities and porosities to calculate bulk densities which consider the effects of erosion, compaction as well as the maximum thickness of the late Cenozoic ice sheet. For the mantle (down to 250 km depth), we implemented a published velocity-density model (Levshin et al., 2007). To calculate an initial density configuration of the crystalline crust, the concept of Pratt's isostasy is applied and the resulting density distribution is used to define an upper and lower crust.

The obtained gravitational response of the parameterized 3D-structural model is compared with the observed gravity field to further investigate the composition of the lithosphere and particularly to define the extent of possible high-density bodies in the crystalline crust. To assess the major controlling factors of the thermal field, the obtained 3D-density model is used to calculate the lithosphere-scale 3D conductive thermal field of the Barents Sea and Kara Sea region. Consequently, the predicted thermal field is validated with measured borehole temperatures. Highest temperature are calculated for the westernmost Barents Sea, which is in accordance with the local rifting history (Fig. 1). Additionally, regions which are known to have experienced strong late Cenozoic uplift and erosion such as the NW Barents Sea and Svalbard reveal higher temperatures (Fig. 1). Beneath the remaining shelf areas minor positive temperature anomalies delineate the geometry of sedimentary basins (Fig. 1). Lowest continental temperatures occur beneath the mainland due to a lack of a thicker sedimentary coverage (Fig. 1).

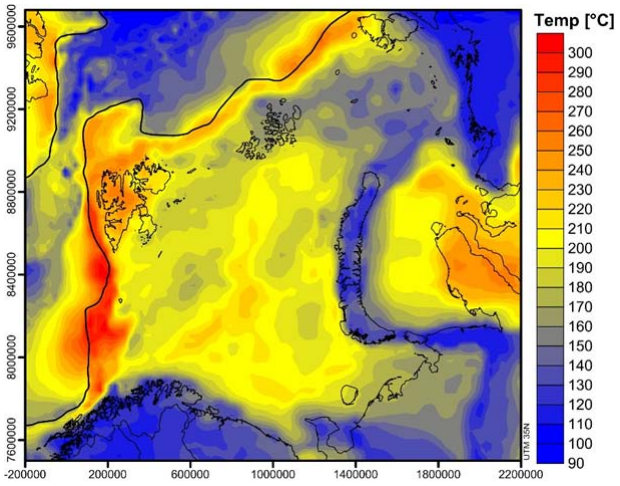

Fig. 1.: Temperature distribution @ −7 km depth.

The developed present-day 3D model provides an ideal base to reconstruct the subsidence/uplift history of the Barents Sea and Kara Sea region through time by considering also the compositional heterogeneities of the crystalline crust and the deeper lithosphere.

References

Breivik, A.J., Faleide, J.I., Gudlaugsson, S.T., 1998. Southwestern Barents Sea margin: late Mesozoic sedimentary basins and crustal extension. Tectonophysics 293, 21–44.

Breivik, A.J., Mjelde, R., Grogan, P., Shimamura, H., Murai, Y., Nishimura, Y., Kuwano, A., 2002. A possible Caledonide arm through the Barents Sea imaged by OBS data. Tectonophysics 355, 67–97.

Clark, S. a., Glorstad-Clark, E., Faleide, J.I., Schmid, D., Hartz, E.H., Fjeldskaar, W., 2013. Southwest Barents Sea rift basin evolution:

comparing results from backstripping and time-forward modelling. Basin Res.

Cocks, L.R.M., Torsvik, T.H., 2005. Baltica from the late Precambrian to mid-Palaeozoic times: The gain and loss of a terrane's identity. Earth-Science Rev. 72, 39–66.

Faleide, J.I., Vågnes, E., Gudlaugsson, S.T., 1993. Late Mesozoic-Cenozoic evolution of the south-western Barents Sea in a regional rift-shear tectonic setting. Mar. Pet. Geol. 10, 186–214.

Gee, D., Bogolepova, O.K., Lorenz, H., 2006. The Timanide, Caledonide and Uralide orogens in the Eurasian high Arctic, and relationships to the palaeo-continents Laurentia, Baltica and Siberia. Geol. Soc. London, Mem. 32, 507–520.

Gudlaugsson, S., Faleide, J.I., Johansen, S.E., Breivik, A.J., 1998. Late Palaeozoic structural development of the South-western Barents Sea. Mar. Pet. Geol. 15, 73–102.

Henriksen, E., Ryseth, a. E., Larssen, G.B., Heide, T., Ronning, K., Sollid, K., Stoupakova, a. V., 2011. Chapter 10 Tectonostratigraphy of the greater Barents Sea: implications for petroleum systems. Geol. Soc. London, Mem. 35, 163–195.

Johansen, S.E.., 1992. Hydrocarbon potential in the Barents Sea region: play distribution and potential. Arct. Geol. Pet. Potential 2, 273–320. Marello, L., Ebbing, J., Gernigon, L., 2013. Basement inhomogeneities and crustal setting in the Barents Sea from a combined 3D gravity and magnetic model. Geophys. J. Int. 193, 557–584.

Levshin, A.L., Schweitzer, J., Weidle, C., Shapiro, N.M., Ritzwoller, M.H., 2007. Surface wave tomography of the Barents Sea and surrounding regions. Geophys. J. Int. 170, 441–459.

Marello, L., Ebbing, J., Gernigon, L., 2013. Basement inhomogeneities and crustal setting in the Barents Sea from a combined 3D gravity and magnetic model. Geophys. J. Int. 193, 557–584.

Otto, S., Bailey, R., 1995. Tectonic evolution of the northern Ural Orogen. J. Geol. Soc. London. 152, 903–906.

Puchkov, V.N., 2009. The evolution of the Uralian orogen. Geol. Soc. London, Spec. Publ. 327, 161–195.

Ritzmann, O., Faleide, J.I., 2007. Caledonian basement of the western Barents Sea. Tectonics 26, 1–20.

Roberts, D., Siedlecka, a., 2002. Timanian orogenic deformation along the northeastern margin of Baltica, Northwest Russia and Northeast Norway, and Avalonian–Cadomian connections. Tectonophysics 352, 169–184.

The effect of melting and crustal production on plate tectonics on terrestrial planets

Diogo L. Lourenço, Paul J. Tackley

Institute of Geophysics, Department of Earth Sciences, ETH Zürich, Switzerland
e-mail: *diogo.lourenco@erdw.ethz.ch*
session: *Geodynamics*

Within the Solar System, Earth is the only planet to be in a mobile-lid regime, whilst it is generally accepted that all the other terrestrial planets are currently in a stagnant-lid regime, showing little or no surface motion. A transitional regime between these two, showing episodic overturns of an unstable stagnant lid, is also possible and has been proposed for Venus (Armann and Tackley, JGR 2012).

Using plastic yielding to self-consistently generate plate tectonics on an Earth-like planet with strongly temperature-dependent viscosity is now well-established, but such models typically focus on purely thermal convection, whereas compositional variations in the lithosphere can alter the stress state and greatly influence the likelihood of plate tectonics. For example, Rolf and Tackley (GRL, 2011) showed that the addition of a continent can reduce the critical yield stress for mobile-lid behaviour by a factor of around 2. Moreover, it has been shown that the final tectonic state of the system can depend on the initial condition (Tackley, G3 2000 – part 2); Weller and Lenardic (GRL, 2012) found that the parameter range in which two solutions are obtained increases with viscosity contrast.

We can also say that partial melting has a major role in the long-term evolution of rocky planets: (1) partial melting causes differentiation in both major elements and trace elements, which are generally incompatible (Hofmann, Nature 1997). Trace elements may contain heat-producing isotopes, which contribute to the heat loss from the interior; (2) melting and volcanism are an important heat loss mechanism at early times that act as a strong thermostat, buffering mantle temperatures and preventing it from getting too hot (Xie and Tackley, JGR 2004b); (3) mantle melting dehydrates and hardens the shallow part of the mantle (Hirth and Kohlstedt, EPSL 1996) and introduces viscosity and compositional stratifications in the shallow mantle due to viscosity variations with the loss of hydrogen upon melting (Faul and Jackson, JGR 2007; Korenaga and Karato, JGR 2008).

We present a set of 2D spherical annulus simulations (Hernlund and Tackley, PEPI 2008) using StagYY (Tackley, PEPI 2008), which uses a finite-volume scheme for advection of temperature, a multigrid solver to obtain a velocity-pressure solution at each timestep, tracers to track composition, and a treatment of partial melting and crustal formation. We address the question whether melting-induced crustal production changes the critical yield stress needed to obtain mobile-lid behaviour as a function of governing parameters.

Our results show that melting and crustal production strongly influence plate tectonics on terrestrial planets. For the same parameters the use of a treatment for melting and crustal production facilitates breaking the stagnant-lid, replacing it with episodic-lid; however, a smoothly evolving mobile lid can also be replaced by episode-lid. Several factors can play a role on these, namely lateral heterogeneities, differences in the lid thickness and internal planetary temperatures induced by melting and crustal production.

3-D numerical modelling of subduction initiation at curved passive margins

F. O. Marques, F. R. Cabral, T. V. Gerya, G. Zhu, D. A. May

Department of Earth Sciences, Swiss Federal Institute of Technology (ETH Zurich), CH-8092 Zurich, Switzerland
e-mail: *fomarques@fc.ul.pt*
session: *Geodynamics*

Subduction initiation at straight passive margins can be investigated with 2-D numerical models, because the geometry is cylindrical (Fig. 1B).

However, on Earth, straight margins rarely occur. The construction of 3-D models is therefore critical in the modelling of spontaneous subduction initiation at realistic, curved passive margins (Fig. 1A).

Here we report on the results obtained from gravitationally driven, 3-D thermomechanical numerical models using a visco-plastic rheology and a passive margin with a single curved section in the middle. The models show that the curvature angle β (Fig. 1A) can control subduction initiation: the greater β is, the more difficult subduction initiation becomes (Figs. 1–3).

The 3-D thermomechanical models provide an in-depth physical understanding of the processes (Figs. 4–6). Temperature is a critical parameter because it controls density, thus affecting stresses and pressure gradients. In the initial stage, isotherms are horizontal, but this configuration rapidly changes with deformation (Fig. DR1). If subduction initiation is fast, as in models 1 and 2, then thermal re-equilibration of the sinking slab with the surrounding mantle is delayed. Hence, the slab remains cold to great depths, the density contrast with the mantle is maintained (cold slab in hot mantle), and the oceanic slab thus sinks rapidly. There is, therefore, a positive feedback between temperature and the sinking velocity of the oceanic slab (e. g., McKenzie, 1977), which can be further enhanced if the cold oceanic slab

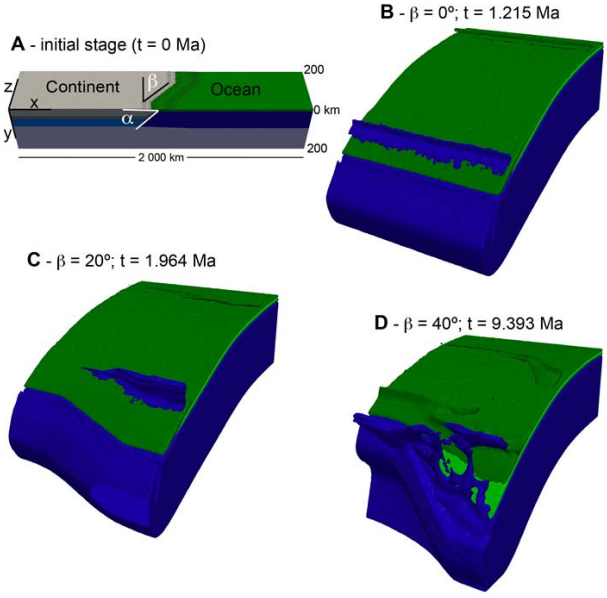

Fig. 1.: Initial stage (A) and final results (B–D) of modelling. The initial stage shows a zig-zag structure to simulate a curved margin, lengths of continent and ocean, and angles α and β. α is the dip of continent-ocean lithospheric boundary surface, and is $45°$ for all models; β is the angle between the trace of the curved section of the margin at the Earth's surface and the z-axis, and is $0°$ (model 1 in B), $20°$ (model 2 in C), or $40°$ (model 3 in D). t – time to subduction initiation

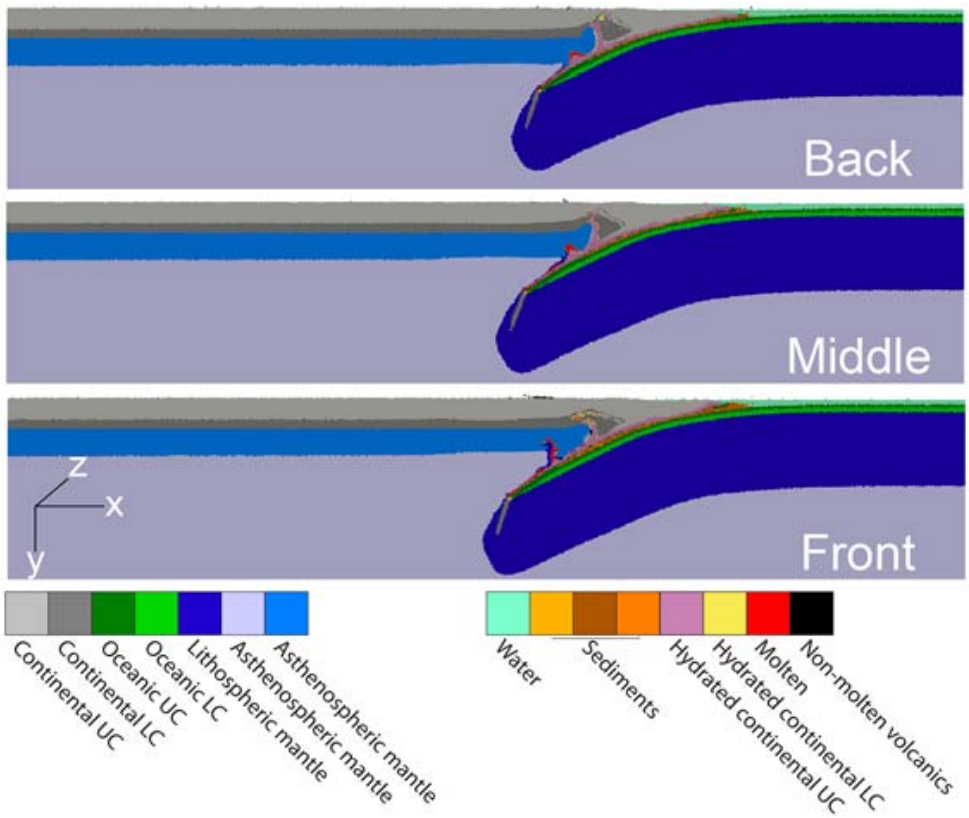

Fig. 2.: Sections through the end result (at $1.964\,\mathrm{Ma}$) of model 2 with $\beta = 20°$, at $z = 0\,\mathrm{km}$ (front wall), $z = 100\,\mathrm{km}$ (middle), and $z = 200\,\mathrm{km}$ (back wall). Note that the oceanic slab reaches $200\,\mathrm{km}$ depth (subduction proper) faster in the front than in the back. UC – upper crust; LC – lower crust.

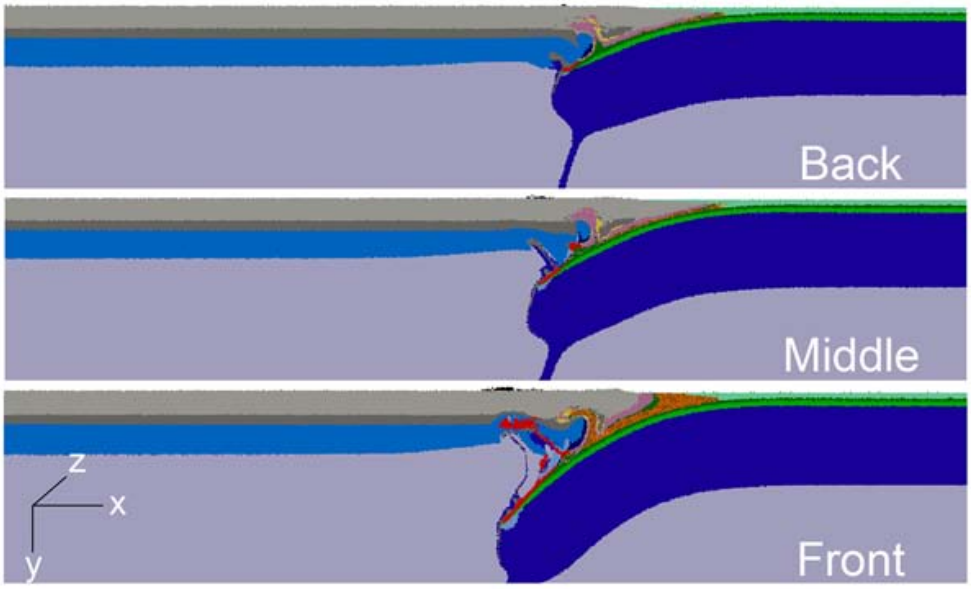

Fig. 3.: Sections through the end result (at $9.393\,\mathrm{Ma}$) of model 3 with $\beta = 40°$, at $\beta = 20°$, at $z = 0\,\mathrm{km}$ (front wall), $z = 100\,\mathrm{km}$ (middle), and $z = 200\,\mathrm{km}$ (back wall). Note that the oceanic slab reaches $200\,\mathrm{km}$ depth (subduction proper) in the front of the model, but not in the back. Colours as in Fig. 2.

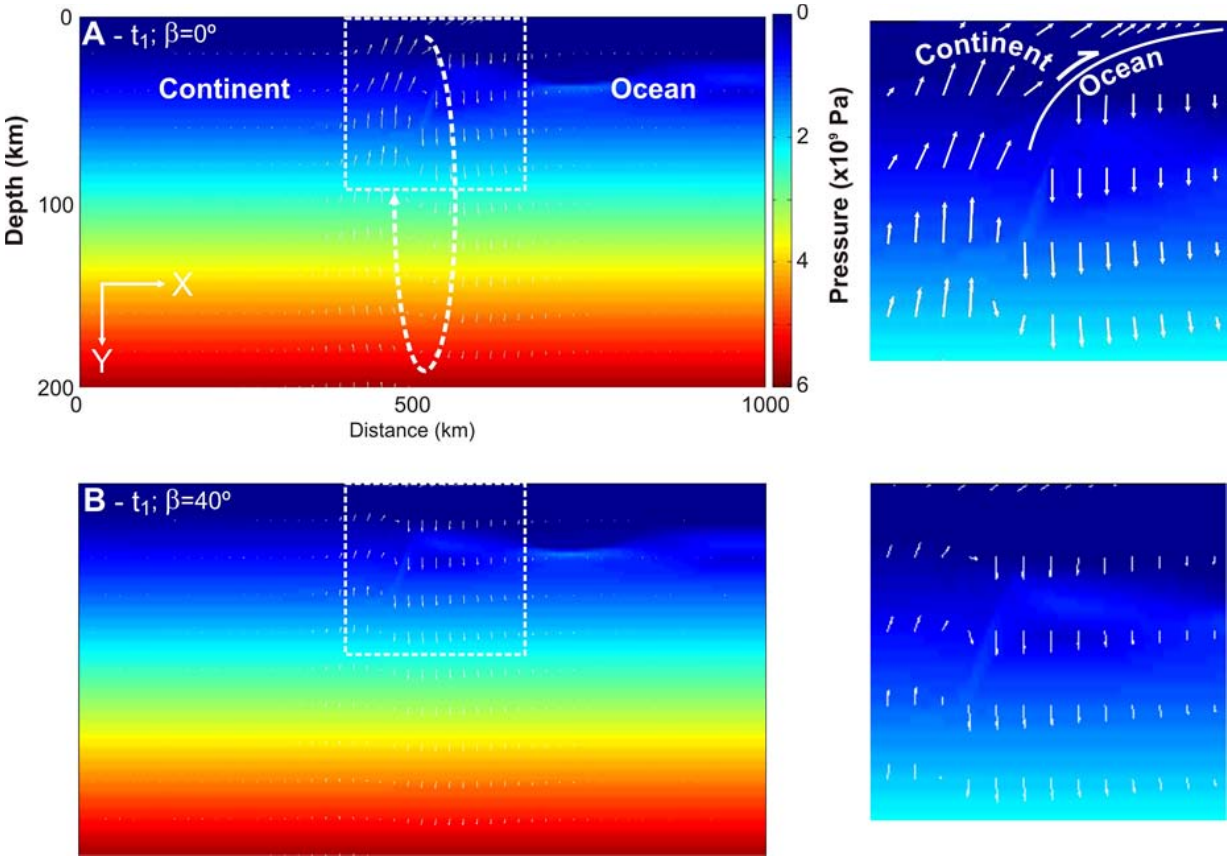

Fig. 4.: Velocity vectors (white arrows) overlain on pressure maps (coloured). The difference in the size of velocity vectors in A (bigger) and B (smaller) indicates why an increase in β hampers subduction initiation. Insets on right are close-ups of the dashed square areas marked in A and B.

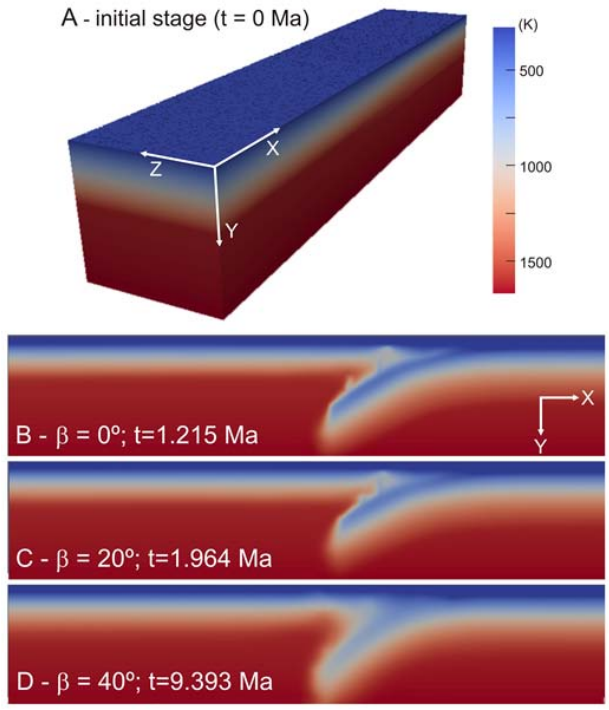

Fig. 5.: Color maps representing the model temperatures in the initial stage (A), and at the front wall in the last stage of Models 1, 2 and 3. Note the higher temperature, from B to D, in the core of the sinking slab.

transforms into high-density eclogite (not modelled).

Specifically, we find that pressure gradients (Fig. 4), arising from density differences between oceanic and continental rocks, drive subduction initiation, and strongly influence the timing. The main difference between straight (cylindrical) and curved margins is that the orientation of the pressure gradient in 3-D is no longer constant, thus producing a horizontal, along-margin component of flow (Fig. 6). We thus conclude that the reason for the impedance of subduction initiation is the result of partitioning of the vertical velocity component into a horizontal component, which therefore decreases the effective slab pull.

We infer that, although favourable for subduction initiation in a 2-D model, because the estimated force balance is adequate, the pronounced curvature in the southeast Brazilian margin is a likely explanation why subduction initiation is hampered there.

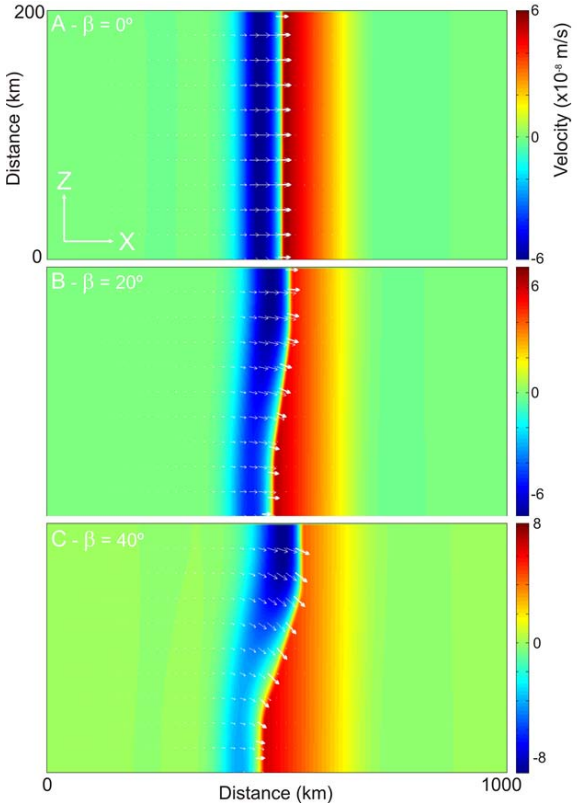

Fig. 6.: XZ plots of the velocity field. In color the Y component, and as vectors (white arrows) the XZ component. A, B and C for Models 1, 2 and 3 respectively. Note the great incorporation of the Z component, towards the front wall (bottom), from A to C. Zero in A, as expected for a 2D equivalent model, and maximum in C. Positive and negative values in the scale bar mean downward and upward flows, respectively.

Crustal deformation and magmatism at the transition between subduction and collisional domains: insight from 3D numerical modeling

Armel Menant[1,2,3], Pietro Sternai[1,2,3], Laurent Jolivet[1,2,3], Laurent Guillou-Frottier[2,1,3], Taras Gerya[4]

[1] *Université d'Orléans, ISTO, UMR 7327, Orléans, France*
[2] *BRGM, ISTO, UMR 7327, 45060 Orléans, France*
[3] *CNRS/INSU, UMR 7327, 45071 Orléans, France*
[4] *Swiss Federal Institute of Technology (ETH), Zurich, Switzerland*
e-mail: *armel.menant@cnrs-orleans.fr*
session: *Geodynamics*

Geodynamic evolution of subduction zones is often complex, due to the variable nature and rheology of interacting lithospheres, 3D slab geometry and related mantle flow. In order to understand the temporal evolution of this dynamics, the long-term geological record should be considered, including the present-day kinematics, the long-term history of deformation and magmatism within the upper plate. This leads to conceptual models that imply complex physical processes that can be tested through numerical modeling.

In this study, we focus on the eastern Mediterranean region where a long-lived subduction zone has been active since the Mesozoic. In this region, the Tethyan active margin is characterized by successive subductions of oceanic and continental ribbons, slab retreat episodes and possible slab tearing processes, notably interpreted from tomographic models showing low-velocity anomaly below Anatolia [Ricou et al., 1986; Piromallo and Morelli, 2003; van Hinsbergen et al., 2005a; Jolivet et al., 2013].

Using G-Plates software, we first modeled the kinematic evolution of the eastern Mediterranean in the last 100 Myrs, accounting for a large number of geological data, including the magmatic occurrences (figure 1). Since 35-30 Ma, the geodynamics of this region has been dominated by the subduction and collision of Arabia with Eurasia and with the development of a large back-arc domain in the Aegean region, resulting from an increase of the rate of slab retreat. This slab retreat is associated with the southward migration of high-potassic magmatism in the back-arc domain with time, and with the southwest fast migration of the Aegean plutons during the middle Miocene from the Menderes to the Cyclades (figure 1).

In addition, a major change occurred in the dynamics of the back-arc opening in the middle Miocene (figure 1) with a new increase of the rate of trench retreat and large-scale block rotations on the edge of this extensional domain in the Hellenides and in western Anatolia [Kissel and Laj, 1988; van Hinsbergen et al., 2005b]. This kinematic change is coeval with the southwest migration of the back-arc plutons and with the increase of their mantle component compared to their crustal component from east to west [Altherr and Siebel, 2002]. Finally, sparse alkaline volcanism emplaced in the Aegean and western Anatolia since ~15 Ma with the same westward migration trend, indicating a hot asthenospheric upwelling associated with a low rate of partial melting [Dilek and Altunkaynak, 2009].

Using high-resolution 3D thermo-mechanical

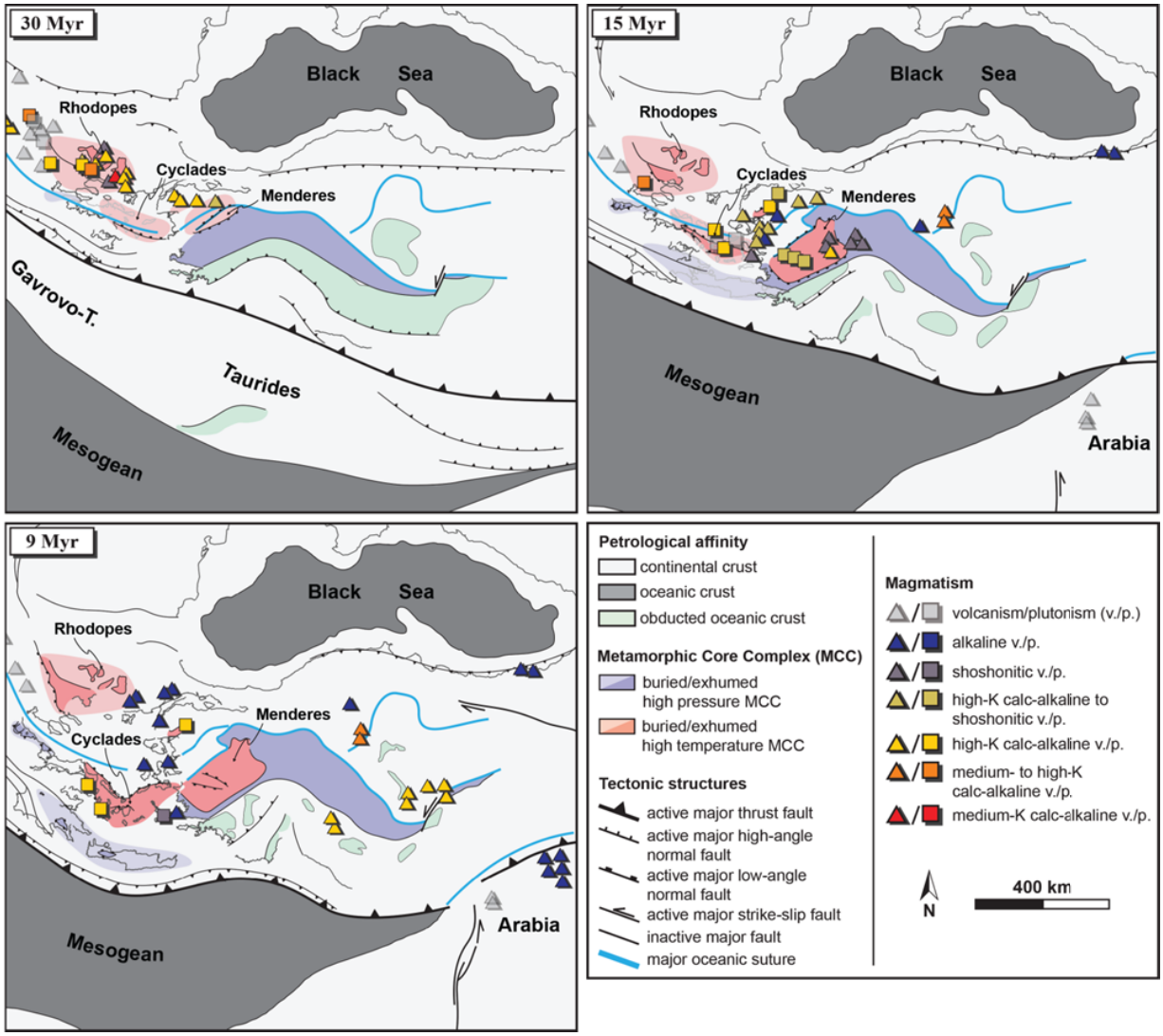

Fig. 1.: Kinematic reconstructions of eastern Mediterranean region at 30, 15 and 9 Ma, highlighting the main metamorphic, tectonic and magmatic features.

numerical modeling, we reproduce a relatively simple model of retreating subduction neighboring a collisional domain that we compare with these geological observations. These numerical experiments are performed with the code I3ELVIS, considering non-newtonian visco-plastic rheologies and notably integrating partial melting and melt extraction processes as well as fluid and melt transport mechanism [Gerya and Yuen, 2003; Zhu et al., 2013]. The resolved grid has a resolution of 3.4, 2.5 and 4.4 km in the x, y and z dimensions respectively and ~130 millions additional randomly distributed moving markers.

The initial model setup shows an oceanic lithosphere and a continental plate (considered as Arabia) converging toward a continental upper plate (considered as Eurasia) (figure 2a). The evolution of the model shows first the subduction of the oceanic crust then of the continental crust below the upper plate margin that is stretched as a result of the trench retreat (figure 2b). When the contient buoyancy and the slab pull forces overstep the strength of the lithosphere, the slab is torn first horizontally then vertically along the subducted continental margins (figure 2c). The slab tear results in the exhumation and the re-

bound of the subducted continental crust and the establishing of a collisional regime (figure 2c). Aside of the collisional domain, the oceanic subduction protracts for longer and slab roll-back and trench retreat occur as faster rates since the slab tearing reduced the along-strike dimension of the slab (figure 2c). Consequently, the upper plate extension rates increase and strike-slip deformation accommodates the rotation of crustal blocks.

The rebound of the subducted continental crust following the slab tearing, combined with 3D mantle flow, carries partially molten mantle wedge toward the base of the stretched upper continental plate (figure 3a). This material then migrates progressively toward the subducting oceanic plate replacing progressively the partially hydrated and molten crustal material previously developed in the back-arc region (figures 3b and 3c). Finally, asthenospheric material rises at the base of the crust, undergoing a possible adiabatic partial melting inducing the development of an alkaline volcanism at the surface (figure 3).

Results from these numerical experiments show a tectonic and magmatic evolution that can be compared to the geological observations across the eastern Mediterranean region. This exercise shows the potential of this double-sided approach involving an independent reconstruction of the long-term evolution of subduction zones based on kinematic reconstructions and 3D thermomechanical numerical modeling to investigate the complex interactions between slab behavior, magmatic history, mantle flow and crustal deformation.

References

Altherr, R., and W. Siebel (2002), I-type plutonism in a continental back-arc setting: Miocene granitoids and monzonites from the central Aegean Sea, Greece, Contributions to Mineralogy and Petrology, 143(4), 397–415, doi:10.1007/s00410-002-0352-y.

Dilek, Y., and S. Altunkaynak (2009), Geochemical and temporal evolution of Cenozoic magmatism in western Turkey: mantle response to collision, slab break-off, and lithospheric tearing in an orogenic belt, Geological Society, London, Special Publications, 311(1), 213–233, doi:10.1144/SP311.8.

Gerya, T. V., and D. A. Yuen (2003), Characteristics-based marker-in-cell method with conservative finite-differences schemes for modeling geological flows with strongly variable transport properties, Physics of the Earth and Planetary Interiors, 140(4), 293–318, doi:10.1016/j.pepi.2003.09.006.

Jolivet, L. et al. (2013), Aegean tectonics: Strain localisation, slab tearing and trench retreat, Tectonophysics, 597-598, 1–33, doi:10.1016/j.tecto.2012.06.011.

Kissel, C., and C. Laj (1988), The Tertiary geodynamical evolution of the Aegean arc: a paleomagnetic reconstruction, Tectonophysics, 146(1-4), 183–201, doi:10.1016/0040-1951(88)90090-X.

Piromallo, C., and A. Morelli (2003), P wave tomography of the mantle under the Alpine-Mediterranean area, Journal of Geophysical Research, 108(B2), doi:10.1029/2002JB001757.

Ricou, L. E., J. Dercourt, J. Geyssant, C. Grandjacquet, C. Lepvrier, and B. Biju-Duval (1986), Geological constraints on the alpine evolution of the Mediterranean Tethys, Tectonophysics, 123(1-4), 83–122, doi:10.1016/0040-1951(86)90194-0.

van Hinsbergen, D. J. J., E. Hafkenscheid, W. Spakman, J. E. Meulenkamp, and R. Wortel (2005a), Nappe stacking resulting from subduction of oceanic and continental lithosphere below Greece, Geology, 33(4), 325, doi:10.1130/G20878.1.

van Hinsbergen, D. J. J., C. G. Langereis, and J. E. Meulenkamp (2005b), Revision of the timing, magnitude and distribution of Neogene rotations in the western Aegean region, Tectonophysics, 396(1-2), 1–34, doi:10.1016/j.tecto.2004.10.001.

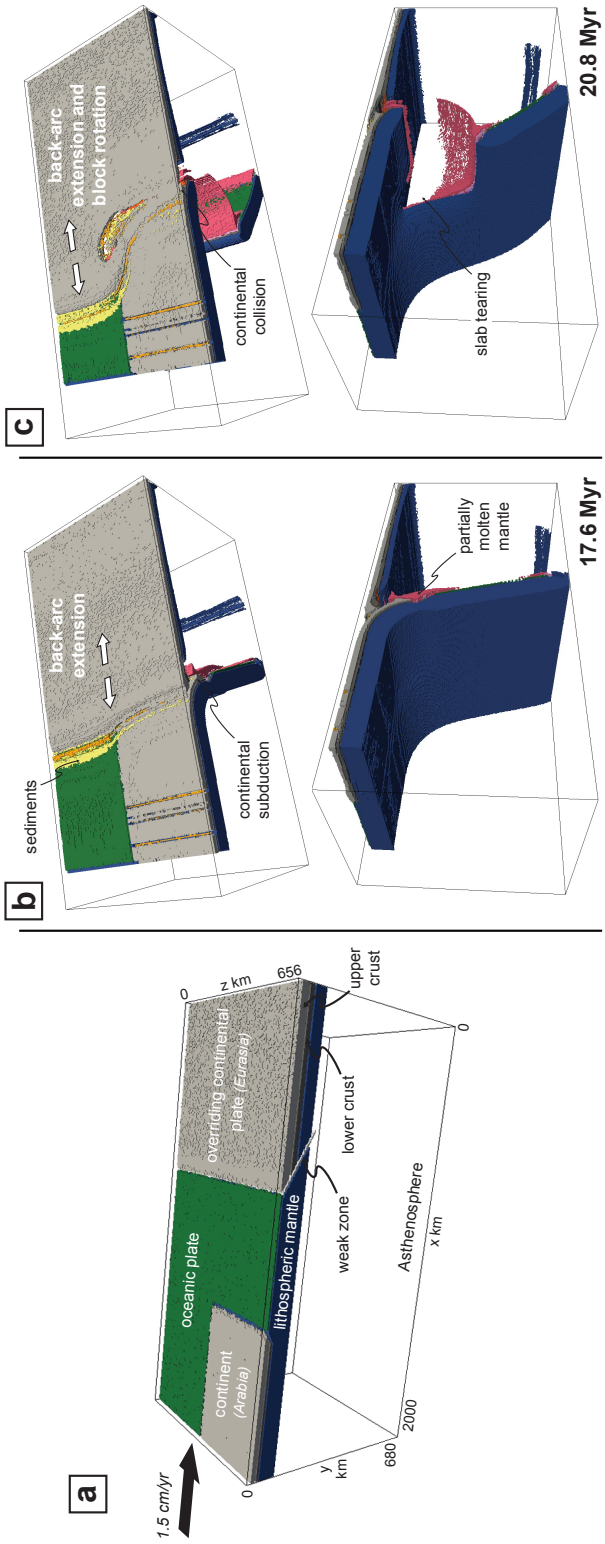

Fig. 2.: 3D thermo-mechanical modeling of retreating subduction neighboring a collisional domain. (a) Initial setup of the 3D model domain with colors showing different rock types. (b, c) Evolution of the reference model at 17.6 and $20.8\,\mathrm{Ma}$. The top layer ("sticky air", $y < 12\,\mathrm{km}$) and the asthenosphere are cut off for clarity.

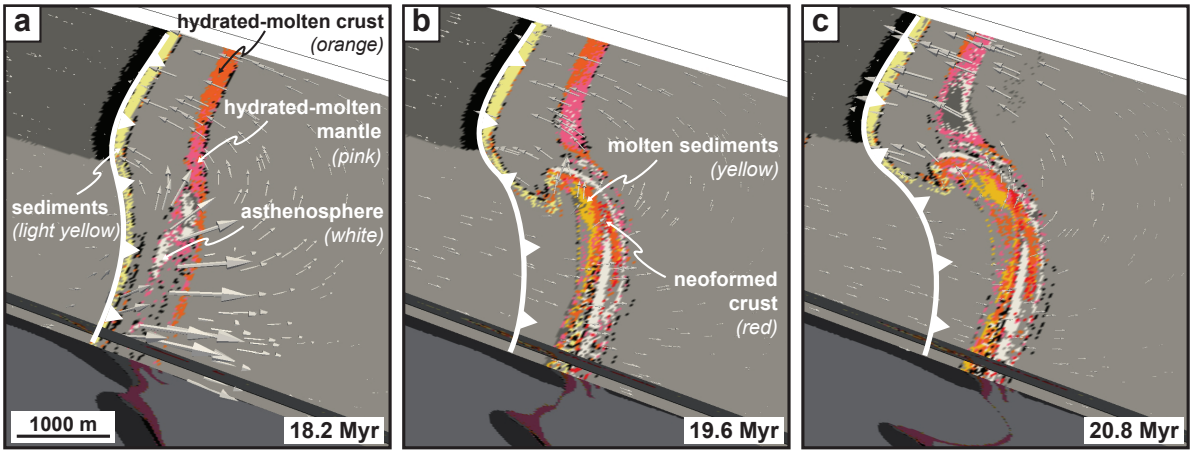

Fig. 3.: 35 km-depth horizontal cross-section of the reference model, corresponding to the base of the stretched continental crust, highlighting the different hydrated and partially molten phases. (a, b, c) Evolution of the model at 18.2, 19.6 and .20.8 Myr.

Zhu, G., T. V. Gerya, P. J. Tackley, and E. Kissling (2013), Four-dimensional numerical modeling of crustal growth at active continental margins, Journal of Geophysical Research: Solid Earth, 118(9), 4682–4698, doi:10.1002/jgrb.50357.

Segregation, Accumulation, and Entrainment of the Oceanic Crust in the Lowermost Mantle: Exploring the Range of Governing Parameters with Numerical Modelling

Elvira Mulyukova[1], Bernhard Steinberger[1,2], Marcin Dabrowski[2,3], Stephan V. Sobolev[1]

[1] *GFZ German Research Center for Geosciences, Physics of the Earth, Potsdam, Germany*
[2] *Physics of Geological Processes, University of Oslo, Oslo, Norway*
[3] *Computational Geology Laboratory, Polish Geological Institute - National Research Institute, Wroclaw, Poland*
e-mail: *mulyukov@gfz-potsdam.de*
session: *Geodynamics*

Introduction

One of the most robust results from tomographic studies is the existence of two antipodally located Large Low Shear Velocity Provinces (LLSVPs) at the base of the mantle, which appear to be chemically denser than the ambient mantle. Results from reconstruction studies (Torsvik et al., 2006) infer that the LLSVPs are stable, long-lived, and are sampled by deep mantle plumes that rise predominantly from their margins.

The amount of the anomalous LLSVP-material that gets entrained into the rising plumes poses a constraint on the survival time of the LLSVPs, as well as on the plume buoyancy, on the lithospheric uplift associated with plume interaction, and geochemical signature of the erupted lavas observed at the Earth's surface. Recent estimates for the plume responsible for the formation of the Siberian Flood Basalts give about 15 % of entrained dense recycled oceanic crust, which made the hot mantle plume almost neutrally buoyant (Sobolev et al., 2011). In order for the entrainment to take place, the destabilizing viscous stresses acting on a volume of anomalously dense material at the CMB must exceed the gravitationally stabilizing stresses associated with its buoyancy. At what conditions are these criteria met in a dynamically active deep mantle?

While hot rising plumes may act as a sink that entrains the dense material away from the CMB, the subducting slabs that bring compositionally dense oceanic crust (OC) into the lowermost mantle, may act as a source of the dense material. A key questions is: at what conditions can a relatively thin (~ 6 km) layer of OC-material segregate at the CMB and contribute to, or even form, the large-scale compositional anomaly?

To investigate this question, we perform high-resolution numerical simulations of thermochemical convection in 2D domains: both Cartesian and hollow cylinder. For this purpose, we have developed a FEM code with particle-in-cell methodology, building on efficient solvers MILAMIN (Dabrowski et al., 2008), together with packages MUTILS (Krotkiewski and Dabrowski, 2013), and Triangle (Shewchuk, 1996) .

Results

In agreement with other studies, we find that the parameters that govern segregation, accumulation, and entrainment of compositional anomalies are the buoyancy ratio (chemical to thermal, where the latter is computed for the temperature difference across the whole layer), as well as the thermally and compositionally induced viscosity variations. An illustrative result of our simulations is presented in Figures 1–3, where the

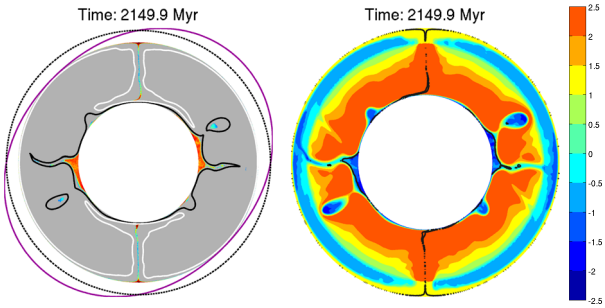

Fig. 1.: Snapshot from one of the simulations to explain the set-up of numerical experimets of segregation of subducted oceanic crust (OC). Left plot: Color-field in the cylinder interior represents the fraction of OC material (computed for each grid-element) – red means pure OC-material. Regions where OC-fraction is less than 0.2 are colored gray. The black and white lines are hot ($T^* = 0.6$) and cold ($T^* = 0.3$) isotherms, respectively (where T^* is the nondimensional temperature). The purple line on the exterior illustrates the direction of the imposed angular velocity boundary conditions (negative means clockwise) – black dashed line indicates the zero angular velocity value. Right plot: Base ten logarithm of viscosity, according to the applied depth- and temperaure-dependent viscosity-profile from (Steinberger & Calderwood, 2006). The black contours represent the OC-fraction value of 0.5. The compositional density anomaly in the presented case is ~1.8 %, corresponding to a buoyancy ratio of ~0.57.

effect of buoyancy ratio of the OC-material on the thermochemical evolution is demonstrated.

The results of our numerical models illustrate that there is both thermal and mechanical feedback between the compositionally distinct materials. The amount of basal heat that flows into the ambient material, and provides the excess buoyancy to drive the convective flow, depends on the volume, or topography, of the anomalously dense material at the CMB. This is largely due to the thermally insulating effect of the latter. The topography of the compositionally dense material, in turn, depends on the flow of the ambient material: the dense material is thickened beneath the upwelling flow, and thinned, or absent, beneath the downwelling flow. The amount of thickening or thinning of the dense basal material is proportional to the strength of the ambient flow.

In cases when the anomalouly dense OC-material manages to accumulate at the CMB, the resulting piles are typically comprised of a mixture of both materials, rather than pure OC-material (based on simulations with two materials: OC and ambient mantle). This is due to two processes. First, the OC-material is introduced into the lowermost mantle as a very thin layer, incapable of complete segregation from its surrounding ambient material. It is, however, capable of slightly reducing the upward flow in its vicinity, albeit on a larger lengthscale. Thus, by retarding its own ascent into the rising plumes, it retards the ascent of the ambient material to which it is viscously coupled, thus both materials end up constituting the piles. The second process that influences the compositional mixture of the dense piles is the convective flow that may develop in the piles interior. This can lead to entrainment of the ambient material into the dense pile-material, further diluting the mixture. The process of convective flow in the dense pile interior leads to a decrease of the piles effective buoyancy ratio over time, increasing its topography and facilitating its entrainment into plumes. The efficiency of this process, compared to the efficiency with which new dense material gets added to the pile, determines the piles survival-time.

References

M. Dabrowski, M. Krotkiewski, and DW Schmid. MILAMIN: MATLAB-based finite element method solver for large problems. Geochemistry Geophysics Geosystems, 9(4):Q04030, 2008. ISSN 1525-2027.

M. Krotkiewski and M. Dabrowski. Mutils - a set of efficient modeling tools for multi-core CPUs implemented in mex. In EGU General Assembly Conference Abstracts, volume 15, page 7877, 2013.

J. Shewchuk. Triangle: Engineering a 2d quality mesh generator and delaunay triangulator. Applied computational geometry towards geometric engineering, pages 203–222, 1996.

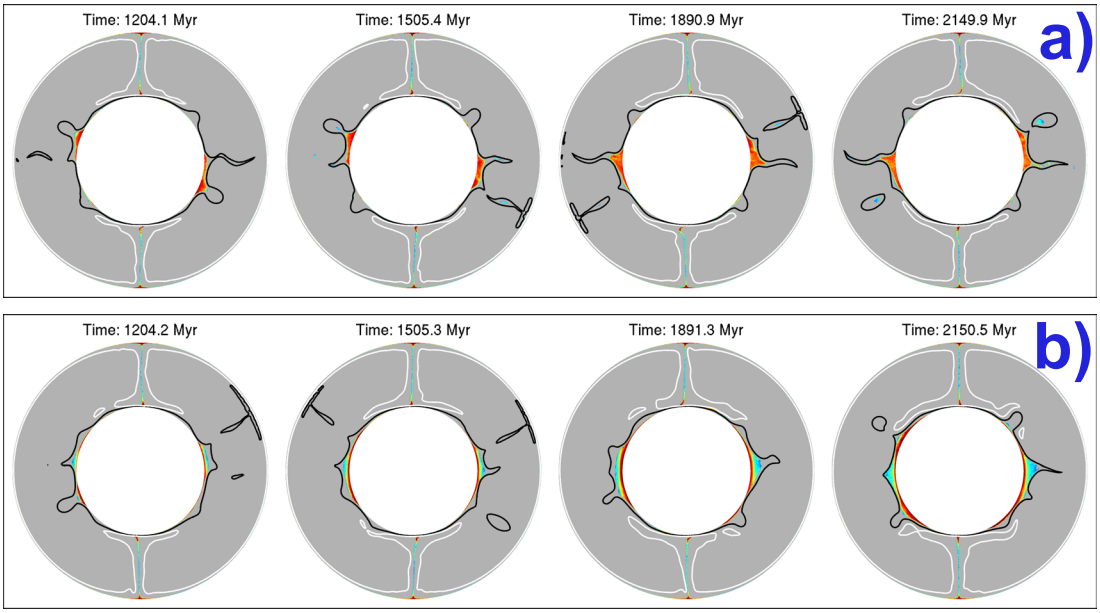

Fig. 2.: Snapshots from the results of two numerical experimets of segregation of subducted oceanic crust (OC), for two different buoyancy ratios (Br). The compositional density anomaly of OC-material is ~1.8 % (Br ~0.57) in the simulation presented in the top row, and ~3.6 % (Br ~1.14) in the bottom row. Explanation of the colors and the set-up is presented in Figure 1. Dense piles of accumulated OC-material formed in case a) have a smaller lateral extent than the piles formed in case b). Further, piles in case a) are constituted by a more homogeneous mixture of OC- and the ambient materials, compared to case b) – where a vertical gradient of the fraction of OC-material within the pile can be observed.

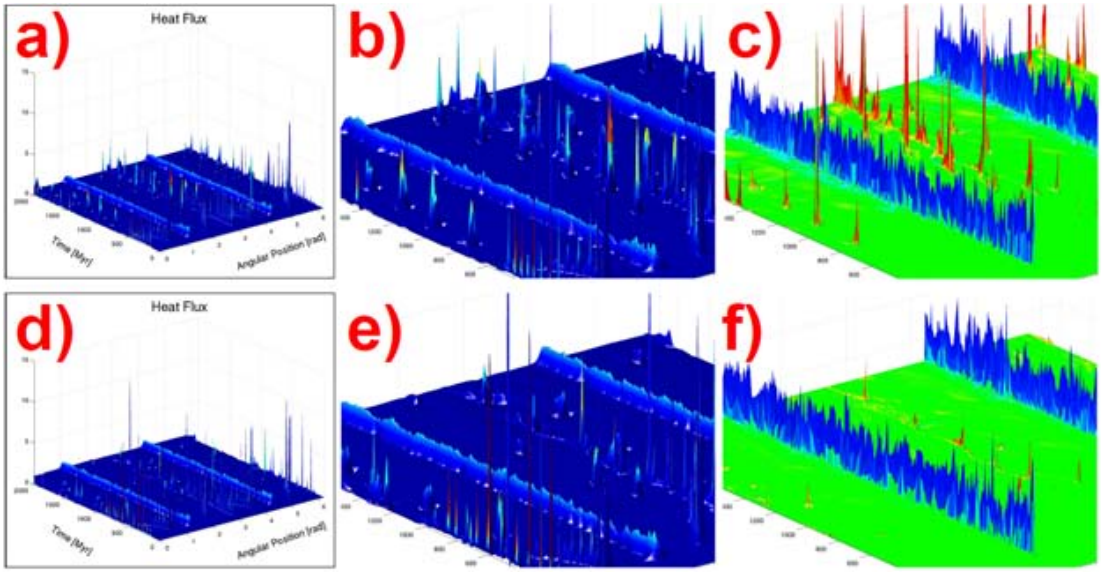

Fig. 3.: Heat (a), b), d), e)) and OC-material (c) and f)) flux over time, measured at mid-depth, for the two simulations presented in Figure 2. Plots b) and e) are zoom-ins on plots a) and d). All values are nondimensional, and scaled to the values measured at the downwelling regions. In plots c) and f) – blue means OC-material flows downwards – towards the CMB, and red means it flows upwards (due to entrainment by rising plumes). Higher heat flux and more efficient entrainment of dense material by plumes can be observed for the simulation with lower buoyancy ratio (case a) in Figure 2).

S.V. Sobolev, A.V. Sobolev, D.V. Kuzmin, N.A. Krivolutskaya, A.G. Petrunin, N.T. Arndt, V.A. Radko, and Y.R. Vasiliev. Linking mantle plumes, large igneous provinces and environmental catastrophes. Nature, 477(7364):312–316, 2011.

T.H. Torsvik, M.A. Smethurst, K. Burke, and B. Steinberger. Large igneous provinces generated from the margins of the large low-velocity provinces in the deep mantle. Geophysical Journal International, 167(3):1447–1460, 2006. ISSN 1365-246X.

Role of extensional strain-rate on lithosphere necking architecture during continental rifting

Nestola, Y.,[1], F. Storti[1], C. Cavozzi[1]

[1]*NEXT – Natural and Experimental Tectonics Research Group, Physics and Earth Science Dept., Università degli Studi di Parma*
e-mail: *yago.nestola@gmail.com*
session: *Geodynamics*

The evolution of lithosphere necking is a fundamental parameter controlling the structural architecture and thermal-state of rifted margin. Among others, parameters such as extensional strain-rate and thermal layering of the lithosphere exert a fundamental control on necking shape and evolution. Despite a large number of analogue and numerical modelling studies on lithosphere extension are available in the literature, a quantitative description of lithosphere necking evolution is still lacking.

We simulated by physical models the progression of lithosphere thinning and necking during orthogonal rifting at different extensional strain-rates. Our models involve a continental 4-layer mechanical lithosphere, which rests on a glucose syrup asthenosphere. Both the topography and the lithosphere base were monitored by time-lapse laser scanning. At the end of deformation, we remove each of the four layers and acquired the surface shape of the underlying ones by laser scanning. This technical approach allowed us to quantify the evolution in space and time of the thinning factors for the crust, mantle, and lithosphere as a whole. Laser-scanning monitoring provided also a detailed picture of the neck shape evolution, which shows a strong dependency on the strain-rate. At low strain-rates, necking is "boxed" with steep flanks and aflat-lying roof. Few deep basins develop at surface. At high strain-rates, more distributed thinning occurs isolating portions of less deformed mantle.A more distributed deformation affects the model topography. Despite large differences in shape, the aspect ratio (height/amplitude) of the necks converge towards very similar values at the end of the experiments.

The significant differences and evolutionary pathways produced by the plate divergence rate on the lithosphere necking profile, suggest that this parameter can exert a fundamental control on the time and space distribution of heat flow during rifting. Following up on this we can speculate on the location and timing of synrift magmatism, which is expected to be preferentially produced on one shoulder for slow plate divergence rate, and more widely distributed and delayed at fast divergence rates.

Toroidal, counter-toroidal, and poloidal flows of the Rivera and Cocos plates

Florian Neumann[1], Alberto Vazquez[2], Gustavo Tolson[3], Juan Contreras[1]

[1] *Graduate School of Earth Sciences, CICESE, Ensenada BC, Mexico*
[2] *Graduate School of Earth Sciences, Institute of Geology, UNAM, Mexico*
[3] *Geology Department, Institute of Geology, UNAM, Mexico*
e-mail: *fneumann@cicese.edu.mx*
session: *Rheology*

Laboratory modeling at a scale 1:4,000,000 was carried out to understand the mantle flow patterns under the Jalisco and Michoacan blocks of the Northern Middle American subduction zone. Scaled model consists of two polyethylene strips that are forced into a tank filled with corn syrup. One of the strips dips 60^{circ} and moves at a velocity of 25 mm/min simulating the Rivera plate. The other one dips 45^{circ}, moves at 75 mm/min and represents the Cocos plate. An acrylic plate 3-mm thick simulates the continental crust of western Mexico. Analysis of pathlines described by embedded markers in the syrup reveal complex, three-dimensional flow patterns in the simulated subduction zone.

The differential motion of the slabs creates a shallow counter-toroidal rotation flow in the simulated mantle wedge from the slow Rivera plate to the fast moving Cocos plate. Similarly, the differential motion gives rise to a deep toroidal flow asthenospheric mantle around the edges of the Rivera slab. Moreover, a hydraulic jump develops in the deep portion of the slow moving strip representing the Rivera slab that causes upwelling poloidal flow under the acrylic plate representing western Mexico. The upwelling eventually merges with the shallow counter-toroidal and poloidal flow of the simulated Cocos slab. Model results are in excellent agreement with seismic anisotropy studies and geochemistry of lavas erupted in the Jalisco and Michoacan blocks. Our results indicate that mantle mixing in the mantle wedge of the Rivera slab is an ongoing process driven by the differential motion between subducting slabs. Rollback of the Rivera plate, if any, likely is a second order effect.

Sponsored by Conacyt

References

Pardo, M. and Suarez, G.. 1995. Shape of the subducted Rivera and Cocos plates in southern Mexico: Seismic and tectonic implications. Journal of Geophysical Research, 100, 357-374.

Soto, L.G. and Ni, J.F. and Grand, S.P. and Sandvol, E. and Valenzuela, R.W. and Guzman-Speziale, M. and Gomez-Gonzalez, J.M. and Dominguez-Reyes. 2009. Mantle flow in the Rivera–Cocos subduction zone. Geophysical Journal International, 179, 1004-1012.

Stubailo, I. and Beghein, C. and Davis, P. M. 2013. Structure and anisotropy of the Mexico subduction zone based on Rayleigh-wave analysis and implications for the geometry of the Trans-Mexican Volcanic Belt. Journal of Geophysical Research, 117, 1–16.

Yang, T. and Grand, S.P. and Wilson, D. and Guzman-Speziale, M. and Gomez-Gonzalez, J.M. and Dominguez-Reyes, T. and Ni, J. 2009. Seismic structure beneath the Rivera subduction zone from finite-frequency seismic tomography. Journal of Geophysical Research 114, 1–12.

Estimating Crustal Thickness of Iran Using Euler Deconvolution Method and EIGEN-GL04C Geopotential Model

Soran Parang

Department of Surveying and Geomatics Engineering, College of Engineering, University of Tehran, Tehran, Iran
e-mail: *soran_parang@ut.ac.ir*
session: *Geodynamics*

The Moho is the boundary between Earth's crust and the mantle. Moho depth is an important parameter in identification of crustal structure and it is also related to geological and tectonic evolution of each zone. The crustal thickness model and Moho depth may be used for studying the state of local and regional isostasy, hence assisting in the characterization of vertical stresses in the lithosphere. These horizontal and vertical stresses are factors that clearly contribute to the seismicity in the upper-to-mid crust. Crustal thickness models are also useful for mineral and geothermal exploration, as areas of thinned crust are sites where the hotter mantle is closer to the Earth's surface. This can result in enhanced plutonic and volcanic activities in the region. In this research, Moho depth is determined according to geopotential models and 3D Euler Deconvolution method. Euler Deconvolution method is not dependent on an initial depth or density limitations. This method is generally used in determining source position and estimating magnetic and gravity anomalies and it is proper to determine depth of vertical and horizontal contacts so it can be used in estimating crust-mantle boundary (Moho depth). In Euler Deconvolution method, Structural index and window size of estimator are important parameters which affect solution very strongly. To estimate crustal thickness using Euler Deconvolution method it is assumed that crust-mantle boundary is a horizontal sheet or it has sill type anomaly which can be expressed in an infinite 2D space. Data used to estimate Moho depth are free air gravity anomaly resulted from expansion of spherical harmonic coefficients of EIGEN-GL04C model (Figure 1), after comparing this model to GPS leveling data, it has been chosen as the most precise model in Iran. In this study Moho depth was estimated for various structural indices and window sizes, in this way the best structural index and window size in the studied region (Iran) and in structural zones of Iran were determined by comparing Moho depth estimated from Euler Deconvolution method and Moho depth calculated by receiver function method in 91 seismic stations of studied region. The results show that for a window size of 45 km and structural index of 0.5 the best Moho depth is estimated for the region, finally the results were also compared to CRUST 2.0 model. Figures 3 to 9 show results of Moho depth estimation using Euler Decovolution method for window sizes of 15 km to 30 km and structural index of 0.5, along 7 profiles in Figure 2.

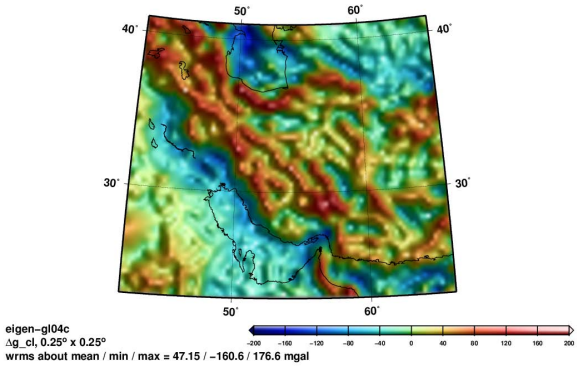

Fig. 1.: Free air gravity anomaly resulted by EIGEN-GL04C model

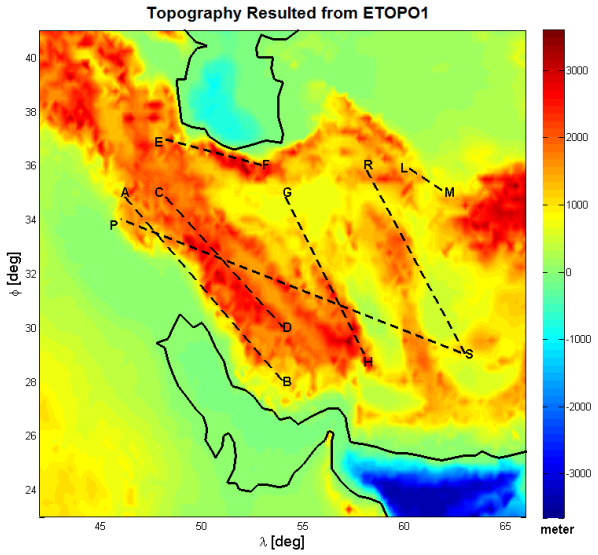

Fig. 2.: Seven considered profiles in Iran

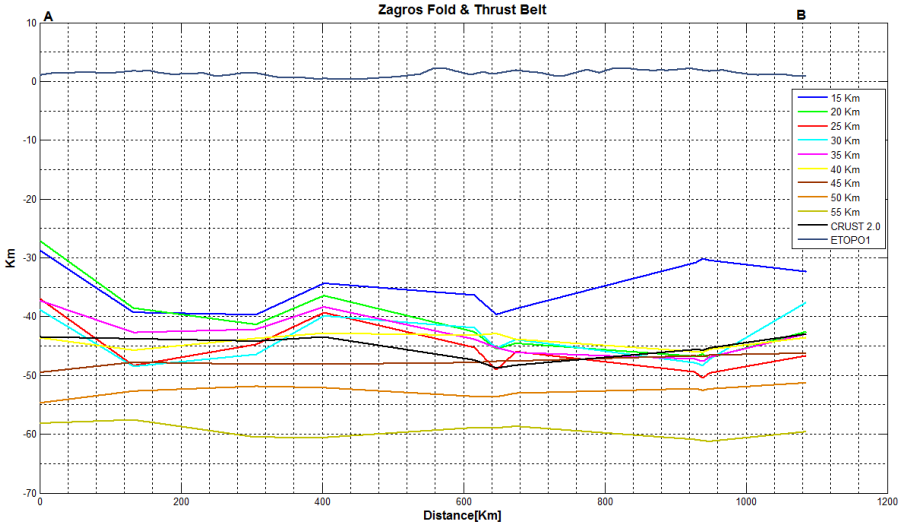

Fig. 3.: Moho depth variation along AB profile located in the Zagros fold & thrust belt

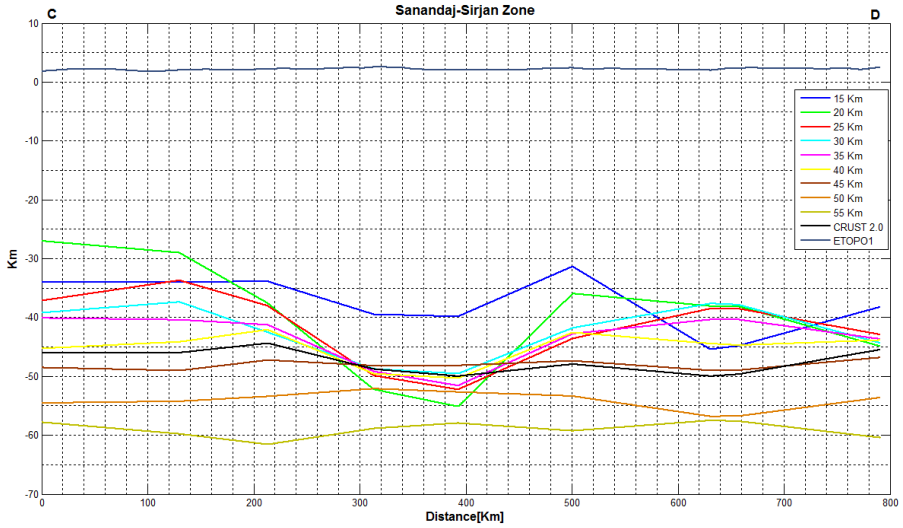

Fig. 4.: Moho depth variation along CD profile located in the Sanandaj-Sirjan zone

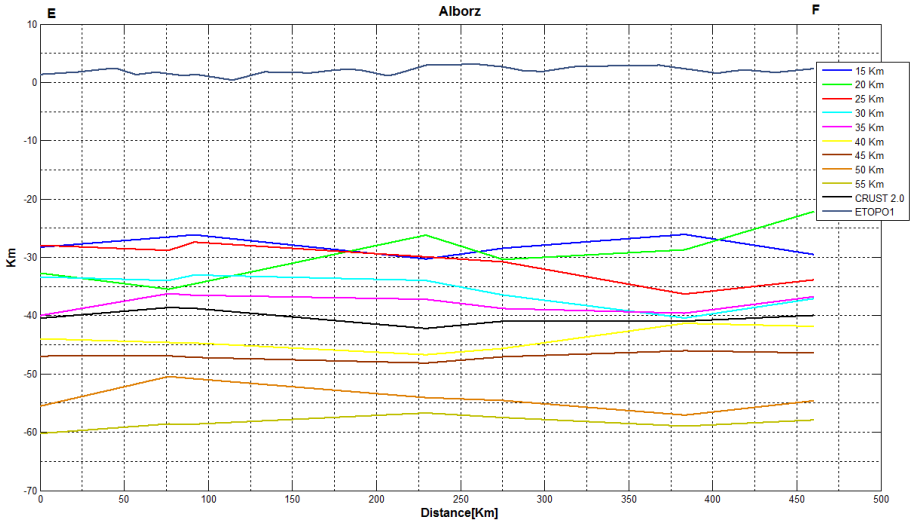

Fig. 5.: Moho depth variation along EF profile located in the Alborz zone

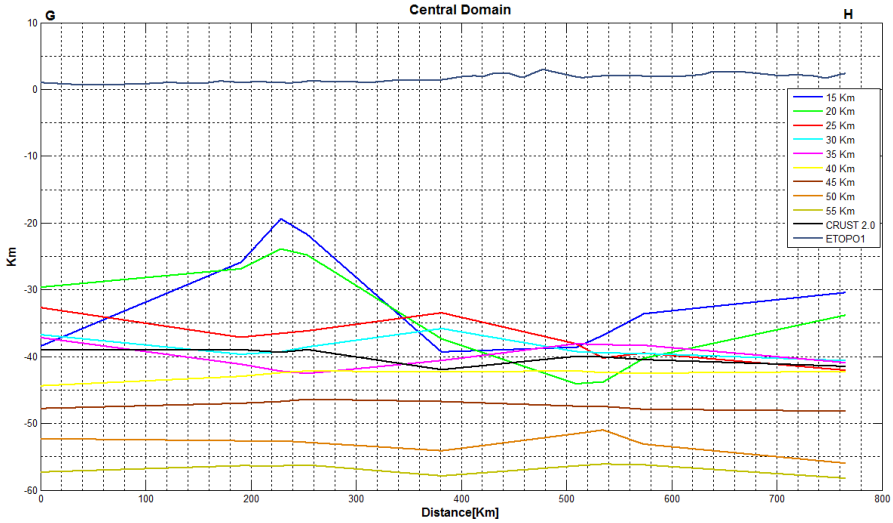

Fig. 6.: Moho depth variation along GH profile located in the Central domain

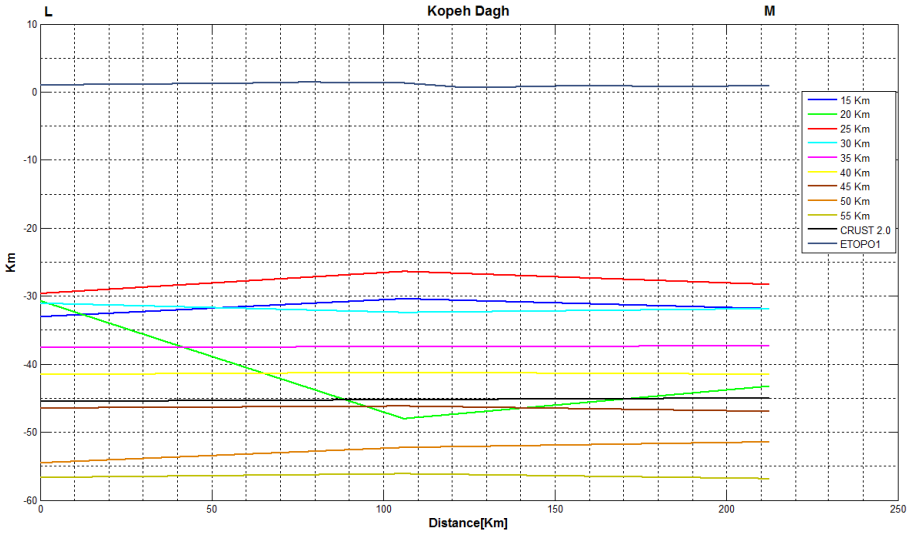

Fig. 7.: Moho depth variation along LM profile located in the Kopeh Dagh zone

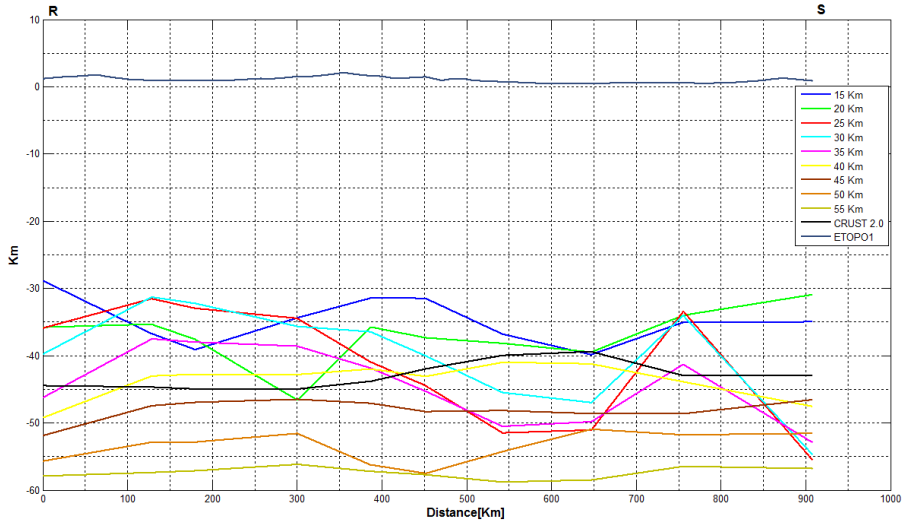

Fig. 8.: Moho depth variation along RS profile

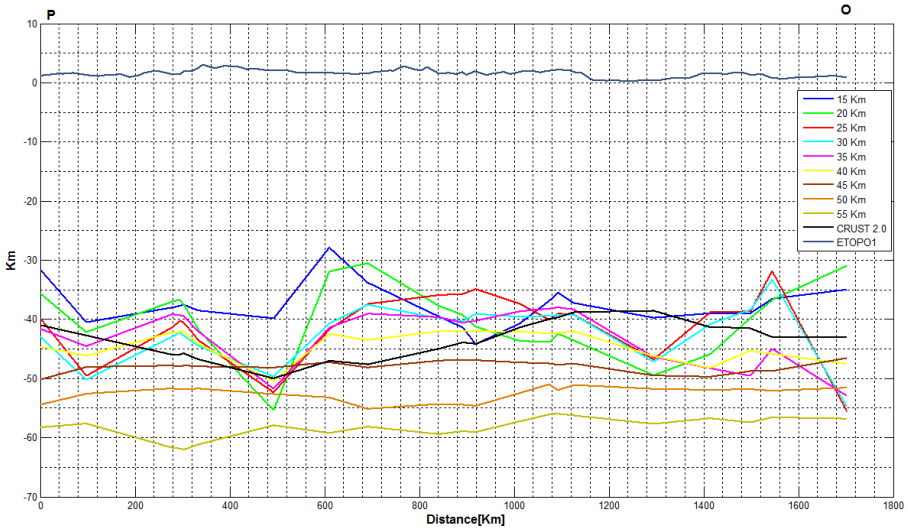

Fig. 9.: Moho depth variation along PS profile

How do weak plate boundaries affect the dynamic topography and geoid?

Alexey G. Petrunin[1], Mikhail K. Kaban[1], Bernhard Steinberger[1], Harro Schmeling[2]

[1] *Helmholtz Centre Potsdam GFZ German Research Centre for Geosciences, Telegrafenberg, D-14473 Potsdam, Germany*
[2] *Goethe-University, D-60323 Frankfurt M, Germany*
e-mail: *alexei@gfz-potsdam.de*
session: *Geodynamics*

The density and viscosity are two major factors controlling mantle dynamics. The geoid, being extremely sensitive to both of them, is a perfect tool reflecting mantle structure. That is why many researchers use the geoid inversion problem to reveal the viscosity-density structure of the lithosphere since decades. The spectral method for solving Navier-Stokes and Poisson equations remains most common technique for such type of problem so far (e. g., Hager and O'Connel, 1981). This method is based on spherical harmonics decomposition of physical fields (e. g., viscosity, density, etc.) that allows obtaining a semi-analytical solution for stress, velocity and gravitational potential with high computational efficiency and preciseness. In its classical formulation, this technique considers the viscosity structure as a number of laterally uniform layers, representing its averaged value for each depth. Most solutions assessing only radial viscosity structure for the mantle that have good fit to the observed geoid, show considerably low value of 1×10^{22} Pa s to 6×10^{22} Pa s for the lithosphere that is too low for the lithospheric plates, and thus do not able to reproduce a plate-like dynamics. Introducing of weak boundaries, dividing strong plates will lead to severe changes in the plate dynamics and, as consequence, in both the geoid and dynamic topography.

So far, most of the studies including strong variation of viscosity have been performed with finite differences (FD)/elements (FE)/volume (FV) methods (e. g. Ratcliff et al., 1997; Yoshida et al., 2001; Tackley, 2008). Using the spectral method on the sphere, we developed the ProSpher code that implies advantages of both spectral-based and FD numerical methods, taking into account strong lateral variations of viscosity, self-gravitation and compressibility, and demonstrates high computational performance and preciseness under high resolution and strong lateral viscosity contrasts (see Petrunin et al., 2013 for more details).

In this study, we intend to determine a pure impact of weak plate boundaries (WPB) on the dynamic topography and geoid. Our numerical experiments assume lateral viscosity variations (LVV) across WPB in uppermost 150 km of the upper mantle only, and only because of effective viscosity decrease along tectonically active plate boundaries (Fig. 1a). In this study we do not intend to construct a self-consistent global model of the mantle, which would require a more extensive work on a joint interpretation of various fields.

To determine a 3D density structure we apply widely-used method connecting shear wave seismic velocity anomalies with density anomalies using standard scaling-factor approach, which has been applied to S40RTS tomography model

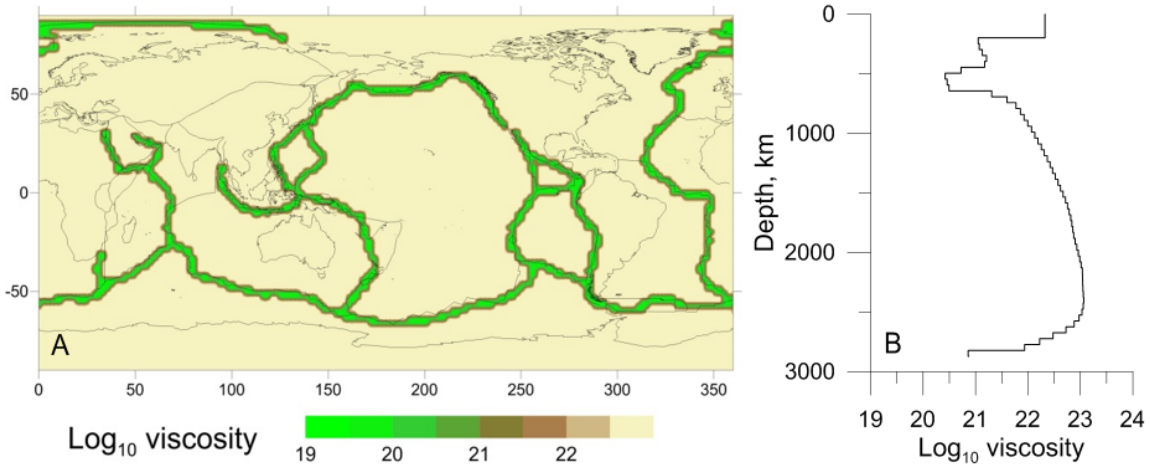

Fig. 1.: WPB based on an integrated global model of plate boundary deformations GSRM (Kreemer et al., 2003); B: radial viscosity model of the mantle (based on Steinberger and Calderwood, 2006)

(Ritsema et al., 2011) as follows:

$$\delta\rho\left(r,\theta,\phi\right) = \alpha\frac{\delta V_{\mathrm{s}}\left(r,\theta,\phi\right)}{V_{\mathrm{s}}\left(r,\theta,\phi\right)}\rho\left(r\right), \qquad \alpha = \frac{d\ln\left(\delta\rho\left(r\right)\right)}{d\ln V_{\mathrm{s}}\left(r,\theta,\phi\right)} \tag{1}$$

where (r,θ,ϕ) are spherical coordinates (radius, latitude and longitude, correspondingly), $\delta\rho$– is density variation, α– is scaling factor and $\frac{\delta V_{\mathrm{s}}(r,\theta,\phi)}{V_{\mathrm{s}}(r,\theta,\phi)}$ is relative shear-wave velocity perturbation. The radial density $\rho\left(r\right)$ profile is obtained from the PREM model (Dzewonski and Anderson, 1981). Taking into account that the presence of WPB changes an average radial viscosity value, that itself affects geoid, we use an algorithm that allows keeping the mean radial viscosity profile unchanged within all models.

The modeling results show that the effect of WPB is significant and may remarkably modify the dynamic topography (Fig. 2) and geoid (Fig. 3). The amplitude of the geoid perturbations reaches −40 m to 70 m with RMS ∼20 m. The maximum changes are found around the big subduction zones at the western margin of South America and over the Southwestern Pacific. The maximum of the observed geoid around South America can be explained by introducing a weak zone separating the Nazca and South American plates. The negative changes of the dynamic geoid are mainly associated with mid-oceanic ridges. Geoid perturbations mainly result from changes of the dynamic topography, which are about −300 m to 400 m.

The amplitude of the geoid undulations grows with increasing of the viscosity contrast between WPB and plates up to values of 2.5–3 orders of magnitude. Further weakening of WPB does not produce significant effect on the geoid. This threshold likely manifests the level when the plates might be considered as decoupled.

The obtained results also show that including WPB may significantly improve the reliability of the global dynamic (snapshot) models and should be considered in future studies.

References

Dziewonski, A.M. & Anderson, D.L. Preliminary Reference Earth Model (PREM), Phys. Earth Planet. Inter. 25, 297-356, (1981).

Hager, B. H. & O'Connell, R. J. A simple global model of plate dynamics and mantle convection. J. Geophys. Res. 86, 4843 (1981).

Kreemer, C., Holt, W. E. & Haines, A. J. An integrated global model of present-day plate motions and plate boundary deformation. Geophys. J. Int. 154, 8–34 (2003).

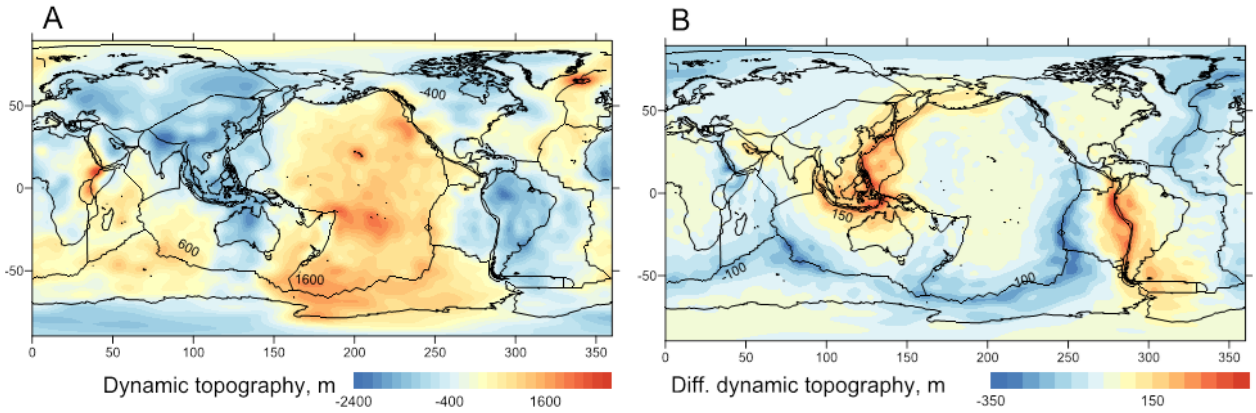

Fig. 2.: A: the calculated dynamic topography for the model with reference radial viscosity profile (Fig. 1b) and plates viscosity of 10^{23}; B: an impact of WPB on the dynamic topography for WPB viscosity contrast of 10^3 with respect to the plate viscosity

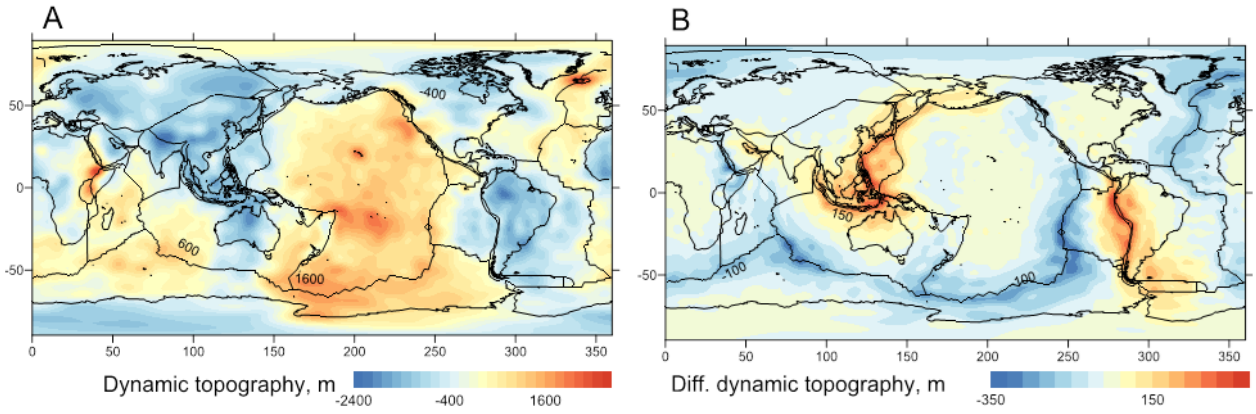

Fig. 3.: A: the resulting geoid for the model with WPB and plate's viscosity of 10^{23}; B: undulations of the geoid as a difference between models with and without WPB. The viscosity at plate boundaries are three orders of magnitude less than the plate's viscosity

Petrunin, A. G., Kaban, M. K., Rogozhina, I. & Trubitsyn, V. Revising the spectral method as applied to modeling mantle dynamics. Geochemistry, Geophys. Geosystems 14, 3691–3702 (2013).

Ratcliff, J. T., Tackley, P. J., Schubert, G. & Zebib, A. Transitions in thermal convection with strongly variable viscosity. Phys. Earth Planet. Inter. 102, 201–212 (1997).

Ritsema, J., Deuss, A., van Heijst, H. J. & Woodhouse, J. H. S40RTS: a degree-40 shear-velocity model for the mantle from new Rayleigh wave dispersion, teleseismic traveltime and normal-mode splitting function measurements. Geophys. J. Int. 184, 1223–1236 (2011).

Steinberger, B. & Calderwood, A. R. Models of large-scale viscous flow in the Earth's mantle with constraints from mineral physics and surface observations. Geophys. J. Int. 167, 1461–1481 (2006).

Tackley, P. J. Modelling compressible mantle convection with large viscosity contrasts in a three-dimensional spherical shell using the yin-yang grid. Phys. Earth Planet. Inter. 171, 7–18 (2008).

Yoshida, M., Honda, S., Kido, M. & Iwase, Y. Numerical simulation for the prediction of the plate motions: Effects of lateral viscosity variations in the lithosphere. Earth, Planets, Sp. 53, 709–721 (2001).

The development of topographic plateaus in an India-Asia-like collision zone using 3D numerical simulations

Adina E. Pusok, Boris Kaus, Anton Popov

Institute of Geosciences, Johannes-Gutenberg University, Mainz, Germany
e-mail: *puesoek@uni-mainz.de*
session: *Geodynamics*

Abstract

The Himalayas and the adjacent Tibetan Plateau represent the most remarkable feature of the Earth's surface as the largest region of elevated topography and anomalously thick crust. Understanding the formation and evolution of the Himalayan-Tibetan region has become of high interest in the scientific community and different models have emerged over the last decades. They range from wholescale underthrusting of Indian lithospheric mantle under Tibet, distributed homogeneous shortening or the thin-sheet model, slip-line field model to the lower crustal flow model for the exhumation of the Himalayan units and lateral spreading of the Tibetan plateau. While some of these models have successfully illustrated some of the basic physics of continental collision, none can simultaneously represent active processes such as subduction, underthrusting, delamination, channel flow or extrusion, which are thought to be important during continental convergence, since these mechanisms require the lithosphere to interact with the underlying mantle.

3D numerical models prove to be powerful tools in understanding the dynamics of coupled systems. However, because of yet recent developments and various complexities, the current 3D models simulating the dynamics of continental collision zones have relied on certain explicit assumptions, either focusing on crustal dynamics or slab-mantle dynamics.

Here, we employ the parallel 3D code LaMEM (Lithosphere and Mantle Evolution Model), using a finite difference staggered grid solver, which is capable of simulating lithospheric deformation while simultaneously taking mantle flow and an internal free surface into account, which allows for the development of topography. We build our model setup to resemble a simplified tectonic map of the India-Asia collision zone and we perform a large number of 3D simulations to investigate the role subduction, continental collision and indentation play on the lithosphere dynamics at convergent margins. The results show that the arrival of a laterally finite continent at the subduction front introduces a strong buoyancy force that changes dramatically the force balance and the dynamics of the system. Trench advance, slab thinning and detachment are processes occurring at the collision zone, while trench retreat, slab roll-back and buckling, coupled with extensive lateral extrusion of material in the upper plate, represent the main processes along the oceanic subduction front. The great variation in slab shape across the subduction-collision zone is consistent with observations from tomographic studies suggesting that 3D models are appropriate to study continental collision settings.

We also analyse the conditions under which large topographic plateaus, such as the Tibetan Plateau can form in an integrated lithospheric and upper-mantle scale model and we discuss the implications these offer for the Asian tectonics. In particular, it has been suggested that slab pull

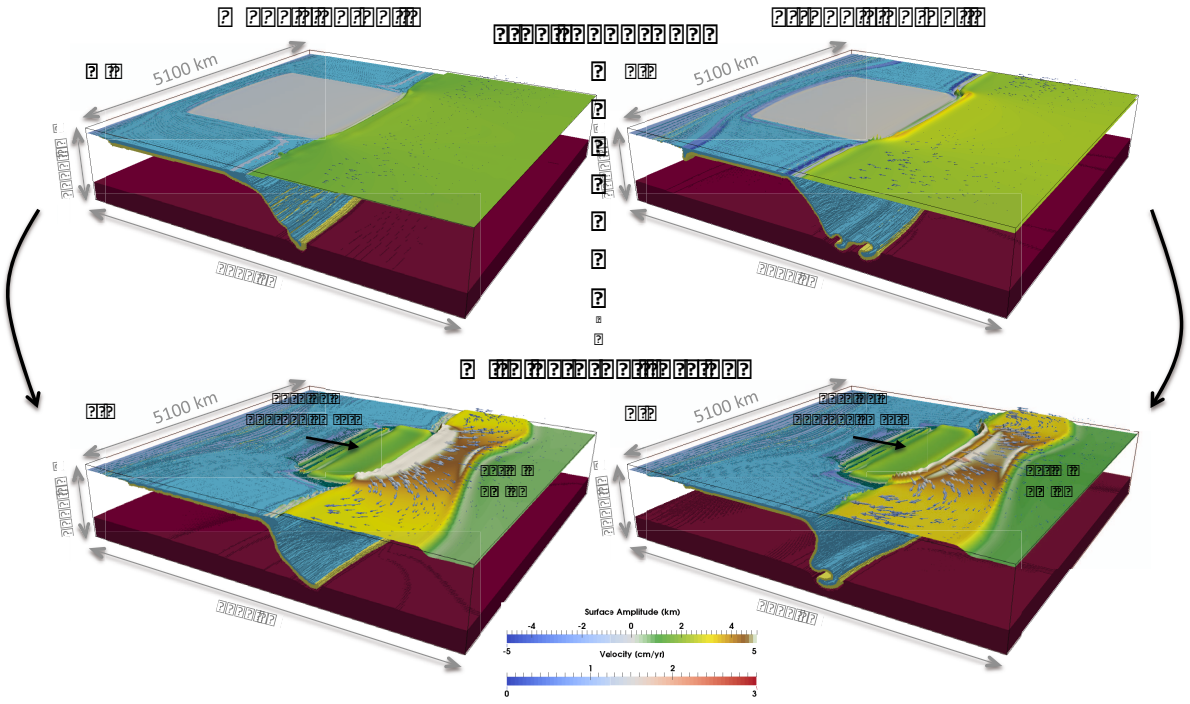

Fig. 1.: The effect of external forcing on upper plate topography in an India-Asia-like setup. (a–b) Simulation results with free subduction after 90 Ma (a) and 70 Ma (b). (c-d) Simulation results with external forcing after 30 Ma. Two additional cases are considered: weak slab-pull (a–c) and strong slab-pull (b-d). External forcing is referred here as an integrated force needed to sustain the present-day convergence of India towards Eurasia ($\sim 5\,\mathrm{cm/a}$) and is implemented numerically as internal Dirichlet boundary conditions. Irregular-shaped crustal blocks such as the Tarim Basin N of the Tibetan Plateau have also been tested (c–d). The subducting slab and the lower mantle are displayed as phases, while topographic maps are shown for the upper plate and continental indentor. Topography has an amplitude exaggeration of x 30 and the velocity arrows represent surface velocity in the upper plate. The results suggest that external forcing and the presence of strong blocks within the Asian lithosphere are necessary to create anomalously high topographic fronts and plateaus, analogous to the Himalayas and the Tibetan Plateau.

is not enough to sustain the on-going convergence of India towards Eurasia, and external forcing, such as ridge push, plume push or slab suction, is important. Furthermore, the presence of strong crustal blocks within the Asian lithosphere such as the Tarim Basin or the Sichuan Basin have also been proposed to be important for the shaping and uplift of the Tibetan Plateau. We test these hypotheses (Figure 1) and show that external factors are necessary to create anomalously high topographic fronts and plateaus, analogous to the Himalayas and the Tibetan Plateau.

Acknowledgements

Funding was provided by the European Research Council under the European Community's Seventh Framework Program (FP7/2007-2013) / ERC Grant agreement #258830. Numerical computations have been performed on MOGON (ZDV Mainz computing center) and JUQUEEN (Jülich high-performance computing center).

Towards quantification of the interplay between strain weakening and strain localisation using analogue models

Malte C. Ritter, Matthias Rosenau, Karen Leever, Onno Oncken

GFZ Potsdam, Lithosphere Dynamics, Potsdam, Germany
e-mail: *malte.ritter@gfz-potsdam.de*
session: *Geodynamics*

Strain weakening is known to be one of the driving factors for the localisation of deformation into discrete faults, entire fault systems and finally into plate boundaries. Nevertheless, the quantitative relationship between weakening and localisation still remains unclear especially when the evolution of whole fault systems is considered. This lack of understanding is at least partly due to the unavailability of geological data with a temporal resolution high enough to image these comparatively fast processes. Physical models using granular materials are able to mimic the process and provide the high temporal and spatial resolution necessary to describe the processes of weakening and localisation with satisfactory precision. Most importantly strain localisation emerges physically self-consistent from simple grain-grain interaction. Physical models therefore seem to be the ideal tool to assess the interplay of both phenomena. However, so far attempts have been made only to quantify either strain weakening (e. g. Lohrmann et al., 2003, using Ring-Shear-Tests) or strain localisation as isolated properties (e. g. Schrank et al., 2008, using the classical Riedel-experiment). While Ring-Shear-Tests are a standard procedure in industry that is correspondingly well developed and yields excellent data on the intrinsic mechanical properties of a granular medium, they do not allow monitoring the process of localisation because of experimental inaccessibility of the shear zone. In Riedel-type strike-slip experiments, on the other hand, no measurements of shear stresses have been available so far. Furthermore, they contain a strong boundary condition in form of a pre-defined linear discontinuity at the base, that might force localisation in otherwise non-localising materials (Schrank et al., 2008).

We developed a new experimental set-up in which deformation of a layer of granular material (sand) in strike-slip mode is driven solely by push from one side and without the need of a basal discontinuity. This is made possible by a layer of low viscosity silicone on which the sand pack rests (cf. fig. 1.) and that reduces the basal drag force to an amount that allows pushing the sand as a rigid block without forming a wedge. The push is applied by a moving indenter, that acts on one half of the sand pack, while the other half is held back by a stationary back wall opposite the indenter, such that in between the two a shear zone forms. The indenter is equipped with a sensor that measures the force integrated over the shear stress along the entire shear zone and the basal drag. The deformation of the sand pack is monitored by a video camera from above. By means of digital image correlation (DIC) displacement- and strain fields can be calculated from the video data, and these in turn can be used to calculate a localisation intensity factor (Schrank et al., 2008). Thus, simultaneous monitoring of shear stress and localisation is possible with this set up.

Here we present data from experiments in this set-up, using materials that show strain weakening to a different amount. These data show a principal pattern of correlated strain weakening and localisation in which overall weakening lags

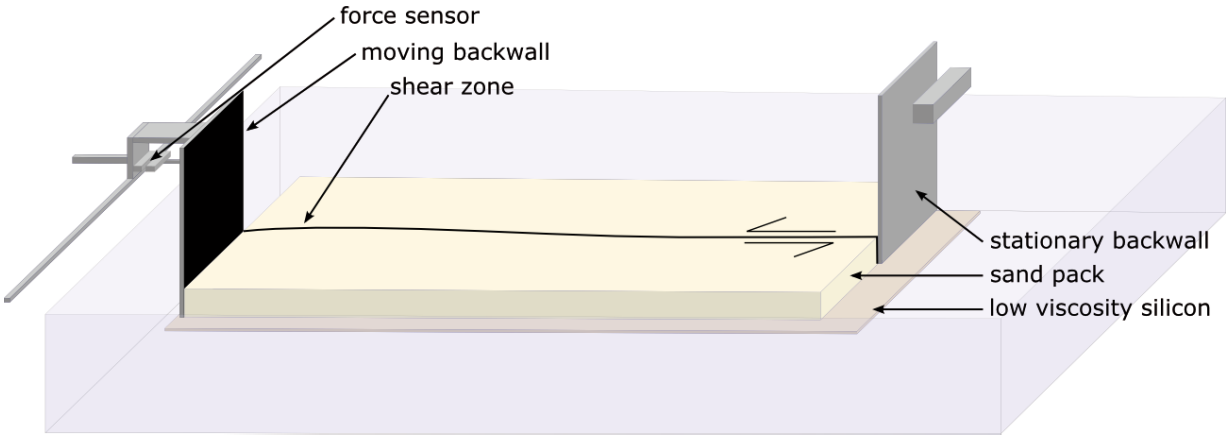

Fig. 1.: Experimental set-up. A sand pack resting on low viscosity silicon is deformed in strike-slip mode by an indenter ("moving back wall") moving against a stationary back wall. The applied integrated shear force is measured by a force sensor connected to the indenter, and the resulting deformation is recorded by a video camera from the top (not shown in figure).

behind the overall localisation (cf. fig. 2). We attribute this lag to the evolution of the fault zone system. More specifically, we hypothesize, that small areas of reduced localisation intensity occurring between adjacent segments of the evolving shear zone act as force bridges that keep up the overall strength, while localisation within the fault segments themselves increases. Only when the bridges rupture, the overall stress decreases, but without a significant increase of overall localisation. Furthermore, we do not measure a direct correlation between the amount of weakening and the amount of localisation, i. e. localisation in the fully evolved shear zone is similar for different materials, independently of the amount of weakening that occurred. The main difference between materials that we observe is the amount of displacement needed to start localisation.

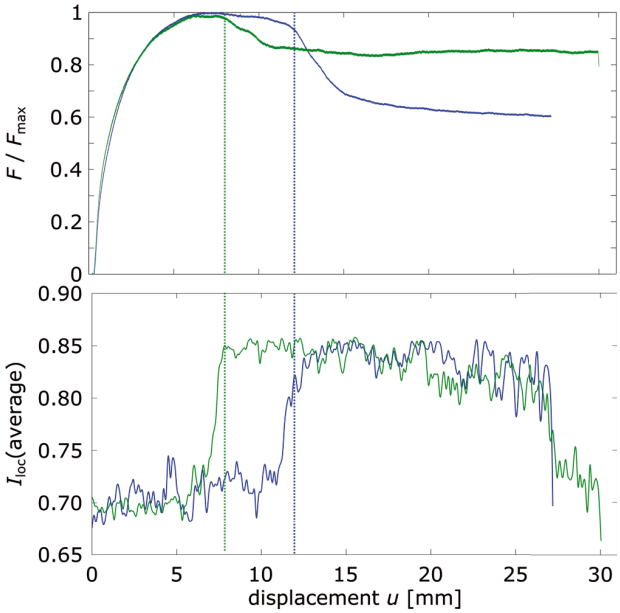

Fig. 2.: Plots showing normalized integrated push force and the amount of localisation (according to Schrank et al., 2008) for two selected experiments, using materials with different strain weakening behaviour (quartz sand, strong weakening, blue, and glass beads, less weakening, green). The amount of localisation is approximately the same, although the amount of weakening is very different. Note the different displacement increments, at which localisation and weakening occur for both materials.

We conclude, that the weakening of lithospheric scale faults strongly depends on their small-scale structural evolution and is to be distinguished from the strain weakening of rock (or sand, in our experiments) as an intrinsic material property. Our experimental set-up, that facilitates simultaneous measurements of force and strain, offers the possibility to evaluate this interplay between lithospheric scale weakening and structural evolution.

References

Lohrmann, J., Kukowski, N., Adam, J., and Oncken, O., 2003, The impact of analogue material properties on the geometry, kinematics, and dynamics of convergent sand wedges: Journal of Structural Geology, v. 25, no. 10, p. 1691–1711, doi: 10.1016/S0191-8141(03)00005-1.

Schrank, C.E., Boutelier, D.A., and Cruden, A.R., 2008, The analogue shear zone: From rheology to associated geometry: Journal of Structural Geology, v. 30, no. 2, p. 177–193, doi: 10.1016/j.jsg.2007.11.002.

Modelling plate kinematics, slabs and LLSVP dynamics – an example from the Arctic and northern Panthalassa

G. E. Shephard, A. L. Bull, C. Gaina

Centre for Earth Evolution and Dynamics (CEED), Department of Geosciences, University of Oslo, Norway
e-mail: *g.e.shephard@geo.uio.no*
session: *Geodynamics*

The Arctic Ocean, one of the world's smallest and shallowest, is also amongst the most tectonically complicated. Bathymetry of the Arctic Ocean is delineated by two major basins, the elongate Eurasia Basin and the larger Amerasia Basin, which are surrounded by extensive continental shelf margins (Figure 1). Our current understanding of its Mesozoic and Cenozoic evolution reveals a history dominated by ocean basin consumption and opening, multiple plate boundary reorganizations and successive magmatic events. While the timing and rates of seafloor spreading within the Eurasia Basin are relatively well constrained, our existing state of knowledge of the evolution of the Amerasia Basin pails in comparison. Some of the most fundamental and outstanding questions about the Amerasia Basin concern the timing of extension and possible seafloor spreading (Jurassic to Cretaceous), style of opening (counter-clockwise, orthogonal or other), location of continental versus oceanic or "transitional" crust, timing of magmatism (High Arctic Large Igneous Province), and quantifying the amount of direction of recent extension (possibly more than 100 %). The opening of the Amerasia Basin is also widely thought to be associated with the closure of an intervening ocean basin, the South Anuyi Ocean, located between Siberia, North America and Panthalassa (Figure 2). Furthermore, considering the Arctic within a global context and with dynamic and connected plate boundaries, demands a consideration of adjacent plate margins, including those within Panthalassa, North America and the nearby Mongol-Okhotsk Ocean.

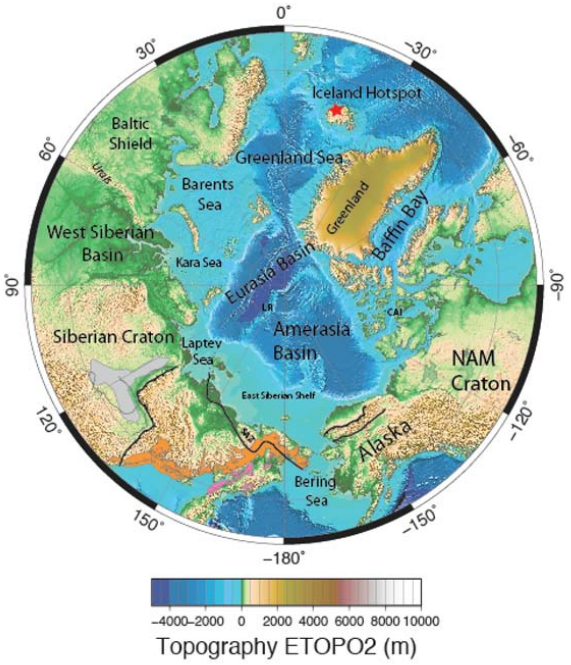

Fig. 1.: Topographic overview of Arctic region with major structural and geographic features labeled.

The onshore geological record and near-surface geophysical data across the circum-Arctic is of variable resolution and coverage, and is compounded by limited accessibility e. g. ice-coverage and expensive reconnaissance and field missions. Ambiguity has permitted a myriad of alternative tectonic scenarios (an example is shown in Figure 2) and there is a need to look to other data-

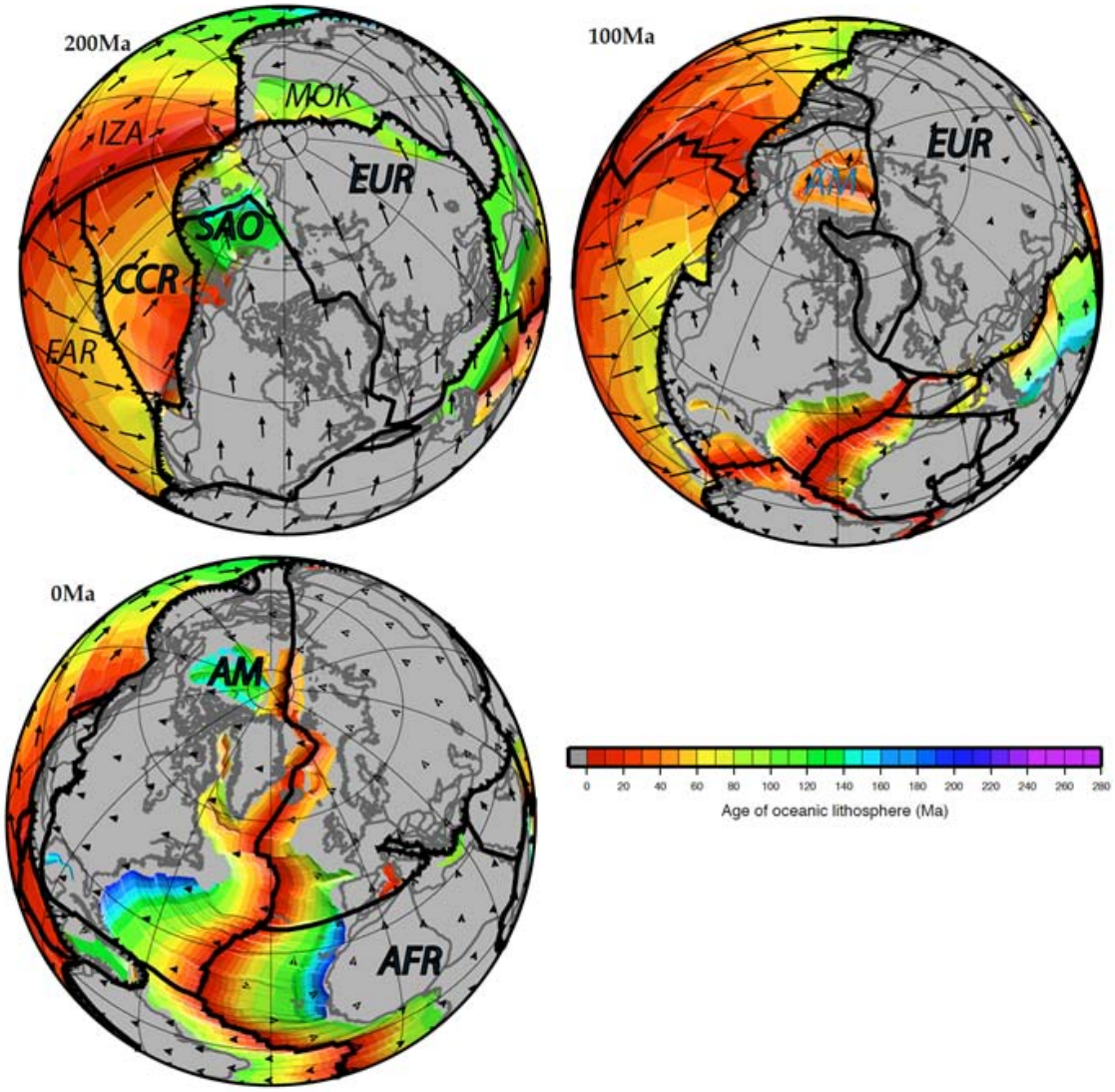

Fig. 2.: Three timesteps from the revised plate reconstruction of the Arctic and Panthalassa region presented in Shephard et al. (2013). Age grid, coloured to age of oceanic lithosphere (Myr), plate velocities in black, continental regions in grey with present-day coastlines in dark grey, plate boundaries in black. Plate and ocean basin acronyms: IZA Izanagi, FAR Farallon, CCR Cache Creek, SAO South Anuyi Ocean, EUR Eurasia, MOK Mongol-Okhotsk, AM Amerasia Basin, AFR Africa.

sets to better constrain surface kinematics and generate refined plate reconstructions. Seismic tomography has the potential to help reveal past kinematic history in regions where subduction processes were sufficiently long-lived to produce considerable amounts of slab that have sunk into the mantle. For example, by assuming vertical sinking of slabs and mantle sinking rates, the location and timing of subduction can be linked to features inferred from seismic tomography (e. g. van der Meer et al., 2012; Sigloch and Mihalynuk 2013, Figure 3). Subduction within the highest Arctic region is suggested to have occurred since at least the Late Jurassic, of which associated slabs can be interpreted to be located under present-day Greenland Siberian Shelf and North America (Shephard et al., 2013; Gaina et al., 2013).

With ever-increasing detail of global plate motion models, advances in numerical modeling and the resolution of seismic tomography, alternative plate reconstructions can now be robustly tested within a geodynamic framework.

Shephard et al. (in press) (Figure 3) compared the spatial and temporal evolution of slabs predicted by two alternative regional reconstructions (Shephard et al., 2013 and Seton et al., 2012) with seismic tomography. While noting an improved match between seismic tomography and a mantle flow model with a refined plate reconstruction, reasonable offsets still remained. Kinematic variability remaining to be further tested includes the timing and location of intra-oceanic and/or continental subduction, subduction polarities, relative plate velocities, convergence and the rate of subduction, age of subducting lithosphere and dip of subducting slabs.

We also present preliminary investigations into the interaction of these regional slabs with the Pacific Large Low Shear Wave Velocity Province (LLSVP). In combination with its antipodal LLSVP located under Africa, these dominant, degree-two features of the lowermost mantle are thought to be of thermochemical origin and have possibly been stable for > 410 Myr (Bull et al., 2014; Torsvik et al., 2008) (Figure 4). However, the specific role of these Arctic and Panthalassa slabs in LLSVP stability and topography as well as plume generation zones and the D" boundaries remains to be further quantified (Bower et al., 2013). By integrating surface kinematics, global mantle flow models and seismic tomography we aim to unravel the complex interaction of surface and mantle dynamics of this region, stretching throughout the Phanerozoic to present-day.

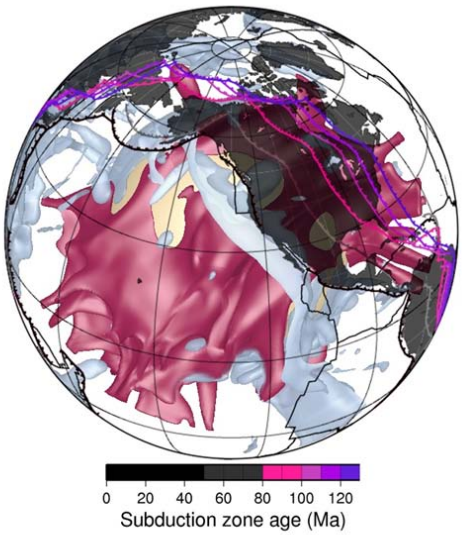

Fig. 4.: Forward modelled mantle structure of Bull et al. (2014) showing residual non-dimensional temperature isosurfaces +/- 0.15 (red/blue respectively) in the lower mantle for the Pacific LLSVP. Present-day coastlines are superimposed in black and reconstructed subduction zones from 0 Ma to 120 Ma shown by coloured lines.

References

Bower, D. J., Gurnis, M. and Seton, M. (2013). Lower mantle structure from paleogeographically constrained dynamic Earth models. Geochemistry, Geophysics, Geosystems v.14 doi:10.1029/2012GC004267

Bull, A.L. Domeier, M., & Torsvik, T.H., (2014). The effect of plate motion history on the longevity of deep mantle heterogeneities. Earth and Planetary Science Letters (in press)

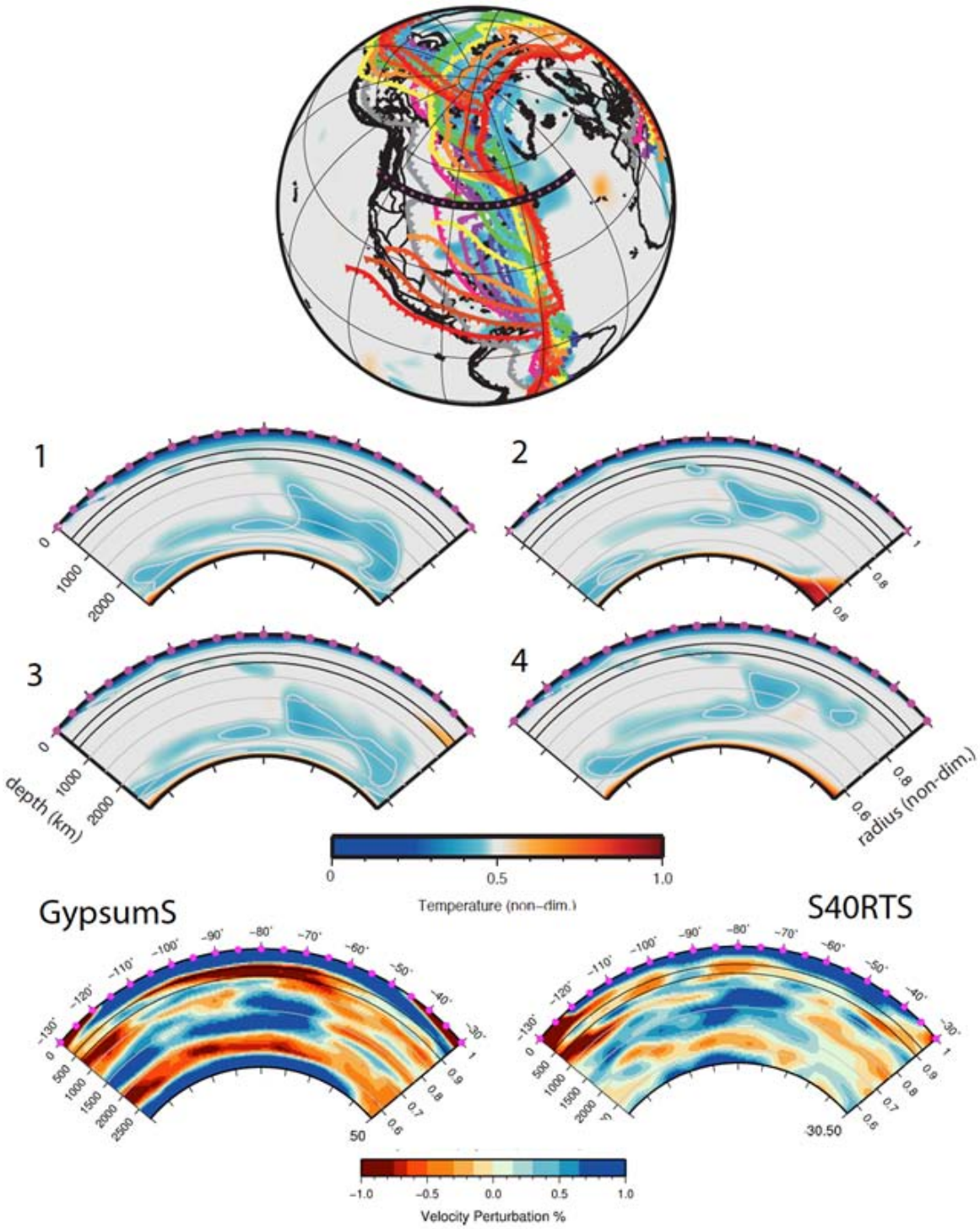

Fig. 3.: Top panel, projection of vertical section, black (50°N, North America) superimposed over reconstructed subduction locations based on Shephard et al., 2013 (230 Ma to 0 Ma). Panels 1–4 forward modeled mantle thermal (slab) structure predicted by four alternative models (differing rheologies). Bottom panels, two seismic tomography models at same vertical section.

Gaina, C., S. Medvedev, T. H. Torsvik, I. Koulakov and S. C. Werner (2013), 4D Arctic: A glimpse into the structure and evolution of the Arctic in the light of new geophysical maps, plate tectonics and tomographic models, Surveys in Geophysics, doi:10.1007/s10712-013-9254-y.

Seton, M., Müller, R.D., Zahirovic, S., Gaina, C., Torsvik, T.H., Shephard, G., Talsma, A., Gurnis, M., Turner, M., Maus, S., Chandler, M. (2012). Global continental and ocean basin reconstructions since 200 Ma. Earth-Science Reviews 113 (3–4), 212–270. doi.org/10.1016/j.earscirev.2012.03.002.

Sigloch, K., and Mihalynuk, M. (2013) Intra-oceanic subduction shaped the assembly of Cordilleran North America. Nature v.496 p.50-56 doi:10.1038/nature12019

Shephard, G.E., Müller, R.D., Seton M., 2013, The tectonic evolution of the Arctic since Pangea breakup: Integrating constraints from surface geology and geophysics with mantle structure. Earth-Science Reviews v.124 p.148-183.

Shephard, G. E., Flament, N., Williams, S., Seton, M., Gurnis, M., and Müller, R.D., In Press. Circum-Arctic mantle structure and long-wavelength topography since the Jurassic. Journal of Geophysical Research

Torsvik, T. H., B. Steinberger, B., L. R. M. Cocks and K. Burke (2008). Longitude: Linking Earth's ancient surface to its deep interior, Earth Planet. Sci. Lett., 276, 273-282, doi:10.1016/j.epsl.2008.09.026

van der Meer, D.G., Torsvik, T.H., Spakman, W., van Hinsbergen, D.J.J. and Amaru, M.L. (2012) Intra-Panthalassa Ocean subduction zones revealed by fossil arcs and mantle structure, Nature Geoscience 5, p. 215-219

Strike-slip movements and Rotation of tectonic blocks in the Kaboodan area, south Khur, Central Iran

Arash Sohrabi, Alireza Nadimi

Department of Geology, Faculty of Science, University of Isfahan, Hazarjirib, P.O.Box 81746-73441, Isfahan, Iran
e-mail: *arashshrbi@yahoo.com*
session: *Geodynamics*

The active tectonics of Iran results from the northward Arabia–Eurasia convergence. At the southwestern and southern boundaries of the Arabia-Eurasia collision zone, the convergence is taken up by the continental collision in the Zagros Mountains, and the active subduction of Makran, respectively. Further north, the northward motion not absorbed by the Makran subduction is expressed as the N-trending right lateral shear between central Iran and Eurasia at a rate of 16 mm/yr (e. g., Regard et al., 2005; Vernant et al, 2004).

The Khur area is located in the central and western part of Central Iran (Stocklin 1968) that characterized by an intricate heterogeneous structures and combination of ancient continental faulty blocks and narrow suture zones. Faults play important role in the tectonic evolution of the area and breaking it into smaller blocks. Major deep and long-lived faults separate structural zones.

Several map-scale NE-SW-trending faults are stretched in the Central Iran. These are Great Kavir, Ordib and Chapedony faults. Ordib fault bounds the Anarak-Khur massif to the southeast. The fault is represented on the surface by a series of sub-parallel vertical reverse faults locally passing into steep thrust dipping to northwest. The width of the fault zone ranges from several hundred meters to 1.5 km to 2 km. The amount of displacement decreases eastward, and the major fault branches out into a series of minor faults which cut practically through all the rock complexes from the Upper Proterozoic to Neogene, even locally through the oldest Quaternary sediments. Many of faults in this zone are accompanied by heavy crushing, schistosity and hydrothermal alteration of the rocks (Aistov, 1984).

It has been recognized that fault blocks in strike-slip tectonic domains must progressively rotate around vertical axes as the overall strike-slip motion continues. Two direct consequences of the deformation mechanism are (1) slip on each of the fault within a domain must be related to the rotation of the blocks bounded by these faults, and (2) the faults themselves must also rotate because they are the boundaries of the blocks (Kissel and Laj 1989). When rotation becomes sufficiently large, slip on the rotating faults ceases because the resolved shear stress on them has decreased and the normal stress has increased to the point where the frictional resistance is too great for further slip. If crustal deformation is to proceed it must be accommodate by a set of new faults, more favorable oriented to the principle direction of the regional stress field (Hogai et al, 1993).

In Kaboodan area the blocks rotated in domino style in different sizes between the strike-slip faults clockwise around vertical axis. These rotations are directly controlled by the orientation of the faults relative to the direction of the principle tectonic shortening.

The following results can be summarized as follows:

1. The Ordib fault and other NE-SW-trending

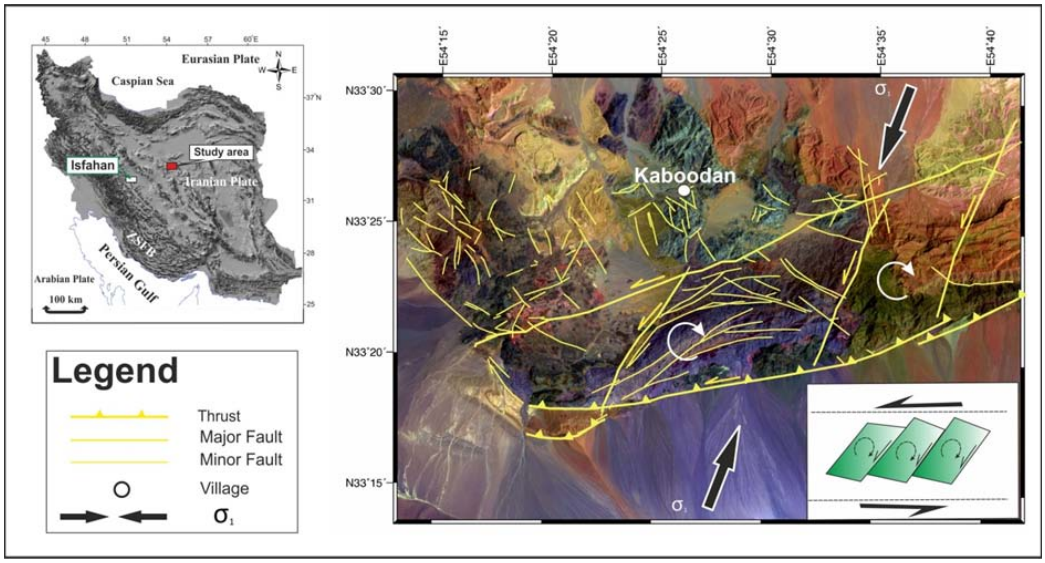

Fig. 1.: Location of the studied area and the Kaboodan structural zones. Fault patterns and the rotated blocks in this area.

faults of the Khur area have important role in tectonic evolution of the Central Iran. Strike-slip movements along the faults have been occurred during northward convergence of the Arabian and Eurasian plates. The movements are created several kinds of smaller faults and have formed different sizes of structural blocks.

2. Clockwise rotation of the structural blocks has been occurred along the major and minor faults of the area.

References

Aistov, L., Melanikov, B., Krivyakin, B., Morozov, L. and Kiristaev, V.(Eds.), (1984) Geology of the Khur Area (central Iran).Explanatory text of the Khur quaderangle map.

Farbod, Y, Bellier, O, Shabanian, E and Abbassi, M.R. (2010) Structural and geomorphic fault segmentations of the Doruneh Fault System, central Iran, Geophysical Research Abstracts, Vol. 12, EGU2010-6576-1.

Hogai, R, Amos, N and Atilla, A (1993) Stress field rotatio or block rotation an example from tha lake mead fault system. J. Geofisica. Vol. XXXVI, N, 2, P. 65-73.

Kisel, C and Laj, C. (1989) Paleomagnetic rotation and continental deformation, Kluwer Academic publishers, 209-228.

Regard, V., Bellier, O., Thomas, J. C., Bourles, D., Bonnet, S., Abbassi, M. R., Braucher, R., Mercier, J., Shabanian, E., Soleymani, S., and Feghhi, K. (2005). Cumulative right-lateral fault slip rate across the Zagros-Makran transfer zone: role of the Minab-Zendan fault system in accommodating Arabia-Eurasia convergence in southeast Iran.Geophysical Journal International 162, 177-203

Stöcklin, J., (1968) Structural history and tectonics of Iran. A review: American Association of Petroleum Geologists Bulletin, v. 52, 7, p. 1229–1258.

Vernant, P., Nilforoushan, F., Hatzfeld, D., Abbassi, M.R., Vigny, C., Masson, F., Nankali, H., Martinod, J., Ashtiani, A., Bayer, R., Tavakoli, F., and Chery, J., 2004. Present-day crustal deformation and plate kinematics in the Middle East constrained by GPS measurements in Iran and northern Oman. Geophysical Journal International, 157, 381–398.

On the relation between plate tectonics, large-scale mantle flow and mantle plumes: Some recent results and many open questions

Bernhard Steinberger[1,2], Rene Gassmoeller[1], Elvira Mulyukova[1], Juliane Dannberg[1], Stephan V. Sobolev[1,3]

[1] *Section 2.5, Geodynamic Modelling, GFZ German Research Centre for Geosciences, Potsdam, Germany*
[2] *Centre for Earth Evolution and Dynamics, University of Oslo, Norway*
[3] *Schmidt Institute of the Physics of the Earth, Russian Academy of Sciences*
e-mail: *bstein@gfz-potsdam.de*
session: *Geodynamics*

Tectonic plate motions are a surface representation of convection in the Earth's mantle. Seismic tomography reveals that most subducted plates eventually sink into the lowermost mantle. Yet the relation of plate tectonics and mantle dynamics remains incompletely understood. The observed stability of the two Large Low Shear Velocity Provinces (LLSVPs) over at least 250 Myr, and possibly much longer, is an important constraint on models of mantle dynamics, and difficult to explain with current models.

Approximately stable LLSVPs that match observed locations and shapes can be reproduced by 3D numerical models with imposed locations and amounts of subduction, as dictated by the plate tectonic reconstructions for the past 250 Myr. In these models, LLSVPs are represented by thermochemically distinct piles, which form when an initially flat and compositionally dense basal layer gets deformed by the ambient mantle flow. The long-term stability of LLSVPs in these models is aided by subduction, which has occurred in similar areas during this period, and mostly stayed away from the LLSVPs; yet it is unclear what could have caused relative stability of subduction zone locations. The fact that the locations of major upwellings (divergent plate tectonic quadrupole; Conrad et al., 2013) have approximately remained stable for the past 250 Myr, but the location of the strongest downwellings (convergent quadrupoles) have moved along the great circle bisecting between the divergent quadrupoles, may suggest that it is the upwellings themselves that maintain stability and orchestrate the global mantle flow. Yet we currently have no dynamically consistent model that explains such behaviour.

Another surface representation of mantle dynamics are hotspots, believed to be caused by mantle plumes. Plumes may interact with spreading ridges, causing increased volcanism and crust production in ridge segments nearby. They may also be instrumental in causing ridge jumps, which may lead to continental fragments in the oceans. Recent results show that plumes and plates also interact at the base of the mantle: the locations and distribution of hotspots can be much better explained with a geodynamic model where plumes are triggered, mainly along the margins of thermochemical piles, by slabs approaching the core-mantle boundary, rather than freely developing (Figure 1).

Important parameters governing the thermochemical evolution of the mantle are buoyancy ratio (chemical vs. thermal), the dependence of viscosity on temperature and chemical compos-

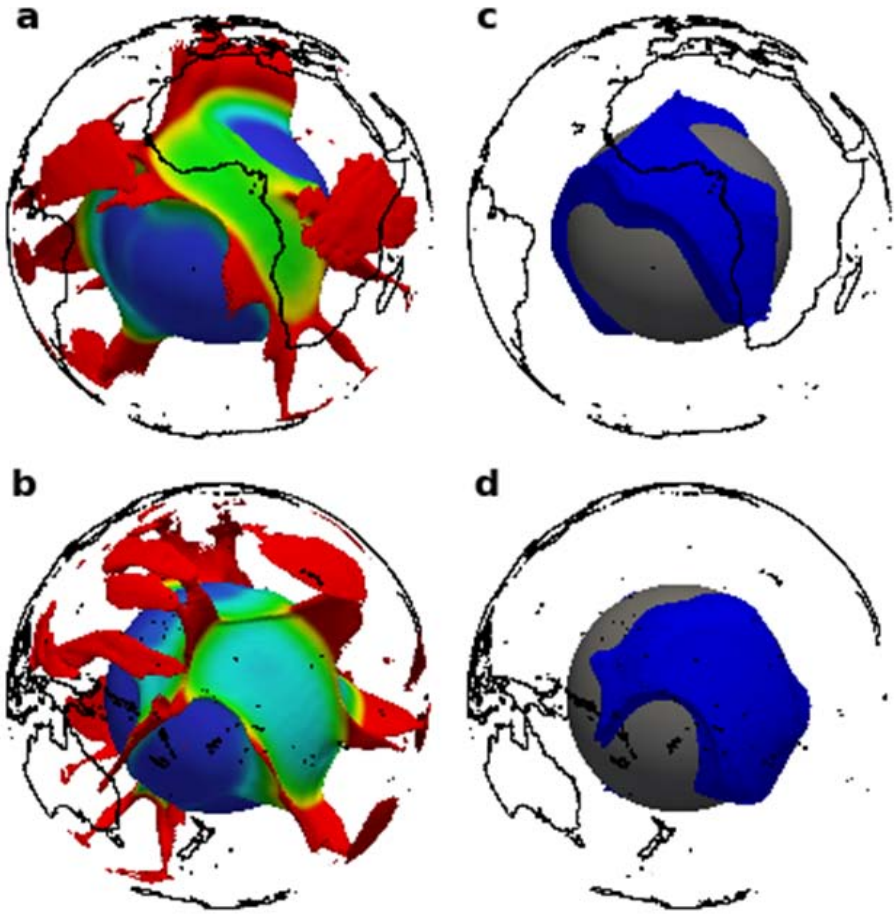

Fig. 1.: Thermo-chemical piles near the core-mantle boundary plotted as chemical isosurface in **c** and **d**, and plumes rising from their margins as isosurface 250 K hotter than the surrounding mantle in **a** and **b**, coloured according to the height above the CMB. The figure shows the model for present-day after 250 Myr of plate motions imposed as surface boundary condition.

ition, as well as the deviation of lower mantle temperature from the adiabatic profile. There is a large uncertainty associated with each of these parameters. For instance, the buoyancy ratio depends on the origin of the chemically anomalous material, which is currently debated. This material, which is responsible for the large scale heterogeneity in the mantle – such as the LLSVPs – may be either primordial, recycled subducted crust, or leaked outer core material – or a combination of these.

Numerical experiments can also show under what circumstances, and to what degree, subducted crust can accumulate in the lowermost mantle, and/or primordial material can remain there for billions of years without being entrained. A modelling result that illustratres how the lower mantle viscosity affects segregation, accumulation, and reentrainment of the subducted oceanic crust is shown in Figure 2.

The behaviour of mantle plumes depends on how much of the chemically different, heavier material is carried upward by them. Numerical models can show under which conditions the low-buoyancy thermochemical plumes could arrive to the lithosphere from the core mantle boundary (Figure 3).

Geodynamic models can be constrained by vari-

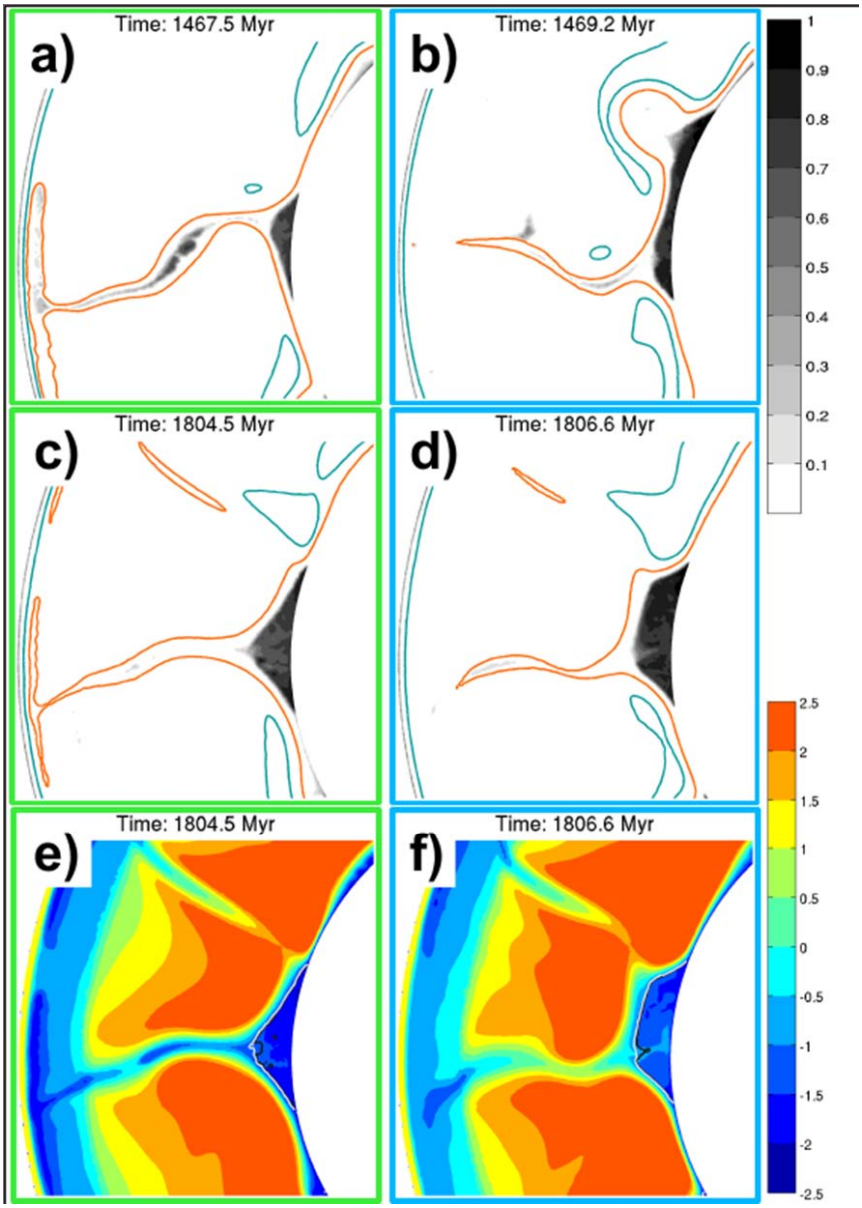

Fig. 2.: Numerical modelling of thermochemical convection in the mantle, illustrating the process of segregation, accumulation, and reentrainment of subducted oceanic crust (OC) for two (subtly) different viscosity-profiles. Left column (figures a), c), and e)) are results obtained with the depth- and temperaure-dependent viscosity-profile from (Steinberger & Calderwood, 2006). Right column (figures b), d), f)) are results obtained with the same profile, but with viscosity lowered by a factor of five in the lowermost $500\,\mathrm{km}$ of the mantle. The top two rows (figures a), b), c) and d)) show the fraction of the OC-material in a small part of the hollow cylinder domain at two different simulation times: $\sim 1.4\,\mathrm{Gyr}$ and $\sim 1.8\,\mathrm{Gyr}$. The red and blue lines are hot ($T^* = 0.6$) and cold ($T^* = 0.4$) isotherms, respectively (where T^* is the nondimensional temperature). The bottom row shows the base ten logarithm of viscosity for the two cases at time $\sim 1.8\,\mathrm{Gyr}$. The black and white lines are isolines for compositional field values 0.6 and 0.4, respectively (where 1 means pure oceanic crust). The main observation is that reducing viscosity in the lower mantle leads to noticably smaller piles, with more ridge-like topography, and composed of a mixture of OC- and ambient material that has a smaller fraction of the OC, compared to the piles produced in a lower mantle with higher viscosity. The compositional density anomaly in both cases is $\sim 1.8\,\%$, corresponding to a buoyancy ratio (chemical to thermal) of ~ 0.57.

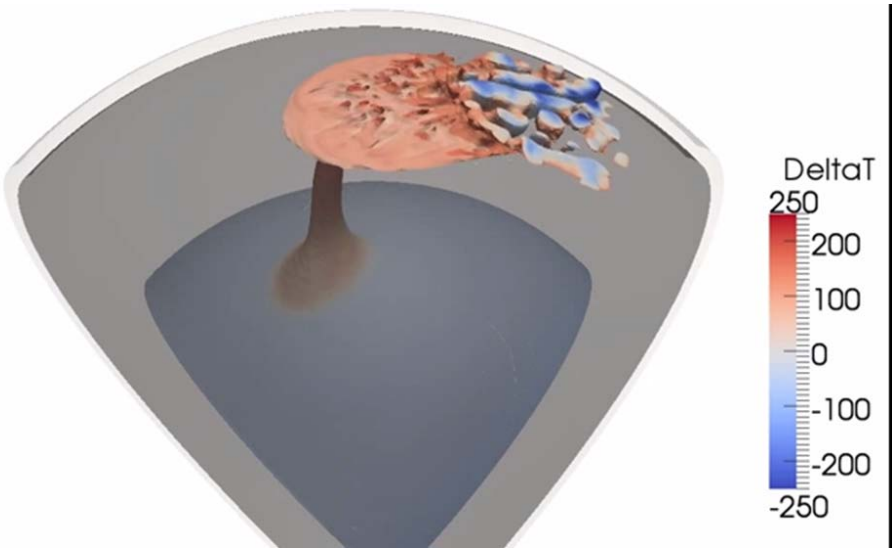

Fig. 3.: A thermo-chemical plume rising from the core-mantle boundary and interacting with an overlying, moving plate. The figure shows the isosurface of the chemical composition (fraction of recycled oceanic crust). The plume is colored by the difference of the local temperature to the adiabatic temperature profile.

ous observations, including geoid, dynamic topography, and lithospheric stresses. Forward model predictions of slabs and plumes can be compared against seismic observations, with the help of recent developments in mineral physics.

The role of crustal thickness and lithospheric rheology on rifted margins width and tectonic subsidence

Anna Eliza Svartman Dias[1,2], Luc. L. Lavier[1,3], Nicholas W. Hayman[1]

[1] *Institute for Geophysics, University of Texas at Austin, USA*
[2] *E&P-EXP, Petrobras, Brazil*
[3] *Department of Geological Sciences, University of Texas at Austin, USA*
e-mail: *annasvartman@gmail.com*
session: *Geodynamics*

Features such as crustal geometry, structural style, amount of magmatism, sedimentary architecture, and subsidence history vary among rifted margins along the world as well as along strike of a single margin. The most variable characteristic is the extent of continental crust deformed by extension. Seismic data from margins around the world exhibit a large variation of the basin width, particularly of the width of a domain where continental crust was thinned to less than 15 km (hyperextended domain), which spans from less than 50 km to more than 150 km in margins such as conjugate Iberia-Newfoundland, the fossil Alpine Tethys, or part of the South Atlantic margin (e. g. Van Avendonk et al., 2006, 2009; Perón-Pinvidic and Manatschal, 2009; Zálan et. al., 2011; Aslanian and Moulin, 2012; Perón-Pinvidic et al, 2013). The South Atlantic Brazilian margin is an extreme example of along strike basin-width variation. The margin width changes from about 600 km in southern Santos Basin to less than 150 km in Camamu Basin (Figure 1). Their hyperextended domains range from 300 km in Santos to about 50 km wide in Camamu Basin. Even though Brazilian margins have features similar to those of the so-called magma-poor conjugate Newfoudland-Iberia, the high volume of early volcanism, especially in Santos and Campos basins, suggest this basins may share some characteristics with magma-rich margins (e. g. Mohriak and Leroy, 2012; Quirk et al., 2013).

Along strike variation in the Brazilian offshore basin-width coincides with changes in the geological provinces in onshore Brazil, from the Ribeira and Araçuaí mobile belts to the São Francisco craton (SFC) (figure 1). The role of initial lithospheric conditions (such as rock rheology and thermal structure) and of the rate of extension on the evolution of rifts and rifted margins have been discussed over the past decades (e. g. Kusznir and Park, 1987; Buck, 1991, 1999; Lavier and Manatschal, 2006; Huismans and Beaumont, 2011). However, the impact of each of these factors on the necking/thinning of the continental crust, particularly on the formation of very wide (> 150 km) asymmetric margins, remains unclear. Therefore, we use numerical experiments to test if there is a physical relationship between initial conditions and the width of the basins; as well as to assess tectonic subsidence histories. We assumed a range of composition (plagioclase, dry or wet quartz dominated crust; and, dry or wet olivine mantle), initial crustal thickness (30 km to 45 km), initial lithosphere thickness (increasing with thermal age varying between 250 Myr and 1 Gyr), initial geotherm (varying with thermal age, crustal thickness and surface heat flow), and velocity of extension (0.5 cm/yr, 1 cm/yr or 2 cm/yr).

We find that small crustal thicknesses (< 35 km) result in narrow margins (< 150 km). Figure 2 a shows the results for a 500 Myr- lithosphere, 30 km crust and strong (dry olivine)

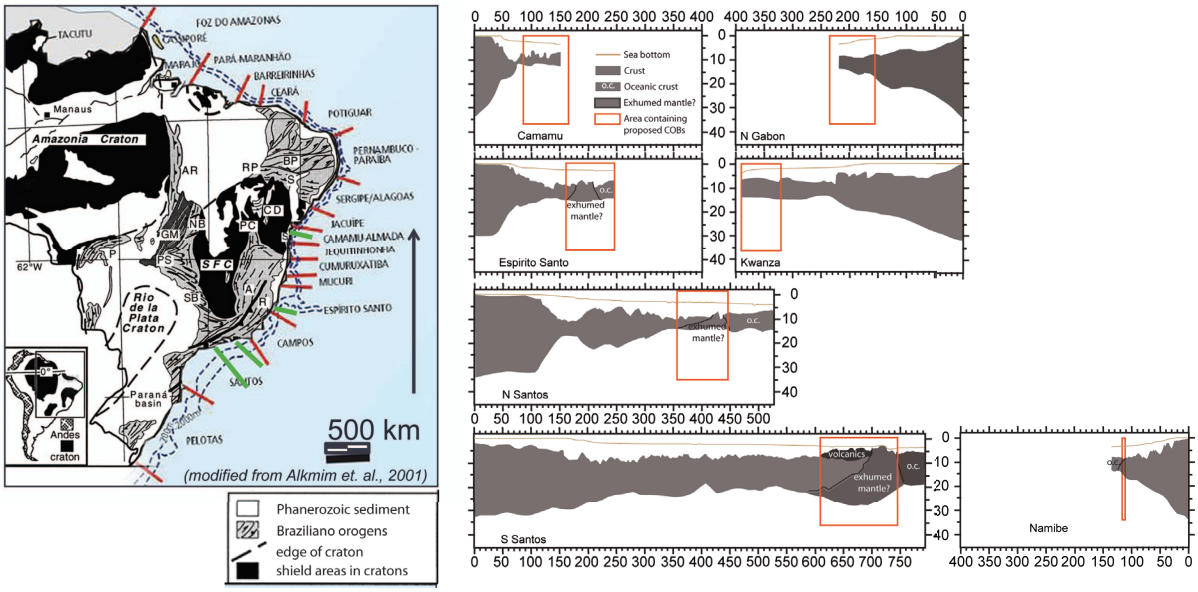

Fig. 1.: On the left, simplified geological map of Brazil depicting the cratonic (black) and mobile belts (grey) domains (modified from Alkimin et al, 2001). Red lines show limits between offshore basins. Green lines show the approximate location of the cross-section of the Brazilian basins displayed on the right. Cross-section cartoons, from bottom to top: Santos Basin and its conjugate at the Namibian margin; Espírito Santo and its conjugate, Kwanza Basin; and, Camamu Basins and its conjugate, Gabon Basin. Orange rectangles encompass various locations proposed for the continent-ocean boundary (COB) in each margin, and interpreted areas of transitional crust or exhumed mantle. Cross-sections and COBs from Sakariasse, (2007), Blaich et al, (2010), Zálan et al. (2011), Heine et al (2013) and references therein.

mantle. Deformation is localized at a narrow area (keystone block H) at the center of the models throughout the rifting process. The thinning and stretching evolution results in a set of narrow conjugate margins (Lavier and Manatschal, 2006; Van Avendonk et al., 2009). Even though there is a delay in thinning the base of the block H in figure 2 a, early crustal necking can occur when the mantle is weak (wet olivine). On the other hand, a wide margin (150 km to $>$ 300 km) can be formed for an initially thick crust ($\geq$ 35 km), a slow rate of extension ($\leq$ 1 cm/yr) and Moho temperatures above 600 °C (figure 2). An initially narrow zone of deformation widens with time and thinning is distributed over a very wide area. The width of the thinning and stretching area also varies with crustal and mantle composition. A wet mantle rheology allows for more widening of the margin than a dry mantle because mantle flow can compensate for crustal thinning and allow for even more distributed deformation even though the mantle is weak (Figure 2 c). The experiment with 45 km crust and a wet olivine upper mantle result in a wide ($>$ 300 km) highly asymmetric lithosphere even for a lithosphere as old as 500 Myr. One margin can be less than one third the width of its conjugate. A young lithosphere/hot geotherm also helps to widen the rift basins. In cold Archean cratonic areas, without significant thickness of ductile lower crust even when the crust is thick, a brittle upper mantle probably controls deformation and early coupling between the crust and mantle forms a block H, leading to a narrow margin. For wide margins, syn-rift subsidence is mostly shallow (300m depth or less), locally reaching 1 km to 1.5 km depths more than 10 Myr after the onset of rifting. For narrow margins, the subsidence curves show a first phase of rapid subsidence during the initiation of block H, followed by a slow uplift accompanying the weakening and deformation of block H (figure 3). However, this uplift alone is

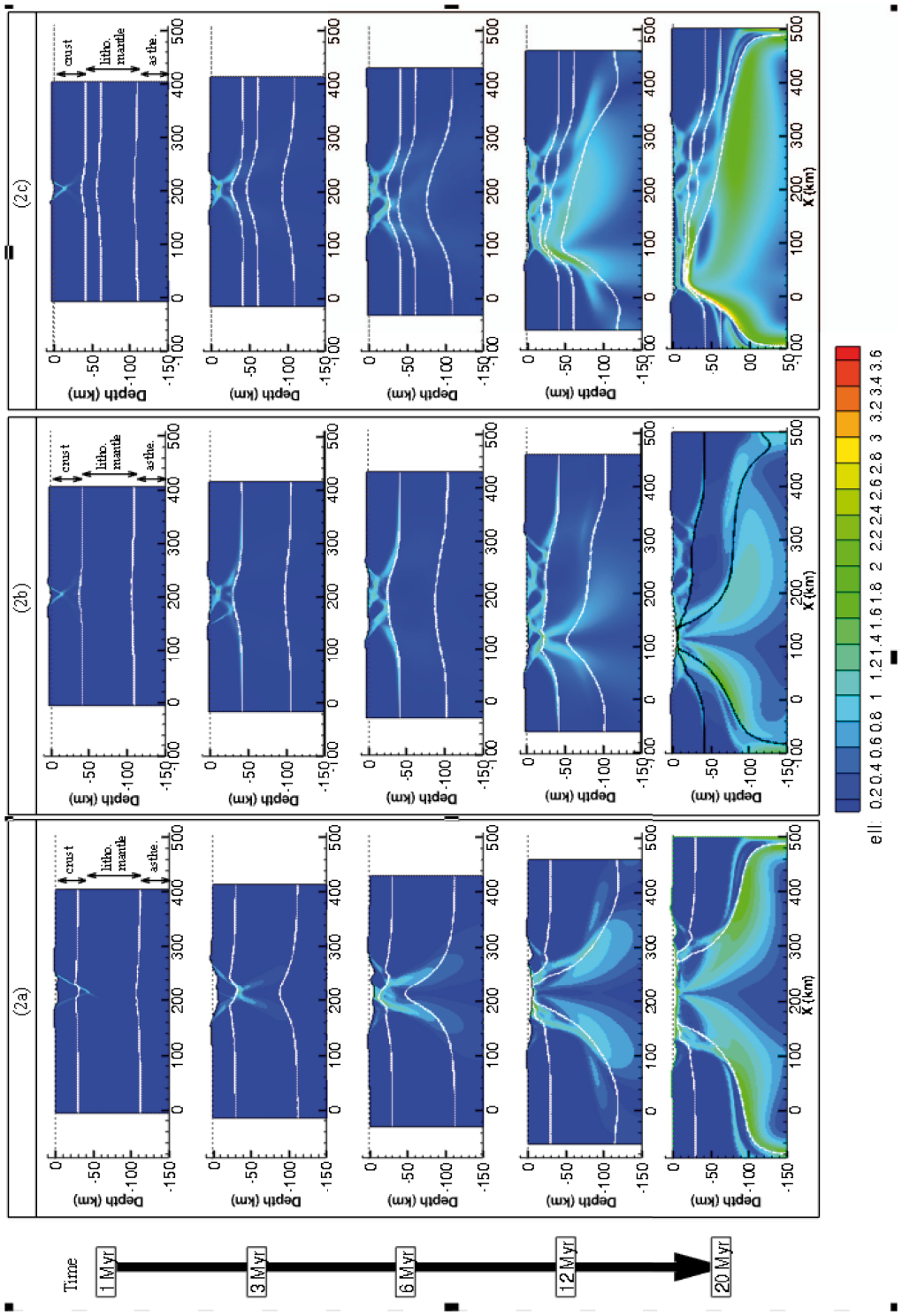

Fig. 2.: Effective accumulated strain field overlay (eII) for models with crust dominated by plagioclase rheology and an initial geotherm corresponding to a $500\,\mathrm{Myr}$ old lithosphere. From top to bottom, the models experience $200\,\mathrm{km}$ of extension over $20\,\mathrm{Myr}$ (extension velocity of $1\,\mathrm{cm/yr}$). At the left, the time after the onset of rifting for each of the five stages of the evolution depicted for the three experiments. (2 a) $30\,\mathrm{km}$ initial crust, and dry olivine mantle; (2 b) $45\,\mathrm{km}$ initial crust, and dry olivine mantle; and, (2 c) $45\,\mathrm{km}$ initial crust, and wet olivine mantle. White solid lines depict the boundaries between crust and mantle (Moho), and between litospheric mantle and asthenosphere (LAB, $1300\,^{\circ}\mathrm{C}$).

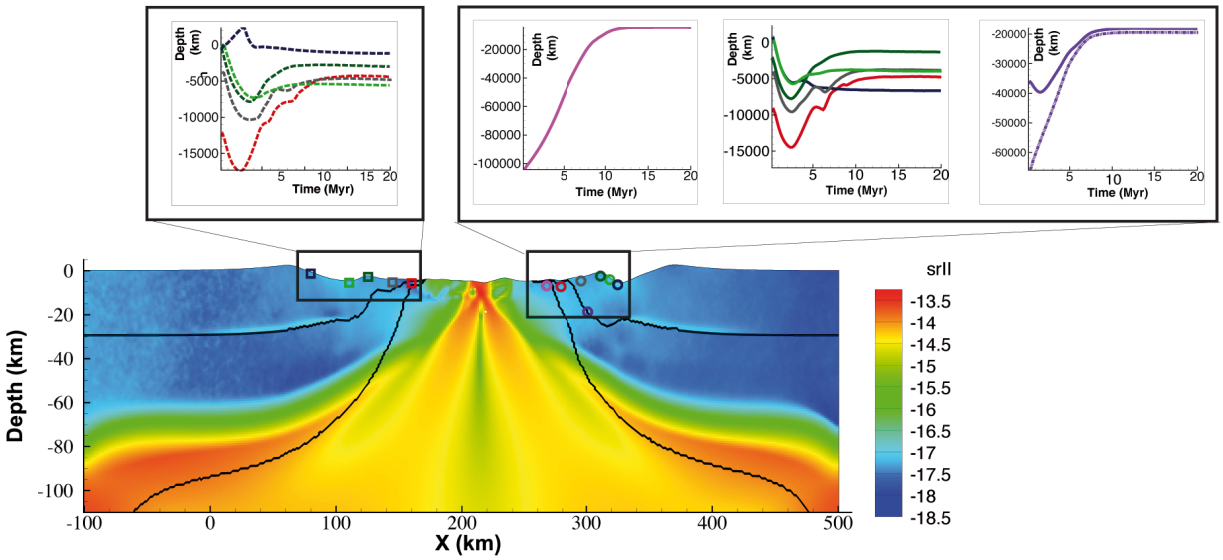

Fig. 3.: On the top, subsidence or exhumation curves (Depth vs. Time) of the particles extracted from the experiment depicted in Figure 2a. Solid lines correspond to subsidence/exhumation histories of particles at the right margins; dashed lines, to the left margin. The color of each line corresponds to the circles (right margin) and squares (left margins) plotted on the section at the bottom, which displays the strain rate of the experiment after 20 Myr of extension.

not enough to result in shallow water conditions.

The processes controlling rif evolution vary depending on initial conditions. We interpret that whether deformation localizes in block H or delocalizes into a wide margin is due to: strengthening of the upper crust, weakening or strengthening of the strong upper mantle below the initial zone of deformation, and the presence or absence of a significant thickness of ductile lower crust. The later is not defined here as a separate layer of the crust with different composition. Ductile lower crust thickness increases with crustal thickness and geothermal gradient (when Moho is above 600 °C significant thickness of the lower crust can flow). Moreover, if the crust is thick, bending stresses are high enough to result in upper crust hardening, forcing the deformation to migrate outside of the initial zone of crustal deformation (Lavier et al., 2000). This lateral migration is later reinforced by three other processes: strengthening of the middle to lower crust due to viscous flow at high strain rates, lateral lower crustal flow from the undeformed to the deformed area, and strengthening of the lithosphere as the mantle uplifts (Buck, 1991) As a result wide margins can form (figure 2). When the strong mantle is weakened sufficiently, deformation localizes there and thinning and exhumation may follow (figure 2, a and b). Brittle faulting or heat transfer in the strong mantle can cause sufficient weakening to initiate thinning and exhumation. But it also possible that diking could provide the necessary weakening.

References

Aslanian, D., & Moulin, M. (2013). Palaeogeographic consequences of conservational models in the South Atlantic Ocean. Geological Society, London, Special Publications, 369(1), 75-90.

Blaich, O. A., Faleide, J. I., Tsikalas, F., Lilletveit, R., Chiossi, D., Brockbank, P., & Cobbold, P. (2010, January). Structural architecture and nature of the continent-ocean transitional domain at the Camamu and Almada Basins (NE Brazil) within a conjugate margin setting. In

Geological Society, London, Petroleum Geology Conference series (Vol. 7, pp. 867-883). Geological Society of London.

Buck, W. R. (1991). Modes of continental lithospheric extension. Journal of Geophysical Research: Solid Earth (1978–2012), 96(B12), 20161-20178.

Buck, W. R., Lavier, L. L., & Poliakov, A. N. (1999). How to make a rift wide.PHILOSOPHICAL TRANSACTIONS-ROYAL SOCIETY OF LONDON SERIES A MATHEMATICAL PHYSICAL AND ENGINEERING SCIENCES, 671-689.

Heine, C., Zoethout, J., & Müller, R. D. (2013). Kinematics of the South Atlantic rift. Solid Earth, 4(2).

Huismans, R., & Beaumont, C. (2011). Depth-dependent extension, two-stage breakup and cratonic underplating at rifted margins. Nature, 473(7345), 74-78.

Kusznir, N. J., & Park, R. G. (1987). The extensional strength of the continental lithosphere: its dependence on geothermal gradient, and crustal composition and thickness. Geological Society, London, Special Publications,28(1), 35-52.

Lavier, L. L., Buck, W. R., & Poliakov, A. N. (2000). Factors controlling normal fault offset in an ideal brittle layer. Journal of Geophysical Research: Solid Earth (1978–2012), 105(B10), 23431-23442.

Lavier, L. L., & Manatschal, G. (2006). A mechanism to thin the continental lithosphere at magma-poor margins. Nature, 440(7082), 324-328.

Mohriak, W. U., & Leroy, S. (2013). Architecture of rifted continental margins and break-up evolution: insights from the South Atlantic, North Atlantic and Red Sea–Gulf of Aden conjugate margins. Geological Society, London, Special Publications, 369(1), 497-535.

Péron-Pinvidic, G., & Manatschal, G. (2009). The final rifting evolution at deep magma-poor passive margins from Iberia-Newfoundland: a new point of view.International Journal of Earth Sciences, 98(7), 1581-1597.

Peron-Pinvidic, G., Manatschal, G., & Osmundsen, P. T. (2013). Structural comparison of archetypal Atlantic rifted margins: A review of observations and concepts. Marine and Petroleum Geology, 43, 21-47.

Quirk, D. G., Hertle, M., Jeppesen, J. W., Raven, M., Mohriak, W. U., Kann, D. J., ... & Mendes, M. P. (2013). Rifting, subsidence and continental break-up above a mantle plume in the central South Atlantic. Geological Society, London, Special Publications, 369(1), 185-214.

Sakariassen, R. (2007). North Namibia margin: regional tectonic evolution based on integrated analysis of seismic reflection and potential field data and modelling.

Van Avendonk, H. J., Holbrook, W. S., Nunes, G. T., Shillington, D. J., Tucholke, B. E., Louden, K. E., ... & Hopper, J. R. (2006). Seismic velocity structure of the rifted margin of the eastern Grand Banks of Newfoundland, Canada. Journal of Geophysical Research: Solid Earth (1978–2012), 111(B11).

Van Avendonk, H. J., Lavier, L. L., Shillington, D. J., & Manatschal, G. (2009). Extension of continental crust at the margin of the eastern Grand Banks, Newfoundland. Tectonophysics, 468(1), 131-148.

Zalán, P. V., Severino, M. D. C. G., Rigoti, C. A., Magnavita, L. P., de Oliveira, J. A. B., & Vianna, A. R. (2011, April). An entirely new 3D-view of the crustal and mantle structure of a South Atlantic passive margin–Santos, Campos and Espírito Santo basins, Brazil. In Americal Association of Petroleum Geology, Annual Convention and Exhibition.

Influence of Melting on the Long-Term Thermo-Chemical Evolution of Earth's Deep Mantle

Paul J. Tackley[1], Diogo Lourenço[2], Ilya Fomin[1], Takashi Nagawaga[2]

[1]*Institute of Geophysics, Department of Earth Sciences, ETH Zurich, Switzerland*
[2]*IFREE, JAMSTEC, Japan*
e-mail: *ptackley@ethz.ch*
session: *Geodynamics*

Melting has always played a key role in Earth evolution. Early solidification of a magma ocean may have left the mantle compositionally stratified and may have continued in the form of a long-lived basal magma ocean (BMO). Ongoing upper mantle/transition zone melting, perhaps associated with water and carbonate, may have caused "internal differentiation", resulting in dense enriched products that sink. Throughout Earth's history melting in the shallow mantle has produced crust, most of which was recycled into the interior and some of which may have segregated above the core-mantle boundary, joining possible enriched products from early differentiation, internal differentiation and BMO solidification to produce a Basal Melange (BAM). Here we investigate the thermal and chemical evolution of Earth's interior from the ~molten state to billions of years later using global-scale numerical simulation. Our previously-published models that included only oceanic crustal production and recycling (e.g. Nakagawa & Tackley, 2014 GCubed) indicated that (i) a layer of subducted crust can rapidly build up above the CMB, (ii) early-formed layering above the CMB may have been necessary to avoid rapid early core cooling and a too-large present-day inner core, (iii) magmatism is the dominant heat transport mechanism early on, (iv) melting acts as a thermostat, buffering mantle temperature. Here we improve the models to handle deep melting including melt fractions of up to 100 %, fractional melting using a eutectic model, segregation of melt and solid, and a parameterized magma ocean treatment at high melt fractions (using an eddy diffusivity based on mixing length theory, similar to previous 1-D treatments). We investigate and characterize the evolution of deep mantle structure in the limits of negatively buoyant melt and positively buoyant melt. We focus on the interplay of deep melting and melt migration, primordial layering, recycled crust and harzburgite, and products of upper mantle internal differentiation, in producing a heterogeneous deep mantle BAM.

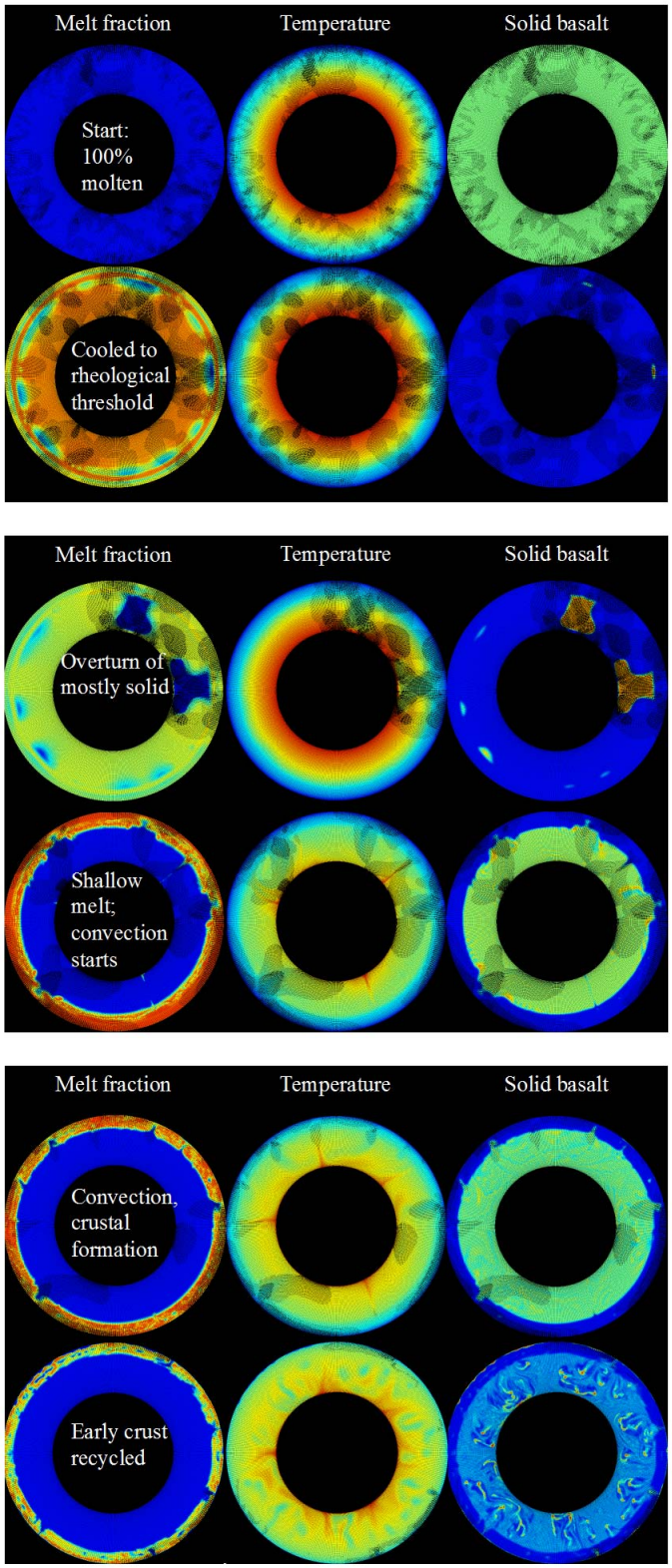

Fig. 1.: Sequence of events in the early ($< 1\,\mathrm{Byr}$) evolution of an Earth-like planet starting from a 100 % molten state. Quantities are scaled to minimum and maximum values.

A two- and three-dimensional numerical modelling benchmark of slab detachment

Cedric Thieulot[1,2], Anne Glerum[1,4], Bram Hillebrand[1], Stefan Schmalholz[3], Wim Spakman[1,2,4], Trond Torsvik[2]

[1] *Utrecht University, Dept. of Earth Sciences, Utrecht, Netherlands*
[2] *Centre for Earth Evolution and Dynamics, Oslo, Norway*
[3] *Institute of Earth Sciences , University of Lausanne, Switzerland*
[4] *The Netherlands Research Centre for Integrated Solid Earth Science*
e-mail: *c.thieulot@uu.nl*
session: *Geodynamics*

Subduction is likely to be the most studied phenomenon in Numerical Geodynamics. Over the past 20 years, hundreds of publications have focused on its various aspects (influence of the rheology and thermal state of the plates, slab-mantle coupling, roll-back, mantle wedge evolution, buoyancy changes due to phase change, ...) and results were obtained with a variety of codes.

Slab detachment has recently received some attention (e. g. Duretz, 2012) but remains a field worth exploring due to its profound influence on dynamic topography, mantle flow and subsequent stress state of the plates, and is believed to have occured in the Zagros, Carpathians and beneath eastern Anatolia, to name only a few regions.

Following the work of Schmalholz (2011), we propose a two- and three-dimensional numerical benchmark of slab detachment. The geometry is simple: a power-law T-shaped plate including an already subducted slab overlies the mantle whose viscosity is either linear or power-law. Boundary conditions are free-slip on the top and the bottom of the domain, and no-slip on the sides.

When the system evolves in time, the slab stretches out vertically and shows buoyancy-driven necking, until it finally detaches. The benchmark is subdivided into several sub-experiments with a gradual increase in complexity. An array of objective measurements is recorded throughout the simulation such as the width of the necked slab over time and the exact time of detachment. The experiments will be run in two-dimensions and repeated in three-dimensional, the latter case being designed so as to allow both poloidal and toroidal flow.

We show results obtained with a multitude of Finite Element and Finite Difference codes, using either compositional fields, level sets or tracers to track the compositions. A good agreement is found for most of the measurements in the two-dimensional case, and preliminary three-dimensional measurements will be shown.

References

Duretz et al (2012), Thermomechanical modeling of slab eduction, JGR, vol. 117.

Schmalholz (2011), A simple analytical solution for slab detachment, EPSL, vol. 304, p 45-54.

The effect of strong heterogeneities in the upper mantle rheology on the dynamic topography and geoid

Anthony Osei Tutu

GFZ German Research Centre for Geoscience (Section 2.5), Potsdam, Germany
e-mail: *oseitutu@gfz-potsdam.de*
session: *Geodynamics*

The undulating nature of the earth surface (topography) on both continents and sea floor and the observed geoid anomaly are influenced by the convective processes within the Earth's mantle driven by density anomalies. Hot, less dense material tends to rise and push the overlying lithosphere upward, whereas cold, denser material tends to sink and pull the lithosphere downward (Steinberger, 2014). This mechanism is simplistically illustrated in figure 1.

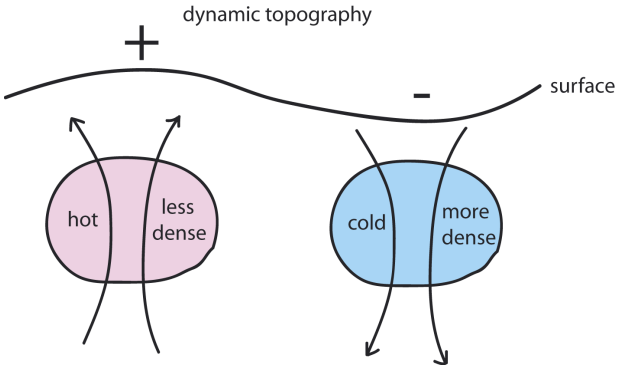

Fig. 1.: The concept of dynamic topography (Steinberger, 2014)

Evidence from ancient coastal areas currently submerged (Hartley et al. 2011) suggests significant changes in topography of several hundred meters relative to the present day Europe. The effect of such changes on the present-day relief and land area would drastically change the face of Europe as shown in figure 2.

The geoid is about 90 % (Hager & Richards, 1989) determined by both the density anomalies driving the mantle flow and the dynamic topography caused at the Earth surface and the core-mantle boundary. The remainder is largely due to strong heterogeneities in the lithospheric mantle and the crust, which also need to be taken into account. Surface topography caused by density anomalies both in the sub-lithospheric mantle and within the lithosphere depend on lithosphere rheology. Here we investigate these effects by assessing the differences between modelled dynamic topography and geoid from the spectral mantle flow code (Hager & O'Connell, 1981) and a fully coupled code of the lithosphere and mantle accounting for strong heterogeneities in the upper mantle rheology (Popov & Sobolev, 2008).

The coupled code approach simulates the visco-elasto-plastic rheology of the lithosphere and the radial and lateral viscosity variations in the material in the uppermost 300 km of the Earth interior including the lithosphere-asthenosphere boundary. In contrast, the mantle flow code simulates a 3-D density structure inferred from shear wave seismic tomography and assumes a radial viscosity variation from the CMB to the surface to compute a deviatoric normal stress, which is then converted to the dynamic topography using a scaling coefficient.

This study is the first step towards, linking global mantle dynamics with lithosphere dynamics using the observed geoid as a major constraint and results from both codes will be presented and compared with the observed geoid and dynamic topography. This effort will also serve as a benchmark of the two existing numerical codes developed for geodynamic modelling.

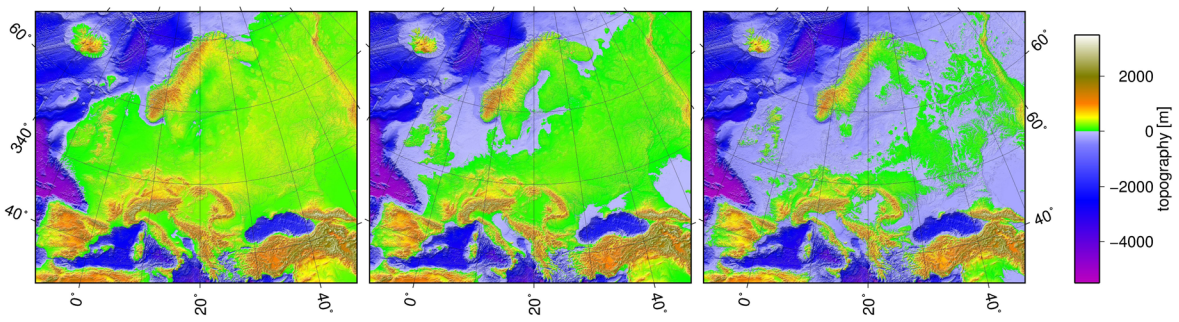

Fig. 2.: Topography of Europe: A) Present-day $+150\,\mathrm{m}$; B) Present-day C) Present-day $-150\,\mathrm{m}$ (Steinberger, 2014)

References

Hager B.H & O'Connell R.J., 1981. A simple global model of plate dynamics and mantle convection, J.geophys. Res. 86, 4843-4867.

Hager B.H. & Richards M.A., 1989. Long-wavelength variations in Earth's geoid: physical models and dynamical implications, Phil. Trans. R. Soc. Lond., A348, 309-327.

Hartley, R.A., Roberts, G.G., White, N. & Richardson, C., 2011. Transient convective uplift of an ancient buried landscape, it Nat. Geosci., 4, 562-565.

Popov A.A., Sobolev S.V., 2008. SLIM3D: A tool for three-dimensional thermomechanical modelling of lithospheric deformation with elasto-visco-plastic rheology.

Steinberger B., 2014. Dynamic topography: Acomparison between observations and models based on seismic tomography.

The role of weak seeds in numerical modelling of continental extensional systems

Iris van Zelst[1], Cedric Thieulot[1,2], Susanne J. H. Buiter[2,3], John Naliboff[3], Wim Spakman[1,2]

[1] *Department of Earth Sciences, Utrecht University, Utrecht, The Netherlands*
[2] *Centre for Earth Evolution and Dynamics, University of Oslo, Oslo, Norway*
[3] *Geodynamics Team, Geological Survey of Norway, Trondheim, Norway*
e-mail: *i.vanzelst@students.uu.nl*
session: *Geodynamics*

Numerical models that investigate the dynamics of the lithosphere and upper mantle need to start from an initial geometry with a set of prescribed mechanical and thermal conditions. Initial conditions are required in order to localize and initiate deformation. Without such initial conditions, deformation may take a long model time to localize, up to millions of years. The reason for this is that these models need to accumulate numerical disturbance to create starting points for the deformation. A method that is often used in models of extension of continental lithosphere to localize deformation faster is to use "seeds" to initiate extension. These seeds are usually small regions that are weaker than the surrounding crust and lithosphere. Multiple ways of prescribing weak seeds are found in the literature.

One way of implementing a weak seed is through thermal effects. A weak region can be achieved by a temperature anomaly in the crust or lithosphere, which can be created by directly imposing a temperature difference, by assigning high radiogenic heat production, by perturbing the basal heat flow, or by modelling a thermal upwelling in the mantle below. For models with a temperature-dependent viscosity, the elevated temperature reduces the viscosity. An advantage of using an imposed temperature anomaly is that it will dissipate with time, thus reducing the impact on later model stages.

Another way of implementing a weak region is to compose the seed of a material with a lower rheological strength than its surroundings. This can be achieved by imposing a lower viscosity, a lower value for the angle of internal friction, or assigning different material properties, such as a von Mises seed in a frictional plastic material. Prescribing the weak seed as a region which already has accumulated strain, leading to strain-weakening, is also a frequently used approach. In the literature a variety of shapes and sizes for this kind of weak seeds can be found. Examples include square seeds, fault-shaped weak inclusions and rectangular seeds with different aspect ratios. Randomly distributed seeds have also been used.

A weak zone can also be created by an abrupt variation in the thickness of the crust and/or lithosphere. A locally thinned crust can be thought to be caused by a previous rifting phase, whereas a thicker crust could represent preceding mountain building. These variations in thickness affect the mechanical strength and impose a thermal anomaly.

The literature is scarce concerning the effects of the different methods of implementing a weak zone on the results of the model. However, the variety in shape, size, orientation, mechanical and thermal properties and depth of the seed(s) begs the question whether these different approaches could have an effect on model evolution. We therefore present a series of numerical models conducted with the codes ELEFANT and SULEC that aims at investigating the role of weak seeds

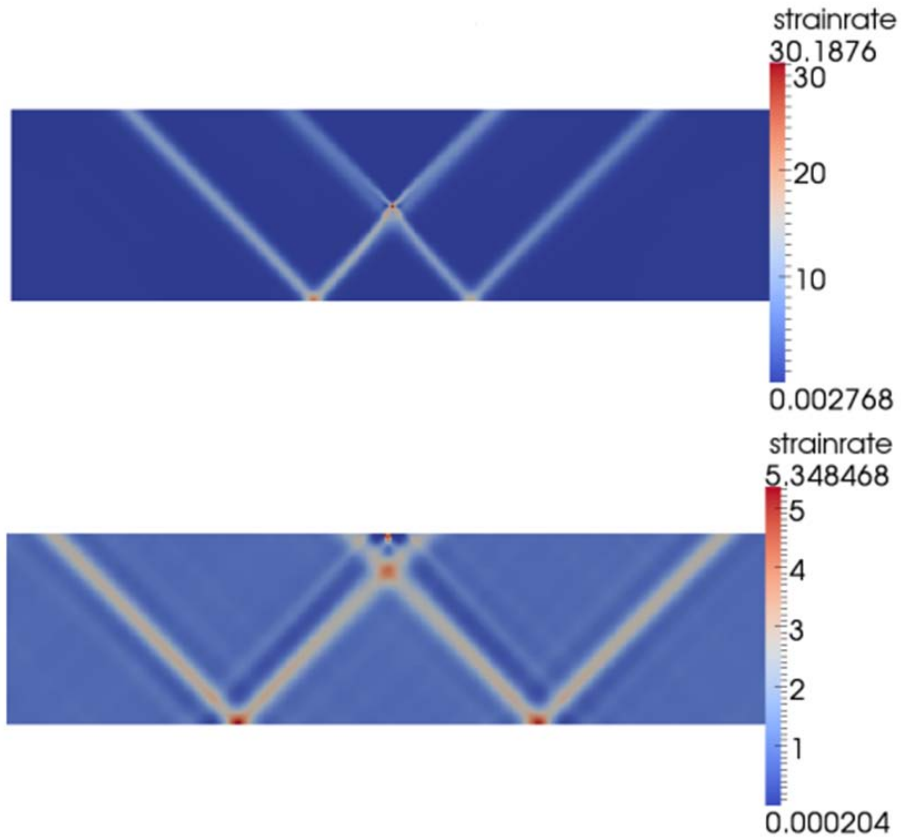

Fig. 1.: Results for different vertical positions of the weak seed in a dimensionless single layer extensional system. The internal angle of friction ϕ is 15. In the top figure, the weak seed is placed in the middle of the model domain, while in the bottom figure the weak seed is placed at the top. Results are calculated with ELEFANT.

in the initial and later stages of continental extension. The basis model is always the same (a multi-layered thermo-mechanically coupled extension model of the upper mantle), the only difference between the models is formed by the size and nature of the weak seed. In figure 1 preliminary results concerning the placement of the weak seed are shown for a simple, dimensionless, one layer model. The viscosity of the layer is 10^5. On the poster for GeoMod2014, results will be presented for the more complex, multi-layered extension model of the upper mantle.

The up side down logic of orogenic collision: on the formation of low-topography mountain ranges

Katharina Vogt[1], Liviu Matenco[1], Taras Gerya[2], Sierd Cloetingh[1]

[1]*Department of Earth Sciences, Utrecht University, Budapestlaan 4, 3584CD Utrecht, Netherlands*
[2]*Institute of Geophysics, ETH Zürich, Sonneggstrasse 5, 8092 Zürich, Switzerland*
e-mail: *k.j.vogt@uu.nl*
session: *Geodynamics*

Abstract

Present models of orogeny generally assume that mountains grow upwards by gradual accretion of crustal material during continental collision. This mechanism is characterized by high topographic build-up and material transport within the pro- and retro-wedge. However, at least half of the mountain ranges worldwide are characterized by low and distributed topographies with little or no exhumation in retro-wedges. In this study we analyse if mountain chains may grow downwards, by active accretion of crustal material to the lower plate. In this model the upper crust is decoupled and deformed, while the lower crust is subducted to mantle depth and subjected to slab retreat. This mechanism allows a foreland shift in the timing of exhumation and the location of the main subduction zone, explaining the often geometrical misfit between the crustal position of the lower plate and the geometry of slabs inferred by teleseismic tomography.

Introduction

When the continental crust reaches a subduction zone continental collision forms generally high topography, because of the excess of low-density material accumulated at the plate margin. Analogue and numerical models demonstrated the gradual accretion of crustal material to the upper plate along retro-shears (Beaumont et al., 1996). In these models continental subduction results in upper plate deformation and formation of double-vergent orogens. Typical examples include the Swiss Alps and the Pyrenees (Schmid et al., 1996; Beaumont et al., 2000). These are dominantly high-convergence orogens with low angles of subduction and where the contact between the collisional plates is positioned in line with the location of slabs detected by teleseismic mantle tomography.

The other half of worldwide orogens forms low-topography mountain ranges at retreating subduction boundaries, where the rapid roll-back of subducted slabs is accommodated by upper plate extension and formation of back-arc basins (e. g., Faccenna et al., 2004). A common feature of these orogens is the geometrical misfit between the crustal position of the lower plate and the geometry of slabs inferred by teleseismic tomography. The aim of this study is to analyse numerically the physical concepts and implications of such low topography mountain ranges.

Methods

The study of collisional systems and the evolution in time of associated deformation was analysed by the means of high-resolution thermo-mechanical numerical modelling designed to investigate the physical processes related to orogenic building. All numerical experiments were performed with the I2VIS code (Gerya and Yuen, 2003). This code is based on conservative finite differences and a marker-in-cell technique. The momentum,

continuity and energy equations are solved on Eulerian frame, and Lagrangian markers that move according to the velocity field interpolated from the fix grid transport physical properties. The model uses non-Newtonian visco-plastic rheologies to simulate multiphase flow.

Model Setup: The computational domain spans 1000 km × 200 km and contains a (600 km wide) high-resolution area of 0.5 km × 0.5 km. Constant velocities are applied to the to simulate a total convergence of 1 cm/a. A rheologically weak zone at the bottom of the continental crust represents a suture zone, separating two continental domains after the closure of an ocean. The continental crust is homogeneous and has a total thickness of 35 km. It is subdivided into 20 km of felsic and 15 km of mafic rocks. The underlying mantle is composed of dry olivine. The initial temperature field of the continental lithosphere was varied. It increases linearly from 0 °C at the surface to 400 °C to 800 °C at the crust-mantle boundary (Moho) and 1300 °C at the lithosphere-asthenosphere boundary at 120 km to 160 km depth. For the asthenospheric mantle a thermal gradient of 0.5 °C km^{-1} is used. To allow for topographic build up of the lithosphere a layer of 20 km and low viscosity (1018 Pa s) and low density (1 kg m^{-3}) is implemented above the lithosphere. The large viscosity contrast between this layer and the lithosphere minimizes shear stresses (< 104 Pa) making it an efficient free surface (e. g. Schmeling et al., 2008). The topography of the model (air/crust interface) evolves according to a transport equation that is solved at each time-step on the Eulerian grid and accounts for erosion and sedimentation (Gorczyk et al., 2007).

Results

Our numerical results indicate that (i) deformation might be localized in lower orogenic plates and (ii) collisional systems are able to develop solely by foreland-vergent deformation and migration of the main subduction zone.

Similar to the orogenic retro-wedge scenarios, the onset of contraction leads to an initially symmetric situation in which pro- and retro- shears display limited offsets at the scale of the orogen. The subsequent localized deformation within the weak (subduction) zone leads to a concentration of deformation almost exclusively in pro-shears. This causes a large-scale asymmetry, where deformation and associated exhumation gradually migrate towards the foreland. The large displacement in the pro-wedge accommodates almost the entire shortening and allows for the subduction of lower crust. The upper crust decouples and records significant internal shortening during the foreland propagation of the deformation front, while the upper orogenic plate is passively exhumed and deformed, although with significant lower values than normally observed in typical retro-wedges. The resulting orogenic geometry is highly asymmetric and almost exclusively oriented towards the foreland, deformation and exhumation migrating in the same direction.

Discussion

Our numerical results indicate that (i) deformation might be localized in lower orogenic plates and (ii) collisional systems are able to develop solely by foreland-vergent deformation and migration of the main subduction zone.

Similar to the orogenic retro-wedge scenarios, the onset of contraction leads to an initially symmetric situation in which pro- and retro- shears display limited offsets at the scale of the orogen. The subsequent localized deformation within the weak (subduction) zone leads to a concentration of deformation almost exclusively in pro-shears. This causes a large-scale asymmetry, where deformation and associated exhumation gradually migrate towards the foreland. The large displacement in the pro-wedge accommodates almost the entire shortening and allows for the subduction of lower crust. The upper crust decouples and records significant internal shortening during the foreland propagation of the deformation front, while the upper orogenic plate is passively ex-

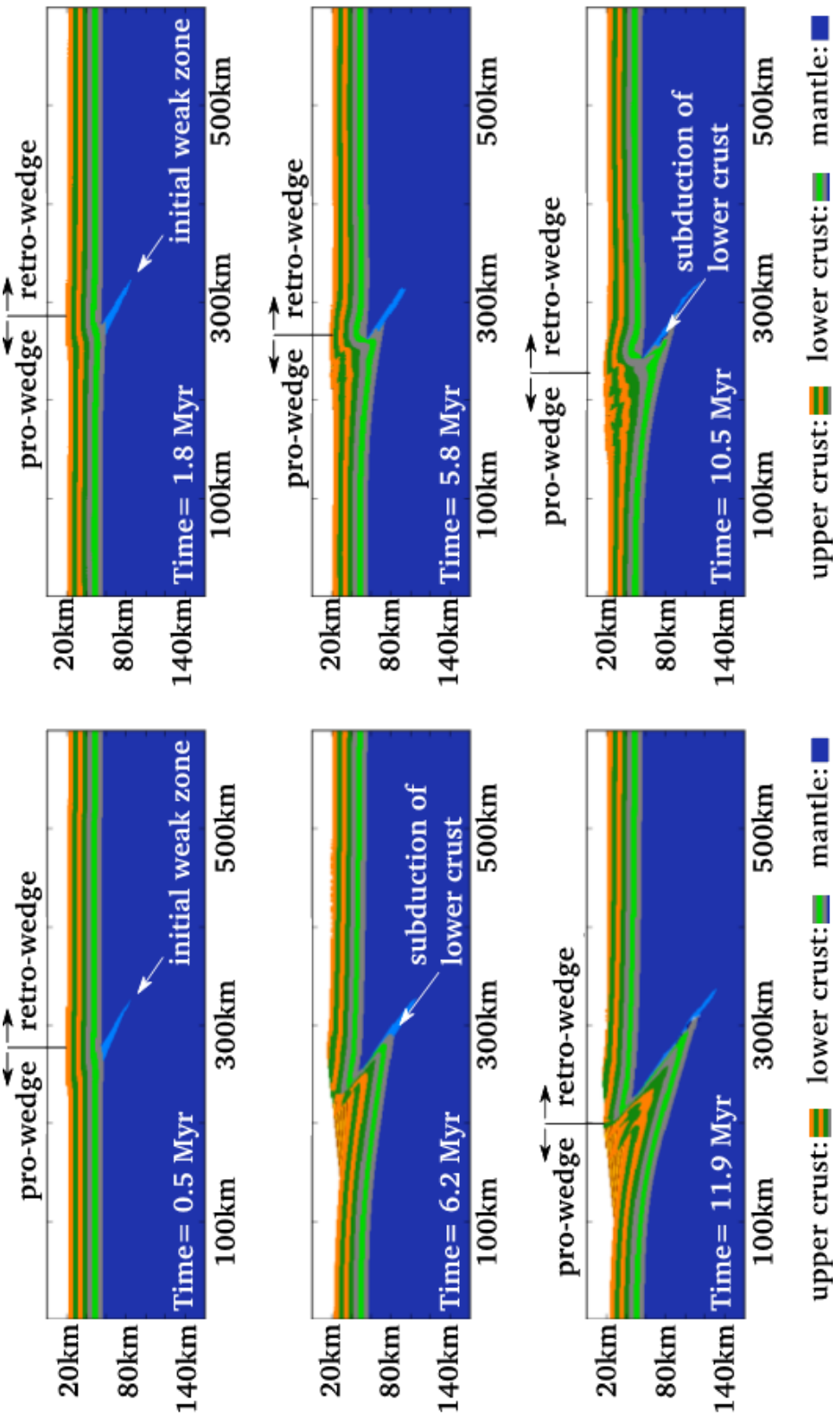

Fig. 1.: Tectonic model of a continent-continent collision zone. Compositional map.

humed and deformed, although with significant lower values than normally observed in typical retro-wedges. The resulting orogenic geometry is highly asymmetric and almost exclusively oriented towards the foreland, deformation and exhumation migrating in the same direction.

References

Beaumont, C., Ellis, S., Hamilton, J., Fullsack, P., 1996. Mechanical model for subduction collision tectonics of Alpine-type compressional orogens. Geology 24, 675-678.

Beaumont, C., Munoz, J.A., Hamilton, J., Fullsack, P., 2000. Factors controlling the Alpine evolution of the central Pyrenees inferred from a comparison of observations and geodynamical models. Journal of Geophysical Research 105, 8121-8145.

Faccenna, C., Piromallo, C., Crespo-Blanc, A., Jolivet, L., Rosetti, F., 2004. Lateral slab deformation and the origin of the western Mediterranean arcs. Tectonics 23, TC1012, doi:1010.1029/2002TC001488.

Gorczyk, W., Willner, A.P., Gerya, T.V. and Connolly, J.A.D. and Burg, J.-P., 2007. Physical controls of magmatic productivity at Pacific-type convergent margins: Numerical modelling. Physics of the Earth and Planetary Interiors. 163, 209–232.

Gerya, T.V., and Yuen, D.A., 2003, Characteristics-based marker-in-cell method with conservative finite differences schemes for modeling geological flows with strongly variable transport properties: Physics of the Earth and Planetary Interiors, v. 140, p. 293–318, doi:10.1016/j.pepi.2003.09.006.

Jolivet, L., Faccenna, C., 2000. Mediterranean extension and the Africa-Eurasia collision. Tectonics 19, 1095-1106.

Schmeling H., Babeyko, A., Enns, A., Faccenna, C., Funiciello, F., Gerya, T., Globalek, G., Grigull, S., Kaus, B., Morra, G., van Hunen, 2008. A benchmark comparison of spontaneous subduction models - toward a free surface. Physics of the Earth and Planetary Interiors 171, 198-223.

Schmid, S.M., Berger, A., Davidson, C., Giere, R., Hermann, J., Nievergelt, P., Puschnig, A.R., Rosenberg, C., 1996. The Bergell pluton (Southern Switzerland, Northern Italy): overview acompanying a geological-tectonic map of the intrusion and surrounding country rocks. Schweizerische Mineralogische und Petrographische Mitteilungen 76, 329-355.

Willingshofer, E., Sokoutis, D., Luth, S.W., Beekman, F., and Cloething, S., 2013. Subduction and deformation of the continental lithosphere in response to plate and crust-mantle coupling. Geology, 41, 1239-1242.

Implementing fluid flow in SLIM-3D

Marius Walter, Javier Quinteros, Stephan V. Sobolev

GeoForschungsZentrum, Telegrafenberg, 14473 Potsdam, Germany
e-mail: *mwalter@gfz-potsdam.de*
session: *Geodynamics*

SLIM-3D is a three-dimensional thermomechanical code capable of simulating lithospheric deformation with elasto-visco-plastic rheology (Popov and Sobolev, 2008). It incorporates an arbitrary Lagrangian Eulerian formulation, free surface, and changes in density and viscosity, due to endothermic and exothermic phase transitions. It has been successfully applied to model different geodynamic processes at divergent (Brune and Autin, 2013; Melnick et al., 2012), convergent (Quinteros and Sobolev, 2013; Quinteros and Sobolev, 2010) and transform (Popov et al., 2012) plate boundaries. However, although SLIM-3D already includes many features, fluid flow has not been incorporated into the model yet.

The aim of the here presented study is to overcome this shortcoming of SLIM-3D. We are especially interested in modeling subduction evolution with respect to fluid flow. Fluids play a crucial role in subduction evolution. For example, excess mechanical weakening along tectonic interfaces, due to excess fluid pressure, may enable oceanic subduction (Dymkova & Gerya, 2013). Hence, the water content may be a critical parameter for subduction initiation. Studies have also shown a correlation between the location of slab dehydration and intermediate seismic activity (Hacker et al., 2003). Furthermore, expelled fluids from the subduction slab affect the melting temperature, consequently, contributing to partial melting in the wedge above the downgoing plate and resulting in chemical changes in earth interior and extensive volcanism (Cagnioncle et al., 2007). In summary, fluids have a great impact on tectonic processes and therefore should be incorporated into geodynamic numerical models.

Here we use existing approaches to implement fluid flow into SLIM-3D (McKenzie, 1984; Morency et al., 2007). The coupling between solid and fluid flow rests upon the assumption that fluids flow through a porous and deformable solid. Thus, we couple the solid momentum equation, continuity equation for solid and fluid, as well as the Darcy equation. This system of equations becomes, however, nonlinear, because permeability is assumed to be a power-law function of porosity. Ultimately, the evolution of porosity is governed by the compaction pressure and the advection of the porous solid.

We plan to show the implementation of the fluid flow into the existing thermo-mechanical finite element code and present first results. Eventually, we will carry out experiments to better understand controls on magma emplacement and variations in the temperature field. We are especially interested in the coupling of subduction processes and the evolution of the magmatic arc. Thereby, we will study the migration of the volcanic front in respect to subduction processes and geometry in order to identify models that best fit the geodynamic evolution of the Central Andes.

References

Brune, S. and Autin, J.: The rift to break-up evolution of the Gulf of Aden: Insights from 3D numerical lithospheric-scale modelling, Tectonophysics, 607, 65–79.

Cagnioncle, A.-M., Parmentier E. M., Elkins-Tanton L. T. (2007). Effect of solid flow above a subducting slab on water distribution and

melting at convergent plate boundaries, J. Geophys. Res., 112 (B09402), 1–19.

Dymkova, D., Gerya, T., 2013. Porous fluid flow enables oceanic subduction initiation on Earth. Geophysical Research Letters 40 (21), 5671–5676.

Hacker, B. R., Peacock S. M., Abers G. A., Holloway S. D. (2003). Subduction factory: Are intermediate-depth earthquakes in subducting slabs linked to metamorphic dehydration reactions?, J. Geophys. Res., 108 (B1), 1–8.

McKenzie, D., (1984). The generation and compaction of partially molten rock. Journal of Petrology 25 (3), 713–765.

Morency, C., Huismans, R., Beaumont, C., Fullsack, P, (2007), A numerical model for coupled fluid flow and matrix deformation with applications to disequilibrium compaction and delta stability, Jour. Geophys. Res., 112 (B10404), 1–24.

Popov, A. A., Sobolev, S. V., 2008. Slim3d: A tool for three-dimensional thermo-mechanical modeling of the lithospheric deformation with elasto-visco-plastic rheology. Physics of the Earth Interiors 171, 55–75.

Quinteros, J., Sobolev, S. V., 2012. Constraining kinetics of metastable olivine in Marianas slab from seismic observations and dynamic models. Tectonophysics 526–529 (0), 48–55.

Quinteros, J. and Sobolev, S. V.: Why has the Nazca plate slowed since the Neogene?, Geology, 41, 31–34, doi:10.1130/G33497.1, 2013.

Quinteros, J., Sobolev, S. V., and Popov, A. A.: Viscosity in transition zone and lower mantle: Implications for slab penetration, Geophysical Research Letters, 37, L09 307, doi:10.1029/2010GL043140, 2010.

The mechanical erosion of refertilized continental lithosphere by plume driven mantle flow

Hongliang Wang[1], Jeroen van Hunen[1], D. Graham Pearson[2]

[1] *Department of Earth Science, University of Durham, Durham, England, United Kingdom*
[2] *Department of Earth & Atmospheric Sciences, University of Alberta, Edmonton, AB, Canada*
e-mail: *godormag@gmail.com*
session: *Geodynamics*

Abstract

Mantle plumes are amongst the most influential thermal events for continental lithosphere as they provide extra heat and strong mantle flow that could change and erode the originally depleted continental root. Xenolith research shows that many Precambian lithospheres show a multistage modification/enrichment through mantle metasomatism process that might change the buoyancy and rheology of continental root. We performed new numerical experiments to explore the lithosphere dynamics of a plume impacting continental lithosphere. A combined rheology with parameters close to dislocation and diffusion creep experiments is applied. Our models demonstrate that the mechanical erosion of lithosphere mainly focuses on the edge of the continental root, and it is strongly affected by the internal buoyancy and rheology of the portion of the root that is exposed to the plume flow. Models with increased plume flux or closer plume proximity, however, are not found to induce more erosion. By either losing their high viscosity or chemical buoyancy, a significant part of continental root might be eroded away during tens of Myrs by the plume impact. Thus, our results indicate that metasomatic refertilization that could change the buoyancy and rheology of lithosphere, is an essentia for the destruction of continental roots. Furthermore, our results demonstrate how a plume event could have caused the significant thinning of Proterozoic lithosphere beneath SW Namibia in southern Africa, at 70 Ma.

Introduction

The heterogeneity of lithosphere with cratonic, platform and oceanic lithosphere, is one of the most salient features of modern plate tectonic. The long lasting thick cratonic lithosphere is considered to be generally stable and not subject to change since it is formed in Archean, at least in terms of geodynamics. However, the finding that North China Craton [Gao et al., 2008; Zhu and Zheng, 2009] has lost significant part of its root shows that craton might also be affected by mantle dynamic activities. With the development of modern geosciences techniques, more and more new evidences show that the physically stable cratons might also experience some mantle dynamics and be modified in different aspects such as seismic properties, chemical composition [Chesley et al., 2004; Carlson et al., 1995, 2005; Simon et al., 2003; James et al., 2001; Griffin et al., 2003a]. Consider the significant lithosphere heterogeneity observed, either from the different thickness of different types of lithosphere or from the geochemical modifications (e. g. mantle metasomatism), the geodynamical modelling of its effects is required. Mantle plumes are suggested to be responsible to some observations related to mantle dynamics. Therefore, it is interesting to know how lithospheric refertilization and mantle plume influence the stability of the continental lithosphere. Numerical experiments are performed to explore the erosion process when a plume impact thick continental root with different buoyancy and strength.

Model setup

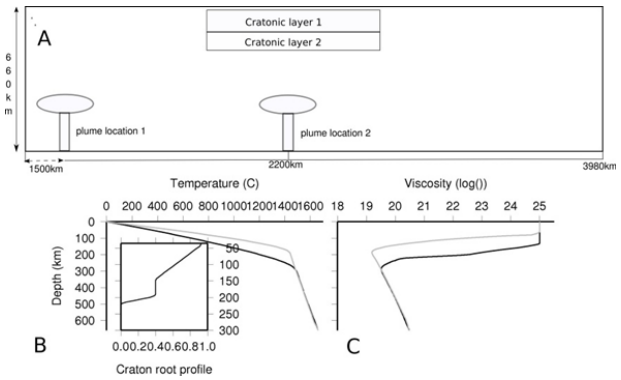

Fig. 1: A) Two-layer Cratonic root setup: 1) a highly depleted layer from Moho to 150 km with the chemically tracking value gradually decrease from 1 to $C\eta$; 2) a less depleted layer from 150 km to 200 km with constant chemically tracking value $C\eta$. B) Typical geotherms of cratonic (black) and normal lithosphere (gray) as the initial thermal condition and chemical profile of cratonic layer (zoomed box). C) Typical viscosity profile corresponding to the geotherms in B.

Results and discussion

Figure 2 show the plume craton interaction for about 125 Myrs through temperature, buoyancy and viscosity evolution. When the plume arrives at around 30 Myrs, the lower cratonic root become relatively more gravitational unstable as the deep blue area indicates and is strongly sheared at the edge by the plume induce flow (30.7 Myr in Fig. 2 B). However, the high viscosity of cratonic root prevent the significant development of gravity instability in this model and only the root material at edge of cratonic root is eroded away. After the major plume flow impact, small scale convection develops underneath the normal lithosphere and it propagates to the edge of cratonic root and cause further erosion (41.7 Myr in Fig. 2 B). Once the plume material cools down, the lower part of cratonic root returns back to neutrally buoyant (125 Myrs in Fig. 2 B). Comparing the cratonic root before and after the plume, we can see the main impact and erosion is focused on the edge of thick continental root.

As the first layer of the root has little effects on the dynamics, we parameterize the chemical buoyancy and strengthening factor ($\Delta\rho$ and $\Delta\eta$ in Fig. 3) of the second layer to explore their effects on the erosion of cratonic root by plumes. We calculate average thermal thickness and chemical root remain at the left cratonic edge at every time step in order to monitor the extent of erosion. Figure 3 A and 3 B show these two quantities at 50 Myr (20 Myrs after the plume rising up) for a range of models. Four models are selected to demonstrate the evolution histories of these two quantities in Figure 3 C and 3 D, in which the impact of plume arrival is clearly indicated by the kink points near 30 Myrs for all of these lines. After the plume, the average thermal thicknesses grows slowly as the mantle cools down (Fig. 3 C), while the erosion of chemical root might still continue (red and blue lines in Fig. 3 D) or slows down (green line in Fig. 3 D). As it shows, the craton edge in the model with $\Delta\rho = 31.5\,\mathrm{kg\,m^{-3}}$ and $\Delta\eta = 4$ maintains an average thermal thickness around 190 km and 90 % of its original cratonic root at 50 Myrs. By either reducing the buoyancy (e. g. $10\,\mathrm{kg\,m^{-3}}$) or the strengthening factor (e. g. < 2), the erosion of cratonic root edge would increase considerably; if both the buoyancy and strengthening factor are reduced, even more significant erosion could be observed (Fig 3 A, 3 B). Therefore, the erosion of cratonic root is strongly depended on the buoyancy and strength of the cratonic root.

Our geodynamical models demonstrate how the continental root would be eroded by the hot mantle flow induced by plume and find the buoyancy and strength of the lowermost root play a dominant role on this process. The effects of plume induced flow on a typical chemical cratonic root with $\Delta\rho \approx 30\,\mathrm{kg\,m^{-3}}$ and mild compositional strengthening factor (3–4) is quite limited. By either losing the chemical buoyancy or reducing the compositional strengthening factor, significant erosion of continental root by plumes could happen. The most likely mechanism for continental root to lose the chemical distinguished characteristics is lithosphere refertilization through mantle metasomatism. By decreasing the Mg#

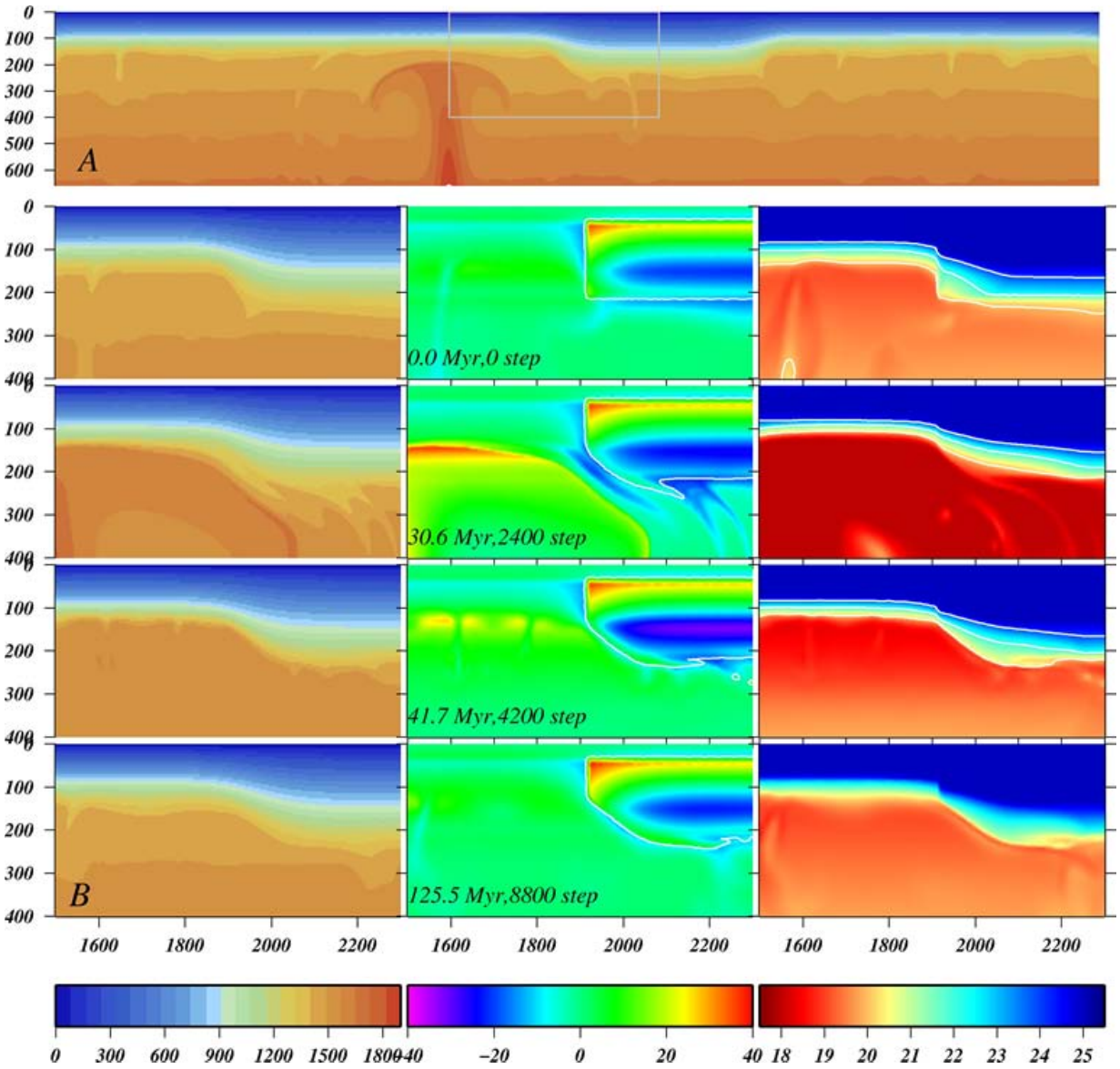

Fig. 2.: A): The full image of temperature field when plume rise up near cratonic root. The area within the gray box is zoomed out in Fig. 2 B. B): The evolution of temperature (left), horizontal buoyancy (middle) and viscosity (right) when plume impact thick cratonic root. The four time snapshots are: 0 Myrs, 30.67 Myr, 41.7 Myr and 125.5 Myrs. The plume rises up at 30 Myr. This model has $\Delta\rho = 21\,\mathrm{kg\,m^{-3}}; \Delta\eta = 3$ as showed in Figure 3.

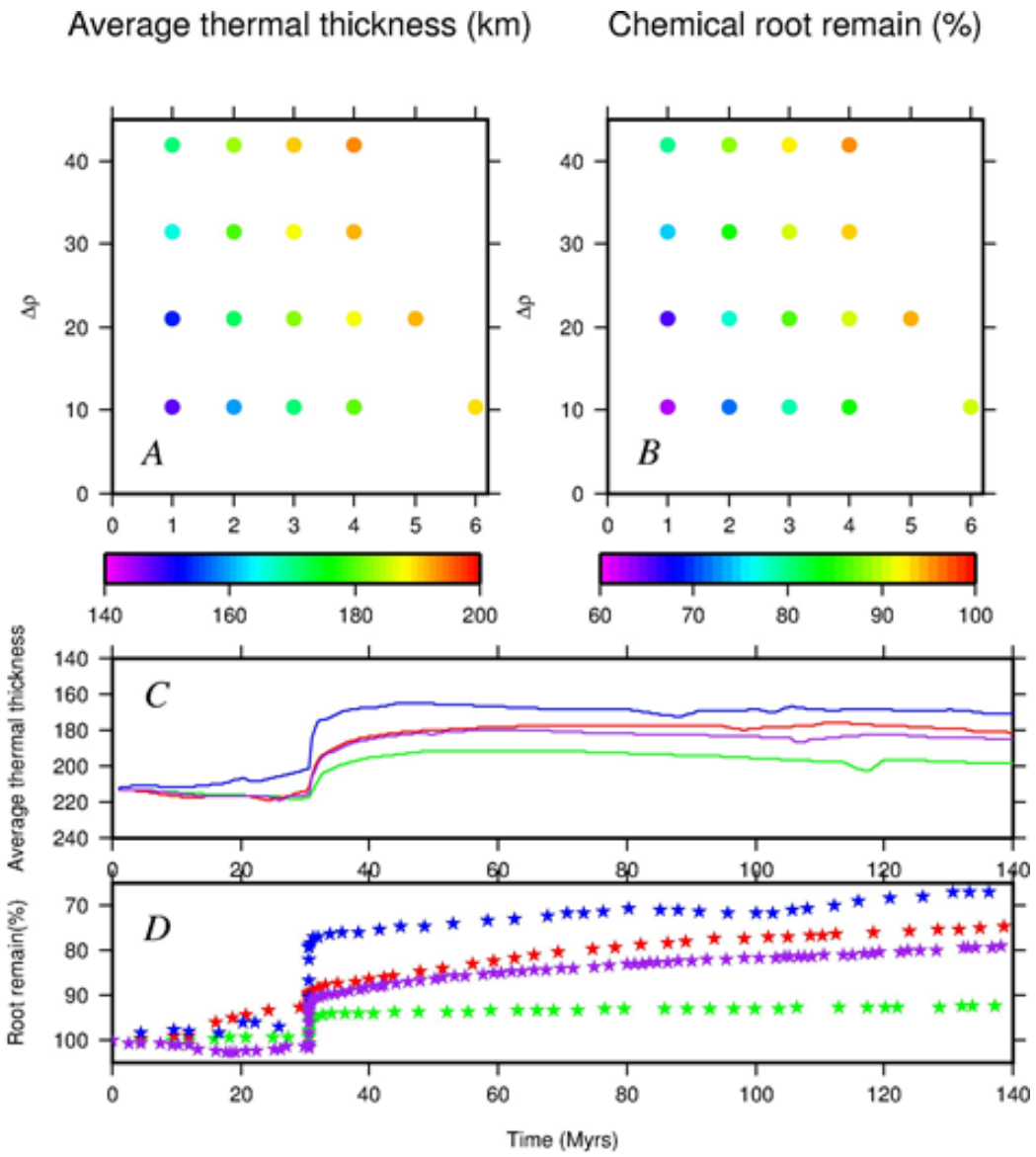

Fig. 3.: Effects of buoyancy and viscosity of the second cratonic layer on the erosion of cratonic root edge. (A) and (B) shows the average thermal thickness and chemical root remain of craton edge ($1914\,\mathrm{km}$ to $2046\,\mathrm{km}$) at 50 Myrs, respectively. C) and D) shows the 140 Myrs evolutions of four selected models in A and B: green lines for ($\Delta\rho = 31.5\,\mathrm{kg\,m^{-3}}; \Delta\eta = 4$); red lines for ($\Delta\rho = 10.5\,\mathrm{kg\,m^{-3}}; \Delta\eta = 4$); blue lines for ($\Delta\rho = 31.5\,\mathrm{kg\,m^{-3}}; \Delta\eta = 1$) purple lines for ($\Delta\rho = 21\,\mathrm{kg\,m^{-3}}; \Delta\eta = 3$).

of the originally depleted continental lithosphere and raising its pyroxene and garnet content, the chemical buoyancy/density of the SCLM would decrease/increase substantially[Griffin et al., 2003(b); Carlson et al., 2005]. Another important aspect of refertilization through mantle metasomatism is thermal effects. Through the heat advection from the metasomatism agents (hot fluid or melts) and enriched radiogenic element, the temperature of refertilized lithosphere would increase accordingly, but its effects would be smaller than the change of Mg# [Griffin et al., 2003(b)]. The influence of metasomatic refertilization on the viscosity of mantle rock is unclear due to the lack of related research, but the research about elastic thickness of Slave province in Canada shows that the metasomatic refertilization might also affects the rheology [Poudjom Djomani et al. 2005]. However, the heating of continental root itself has a rheological effect as the temperature is the main factor of mantle rheology, especially for the root material at the rheological boundary. Therefore, it's reasonable to link the change of buoyancy and strengthening factor in our models to metasomatic refertilization that happen to the continental root, even though we didn't include this process in our numerical models due to the lack of mathematic description.

Conclusion

1. For any significant thinning of cratonic root, it is most likely that one of the factor of buoyancy and viscosity or both were changed significantly, otherwise the chemically buoyant and strengthened root would strongly resist the erosion and deformation.

2. Metasomatic refertilization, as the main mechanism to change the composition of continental root, has an important geodynamic meaning for the continental lithosphere.

References

Carlson, R. R. W., D. G. Pearson, and D. D. E. James (2005), Physical, chemical, and chronological characteristics of continental mantle, Rev. Geophys., (2004), 1–24, doi:10.1029/2004RG000156.1.INTRODUCTION.

Djomani, Y. P., and S. O'Reilly (2001), The density structure of subcontinental lithosphere through time, Earth Planet. Sci. Lett., 184, 605–621.

Gao, S. et al. (2008), Recycling deep cratonic lithosphere and generation of intraplate magmatism in the North China Craton, Earth Planet. Sci. Lett., 270(1-2), 41–53, doi:10.1016/j.epsl.2008.03.008.

Griffin, W., S. O'Reilly, L. Natapov, and C. Ryan (2003a), The evolution of lithospheric mantle beneath the Kalahari Craton and its margins, Lithos, 71, 215–241, doi:10.1016/j.lithos.2003.07.006.

Griffin, W. ., S. . O'Reilly, N. Abe, S. Aulbach, R. . Davies, N. . Pearson, B. . Doyle, and K. Kivi (2003b), The origin and evolution of Archean lithospheric mantle, Precambrian Res., 127(1-3), 19–41, doi:10.1016/S0301-9268(03)00180-3.

Simon, N., G. R. Irvine, and G. Davies (2003), The origin of garnet and clinopyroxene in "depleted" Kaapvaal peridotites, Lithos, 71(2-4), 289–322, doi:10.1016/S0024-4937(03)00118-X

James, D. E., M. J. Fouch, J. C. Vandecar, and S. Van Der Lee (2001), Tectospheric structure beneath southern Africa, Geophys. Researc Lett., 28(13), 2485–2488.

Chesley, J., K. Righter, and J. Ruiz (2004), Large-scale mantle metasomatism: a Re–Os perspective, Earth Planet. Sci. Lett., 219(1-2), 49–60, doi:10.1016/S0012-821X(03)00698-8.

Deformation of forearcs during ridge subduction

Stefanie Zeumann, Andrea Hampel

Institut für Geologie, Leibniz Universität Hannover, Callinstraße 30, 30167 Hannover
e-mail: *zeumann@geowi.uni-hannover.de*
session: *Geodynamics*

Subduction of oceanic ridges causes considerable deformation of the forearc. Depending on the orientation of the ridge relative to the plate convergence direction, the ridge may either be stationary (e. g. Cocos Ridge at the Central American margin) or migrate along the margin (e. g. Nazca Ridge at the Peruvian margin). Here we use the finite Element program Abaqus to investigate the tectonic evolution of forearcs affected by ridge subduction.

The 3D models consist of a wedge-shaped forearc, under which an oceanic plate carrying the ridge is subducted (fig. 1). Following the approach of Cailleau and Oncken (2008) we use a cylindrical shape with a radius of 225 km for the subducting plate. Since the focus is on the deformation of the forearc we consider the oceanic plate as rigid. The plate interface is divided into the coupling zone with a variable friction coefficient and a frictionless section. The coupling zone along the plate interface is up to 30 km deep (fig. 1).

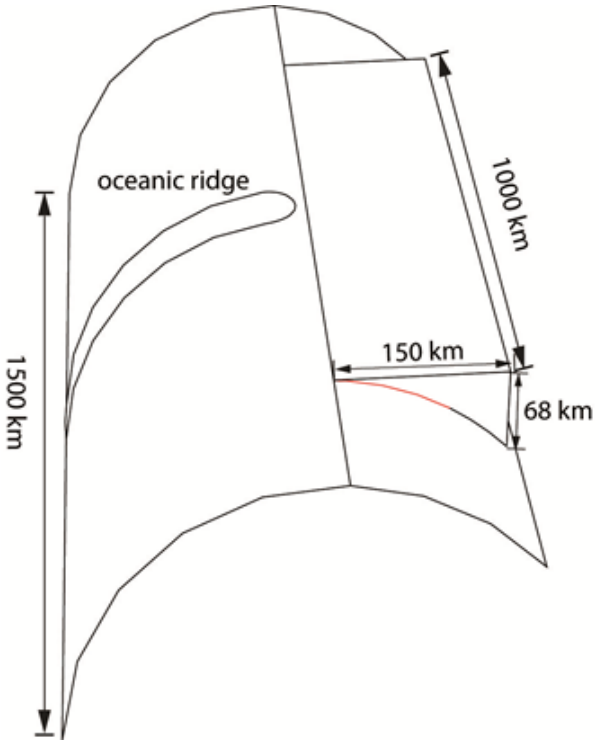

Fig. 1.: Model geometry includes a deformable wedge and a rigid slab carrying the oceanic ridge. The red line indicates the coupling zone along the plate interface.

In a systematic series of experiments, we consider migrating and non-migrating ridges by changing the angle between ridge and plate convergence direction. We further varied the ridge shape, the mechanical strength of the forearc and the frictional behaviour of the plate interface to identify the most crucial parameter for forearc deformation.

First results with a purely elastic forearc show that in all models the forearc is uplifted (fig. 2 a) and moved sideward during ridge subduction. For a stationary ridge, where the plate convergence direction is parallel to the ridge and perpendicular to the trench, the deformation pattern is symmetrical with respect to the ridge axis (fig. 2 a-d). The strain components show co-existing domains of both shortening and extension. Along the ridge axis, contraction occurs at the ridge tip and extension behind it (Fig 2 b). The strain component parallel to the margin (i. e. perpendicular to the ridge axis) reveals extension at the ridge tip and contraction above the flanks of the ridge (fig. 2 d-e). In models with a migrating ridge, the strain field becomes asymmetric with respect

to the ridge axis (fig. 2 e-f). The maximum contraction is found above the leading flank of the ridge.

A preliminary parameter study shows that the displacement and strain fields depend on the ridge shape (height, width), on the friction coefficient along the plate interface and, to a lesser extent, on the Young's moduli of the forearc. A higher ridge increases the amount of uplift whereas a broader ridge enlarges the region of uplift. A higher friction coefficient results in lower uplift for constant ridge height. Shortening and extension perpendicular to the margin increase with increasing ridge height or decreasing Young's moduli of the forearc layers. In contrast, a higher friction coefficient leads to lower extension but higher contraction. The strain component parallel to the margin is primarily affected by the ridge shape whereas material properties of the forearc and friction coefficient along the plate interface have nearly no influence. Increasing the ridge height increases the magnitude of both the extension at the ridge tip and the contraction above the ridge flanks. In contrast, a wider ridge decreases the overall amount of strain. In all models the ridge indents the forearc wedge (fig. 2 c). The indentation increases if a) the Young's moduli of the forearc layers decrease, b) the ridge is higher and c) the friction coefficient of the plate interface is increased. For example, increasing the ridge height from 1000 m to 2000 m enlarges the indentation by nearly 300 m after one million years of modelling time. Furthermore, the indentation depends on the frictional coupling between the two plates, with higher friction coefficients leading to larger re-entrants.

Future models will include the implementation of plastic behaviour to investigate the permanent deformation of forearcs during ridge subduction.

References

Cailleau, B. and O. Oncken (2008), Past forearc deformation in Nicaragua and coupling at the megathrust interface: Evidence for subduction retreat?, Geochem. Geophys. Geosyst., 9, Q03016, doi:10.1029/2007GC001754

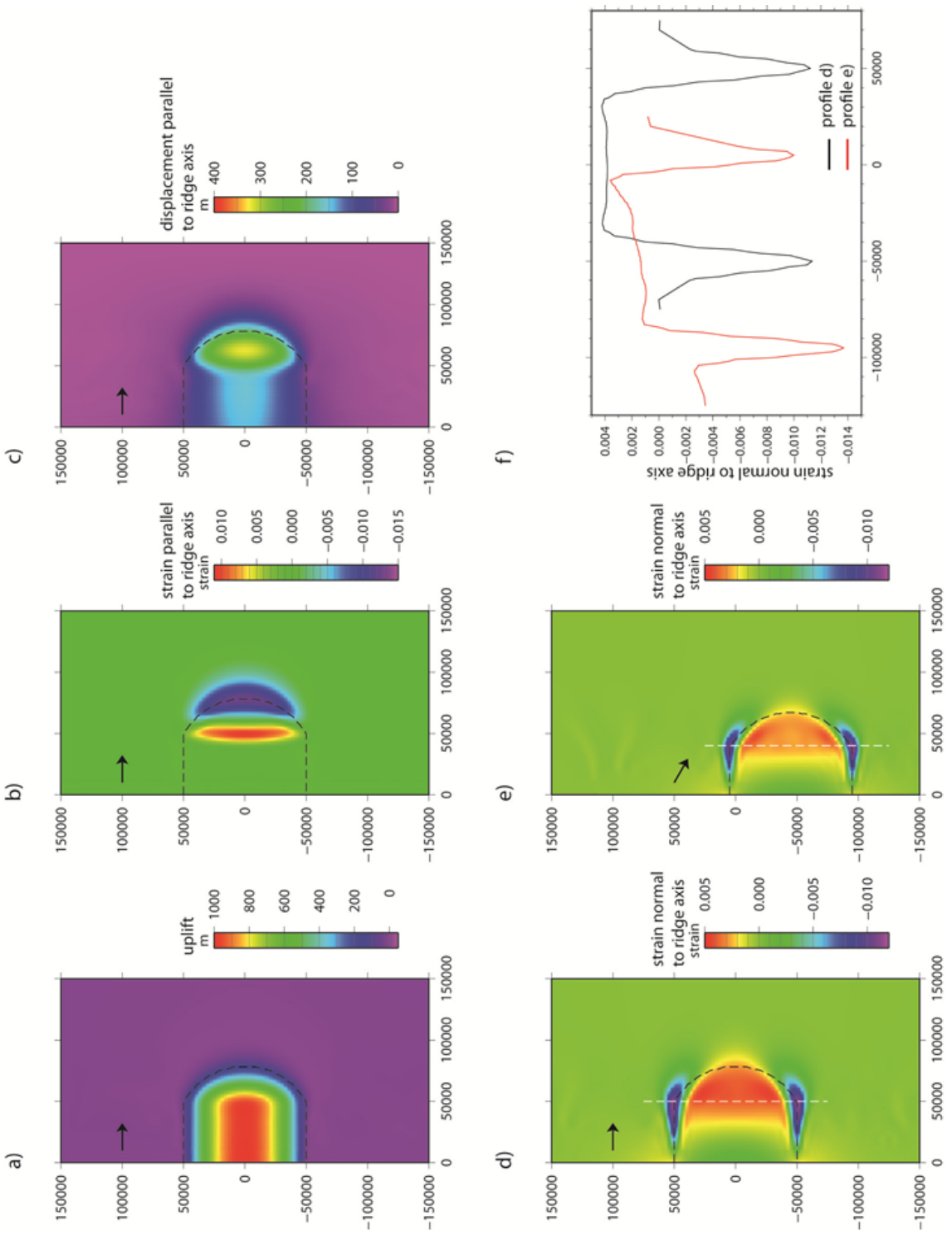

Fig. 2.: Central part of the model surface at 1 Ma of model time for a $100\,\mathrm{km}$ broad and $1\,\mathrm{km}$ high ridge. Black arrows indicate the plate convergence direction and black dashed line mark the ridge position. a) Uplift, b) strain component along the ridge axis, c) displacement along the ridge axis, and d) strain component normal to the ridge axis for a model with a plate convergence direction normal to the margin. e) Strain component normal to the ridge axis for a model with a plate convergence direction $60°$ oblique to the margin. f) Comparison of the strain component normal to the ridge axis for the white profiles in pictures d (black) and e (red).

GFZ
Helmholtz Centre
POTSDAM

GeoMod 2014

Modelling in Geosciences

Programme & Extended Abstracts

31 August - 5 September 2014

Editors:
Kirsten Elger
Øystein Thordén Haug
Malte Ritter

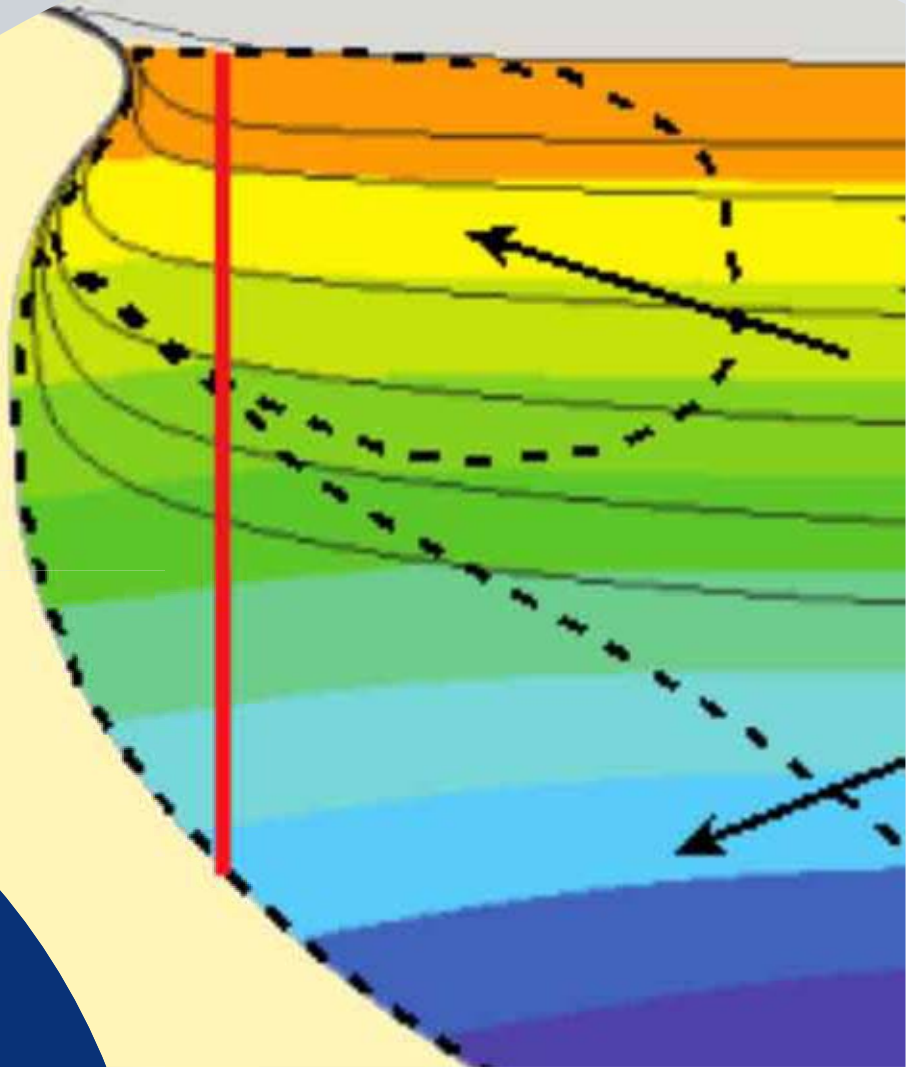

Session V
Rheology

Conveners:
Georg Dresen (GFZ/U Potsdam)
Hiroki Sone (GFZ)

DFG Geo.X Geo.Sim

Session V.

Rheology

Session Description: Rheology

Conveners: Georg Dresen (GFZ/U Potsdam), Hiroki Sone (GFZ)

Rheology of the Lithosphere – What's new and where is this going? Localized and episodic deformation in the upper crust is intimately coupled to viscous flow of deeper layers of the upper lithosphere. The nature of this coupling in actively deforming regions such as mountain belts and large plate-bounding fault zones is complex and involving a broad range of governing physical processes potentially varying in space and time. In this session we wish to address open questions related to the rheology of crustal and upper mantle rocks and in particular span a bridge between constraints provided by laboratory and field studies to numerical modelling approaches of ductile deformation processes over a range of spatial and temporal scales.

Fold Geometry Toolbox 2: A New Tool to Estimate Mechanical Parameters and Shortening from Fold Geometry

Marta Adamuszek[1], Marcin Dabrowski[1,2], Daniel W. Schmid[2]

[1] *Polish Geological Institute – National Research Institute, Lower Silesia Branch, Poland*
[2] *Physics of Geological Processes, University of Oslo, 0316 Oslo, Norway*
e-mail: *marta.adamuszek@pgi.gov.pl*
session: *Rheology*

Rheological properties of rocks, deformation condition, and amount of shortening significantly influence shape of buckle folds during deformation. Understanding the relation between these parameters and the fold shape gives a possibility to interpret natural fold structures and consequently gain an insight into rock deformation at the geological scale. Range of mathematical relationships has been derived from the mechanical theory of folding to estimate material parameters and amount of shortening from the fold shape. The use of these relationships requires determination of the fold geometrical parameters such as fold arclength, amplitude, wavelength and thickness. An accurate estimation of the geometrical parameters is essential for the correct fold shape analysis. The major challenge in the fold geometry study is rooted in curvature analysis, which is highly sensitive to the presence of noise. The noise corrupts the curvature analysis and thus affects identification of hinges and inflection points, which are the reference points necessary to determine all the fold shape parameters.

In order to promote the accurate fold shape analysis, we developed Fold Geometry Toolbox (FGT) (Adamuszek et al., 2011). The toolbox deals with noisy interfaces and automatically determines the four parameters for a generic fold shape. The parameters are further employed in estimation of shortening and material properties using: Biot (1961, 1965), Currie et al. (1962), Sherwin and Chapple (1968), Fletcher (1974, 1977), Fletcher and Sherwin (1978) and Schmalholz and Podladchikov (2001) methods. FGT is open source, written in MATLAB. It is easy to use and comes with a graphical user interface.

The new version of FGT includes significant new functionality aimed at improving the fold shape analysis and presentation of the final results in a form of exportable tables and figures. The new enhancements also involve implementation of new methods for estimating shortening and mechanical parameters based on e.g. stretching of the folded layer back to the planar orientation using analytical Large Amplitude Folding method (Adamuszek et al., 2013) and finite element method based tools. Further changes in the toolbox include a possibility to: a) make a correction for obliquity of the fold section, b) modify manually the position of hinges and inflection points on the fold interfaces, c) analyse a single fold interface, d) exclude part of the fold train from the final fold analysis, and e) apply different filtering on different fold interfaces.

One of the new key features in FGT is EduFold application. The application is desired to illustrate the fold evolution with progressing shortening for user defined initial geometrical and mechanical parameters and amount of shortening. The evolution of the fold shape and the fold shape parameters can be illustrated for each time step on diagrams (Figure 1). The folding process is simulated using finite element method based MIL-

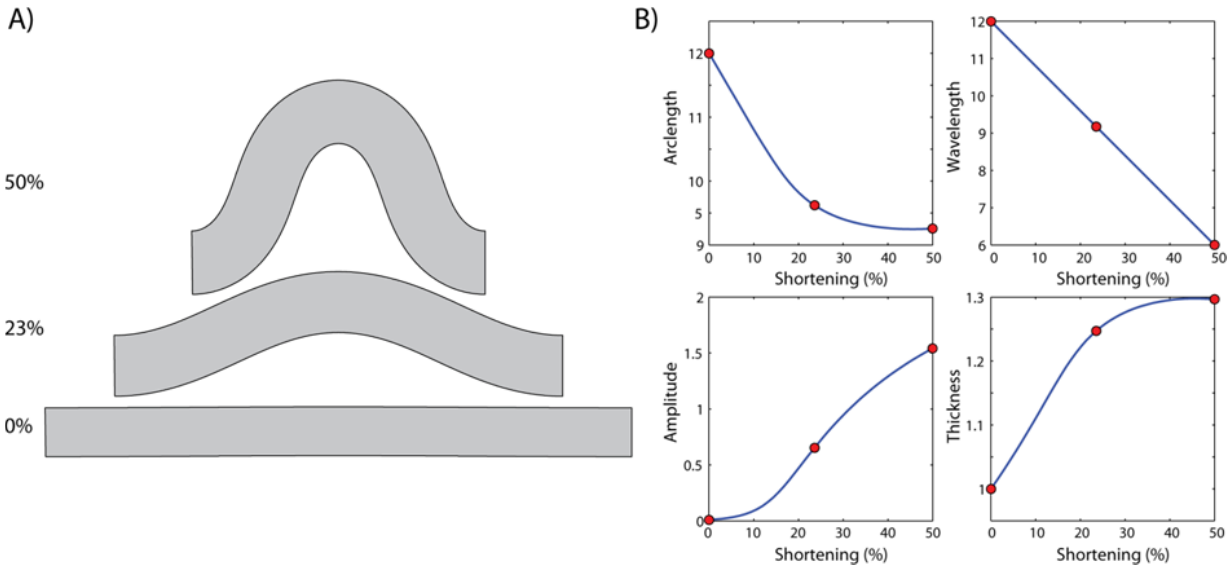

Fig. 1.: Results of the numerical simulation of fold evolution using EduFold application for initial amplitude A0=0.01, wavelength λ=12, thickness H=1, viscosity ratio R=100, and stress exponent n=1. A) Fold shape at shortening of 0%, 23%, and 50%. B) Evolution of fold geometry parameters as a function of shortening. Three points on the four diagrams refer to three shortening values 0%, 23%, and 50%.

AMIN solver (Dabrowski et al., 2008). The fold shape generated in the application can be further analysed in the toolbox. As a result, EduFold application has a great educational value. Geometrical analysis of the synthetically generated fold allows to investigate the relation between the input and output parameter values. This gives a user an opportunity to explore advantages and limitations of the mathematical relationships desired to analyse the fold shape.

References

Adamuszek M., Dabrowski M., Schmid D.W. 2011. Fold Geometry Toolbox - Automated determination of fold shape, shortening, and material properties Journal of Structural Geology, Vol. 33, p. 1406-1416

Adamuszek M., Schmid D.W., Dabrowski M., 2013, Theoretical analysis of large amplitude folding of a single viscous layer, Journal of Structural Geology, Vol. 48, p. 137–152

Biot, M.A., 1961. Theory of folding of stratified viscoelastic media and its implications in tectonics and orogenesis. Geological Society of America Bulletin 72 (11), 1595-1620.

Biot, M.A., 1965. Theory of similar folding of first and second kind. Geological Society of America Bulletin 76 (2), 251.

Currie, J.B., Patnode, H.W., Trump, R.P., 1962. Development of folds in sedimentary strata. Geological Society of America Bulletin 73, 655-674.

Dabrowski, M., Krotkiewski, M., Schmid, D.W., 2008. MILAMIN: MATLAB-based finite element method solver for large problems. Geochemistry Geophysics Geosystems 9.

Fletcher, R.C., 1974. Wavelength selection in folding of a single layer with power-law Rheology. American Journal of Science 274 (9), 1029-1043.

Fletcher, R.C., 1977. Folding of a single viscous layer: exact infinitesimal-amplitude solution. Tectonophysics 39, 593-606.

Fletcher, R.C., Sherwin, J.A., 1978. Arc lengths of single layer folds - Discussion of comparison

between Theory and Observation. American Journal of Science 278(8), 1085-1098.

Sherwin, J.A., Chapple, W.M., 1968. Wavelengths of single layer folds - a comparison between theory and observation. American Journal of Science 266 (3), 167-179.

Schmalholz, S.M., Podladchikov, Y.Y., 2001. Strain and competence contrast estimation from fold shape. Tectonophysics 340 (3-4), 195-213.

Mechanical anisotropy development and localization in two-phase composite rocks.

Marcin Dabrowski[1,2]

[1] *Computational Geology Laboratory, Polish Geological Institute - National Research Institute, Wroclaw, Poland*
[2] *Physics of Geological Processes, University of Oslo, Oslo, Norway*
e-mail: *mdabr@pgi.gov.pl*
session: *Rheology*

Introduction

An isotropic composite medium subject to viscous deformation develops compositional layering, which is initially parallel to the instantaneous stretching direction. The development of such structural anisotropy results in effectively anisotropic viscous properties, which favor layer-parallel shearing over layer-parallel stretching or shortening. Thus, to a first order approximation, monotonic hardening is expected in pure shear deformation. Non-coaxial deformation paths such as simple shear can lead to an initial hardening phase followed by overall weakening (Dabrowski et al, 2012). The behavior reflects a successive build-up of the shape and mechanical anisotropy concurrent with a progressive reorientation of the compositional layering into the shear direction. This results in a growing dominance of the weaker component (shear viscosity) over the stronger component (normal viscosity) of the effective anisotropic viscosity in determining the effective mechanical response of a composite rock in simple shear. The level and the rate of mechanical weakening available in two-phase composite systems consisting of weak inclusions depend chiefly on the inclusion fraction and the viscosity ratio. A varying inclusion fraction in a rock column subject to simple shear results in a non-homogeneous distribution of the shear rate. With strain-dependent weakening due to fabric development, which provides a positive-feedback mechanism, strain localization can occur. However, deforming anisotropic rocks may experience mechanical instabilities, e.g., internal boudinage or folding may develop during layer-parallel extension or shortening, respectively, resulting in both cases in a prominent overall weakening. In fact, the question that arises is as to whether viscous deformation of initially isotropic composite rocks can lead to a well-developed compositional layering before it is hampered by boudinage formation. With regard to the issue, the three critical questions are: (1) How does the rock fabric evolution depend on the mechanical properties of rock constituents, the inclusion fraction and the initial microstructure? (2) How does the mechanical (viscous) anisotropy relate to the overall shape anisotropy of a composite rock? (3) How does the internal boudinage development manifest in composite materials consisting of elongated inclusions rather than well-developed layers?

Methods

I will numerically investigate the development of shape preferred orientation and mechanical anisotropy in a composite two-phase rock undergoing stretching. A two-dimensional inclusion-host type of composite, in which an interconnected host embeds non-overlapping inclusions, is considered. Different inclusion fractions, shapes and size distributions are studied. The initial spatial distribution of the inclusions is intended to be

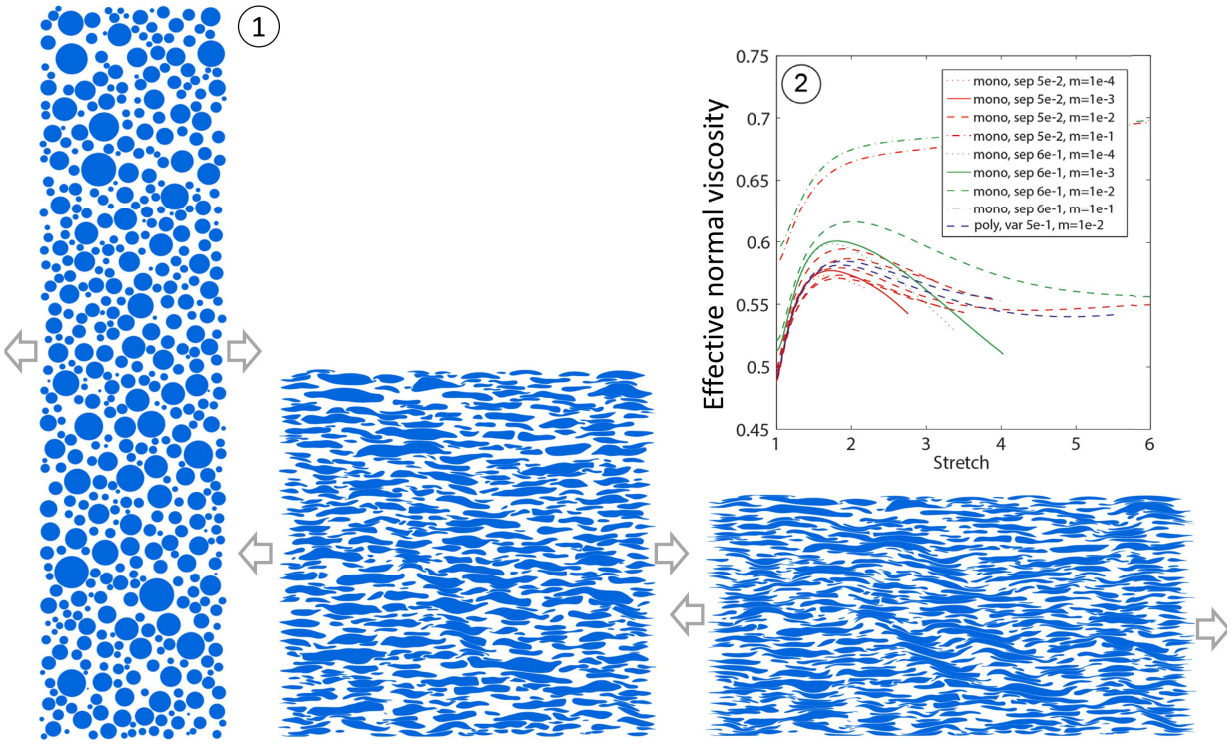

Fig. 1.: Fabric development in a poly-disperse inclusion-host composite subject to pure shear. Linear viscosity is used and the viscosity ratio was set to 1e-2. The inclusion fraction is 30% and the coefficient of variation of the log-normal distribution used for inclusion diameters was set to 0.5. 2) The effective normal viscosity normalized by the host viscosity as a function of stretch. The inclusion fraction is 30%. sep: minimum initial separation among the inclusions (scaled upon the smaller of the local radii), var: the coefficient of variation of the log-normal distribution, m: viscosity ratio between the inclusions and the host

random, statistically homogeneous (no clustering) and isotropic. In a series of complementary simulation runs, periodic inclusion arrays are analyzed. Both the inclusion and host materials are considered as viscous fluids and the intrinsic viscosities of the inclusion and the host phases are isotropic. A coherent inclusion-host interface is assumed and interfacial processes such as surface tension or diffusional mass transfer are neglected. The deformation is studied in the Stokes limit and under no gravity. A self-developed FEM code (www.milamin.org, Dabrowski et al., 2008) is used to find the velocity vectors at the inclusion interfaces. Unstructured triangular computational meshes adapting to or fitting all the internal inclusion boundaries are used in the simulations. To achieve the necessary resolution of the complex geometry of evolving inclusion-host interfaces, a large number of computational points is required. A test case is presented to demonstrate the performance of different ODE solvers and the accuracy of competing geometrical representations.

Results

Figure 1 shows that subjecting a two-phase composite consisting of weak inclusions (the viscosity

ratio of 1e-2) to pure shear deformation results in the development of stretched inclusions with complex sigmoidal shapes organizing into conjugate bands, which gives an overall impression of a structure resembling internal boudinage. The system undergoes hardening in the initial stages of stretching (the blue curves in the inset plot in Fig. 1). This behavior can be attributed to the development of shape preferred orientation, which results in an effectively anisotropic viscosity. The harderning phase is followed by an overall weakening phase, which can be correlated with the development of internal boudinage-like structures. The weakening phase occurs both in mono- and polydisperse composites. The peak of the hardening phase increases with increasing the initial separation between the inclusions. No weakening phase is observed for the viscosity ratio of 1e-1. A significant increase in the rate of weakening is observed with decreasing the viscosity ratio from 1e-2 to 1e-3.

References

Dabrowski, M., Krotkiewski, M., and Schmid, D. W. MILAMIN: MATLAB-based finite element method solver for large problems, Geochem. Geophys. Geosyst., 9, Q04030, 2008

Dabrowski, M., Schmid, D.W. and Podladchikov, Y.Y. A two-phase composite in simple shear: Effective mechanical anisotropy development and localization potential. Journal of Geophysical Research 117, 2012

Numerical models of ductile roots of mature strike-slip faults

Yuri Fialko[1]

[1] *Insitute of Geophysics and Planetary Physics, Scripps Insitution of Oceanography, University of California San Diego, La Jolla, CA 92093, USA*
e-mail: *yfialko@ucsd.edu*
session: *Rheolohy*

The degree to which strain is localized in the ductile part of the lithosphere below major faults is a major unresolved question in continental tectonics. Two classes of models have been proposed: one postulating a broadly distributed viscous deformation in the lower crust and upper mantle (the "thin lithosphere" model), and another one postulating extension of localized shear well below the brittle-ductile transition (the "thick lithosphere" model). Understanding the mechanics of lithospheric shear zones is essential for a number of problems in continental tectonics, including the long-term strength of the Earth's crust and upper mantle, stress transfer from the relative plate motion to seismogenic faults, and, ultimately, seismic hazards. Geological and geophysical evidence has been presented in support of both the "thin" and "thick" lithosphere models, possibly indicating differences in deformation styles between various locations, tectonic settings, deformation rates, and total displacements. If such variability exists, it is of interest to establish the main controlling factors and governing mechanisms on the observed deformation styles.

We investigate the long-term deformation and strain evolution due to major strike-slip faults in the continental crust. In particular, we use numerical models to evaluate the efficiency of various strain-softening mechanisms, such as thermomechanical coupling, grain-size reduction, and mylonitic fabric, and assess the degree to which they promote or inhibit strain localization, individually and in combination, in response to long-term fault slip. This is accomplished using finite element models that incorporate realistic geotherms, far-field loading rates and loading histories, depth-dependent compositions, and constitutive relationships inferred from laboratory experiments. Our simulations investigate conditions under which permanent shear zones may develop in an initially unstrained ductile substrate. We evaluate the magnitude and distribution of deviatoric stresses in the ductile lower crust and upper mantle, and make inferences about the long-term strength of continental lithosphere as a function of temperature regime, composition, deformation rate, total displacement, and other relevant factors. Observables that are brought to bear on the model predictions include grain size distributions from the exposed mid-to-lower crustal shear zones, inferences of deviatoric stress from petrologic and micro-structural data, seismic structure and anisotropy below active fault zones, and geodetic observations of transient and secular deformation due to major strike-slip faults.

The degree of strain localization in the ductile substrate depends on a number of factors such as the host rock composition, water content, geothermal gradient, and fault slip rate. Stiffer rheologies, lower ambient temperatures, and higher slip rates give rise to narrower shear zones. For the "San Andreas- ike" parameters used in our models, the predicted width of the thermally induced shear zone in the lower crust is of the order of a few km (*Takeuchi and Fialko*, 2012). Thus

much of the relative plate motion is accommodated by a "deep fault root" that extends into the lower crust, and further down into the upper mantle.

In models of (*Takeuchi and Fialko*, 2012), the behavior of the ductile substrate was governed by the constitutive relation for temperature- and stress- ependent power law dislocation creep. In these models, the thermally-activated power-law rheology was used as a proxy for all strain-weakening mechanisms. Such an approach does take into account diffusion creep, provided that contributions of dislocation creep and diffusion creep to the total strain rate are approximately equal (e. g., *De Bresser et al.*, 1998). We have also experimented with including into our models two additional mechanisms of ductile deformation that may be important in the lower crust and/or the upper mantle: grain size reduction and mylonitic fabric.

Grain size reduction

Grain size evolution is included in the viscous constitutive equation through the addition of grain size-dependent diffusion creep,

$$\dot{\varepsilon}_{diff} = A_{diff} d^{-m_{diff}} \sigma^{n_{diff}} \exp(-\frac{Q_{diff}}{RT}) \quad (1)$$

where d is grain size, n_{diff}=1, and A_{diff}, Q_{diff}, and m_{diff} are empirically determined parameters. Grain size reduction has been proposed as one of the mechanisms that can give rise to ductile shear zones observed in nature [e. g., *Fitz Gerald and Stüunitz* , 1993; *Jin et al.*, 1998] and laboratory experiments [e. g., *Tullis and Yund*, 1985; *Rutter* , 1995]. The grain size d is allowed to vary through a combination of static grain growth

$$\dot{d}_{+} = p^{-1} d^{1-p} G_0 exp(\frac{-H}{RT}) \quad (2)$$

and dynamic recrystallization

$$\dot{d}_{-} = -\lambda d \dot{\varepsilon}_{dis} \quad (3)$$

where G,p, and λ are empirical constants [*Hall and Parmentier*, 2003]. The constitutive equation for grain size evolution may either reflect a balance between the static grain growth and dynamic recrystallization [*De Bresser et al.*, 1998; *Montéesi and Hirth*, 2003; *Hall and Parmentier*, 2003], or evolution of the grains towards a stress-dependent equilibrium grain size $D = D_0 \sigma^{-r}$ where D_0 and r are material properties [*Van Der Wal et al.*, 1993; *Braun et al.*, 1999].

Grain size reduction may also be included with the addition of the grain size-dependent grain boundary sliding deformation mechanism. Grain boundary sliding allows for non-linear stress dependence similar to that of dislocation creep, while also allowing for grain size dependence similar to diffusion creep [*Hirth and Kohlstedt*, 1995]. Laboratory experiments have shown that deformation by grain boundary sliding is governed by a flow law similar to that of dislocation/diffusion creep [[*Hirth and Kohlstedt*, 1995; *Hansen et al.*, 2011].

$$\dot{\varepsilon}_{GBS} = A_{GBS} d^{-m_{GBS}} \sigma^{n_{GBS}} \exp(-\frac{Q_{GBS}}{RT}) \quad (4)$$

where A_{GBS}, n_{GBS}, Q_{GBS}, and m_{GBS} are empirically determined. Grain size evolution within the grain boundary sliding regime is governed by the same combination of static grain growth and dynamic recrystallization as described above.

Each of the three potential deformation mechanisms (dislocation creep, diffusion creep, and grain boundary sliding) may contribute to the total viscous strain rate,

$$\dot{\varepsilon}_{total} = \dot{\varepsilon}_{dis} + \dot{\varepsilon}_{diff} + \dot{\varepsilon}_{GBS}. \quad (5)$$

which requires only that constitutive parameters for each regime (readily available in references cited above) are defined to control the evolution of strain as a function of stress, temperature, and grain size during model execution.

Mylonitic fabric

We also assess the efficiency of fabric development due to large strains that give rise to differentiation of mineral phases and laminated textures, as observed in the exposed mylonite zones (*Berthe et al.*, 1979; *Büurgmann and Dresen*, 2008; *Mehl*

and Hirth, 2007; *Sibson*, 1978). The net result is formation of quasi-continuous layers of different mineral composition. Creep rate of each mineral phase is governed by equation 5 (any combination of deformation regimes may again be assumed). The total strain rate for a given volume of rock of multi-phase composition (or finite element, in case of a numerical model) is a volume-weighted superposition of the individual strain rates for each phase

$$\dot{\varepsilon}_{total} = \sum_{i=1}^{N} \dot{\varepsilon}_i \phi_i; \qquad \sum_{i=1}^{N} \phi_i = 1 \tag{6}$$

where ϕ_i are the volume proportions of the various phases, respectively [*Handy*, 1994].

In our models, we use a constitutive relationship for a laminated material, in which bands of a rheologically weak phase are interspersed within bands of stronger phases. Under a given applied shear stress, the total strain across a given volume of rock is insensitive to the details of band spacing, as long as the volume proportions of each phase are preserved. For example, for a two-phase mylonite composed of a weak phase and a strong phase subjected to a shear stress parallel to foliation, the total velocity across a 2-band layer having thickness $x + y$, where x is the thickness of a weak phase and y is the thickness of a strong phase, is identical to the velocity across the layer of the same thickness, composed of 10 weak and 10 strong bands having individual thicknesses of $0.1x$ and $0.1y$, respectively. One can then compute the total strain rate for a given volume as

$$\dot{\varepsilon}_{total} = \dot{\varepsilon}_w \phi_w + \dot{\varepsilon}_s \phi_s + \dot{\varepsilon}_a \phi_a \tag{7}$$

where ϕ_w and ϕ_s are the volume proportions of the weak and strong phases, respectively, and ϕ_a is the volume proportion of the aggregate rock. To illustrate this formulation, we use laboratory-derived constitutive relations for synthetic anorthite-diopside aggregates (*Dimanov and Dresen*, 2005), which have been used as a proxy for lower crustal rocks of gabbroic composition (e. g., *Mehl and Hirth*, 2007). *Dimanov and Dresen* (2005) presented dislocation and diffusion creep flow law parameters (equation 5) for pure anorthite, pure diopside, and two-phase mixtures with various volume proportions of each phase. Using these parameters, we calculate the effective viscosity of the phases for a given stress and temperature.

Figure 1 shows the distribution of velocity across a simulated volume of a material comprised of three different laminated rheologies; 0-10 cm: 5 cm pure wet anorthite and 5 cm pure wet diopside (fully laminated rheology- ϕ_w=0.5, ϕ_s=0.5, ϕ_a=0); 10-20 cm: 2.5 cm pure wet anorthite, 2.5 cm pure wet diopside, 5 cm wet 50% anorthite-50% diopside mixture (partially laminated rheology- ϕ_w=0.25, ϕ_s=0.25, ϕ_a=0.5); 20-30 cm: 10 cm wet 50% anorthite-50% diopside mixture (unlaminated rheology- ϕ_w=0, ϕ_s=0, ϕ_a=1), subjected to a shear stress of 10 MPa and a temperature of 500°C. Though the total composition of the rock (50% anorthite and 50% diopside) is preserved within each 10 cm band, greater deformation occurs in regions with high volume proportions of weak anorthite. If we assume that the volume proportions for each phase vary either (i) as a function of distance from the fault (time-invariant distribution) or (ii) as of function of total strain (in this case, the volume proportions would evolve during the simulation), deformation will localize in proportion to the degree of phase separation.

Figure 2 shows preliminary simulations that include the effects of thermomechanical coupling and grain size evolution. Subplots (a)-(c) in Figure 2 illustrate strain rates through 10 Myr of deformation, under the same boundary conditions as described above. The model consists of a 12 km thick elastic crust underlain by a ductile substrate that deforms by a combination of dislocation and diffusion creep. For simplicity, we assume the rheology of a wet olivine ($A_{dis} = 3.6e5$ MPa$^{-3.5}$s^{-1}; $n_{dis} = 3.5$; $Q_{dis} = 480e3$ kJ mol^{-1}; $A_{diff} = 1e9$ MPa^{-1}s^{-1}, $n_{diff} = 1$; $Q_{dis} = 335e3$ kJ mol^{-1}; A_{dis} and A_{diff} have a constant water content C_{OH} = 1000 H/10^{6}Si folded in, [*Hirth and Kohlstedt*, 2003; *Freed and Büurgmann*, 2004]) for the entire substrate. Strain localization occurs in these models by (a) grain size evolution

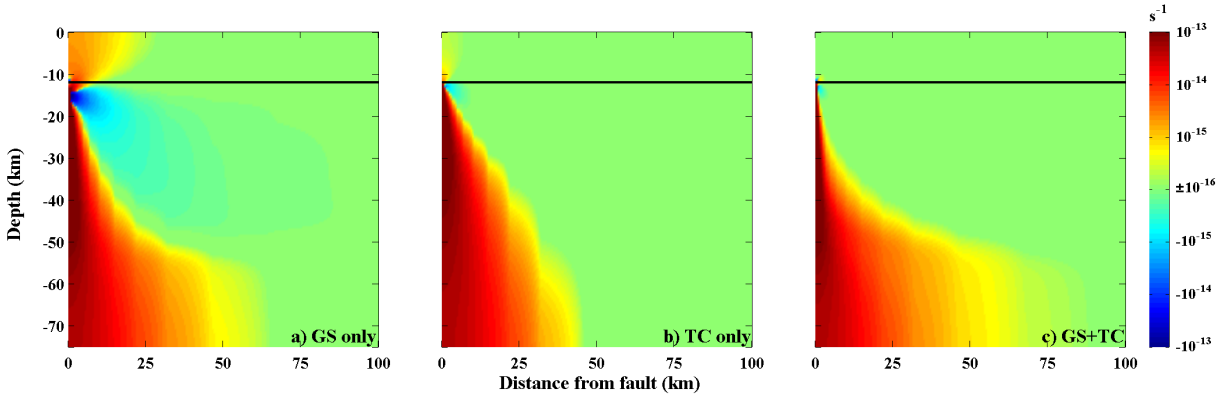

Fig. 2.: Preliminary results from a coarse-meshed model showing strain rate vs. depth and distance from fault through 10 Myr of simple shear. a) Grain size evolution (diffusion and dislocation creep); b) thermomechanical coupling (dislocation creep only); c) grain size evolution and thermomechanical coupling (diffusion and dislocation creep). Solid black line denotes the elastic-viscoelastic transition at 12 km depth.

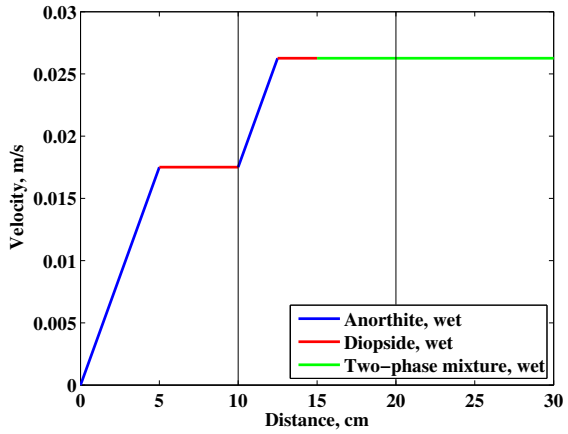

Fig. 1.: Distribution of velocity across a 30 cm-thick layer of simulated material composed of three laminated rheologies: 0-10 cm: 5 cm pure wet anorthite (blue) and 5 cm pure wet diopside (red); 10-20 cm: 2.5 cm pure wet anorthite (red), 2.5 cm pure wet diopside (blue), 5 cm wet 50% anorthite-50% diopside mixture (green); 10 cm wet 50% anorthite-50% diopside mixture (green), subjected to a shear stress of 10 MPa at a temperature of 500°C. All phases deform by dislocation creep, with flow law parameters from *Dimanov and Dresen* (2005).

($p = 3$; $G_0 = 4.3e-1$ m^{3}s^{-1}; $H = 600$ kJ mol^{-1}; $\lambda = 1$, equations 2 and 3 [*Hall and Parmentier*, 2003], assuming deformation by diffusion and dislocation creep); (b) shear heating and thermomechanical coupling, assuming deformation by dislocation creep only; and (c) a combination of grain size evolution and thermomechanical coupling, assuming deformation by diffusion and dislocation creep. All models assume an initial geotherm of 20°C/km. The initially one-dimensional temperature field is modified by shear heating and heat conduction in models (b) and (c). Initial grain sizes are 1 mm for models (a) and (c). Each model exhibits development of a shear zone below the elastic layer, with most intense strain located within 30 km of the fault plane (horizontal coordinate of 0). Models incorporating grain size evolution (a and c) show a significant delocalization of deformation towards the bottom of the domain, owing to the relatively high temperatures and enhanced grain growth (equation 2) at depth. Notably, the model combining grain size evolution and thermomechanical coupling (model c) shows robust localization within ∼3 km of the fault plane in the depth interval ∼12-30 km. Localization in this region is more pronounced relative to that in models accounting for the grain size evolution or thermomechanical coupling alone (Figure 3). In fact, the degree of strain localization in this case appears to be

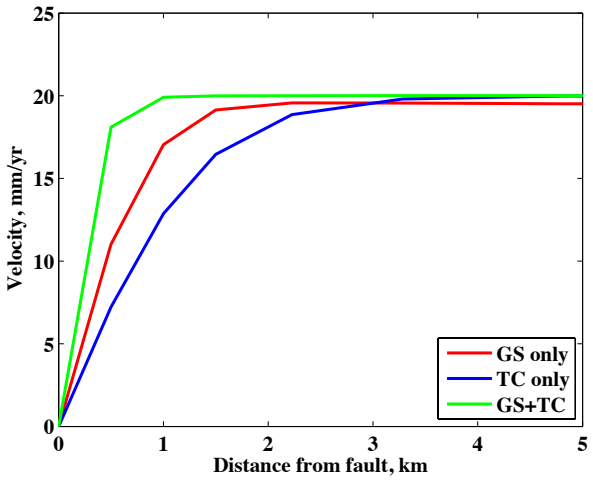

Fig. 3.: Profiles of fault-parallel velocity at depth of 20 km, for the deformation mechanisms illustrated in Figure 2: grain size evolution (red line), thermomechanical coupling (blue line), and a combination of the grain size evolution and thermomechanical coupling (green line).

limited by the mesh size, and we expect it to be even more pronounced upon a suitable mesh refinement. Our preliminary results shown in Figures 2 and 3 suggest that thermomechanical coupling and grain size reduction can work in concert to enhance strain localization in the lower crust and the upper mantle.

References

Handy, M., Flow laws for rocks containing nonlinear viscous phases: a phenomenological approach, J. Struct. Geol., 16, 287-301, 1994.

Hansen, L., M. Zimmerman, and D. Kohlstedt, Grain boundary sliding in San Carlos olivine: Flow law parameters and crystallographic-preferred orientation, J. Geophys. Res., 116, B08201, doi:10.1029/2011JB008220, 2011.

Hirth, G., and D. Kohlstedt, Experimental constraints on the dynamics of the partially molten upper mantle 2. Deformation in the dislocation creep regime, J. Geophys. Res., 100, 15,441-15,449, doi:10.1029/95JB01292, 1995.

Hirth, G., and D. Kohlstedt, Rheology of the upper mantle and mantle wedge: A view from the experimentalists, in Inside the Subduction Factory, Geophys. Monogr. Ser., vol. 138, edited by J. Eiler, pp. 83-105, AGU, Washington, D. C, 2003.

Jin, D., S.-I. Karato, and M. Obata, Mechanisms of shear localization in the continental lithosphere: Inference from the deformation microstructures from the Ivrea zone, Northwest Italy, J. Struct. Geol., 20, 195-209, 1998.

Mehl, L., and G. Hirth, Plagioclase preferred orientation in layered mylonites: Evaluation of ow laws for the lower crust, J. Geophys. Res., 113, B05202, doi:10.1029/2007JB005075, 2007.

Montéesi, L., and G. Hirth, Grain size evolution and the rheology of ductile shear zones: From laboratory experiments to postseismic creep, Earth Planet. Sci. Lett., 211, 97-110, doi:10.1016/S0012-821X(03)00196-1, 2003.

Rutter, E., Experimental study of the in uence of stress, temperature, and strain on the dynamic recrystallization of Carrara marble, J. Geophys. Res., 100, 24,651-24,663, doi:10.1029/95JB02500, 1995.

Sibson, R., Fault rocks and fault mechanisms, Journal of the Geological Society, 133, 191-213, 1978.

Takeuchi, C., and Y. Fialko, Dynamic models of interseismic deformation and stress transfer from plate motion to continental transform faults, J. Geophys. Res., 117, B05403, doi:10.1029/2011JB009056, 2012.

Tullis, J., and R. Yund, Dynamic recrystallization of feldspar: A mechanism for ductile shear zone formation, Geology, 91, 238-241, 1985.

Van Der Wal, D., P. Chopra, M. Drury, and J. Fitz Gerald, Relationships between dynamically recrystallized grain size and deformation conditions in experimentally deformed olivine rocks, Geophys. Res. Lett, 20, 1,479-1,482, doi:10.1029/93GL01382, 1993.

Present-day intra-plate deformation of the Eurasian plate

Candela Garcia-Sancho[1], Rob Gover[1], Karin N. Warners-Ruckstuhl[2], Magdala Tesauro[1]

[1] *Utrecht University, Faculty of Geosciences, Earth Science Dept, Utrecht, The Netherlands*
[2] *Shell Global Solutions, Kesslerpark 1, 2288 GS, Rijswijk, The Netherlands*
e-mail: *C.GarciaSancho@uu.nl*
session: *Rheology*

We build on the results of two recent, yet independent, studies. In the first (Warners-Ruckstuhl et al., 2013) the forces on, and stresses within the Eurasian plate were established. In the second (Tesauro et al., 2012) the distribution of mechanically strong and weak parts of the Eurasian plate was found. The aim of our work is to predict lithospheric deformation of the Eurasian plate and to compare it with observations. This constitutes a test of both the force/stress results and of the strength results. Specific questions are to which extent stresses localize in specific regions and whether micro-plates as identified by geodesists arise naturally from the results.

Importantly, Warners-Ruckstuhl et al. (2013) found an ensemble of mechanically consistent force models based on plate interaction forces, lithospheric body forces and convective tractions. Each of these force sets is in mechanical equilibrium. A subset drives Eurasia in the observed direction of absolute motion and generates a stress field in a homogeneous elastic plate that fits observed horizontal stress directions to first order (Fig 1.). Deformation models constitute a further test and a possibility to discriminate between the remaining force sets.

Following Tesauro et al. (2012) we assume five different compositions for the upper and lower crust according to the age of the geological provinces (Fig 2.). We use their geotherms and crustal thickness maps to estimate vertical distributions of strength at any location within the Eurasian plate. We compute de vertical distribution of strength for each element of the domain, and integrate it up to the value of the previously calculated stress field to obtain the lithospheric strength of each element of the model.

From the power-law relationship between strength and viscosity, and based on the assumption that horizontal strain rates do not vary with depth, we estimate the vertically averaged viscosity of each element of the domain.

We compute deformation in our model by solving the mechanical equilibrium equation using finite element code GTECTON. It is computed in a spherical shell using plane stress approximation. We plan to include major active faults in our mechanical model.

We compare our results with GPS velocities, InSAR, seismic, and paleomagnetic observations, which capture present-day and long-term deformation. We discuss various causes for differences.

References

Warners-Ruckstuhl et al., Tethyan collision forces and the stress field of the Eurasian plate, Geophys.J.Int., 219, 2013.

Tesauro et al., Global strength and elastick thickness of the lithosphere, Global Plan. Chang., 90-91, 51-57, 2012.

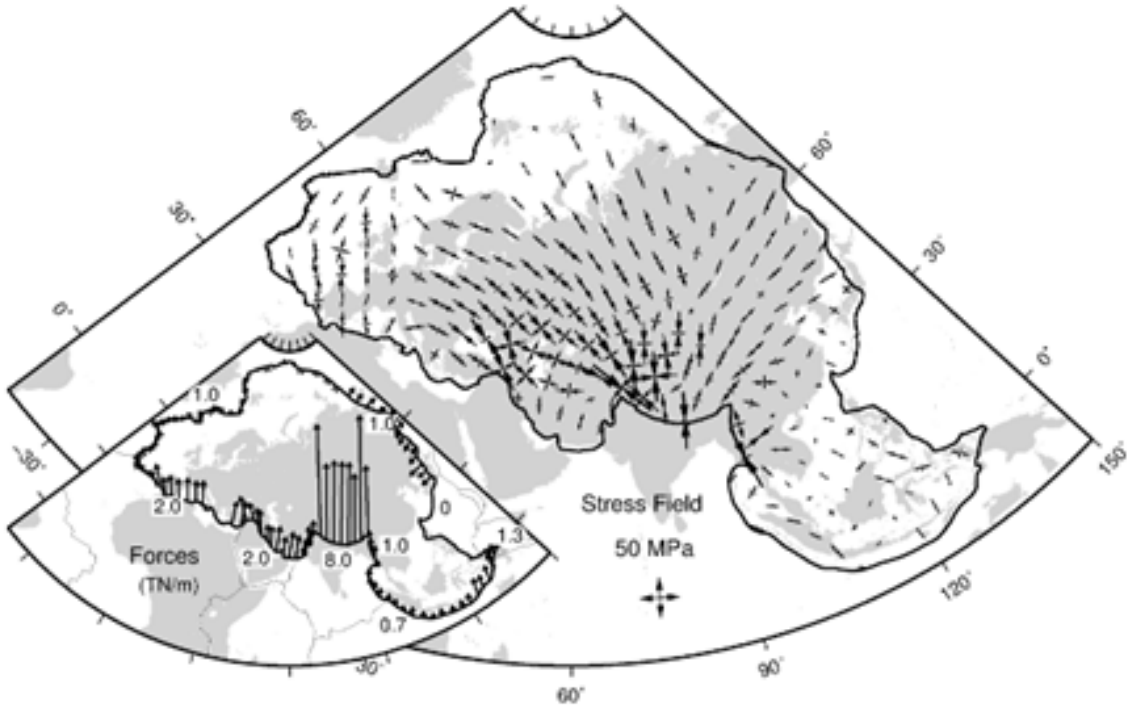

Fig. 1.: Principal axes of the stress field (MPa). Corresponding average edge forces are displayed in the inset (TN/m).

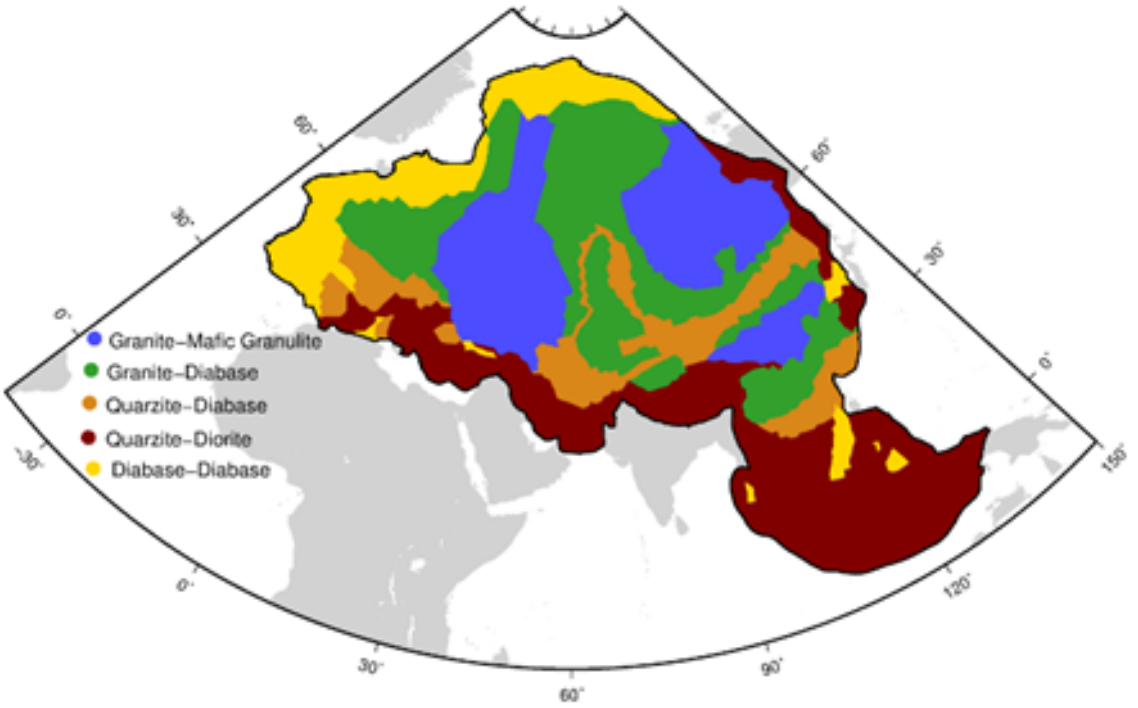

Fig. 2.: Eurasia composicioal types of the upper and lower crust over dry olivine lithospheric mantle

Localization of deformation in a polymineralic material

Suzon Jammes[1], Luc L. Lavier[1], Jacqueline E. Reber[1]

[1]*Institute for Geophysics, University of Texas at Austin, USA*
e-mail: *suzon.jammes@austin.utexas.edu*
session: *Rheology*

Even though ninety-five volume percent of all rocks are polymineralic, metric and crustal scale numerical experiments mainly used monomineralic material composed of wet or dry, plagioclase, quartz or olivine to approximate rock behavior. This approach presumes that the rheology of the crust or mantle is mainly controlled by the weakest or the most abundant mineral phase. An assumption that can be debated in regards to experimental and theoretical studies realized on bimineralic and polymineralic rocks, which show that their bulk strength depends also on the proportion, shape, distribution, and strength ratio of the minerals [Handy, 1990; Jordan, 1988]. Moreover, since the transition from brittle to ductile deformation depends on the individual brittle ductile transition of each mineral phase it is expected that under certain conditions some deform brittle while others show ductile deformation. Natural observations show that minerals that are harder than their surrounding matrix tend to remain as only slightly deformed porphyroclasts or that they can exhibit localized fractures while the rest of the material presents evidence of ductile deformation [Mitra, 1978; Wakefield, 1977; White et al., 1980], inferring that a mixed brittle-ductile or semi-brittle rheology is at play.

Evidence for such a behavior can be observed in a wide range of examples at different length scales (from microscopic to crustal scale) and in different types of materials such as quartzofeldspatic rocks [Tullis et al., 2000] or olivine rich mantle rocks in the presence of serpentine or plagioclase [Kaczmarek and Müntener, 2008]. All these observations suggest that a polymineralic composition has a strong influence on deformation processes and localization of the deformation from the microscopic to the lithospheric scale.

Here, we consequently investigate the relation between polymineralic composition and localization of the deformation. To simplify our experiments and to reduce the number of parameters, we perform metric scale numerical models with a bimineralic composition using shearing boundary conditions leading to a fracture-like localization at different temperatures and strain rates (Figure 1). With this approach we seek to answer: how does localization occur in bi-mineralic materials? What impact has the percentage of weak versus strong phase on the localization of the deformation? And how does the temperature and strain rate, controlling the strength difference between the two minerals, affect the localization and deformation processes?

This study shows that the deformation localization is highly dependent on the fraction of the weak phase as well as the strength ratio between the phases. We identify four domains where the deformation can be characterized as brittle, semi-brittle, semi-ductile, or ductile depending on the mechanical behavior and strength ratio between the two phases. Similar to Handy [1990]'s classification, we define three deformation types to characterize the degree of localization within the shear zone. Type I deformation is controlled by the strong phase. In presence of a weak phase, the strong phase forms an interconnected load bearing framework surrounding the weak phase and deformation is accommodated along a straight and thin shear zone. Type II is characterized by the formation of anastomosing structures controlled by the distribution of the weak phase while

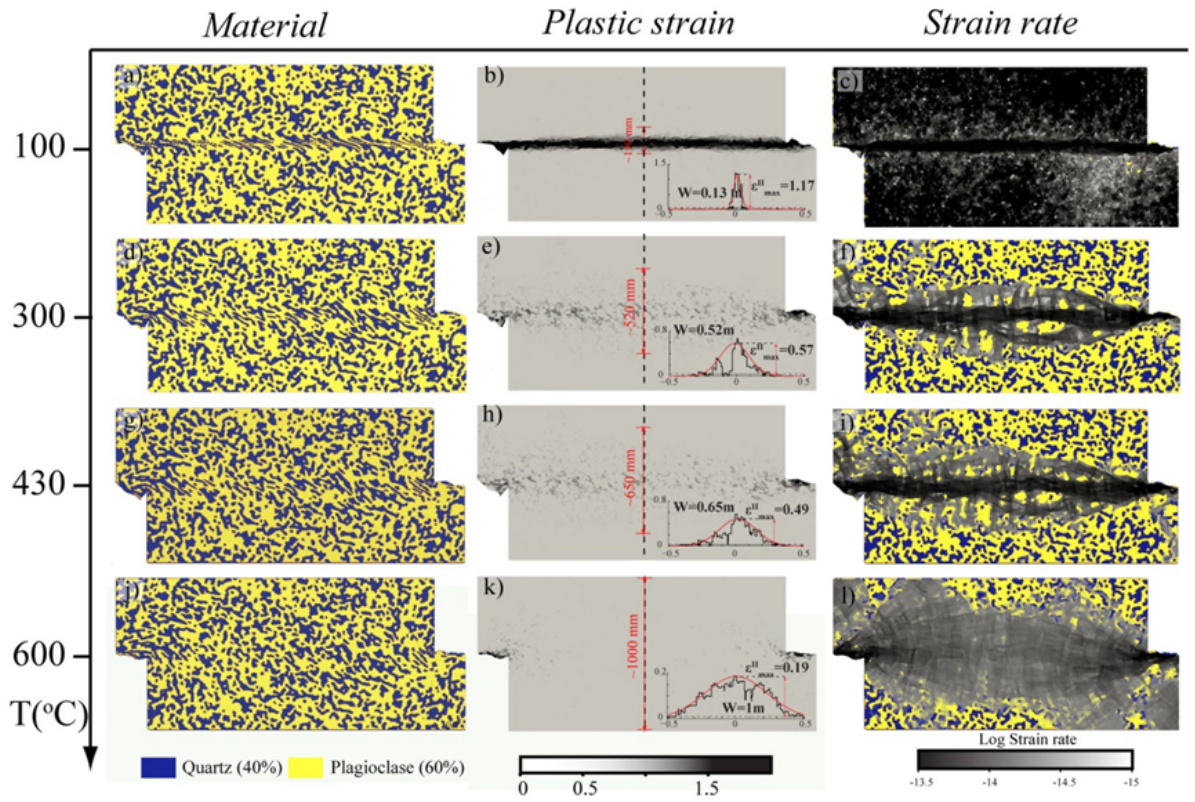

Fig. 1.: Example of a numerical experiment realized for a concentration of quartz equal to 40% with a temperature set at: a-c) 100 °C, d-f) 300 °C, g-i) 430 °C and j-l) 600 °C. Left: material distribution. Middle: Distribution of the accumulated plastic strain. The inset in the right bottom corner of each model shows the distribution of the second invariant of the strain or effective strain (ϵ^{II}) with a corresponding Gaussian approximation along a cross-section through the central part of the model, an estimation of the maximum value of ϵ^{II}_{max} and the width of the shear zone (W). Right: Representation of the logarithmic value of the strain rate when strain is equal to 0.2 superimposed on the material distribution.

the strong phase forms elongated augen; the significant strain in both phases indicates that they are both rheologically active. In type III the strong phase forms relatively undeformed clasts in a weak matrix and is consequently inferred to be rheologically passive and a delocalized shear zone can be observed.

Our results are summarized in the Figure 2 where we correlate the depth dependent strength profile of wet quartz and plagioclase (the reference strain rate is equal to 10-14 s-1) (Figure 2a) to a phase diagram showing the different deformation types observed in the numerical experiments depending on the quartz concentration (Figure 2b). This correlation between the deformation types and the different domains allows us to determine the impact of the phase ratio and the strength ratio on the shear localization. The results can be resumed as follow. At low temperature (brittle domain) both mineral behave in a brittle manner and a narrow shear zone forms (Type I). In the semi-brittle domain, one mineral phase deforms in a brittle manner and the other deforms ductily and all three types of deformation can be observed depending of the amount of the weak phase. If the weak phase ratio is low enough the deformation is mainly brittle (Type I) whereas anastomoses occurs (Type II) when the amount of weak phase increases. For a high weak phase ratio the shear zone is fully ductile, the shear zone is very wide and no deformation of the strong mineral phase is occurring (Type III). In

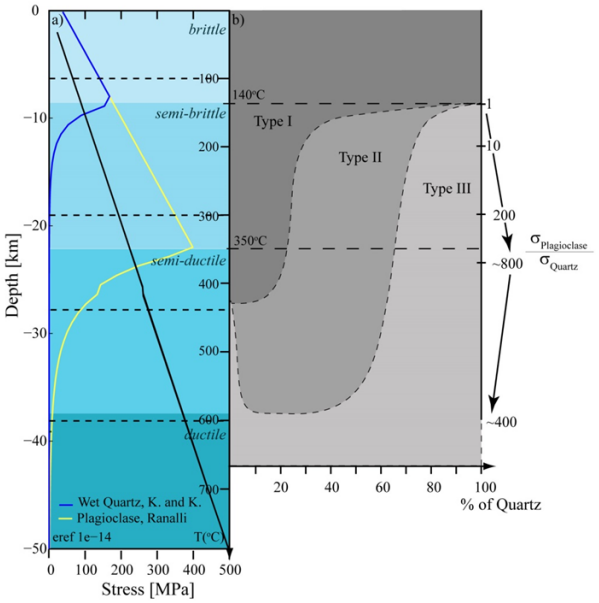

Fig. 2.: a) Depth dependent strength profile of wet quartz and plagioclase calculated for a reference strain rate equal to 1e-14. b) Phase diagram showing the different types of deformation observed in the numerical experiments depending on the quartz concentration, the temperature and corresponding strength ratio between the two phases.

the semi-ductile domain, both mineral phases are expected to behave in a ductile manner. However, contrary to what is expected from the dislocation creep law, plagioclase still exhibits brittle behavior in presence of quartz and therefore displays the characteristics of type II deformation. For a high amount of quartz both phases are behaving in a ductile manner leading to the formation of a wide shear zone (Type III). Fully ductile deformation independent of the weak phase ratio (Type III) only occurs for high temperatures.

Finally, this study demonstrates that in the semi-ductile domain deformation in monomineralic rocks (0% of quartz) is strongly delocalized (Type III) whereas in polymineralic rocks, with the addition a small amount of weak phase, the deformation will localize with an intensity depending on the amount of the weak phase (Type II). It appears therefore that the insertion of a small amount of weak phase can revert the mechanical behavior of the strong phase and lead to the formation of a narrow semi-brittle shear zone (Type II) where a fully ductile (Type III) behavior is expected. This highlights the importance of a bi-mineralic material on the deformation localization and furthermore on large scale deformation processes.

References

Handy, M. R. (1990), The solid-state flow of polymineralic rocks, Journal of Geophysical Research: Solid Earth (1978–2012), 95(B6), 8647-8661.

Jordan, P. (1988), The rheology of polymineralic rocks - an approach, Geologische Rundschau, 77(1), 285-294.

Kaczmarek, M.-A., and O. Müntener (2008), Juxtaposition of melt impregnation and high-temperature shear zones in the upper mantle; field and petrological constraints from the Lanzo Peridotite (Northern Italy), Journal of Petrology, 49(12), 2187-2220.

Mitra, G. (1978), Ductile deformation zones and mylonites; the mechanical processes involved in the deformation of crystalline basement rocks, American Journal of Science, 278(8), 1057-1084, doi:10.2475/ajs.278.8.1057.

Tullis, J. A., H. Stünitz, C. Teyssier, and R. Heilbronner (2000), Deformation Microstructures in Quartzo-feldspathic Rocks, in Stress, Strain and Structure, A volume in honour of W D Means, edited by M. W. Jessell and J.L.Urai., Journal of the Virtual Explorer.

Wakefield, J. (1977), Mylonitization in the Lethakane shear zone, eastern Botswana, J. geol. Soc. Lond., 133, 262-275.

White, S., S. Burrows, J. Carreras, N. Shaw, and F. Humphreys (1980), On mylonites in ductile shear zones, Journal of Structural Geology, 2(1), 175-187.

Localization processes on Earth, Mars, and Venus

Laurent G.J. Montési[1], Frédéric Gueydan[2]

[1] *University of Maryland, Department of Geology, USA*
[2] *Université Montpellier 2, Géosciences Montpellier, France*
e-mail: *montesi@umd.edu*
session: *Rheology*

Introduction

Few problems in Earth Science are as fundamental as the origin of plate tectonics. Our planet has adopted a global tectonic regime that appears unique in the solar system [1]. A fundamental characteristic of plate tectonics is that deformation is localized in narrow deformation zones. As strike-slip faults in particular do not contribute to removing heat from the interior of the planet, localized shear zones must instead act as zones of weakness [2]. Although weakness is often construed as a reduction in stress required to deform a rock at given strain rate, a more geological relevant definition of weakness is that the strain rate is higher than outside the shear zone, whereas stress is probably the same in the shear zone and in the host rock (at least in simple shear).

Localization seen as the consequence of weakening leads to an energy conundrum that can only be resolved is rock rheology depends on deformation history through a state variable. As ductile rheologies are fundamentally strain rate hardening, the high strain rate inside a narrow shear zone leads to higher energy dissipation rate than in a broad shear zone. Therefore, localization must involve a weakening process to make deformation in a localized more favored over distributed deformation [3].

I summarize here localization processes proposed to be active on Earth, their effect, and whether or not they may be active in other terrestrial bodies.

Efficiency of localization processes

Rocks deform following brittle processes at relatively shallow pressure and temperature and plastic mechanisms are greater depth. Geological observations on Earth show that deformation can localize under both conditions [4], even though plastic rheologies, being strain-rate hardening, are fundamentally stable in the laboratory [3, 5]. Localization can be understood in either case if a state variable enables rock strength to weaken as strain accumulates.

Brittle processes involve the formation of, and sliding along, cracks between and inside grains that form a rock. It is therefore not surprising that brittle failure should result in a localized shear zone. Additional processes that weaken brittle shear zones include nucleation of weak minerals like serpentine, graphite, and mica [6] and the development of a foliated cataclastic zone [7]. All these phenomena contribute to decrease the coefficient of friction from 0.6 to 0.1. A key to achieve such weakness is that fault gouge adopts a fabric that allows the weak phase to form a through-going layer [8].

Localization in the ductile regime is harder to understand, because of the fundamental strain-rate hardening behavior of plastic deformation process. Montési [5] describes how modifying a well-chosen state variable inside a narrow domain (the shear zone) can reduce the energy required for deformation, compensating for the high deformation rate in the shear zone. His method allows the localization of a localization potential that describe how narrow a shear zone can be

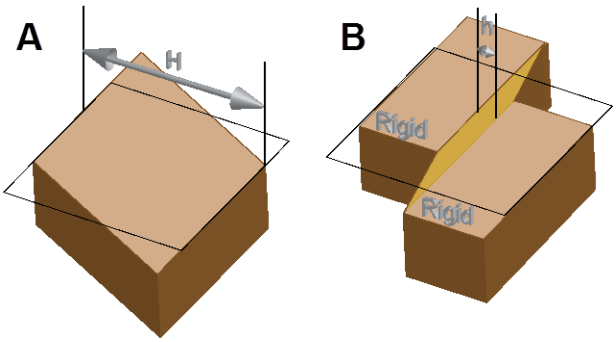

Fig. 1.: Schematics diagrams illustrating (A) the reference non-localized deformation state and (B) the localized states, where the different shade of the shear zone indicates a different temperature or microstructure. The localization potential $L = h/H$ is computed by comparing energy dissipation between configurations A and B (Montési, 2013).

produced by a change in state variable before it is no longer energetically favorable (Figure 1).

Only a few state variables are efficient enough to lead to localized deformation, at least if the change is limited to what is observed in geological example [5]. Other characteristics of shear zones should be regarded as consequences of the large strain in the shear zone but do not have a significant rheological effect.

The most efficient localization process active in the continental crust appears to be the development of a layered fabric. Ductile shear zones are formed of anastomosing high-strain bands at many scales [4, 9]. The high-strain zones are often rich in phyllosilicates, sometimes to the point of being classified as phyllonite. Development of a layered fabric enables the weakest phase to control the rheology of the deforming rock. If that phase is weak or highly nonlinear, like micas, pronounced weakening is associated with the appearance of a layered fabric [5]. This localization process is clearly limited to temperatures are which micas are stable ($\sim 450\,^{\circ}\mathrm{C}$).

In the mantle ductile shear zone rocks are often synonym with mylonites, i.e., they are characterized by a reduced grain size [10-13]. Reducing grain size is possible only when dislocations are active inside the rocks [e.g. 14]. However, it leads to weakening only if grain boundary sliding and diffusion are dominant. Therefore, grain size reduction is a viable localization process only in the dislocation-accommodated Grain Boundary sliding regime (dis-GBS, [15]). The mantle can localize in this regime at temperatures less than less than $800\,^{\circ}\mathrm{C}$ [16].

Application to terrestrial planets

The localization potential analysis described above reveals that localization is possible not only in the brittle levels of the lithosphere but also in the ductile regime at relatively low temperatures where either micas are present or dis-GBS is active (mantle at temperature less than $800\,^{\circ}\mathrm{C}$).

Applying this insight to the continental lithosphere, we see that localization can take place in the middle crust and uppermost mantle, but not in the lower crust that separates them. Gueydan et al. [16] developed from these constraints the concept of strain-dependent lithospheric strength. At low strain, the upper mantle and upper crust are the strongest regions of the lithosphere. However, fabric evolution reduces strength in the upper crust (brittle fabric), middle crust (fabric in presence of mica) and upper mantle (grain size reduction). The reduced strength of the lithosphere as a whole leads to increased strain rate if the loading stress, controlled by large-scale tectonics, does not change. The lower crust, which does not weaken, becomes the load-bearing layer at high strain. This model is able to reconcile different views of the lithospheric strength profile by associating the classic "jelly sandwich" model to low strain areas and the "crème brûlée" model to high strain areas [17].

It should be noted that the localizing uppermost mantle is expected to be absent in regions of thickened crust, like the Tibetan plateau, and regions with high heat flux, like the Basin and Range province of the Western United States. Accordingly, deformation remains diffuse in these regions.

The oceanic lithosphere is simple to understand as it does not require considering the complica-

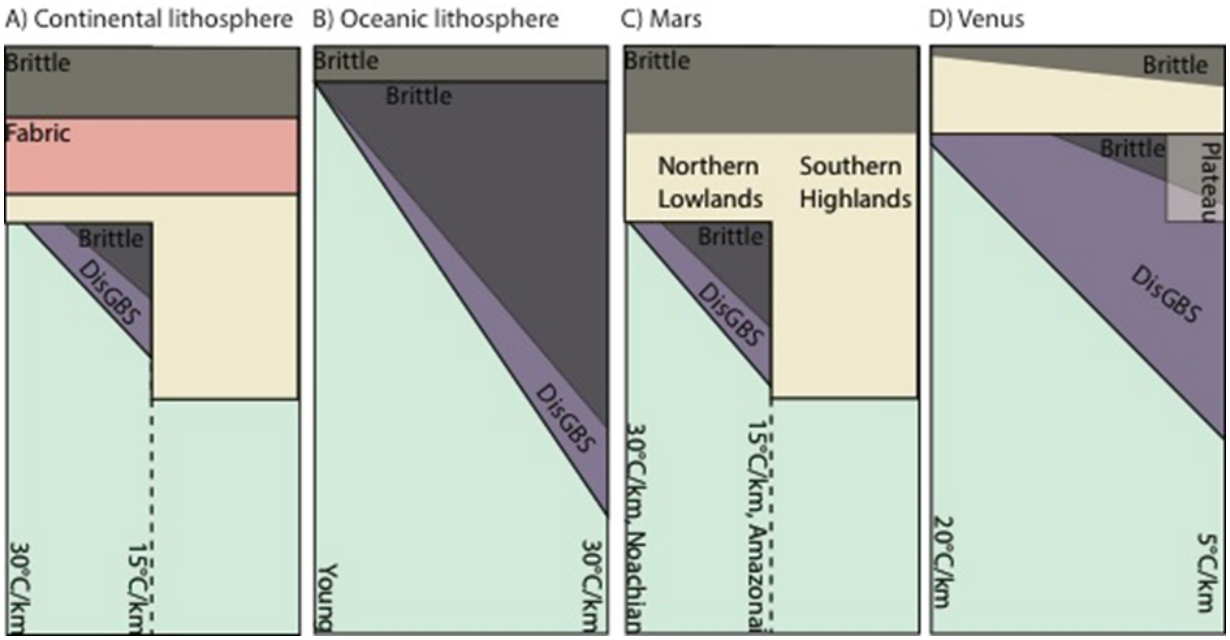

Fig. 2.: Representation of localization processes in planetary lithospheres. Green: mantle, no localization. Purple: mantle, localization by grain size reduction in presence of dis-GBS. Brown: crust, no localization. Pink: crust, localization by fabric development in presence of micas. The vertical axis represents depth with an approximate scale of 1.5mm/km. The horizontal axis corresponds to different tectonic environments or geotherm (as indicated).

tions of layer development in the crust. Localization is possible in a brittle lithospheric mantle with a thickness that increases with age. Dis-GBS lines the base of this brittle mantle but does not affect much the general organization of the lithosphere. It should be noted that it is in the oceans that the most localized shear zones are observed [2].

The rheological profile of Mars resembles that of the continental crust with brittle upper crust and upper mantle separated by a non-localizing lower crust. Here again, the localizing uppermost mantle is absent if the crust is too thick (Southern Highlands) or too hot. Ductile shear zone development is not expected in the crust because its basaltic composition [18] is not conducive to the presence of micas similar to those observed in terrestrial shear zones [19]. Therefore, the lower crust constitutes a more efficient impediment to failure of the lithosphere as a whole than it does on Earth. More importantly, the uppermost mantle can only be localizing only if the geotherm is less than 25 °C/km, which corresponds to the middle Hesperian period. By then, the convective vigor may have decreased below what is necessary for plate tectonics to form. The absence of plate tectonics in the Martian geological records may be ascribed to the disconnection between driving forces and localization potential over time.

Venus appears unlike the Earth in that localization can only occur in a thin brittle layer at the surface or in a thick region of the mantle where dis-GBS is active. If this mantle is able to generate localized shear zones, these may be sufficiently far from the surface that they do not have a evident effect on surface geology. Alternatively, it may be that brittle failure in contact with dis-GBS mantle is necessary to trigger localization and that otherwise the localization in the uppermost mantle is stabilized by interaction with adjoining non-localizing regions.

References

[1] O'Neill, C., Jellinek, A.M., Lenardic, A., (2007). Conditions for the onset of plate tectonics on terrestrial planets and moons, Earth and Planet. Sci. Lett. 261, 20– 32.

[2] Bercovici, D., Ricard, Y., Richards, M.A. (2000). The relation between mantle dynamics and plate tectonics: A primer. In: Richards, M., Gordon, R., van der Hilst, R. (Eds), The History and Dynamics of Global Plate Motions, Geophys. Monograph 121, 1–46.

[3] Montési, L.G.J., and Zuber, M.T. (2002), A unified description of localization for application to large-scale tectonics, J. Geophys. Res., 102, doi:10.1029/2001JB000465.

[4] Vauchez, A., A. Tommasi, and D. Mainprice (2012). Faults (shear zones) in the Earth's mantle, Tectonophysics 558-559, 1-27, doi: 10.1016/j.tecto.2012.06.006.

[5] Montési, L.G.J. (2013) Fabric development as the key for forming ductile shear zones and enabling plate tectonics, J. Struct. Geol. 50, 254–266.

[6] Lockner, D.A., et al. (2011). Low strength of deep San Andreas fault gouge from SAFOD core, Nature 472, 82-85.

[7] Collettini, C., A. et al., (2009), Fault zone fabric and fault weakness, Nature 462, 907-911.

[8] Rutter, E.H. et al. (2013). Reduction of friction on geological faults by weak-phase smearing, J. Struct. Geol. 51, 52-60, doi: 10.1016/j.jsg.2013.03.008.

[9] Gerbi, C., N. Culshaw, and J. Marsh (2010), Magnitude of weakening during crustal-scale shear zone development, J. Struct. Geol. 32, 107– 117.

[10] Drury, M.R. et al. (1991), Strain localization in upper mantle peridotites, Pure Appl. Geophys. 137, 439– 460, doi:10.1007/BF00879044 .

[11] Jin, D., S.-I. Karato, , and M. Obata (1998). Mechanisms of shear localization in the continental lithosphere: Inference from the deformation microstructures from the Ivrea zone, Northwest Italy, J. Struct. Geol. 20, 195– 209.

[12] Precigout, J., and F. Gueydan (2009), Mantle weakening and strain localization: Implications for the long-term strength of the continental lithosphere, Geology, 37, 147-150. doi:10.1130/G25239A.1.

[13] Platt J. P., and W. M. Behr (2011). Grainsize evolution in ductile shear zones: Implications for strain localization and the strength of the lithosphere.= J. Struct. Geol. 33, 537– 550, doi:10.1016/j.jsg.2011.01.018.

[14] de Bresser J.H.P., J.H. ter Heege, and C.J. Spiers (2001). Grain size reduction by dynamic recrystallization: Can it result in major rheological weakening? Int. J. Earth Sci. 90, 28–45.

[15] Hirth, G., and D.L. Kohlstedt (2003). Rheology of the upper mantle and the mantle wedge: a view from the experimentalists. In: Eiler J. (Ed.), The Subduction Factory, Geophys. Monograph 138, 83– 105.

[16] Gueydan, F., J. Précigout, and L. Montési (2014). Strain weakening enables continental plate tectonics, Tectonophysics, in press, doi:10.1016/j.tecto/2014.02/005.

[17] Jackson, J. (2002). Strength of the continental lithosphere: time to abandon the jelly sandwich? GSA Today September, 1-9.

[18] Wray et al. (2013) Prolonged magmatic activity on Mars inferred from the detection of felsic rocks, Nature Geosci. 6, 1013-1017, doi: 10.1038/ngeo1994.

[19] Gueydan, F. et al. (2003). Analysis of continental midcrustal strain localization induced by microfracturing and reaction-softening, J. Geophys. Res. 108, 2064 doi:10.1029/2001JB000611.

Rheology of bubble- and crystal-bearing magma: new analogue experimental data and an effective-medium model

S. P. Mueller[1], J.M. Truby[2], E.W. Llewellin[2], H.M. Mader[3]

[1]*Institute of Geosciences, Johannes Gutenberg University Mainz, 55099 Mainz, Germany*
[2]*Department of Earth Sciences, Durham University, Durham DH1 3LE, UK*
[3]*School of Earth Sciences, University of Bristol, Bristol, BS8 2JJ, UK*
e-mail: *sebastian.mueller@uni-mainz.de*
session: *Rheology*

Introduction

Magma is a multiphase suspension: a complex mixture of a viscous silicate melt, a solid phase (crystals), and a gas phase (bubbles). The degree of interaction between bubbles and crystals, and the relative proportions of these phases, exert a major control on the bulk flow behaviour of the magma or lava. Characterizing, modelling, and predicting the flow of such a suspension requires a constitutive rheological model, encapsulating the viscosity of the suspension as a function of the properties of the suspending liquid and the volume fraction and properties of the suspended phase(s).

In contrast to two-phase mixtures (solid-liquid, gas-liquid), very little research has been directed at understanding the rheology of three-phase suspensions – primarily owing to the complexity of the problem – and no experimentally-validated constitutive rheological model has been published to-date. Constraining three-phase rheology therefore remains an important, yet outstanding, problem in geosciences, as well as in multiphase fluids research.

Here, we build on published two-phase constitutive equations to generate a three-phase model, by using an 'effective-medium' method in which the bubble suspension is treated as a continuous medium which suspends the particles. We validate the model against a set of new experimental data for three-phase suspensions of bubbles and spherical particles in the low capillarity regime (in which flow is steady and bubble deformation is small).

On the rheology of two-phase suspensions

Bubble suspensions

When a bubble suspension flows, viscous stresses cause the bubbles to deform. In a steady flow the bubbles reach an equilibrium deformation, which is described by the capillary number

$$Ca = \lambda\dot{\gamma} \tag{1}$$

where λ is the bubble relaxation time and $\dot{\gamma}$ the shear strain rate (Taylor 1934; Llewellin et al. 2002, Rust & Manga 2002). The relaxation time describes the characteristic timescale over which the bubble adjusts towards a new equilibrium deformation in response to a change in the strain environment, and depends on the liquid-gas interfacial tension Γ and the bubble radius a : $\lambda = \mu a/\Gamma$. For steady flow, the relative viscosity η_{r_b} of a bubble suspension is given by (Mader et al. 2013)

$$\eta_{r_b} \equiv \frac{\eta_b}{\mu} = \eta_{r,\infty} + \frac{\eta_{r,0} - \eta_{r,\infty}}{1 + (\frac{6}{5}Ca)^2} \tag{2}$$

where η_b is the viscosity of the bubble suspension, and $\eta_{r,0}$ and $\eta_{r,\infty}$ are, respectively, the relative viscosity of the bubble suspension at low and high Ca. For non-dilute suspensions, $\eta_{r,0}$ and $\eta_{r,\infty}$ are given by (Llewellin & Manga 2005; Mader et al. 2013)

$$\eta_{r,0} = (1 - \phi_b)^{-1} \tag{3}$$

and

$$\eta_{r,\infty} = (1 - \phi_b)^{5/2} \tag{4}$$

where ϕ_b is the bubble volume fraction.

Particle suspensions

Suspensions of solid particles are non-Newtonian (mostly shear-thinning) when non-dilute and their rheology is often described using a power law of the form

$$\eta_p = K\dot{\gamma}^{n-1} \tag{5}$$

where η_p is the apparent viscosity of the suspension, K is the consistency and n is the flow index which defines the degree of shear thinning. Mueller et al. (2011) demonstrate that the dependence of the relative consistency K_r on particle volume fraction ϕ_p is well described by the Maron-Pierce relationship (Maron & Pierce 1956)

$$K_r \equiv \frac{K}{\mu} = (1 - \frac{\phi_p}{\phi_m})^{-2} \tag{6}$$

where ϕ_m is the maximum packing fraction. The relative consistency is defined by analogy with the relative viscosity of the particle suspension $K_r \approx \eta_{r_p} \equiv \eta_p./\mu$. (Note that, strictly, the relative consistency is dimensionless only if $n = 1$, and is numerically equal to η_{r_p} only if $n = 1$ or $\dot{\gamma} = 1$. However, Mader et al. (2013) demonstrate that, in practice, K_r and η_{r_p} can be treated as equivalent for $10^{-3} \lesssim \dot{\gamma} \lesssim 10\ s^{-1}$ and $\phi_p/\phi_m \lesssim 0.5$).

The maximum packing fraction ϕ_m is a function of particle shape (i.e., particle aspect ratio, r_p) and roughness; Mader et al. (2013) give the following equation for rough particles (representative for crystals in magma):

$$\phi_m = 0.5\Big[- \frac{(log_{10} r_p)^2}{2}\Big] \tag{7}$$

A model for the rheology of three-phase suspensions

Equation (6) gives the consistency of a suspension of particles in a liquid with viscosity μ. If we suppose that the particles are instead suspended in a bubble suspension with viscosity η_b (i.e. we treat the bubble suspension as an 'effective medium') we obtain

$$\frac{K}{\eta_b} = \Big(1 - \frac{\phi_p}{\phi_m}\Big)^{-2} \tag{8}$$

At low Ca, from equations (2) and (3), we have $\eta_b = \mu(1 - \phi_b)^{-1}$, hence

$$K_r = (1 - \phi_b)^{-1}\Big(1 - \frac{\phi_p}{\phi_m}\Big)^{-2} \tag{9}$$

If, as in our model, the bubble suspension is treated as effective medium and continuous phase, particle and bubble volume fractions are commonly defined as

$$\phi_b = \frac{V_b}{V_l + V_b} \tag{10}$$

$$\phi_p = \frac{V_p}{V_l + V_b + V_p} \tag{11}$$

where V_l, V_b and V_p are the volumes of the liquid, bubble and particle phases, respectively.

For many three-phase applications, however, it makes more sense to consider the effect of *adding* bubbles to a particle suspension, rather than replacing liquid with gas. For example, a magma that contains solid crystals may be bubble-free at depth, but become increasingly bubble-rich during ascent. In this case, it is more intuitive to define a particle volume fraction and bubble volume fraction as follows:

$$\phi_b^* = \frac{V_b}{V_l + V_b + V_p} \tag{12}$$

$$\phi_p^* = \frac{V_p}{V_l + V_p} \tag{13}$$

In this formulation, the particle volume fraction does not change from its initial value as bubbles grow, and the bubble volume fraction reflects the value that would be measured using Archimedes' principle.

Analogue experiments

We performed a series of 42 rheology tests on three-phase analogue samples. The samples were prepared by adding spherical glass beads (Potters Ballotini; density 2448 kg/m^3, size fraction 63 to 125 μm) to a sugar syrup (Tate & Lyle Golden Syrup; density 1438 kg/m^3) and aerating with a domestic electric whisk. The rheology of the pure syrup was determined individually for each sample batch and found to be strictly Newtonian. Particle volume fraction was controlled by adding a known mass of beads to a known mass of syrup (typically equating to 100-150 ml) to prepare sample suites of similar initial (bubble-free) particle volume fraction ϕ_p = 0:05, 0.1, 0.2, 0.3, 0.4, and 0.5. Gas volume fraction was varied by adjusting the duration and speed of whisking, and suspension temperature. The bubble size distribution of each sample was determined using a sample image and the image analysis software JMicroVision.

Rheometric data were collected using a ThermoScientific Haake MARS II rheometer in concentric cylinder arrangement, at 20 °C. At steady flow experiments, a ramp of 20 incrementally increasing shear stresses (up to 500 Pa), and the corresponding strain rate values, is recorded - followed by a 20-step down-ramp. The consistency of each samples is determined by fitting the Herschel-Bulkley model to the corresponding τ vs $\dot{\gamma}$ flow curve (Figure 1, blue line):

$$\tau = \tau_0 + K\dot{\gamma}^n \qquad (14)$$

For some samples, the highest experimental strain rates are sufficient that the bubbles cannot be assumed to be in the low capillarity regime. We filter data to remove these datapoints by calculating a typical capillary number for each point. For this calculation, we assume the effective strain-rate in the bubbly effective medium to be approximately given by $\dot{\gamma}' = \dot{\gamma}/(1-\phi_p)$ (neglecting solid-body rotation of the particles). To determine a typical bubble radius for a sample, we calculate the volume-mean-radius $< a >= \Sigma a^4/\Sigma a^3$ where summation

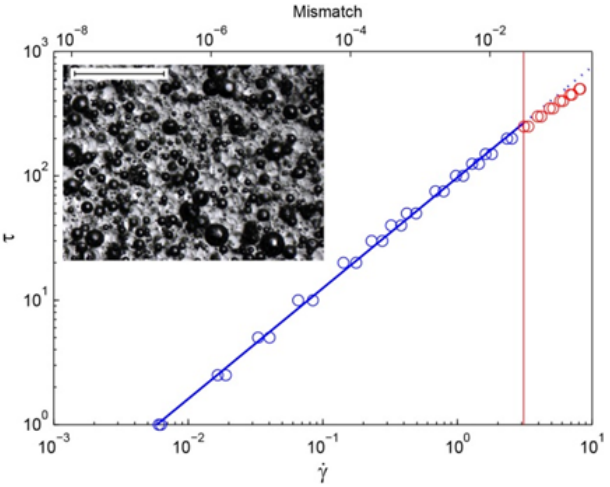

Fig. 1.: Exemplary flow curve of shear stress τ against strain rate $\dot{\gamma}$. Datapoints are collected during both the up-ramp and down-ramp, and fitted with the Herschel-Bulkley model (equation 14, blue line). Datapoints for which the deviation of the viscosity of the bubbly effective medium from the low capillarity assumption is greater than 5% are discarded (red line). Inset shows photomicrograph of a sample ($\phi_p = 0.42$; $\phi_b = 0.29$), in which dark-rimmed spheres are bubbles, and glass beads are light and translucent.

is over all measured bubbles in that sample (following Mader et al. 2013). Using $\dot{\gamma}$ and $< a >$ in equation (1) we obtain an effective capillary number Ca‘ for each datapoint, and a corresponding value of η_{r_b}. If the discrepancy between η_{r_b}b (which accounts for variable capillarity; eq. 2) and $\eta_{r,0}$ (which assumes $Ca \ll 1$; eq. 3) is greater than 5%, the datapoint is discarded (Figure 1, red line). After filtering, all flow curves comprise at least 14 datapoints.

Results

The resulting K_r values of 42 rheometric experiments on samples with 0 to 45 vol% particles and 0 to 28 vol% bubbles are displayed in Figure 2. From both Figure 2a and 2b, it becomes evident that the effect of adding bubbles a particle suspension depends upon the initial particle concentration ϕ_p^*. For dilute particle suspensions ($\phi_p^* \lesssim 0.25$), adding bubbles increases the bulk consistency, whereas for concentrated suspensions

with $\phi_p^* \gtrsim 0.25$ adding bubbles decreases bulk consistency.

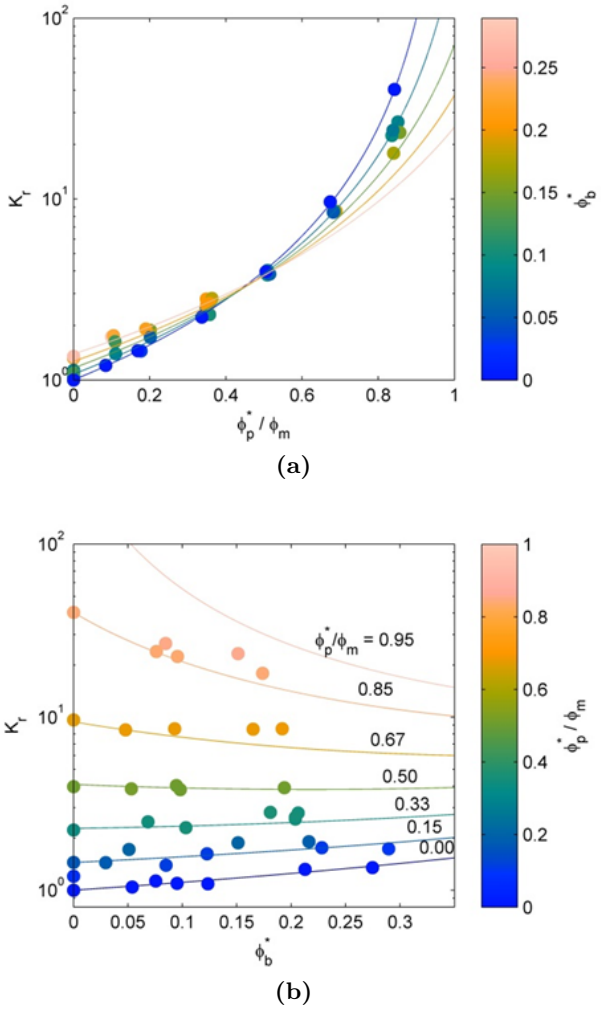

Fig. 2.: (a) Relative consistency K_r plotted against the particle concentration ϕ_p^* (normalized by the maximum packing fraction ϕ_m); circles are coloured according to ϕ_b^*. Solid lines are the three-phase model (equation 9). (b) K_r against gas volume fraction ϕ_b^*, with datapoints coloured according to ϕ_P^*. Again, solid lines are fits of equation 9.

The physical explanation for this behaviour is straightforward, and relies on two competing processes. The intrinsic effect of the addition of low capillarity (i.e. spherical) bubbles to a fluid is to increase its consistency. For dilute particle suspensions, this is the dominant trend, hence our data show an increase in consistency with increasing bubble content for $\phi_p^* \lesssim 0.25$. Opposing this is a 'dilution' process, in which the addition of bubbles to a suspension of particles moves the particles further apart; this decreases the particle volume fraction ϕ_p, reduces the impact that particle-particle interactions have on suspension rheology, and reduces suspension consistency. This process dominates for concentrated particle suspensions because the Maron-Pierce relationship is a power law; hence, the higher the initial particle volume fraction, the greater the impact the same dilution will have.

References

Llewellin, E. W., Mader, H. M. & Wilson, S. D. R. (2002) The rheology of a bubbly liquid. Proceedings of the Royal Society A: Mathematical, Physical and Engineering Sciences 458, 987-1016.

Llewellin, E. W. & Manga, M. (2005) Bubble suspension rheology and implications for conduit flow. Journal of Volcanology and Geothermal Research 143 (1-3), 205-217.

Mader, H. M., Llewellin, E. W. & Mueller, S. (2013) The Rheology of Two-Phase Magmas : A Review and Analysis. Journal of Volcanology and Geothermal Research 257, 1-51.

Maron, S. H. & Pierce, P. E. (1956) Application of Ree-Eyring generalized flow theory to suspensions of spherical particles. Journal of Colloid Science 11, 80-95.

Mueller, S., Llewellin, E. W. & Mader, H. M.(2011) The effect of particle shape on suspension viscosity and implications for magmatic flows. Geophysical Research Letters 38.

Rust, A. C. & Manga, M. (2002) Effects of bubble deformation on the viscosity of dilute suspensions. Journal of Non-Newtonian Fluid Mechanics 104, 53-63.

Taylor, G. I. (1934) The formation of emulsions in definable fields of flow. Proceedings of the Royal Society A: Mathematical, Physical and Engineering Sciences 146, 501-523.

Modeling stress evolution around a rising salt diapir

Maria A. Nikolinakou[1], Peter B. Flemings[1], Michael R. Hudec[1]

[1] *Bureau of Economic Geology, The University of Texas at Austin*
e-mail: *mariakat@mail.utexas.edu*
session: *Rheology*

Overview

We simulate the evolution of a salt diapir during sedimentation and study how deposition and salt movement affect stresses close to the diapir (Figure 1). We model the wall rocks as porous elastoplastic materials. Our analysis shows that stresses rotate near a salt diapir, such that the maximum principal stress is perpendicular to the contact with the salt. The minimum principal stress is in the hoop direction, and drops near the salt, resulting in a reduced range of acceptable drilling mud weights. The mean stress increases near the upper parts of the diapir, leading to a porosity that is lower than predicted for uniaxial burial at the same depth.

Because we simulate sedimentation simultaneously with the movement of the salt, our study offers two major achievements distinct from previous work on salt-diapir and sediment interaction: the salt is not kinematically prescribed and the stresses within the basin develop as a function of both the depositional process and the loading from the salt. Consequently, the porosity-depth profile in our model differs from that of a basin that has been uniaxially deposited; here, the wall rocks are denser near the growing dome.

Finite-element model

We built our numerical model within the finite-element program Elfen®(Peric and Crook, 2004, Rockfield, 2010, Thornton et al., 2011). We study the evolution of a three-dimensional salt diapir using an axisymmetric model (360° rotation of the vertical section shown in Figure 2). There is no slip between the diapir and the basin. The base and side boundaries are rollers (zero-normal-displacement, free-slip boundaries), and the model is wide enough that the side boundary is unaffected by any stress perturbations. The initial stresses in the model are geostatic (K_0=0.8). Pore pressures are assumed hydrostatic and do not change during the analysis (drained simulation). We simulate sedimentation by aggrading the top of the model 400 m every half million years.

We model the salt as a solid viscoplastic material with an equivalent salt viscosity between $10^{18} - 10^{20}$ Pas, using a reduced form of the Munson and Dawson formulation (Munson and Dawson, 1979). Basin sediments are modeled as porous elastoplastic, using the SR3 constitutive model, which is based on the principles of Modified Cam Clay (Muir Wood, 1990, Rockfield, 2010)

Stresses within the wall rocks

Rise of a salt diapir loads the wall rocks, because the salt expands out as it moves up. In the circumferential (hoop) direction, the diapir radius increases, leading to significant extensional hoop strains; as a result, the hoop (or circumferential) stress decreases in comparison to the far-field horizontal/hoop stress (Figure 3b). On the other hand, as the salt diapir is pushing outwards, it radially compresses the sediments (Figure 3a). This increases the horizontal stress (green solid line in Figure 3b) above its far-field value (dotted gray line) and to values even higher than the integration of the overburden (dashed gray line)

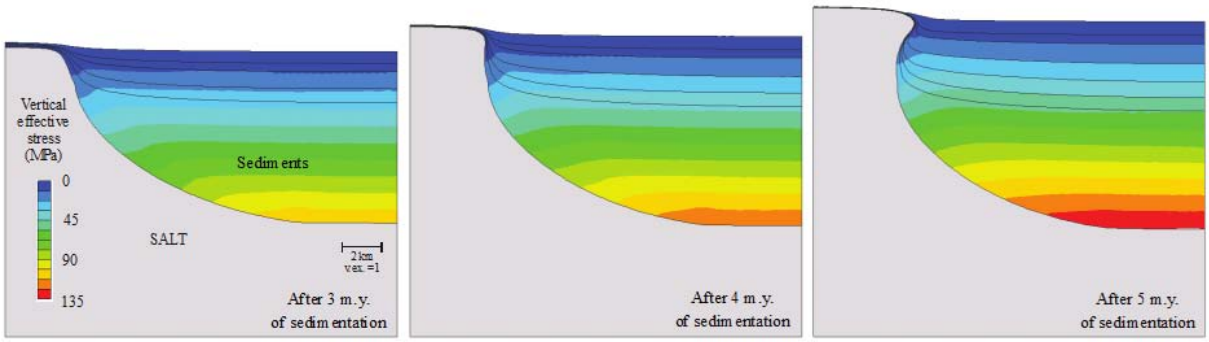

Fig. 1.: Vertical sections predicted by the numerical model after 3, 4, and 5 m.y. of sedimentation. Contours illustrate changes in vertical stress due to sedimentation and simultaneous salt movement (Nikolinakou et al., 2014).

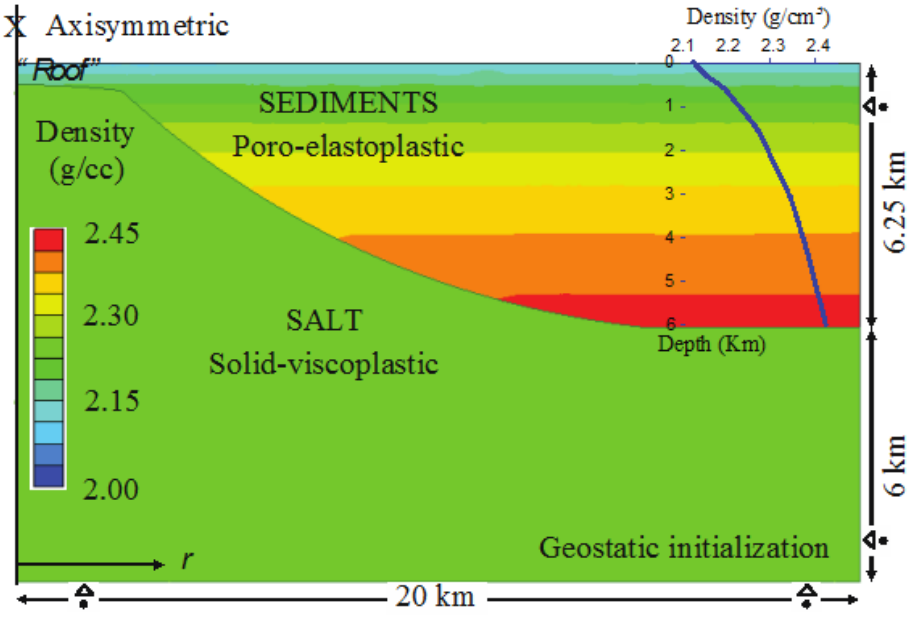

Fig. 2.: Plane of revolution for axisymmetric numerical model (vertical section). Contours and inset plot show density-depth profile of initial section (Nikolinakou et al., 2014).

close to the upper parts of the diapir. The vertical stress (dotted solid purple line in Figure 3b) decreases in the sediments next to the salt diapir. This decrease is associated with a rotation of the principal stresses near the salt-sediment interface. The maximum principal stress (σ_1) becomes perpendicular to the salt face and increases to a value equal to the stress inside the salt. Near the dome, the minimum principal stress is in the circumferential (hoop) direction, because of the circumferential expansion of the diapir during its rise.

The combination of the stress changes near the salt (Figure 3) leads to a net increase of the mean stress close to the upper parts of the diapir, and a decrease near the base of the diapir, compared to the far-field values at the same depth (Figure 4a). Consequently, the porosity near the vertical parts of the salt diapir is lower than the porosity predicted by a uniaxial compression model (Figure 4b), as the sediments have been locally compressed to a higher stress level.

Discussion

Our results show that near a rising salt diapir, the minimum principal stress is in the circumferential (hoop) direction. This suggests that radial normal faults should be favored near the diapir, as is commonly observed (Davison et al., 2000, O'Brien and Lerch, 1987, Stewart, 2006). The predicted decrease in the hoop stress also means that the fracture gradient is reduced near the salt; in practice, this suggests a narrower range of admissible drilling mud weights. Indeed, reduced stress values at the circumferential (hoop) direction are often reported near salt diapirs and such stresses are associated with borehole instabilities and loss of circulation (Bradley, 1978, Seymour et al., 1993, Dusseault et al., 2004). Furthermore, our model predicts a higher mean stress near the upper parts of the diapir; indeed, denser sediments have been observed near the "shoulders" of salt diapirs in the North Sea (Dusseault et al., 2004)

Such comparisons illustrate that evolutionary models can provide a detailed understanding of the stress history of mudrocks close to salt diapirs and hence improve predictions of stresses, possible fault directions, shear/tensile strength, and material properties of the wall rocks.

References

Bradley, W. B., 1978, Borehole failure near salt domes: Society of Petroleum Engineers Annual Fall Technical Conference and Exhibition, 10/01/1978, at Houston, Texas

Davison, I., I. Alsop, P. Birch, C. Elders, N. Evans, H. Nicholson, P. Rorison, D. Wade, J. Woodward, and M. Young, 2000, Geometry and late-stage structural evolution of Central Graben salt diapirs, North Sea: Marine and Petroleum Geology, 17, no. 4, 499-522. doi: http://dx.doi.org/10.1016/S0264-8172(99)00068-9.

Dusseault, M. B., V. Maury, F. Sanfilippo, and F. J. Santarelli, 2004, Drilling Around Salt: Risks, Stresses, And Uncertainties, 5-9 June 2004 Muir Wood, D., 1990, Soil behaviour and critical state soil mechanics: Cambridge University Press.

Munson, D. E., and P. R. Dawson, 1979, Constitutive model for the low temperature creep of salt (with application to WIPP), in SAND79-1853Sandia National Laboratories, Albuquerque, NM

Nikolinakou, M. A., P. B. Flemings, and M. R. Hudec, 2014, Modeling stress evolution around a rising salt diapir: Marine and Petroleum Geology, 51, 230-238. doi: http://dx.doi.org/10.1016/j.marpetgeo.2013.11.021.

O'Brien, J. J., and I. Lerch. 1987, Modellingof the deformation and faulting of theformations overlying an uprising saltdome., in I. Lerche and J. J. O'Brien, eds., Dynamical Geology of Saltand Related Structures: Academic Press, London. 419–455.

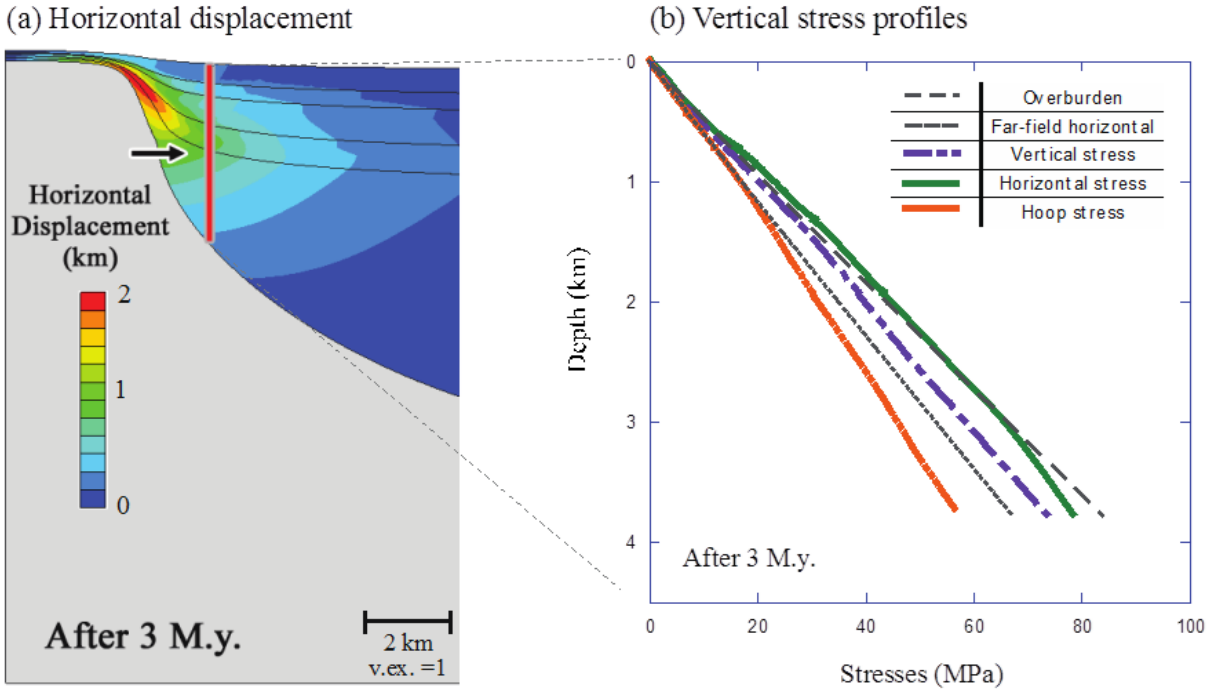

Fig. 3.: (a) Vertical section with contours of horizontal displacement next to rising salt dome, after 3 m.y. of deposition; (b) Stress profiles of horizontal, vertical, and hoop stresses along well next to salt. (Nikolinakou et al., 2014).

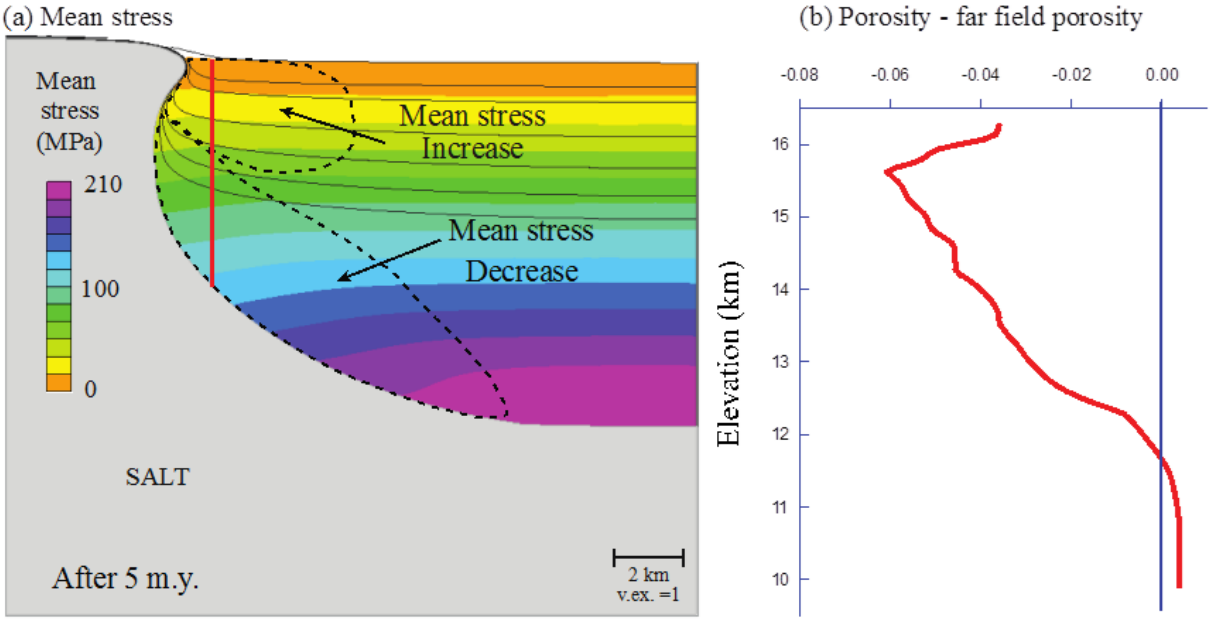

Fig. 4.: (a) Vertical section showing mean stress contours near rising salt dome after 5 m.y. of deposition; b) profile along vertical well plotting difference between measured and far-field porosity (Nikolinakou et al., 2014).

Peric, D., and A. J. L. Crook, 2004, Computational strategies for predictive geology with reference to salt tectonics: Computer Methods in Applied Mechanics and Engineering, 193, no. 48,Äì51, 5195-5222. doi: http://dx.doi.org/10.1016/j.cma.2004.01.037.

Seymour, K. P., G. Rae, J. M. Peden, and K. Ormston, 1993, Drilling close to salt diapirs in the North Sea: Offshore Europe, 09/07/1993, at Aberdeen, U.K.

Stewart, S. A., 2006, Implications of passive salt diapir kinematics for reservoir segmentation by radial and concentric faults: Marine and Petroleum Geology, 23, no. 8, 843-853. doi: http://dx.doi.org/10.1016/j.marpetgeo.2006.04.001.

Thornton, D. A., D. T. Roberts, A. J. L. Crook, and J. G. Yu, 2011, Regional scale salt tectonics modelling: Bench-scale validation and extension to field-scale propblems.: Beyond balanced sections: Geological Society of America Conference, at Minneapolis, USA.

Numerical bifurcation analysis of spontaneous strain localization resulting in necking of a layer

M. Peters[1], T. Poulet[2], M. Veveakis[2], A. Karrech[3], M. Herwegh[1], K. Regenauer-Lieb[2,4]

[1]*Institute of Geological Sciences, University of Bern, Switzerland*
[2]*CSIRO Earth Science and Resource Engineering, Kensington, Western Australia*
[3]*School of Civil and Resource Engineering, The University of Western Australia*
[4]*School of Earth and Environment, The University of Western Australia*
e-mail: *max.peters@geo.unibe.ch*
session: *Rheology*

Introduction

During necking of a mechanically stiff layer embedded in a weaker matrix, relatively large amounts of strain localize in small areas. As this deformation style appears under distinct geological conditions, necking phenomena, e.g. *boudinaged* mineral veins, are associated with a variety of deformation modes. These modes have been identified and recently numerically modeled as extensional fracturing (Abe and Urai, 2012), bookshelf-gliding or pinch-and-swell structures (Schmalholz and Maeder, 2012). In the latter case, i.e. *continuous necking*, symmetric boudins are interpreted as the result of dominant viscoplastic deformation (Goscombe et al., 2004). This study focuses on such deformation structures and the origin of the instabilities provoking necking. Indeed the driving mechanisms are currently not very well understood. In this light, we will explore their role as precursory structures, i.e. storage and potential localization of elastic energy affecting further plastic deformation (e.g. Regenauer-Lieb & Yuen, 1998; 2004; Karrech et al., 2011a) and the flow regime during localization. With this respect coupling of state, rheology and thermal-mechanics was chosen.

Method

In this work we have implemented the coupled model, recently presented by Herwegh et al. 2014, comprising multiple rheologies (elastic, rate-independent plasticity, diffusion creep, dislocation creep) and accounting for grain size variations. The resulting system of equations was solved in a shear box setting, for constant velocity conditions with a finite element solver (Karrech et al, 2011a). We simulate a pure-shear box with constant velocity boundary condition, using finite elements of which each element represents a grain size distribution. The box is built up by 3 layers, consisting of a central layer of coarse-grained populations that are allowed to evolve with time, surrounded by finer-grained populations with fixed grain sizes. The rheology of the central layer evolves from transient stages (linear elasticity and strain hardening) to composite viscous flow (dislocation + diffusion creep) with increasing shear strain. The small grain sizes in top and bottom layers are strain-invariant and limited in their growth (comparable to *Zener pinning* in nature) forcing the matrix to exclusively deform by diffusion creep. In contrast, the initially coarse-grained central layer is allowed to adapt to the physical deformation conditions by either grain growth (subscript g) or grain size reduction (subscript r) following the *Paleowattmeter* of Austin and Evans (2007; 2009):

$$d_s = k' \sigma^{-m'} exp\Big(\frac{-Q'}{RT}\Big)$$

where

$$k' = \Big[\frac{c\gamma A_g}{\lambda P A_{dis}}\Big]^{1/(p+1)}$$

$$m' = \frac{n+1}{p+1}$$

$$Q' = \frac{Q_g - Q_r}{p+1}$$

where d_s is the steady-state grain size, σ the flow stress, Q the activation enthalpy, R the gas constant, T the absolute temperature, c a geometric constant (π for spherical grains), γ the grain boundary energy, A the pre-exponential factor of the corresponding power-law creep behavior, λ the energy fraction deposited in the microstructure, p the grain growth exponent and n the stress exponent.

We embedded the grain size evolution in the thermodynamic approach of Regenauer-Lieb and Yuen (2004) and expended it to the transient regime. The total energy budget reads:

$$\underbrace{\rho c_p \frac{dT}{dt}}_{\text{energy budget}} = \underbrace{\chi\left(\sigma_{ij}\dot{\varepsilon}_{ij} - \rho\frac{\partial\psi}{\partial\varepsilon_{ij}^{el}}\dot{\varepsilon}_{ij}^{el} - \rho\frac{\partial\psi}{\partial d}\dot{d}\right)}_{\text{dissipative work}} + \underbrace{\rho T\frac{\partial^2\psi}{\partial\varepsilon_{ij}^{el}\partial T}\dot{\varepsilon}_{ij}^{el}}_{\text{thermal-elastic heat}} + \underbrace{\rho T\frac{\partial^2\psi}{\partial d\partial T}\dot{d}}_{\text{grain size heat}} + \underbrace{\kappa\nabla^2 T}_{\text{heat conduction}}$$

where ρ is the mass density, c_p the specific heat, χ the Taylor-Quinney coefficient ($\chi = 1 - \lambda$), ϵ the elastic strain, d the mean grain size, ψ the Helmholtz free energy and κ the thermal conductivity. For a detailed description of the modeling technique the reader is referred to Herwegh et al. (2014).

In addition, linear perturbation analyses were performed in order to evaluate the imperfection sensitivity in the elastic (and viscous) regimes. We perform a classical modal analysis to determine the natural mode shapes and frequencies of the geological structure during arbitrarily imposed vibrations. This analysis aims at detecting the *eigenmodes* of the system, which are sinusoidal vibrations with geometry specific modal shapes and frequencies. The *eigenvalues* represent the nodal points where the onset of (visco)-elasto-plastic localization can initiate in the structure (Rice, 1976). The *eigenmodes*, *eigenvalues* and *eigenvectors* are highly sensitive to the layer-box aspect ratio and material properties, i.e. differences in Young's moduli, or effective viscosity, respectively. These preloading structures were then used as seeds for imperfections in the succeeding modeling of boudinage in order to overcome instabilities that may arise from geometry and to reduce computational time. Moreover, further sensitivity studies were performed in order to exclude boundary effects, such as mesh or rheological parameter sensitivities or perturbations from numerical noise.

Results

Bifurcation from homogeneous state

With increasing extensional strain, grain sizes converge to a steady state, i.e. viscous relaxation of the calcite (Fig. 1). It becomes obvious that localization then occurs from steady state. The total energy budget thus reduces to the terms of dissipative work and heat conduction. By means of an instability analysis, first described by Gruntfest (1963), we can uncover the time-independent critical threshold for which localization will occur in terms of the ratio of mechanical energy, which is converted into heat, over the diffusive capacity of the system, also known as the *Gruntfest number*, or critical dissipation, in dependence of the layer dimension $ł_y$:

$$Gr = \chi\frac{A_{dis}l_y^2}{\kappa T_{boundary}}\sigma^{n,disl}exp\Big(\frac{-Q_{disl}}{RT_{boundary}}\Big)$$

Post-localization viscous creep

Depending on the dissipated energy, grain sizes in the modeled domains vary substantially in space and time. While low stresses in the swells favor grain growth and diffusion creep, high stresses in the pinches provoke dramatic grain size reduction with an increasing contribution of dislocation creep. The development of symmetric necks thus seems to coincide with the transition from dislocation to diffusion creep dominated flow with continuous grain size reduction in the necks and growth in the swells, respectively. Linked with the grain size reduction is strain localization within the necks at relatively low extensional strains.

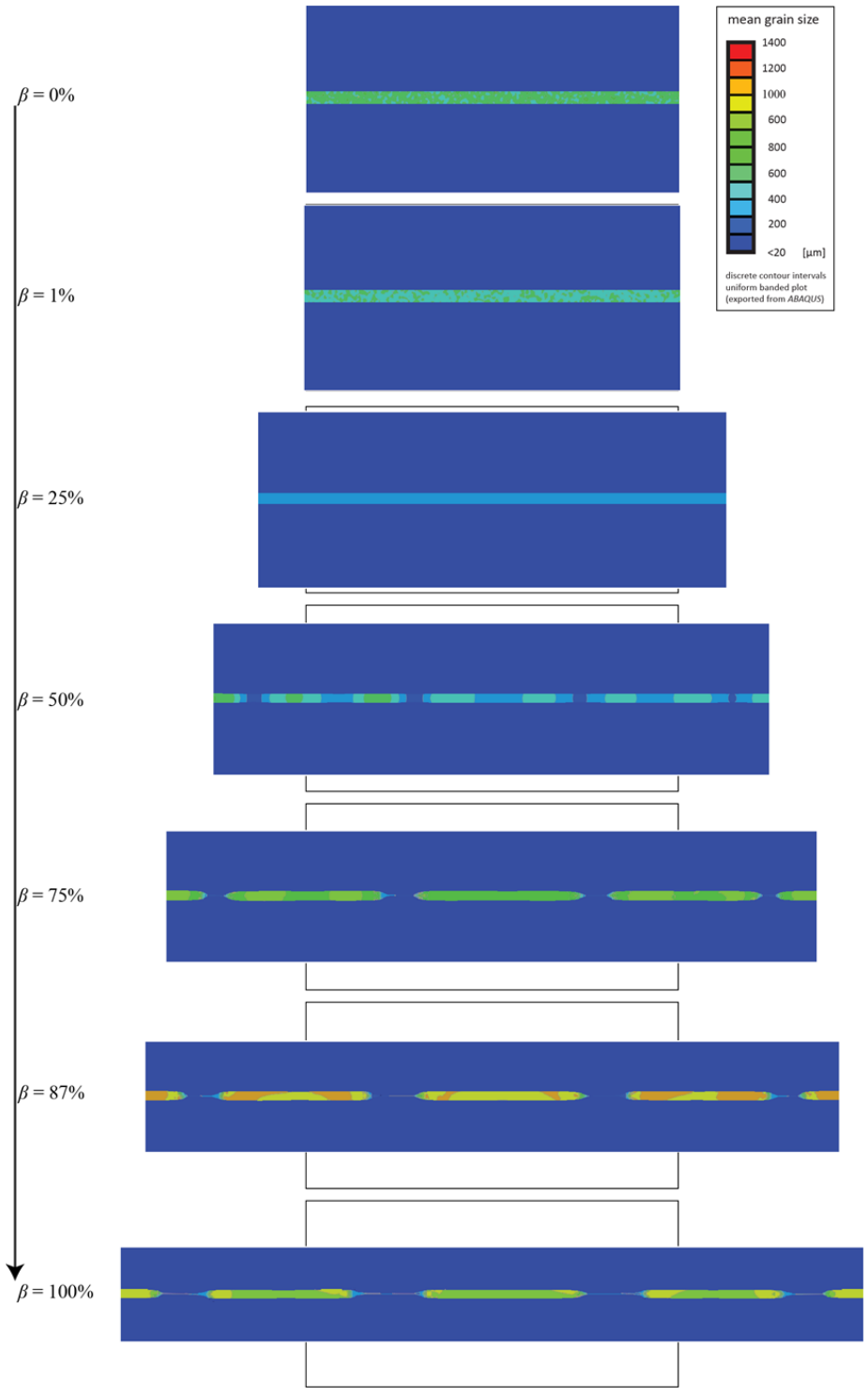

Fig. 1.: Numerical simulation of a coarse-grained ($500\mu m \pm 2\sigma$) calcite layer embedded in a finer-grained ($10\mu m \pm 2\sigma$) calcitic matrix. Boundary conditions: Strain rate=1.0E-14 $^{s-1}$, Temperature=300°C. β=relative extensional strain.

Concluding remarks

The focus of our ongoing work is to understand necking phenomena and the comparison between numerical simulations and natural microstructures. We have shown that visco-plastic necking of a numerical calcite layer occurs for natural deformation conditions and deformation mechanisms from *steady-state* composite viscous creep. The difference in effective viscosity between layer and matrix is around 1 order of magnitude, which underlines the contribution of an additional weakening effect, i.e. shear heating. Moreover, the thermo-dynamic feedbacks allow microstructural work, acting as an energy sink, which limits the actual contribution of shear heating to less than 2 K. Nevertheless, an instability study (Gruntfest, 1963) reveals the amount of critical dissipation necessary to trigger a perturbation resulting in localization.

Furthermore, we reveal that elastic stress concentrations control localized visco-plastic deformation, which is expressed by plastic strain energy increase in necking structures, as previously discussed by Regenauer-Lieb and Yuen (2004). This finding underlines the importance of the *transient* deformation regime as trigger for plastic deformation and the need for thermodynamics-based (total) energy considerations. Finally, we will discuss the effects of perturbations, which seem to be a prerequisite for solely mechanics-based simulations in which localization is driven by geometry, compared to our case, in which the microphysical deformation behavior of the system drives strain localization.

References

Abe, S. and Urai, J.L. (2012). Discrete element modeling of boudinage: insights on rock rheology, matrix flow, and evolution of geometry. Journal of Geophysical Research, 117.

Austin, N. and Evans, B. (2007). Paleowattmeters: A scaling relation for dynamically recrystallized grain size. Geology, 35.

Austin, N. and Evans, B. (2009). The kinetics of microstructural evolution during deformation of calcite. Journal of Geophysical Research, 114.

Goscombe, B.D., Passchier, C.W. and Hand, M. (2004). Boudinage classification: End-member boudin types and modified boudin structures, Journal of Structural Geology, 26.

Gruntfest, I.J. (1963). Thermal feedback in liquid flow; plane shear at constant stress. Transactions of the Society of Rheology, 7.

Herwegh, M., Poulet, T., Karrech, A. and Regenauer-Lieb, K. (2014). From transient to steady state deformation and grain size: A thermodynamic approach using elasto-visco-plastic numerical modeling, J. Geophys. Res. Solid Earth, 119.

Karrech, A., Regenauer-Lieb, K. and Poulet, T. (2011a). A Damaged visco-plasticity model for pressure and temperature sensitive geomaterials. Journal of Engineering Science, 49.

Regenauer-Lieb, K., Yuen, D. (1998). Rapid conversion of elastic energy into plastic shear heating during incipient necking of the lithosphere. Geophysical Research Letters, 25.

Regenauer-Lieb, K., Yuen, D. (2004). Positive feedback of interacting ductile faults from coupling of equation* of state, rheology and thermal-mechanics. Physics of the Earth and Planetary Interiors, 142.

Rice, J. R. (1976). The localization of plastic deformation. Theoretical and Applied Mechanics, 1.

Schmalholz, S.M. and Maeder, X. (2012). Pinch-and-swell structure and shear zones in visco-plastic layers. Journal of Structural Geology, 37.

Finite element model investigation of fault shear stress accumulation due to elastic loading and viscous relaxation.

Hiroki Sone[1]

[1] *German Research Centre for Geosciences, Potsdam, Germany*
e-mail: *sone@gfz-potsdam.de*
session: *Rheology*

Recent seismological observations from megathrust earthquakes in subduction zones (e.g. Sumatra, Maule, Tohoku) show that sources of relatively high and low frequency seismic waves are not necessarily co-located along a ruptured fault plane. As frequency of seismic waves reflect the rupture style which is influenced by preexisting shear stresses on the fault, some authors have accordingly suggested that the nature of the spatial stress heterogeneity along the subduction zone is depth dependent (Lay et al., 2012). However, we have little specific understanding about how such stress heterogeneities arise along fault planes, how they evolve throughout an earthquake cycle, or how it is affected by depth-dependent rheology. It is important to understand these interseismic processes because the initial stress condition prior to an earthquake has first order controls on how large an earthquake grows.

The focus of this study is to explore how stress concentrations on faults behave between earthquakes under some assumptions about the fault zone and host rock rheology. A generic fault zone model in a finite element code is used to investigate how the accumulation of shear stress along faults are influenced by the type of asperity (geometrical vs. stress), interseismic loading rate, and the mechanical properties of the fault zone and host rock materials. Fault stress accumulation is usually modeled by considering a frictionally locked fault interface embedded in an elastic lithosphere. However, many rocks exhibit viscoelastic behavior over geological time scales, especially true for fault related rocks which can

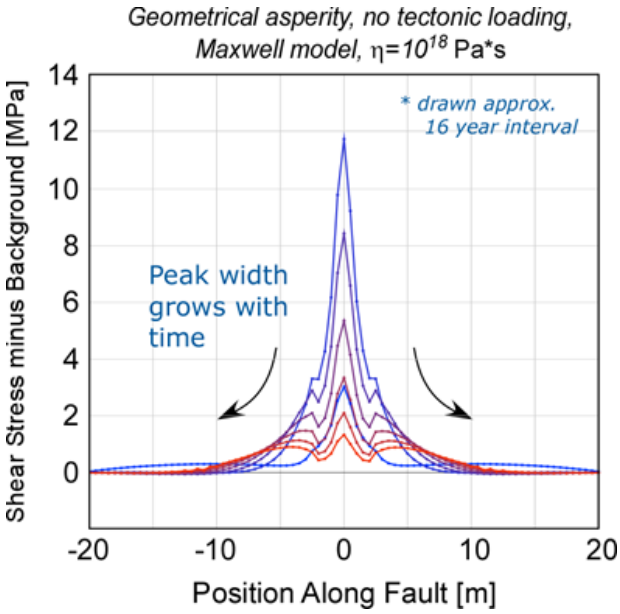

Fig. 1.: Relaxation of a stress concentration due to a geometrical asperity on the fault plane. The shear stress profile relative to the background level is drawn against the position along the fault plane. The profile evolves from blue to red, describing the growth in length scale of the stress concentration.

be clay-rich and in-cohesive relative to the surrounding rocks. Thus particular emphasis of this study is to use viscoelastic rheology for the fault zone material to account for not only the elastic tectonic loading on faults, but also the viscous relaxation of stress over time.

Results of the modeling suggest that spatial diffusion of stress heterogeneities can occur due to viscoelastic effects especially when geometrical complexity is introduced at the fault surface.

(Figure 1) That is, the length scale of the stress concentration can grow over time as viscous deformation takes place in the viscoelastic fault zone. It is also found that the time scale required for the spatial diffusion of stress is influenced by the effective viscosity of the fault zone. This suggests that rheological properties can influence the size of stress patches, or "asperities", that can develop along a fault over a certain interseismic loading period. Comparison of results between different viscoelastic rheology and different tectonic loading rates will also be investigated to identify the relevance to natural settings.

References

Lay, T., Kanamori, H., Ammon, C.J., Koper, K.D., Hutko, A.R., Ye, L., Yue, H., and Rushing, T.M., Depth-varying rupture properties of subduction zone megathrust faults. Journal of Geophysical Research, 117, B04311, doi:10.1029/2011JB009133, 2012.

Lithospheric strength and elastic thickness variations in the North American continent

Magdala Tesauro[1,2], Mikhail K. Kaban[2], Sierd Cloetingh[1], Walter D. Mooney[3]

[1] *Department of Earth Sciences, Utrecht University, The Netherlands*
[2] *German Research Center for Geosciences (GFZ), Potsdam, Germany*
[3] *USGS, Menlo Park, USA*
e-mail: *magdala@gfz-potsdam.de*
session: *Rheology*

We estimate the strength and effective elastic thickness (*Te*) of the North American (NA) lithosphere (Tesauro et al., 2014a). To this purpose, we use two thermal models, which are corrected for compositional variations and anelasticity effect in the upper mantle (Figs. 1a-b), obtained in a joint inversion of the gravity data and two recent seismic tomography models NA07 (Bedle and van der Lee, 2009) and SL2013sv (Shaffer and Lebedev, 2013).

The method implies the construction of a preliminary 3D density model (Kaban et al., 2014), reflecting the effect of both thermal and compositional variations of the upper mantle. Such a model was obtained from a joint inversion of the residual mantle gravity anomalies, estimated by subtracting the gravity effect of the crust from the observed gravity field, and the residual topography. Afterwards, the two tomographic models were inverted for temperature using mineral physics equations (e.g., Stixrude and Lithgow-Bertelloni, 2005). In the initial inversion a uniform fertile composition was used. The initial thermal models made it possible to separate the effect of temperature and composition in the mantle residual gravity anomalies (Kaban et al., 2014). These preliminary results are obviously biased by not considering composition variations in the constructed thermal model (e.g., Griffin et al., 2003). To overcome this problem the initial compositional density anomalies under the cratons are interpreted in terms of degree of depletion in heavy constituents (CPX, garnet and *Fe*), and thus the thermal model is re-estimated, using the new composition (Tesauro et al., 2014b). These steps are repeated until the convergence is reached.

The crustal rheology is assigned using NACr14 (Tesauro et al., 2014c), the most recent NA crustal model, providing velocity and thickness for the three layer model of the crystalline crust. According to NACr14, we assign a 'hard' rheology (Type 5, Fig.2) represented by granite-diabase-mafic granulite to the regions characterized by high crustal velocities (e.g., the northern Rocky Mountains) and a 'soft' rheology (Type 1, Fig.2), represented by quartzite-diorite to regions with low crustal velocities (e.g., the continental margins). Between these two end-members we define several other rheologies given by a combination of these lithotypes, assigned to the areas with intermediate crustal velocities (Fig. 2).

The obtained strength models (Figs. 3-ab), identified with the same names as of the tomography models, evidence a sharp contrast between the weak off-cratonic regions, where the strength is prevalently localized in the crust, and the inner part of the cratons, characterized by strong lithosphere. Such a difference has been already observed in global strength models (e.g., Tesauro et al., 2012), but differently from previous results, the new models show that the Phanerozoic structures close to the edge of the cratons, as the Appalachians, are characterized by low strength,

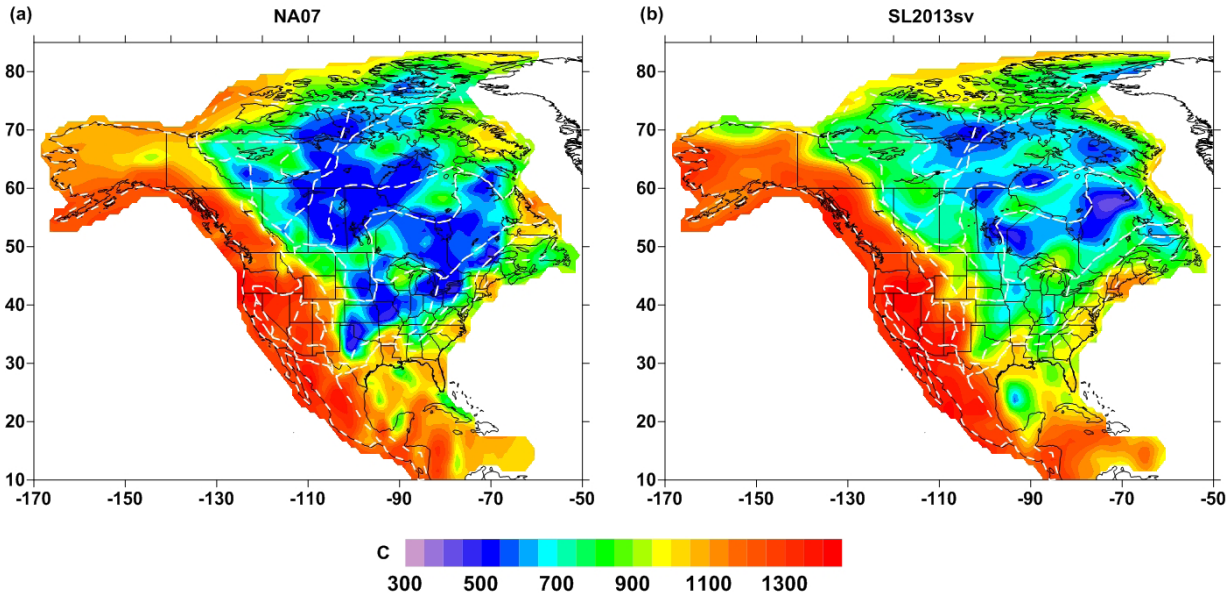

Fig. 1.: Temperature variations in the upper mantle (C°), 100 km depth (Tesauro et al., 2014b), estimated from joint inversion of the gravity and tomography data. Two tomography models have been employed: (left) the regional tomography model NA07 and (right) the global tomography model SL2013sv. White dashed contours as in Figs. 2-4 show the boundaries between tectonic provinces.

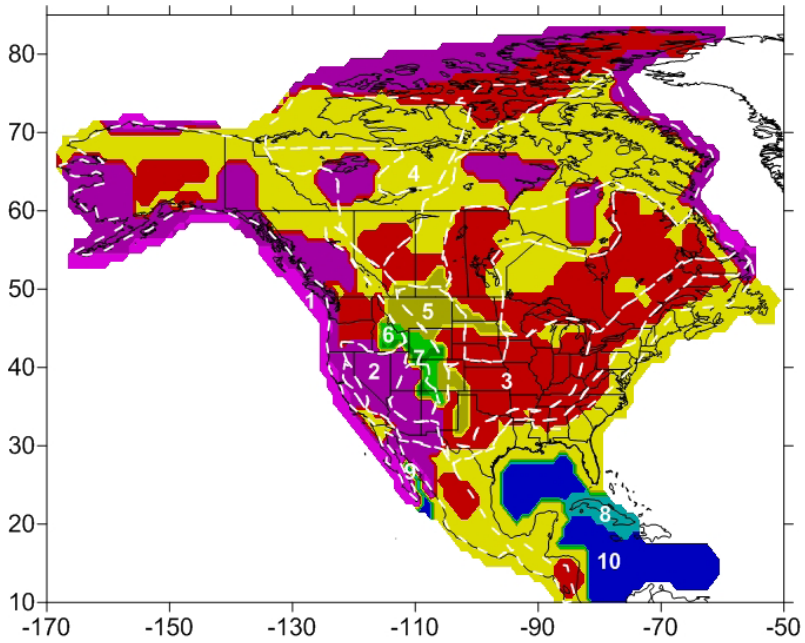

Fig. 2.: Rheological types of the crustal layers (Tesauro et al., 2014a), assigned on the base of the crustal velocity variations in NACr14 (Tesauro et al., 2014c), are identified by colours and white numbers, as follows: 1, Dry Quartzite-Wet Diorite-Wet Diorite; 2, Dry Quartzite-Wet Diorite-Dry Diabase; 3, Dry Granite-Wet Diorite-Mafic Granulite; 4, Dry Granite-Wet Diorite-Dry Diabase; 5, Dry Granite-Dry Diabase-Mafic Granulite; 6, Dry Quartzite-Dry Diabase-Dry Diabase; 7, Dry Quartzite-Wet Diorite-Mafic Granulite; 8, Dry Granite-Mafic Granulite; 9, Wet Quartzite-Wet Diorite; 10, Diabase.

while zones of local weakness are also present within the cratons. NA07 and SL2013sv differ chiefly in some peripheral parts of the cratons, as the Proterozoic Canadian Platform, the Grenville and the western part of the Yavapai-Mazatzal province, where the integrated strength in NA07 is ten times larger than in SL2013sv, reflecting the difference in the uppermost mantle temperatures (>200°C).

In terms of *Te* (Figs. 4a-b) estimated from the strength distribution the differences between the two models are less pronounced. In both of them only the most peripheral parts of the cratons, comprising Proterozoic regions reactivated by Meso-Cenozoic tectonics (e.g., Rocky Mountains and the Mississippi Embayment), are weak due to the absence of a mechanically strong part of the mantle lithosphere and thus more prone to instability. Intraplate earthquakes are distributed along the edges of the cratons, demonstrating that tectonic stress accumulates there more easily, while the core of the cratons remains undeformed. In both models half or more of these events occur in the weak lithosphere with the values of the integrated strength and *Te*, limited to a small range ($\sim 0.5 \times 10^{13}$ Pa s and ∼15 km, respectively), while the remaining part is located in the lithosphere characterized by pronounced contrast of strength and *Te*.

References

Bedle, H., van der Lee, S., 2009. S velocity variations beneath North America. J. Geophys. Res., 114, B07308, doi:10.1029/2008JB005949.

Griffin, W.L., O'Reilly, S.Y., Abe, N., Aulback, S., Davies, R.M., Pearson, N.J., Doyle, B.J., Kivi, K., 2003. The origin and evolution of Archean lithospheric mantle. Precambrian Res., 127, 19–41.

Kaban, M.K., M., Tesauro, M., Mooney, W.D., Cloetingh, S.A.P.L., 2014. Density, temperature and composition of the North American lithosphere: new insights form a joint analysis of seismic, gravity and mineral physics data. Part I: Density structure of the crust and upper mantle. Geophys. Geochem. Geosyst. (submitted).

Schaeffer, A.J., Lebedev S., 2013. Global shear-speed structure of the upper mantle and transition zone. Geophys. J. Int., 194, (1), 417-449.

Schulte, S., Mooney, W.D., 2005. An updated global earthquake catalogue for stable continental regions: reassessing the correlation with ancient rifts. Geophys. J. Int. 161, 707–721.

Stixrude, L., Lithgow-Bertelloni, C., 2005. Thermodynamics of mantle minerals – I. Physical properties. Geophys. J. Int., 162, 610–632.

Tesauro, M., Kaban, M.K., Cloetingh, S.A.P.L., 2012a. Global strength and elastic thickness of the lithosphere. Global and Planetary Change 90–91, 51–57.

Tesauro, M., Kaban, M., Mooney, W.D., Cloetingh, S.A.P.L., 2014a. Lithospheric strength and elastic thickness variations in the North American continent. Earth and Planetary Science Letters (submitted).

Tesauro, M., Kaban, M., Mooney, W.D., Cloetingh, S.A.P.L., 2014b. Density, temperature and composition of the North American lithosphere: new insights form a joint analysis of seismic, gravity and mineral physics data. Part II: Thermal and compositional model of the upper mantle. Geophys. Geochem. Geosyst. (submitted).

Tesauro, M., Kaban, M., Mooney., W.D., Cloetingh, S.A.P.L., 2014c. A 3D model for the crustal structure of the North American Continent. Tectonophysics, in press.

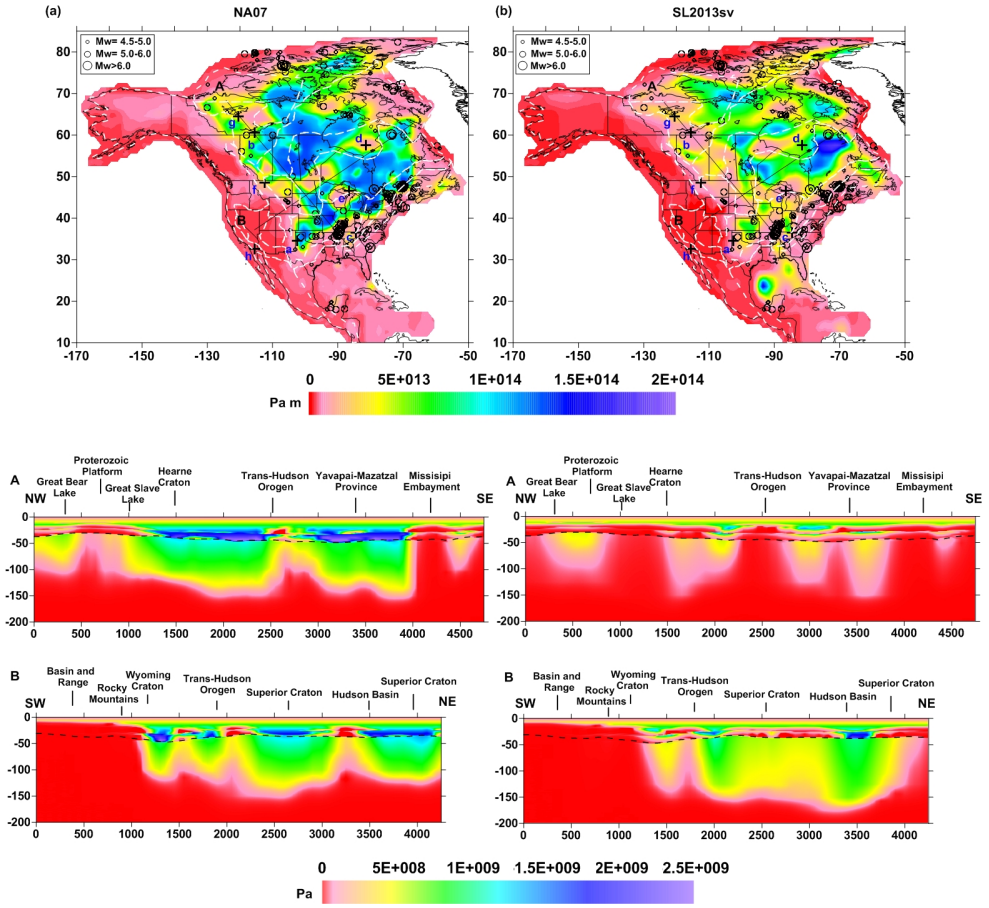

Fig. 3.: Integrated lithospheric strength (Pa m) and strength variations (Pa) along two cross-sections estimated for a compressional regime using the crustal rheological types (Fig. 2) and (a) the NA07 thermal model (Fig. 1a); (b) the SL2013sv thermal model (Fig. 1b). Black circles as in Figs. 4(a-b) show the intraplate earthquakes location from the seismic catalog for stable continental regions (SRCs) of Schulte and Mooney (2005).

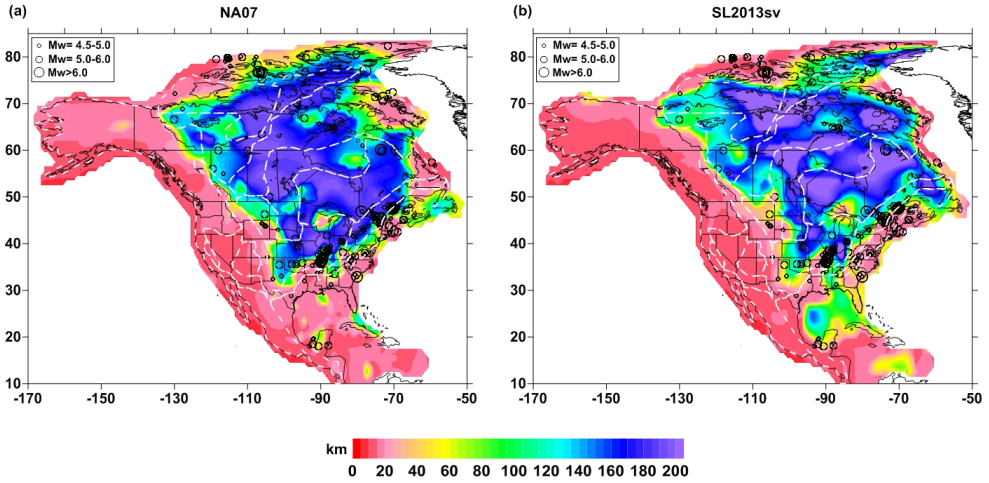

Fig. 4.: Effective elastic thickness (Te) of the lithosphere (km) (Tesauro et al., 2014a) for (a) NA07 and (b) SL2013sv.

GFZ
Helmholtz Centre
POTSDAM

GeoMod2014

Modelling in Geosciences

Programme & Extended Abstracts

31 August - 5 September 2014

Editors:
Kirsten Elger
Øystein Thordén Haug
Malte Ritter

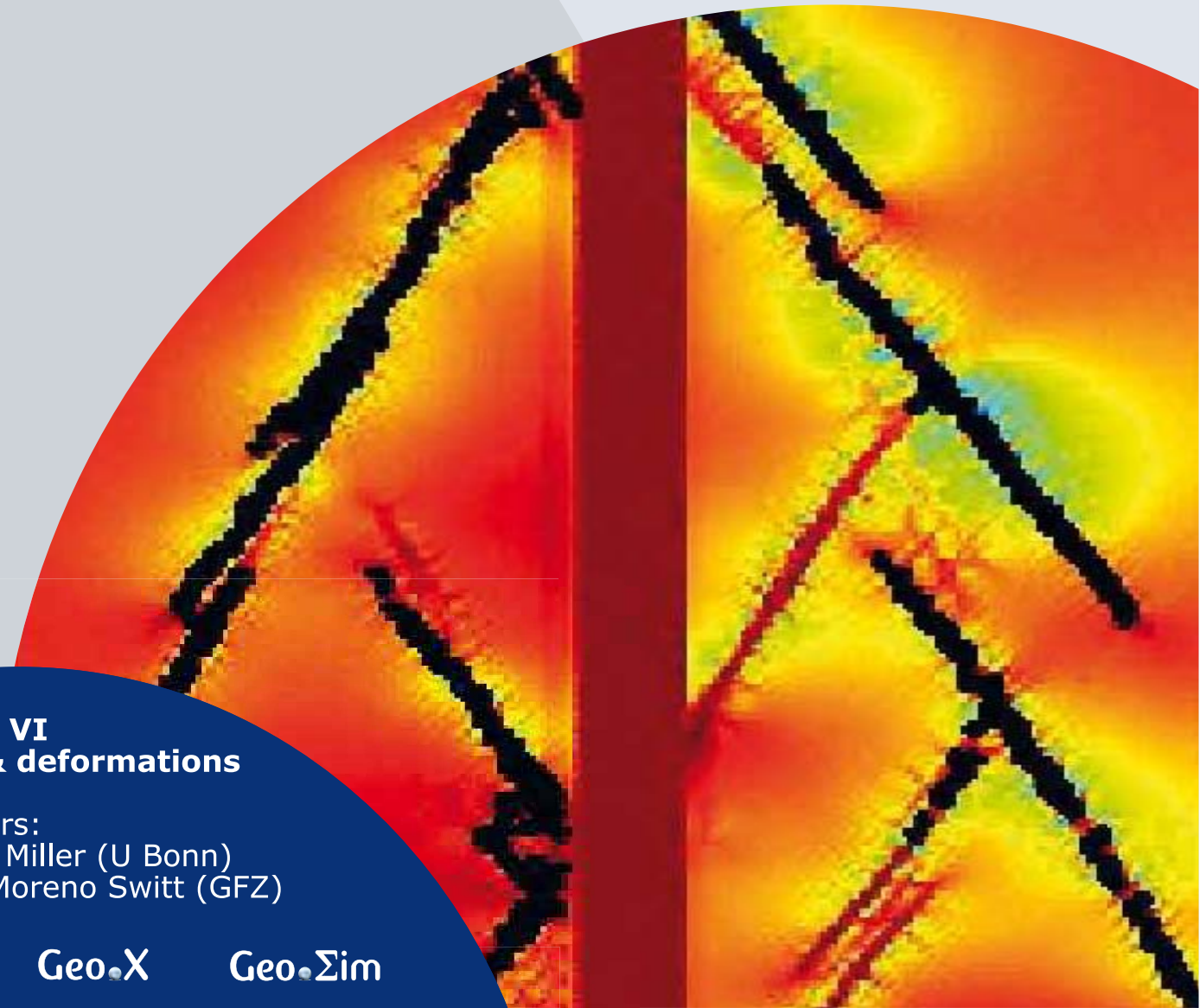

Session VI
Fluids & deformations

Conveners:
Stephen Miller (U Bonn)
Marcos Moreno Switt (GFZ)

DFG Geo.X Geo.Sim

Session VI.

Fluids and Deformation

Session Description: Fluids and Deformations

Conveners: Stephen Miller (U Bonn), Marcos Moreno Switt (GFZ)

This session is focused on the interactions between elastic and inelastic deformation, brittle failure (earthquakes), how fluids affect and are affected by, coupled deformation, as well as the importance of flow for numerous geodynamic processes. These include, but are not limited to, non-volcanic tremor and slow-slip earthquakes, enhanced geothermal systems, post-seismic deformation, earthquake swarms, and aftershocks. Although the interactions between fluids and deformation are conceptually straightforward, complexity arises due to multiple feedbacks between crack nucleation, growth, and coalescence combined with the initiation of fluid flow and an evolving pore-elastic/ fracture stress state. Modeling these processes is numerically challenging because the underlying physics require high-resolution simulations over a wide range of timescales. This session aims to understand fluids and deformation of a wide range of space and time scales, using recent advances in numerical modeling to compare with observations from experimentalists, geodesists, and geologists.

Effect of Fluid Circulation on Intermediate-Depths Subduction Dynamics: From Field Observations to Numerical Modelling

S. Angiboust[1,2], S. Wolf[1], E. Burov[1], P. Agard[1], P. Yamato[3]

[1] *ISTeP, Univ. P.M. Curie-Paris 6, Paris, France*
[2] *Lithosphere dynamics laboratory, GFZ Potsdam, Germany*
[3] *Laboratoire de Tectonique, Univ. Rennes 1, France*
e-mail: *samuel.angiboust@gfz-potsdam.de*
session: *Fluids and Deformation*

A wide range of geophysical/petrological data indicates that large amounts of water are released in subduction zones during the burial of oceanic lithosphere through metamorphism and associated dehydration reactions. Large volumes of aqueous fluids are expected and observed in the mantle wedge, just below the continental Moho. Recent estimates suggest that the mantle wedge is heterogeneously serpentinized (generally 20-30 %). This serpentinization is believed to cause a significant weakening of the mantle wedge and therefore may critically control the depth of interplate seismogenic coupling. However, data constraining mechanisms driving deep (50 km to 200 km) fluid circulation are lacking and fluid-rock interaction processes remain weakly constrained at the km-scale.

We herein propose a new fluid migration algorithm based on field relationships and thermodynamic modelling (PerpleX) where fluids are free to migrate, driven by rock fluid concentration, non-lithostatic pressure gradients and deformation. Oceanic subduction is then modelled using a forward visco-elasto-plastic thermomechanical code (FLAMAR algorithm) in which fluid transport and rheological effect is implemented. After 15 Ma of convergence between the two plates, we show that deformation is accommodated along a low-strength shear zone in the wall of the subduction thrust interface, characterized by a weak (10-25 % serp.) and relatively narrow (between 3 km to 6 km) serpentinized front/channel.

Our results also show that dehydration associated with eclogitization of oceanic crust (60 km to 75 km and serpentinite breakdown (110 km to 130 km) significantly weakens the mantle wedge at these depths, thereby favoring underplating of oceanic plate material in the deep mantle wedge (Angiboust et al., 2012). Hydration of the subduction interface also significantly weakens the interface and enables detachment and stacking of slices from the downgoing slab. We finally show that modelled geometries are in good agreement with reconstructions derived from field structural observations made along the Western Alps eclogite-facies ophiolitic belt, where large, coherent slices were detached at c. 80 km depth in the Alpine subduction zone (Fig. 1).

References

Angiboust, S., Wolf, S., Burov, E., Agard, P., & Yamato, P. (2012). Effect of fluid circulation on subduction interface tectonic processes: Insights from thermo-mechanical numerical modelling. Earth and Planetary Science Letters, 357, 238-248.

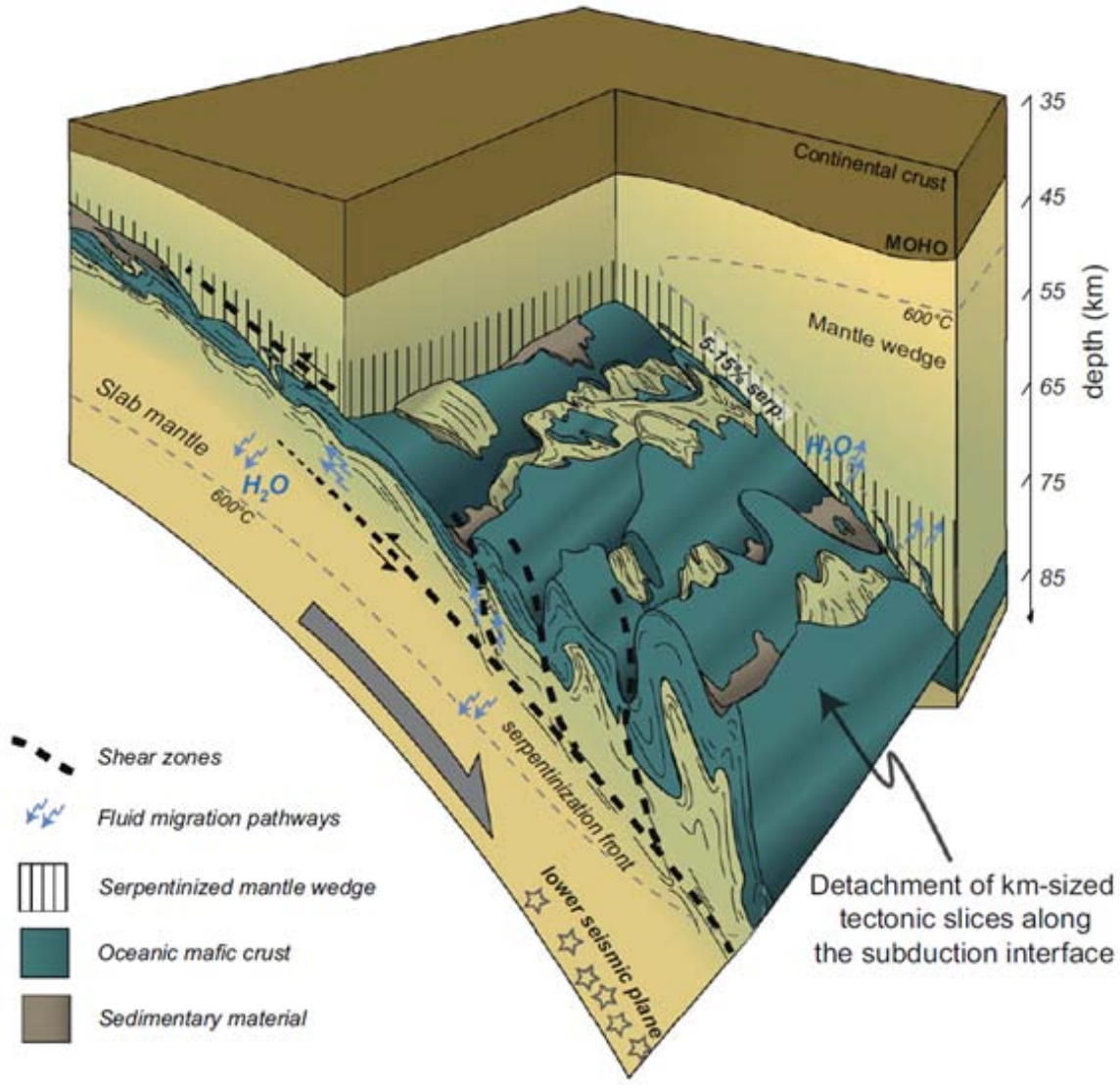

Fig. 1.: Schematic view drawn from field and numerical modeling results of the subduction interface region showing the detachment of large slices of oceanic lithosphere between $60\,\mathrm{km}$ and $80\,\mathrm{km}$ depths (Angiboust et al., 2012).

Assessment of microbial contamination of groundwater near solid waste dumpsites in basement complex formation, using total plate count method

Biodun Suraj Badmus

Federal University of Agriculture Abeokuta
e-mail: *badmusbs@yahoo.co.uk*
session: *Fluids and Deformation*

Abstract

Microbial analysis of water samples collected from two selected dumpsites within Ibadan metropolis were carried out in order to ascertain the effects of leachates generated by dumpsite on groundwater quality. Water samples were collected from surrounding wells and stream near Aba-Eku and Ajakanga solid waste landfill in Southwestern part of Nigeria. The samples were analysed for coliform count and Escherichia Coli through total plate count method. The result of the microbial analysis reveals high presence of coliform in all the water samples while two wells around Aba Eku dumpsite have E. Coli presence and none is detected in wells and stream around Ajakanga landfill. High values of microbial counts are principal indicators of suitability of water for domestic purpose and also sign of groundwater contamination in the surrounding wells. The sign of groundwater contamination was noticed in many surrounding wells around the two dumpsites resulting in high number of coliform bacteria. The presence of E. coli in wells 2 and 7 in Aba Eku requires control measures before consumption.

Physico-chemical properties of soil samples and environmental impact of dumpsite on groundwater quality in basement complex terrain, south western Nigeria

Biodun Suraj Badmus

Federal University of Agriculture Abeokuta
e-mail: *badmusbs@yahoo.co.uk*
session: *Fluids and Deformation*

Abstract

Physiochemical and microbial analyses of water samples from hand-dug wells were carried out around active dumpsite and or soil samples to ascertain the effect of wastes on the groundwater and soil quality. Soil samples were collected up to depth of 100 cm with the aid of soil auger while water samples were collected inside a 2 L PVC bottle. Soil pH, EC, % OM, % OC values ranged from 5.45–6.45, 5.03–6.63, 2.39–9.14 and 1.39–5.30. The mean values of soil pH, EC, % OM, % OC are high when compared with control. For water samples, the parameters of interest for microbial analysis are: coliform count and E. coli while parameters determined for physio-chemical analysis are: pH, Total Dissolved Solid (TDS), Electrical Conductivity (EC), Hardness, Carbonate, Bicarbonate, Chloride, Nitrate, Sulphate, Calcium, Magnesium, Potassium and Sodium ions. Microbial analysis revealed severe pollution in all samples while most of physiochemical parameters indicated traceable pollution which were below the World Health Organization (WHO) standard for human consumption as well as the Nigerian Standard for Drinking Water Quality (NSDWQ) limits. However, Well 5 which is close to the landfill has high values for all analyzed parameters when compared with other wells.

Towards a general simulation tool for complex fluid-rock lithospheric processes: merging pre-processing, processing and post-processing in state-of-the-art computational devices

Boris Galvan, Sahar Hamidi, Thomas Heinze, Mohammad Khatami, Gunnar Jansen, Stephen Miller

Geodynamics/Geophysics, University of Bonn
e-mail: *galvan@geo.uni-bonn.de*
session: *Fluids and Deformation*

Study of flow through porous and fractured media is a very active research area, with many different models and numerical tools available. Most of these tools are designed to study coupled processes of fluid flow, heat flow, and chemistry, and results from these models have proven valid in many real world applications.

However, the development of new engineering techniques requires new tools to address more complex scenarios. For example, fracking, enhanced geothermal systems, and CO2 /gas sequestration and storage play a very important role in the world's energy and environmental requirements. This tendency will likely steeply increase in the future.

The principle problem for the general applicability of all these techniques relates to uncontrolled and unexpected effects of fluid-triggered rock deformation. For example, induced seismicity can disturb the population, with possible infrastructure damage or unplanned flow paths that may lead to aquifers and soil pollution.

Therefore, there is need for new tools that consider the full coupling between rock deformation and fluid flow that use state-of-the-art fluid flow and rock deformation models. Desired fluid flow models should include saturated and unsaturated porous media and multiphase-multicomponent flow with local and nonlocal thermal equilibrium. They are few tools available that are capable of solving such models and, to the best of our knowledge, none of these models include the case for non-local thermal equilibrium. Such models are necessary to address real world problems like the stimulation stages in enhanced geothermal systems or fracking (Figure 1).

Rock deformation models should include poro-elasto-plastic rheology with thermal stresses and hardening-weakening effects, and include damage models when cycled loading-unloading is of interest (Figure 2). Another important factor for real world cases is seismic risk assessment, and is such cases a simulation tool should be able to adequately assess mechanistic seismic hazard, including expected maximum magnitude (Figure).

Numerical implementation of these models requires state of the art numerical schemes capable of dealing with complex geometries while maintaining high accuracy and numerical resolution.

Finite differences, finite volumes and mixed finite elements are well suited for fluid flow simulations in complex domains, while finite elements and mesh free methods have been applied for rock deformation simulations (Figure 4).

Solutions of these coupled models using advanced numerical schemes at high resolution is computational expensive and requires very long computational times. Graphical Processor Units

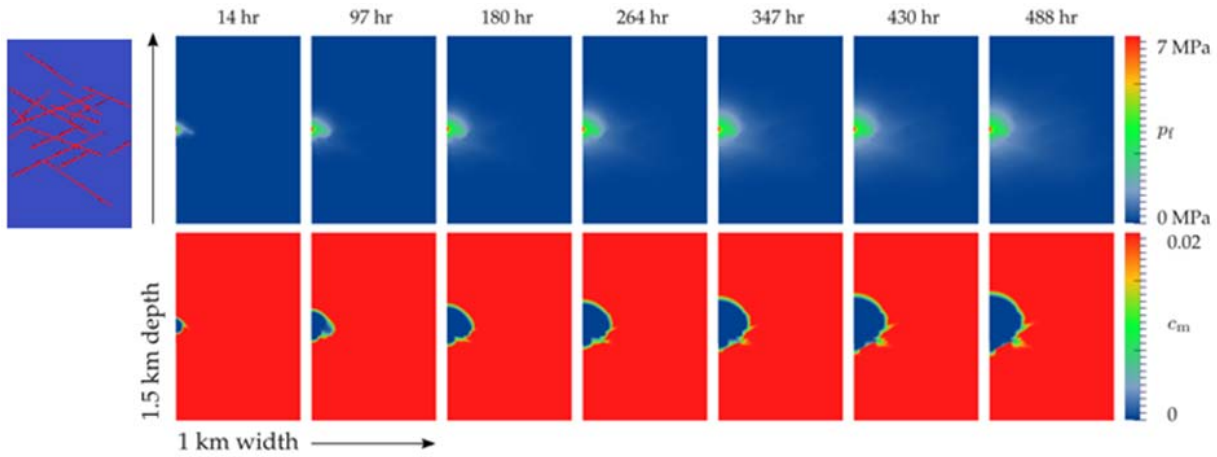

Fig. 1.: Results of a geothermal system simulation. Fresh cold water is injected in a hot fractured porous rock which is saturated with saline water. Figures on top show the pressure of the system while on bottom are the corresponding mass fraction diagrams

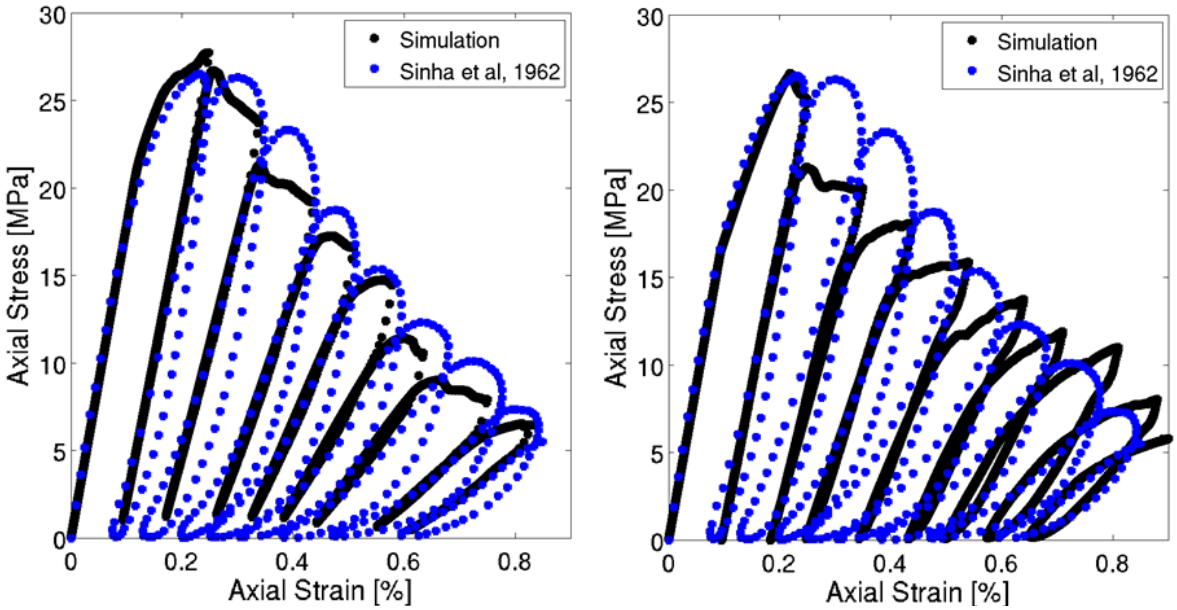

Fig. 2.: Comparison of two damage models with experimental data cycling compression test. A) Damage operator as a function of effective plastic strain. b) Double surface damage-yield functions model.

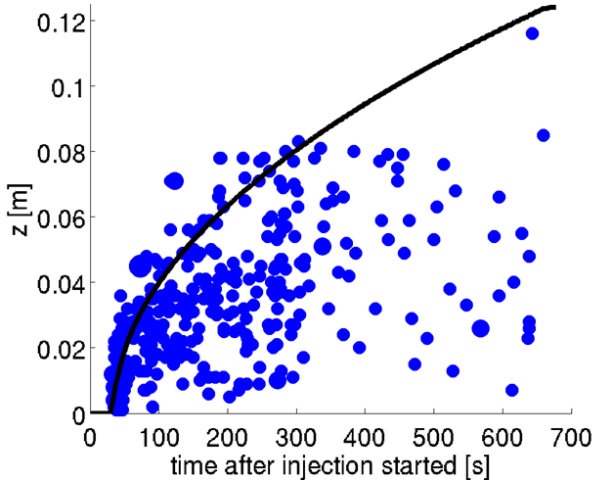

Fig. 3.: Propagation of acoustic emissions during fluid injection in a drained specimen. Results form poro-elasto-plastic model simulation. Black curve represent fluid front as solution of saturation equation. Blue dots are numerical acoustic emissions. Following experimental data from Stanchits et al. 2011.

(GPUs) resend a new programming paradigm that allows shorter computational times in comparison to CPU programming. However, for correct and efficient implementation of numerical algorithms in GPUs it is necessary to manage different memory protocols and specialized programming techniques, which adds additional complexity to the problem. In addition, usage of distributed GPU clusters for numerical simulations and even the implementation of well-known numerical algorithms, is a very new research area.

Under these circumstances of complex physical models and high numerical resolution, post processing may become a bottleneck. Fast analysis of the data requires fast and informative post processing techniques, and real time visualization techniques might allow rapid analysis of large data sets. In particular, for 3D simulations, visualization plays an important role. The question is how to present 3D information in the most informative way while maintaining computationally efficiency (Figure 5). Particularly for GPU systems, communication from GPUs to CPUs to apply rendering techniques slows down the entire computation, so new rendering algorithms appropriate for GPUs must be developed.

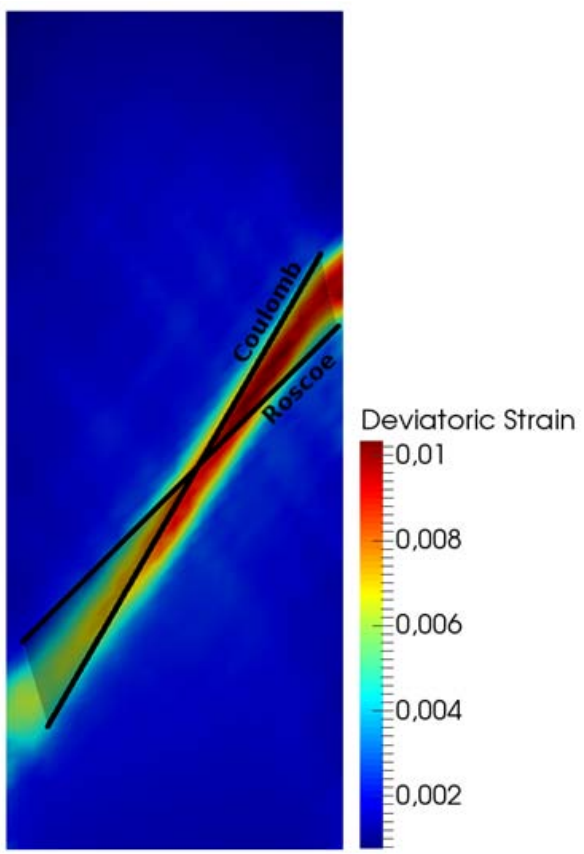

Fig. 4.: Shear bands for strain for uniaxial experiment simulation. Simulation of poro-elasto-plastic model using mesh free methods.

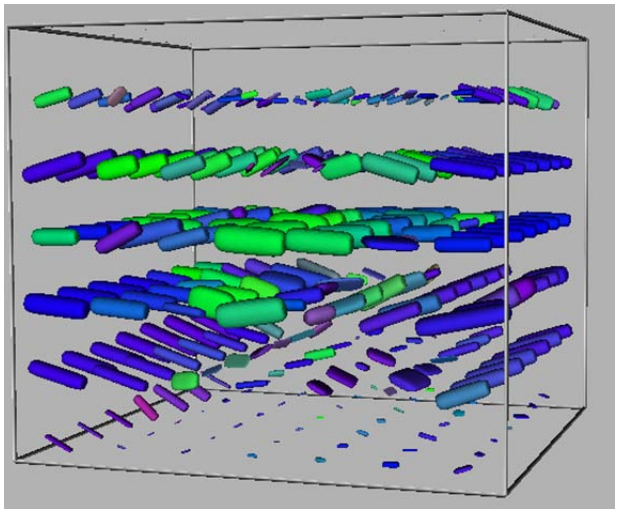

Fig. 5.: Visualization of 3D stress tensor using glyphs.

The description and representation of complex geometries, as they are encountered in real world cases, is a complicated task. Some tools rely on third party programs to create a suitable numerical representation of the geometry of the case under study. In other cases an over-simplification of the geometry is required. These procedures may result in limited applicability or usage of the simulation tool.

Tactile devices that allow a more intuitive and faster interaction with computational tools may increase the use of scientific simulation programs. Programming of a general multifunctional modeling tool for lithospheric fluid-rock processes is a very complex task. In this talk, we present different steps that we have taken toward this goal. This includes the development of new physical models, application to real cases and implementation of these models using advanced numerical schemes. We also describe some programming techniques for object oriented implementation in CPU, GPU and cluster of GPUs, pre-processing using tangible devices and visualization techniques for CPU and GPU based programs.

THC modelling of an Enhanced Geothermal System

Sahar Hamidi, Thomas Heinze, Boris Galvan, Stephen Miller

Geodynamics/Geophysics, University of Bonn
e-mail: *hamidi@geo.uni-bonn.de*
session: *Fluids and Deformation*

Fluid-rock interactions play an essential role in many earth processes, from a likely influence on earthquake nucleation and aftershocks, to enhanced geothermal system, carbon capture and storage (CCS), and underground nuclear waste repositories. Coupled thermal-hydraulic-chemical models (THC) are important for investigating these processes. Our objective is to develop algorithms for coupling the fluid processes to the rock mechanics that control rock deformation and fracture. To that aim, we present a two-dimensional numerical simulation of a fully coupled non-isothermal non-reactive solute flow flexible for field as well as laboratory scales.

In THC models, two-way interactions between different processes (thermal, hydraulic and chemical) are present. Fluid flow influences the permeability of the rock especially if chemical reactions are taken into account. On one hand solute concentration influences fluid properties while, on the other hand, heat can affect further chemical reactions.

The flow process of the model includes a nonlinear Darcian flow for either saturated or unsaturated scenarios. The governing equation for the saturated case is:

$$\frac{\partial}{\partial t}\left(\phi\rho\right) + \nabla\left(\rho\boldsymbol{v}\right) = Q \tag{1}$$

where ρ is the mass density of the fluid, ϕ the rock porosity, Q the source/sink term and $\boldsymbol{v}$ Darcy velocity:

$$\boldsymbol{v} = \frac{-\kappa}{\mu}\left(\nabla P - \rho\boldsymbol{g}\right) \tag{2}$$

where κ is the permeability, μ the dynamic viscosity of the fluid and $\boldsymbol{g}$ the gavitational acceleration. For the variably saturated systems in laboratory scale, Richards' Approximation is used (Kolditz, 2002) and the relative permeabilities are derived from van Genuchten relations (van Genuchten, 1980). Permeability and porosity of rock are stress and pressure dependent (Rutqvist et al., 2002). Additionally, the gravitation effects can be switched on and off depending on the simulation case.

The non-reactive mass transport is described as (Ackerer et al., 1999) :

$$\phi\frac{\partial C_m}{\partial t} + \boldsymbol{v}\nabla C_m - \nabla\left(D_{\mathrm{m}}\nabla C_m\right) = 0 \tag{3}$$

with C_m mass fraction and D_{m} molecular diffusion coefficient.

The thermal part of the simulation models heat transfer processes for either local thermal nonequilibrium or equilibrium cases. For the former one, conservation of energy for fluid and rock is expressed as (Shaik et al., 2011):

$$\phi c_{p,\mathrm{f}}\rho_{\mathrm{f}}\frac{\partial T_{\mathrm{f}}}{\partial t} + \boldsymbol{v}\nabla T_{\mathrm{f}} - \lambda_{\mathrm{f}}\nabla^2 T_{\mathrm{f}} + Q_T = 0 \tag{4}$$

$$\left(1-\phi\right)c_{p,\mathrm{r}}\rho_{\mathrm{r}}\frac{\partial T_{\mathrm{r}}}{\partial t} - \lambda_{\mathrm{r}}\nabla^2 T_{\mathrm{r}} - Q_T = 0 \tag{5}$$

$$Q_T = hA\left(T_{\mathrm{f}} - T_{\mathrm{r}}\right) \tag{6}$$

where T is temperature, c_p thermal capacity, λ thermal conductivity, Q_T heat transfer between rock and fluid, h heat transfer coefficient and A heat transfer area. Assuming local thermal equilibrium, we can rewerite the temparature equation (Kolditz, 2002):

$$c_p\rho\frac{\partial T}{\partial t} + c_{p,\mathrm{f}}\rho_{\mathrm{f}}\phi\boldsymbol{v}\nabla T - \lambda\nabla^2 T = 0 \tag{7}$$

$$c_p = \phi c_{p,\mathrm{f}} \rho_\mathrm{f} + (1-\phi)\, c_{p,\mathrm{r}} \rho_\mathrm{r} \quad (8)$$

$$\lambda = \phi \lambda_\mathrm{f} + (1-\phi)\, \lambda_\mathrm{r} \quad (9)$$

Estimating heat production from a naturally fractured geothermal systems remains a complex problem. Previous works are typically based on a local thermal equilibrium assumption and rarely consider the salinity. The dissolved salt in fluid affects the hydro- and thermodynamical behavior of the system by changing the hydraulic properties of the circulating fluid. For studying such a system, we consider a given fracture network saturated with saline water and inject high pressure fresh water into it. We compare the results of different assumptions (e. g. local thermal equilibrium an non-equilibrium) with field observations (Figure 2).

References

Ackerer et al. Modeling variable density flow and solute transport in porous medium: 1. Numerical model and verification. Transport in Porous Media 35.3 (1999): 345-373.

Kolditz, Olaf. Computational methods in environmental fluid mechanics. Springer (2002)

Rutqvist, J., et al. A modeling approach for analysis of coupled multiphase fluid flow, heat transfer, and deformation in fractured porous rock. International Journal of Rock Mechanics and Mining Sciences 39.4 (2002): 429-442.

Shaik, Abdul Ravoof, et al. Numerical simulation of Fluid-Rock coupling heat transfer in naturally fractured geothermal system. Applied Thermal Engineering 31.10 (2011): 1600-1606.

Stanchits, Sergei, et al. Fracturing of porous rock induced by fluid injection. Tectonophysics 503.1 (2011): 129-145

Van Genuchten, M. Th. A closed-form equation for predicting the hydraulic conductivity of unsaturated soils. Soil Science Society of America Journal 44.5 (1980): 892-898.

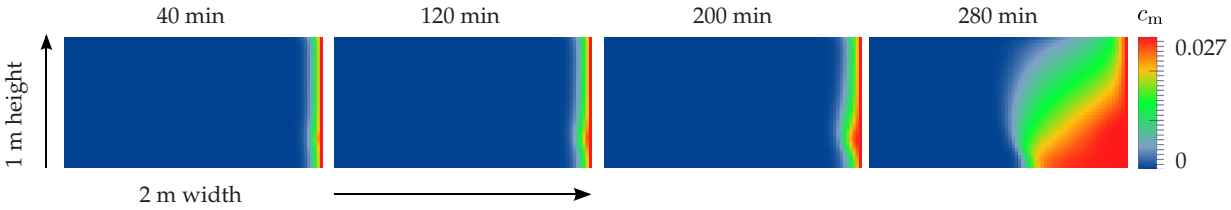

Fig. 1.: The Henry saltwater intrusion problem describes the steady state solution of a diffused saltwater front in an initially saturated fresh water confined aquifer. Results of the simulation for $\kappa = 1 \times 10^{-12}\,\mathrm{m}^2$ and $D_\mathrm{m} = 1.886 \times 10^{-6}\,\mathrm{m}^2\,\mathrm{s}^{-1}$.

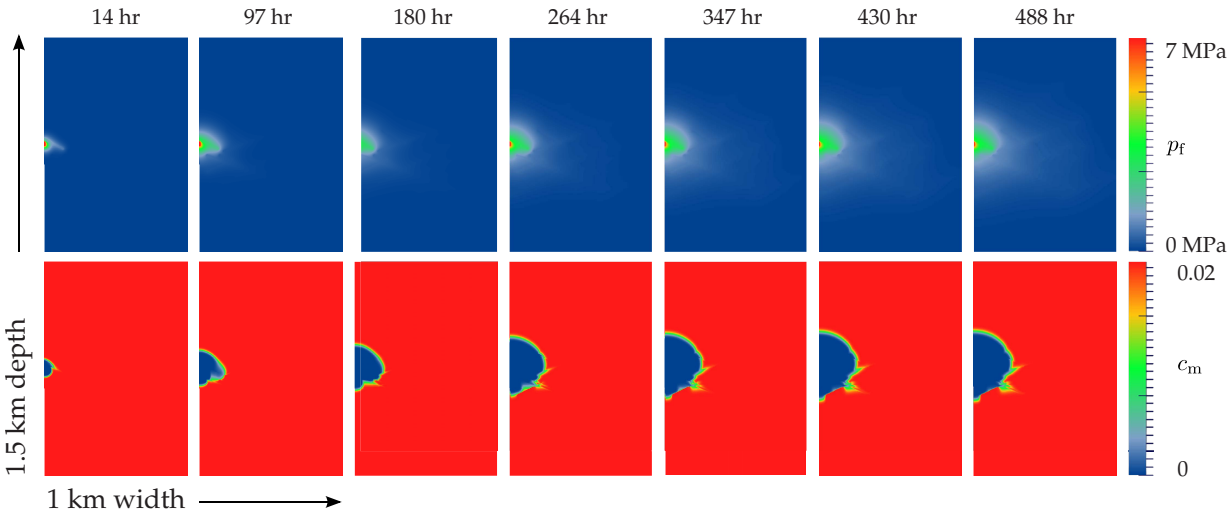

Fig. 2.: Results of a geothermal system simulation. Fresh cold water is injected in a hot fractured porous rock which is saturated with saline water. Figures on top show the pressure of the system while on bottom are the corresponding mass fraction diagrams.

Numerical Modelling of earthquake swarms in the Vogtland / West-Bohemia

Thomas Heinze, Sahar Hamidi, Boris Galvan, Stephen Miller

Geodynamics/Geophysics, Bonn University
e-mail: *heinze@geo.uni-bonn.de*
session: *Fluids and Deformation*

Introduction

An earthquake swarm is defined as a sequence without a single, dominant event (Yamashita, 1998). Field observations and numerical simulations suggest that fluid flow is an important component in the generation of earthquake swarms (Hainzl, 2004). In West Bohemia / Vogtland, earthquake swarms coincide with degassing of CO2 originating from the mantle. Young Quaternary volcanism with a magmatic body associated with a local Moho updoming is the assumed source for the CO2 that propagates through a pre-existing and re-stimulated fracture network (Weinlich et al., 1999). The fluids are suggested as a main trigger for earthquake activity in the region (e. g. Spicak & Horalek, 2001, Weise et al., 2001, Bräuer et al. 2003).

Earthquake swarms over the last decades concentrated in the Novy Kostel area (Czech Republik) within a region of several square kilometers. The earthquake swarms, with a maximum magnitude of 4.5, include several thousand micro-seismic events with hypocenters ranging between 6.5 km and 11 km, with some deeper around 13 km, and occur along a steeply dipping fault plane (Fischer & Horalek, 2003). Registered swarms occurred in 1985/1986, 1997, 2000, 2008 and 2011, during which previously ruptured areas were reactivated (Fischer et al., 2014).

Several numerical models have been applied to the West- Bohemian earthquake swarms, including a poro- elasto plastic finite element model to calculate stresses and strains (Kurz et al., 2003). These studies demonstrated that the regional stress field is insufficient to cause earthquake swarms, but when combined with fluid migration they show reasonable rates of deformation capable of earthquake swarms. Statistical approaches can reproduce the seismic pattern of the 2000 swarm (Hainzl, 2004), where a brittle patch surrounded by an elastic half- space is loaded by fluid migration and stress changes. The spatio-temporal distribution of the seismic events is shown to be dominated by stress triggering, with fluid migration acting as the initiator. Linear diffusion models (Parotidis et al., 2005) focused on a single fluid source to determine overall diffusivity.

In this work we develop and apply a model to simulate the flow of supercritical CO2 through a fracture network assuming non- linear diffusion with a stress and pressure dependent permeability and porosity (Rutqvist et al., 2002). We solve the diffusion-advection equations for the temperature of the rock and CO2, assuming local equilibrium. Stresses are calculated with a full poro-thermo-elasto- plastic rheological model taking hardening, softening and damage effects into account. Plastic deformation of rocks is modeled using the Griffith and Mohr-Coulomb criteria. Cohesion and internal friction angle are mobilized in terms of a cohesion weakening and frictional strengthening model (CWFS) (Hajiabdolmajid et al., 2002). The mobilized values for friction angle, cohesion and dilatancy angle are calculated as functions of the effective plastic stresses and a damage variable is calculated as a functions of plastic strain. Our theoretical model is implemented in

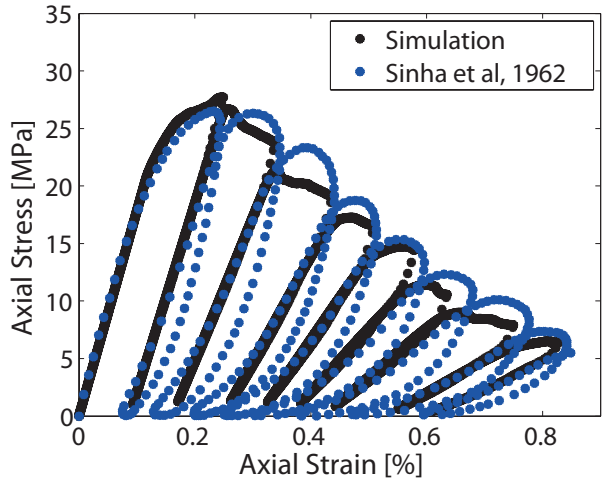

Fig. 1.: Comparison of experimental and simulated stress- strain response curve of an uniaxial compression cycling test of a concrete specimen. Experimental data taken from (Sinha et al., 1962).

a numerical scheme using finite differences on a staggered grid to simulate the dynamic behavior during loading and fluid injection. The numerical results of the model show very good agreement with laboratory results (figure 1). Coincidence was achieved for stress – strain relationships, volumetric and inelastic strain, fracture propagation and stress drop during fluid injection.

Estimating the seismic moment of a fracture generation or -propagation is of great interest in numerical simulations. Most published models are able to reproduce important features and behavior of the seismic events like the propagation of the seismic cloud from the borehole, the Kaiser- Effect and also give reasonable values for magnitudes and the overall distribution of the events. They are mainly tested at shale gas fields or geothermal sides.

We present an approach based on continuum mechanics to derive the seismic magnitude using the deviatoric strain as an indicator for rupture processes. A peak- detection algorithm is used to identify rapid changes that are then marked as seismic events. This method works very well on laboratory scale for dry and hydraulic fracturing (figure 2). In this work we apply the same mechanism to field scale to match the seismic characteristics of the earthquake swarm in the

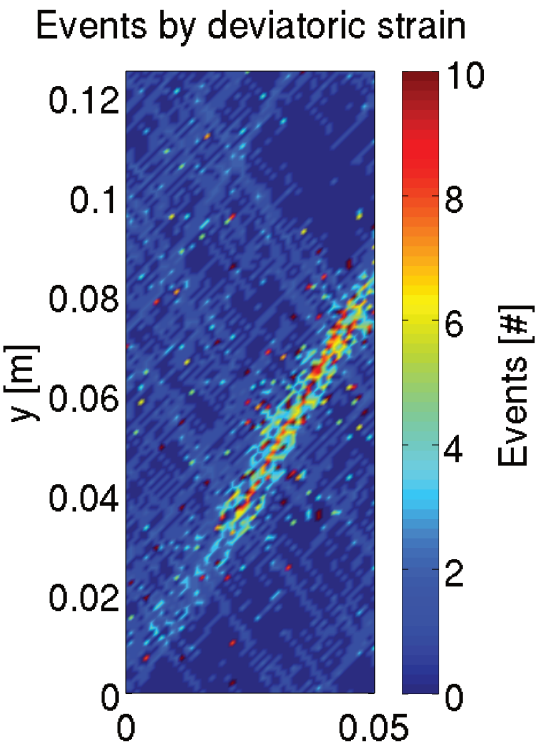

Fig. 2.: Numerical simulation of a confined compression experiment. Acoustic emissions are simulated using the deviatoric strain as a marker. Simulation results of acoustic emission fit to experimental observations (cf. Stanchits et al., 2011).

Vogtland / West Bohemia.

We numerically simulate the flow of hot, overpressured CO2 rising from below in a region from 5 km to 15 km depth mainly taking place in a preexisting fracture network (figure 3) which evolves during high pressure flow. We compare the results to field observations and the seismic measurements during the swarm activity, paying special attention to the seismic characteristics of the region.

References

Yamashita, T. (1998). Simulation of seismicity due to fluid migration in a fault zone. Geophysical Journal International, 132, p. 674-686.

Hainzl, S. (2004). Seismicity patterns of earth-

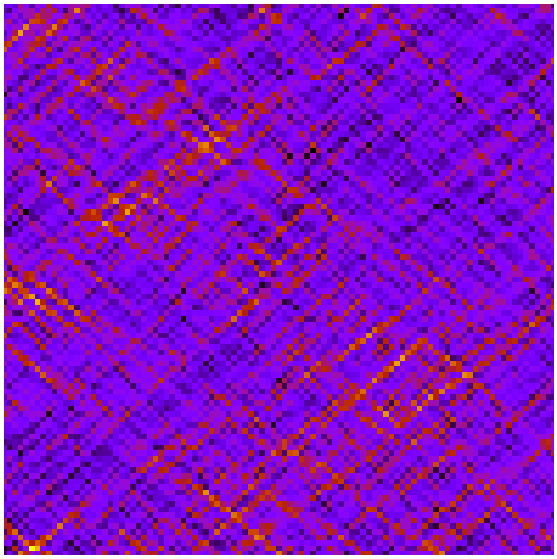

Fig. 3.: Deviatoric strain of a fracture network obtained from a numerical simulation of a compressive environment. Dimensions are 2 km x 2 km.

quake swarms due to fluid intrusion and stress triggering . Geophysical Journal International, 159, p.1090-1096.

Weinlich, F.H., Bräuer, K., Kämpf, H., Strauch, G., Tesar, J. Weise, S.M. (1999). An active subcontinental mantle volatile system in the western Eger rift, Central Europe: Gas flux, isotopic and compositional fingerprints. Geochimica et Cosmochimica Acta, 63(21), p. 3653-3671.

Spicak, A., Horalek, J. (2001). Possible role of fluids in the process of earthquake swarm generation in the West Bohemia/Vogtland seismoactive region. Tectonophysics, 336, p.151-161.

Weise, S.M., Bräuer, K., Kämpf, H., Strauch, G., Koch, U. (2001).Transport of mantle volatiles through the crust traced by seismically released fluids: a natural experiment in the earthquake swarm area Vogtland/NW Bohemia, Central Europe. Tectonophysics, 336, p.137-150.

Bräuer, K., Kämpf, H., Strauch,. G., Weise, S.M. (2003). Isotopic evidence (3He/4He, of fluid-triggered intraplate seismicity. Journal of Geophysical Research. 108(82).

Fischer, T., Horalek, J. (2003). Space-time distribution of earthquake swarms in the principal focal zone of the NW Bohemia/Vogtland seismoactive region: period 1985–2001. Journal of Geodynamics. 35, p. 125-144.

Fischer, T., Horalek, J., Hrubcova, P., Vavrycuk, V., Bräuer, K., Kämpf, H. (2014). Intracontinental earthquake swarms in West- Bohemia and Vogtland: A review. Tectonophysics, 611, p.1-27.

Kurz, J.H., Jahr, T., Jentzsch, G. (2003). Geodynamic modelling of the recent stress and strain field in the Vogtland swarm earthquake area using the finite element method. Journal of Geodynamics. 35, p. 247-258.

Parotidis, M., Shapiro, S.A., Rothert, E. (2005). Evidence for triggering of the Vogtland swarms 2000 by pore pressure diffusion. Journal of Geophysical Research, 110.

Rutqvist, J., Wu, Y.S., Tsang, C.F., Bodvarsson, G. (2002). A modeling approach for analysis of coupled multiphase fluid flow, heat transfer, and deformation in fractured porous rock. International Journal of Rock Mechanics & Mining Sciences, 39, p.429-442.

Hajiabdolmajid, V., Kaiser, P.K., Martin, C.D. (2002). Modelling brittle failure of rock. International Journal of Rock Mechanics & Mining Sciences, 39, p.731-741.

Sinha, B.P., Kurt, H. Gerstle, Tulin, L.G. (1964). Stress- Strain Relations for concrete under cyclic loading. Journal of the American Concrete Institute, 61(2), p.195-211.

Stanchits, S., Mayr, S., Shapiro, S., Dresen, G. (2011). Fracturing of porous rock induced by fluid injection. Tectonophysics, 503, p.129-145.

Modelling of fractured reservoirs: fluid-rock interactions within fault domains

Antoine Jacquey[1], Mauro Cacace[1,3], Guido Blöcher[1], Magdalena Scheck-Wenderoth[1,2]

[1]*Helmoltz Centre Potsdam, GFZ German Research Center for Geosciences, Potsdam, Germany*
[2]*RWTH Aachen, Germany*
[3]*Potsdam University, Potsdam, Germany*
e-mail: *ajacquey@gfz-potsdam.de*
session: *Fluids and Deformation*

The presence of a major fault can have significant impacts on the hydraulic and mechanical properties of the hosting rock. Different domains in terms of fluid and mechanical properties can be identified within a faulted region such as a low permeability fault core, a damage zone usually extending on both sides of the core where rocks are highly fractured and permeability increases and poorly fractured or intact rocks situated far away from the fault core [4, 7, 12], see figure 1. During geothermal operations, injection and production of fluid can induce significant pore pressure changes which impact the stress field thus affecting the reservoir rocks. In this context, the elastic and hydraulic properties of the porous rock can be altered by deformation of the pore and bulk volumes which in some cases may compromise the productivity of the geothermal system [3, 5]. Therefore special interest is given to porosity and permeability temporal evolutions as main properties controlling fluid transport processes within such systems.

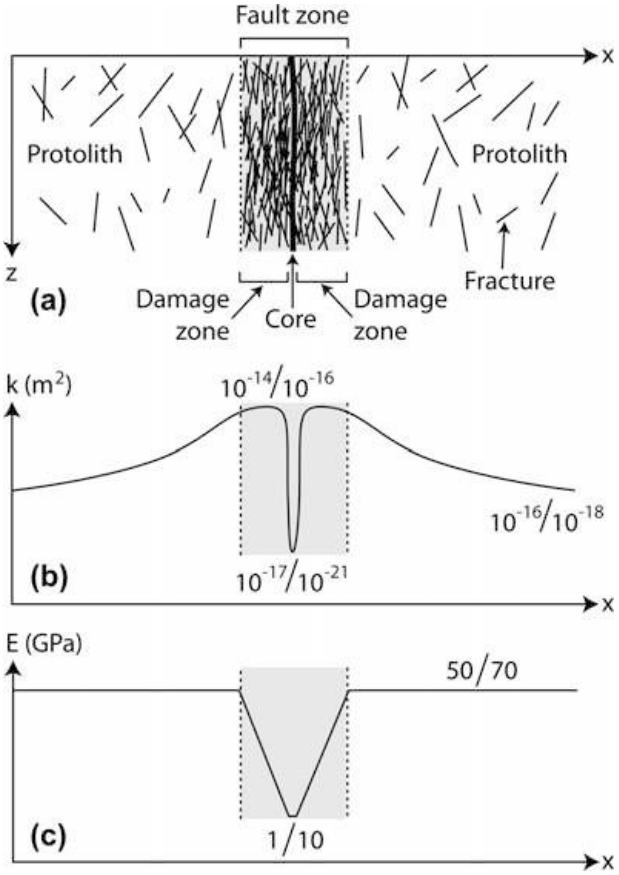

Fig. 1.: Fault zone configuration - example of the permeability and Young's modulus distributions [4]

The presence of fractures, their density, apertures and interconnectivity play a major role in affecting poroelastic processes within fault zones. While for a non fractured rock hydraulic properties will depend only on changes in pore volume as induced by elastic deformation of the pores, closure of fractures can induce important nonlinearities on the stress-strain relations [9]. Typical distributions are schematically shown in figure 1 for permeability (b) and Young's modulus (c).

Different behaviors in these two properties nicely illustrate how fractures may significantly impact processes occurring in these domains.

The aim of this project is to deepen current understanding of fundamental processes controlling fluid-rock interactions in fault zones. In a first step poroelastic formulations are derived which are based and validated on laboratory experiments on undamaged and damaged samples [2, 1, 8]. Porosity and permeability relations are the major focus of this project and their evolution is linked with the stress field or with pore pressure changes. An important interest will be given to the continuity of the formulations at the interface between two zones of the fault region. These formulations, implemented in a simulation software will be used in a future step to simulate a faulted geothermal system at the reservoir scale thus abling to analyze fluid-rock interactions within the fault and the impact of major fault zones on the system productivity.

Simulations are conducted using the open-source 3-D finite element method-based simulator OpenGeoSys [14, 16, 15, 10] which offers the possibility of solving coupled processes within a hybrid approach combining discrete fractures and continua models for fractured porous rocks. Porosity and permeability relations previously defined and validated have been implemented in the simulator.

The current results of the project will be presented, including porosity and permeability relations for undamaged samples. From [1], experimental data for porosity of two kinds of sandstone are presented. The availability of these data lead to first consider for this project these two sandstones: Flechtinger sandstone, a Lower Permian (Rotliegend) sedimentary rock from an outcrop near Flechtiner, Germany [11] and Bentheimer sandstone, a Lower Cretaceous sedimentary rock from an outcrop near Bentheim, Germany [6]. Unlike the Bentheimer sandstone which is very homogeneous (95 % quartz, 3 % kaolinite and 2 % orthoclase), Flechtinger sandstone is composed of quartz (55 – 65 %), rock fragments of volcanic origin (20 – 25 %) and feldspars (15 – 20 %). Different models [1, 13, 8] for sandstones have been investigated and compared to the laboratory measurements. From [13], porosity changes depend on the mean effective stress:

$$\phi = (\phi_0 - \phi_\mathrm{r})\, e^{A\sigma'_\mathrm{M}} + \phi_\mathrm{r} \tag{1}$$

Where ϕ_0 and ϕ_r are the initial and residual porosity (at high stresses), σ'_M the mean effective stress and A a coefficient.And from [1], porosity changes depend on drained experiment quantities such as the drained volumetric strain (equation (2)) or the drained bulk compressibility (equation (3)):

$$\phi = \frac{V_\phi^0 - e_V V_\mathrm{b}^0 + e_V^\mathrm{u}\left(V_\mathrm{b}^0 - V_\phi^0\right)}{V_\mathrm{b}^0 - e_V V_\mathrm{b}^0} \tag{2}$$

$$d\phi = -\left((1-\phi_0)\, C - C_\mathrm{s}^\mathrm{u}\right) dp_\mathrm{e} \tag{3}$$

Where V_ϕ^0 and V_b^0 are initial pore and bulk volumes, e_V and e_V^u the volumetric strains under drained and unjacketed conditions. C is the dreained bulk compressibility, C_s^u the unjacketed solid compressibility and p_e the Terzaghi effective pressure.

The validity of new poroperm relations is tested by simulating isothermal hydrostatic tests with increasing pore pressure on 3-D cylindrical rock samples under the same conditions as the laboratory experiments (see figure 2). In such configuration, the confining pressure is equal to the pore pressure. Experimental results from a drained hydrostatic test are used for some of the models in order to obtain poroperm relations fitting laboratory measurements [9]. An acting pressure from 0.1 MPa up to 70 MPa is considered with an increasing rate of 10 MPa h^{-1}. In these conditions the porosity decreases with increasing acting pressure due to changes in pore and bulk volumes.

Figure 3 shows the porosity evolution depending on the acting pressure for an undamaged sample of Flechtinger sandstone (sub-figure 3 a) and Bentheimer sandstone (sub-figure 3 b). For an acting pressure of 70 MPa, a decrease of 8,1 % and 1,4 % for the Flechtinger sandstone and for the Bentheimer sandstone are respectively observed. Two different domains are identified: under a certain acting pressure (20 MPa

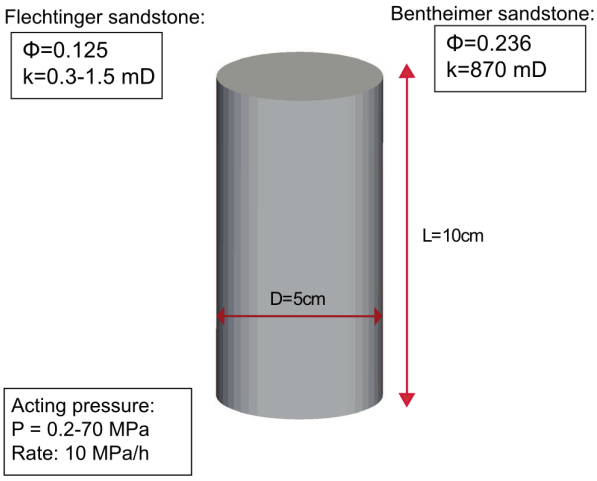

Fig. 2.: Simulation setup of the hydrostatic test and initial properties of the two sandstones

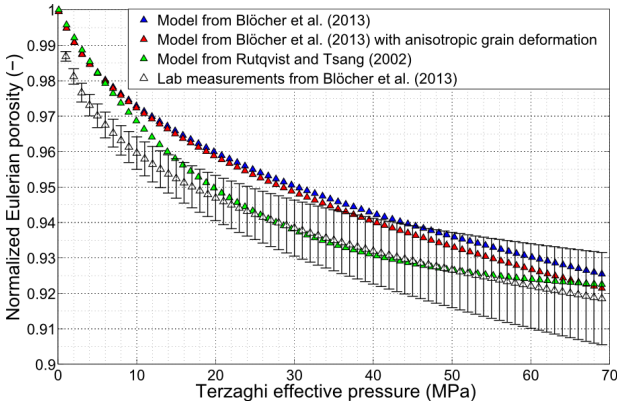

(a) Flechtinger sandstone

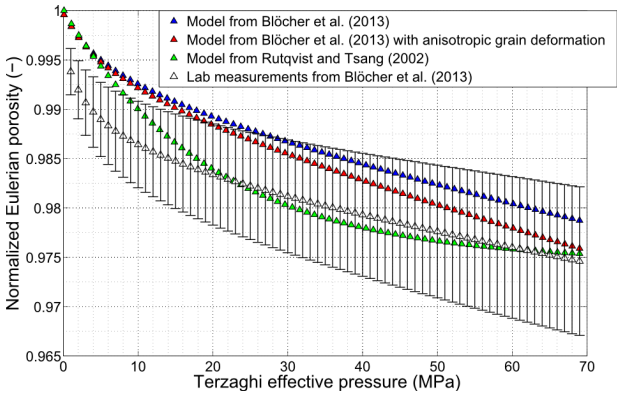

(b) Bentheimer sandstone

Fig. 3.: Normalized porosity evolution for the two mentioned sandstones

for Flechtinger sandstone and 10 MPa for Bentheimer sandstone) the porosity decreases non-linearly and linearly above this acting pressure. These two domains can be identified in the porosity computed with models from [1] but the model from [13] gives a better precision for the porosity in the considered acting pressure range. These results show that the porosity of the Flechtinger sandstone is more sensitive to a change of pore pressure than the porosity of the Bentheimer sandstone.

Permeability changes are linked to porosity changes and pore shape changes using the Kozeny-Carman permeability derived from the Hagen-Poiseuille equation. Following this approach, permeability changes can be expressed as a function of porosity changes and a Kozeny-Carman coefficient [9]:

$$k = A\frac{\phi^3}{(1-\phi)^2} \qquad (4)$$

Where A is a parameter which depends on the geometry of the pore and ϕ is the porosity. In [2], this poroperm relation has been evaluated for the Flechtinger sandstone and validated by comparison with experimental measurements of permeability. Figure 4 shows the computed permeabilites computed with equation (4). With this model, the permeability decrease shows the same evolution trend as for the porosity. A decrease of 27 % and 8 % for the Flechtinger and Bentheimer sandstones permeability respectively are observed for an acting pressure of 70 MPa. Such decrease can have significant impacts on fluid flow and accordingly also on a geothermal system productivity.

Different models have been tested for porosity and permeability changes under increasing pore pressure after being implemented in the finite element method-based simulator OpenGeoSys. Models for porosity which depend on measurements made in laboratory under drained conditions show a good trend but are strongly dependent on the available experimental data. In future work, changes for mechanical properties such as the bulk compressibility will be investigated for undamaged samples to generalize these porosity relations for different kind of sandstones. Then

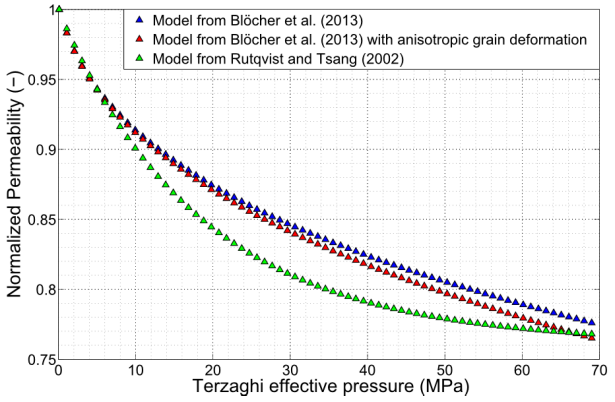

(a) Flechtinger sandstone

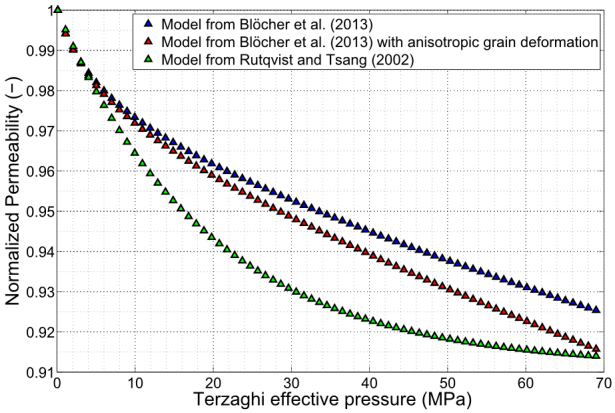

(b) Bentheimer sandstone

Fig. 4.: Normalized permeability evolution for the two mentioned sandstones

in next steps, the study of damaged sandstones will be performed in parallel with laboratory experiments with different fractures densities to complete the fault zone model.

References

[1] Guido Blöcher, Thomas Reinsch, Alireza Hassanzadegan, Harald Milsch, and Günter Zimmermann. Direct and indirect laboratory measurements of poroelastic properties of two consolidated sandstones. International Journal of Rock Mechanics and Mining Sciences, 67:191–201, April 2013.

[2] Guido Blöcher, Günter Zimmermann, and Harald Milsch. Impact of Poroelastic Response of Sandstones on Geothermal Power Production. Pure and Applied Geophysics, 166(5-7):1107–1123, May 2009.

[3] Mauro Cacace, Guido Blöcher, Norihiro Watanabe, Inga Moeck, Nele Börsing, Magdalena Scheck-Wenderoth, Olaf Kolditz, and Ernst Huenges. Modelling of fractured carbonate reservoirs: outline of a novel technique via a case study from the Molasse Basin, southern Bavaria, Germany. Environmental Earth Sciences, 70(8):3585–3602, March 2013.

[4] Frédéric Cappa. Modelling fluid transfer and slip in a fault zone when integrating heterogeneous hydromechanical characteristics in its internal structure. Geophysical Journal International, 178(3):1357–1362, September 2009.

[5] Y. Cherubini, Mauro Cacace, Magdalena Scheck-Wenderoth, and V. Noack. Influence of major fault zones on 3-D coupled fluid and heat transport for the Brandenburg region (NE German Basin). Geothermal Energy Science, 2(1):1–20, April 2014.

[6] Jeremie Dautriat, Nicolas Gland, Jean Guelard, Alexandre Dimanov, and Jean L. Raphanel. Axial and Radial Permeability Evolutions of Compressed Sandstones: End Effects and Shear-band Induced Permeability Anisotropy. Pure and Applied Geophysics, 166(5-7):1037–1061, May 2009.

[7] D.R. Faulkner, C.a.L. Jackson, R.J. Lunn, R.W. Schlische, Z.K. Shipton, C.a.J. Wibberley, and M.O. Withjack. A review of recent developments concerning the structure, mechanics and fluid flow properties of fault zones. Journal of Structural Geology, 32(11):1557–1575, November 2010.

[8] Alireza Hassanzadegan, Guido Blöcher, Harald Milsch, Luca Urpi, and Günter Zimmermann. The Effects of Temperature and Pressure on the Porosity Evolution of Flechtinger Sandstone. Rock Mechanics and Rock Engineering, 47(2):421–434, April 2013.

[9] Alireza Hassanzadegan and Günter Zimmermann. A Poroelastic Description of Permeabil-

ity Evolution. Pure and Applied Geophysics, October 2013.

[10] O. Kolditz, S. Bauer, L. Bilke, N. Böttcher, J. O. Delfs, T. Fischer, U. J. Görke, T. Kalbacher, G. Kosakowski, C. I. McDermott, C. H. Park, F. Radu, K. Rink, H. Shao, H. B. Shao, F. Sun, Y. Y. Sun, a. K. Singh, J. Taron, M. Walther, W. Wang, N. Watanabe, Y. Wu, M. Xie, W. Xu, and B. Zehner. OpenGeoSys: an open-source initiative for numerical simulation of thermo-hydro-mechanical/chemical (THM/C) processes in porous media. Environmental Earth Sciences, 67(2):589–599, February 2012.

[11] Harald Milsch, Guido Blöcher, and Silvio Engelmann. The relationship between hydraulic and electrical transport properties in sandstones: An experimental evaluation of several scaling models. Earth and Planetary Science Letters, 275(3-4):355–363, November 2008.

[12] T.M. Mitchell and D.R. Faulkner. The nature and origin of off-fault damage surrounding strike-slip fault zones with a wide range of displacements: A field study from the Atacama fault system, northern Chile. Journal of Structural Geology, 31(8):802–816, August 2009.

[13] J. Rutqvist, Y.-S. Wu, C.-F. Tsang, and G. Bodvarsson. A modeling approach for analysis of coupled multiphase fluid flow, heat transfer, and deformation in fractured porous rock. International Journal of Rock Mechanics and Mining Sciences, 39(4):429–442, June 2002.

[14] Wenqing Wang and Olaf Kolditz. Object-oriented finite element analysis of thermo-hydro-mechanical (THM) problems in porous media. International Journal for Numerical Methods in Engineering, 69(May 2006):162–201, 2007.

[15] Nori Watanabe, W Wang, J Taron, U. J. Görke, and O Kolditz. Lower-dimensional interface elements with local enrichment : application to coupled hydro-mechanical problems in discretely fractured porous media. International Journal for Numerical Methods in Engineering, pages 1010–1034, 2012.

[16] Norihiro Watanabe, Wenqing Wang, Christopher I. McDermott, Takeo Taniguchi, and Olaf Kolditz. Uncertainty analysis of thermo-hydro-mechanical coupled processes in heterogeneous porous media. Computational Mechanics, 45(4):263–280, November 2009.

Heat transport mechanisms at different scales – a 3D modelling workflow

Magdalena Scheck-Wenderoth[1,2], Mauro Cacace[1,3], Judith Sippel[1], Yuriy Petrovich Maystrenko[1,4], Yvonne Cherubini[1,3], Vera Noack[1,3,5], Björn Onno Kaiser[1,3,6], Björn Lewerenz[1]

[1]*Helmholtz Centre Potsdam GFZ German Research Centre for Geosciences, Telegrafenberg, D-14473 Potsdam, Germany*
[2]*RWTH Aachen, Germany*
[3]*Potsdam University, Potsdam, Germany*
[4]*Geological Survey of Norway (NGU), Trondheim, Norway*
[5]*Bundesanstalt für Geowissenschaften und Rohstoffe, Dienstbereich Berlin, Germany*
[6]*DHI-WASY GmbH, Berlin, Germany*
e-mail: *sippel@gfz-potsdam.de*
session: *Fluids and Deformation*

Temperature plays a crucial role for many processes affecting the lithosphere, from fluid-rock interactions on the micro scale to the rheology-dependent deformation of an entire lithospheric plate. The thermal field of the lithosphere is controlled by heat transport mechanisms – namely conduction, advection, and convection – with diverse relative importance at different scales. We compare differently detailed 3D structural models from the Central European Basin System (CEBS) to assess the sensitivity of temperatures to (1) the heat transport mechanisms considered, (2) the configuration of the lithosphere in terms of 3D distribution of thermal and hydraulic properties and (3) fault-controlled groundwater flow. Based on the analysis of differently scaled models, we propose a strategy for modelling the geothermal field of sedimentary basins from the lithospheric to the local (reservoir) scale (Scheck-Wenderoth et al., 2014). This workflow has a hierarchical structure and shows how the results of larger scale simulations can be used as input and boundary conditions for smaller and more detailed models. The general applicability of this workflow and the resulting 3D temperature distributions make it of interest for a broad range of geoscientific studies including thermo-mechanical modelling of lithospheric deformation or geothermal utilisation.

3D thermal models of the entire CEBS (e. g. Scheck-Wenderoth & Maystrenko, 2013; Fig. 1, 2) have shown that conduction is the dominant heat transport mechanism on the lithospheric scale. The thermal field is thus strongly controlled by the distribution of thermal conductivities caused by compositional and thickness variations of the highly conductive lithospheric mantle and crystalline crust as well as the insulating sedimentary cover. Among the sediments, rock salt plays an exceptional role because of its strongly varying thicknesses in the region and its very high thermal conductivity, which together produce strong (even though short-wavelength) thermal anomalies. Variable thicknesses of the upper crystalline crust induce thermal anomalies of larger wavelengths related to the large amount of radiogenic heat produced by these felsic rocks. Finally, the depth distribution of the thermal lithosphere-asthenosphere boundary (LAB) controls the basin-wide temperature distribution as

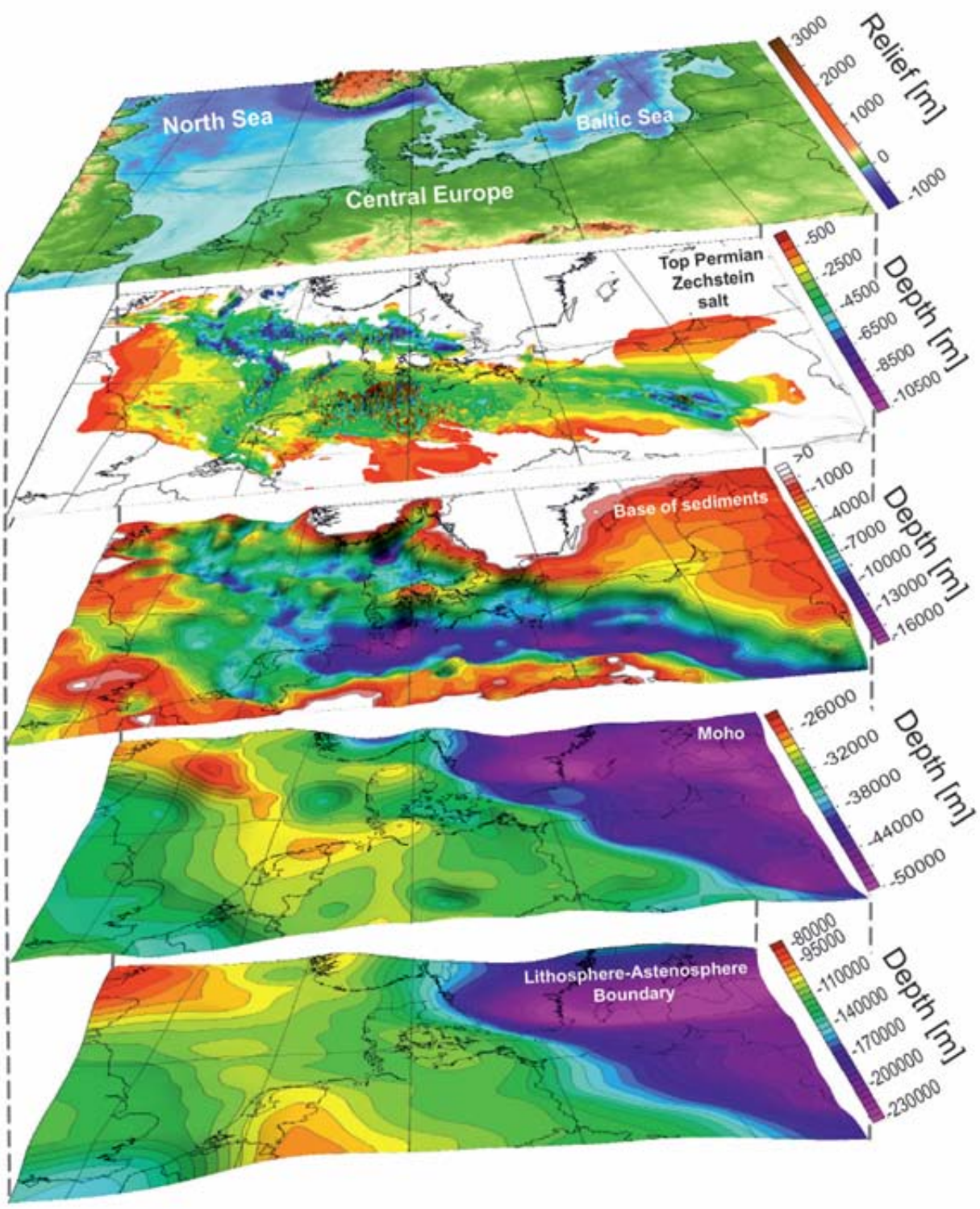

Fig. 1.: 3D structural model of the CEBS used for purely conductive thermal simulations (Scheck-Wenderoth & Maystrenko, 2013). The selected surfaces are relevant for the thermal field. The lithosphere-scale model covers an area of about 1000x1800 km with a horizontal resolution of $\sim 4\,\mathrm{km}$. It resolves eight sedimentary units (including a layer of mobilised Upper Permian Zechstein salt), two layers of the crystalline crust and the lithospheric mantle (after Maystrenko & Scheck-Wenderoth, 2013).

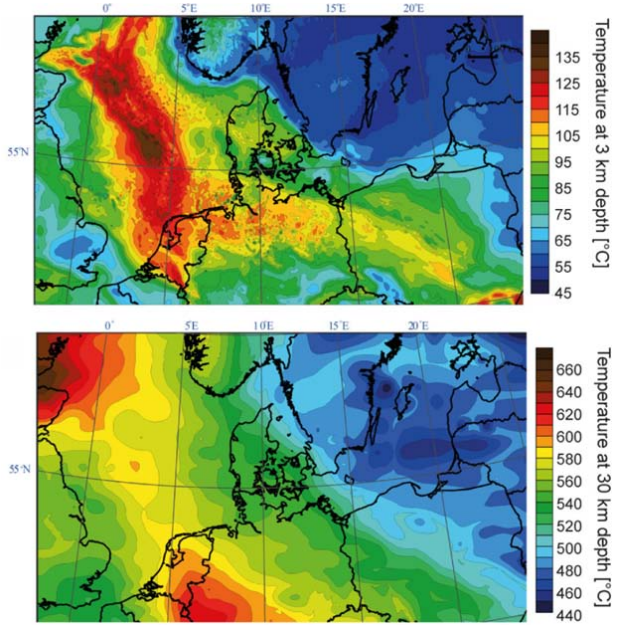

Fig. 2.: Results of the 3D thermal model of the CEBS with modelled temperature at 3 km and 30 km depth (below sea level; Scheck-Wenderoth & Maystrenko, 2013).

it represents the depth of commencing partial melting of the mantle and thus an isotherm (of ~1300 °C). Knowing the depth of this isotherm thus provides a suitable lower boundary condition for thermal models of entire sedimentary basins.

The same factors (thermal conductivity, radiogenic heat production, and depth of the LAB) decide upon the distribution of temperatures on the regional scale, such as over the subsurface of the federal state of Brandenburg (e. g. Noack et al., 2012). For this reason, it is essential to consider information on the configuration of the deep crust and upper mantle also on the regional scale. However, local deviations of modelled temperatures from measured (borehole) temperatures also provide indications for moving fluids. Modelling the coupled transport of heat and fluid is numerically far more expensive and requires higher resolution of the subsurface geology and hydrogeology. Therefore, only models of a limited size can be studied with such simulations. Accordingly, the influence of fluid flow on the regional thermal field was successfully assessed for the area of Brandenburg down to a depth of 6 km (below sea level; Noack et al., 2013), thereby using well-constrained lower boundary conditions derived from lithosphere-scale thermal models of the CEBS.

On the local scale, groundwater flow and the corresponding temperature and pressure distributions might be influenced by the existence of faults and the related variations in hydraulic properties (Cherubini et al., 2014). Permeable faults may focus fluid flow and cause local convective instabilities along the fault area. Furthermore, 3D models show that free (density-driven) convection can occur locally, namely where the permeability and the thickness of geological layers are large enough and the hydraulic gradients low (e. g. Kaiser et al., 2011). To numerically reproduce such local processes related to coupled heat and groundwater transport along faults or the development of stable convective cells, even higher-resolved 3D models are required providing a high degree of detail on the distribution of hydraulic properties. Again, results from larger scale models can be exploited to extract suitable thermal and hydraulic boundary conditions for local high-resolution models.

References

Cherubini, Y., Cacace, M., Scheck-Wenderoth, M., Noack, V. (2014): Influence of major fault zones on 3-D coupled fluid and heat transport for the Brandenburg region (NE German Basin). Geoth. Energ. Sci., 2, 1–20, 2014; doi:10.5194/gtes-2-1-2014.

Kaiser, B. O., Cacace, M., Scheck-Wenderoth, M., Lewerenz, B. (2011): Characterization of main heat transport processes in the Northeast German Basin: Constraints from 3D numerical models. Geochemistry, Geophysics, Geosystems 12 (7), 1-17; doi:10.1029/2011GC003535.

Maystrenko, Y. P., Scheck-Wenderoth, M. (2013): 3D lithosphere-scale density model of the Central European Basin System and adjacent areas. Tectonophysics 601, 53-77.

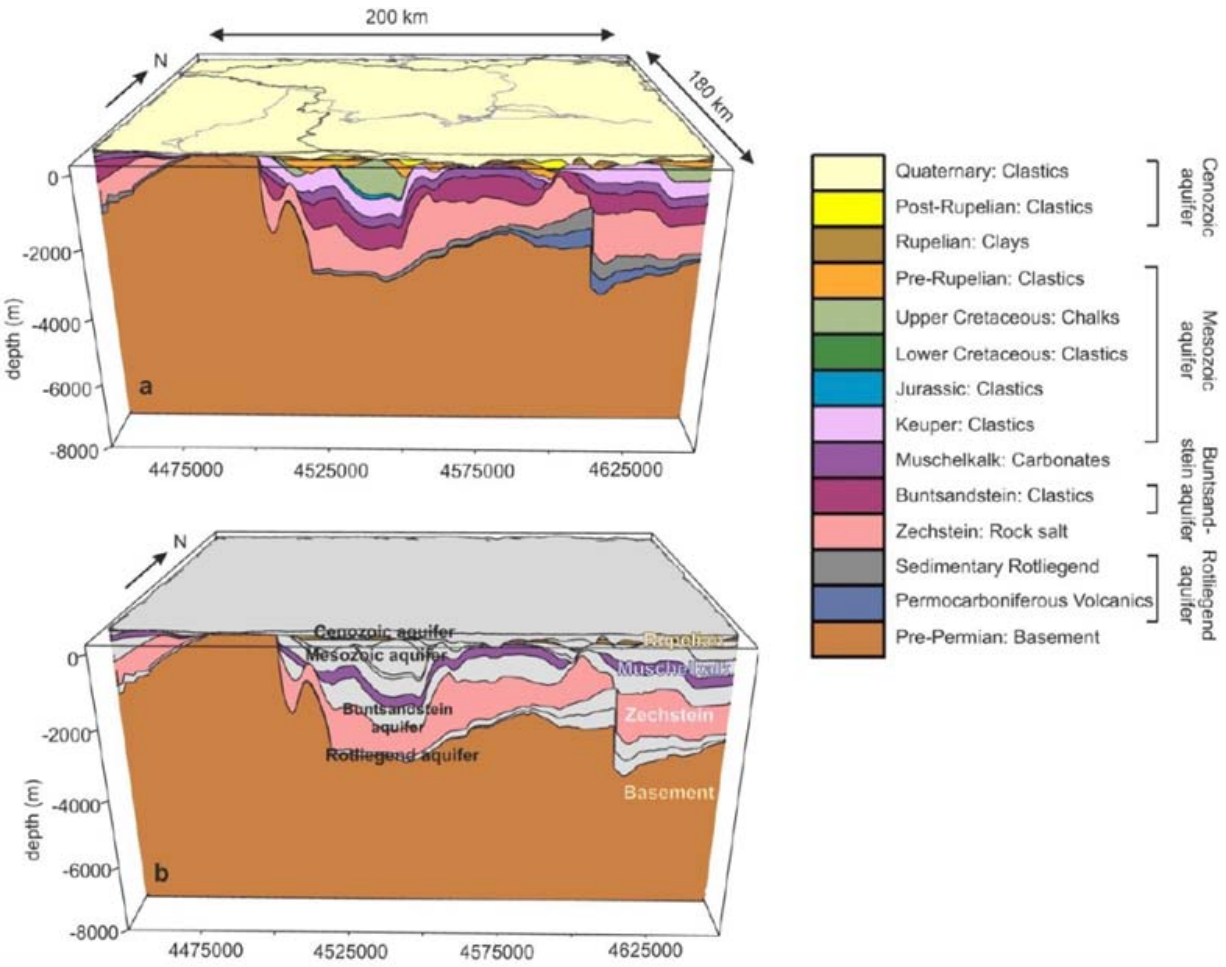

Fig. 3.: 3D geological model of Brandenburg (Noack et al., 2013) used for 3D coupled fluid and heat simulations (e. g. Cherubini et al., 2014); a) stratigraphic layers; b) aquitards (white) and aquifers (black).

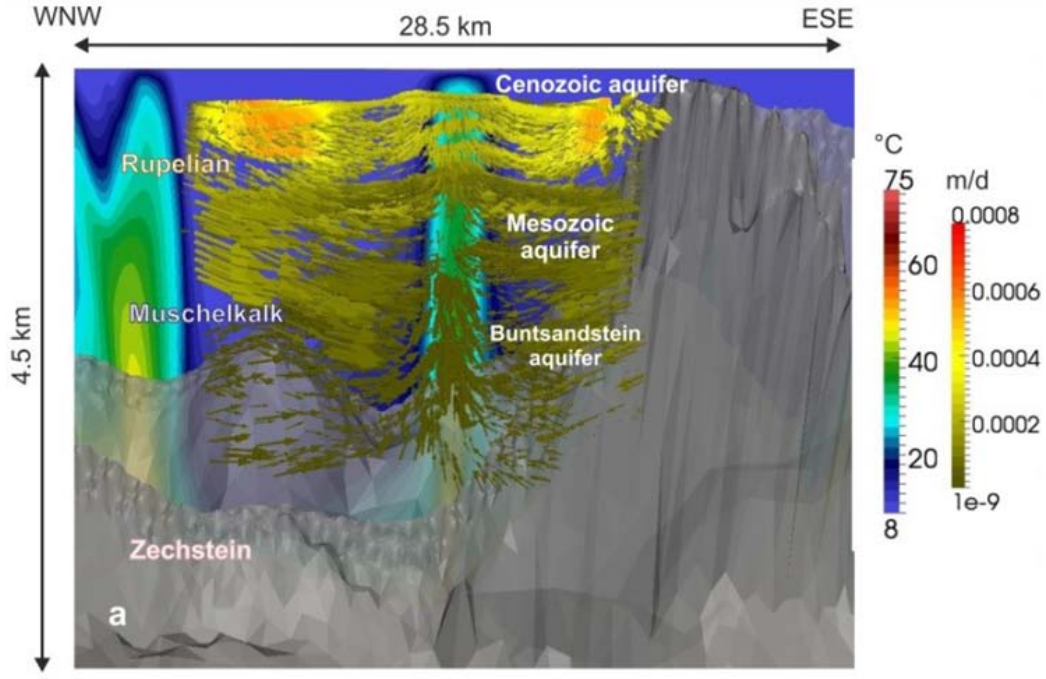

Fig. 4.: 3D flow field around a permeable fault zone (Cherubini et al., 2014). Grey-shaded is the impervious Permian Zechstein salt layer. The Gardelegen fault zone is presented by its temperature distribution in the background. Groundwater flow is directed from the surrounding aquifers towards the fault zone (velocity vectors).

Noack, V., Scheck-Wenderoth, M., Cacace, M. (2012): Sensitivity of 3D thermal models to the choice of boundary conditions and thermal properties: a case study for the area of Brandenburg (NE German Basin). Environ. Earth. Sci. (2012) 67:1695–1711; doi: 10.1007/s12665-012-1614-2.

Noack, V., Scheck-Wenderoth, M., Cacace, M., Schneider, M. (2013): Influence of fluid flow on the regional thermal field: results from 3D numerical modelling for the area of Brandenburg (North German Basin). Environ. Earth. Sci. (2013) 70: 3523-3544, doi: 10.1007/s12665-013-2438-4.

Scheck-Wenderoth, M., Maystrenko, Y. P. (2013): Deep control on shallow heat in sedimentary basins. Energy Procedia 40, 266-275.

Scheck-Wenderoth, M., Cacace, M., Maystrenko, Y. P., Cherubini, Y., Noack, V., Kaiser, B. O., Sippel, J., Lewerenz, B. (2014): Models of heat transport in the Central European Basin System: Effective mechanisms at different scales. Marine and Petroleum Geology, doi: 10.1016/j.marpetgeo.2014.03.009.

Digital rock physics: Insight into fluid flow and elastic deformation of porous media

Takeshi Tsuji

International Institute for Carbon-Neutral Energy Research, Kyushu University
e-mail: *tsuji@i2cner.kyushu-u.ac.jp*
session: *Fluids and Deformation*

Introduction

Digital rock physics combines modern microscopic imaging with numerical simulation for analysis of the physical and hydrological properties (e. g., Saenger et al., 2011). Recent technology developments of X-ray microcomputed tomography (micro-CT) as well as computational capacity for numerical simulation enable us to apply digital rock physics to realistic rock samples. Using digital pore models (Fig. 1), we study porous flow, fluid-solid interaction, interfacial phenomena, elastic and inelastic deformation, and mineral precipitation within real pore space. Since it allows us to estimate hydrological and elastic properties under several subsurface conditions (e. g., pressure), we can conduct virtual laboratory experiments in various reservoir conditions (e. g., Saenger et al., 2010; Tsuji et al., 2012; Jiang et al., 2014).

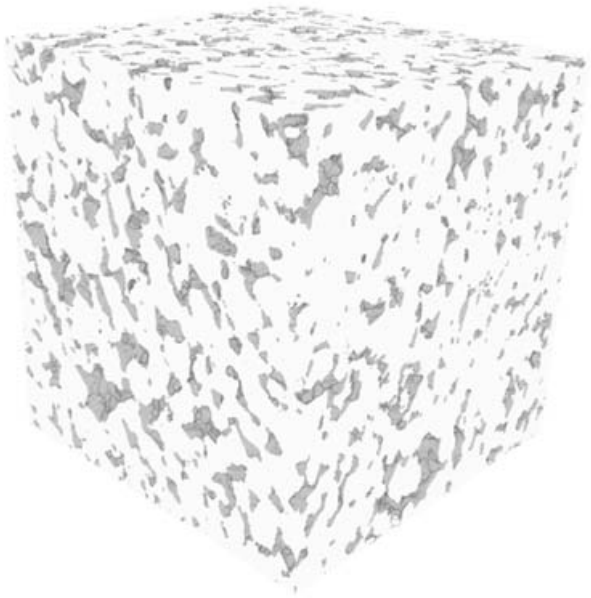

Fig. 1.: Three-dimensional pore geometry of Berea sandstone reconstructed from scanned micro tomographic image. Gray indicates the pore space.

Here we mainly show the application of digital rock physics for Carbon dioxide Capture and Storage (CCS). In CCS projects, CO_2 injected into the subsurface reservoir can be trapped according to several mechanisms, including structural and stratigraphic trapping, capillary trapping, dissolution, and chemical reaction (or mineral precipitation). The behavior of CO_2 inside pore space can be characterized as two-phase flow in a porous media system, which is usually influenced by interfacial tension, pore structure, pressure, wettability, and etc. Therefore, we believe that digital rock physics significantly contributes to reveal multi-phenomena in porous medium occurred in the CCS project.

To characterize properties of CO_2 injection reservoirs, we can apply digital rock physics to geophysical properties (e. g., seismic velocity). We usually use rock physics models (analytical models; Tsuji and Iturrino, 2008) or empirical relations (Tsuji et al., 2011) in order to estimate physical properties from seismic velocity. Using rock physics models, for example, we predict pore pressure distribution from high-resolution seismic velocity derived from waveform tomography (Tsuji et al., 2014). However, the analytical models (e. g., differential effective medium theory) can

be applied only for the limited or simplified pore geometry (e. g., crack). The digital rock physics can construct the relationship between elastic properties and subsurface properties by considering realistic pore geometry and various reservoir conditions. Here we also show our recent studies of digital rock physics to construct the relationship between elastic properties and subsurface properties under several conditions (Tsuji et al., 2012).

To predict long-term CO_2 behavior within the reservoir in CCS projects, we use reservoir simulation. A key parameter in the reservoir simulation is "relative permeability". Although the hydrological properties are significantly influenced by mineral precipitation due to CO_2 injection (e. g., change of pore space) and dissolution, it is difficult to estimate time evolution of these properties. The elastic properties (e. g., P-wave velocity) derived from time-lapse seismic survey are also influenced by mineral precipitation. Using digital rock approach, we can simulate mineral precipitation and estimate time-evolution of (1) hydrological properties (e. g., relative permeability) for reservoir simulation and (2) elastic properties for geophysical monitoring. Recently we have developed numerical calculation methods to model carbonate precipitation during long-term CO_2 storage (Jiang and Tsuji, in revision).

Digital rock model

The digital rock model used in this study was extracted from images of a cylindrical core of Berea sandstone obtained by multi-slice micro-CT scanner (Fig. 1). Berea sandstone is well-sorted sandstone with relatively large size of grain. The resolution of the scanned images is 3.2 µm. Total data sets are composed of 396 slices with interval of 5 µm. In the image data, each pixel corresponds to CT value, which is proportional to the density of the material. To identify and label the pore and grain phases within the images, the segmentation process is carried out by using a single grayscale threshold method to match typical porosity of Berea sandstone (~21 %). Consequently, these segmented 2D pixel images are linearly interpolated to generate voxel-based 3D volume with 3.2 µm (Fig. 1).

Two-phase LBM modeling

The fluid velocity field within the 3D pore spaces is calculated using the two-phase lattice Boltzmann method (LBM). In this study, we show the results using the color gradient model (Tölke et al., 2006) to treat the multi-phase problem. No-slip boundary conditions are imposed at all solid nodes including the precipitated minerals via a half-way bounce-back scheme. To increase the computation efficiency, we applied the graphics processor unit (GPU) parallel computing technique (e. g., Jiang et al., 2014). The advantages of GPU computing, including large memory bandwidth and low cost, make it suitable for conducting large-scale computation on a small-scale GPU-based cluster (Tölke and Krafczyk, 2008). Using this technique, we can conduct two-phase LBM simulation for the largest grid size in the world (~1000^3; Fig. 2). The two-phase LBM simulation was often applied to the pore-scale model in order to characterize fluid flow within one pore throat with micrometer scale. Due to the GPU utilization, however, size of the digital rock is approaching to laboratory-scale (~centimeter scale). Therefore, the GPU computation could bridge a gap between pore-scale phenomena and laboratory-scale phenomena.

We estimate hydrological properties under several reservoir conditions (e. g., interfacial tension) from CO_2 behavior within pore space (Fig. 3). The relative permeability decreases with increasing IFT because of growing capillary trapping intensity (Fig. 3). In extremely low IFT conditions, the capillary trapping phenomenon disappears, and the curvatures of the relative permeability curves diminish (Jiang et al., 2014). The relative permeability estimated for several reservoir conditions is crucial information in reservoir simulation.

The elastic properties (e. g., P-wave and S-wave velocities) of CO_2 saturated rock sample

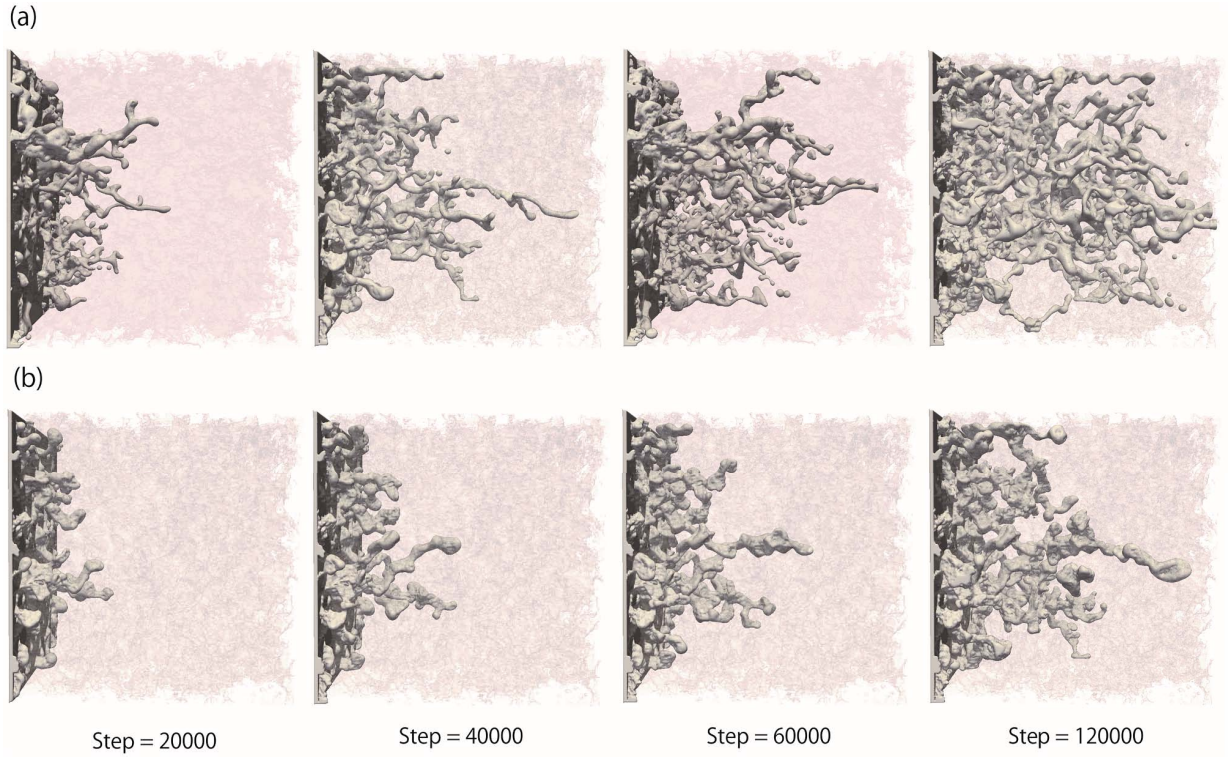

Fig. 3.: Non-wetting fluid invasion simulation of (a) low interfacial tension case and (b) high interfacial tension case (Jiang et al., 2014). The solid phase is shown in light gray, and the wetting fluid is transparent. The non-wetting white fluid is injected from left to right. The size of the calculated cube is 1.024 mm.

obtained via LBM (Fig. 3) are calculated by applying staggered finite-difference time-domain (FDTD) method (Saenger et al., 2011; Fig. 4). By using different frequency of source Ricker wavelet, we can estimate frequency dependence of elastic properties. Seismic velocity and quality factor can be estimated under several reservoir conditions (e. g., interfacial tension). We further obtain the relationships between seismic velocity and CO_2 saturation in drainage and imbibition processes.

Mineral precipitation modeling: Time-evolution of hydrological and elastic properties

In CCS project, the injected CO_2 would be precipitated. The carbonate precipitation process is represented as a two-component system of Ca^{2+} and CO_3^{2-}. The rate of precipitation is controlled by both changes in Ca^{2+} and CO_3^{2-} concentration in the fluid. Here, considering the equilibrium conditions, we only calculate one-component fluid with calcite for convenience (Yoo et al., 2013; Jiang and Tsuji, in revision). The calcite deposition within the pore space is calculated by using an advection–reaction formulation solved by finite volume method (FVM); we model the precipitated rock by transferring the fluid node to solid node according to the calcium concentration level. The clogging model updates the solid phase according to precipitation process and consequently changes the geometry and porosity of the sample rock. Then fluid solver is called to recalculate the flow field based on the evolved pore microstructures. Our calculation shows that deposition location depends on not only the fluid velocity field but also the rock structure. To validate our method, the carbonate precipitation simulation is carried out on a beads pack model and compared with laboratory experiment (Yoo et al.

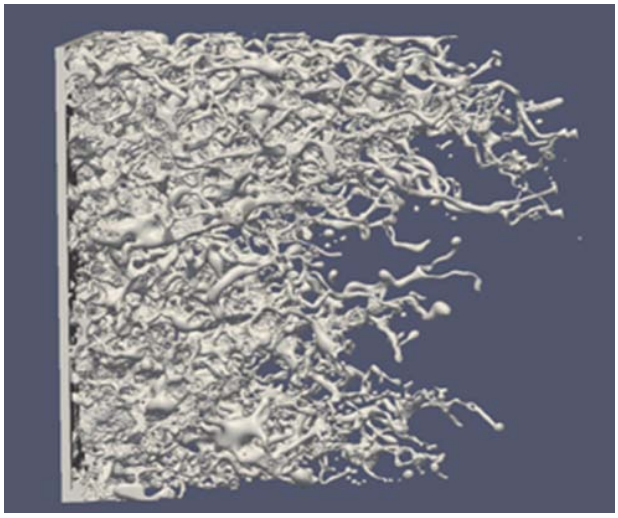

Fig. 2.: Example of CO_2 behavior within pore space of Berea sandstone using two-phase lattice Boltzmann method. The left is inflow side. White indicates the injected CO_2. This grid size is 1000x1000x1000.

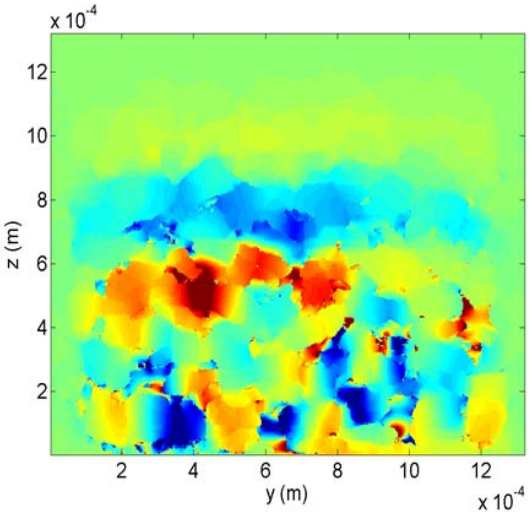

Fig. 4.: Elastic deformation of the LBM-derived CO_2 saturated rock (Fig. 3). Elastic wave propagates from bottom to top. Color shows the velocity distribution.

2013). Since the simulation results are in consistent well with the experiment data, our method can simulate realistic mineralization process.

The calculated permeability variation due to the carbonate precipitation demonstrates that evolution of pore structure significantly influences the absolute permeability, while it only affects the relative permeability of non-wetting phase at low water saturation conditions. Because the non-wetting phase occupies most of the pore spaces at low wetting saturation conditions, the movement of non-wetting fluid is suppressed due to the increased capillary pressure associated with mineralization. Whereas, for high wetting saturation conditions, the relative permeability is less influenced because the non-wetting fluid inside the pore turns to separated droplets and it is possible for those droplets to pass the pore throat. These observations can be used in the long-term reservoir simulation to estimate future CO_2 behaviors.

The elastic properties obtained via FDTD to the mineralized digital rock samples demonstrate that elastic properties are much influenced by the mineralization features. The relationship between seismic velocity and porosity derived from our mineralization simulation is different from that derived from other mineralization methods (i. e., CT threshold adjacent method; Jiang and Tsuji, in revision). This information related to the time-evolution of elastic properties can be used in geophysical monitoring for the injected CO_2.

Acknowledgement

I worked this study with Drs. F. Jiang and T. Ikeda. We gratefully acknowledge the support of the I2CNER, sponsored by the World Premier International Research Center Initiative (WPI), MEXT, Japan.

References

Jiang, F., T. Tsuji, and C. Hu (2014), Elucidating the role of interfacial tension for hydrological properties of two-phase flow in natural sandstone by an improved lattice Boltzmann method, Transport in Porous Media, doi:10.1007/s11242-014-0329-0.

Jiang, F., and T. Tsuji (2014), Evolution of Pore-geometry and Relative Permeability due to Carbonate Precipitation in Porous Media, Physical Review E, in moderate revision.

Saenger, E.H., F. Enzmann, Y. Keehm, H. Steeb (2011), Digital rock physics: Effect of fluid viscosity on effective elastic properties, Journal of Applied Geophysics, 74, 236-241.

Tölke, J., et al. (2006), An adaptive scheme using hierarchical grids for lattice Boltzmann multiphase flow simulations, Computers & Fluids, 35, 820-830.

Tölke, J. and M. Krafczyk (2008), Tera FLOP computing on a desktop PC with GPUs for 3D CFD, International Journal of Computational Fluid Dynamics, 22, 443-456.

Tsuji, T., and G. Iturrino (2008), Velocity-porosity relationships of oceanic basalt from eastern flank of the Juan de Fuca ridge: The effect of crack closure on seismic velocity, Exploration Geophysics, 39, 41-51.

Tsuji, T. et al. (2011), In situ stress state from walkaround VSP anisotropy in the Kumano basin southeast of the Kii Peninsula, Japan, Geochem. Geophys. Geosyst., 12, Q0AD19, doi:10.1029/2011GC003583.

Tsuji, T., H. Yamabe, T. Matsuoka (2012), LBM simulation for CO2 saturation monitoring from elastic velocity and resistivity: Migration of supercritical CO2 in porous media under several PT conditions, AGU fall meeting, GC51A-1176.

Tsuji, T., R. Kamei, and G. Pratt, (2014), Pore pressure distribution of a mega-splay fault system in the Nankai Trough subduction zone: Insight into up-dip extent of the seismogenic zone,Earth and Planetary Science Letters, 396, 165-178, doi:10.1016/j.epsl.2014.04.011.

Yoo, S.Y., et al. (2013), A geochemical clogging model with carbonate precipitation rates under hydrothermal conditions, Applied Geochemistry, 30, 67-74.

GFZ
Helmholtz Centre
POTSDAM

GeoMod2014

Modelling in Geosciences

Programme & Extended Abstracts

31 August - 5 September 2014

Editors:
Kirsten Elger
Øystein Thordén Haug
Malte Ritter

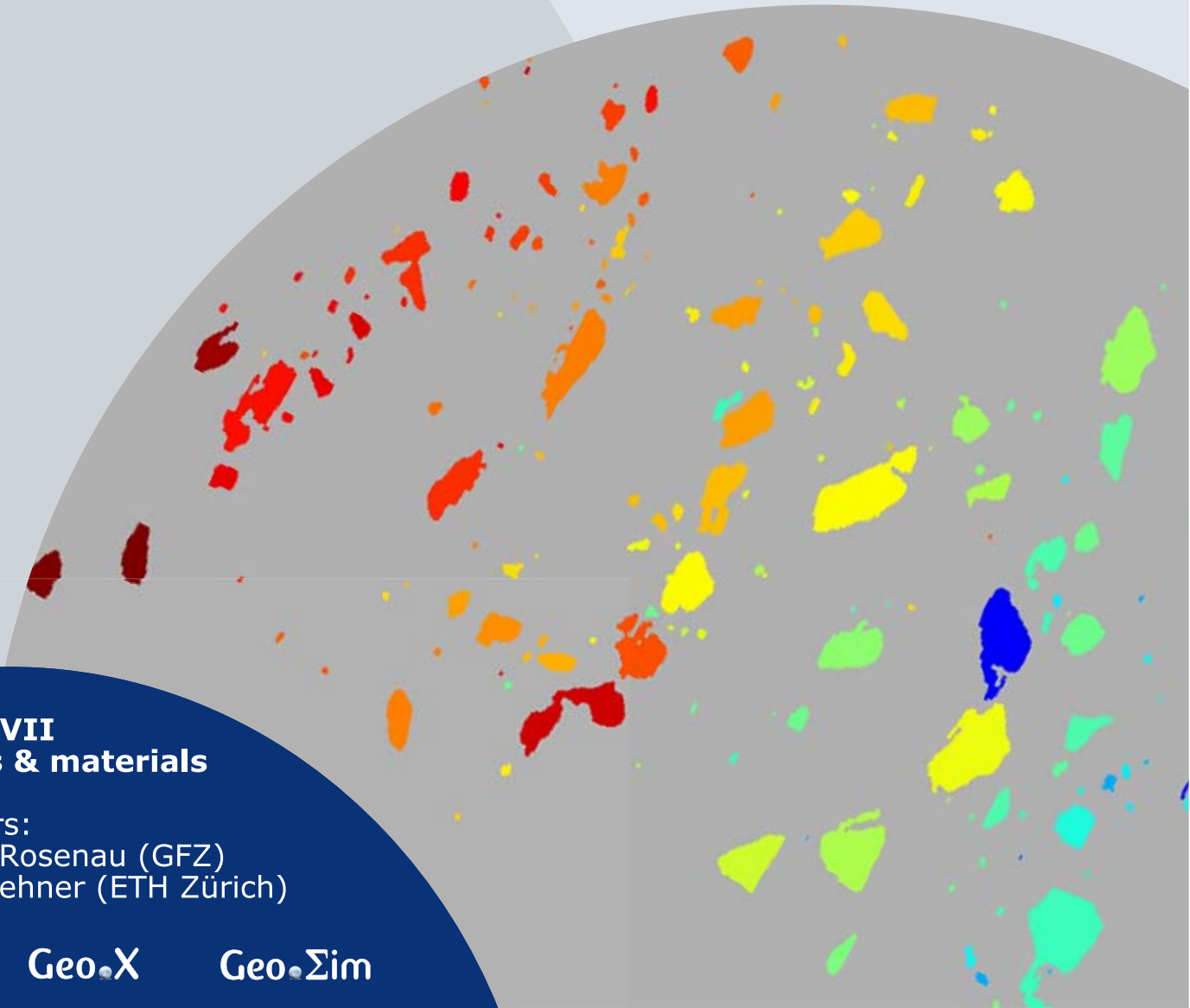

Session VII
Methods & materials

Conveners:
Matthias Rosenau (GFZ)
Marcel Frehner (ETH Zürich)

DFG Geo.X Geo.Sim

Session VII.

Methods and Materials

Session Description: Methods and Materials

Conveners: Matthias Rosenau (GFZ), Marcel Frehner (ETH Zürich)

In parallel to contributions to the thematic sessions of GeoMod 2014 we encourage all participants to present methodological advances in modelling, both analogue and numerical, in a special session which will consist of posters only. Contributions might include but are not limited to e.g. the development of new analogue materials, experimental setups, monitoring techniques as well as technical advances in mathematical approaches of simulation, analysis, visualization, data assimilation, etc.

Seismological monitoring of labscale landslides: Method & bouncing ball benchmark

Zahra Amirzada[1], Øystein Thordén Haug[1], Arnaud Burtin[1], Tuna Eken[1], Matthias Rosenau[1]

[1] *Helmholtz-Zentrum - GFZ Potsdam*
e-mail: *lg020@zedat.fu-berlin.de*
session: *Methods and Materials*

Introduction

Seismological monitoring of landslides, the remote detection and quantification of slope processes by seismometers, is an emerging field in earth and environmental science integrating geomorphological and geophysical methods (Petley, 2013; Burtin et al., 2013). The potential of the method is to invert seismic signals for a suite of aspects of event dynamics such as volume, velocity as well as details of the fragmentation process. For a sound interpretation of landslide signals in nature, knowledge of the responsible seismic sources and how the energy is transferred to the detector is paramount. However, because most events lack direct observations by other methods (e.g. cameras), the source-signal relationship remains often obscure. In order to shed light on the source-signal relationships in the context of seismological landslide monitoring, we started controlled laboratory experiments using analogue landslide models. Here we present the results of a first benchmark test including a controlled source, i.e. a ballistic steel ball impacting vertically a base made of various materials. This bouncing ball tests intend to calibrate and verify the monitoring method by relating a set of seismic metrics to the impact energy.

Benchmark setup & analysis

The benchmark setup allows a vertical free fall of a steel ball through air under earth's acceleration onto a horizontal base plate (glass, plastic, rubber) followed by several ball bounces. Steel balls of variable size (c. 1 – 10 mm diameter) are released from variable height above the base plate (<45 cm) in order to generate impact events covering a large range of energy (10^{-4} – 10^{-2}) Nm). The elastic deformation of the base plate in response to the impact is measured using triaxial capacitive accelerometers at a sampling frequency of 20 kHz. The potential energy of the steel ball is estimated from digital optical images of the impact taken at 250 Hz. We assume that the impact is perfectly elastic, i.e. that the difference in potential energy of the steel ball before and after the impact equals the impact energy which is transmitted and attenuated through the base plate and picked up by the sensors.

Signal processing includes: (1) low pass filtering the readings to <1500 Hz corresponding to the flat response regime of the sensors; (2) converting voltage to acceleration following a calibration procedure; (3) integrating the signal over time and high pass filtering to >100 Hz to retrieve the ground velocity (Figure 1).

Based on the ground velocity data start and end of the events were picked automatically using a standard STA/LTA trigger technique and the low pass-filtered Hilbert transform was used to derive the signal envelope. From the latter a series of seismic metrics following Dammeier et al (2011) were derived (Figure 1). These include:

- DUR: Duration of the event (s)
- RT: Risetime, i.e. time from start of event to velocity peak (s)

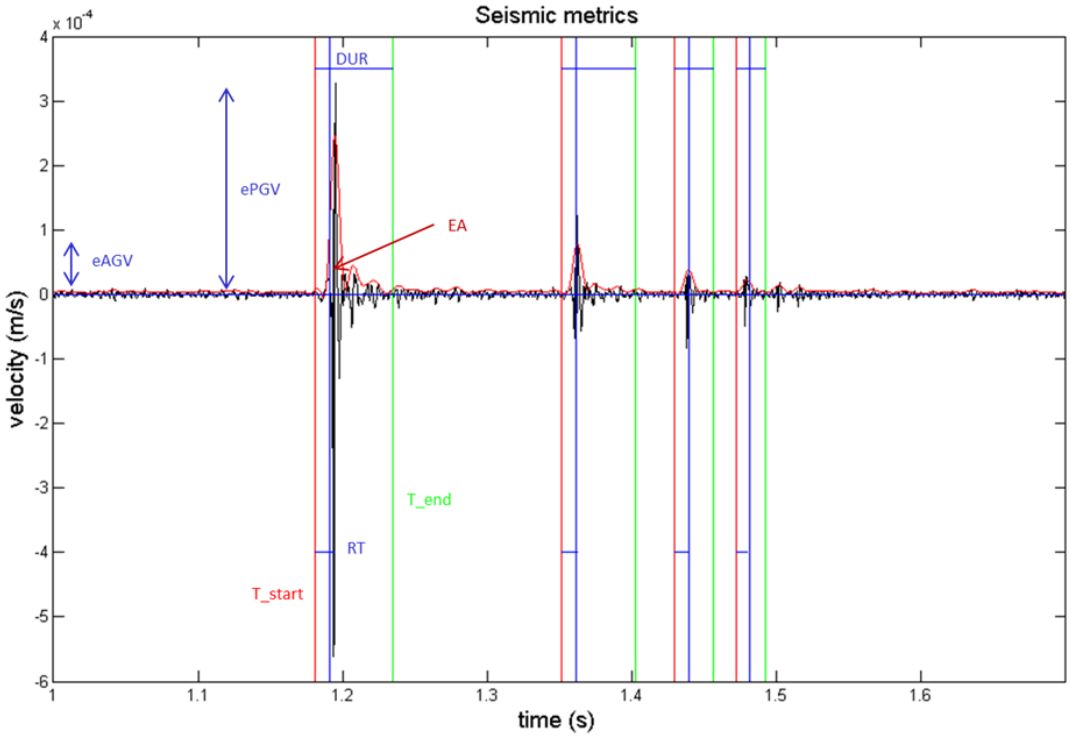

Fig. 1.: Example of "seismic" signal excited by successive impacts from a bouncing steel ball and recorded by an accelerometer in the benchmark setup. Seismic metrics according to Dammeier et al. (2011) indicated.

- ePGV: Peak ground velocity of signal envelope (m/s)
- eAGV: Average ground velocity of signal envelope (m/s)
- EA: Envelope area as a proxy for the energy of the triggering event (m)

Additionally, spectral analysis (Figure 2) based on the Fast Fourier Transform allowed quantifying the frequency content of the impact signal with high energy ("brightness") over time by means of the spectral centroid (SC in Hz).

Bivariate regression analysis finally has been used to find the relationships between the seismic metrics as defined above and the ballistic parameters, e.g. impact energy, in order to quantify the source-signal scaling relationships.

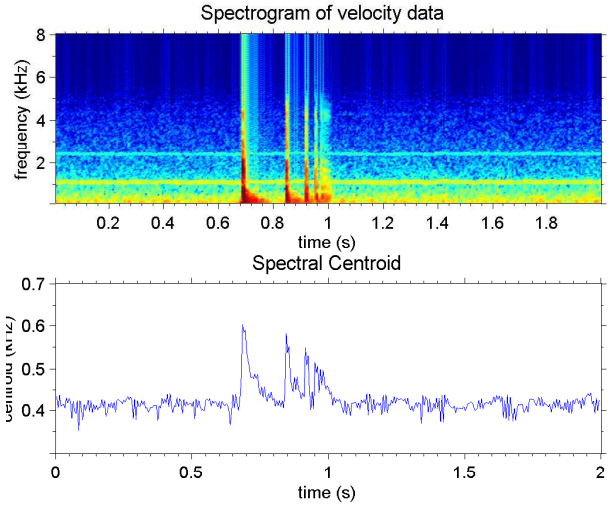

Fig. 2.: Spectrogram and spectral centroid of the bouncing ball signal in Figure 1. Note the decrease in centroid (= lowering the "tone") of successive impacts.

Scaling of seismic metrics to ballistic parameters & nature

Scaling, or similarity analysis, the comparison between the behavior of a labscale model and its natural prototype, helps to quantitatively relate labscale observation to nature and verifies the simulation method.

Our analogue models are generally setup at a length scale L*/L of 1:1.000 to 1:3.000 (i.e. a centimeter scales up to 10 – 30 meters). To assure dynamic similarity, the acting forces have to scale down consistently (Hubbert, 1937).

From this and Newton's 2nd Law ($F = m \cdot a$) it follows that for experiments conducted under earth's gravity field, all other accelerations in the model have to be same as in nature. Consequently, the time and velocity scales of the models both have to be the square root of the length scale, i.e.

$$T^*/T = v^*/v = (L^*/L)^{0.5} \sim 30 - 50 \quad (1)$$

We observe ground velocities and frequencies triggered by the ballistic impact in our setup that are in the order of $v^* = 10^{-4}$ m/s and $f^* = 10 - 1000$ Hz, respectively (Figure 1 and 2). According to (i) this scales to $v = 10^{-6}$ m/s and f = 1 – 20 Hz in nature which fits very well to observations (e.g. Burtin et al., 2013; Dammeier et al., 2011).

Preliminary analysis of a first set of experiments where we varied fall height of a 5 gram steel ball impacting glass, rubber and glass-on-plastic base plates shows positive correlations between the seismic metrics and fall height for all materials (Figure 3).

Data shown in Figure 3 indicate a linear correlation ($R^2 > 0.9$) between peak ground velocity, envelope area (as a proxy for energy) and fall height (as a proxy for impact energy). This verifies the potential of finding a simple relationship between impact energy and accelerometer response and marks the approach feasible.

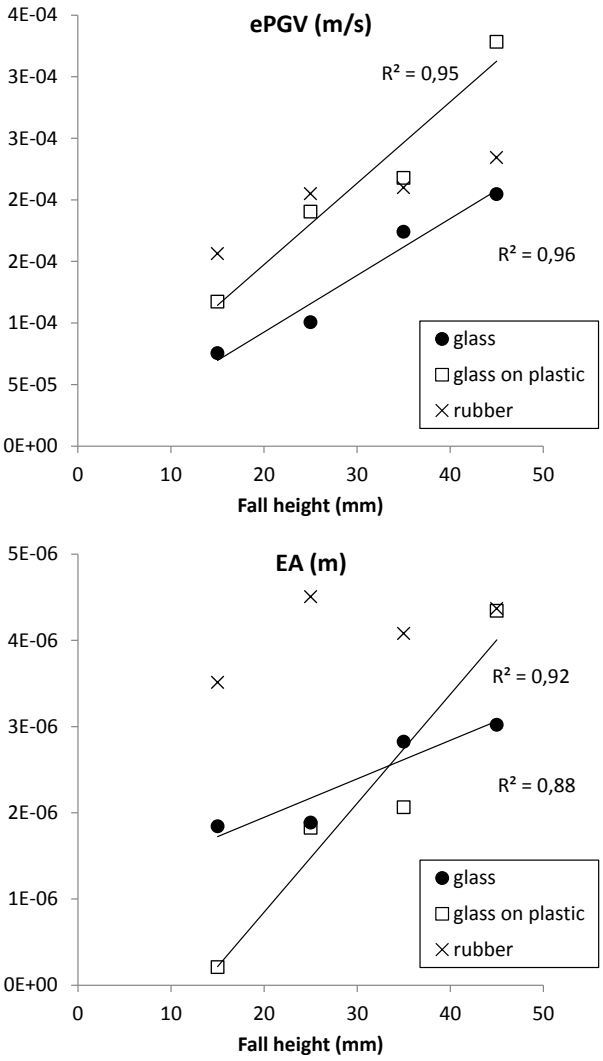

Fig. 3.: Relationship between seismic metrics (ePGV, envelope peak ground velocity, and EA, envelope area) and fall height of a 5 gram steel ball on various bases.

Outlook: Application to fragmenting labscale landslides & nature

Once we verified the monitoring method we plan to apply it to analogue models of fragmenting landslides. Preliminary test using loose sand avalanches versus cemented sand slides demonstrated the potential to differentiate between these two endmembers by means of their seismic signals and monitor the internal deformation and fragmentation process remotely. Besides having a new

monitoring technique for labscale experiments we aim at better understanding the signal-source relationship in nature. This includes questions revolving around the controls of the seismic energy released by gravitational mass movements: Which are the mechanisms contributing to the seismic signal (e.g. fragmentation, impact, sliding friction, collision)? What is their relative importance in the total and time variable seismic energy of an event? Can they be differentiated e.g. by the frequency domain they occupy?

References

Burtin, A., N. Hovius, D. T. Milodowski, Y.-G. Chen, Y.-M. Wu, C.-W. Lin, H. Chen, R. Emberson, and P.-L. Leu (2013), Continuous catchment-scale monitoring of geomorphic processes with a 2-D seismological array, Journal of Geophysical Research-Earth Surface, 118(3), 1956-1974, doi:10.1002/jgrf.20137.

Dammeier, F., J. R. Moore, F. Haslinger, and S. Loew (2011), Characterization of alpine rockslides using statistical analysis of seismic signals, Journal of Geophysical Research-Earth Surface, 116, doi:10.1029/2011jf002037.

Hubbert, M. K. (1937), Theory of scale models as applied to the study of geological structures, Geological Society America Bulletin, 48, 459-1520.

Petley, D. N. (2013), Characterizing Giant Landslides, Science, 339(6126), 1395-1396, doi:10.1126/science.1236165.

Small-scale modelling of ice flow perturbations induced by sudden ice shelf breakup

Giacomo Corti[1], Antonio Zeoli[2], Irene Iandelli[2]

[1] *Consiglio Nazionale delle Ricerche – Istituto di Geoscienze e Georisorse, Unità Operativa di Firenze, via G. La Pira, 4, 50121 Firenze, Italy*
[2] *Museo Nazionale Antartide, Università degli Studi di Siena, via del Laterino, 8, 53100 Siena, Italy*
e-mail: *giacomo.corti@igg.cnr.it*
session: *Methods and Materials*

Many glaciers in Greenland and Antarctica flow into the sea, terminating in extensive ice shelves which act as a buttress for their glaciers and slow their flow. A sudden marine shelf break up is expected to induce an increase in glacier speed, as flowing glaciers no longer encounter resistance on reaching the ocean, until a new equilibrium is established. The collapses of Antarctic Peninsula's Larsen-A and Larsen-B ice shelves between 1995 and 2002 confirmed these inferences. Glaciers draining the Larsen A ice sheet accelerated up to threefold after its 1995 collapse, whereas after disintegration of Larsen B ice shelf in 2002 some of the glaciers (Hektoria, Green and Evans glaciers) accelerated up to eightfold. Concomitant with the increase in velocity, glaciers significantly stretched and thinned close to their grounding line. These abrupt variations in the evolution of the glaciers have been mainly attributed to the removal of the buttressing ice shelf, a finding supported by the observation that glaciers that remained well buttressed by the remnant Larsen B shelf did not accelerate. This process can cause severe depletion of continental ice levels with obvious implications for eustatic sea level rise. Several numerical models have analyzed the process, but the complex boundary conditions adopted and the different modelling approaches make it difficult to isolate the role of ice-shelf buttressing on the large-scale dynamics of ice sheets, whose role thus remains controversial.

In this work we use simple small-scale laboratory models to reproduce the flow of a valley glacier draining an ice sheet into an ice shelf and to investigate the flow perturbations induced by ice shelf collapse. The analogue models, which apply to ice sheets grounded above sea level (e.g., East Antarctic Ice Sheet; Antarctic Peninsula and the Larsen Ice Shelf), were performed at the Tectonic Modelling Laboratory of CNR-IGG of Florence, Italy and at the Museo Nazionale Antartide, University of Siena, Italy. The flowing ice was simulated by using Polydimethilsyloxane (PDMS), a transparent Newtonian silicone that has been shown to well approximate the rheology of natural ice. Instability of glacier flow was induced by manually removing a basal silicone platform (floating on water) exerting backstresses to the flowing analogue glacier: the simple set-up adopted in the experiments isolates the effect of the removal of the buttressing effect that the floating platform exerts on the flowing glaciers, thus offering solid insights into the influence of this parameter on the flow perturbations resulting from a collapse event.

The experimental results show a significant increase in glacier velocity close to its outlet following ice shelf breakup, a transient effect that does not significantly propagate upstream towards the ice sheet, rapidly decays with time and is accompanied by significant ice thinning. This pattern closely matches the time-space evolution of flow perturbations observed on tributary glaciers of the Larsen B ice shelf after its 2002 collapse. Basal lubrication and variations in ice thickness do not significantly influence the process that

thus leaves the ice sheet almost unaffected by flow perturbations. Extrapolation of the experimental finding to the Larsen B case supports the importance of the removal of the buttressing effect on the dynamics of glaciers draining the Antarctic Peninsula. However, for reasonable values of ice thickness (typically <1000-1500m) the models indicate no propagation of the flow perturbation up to the ice sheet, suggesting that the removal of buttressing alone do not represent the major factor inducing depletion of ice sheets and threatening their stability, at least in case of valley glaciers for which the feeding ice sheet is grounded above the sea level (e.g., East Antarctic Ice Sheet; Antarctic Peninsula and the Larsen Ice Shelf).

Carbopol® for experimental tectonics: a rheological benchmark study

E. Di Giuseppe[1], F. Corbi[2], F. Funiciello[3], A. Massmeyer[4,5], T.N. Santimano[2]

[1]*Institut de Physique du globe de Paris, Sorbonne Paris Cite, Université Paris-Diderot, CNRS, 1 rue Jussieu, F-75005 Paris, France.*
[2]*Deutsches GeoForschungsZentrum GFZ, Helmholtz-Zentrum Potsdam, 14473 Potsdam, Germany.*
[3]*LET, Laboratory of Experimental Tectonics, Universita' 'Roma Tre', L.go S. Leonardo Murialdo, 1, 00146 Rome, Italy.*
[4]*RWTH Aachen, Lehrstuhl für Wärme- und Stoffübertragung, Augustinerbach 6, 52056, Aachen, Germany.*
[5]*Laboratoire FAST, CNRS/Université Paris Sud, Bat. 502 Rue du Belvedere, 91405 Orsay, France.*
e-mail: *digiuseppe@ipgp.fr*
session: *Methods and Materials*

Summary

As a prerequisite in experimental tectonics, in-depth analysis of the rheology of any analogue rock material is necessary to test its suitability for modelling a geophysical process in laboratory. Here we report a systematic characterization of physical and rheological properties of a large variety of polymeric hydrogels, known as Carbopol® , as a function of concentration, composition, pH, temperature and aging. These fluids feature a visco-elasto-plastic rheology which is described by the Herschel-Bulkley model. Benchmark tests are performed with three different types of rheometers at four institutes (FAST, GFZ, IPGP and LET), and a preliminary benchmark that tested the comparability of results is proposed.

Polymer rheology

Carbopol® identifies a polymer family based on modified crosslinked acrylic acid chemistry. Such polymers are available as fluffy white powders of 0.2-0.6 μm particles that absorb water, hydrate and swell creating a transparent gel-like texture if properly neutralized. The presence of neutralizer agents causes the creation of negative charges along the polymer backbone and, consequently, changes the interactions and the entanglements of its network. Therefore, when submitted to a stress τ, it deforms elastically when τ is lower than a critical value τ_y and is shear-thinning when $\tau > t_y$. Carbopol® polymers are commonly used in industry, i.e. cosmetic products, personal care and pharmaceutical merchandise, as thickeners, suspending agents and stabilizers. In the last years, Carbopol® has been employed in experimental tectonics and geodynamics including thermal convection experiments (e.g. Davaille et al., 2013), gravity-driven flow experiments (e.g. Chambon et al., 2013), and strain localization experiments (Schrank et al., 2008) because of its versatility to provide a large range of yield stress values and shear thinning behavior, and excellent transparency. Satisfying the rheological similarity criteria is a great advantage for modelers, but at the same time characterizing Carbopol® rheology is complex, requires time-consuming efforts, and the results may be affected by several physical parameters. This limited the use of this material in the last years.

Conscious that a deep knowledge of the physical and rheological properties of the working

fluid is pivotal for modeling properly a geophysical process, we decided to carry out an extensive study of the rheology of different Carbopol® types as a function of concentration, composition, pH, temperature and aging. Their flow behavior is described as well as their visco-elastic VE properties.

Selected Carbopol® samples, methods and rheometers

Here we report rheological measurements of six different types of Carbopol® , namely: ETD2050, ETD2623, Ultrez10 (U10), Ultrez21 (U21), EZ2, EZ3. Our selection aims at covering the widest range of rheological behaviour according to preliminary data provided by the producing company (*Lubrizol* – http://www.lubrizol.com) and the ease of preparation. The samples have been prepared at intermediate to high concentrations, ranging from 0.1 to 1.0 wt%. All the samples have been prepared following a standard procedure including neutralization (pH = 7) to always work with the maximum viscosity. The viscous behaviour and yield stress are evaluated by means of rotational and oscillatory tests.

In a first set of tests, we imposed a torsional flow to the sample in a rotational regime. The rheological tests consist of imposing a wide range of shear rate ($\gamma = 106{-}3 - 10^3$ s^{-}1) and measuring the stress (i.e. strain rate controlled) or vice-versa (i.e. stress controlled). Each flow curve is then fitted with a Herschel-Bulkley (HB) model, a rheological model that successfully describes Carbopol® flow properties. This procedure allows the estimation of the amount of stress that the sample experiences before yielding, τ_y, the flow index n (that describes degree of shear thinning), and sample consistency, K_y (a constant of proportionality between stress and strain rate).

A second set of tests in oscillatory regime are used to examine the VE behavior of Carbopol® . The standard procedure adopted in Material Science consists of measuring the energy stored in the sample during deformation and the energy lost afterwards. These two quantities are expressed, respectively, by the storage (G') and the loss (G") moduli, over a broad range of deformation and deformation rates (Mezger, 2002). The amplitude sweep test applies shear strain amplitude, γ, ranging between 10^{-2} and 10^3 % at constant frequency ($\omega = 1$ s^{-1}). The plateau of the G' curve determines the linearity of the VE behavior and its threshold γ_{LVE}, that is the amount of strain after which the sample structure is irreversibly changed. The *frequency sweep test* applies a constant amplitude oscillation (where $\gamma < \gamma_{LVE}$) with frequency ranging from 10^2 to 10^{-2} s^{-1}. The region in the frequency domain where the G' intersect the G" curve is equivalent to the Maxwell relaxation time, while the elastic shear modulus is identified as the value of G' obtained at the highest frequencies, where the plateau is reached.

This benchmark study has been conducted in synergy between four laboratories equipped with different rheometers. Rheometric measurements at the IPGP are performed on a RheoStress RS60 (ThermoHAAKE). Measurements at FAST are performed on a Physica MCR501 (Anton Paar). Measurements performed at LET and GFZ are performed on a Physica MCR301 (Anton Paar). All the rheometers employed in this study, are equipped with a Peltier element to control the temperature and with a solvent trap to minimize sample evaporation. The measurement systems used vary between the different labs and include plate-plate and cone-plate geometries as well as different surface roughness (sandblasted, polished).

Carbopol® ETD2050 benchmark

Samples of 1.0 wt% Carbopol®ETD2050 are prepared following a standard procedure in each laboratory. All the Peltier elements are set at T = 23 °C, which is the typical room temperature in laboratory. Viscosity and shear stress values obtained by the different rheometers are in very good agreement for $\dot{\gamma} > 1$ s^{-1} (Fig.1). However, assessment of τ_y provides larger variability, i.e. τ_y undergoes a variation up to a factor

of 3. We attribute this variation to the different measurement system geometries (i.e. plate-plate vs. cone-plate) adopted that may cause wall slip and/or transitional effects. Measurements carried out with the oscillatory methods to assess the viscoelastic behaviour of our samples show a much better reproducibility. Both amplitude and frequency sweep tests reveal an excellent agreement of measurements of the G' and G" moduli on the different rheometers. G' measured in amplitude sweep test with MCR301 (LET) shows the same values measured with the MCR501 (FAST), but differs by 7 % from the curve obtained with the same device (MRC301 - GFZ), and by only 3 % from data obtained with RS600 (IPGP). G" variability is in the same range and $\gamma_{LVE} =$ 10 % for all measurements. For the frequency sweep test, G' measured with MCR301 (LET and GFZ) shows a difference of almost 20 %, while there is a difference of 5 % between RS600 (IPGP) measurements and MCR301 (GFZ). Despite some uncertainty of τ_y in rotational tests, we consider our benchmark successful and conclude that Carbopol® allows in general to obtain reproducible results if preparation follows a strict procedure.

Systematics of Carbopol® rheology: Effects of concentration, composition, pH, temperature and aging.

Effect of concentration:

The viscosity curve of ETD2050 and ETD2623 exhibit an increase of approximately two orders of magnitude as the concentration is increased from 0.1 to 1.0 wt% accompanied by an increase of the shear thinning behaviour. U10 viscosity increases by 2 orders of magnitude as concentration increases from 0.1 to 0.5 wt%, and 3 orders of magnitude as concentration increases from 0.5 to 1.0 wt%. ETD2050 linear viscoelastic range increases by 6 times when concentration increases from 0.1 wt% to 1.0 wt%. An increase of concentration of the same amount provokes an increase of the linear viscoelastic range of about 16 times for U10 and ETD2623. Independently of the type of Carbopol® , increasing the concentration causes an increase of the viscosity and shear thinning behaviour, of γ_{LVE} and G'.

Effect of composition:

The composition of the molecules forming the Carbopol® gels strongly affects their rheology. At low concentration, 0.1 wt%, both ETD samples show higher viscosity and G' modulus than Ultrez samples. An inverse behavior is observed at higher concentration, i.e. 1.0 wt%: Ultrez and EZ samples show a similar flow behavior, ETD2050 reaches the lowest viscosity values and ETD2623 curves have intermediate values. Storage modulus attains the highest values for Ultrez and EZ samples.

Effect of pH:

Non-neutralized samples have a pH ranging between 2.5 and 3.5 and have very low viscosities, especially ETD and Ultrez. Independently from Carbopol® composition, the viscosity has the highest values for pH in the 6 to 9 range. The viscosity decreases for pH values above 9.0. Actually, adding a large amount of neutralizer causes an excess of electrolytes that produces the moistening of the electrostatic repulsions.

Effect of temperature:

Our results show an inverse relationship between temperature and viscosity. For T varying between 15 and 40 °C, the viscosity decreases by 30% for ETD2623 (0.1 and 1.0wt%) and U10 (0.1 wt%), U21 (0.1 wt%) viscosity is more sensible to temperature with a reduction of 46% in the same temperature range, while ETD2050 viscosity (0.1 wt%) is less sensible with a viscosity reduction of 10%.

Effect of aging:

According to technical sheets, Carbopol® polymers are very stable in time, however we suggest

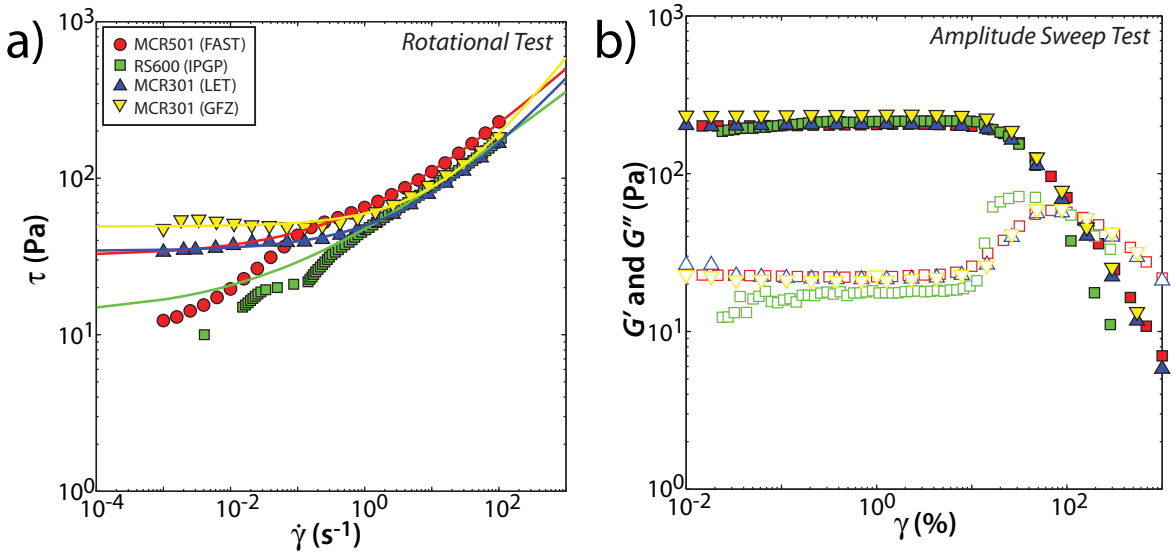

Fig. 1.: Results of the benchmark tests performed on ETD2050 Carbopol® samples of 1.0 wt% and T = 23 °C. a) Results of the flow test (rotational regime): shear stress versus shear rate; b) results of amplitude sweep test (oscillatory regime): G' and G" moduli versus deformation amplitude. Symbols identify the laboratory and the rheometer used for the benchmark. Filled symbols mark the storage modulus G', open symbols the loss modulus G".

using this material within a few days after preparation. Our measurements 2.5 - 5 weeks after samples' preparation revealed a decrease of viscosity values by almost 30% for samples with concentration 0.1 wt% anddecrease of 10% for samples with concentration 1.0 wt%.

References

Chambon, G., Ghemmour, A., Mohamed, N., 2013. Particle migration within free-surface flow of a viscoplastic flow. EGU General Assembly.

Davaille, A., Gueslin, B., Massmeyer, A., Di Giuseppe, E., 2013. Thermal instabilities in a yield stress fluid: existence and morphology. J. Non-Newtonian Fluid Mech. 193, 144-153.

Mezger, T., 2002. The Rheology Handbook: For Users of Rotational and Oscillatory Rheometers. Vincentz Verlag Hannover.

Schrank, C., Boutelier, D., Cruden, A., 2008. The analogue shear zone: From rheology to assoiciated geometry. J. Struct. Geol. 30, 177-193

Initiation process of the frontal thrust revealed from detailed analogue experiments

T. Dotare[1], Y. Yamada[1,2], T. Hori[2], H. Sakaguchi[2]

[1] *Graduate School of Engineering, Kyoto University, Kyoto, Japan*
[2] *Japan Agency for Marin-Earth Science and Technology (JAMSTEC), Yokohama, Japan*
e-mail: *dotare.tatsuya.76s@st.kyoto-u.ac.jp*
session: *Methods and Materials*

Summary

Discontinuity surfaces (e.g. fractures, faults) in rocks significantly influence fluid permeability, thus their distributions have to be evaluated in detail for hydrocarbon exploration / production. To establish a fracture distribution model, a series of analogue experiments were conducted and the fault initiation process in the experiments was analyzed in detail by using a digital image correlation technique. The result of our shortening experiments identified a number of weak shear bands prior to the later initiation of a frontal thrust. Such minor shear bands have been reported in the toe area of the Nankai accretionary prism, SW Japan. By comparing with several transects at this subducting margin, we can classify lateral variations in the structural geometry into deformation stages we identified in the models.

Introduction

Discontinuity surfaces, such as fractures and faults, have been an important target of oil and gas exploration and production. Recent hydrocarbon production from shale requires detecting areas of better initial permeability, can be regarded as 'sweet spots', due to rich discontinuity surfaces. Such surfaces are generally of subseismic scale and hard to detect from surface investigations.

Analogue modeling is a useful tool for evaluating how geologic structure is formed and constructing detailed structural models including minor deformation features. In recent study, digital image correlation technique (e.g. DIC) enables us to detect the deformation in the analogue model quantitatively and in high spatial and temporal resolution. Previous studies demonstrated that this technique can reveal detailed styles of strain accumulation in analogue models (e.g., Adam et al., 2005, Hoth et al., 2007), and the technique is now widely applied to analogue experiments to reveal structural evolution quantitatively.

In this study, we aimed to observe small scale structures (i.e. fractures or minor faults) developed during deformation process in shortening experiments. Our observations focused on the frontal thrust area whose detailed deformation was analyzed with DIC technique.

Experimental setup

The setup of our shortening experiments is summarized in Figure 1. The experimental material is beach dry sand (Toyoura sand) and its cohesion is ca 100Pa. Scaling factor is $10^4 \sim 10^5$. During shortening the material, deformation at the frontal thrust was recorded every 27μm shortening. (Figure 2), with two digital cameras (cannon EOS 7D) through a transparent side-wall.

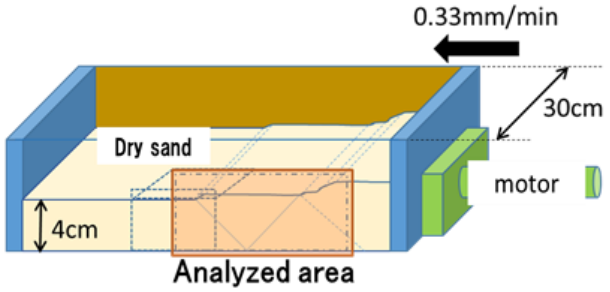

Fig. 1.: Experimental setup

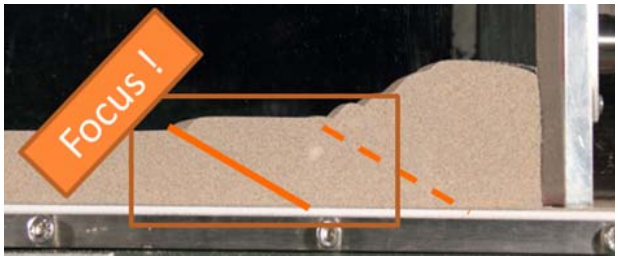

Fig. 2.: Analyzed area

Experimental results

When the old (pre-existing) frontal thrust is active (a in Figure 3 and 4), shear strain shows a constant value. After this, the activity of the old (pre-existing) frontal thrust decreases (b in Figure 4), and several weak shear-strain bands appeared in front of the old thrust (Figure 3b). The activity of each band is very short (can be detected in only 1 or 2 snapshots), and locations are systematically but rapidly changing. Then, the shear bands starts to localize at a specific location (Figure 3c) and the shear strain along the old thrust significantly decreases (c in Figure 4). Finally, the activity of the weak shear bands ceases and a new frontal thrust is generated showing a constant value of shear strain (d in Figure 3 and Figure 4)

Discussion and implication to real geology

From our experimental results, we can divide the initiation process of the frontal thrust generation into three stages:

Stage 1: Deformation propagating stage (b in Figure 3 and Figure 4). Characterized by short-life minor "weak shear bands" in front of the old frontal thrust of decreasing activity.

Stage 2: Strain localizing and thrust initiation stage (c in Figure 3 and Figure 4). The shear strain starts to localize and the location of the new frontal thrust seems to be selected among previous minor weak shear bands during the localizing process.

Stage 3: Active frontal thrust stage (d in Figure 3 and Figure 4). The newly initiated thrust is the only active fault showing a constant strain value. No weak shear band observed.

As a natural example, we have looked at the proto thrust zone (PTZ) at the toe of the Nankai accretionary prism, SW Japan. The Nankai accretionary prism is formed by the subduction of the Philippine Sea plate underneath the southwest Japan arc (Eurasian plate) and active sediment accretion is presently taking place (Moore et al., 2001). It has been reported that the structural domain varies between two parallel transects; Ashizuri and Muroto transects. While the Ashizuri transect has a well-developed PTZ containing a series of subparalell dipping discontinuities (Figure 5 Toe of Ashizuri Transect (Morgan et al., 1995)Figure 5), the Muroto transects has a few discontinuity features and narrow proto-thrust zone (Moore et al., 2001) (Figure 6). Moore et al. (2005) also attributed these variations to differences in mechanical properties and/or pore pressures, but this has not been confirmed.

Based on the deformation stages as proposed above, the sub-parallel discontinuities may correspond to the 'weak shear bands' observed in experimental results, and the along-strike variation may be not due to the mechanical property but the initiation stages of the frontal thrust. Since the surface topography of the Muroto transect PTZ is more deformed than that of the Ashizuri transect, the Muroto PTZ is in the later stage; i.e. the Ashizuri PTZ may be in the Stage 1, Muroto PTZ may be in the Stage 2. The Muroto PTZ could have been wider in the past with more discontinuity surfaces but now these minor features may have all disappeared and cannot be

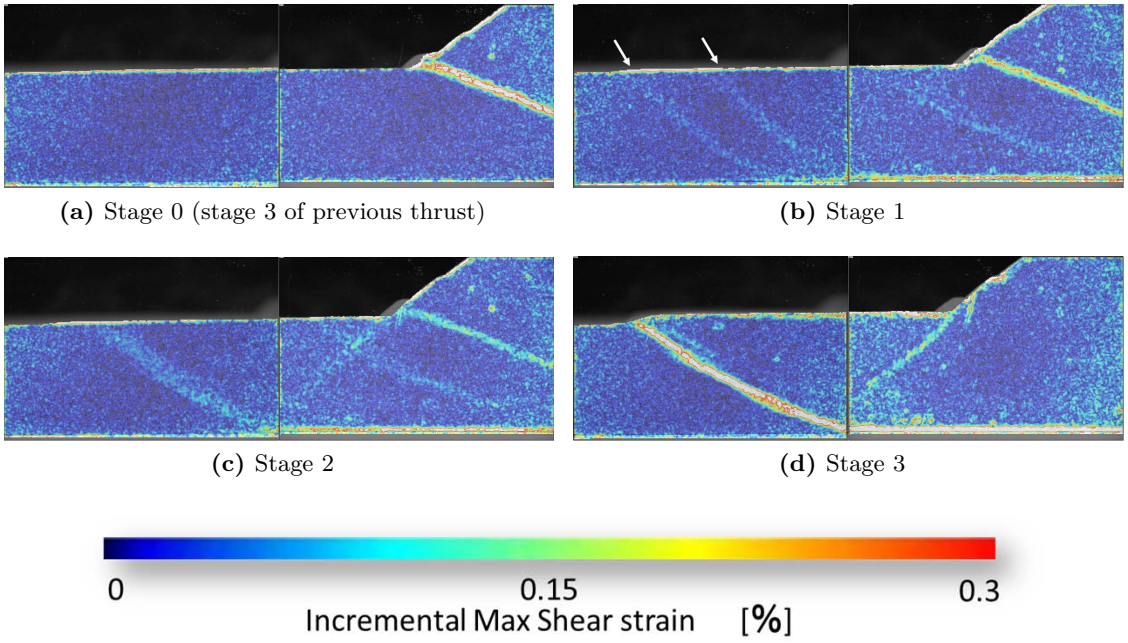

(a) Stage 0 (stage 3 of previous thrust)

(b) Stage 1

(c) Stage 2

(d) Stage 3

(e) Stage 2

Fig. 3.: Snapshots of experimental results. (a) ∼ (d) correspond to deformation stages. Each picture shows the incremental max shear strain distribution calculated every 27μm shortening.

detected.

Moore et al (1995) mentioned that the Cascadea accretionary margins PTZ has a lot of subparallel protothrusts with some negative-polarity reflection in the seismic dataset. This suggests possible fluid migration along these faults. During Stage1, 'weak shear bands' rapidly change their location and may develops a lot of subparalell active protothrusts, but previous protothrusts became inactive once the frontal thrust initiated. Fluid migration paths may focus on the new active frontal thrust and previous protothrusts may not show clear seismic anomaly (negative-polarity). This assumption is consistent with the different deformation stage of Ashizuri (Stage1) and Muroto (Stage2) protothrust zones.

Conclusion

We conducted the detailed analogue sandbox modelling focusing on the initiation of the frontal thrust, and found 'weak shear bands' before new fault initiates and strain concentration at the area of the new thrust formation. By comparing to the toe geometry at the Nankai accretionary prism, we inferred the along-strike variation of structural geometry may be due to the different deformation stages.

References

Adam, J. et al.; 2005: Shear localization and strain distribution during tectonic faulting—new insights from granular-flow experiments and high-resolution optical image correlation techniques. Journal of Structural Geology, 27(2), 283–301.

Hoth, S. et al.; 2007: Frontal accretion: An internal clock for bivergent wedge deformation and surface uplift. Journal of Geophysical Research, 112(B6), B06408.

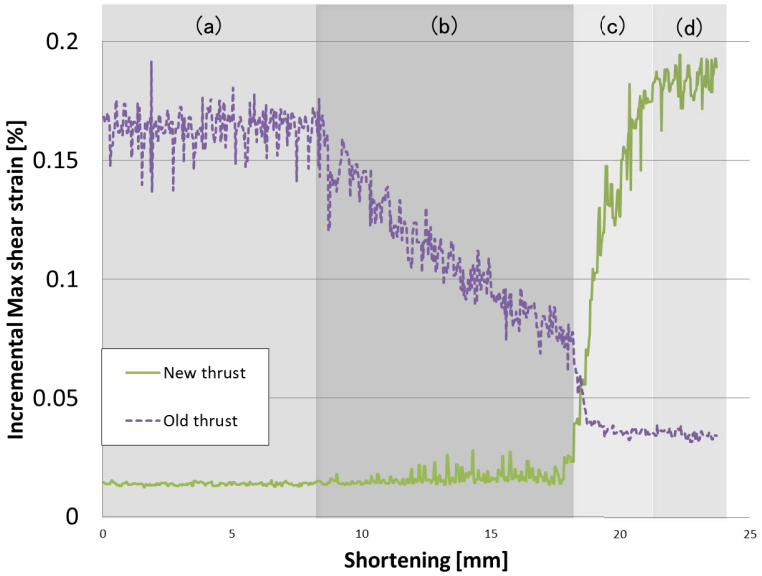

Fig. 4.: Time series of old and new thrust activation (incremental shear strain). (a) (d) correspond to Figure 3. Each value are calculated around 1cm×1cm square area where both thrusts intersect.

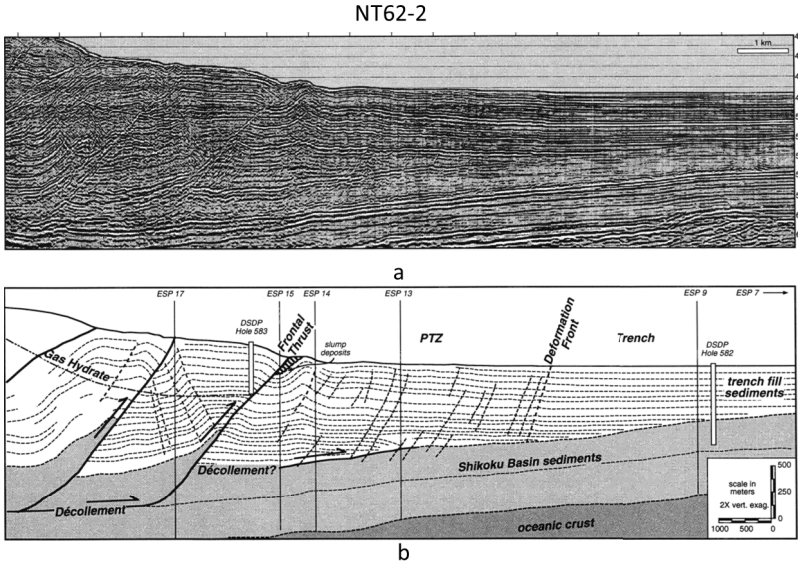

Fig. 5.: Toe of Ashizuri Transect (Morgan et al., 1995)

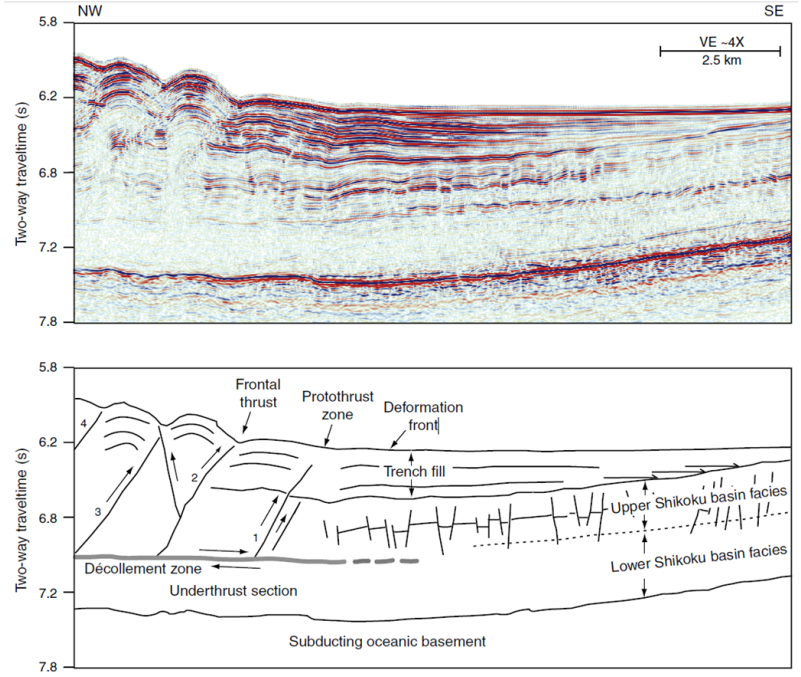

Fig. 6.: Toe of Muroto Transect (Mikada et al, 2005)

The Use of Scaling Theory in Geological Laboratory Models

Olivier Galland[1], Eoghan Holohan[2], Guillaume Dumazer[3]

[1] *Physics of Geological Processes (PGP), University of Oslo, Norway*
[2] *German Research Centre for Geosciences (GFZ-Potsdam), Germany*
[3] *Physics Department, University of Oslo, Norway*
e-mail: *olivier.galland@fys.uio.no*
session: *Methods and Materials*

The main advantage of laboratory modelling, *i.e.* that geological processes are simulated within the limits of a laboratory and the working time of the researcher, at the same time represents the method's biggest problem: the difference in scale between geological systems and the experimental setup in the laboratory can be enormous. It is this scale gap that often leads to scepticism among Earth scientists regarding the applicability of laboratory models.

The geological applicability of laboratory results requires a robust scaling analysis [Hubbert, 1937; Ramberg, 1967]. Nevertheless, there is a lot of confusion among Earth scientists about scaling of laboratory models to geological systems, and first of all about the meaning of "scaling". The main confusion is related to the goals of laboratory models. They are not designed to mimic a given geological system, as many Earth scientists think, but to understand generic processes, either individually or in combination, and to identify or demonstrate physical laws governing these processes. In order to prove that any physical laws identified in laboratory experiments apply to geological systems, these laws should be dimensionless, *i.e.* they are independent of the length scale, time scale, etc... If an established law depends on the observational dimensions, the physical generality fails and the laboratory results cannot be extrapolated to geological systems.

The procedure for establishing dimensionless scaling laws involves two steps: (i) a *dimensional analysis* of the considered physical problem, to identify the dimensionless governing parameters, and (ii) a *comparison of laboratory and geological values of these dimensionless parameters (called similarity)* to test the geological relevance of the experimentally-derived physical laws.

Dimensional analysis

The principles of dimensional analysis are described in detail by *e.g.* Barenblatt [2003]. The approach consists in identifying the dimensionless physical parameters that govern the processes to be addressed.

The first step is to list the n parameters with dimensions that are relevant for the processes to be studied. In mechanical systems, usual dimensions are those of length (L), mass (M) and time (T). From this list of parameters, the experimentalist should separate the governing parameters, *i.e.* those known and controlled, from the output parameters to be measured. In the field of phase transition the notions of 'control parameters' and 'order parameter' are often in use.

The second step is to identify the number k of the governing parameters with independent dimensions. A set of parameters has independent dimensions if their dimensions cannot be expressed as a function of each other's [Barenblatt, 2003]. For instance, the height of a volcanic edifice and the density of the rock have independent dimensions, because the dimension of the density ($[\rho] = ML^{-3}$) cannot be expressed as a function of the dimension of the depth ($[h] = L$) only. In contrast, the rock cohesion ($[C] = ML^{-1}T^{-2}$), the density ($[[\rho] = ML^{-3}$),

the gravity ($[g] = LT^{-2}$) and the height of, *e.g.* a volcanic edifice ([h]=L) do not have independent dimensions, given that the dimension of C is a function of the dimensions of ρ, g and h:

$$\begin{aligned}[C] &= ML^{-1}T^{-2} = [\rho] \times [g] \times [h] \\ &= (ML^{-3}) \times (LT^{-2}) \times (L)\end{aligned} \quad (1)$$

The third step is to calculate the number m of dimensionless parameters that characterise the physical system to be simulated in the experiments. This number is easily calculated by using the Π-theorem (or Buckingham Π-theorem), which is the central theorem in dimensional analysis. It states that "*a physical relationship between some dimensional (generally speaking) quantity and several dimensional governing parameters can be rewritten as a relationship between a dimensionless parameter and several dimensionless products of the governing parameters; the number of dimensionless products is equal to the total number of governing parameters minus the number of governing parameters with independent dimensions*" [Barenblatt, 2003]. This means that the number m of dimensionless parameters to be defined is easily calculated by $m = n - k$.

Once the number of dimensionless parameters $\Pi_{i(1 \leq i \leq m)}$ governing the modelled system is calculated, the next step is to identify each of them by combining the dimensional laboratory parameters. Among the n dimensional parameters, if the model output has a measurable quantity x, one dimensionless output number Π should contain x, and the $m - 1$ other dimensionless numbers can be defined as input parameters.

If the dimensional analysis is relevant, the defined dimensionless numbers should have a physical meaning. A good example is the Reynolds number (Re), which quantifies the relative contributions of inertial forces with respect to viscous forces in a flowing fluid: a critical value (Re_c) of the Reynolds number marks the transition between a laminar flow regime ($Re < Re_c$) and a turbulent flow regime ($Re > Re_c$).

The dimensionless parameters identified during the dimensional analysis represent the foundation for the experimental strategy and the analysis of experimental results. Two different approaches can be adopted, depending on the nature of the model outputs.

If the model output is a measured quantity, the aim of the experimental procedure will be to establish a correlation between the measured dimensionless parameter Π and the dimensionless input parameters Π_i (Figure 1a). The Π-theorem states that the output dimensionless quantity Π can be rewritten as a function of the other $m - 1$ Π-numbers, such as:

$$\Pi = F(\Pi_1, \Pi_2, \ldots, \Pi_{m-1}) \quad (2)$$

The function F is the physical law that governs the simulated processes. This relationship between the dimensionless output and the dimensionless input parameters should dictate the experimental strategy. In order to test the effects of each dimensionless parameter Π_i during an experimental project, the dimensional experimental parameters should be varied such that Π_i is systematically varied, while the others are kept constant. Applied to each Π_i-number, the experimental results will contribute to derive the physical laws that govern the processes to be understood by constraining the function F. If the parameters Π and Π_i are well defined, they are expected to correlate (Figure 1a).

If the model output is not a measured quantity, but contrasting physical behaviours, the aim of the experimental procedure will be different. We already mentioned the turbulent and laminar regime in fluid mechanics. Another example of contrasting behaviour is the formation of dykes or cone sheets in volcanic systems [see abstract by Galland et al., session Volcanism and Volcanotectonics; Galland et al., in revision]. Here the aim will be to vary systematically the values of the m dimensionless parameters Π_i and then to map under which conditions these contrasting physical behaviours occur (Figure 1b). This procedure is equivalent to building a phase diagram, the contrasting physical behaviours being analogue to physical phases.

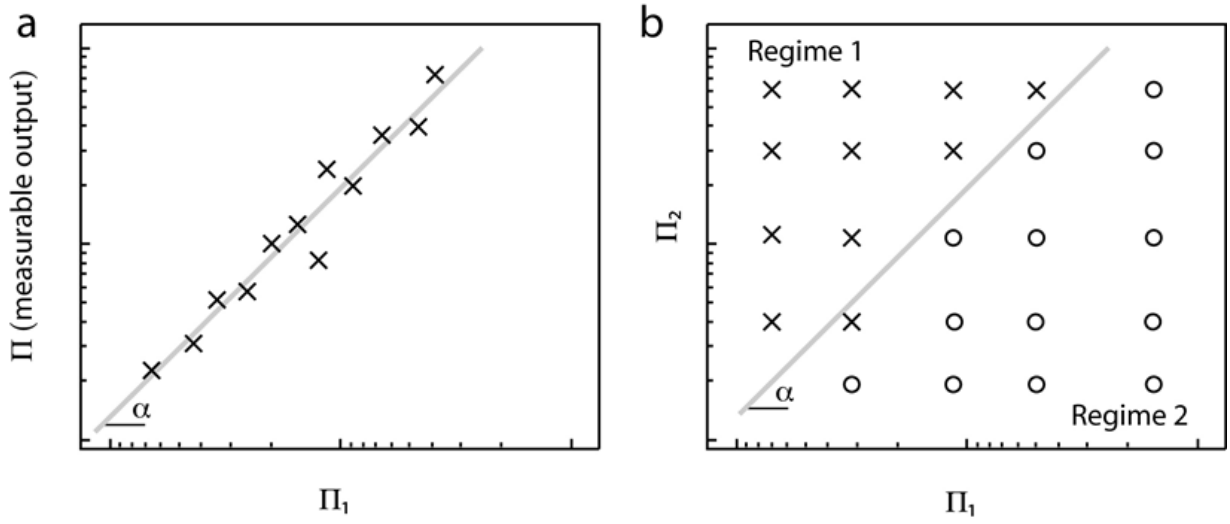

Fig. 1.: Conceptual diagrams illustrating how the nature of the experiment output dictates the analysis of that output in terms of the dimensionless model parameters. a. If the model output is a measured quantity Π, the results will be displayed as a correlation between Π and the input parameters Π_i. b. If the model output is a physical regime, the results will be displayed as a dimensionless phase diagram.

Similarity to geological systems

Following the dimensional analysis and the identification of the Π-numbers, and after obtaining the experimental results that quantify the scaling laws governing the modelled processes, one needs to test the geological relevance and applications of these laws. In other words, we need to test whether the processes simulated in the laboratory are physically similar to the geological processes. This concept of *physically similar phenomena* is central to geological laboratory modelling. *Two systems are considered similar if the values of the dimensionless parameters are identical, even if the values of the governing dimensional parameters differ greatly* [Barenblatt, 2003]. It means that although the scales of the laboratory models are drastically different to the scales of the geological systems they aim to simulate, the laboratory models will be physically similar to their geological equivalents if their respective Π-numbers, as identified in the dimensional analysis, have the same values. Therefore, the experimentalist must compare the values of each Π-number in the laboratory with the values of these numbers in the geological system: if the ranges of values overlap, the two systems are similar, and the experimental results are relevant to the geological system [see abstract by Galland et al., session Volcanism and Volcanotectonics; Galland et al., in revision].

Discussion

A classical approach of laboratory modelling is to use the scaling analysis to justify that the models are representative of their geological prototypes, *i.e.* to use the similarity principle only. Hence, this approach ignores the first part of the scaling procedure, *i.e.* identifying the governing dimensionless parameters to establish the experimental strategy. In most studies, the model results are plotted in dimensional graphs that are scale-dependent, making it very hard to quantitatively compare laboratory results with geological data. Therefore, these studies underuse the fundamental implications of the scaling theory.

Conversely, using the full procedure dictated by the scaling theory offers several crucial advantages:

- the fundamental dimensionless parameters that govern the modelled physical system are identified;

- the list of dimensionless parameters helps to define and focus experimental strategy;
- plotting the model outputs in dimensionless forms reveals the fundamental scale-independent physical laws that govern the modelled processes;
- consequently, it is possible to quantitatively compare laboratory results and geological data in the same dimensionless plots to test the geological relevance of the laboratory results.

References

Barenblatt (2003), Scaling, 171 pp., Cambridge University Press, Cambridge.

Galland et al. (in revision), Toward a unified model for dykes versus cone sheets in volcanic systems, J. Geophys. Res.

Hubbert (1937), Theory of scale models as applied to the study of geologic structures, Geol. Soc. Am. Bull., 48.

Ramberg (1967), Gravity, deformation and the Earth's crust as studied by centrifuge models, 452 pp., Academic Press, New York.

Testing tools for the generation of an unstructured tetrahedral grid on a realistic 3D underground model

Ines Görz[1], Felix Träger[1], Björn Zehner[2], Jeanne Pellerin[3]

[1]*Department of Geophysics and Geoinformatics, TU Bergakademie Freiberg, Gustav-Zeuner-Str. 12, 09599 Freiberg, Germany*
[2]*Bundesanstalt für Geowissenschaften und Rohstoffe, Dienstbereich Berlin, Wilhelmstraße 25-30, 13593 Berlin, Germany*
[3]*IUniversité de Lorraine, GeoRessources UMR7359, CNRS, CREGU, ENSG, 2 rue du doyen Marcel Roubault, TSA 70605, 54518 Vandoeuvre-Lès-Nancy Cedex, France*
e-mail: *IGo@geo.tu-freiberg.de*
session: *Methods and Materials*

Introduction

Numerical simulations of stress field, heat flux and groundwater flow are important for modern investigations of the geological underground performed by geo-consulting and resource exploration companies. However, the simulation results are only meaningful if the geology of the research region is represented adequately.

Realistic underground models are generated with dedicated geomodeling software like Petrel, Move3D, Gocad and Skua, which integrate all available data while respecting geological concepts and the data as geometry and property constraints. The structural models generated by the geomodeling software usually describe the geometry of the subsurface by boundary surfaces. From these surfaces, a boundary representation model can be created (Weiler, 1988; Duvinage et al., 1999). A coherent boundary representation is achieved when the volume of the body is completely confined and partitioned by surfaces without holes and overlaps (Caumon et al., 2004). If the model is to be used for calculations, its volume has to be discretized into cells each of which belongs to one unique geological unit. Depending on the method of computation to be applied, different cell types are used.

Unstructured grids are often used with finite element (FE) based software codes (Schwarzbach et al., 2011, Afanasjew et al., 2013). Unstructured grids consist of an irregular pattern of grid points with neither a pre-defined topology nor fixed cell geometry. Unstructured meshes do not have a regular connectivity, i.e. their vertices do not all have the same number of neighbors. Tetrahedral meshes are the most versatile unstructured meshs, therefore they can represent any geometry. They can be built automatically respecting predefined mesh properties. In this study, we created a structural 3D model with the Paradigm Skua software and tested workflows for generating a tetrahedral unstructured grid suitable for FE simulations on this model.

Skua uses a fully-volume based modeling approach, which interpolates geological horizon surfaces implicitly as iso-surfaces on a tetrahedral mesh, while accounting for faults. The cells of the primary tetrahedral mesh cross horizon boundaries, therefore the resulting structural model has to be transformed into a boundary representation and then be re-meshed by a tetrahedral grid which respects all geological boundaries.

The first step towards creating a tetrahedral mesh consists of generating and combining loose surfaces to make a boundary representation. Since Gocad/Skua creates and edits the triangular surfaces (TSurfs) independently of each other, the nodes of two surfaces at one surface contact

are usually not identical.

Each workflow has to generate triangulated surfaces that have the same geometry along their lines of intersection, i.e. they must have identical vertices and segments. The tetrahedrons should have a suitable quality, which means the aspect ratio should not be too great because numerical instabilities can occur in such tetrahedrons. Mesh quality definition completely depends on the application. Typically a set of quality criteria on the size, shape, and orientation is taken into account at the mesh generation step.

In order to formulate boundary conditions, certain points or lines are often required to be part of the mesh. The workflow has to be able to add these objects as constraints to the tessellation.

If, for example, a geophysical measurement is simulated, the mesh resolution also needs to be adapted to the measurement method. In particular, the mesh has to be refined in the vicinity of the source and receivers to avoid aberrations across the whole modeling domain.

Test case "relay ramp"

We used the 3D structural model of a normal fault relay ramp to test the tessellation workflows.

The structure consists of two overlapping fault segments connected by a soft linkage zone that transfers displacement from one fault segment to the other. The model includes three stratigraphic horizons displaced along the two normal faults, both of which terminate in the modeling domain (fig. 1). Generation of a tetrahedral mesh in this model is challenging since:

- the horizon-fault contact lines cut one another at narrow angles, such that flat acute-angled tetrahedrons are generated;
- the two faults end inside the model;
- the triangulation of the fault surfaces has to respect vertices of the fault-contact lines, which usually cross one another, such that a constrained triangulation including crossing lines is necessary in order to create a conformal triangulation.

Workflows

Skua Finite Element Mesh Constructor

Gocad/Skua provides a commercial module for constructing tetrahedral meshes, the Finite Element Mesh Constructor (FEMC). This tool works with a Weiler boundary representation (Weiler, 1988), the so-called Model3D, which can be transformed into a tetrahedral mesh using the FEMC. This module works fully automatically: only the number of tetrahedrons has to be specified. The tetrahedral mesh consists of parts representing the geological units, and the vertices at the boundary of each part are duplicated. The FEMC in combination with Skua generates an overall good mesh quality in many cases. However, tessellation of the relay ramp model failed during re-meshing the surfaces.

Gmsh and TetGen via Skua plugin CompGeom

This workflow combines Skua and Gocad with the opensource softwares Gmsh (Geuzaine and Remacle, 2009) and TetGen (Si, 2011). In order to manipulate Skua and Gocad objects and to communicate with Gmsh and TetGen, Gocad/Skua was extended by implementing the CompGeom plugin (Zehner, 2011). First, a framework of all surface outlines and contacts has to be extracted in Skua. In order to smooth the curves or to get a regular spacing of the curve nodes, the curves can be resampled with a cubic spline function which conserves the original shape of the objects. The line framework of each surface is exported to Gmsh. Gmsh creates a triangulation incorporating all nodes of the framework. The resulting triangulated surfaces are read back to Skua and the surfaces are transformed back to their 3D geometry. In this way, all surfaces have to be re-meshed until a watertight boundary representation is obtained. During this re-meshing process, further lines and points can be added, so that they are part of the triangulation. This option can be used to provide the necessary geometry for defining boundary conditions at the surface or to enforce local refinements of the mesh. Next, the

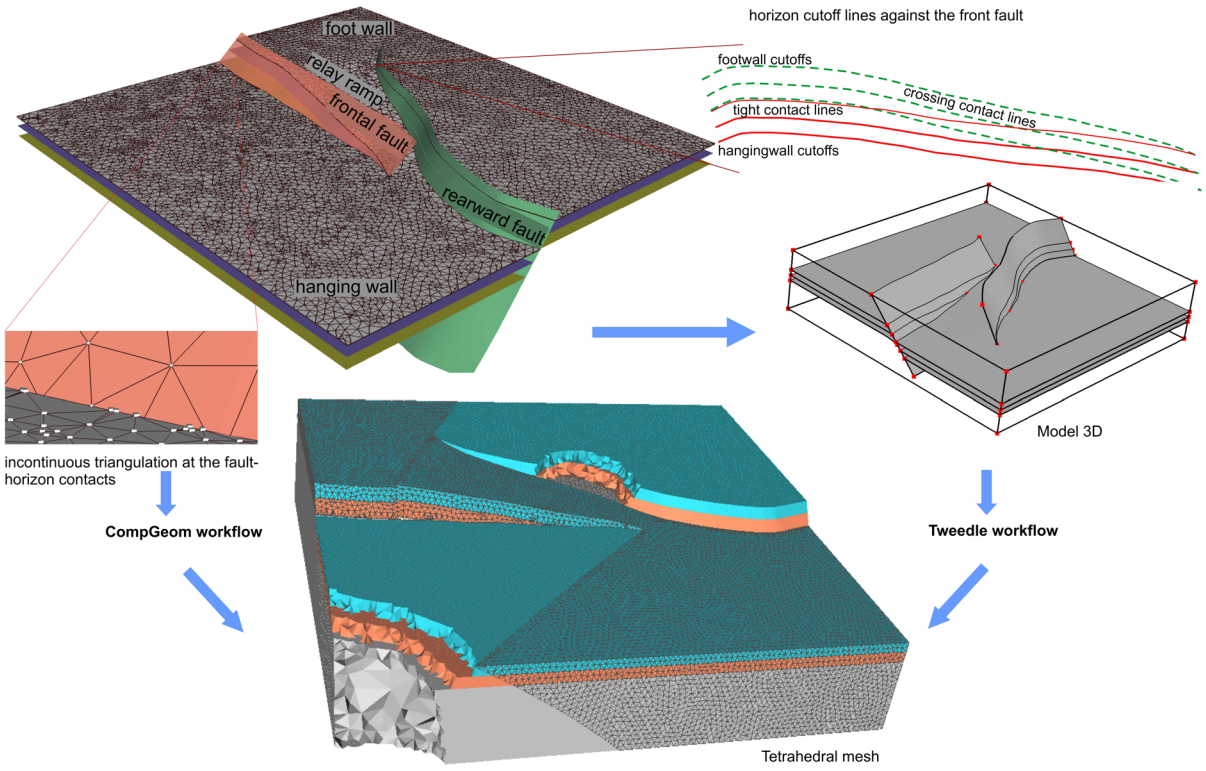

Fig. 1.: 3D model of a relay ramp consisting of triangulated boundary surfaces and a tetrahedral mesh.

finite element mesh can be produced. To accomplish this, all surfaces of the model are exported to a TetGen input file. This file contains duplicate but identical vertices as one global point. If the model is partitioned by internal surfaces, TetGen can recognize this, and each tetrahedron is assigned a number indicating the partition it belongs to. This number can be later used for setting material parameters. The TetGen output can be used as input for the simulation software or be imported back into Gocad/Skua for quality control and further processing.

Graphite Voronoi based re-meshing via the Skua plugin Tweedle and TetGen

When using the surface structural model built by Skua, it is necessary to re-mesh these surfaces. This means improving their quality and adapting triangle sizes. We use the surface re-meshing method recently proposed by Pellerin et al. (2014). This method, specifically developed for geological models, is based on the notion of Centroidal Voronoi Diagrams (Du et al. 1999). The two main steps of the method are (1) to optimize the positions of the vertices of the output mesh and (2) to consider a 3D subdivision of the model, determined from these points, to build the triangles of the output mesh. The method is automatic, it re-meshes all surfaces and contact lines at the same time with a controlled number of triangles, and the output mesh triangle quality does not depend on the input mesh quality. This mehtod is implemented in a plugin of the research modeling software Graphite (`http://alice.loria.fr/index.php?option=com_content&view=article&id=22`) that is interfaced in Gocad through the plugin Tweedle Pellerin et al. (2010). The resulting set of surfaces was exported to TetGen.

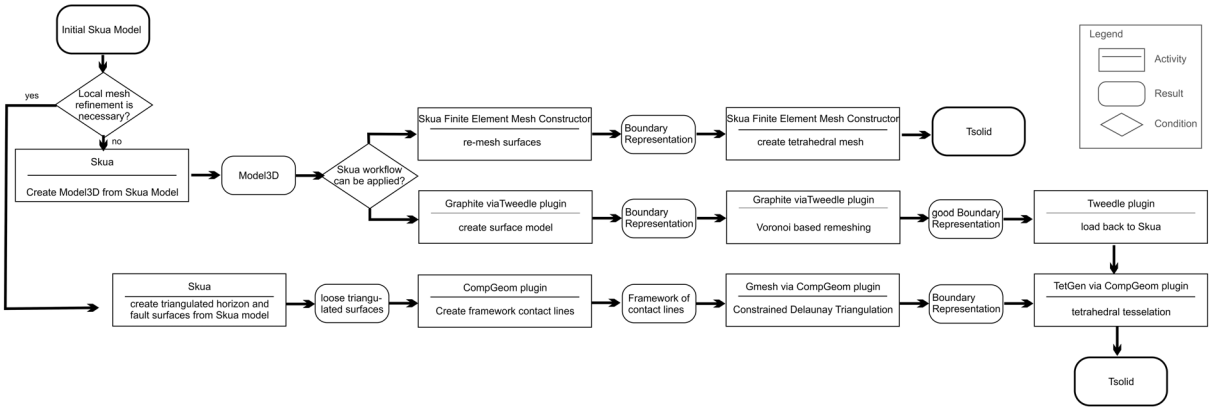

Fig. 2.: Workflows for generating a 3D tetrahedral grid.

Results

While preparing a 3D Skua model for a FE simulation on an unstructured tetrahedral grid, the major part of the work consists in generating a continuous triangulation of the geological boundary surfaces in a good quality (fig. 2). The meshing software has to handle crossing contact lines and non-manifold surfaces and to provide a good mesh quality for running a numerically stable process simulation.

The tools developed by Pellerin et al. (2014) permit to re-mesh the surfaces of our boundary representation model with triangles as equilateral as possible in a short time of approximately 30 minutes. The size of the triangulation can be specified by setting the desired number of vertices in the final mesh. If surface contact lines are situated very tight up against one another, the model can be simplified automatically by setting a merging distance. In the current version, the mesh cannot yet be locally refined.

Creating the boundary representation with the CompGeom plugin requires much more working time - in the case of our relay ramp model approx. 2 days. However, the CompGeom plugin in combination with Gmsh allows the mesh geometry and quality to be controlled in detail. The user can specify the distance of the triangle nodes along the contact lines, add lines and points to the triangulation and refine the triangulation locally.

Conclusions

Currently the use of external software is often necessary if a Skua model has to be prepared for a FE simulation. In this study, we tested the Tweedle and CompGeom research plugins, which are both well suited to performing this task. Tweedle is comfortable to handle and a very fast tool, which automatically re-meshs a boundary representation. CompGeom allows for very detailed control over the triangulation, but requires a lot of manual work. Working with both plugins, the surface meshes obtained had to be reworked by hand in order to generate a perfect triangulation which can be used for the generation of an unstructured tetrahedral mesh.

References

Afanasjew M., Börner R.-U., Eiermann M., Ernst O., Spitzer K. (2013): Efficient Three-Dimensional Time Domain TEM Simulation Using Finite Elements, a Nonlocal Boundary Condition, Multigrid, and Rational Krylov Subspace Methods. Expanded Abstracts, 5th International Symposium on Three-Dimensional Electromagnetics, May 7 – 9, 2013, Sapporo, Japan, 4p.

Caumon G.,Lepage F., Sord C.H., Mallet J.-L. (2004): Building an Editing a Sealed Geological Model. Mathematical Geology, 36/4, 405-424. Du Q., Faber V., Gunzburger M. (1999):

Centroidal Voronoi Tesselations: Applications and Algorithms. SIAM Review 41/4, 637-676.

Duvinage I., Mallet J. L., Dulac J. C. (1999): Extracting information from faulted horizon boundaries for building and updating of a 3D model. Annual Meeting Expanded Abstracts, American Association of Petroleum Geologists, A35.

Geuzaine C., Remacle J.-F. (2009): Gmsh: a Three-Dimensional Finite Element Mesh Generator with Built-in Pre- and Post-Processing Facilities. International Journal for Numerical Methods in Engineering 79, 1309 – 1331.

Moyen R. (2005): Throw modeling on unstructured Objects. 25th Gocad Meeting, Nancy, 19pp.

Muron P. (2005): Handling faults in 3D structural restoration. 25th Gocad Meeting, Nancy, 15pp.

Schwarzbach C., Börner R.-U., Spitzer K. (2011): Three-dimensional adaptive higher order finite element simulation for geo-electromagnetics—a marine CSEM example. Geophys. J. Int., 187, 63-74.

Pellerin J., Levy B., Caumon G. (2010): Advanced geometry processing in Gocad using Graphite. 30th Gocad Meeting, Nancy, 8 pp.

Pellerin J., Levy B., Caumon G., Botella A. (2014): Automatic surface remeshing of 3D structural models at specified resolution: A method based on Voronoi diagrams. Computers and Geosciences 62, 103-116.

Si H. (2011): TetGen, A Quality Tetrahedral Mesh Generator and a 3D Delaunay Triangulator. http://wias-berlin.de/software/tetgen//, last time visited July 2014.

Weiler K., (1988): The radial edge structure: A topological representation for non-manifold geometric boundary modeling. In Wozny M., McLaughlin H., Encarna, eds., Geometric modeling for CAD application. Elsevier Amsterdam, 3–36.

Zehner B. (2011): Constructing Geometric Models of the Subsurface for Finite Element Simulation. Conference of the International Association of Mathematical Geosciences (IAMG 2011), Salzburg, Austria, 5th-9th September 2011, doi:10.5242/iamg.2011.0069.

Flanking structures – New insights from analogue models

C. J. S. Gomes[1], Rodrigues, B. A.[1], Endo, I.[1]

[1] *Departamento de Geologia, Universidade Federal de Ouro Preto, Morro do Cruzeiro s/no; 35.400-000 Ouro Preto, Minas Gerais (Brasil)*
e-mail: *caroline.janette@gmail.com*
session: *Methods and Materials*

Introduction

Flanking folds are deflections of planar or linear fabric elements in the vicinity of crosscutting objects (Grasemann & Stüwe 2001; Passchier 2001) that occur in a wide range of tectonic environments and rock types. These structures challenged geologists because of their common counter-intuitive behavior as they may show shear sense opposite to the effect of fault drag. Thus flanking folds, collectively termed flanking structures by Passchier (2001), must be used with caution as shear sense indicators.

Several explanations have been proposed to explain the origin of the flanking folds in shear zones, such as the reduction of the flow velocity alongside veins, dykes or faults, the type of ductile flow and the initial orientation of the crosscutting element (e.g. Passchier 2001; Grasemann & Stüwe 2001; Grasemann et al. 2003; Wiesmayr & Grasemann 2005).

Numerous numerical modeling studies concerning the kinematics of flanking structures have been presented but analogue models are not common. Hudleston, in 1989, was the first author who generated flanking structures in analogue experiments. He used plasticene in simple shear and showed that the progressive rotation of an extensional fracture causes the formation of folds not by slip along the fracture margins but passively by a local contraction.

Odonne (1990) employed horizontal paraffin wax layers to analyse the deformation intensity around a fault, by uniaxial compression. He concluded that a fracture locally disturbs stress and deformation fields producing a non-coaxial strain history.

Exner et al. (2004) used silicone, a linear viscous material, in a ring shear rig, to test and extend previous numerical models of type-s flanking folds to higher shear strains. The authors showed that both offset and deflection of type-s flanking folds along a central discontinuity document a local contraction of the planar fabric elements parallel to the shear zone boundary. In addition, they suggest that, as the crosscutting element itself co-rotates, in principle, at high shear strain all flanking structures may evolve to type-s flanking folds.

The aim of this work is to present new analogue models of flanking folds above a single strike-slip fault using a linear viscous silicone of low viscosity and compare them with those presented by Exner et al. (2003).

Model set up and procedure

Seven models were built and deformed in a rectangular box, 33 cm long, 20 cm wide and 1.5 cm deep. An electric motor displaced one half of the box horizontally, producing a sinistral fault slip at shear strain rate of 6.9×10^{-3} s^{-1}(2 cm/h). As the shear zones in our experiments were only 6 cm large, the lateral boundaries had no effect on deformation. Figure 1 shows the set-up of one of the seven experiments, with the five horizontal lines representing marker lines (the planar fabric elements), and a thin metal plate the crosscutting element. Following Exner et al. (2004), we used liquid soap as a lubricant along the metal plate

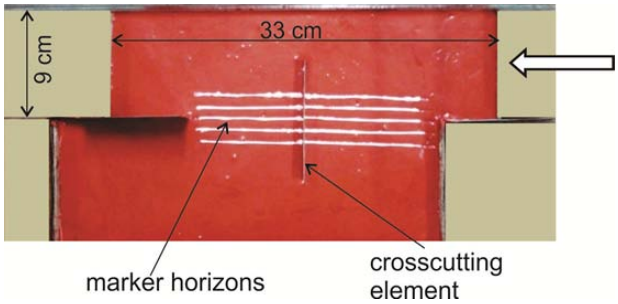

Fig. 1.: The initial set-up of our experiments shown by model CIS90. Arrow shows the direction of the movement.

to simulate slip along an active fault.

The silicone used as a ductile matrix was a mixture between mastic silicone rebondissant 36 (from E^{ts}E. H. Roberts et Cie, CRC) and alcohol, with a resulting viscosity $\mu = 1.7 \times 10^4$ Pa s, at 21 °C. The models were deformed by a total shear strain of $\gamma = 1.3$, that corresponds to 8 cm of linear dislocation.

Based on Grasemann et al. (2003) and Exner et al. (2004), we used seven different initial angles ϕ of the crosscutting element to the shear zone boundary ($\phi = 15°$, 30°, 70°, 90°, 110°, 150° e 165°). The experiments were named according to their angle ϕ: CIS15, CIS30, CIS70, CIS90, CIS110, CIS 150 and CIS165, and to facilitate we used the terminology provided by Grasemann et al. (2003) for the experimental result descriptions. To ensure reproducibility we performed each experiment twice.

Results

The line drawings of figure 2 summarize our experiments. Models are shown prior to and at final stage of deformation, followed by an interpretative sketch and the flanking structure classification.

The most interesting feature of our experiments is the markedly different amount of offsets of the marker lines that led to thickening and thinning of the silicone at crosscutting element terminations. The offsets varied along the crosscutting element (sense and magnitude) both among the five marker lines of one experiment and among the seven experiments. The deflections of the marker-lines, adjacent to the crosscutting element, were also heterogeneous as they vary over the length of the crosscutting element. In addition, if considering only the upper marker lines, all experiments except the models CIS15 and 30 show contractional deflection. However, analyzing the central marker line (accordingly to Grasemann et al. 2003) it is notable that offsets were extensional in models CIS15, 70, 90, 110 and 165 and despicable in the models CIS 30 and 150. At final deformation, we classified the instantaneous flanking structures as extensional normal a-type, extensional reverse a-type, shear band and n-type flanking folds (Fig. 2).

Discussion/Conclusions

The deviation of the square grid, marked on an additional experiment set up without the crosscutting element, showed the silicone flow trajectory (Fig. 3). This trajectory suggests that the introduction of a discontinuity acted as an obstacle modifying the flow field. As thickening and thinning of silicone at crosscutting terminations are consistent with sinistral simple shear, the modelled flanking folds should have formed by perturbation strain. We suggest that this deformation occurred in our experiments because of the relative low viscosity of the silicone.

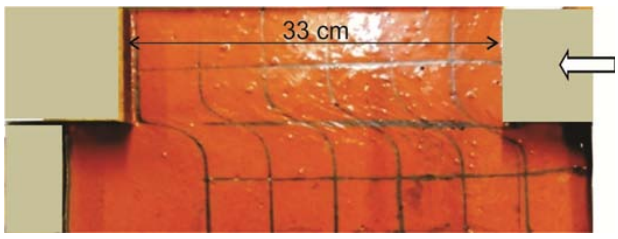

Fig. 3.: The silicone flow trajectory after the sinistral simple shear in an additional model set up with an initial square grid and without the crosscutting discontinuity. Arrow indicates the direction of the movement.

In the literature, natural examples of flanking folds, comparable to the model results, are

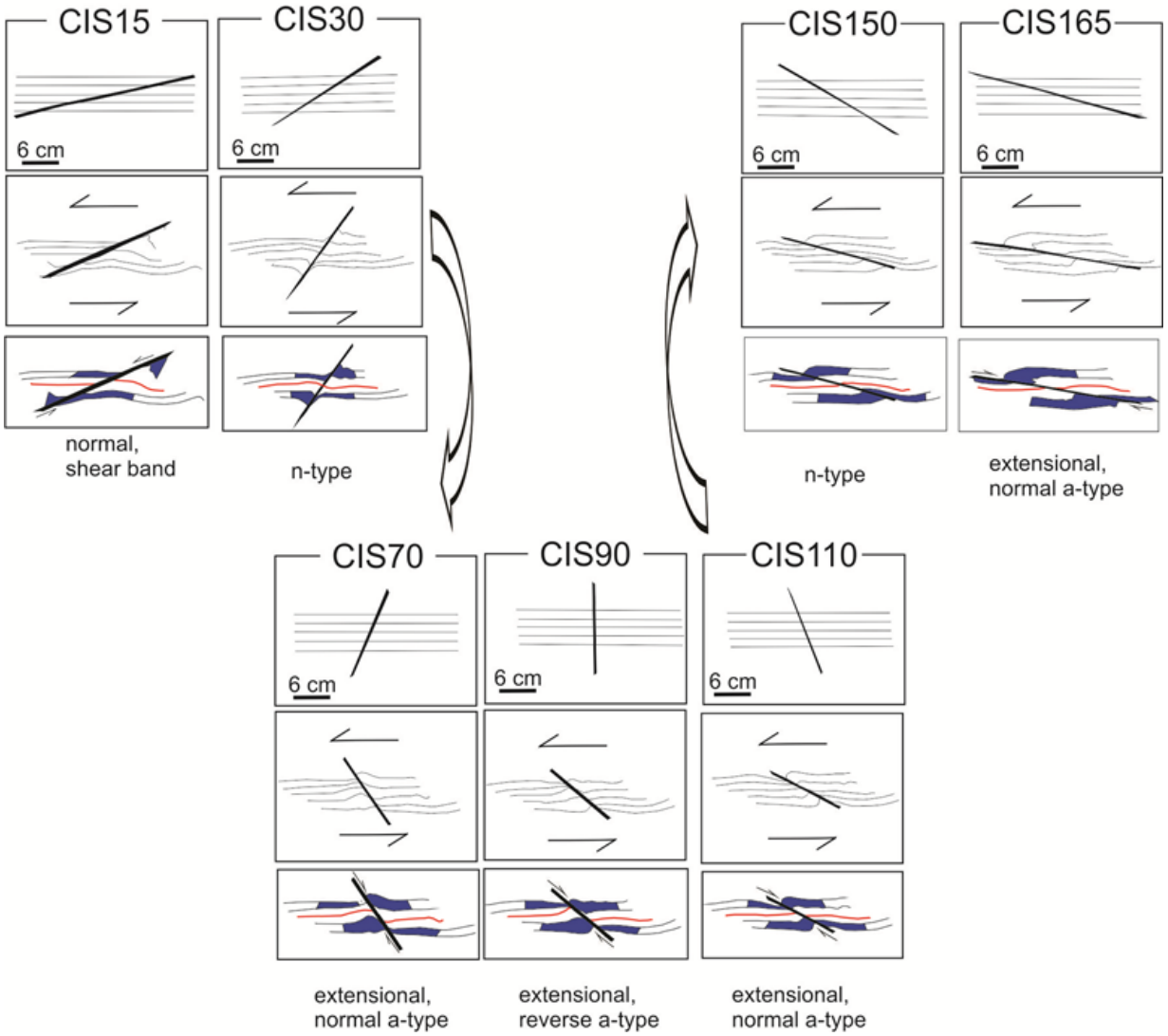

Fig. 2.: Line drawings of the seven analogue experiments with initial angle $\phi = 15°$ (CIS15), 30° (CIS30), 70° (CIS70), 90° (CIS90), 110° (CIS110), 150° (CIS150) and 165° (CIS165) to the shear zone boundary. Each experiment is shown at $\gamma = 0$ and at final $\gamma = 1.3$, without and with interpretation of instantaneous flanking fold type. Note thickening and thinning of the silicone at opposite terminations of the crosscutting element.

common in medium to high grade metamorphic rocks. Thus, our experiments suggest that the flow characteristics constitute an additional factor controlling flanking fold geometries.

Acknowlegments

We acknowledge Fundação de Amparo à Pesquisa do Estado de Minas Gerais (Fapemig) (CRA-APQ-01672-11 and CRA-PPM-00531-13) for financial support.

References

Exner U., Mancktelow N.S., Grasemann B. 2004. Progressive development of s-type flanking folds in simple shear. Journal of Structural Geology 26: 2191-2201.

Grasemann, B., Stüwe, K. 2001. The development of flanking folds during simple shear and

their use as kinematic indicators. Journal of Structural Geology 23: 715-724.

Grasemann B., Stüwe K., Vannay J.-C. 2003. Sense and non-sense of shear in flanking structures. Journal of Structural Geology 25: 19-34.

Hudleston P. 1989. The association of folds and veins in shear zones. Journal of Structural Geology 11: 949-957.

Odonne, F. 1990. The control of deformation intensity around a fault: natural and experimental examples. Journal of Structural Geology, 12: 911–921.

Passchier C.W. 2001. Flanking structures. Journal Structural Geology 23, 951–962.

Wiesmayr G. & Grasemann B. 2005. Sense and non-sense of shear in flanking structures with layer-parallel shortening: implications for fault-related folds. Journal of Structural Geology 27: 249-264.

The Ribbon Tool

J. Großmann[1], J. F. Ellis [1], H. Broichhausen[1]

[1] *Midland Valley Exploration, 2 West Regent Street, Glasgow G2 1RW, United Kingdom*
e-mail: *johannes@mve.com*
session: *Methods and Materials*

3D geological modelling may inherit a high level of uncertainty, being representations of the interpreters understanding of reality. As predictions made always rely on assumptions all the results a geologist gains from geological models comprise interpretational problems that have to be faced by building more constrained models. One approach for constraining and validating a given 3D model is to use the intrinsic rules in a predictive way during the model building process. This way, geometric objects like 3D lines and surfaces can be used to aid the model building process.

Structural traces such as outcrop traces intersecting with elevation contours allow the geologist to predict the geometry of a horizon in the subsurface (Groshong, 1999). Transferring these 2D or 2.5D horizons into 3D is laborious work and a lot of uncertainty may remain. A direct use of 3D lines formed from the intersection of structural traces on a 3D topography represents an alternative method.

Software often provides the possibility of creating 3D surfaces based on 3D line data, by extending a line into the third dimension according to a certain dip and dip azimuth. This method produces simple geometries and can provide reasonable results for subsurface models. However, Midland Valley's Move^{TM} software improves on this method with the 3D dip domain construction in the Ribbon Tool. It provides a distinctive approach which allows the creation of surfaces with varying orientation along its length (Fig. 1). It can be used as a predictive tool in geological models with complex geometries.

In Move, Ribbon construction is based on the three-point approach which involves using three points with known x, y, z coordinates and calculating the orientation (azimuth and dip) of a planar triangle fitting the three points. The reliability of the computation depends on the number of points selected and on their sample spacing along the line. Developed on the method of Fernandez (2004), where the mean principle orientation is calculated on a radial bias function, the algorithm now calculates the mean principal orientation of each triangle created for every three points along the line. The Ribbon construction in Move 2014 defines an additional search window interval based on a set distance from the center point of a triangle. It then averages the mean principal orientation of the included triangles and produces several 3D dip domains along the line (Fig. 2). These are projected as sticks in 3D and can be displayed and created as coherent Ribbon surfaces (Fig. 3, right).

Working with the mean principal orientations of the defined dip domains provides a statistical control towards the shape and strength of the created surface. This information is illustrated in a Fisher plot and classified according to the cluster/girdle classification after Woodcock (1977) (Fig. 3, left). A low K-value represents girdle and a high K-values represents cluster shape mean principal orientations of the dip domains. The M-value is a measure of the statistical strength of the mean principal orientations.

It is important to understand that Ribbon surfaces created on the basis of 3D line data formed from the intersection of geological surfaces are merely a statistical approach and cannot always

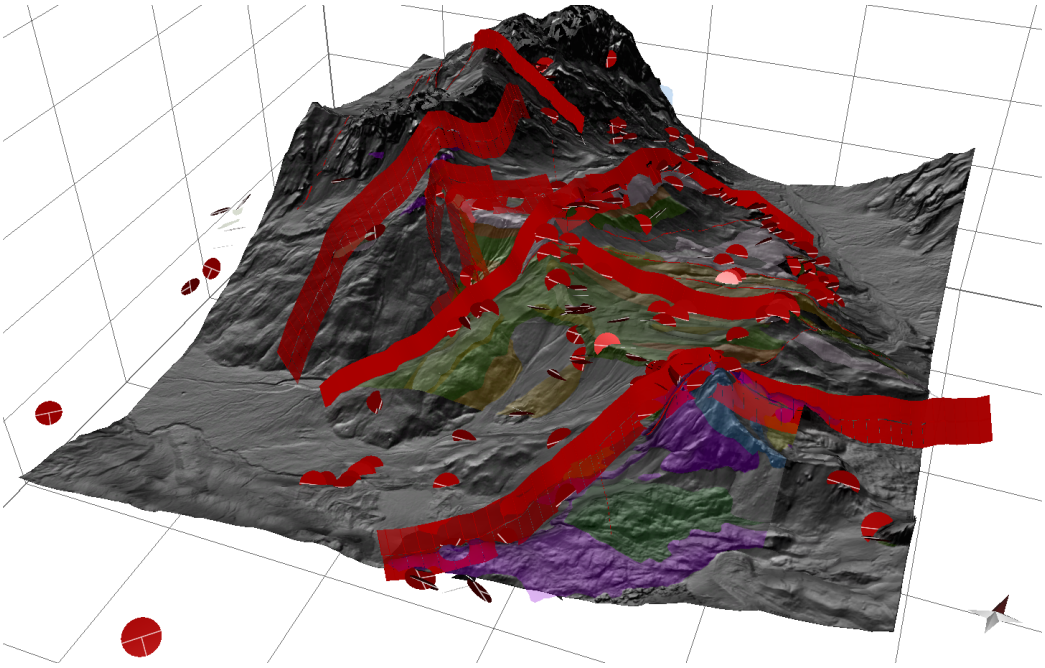

(a)

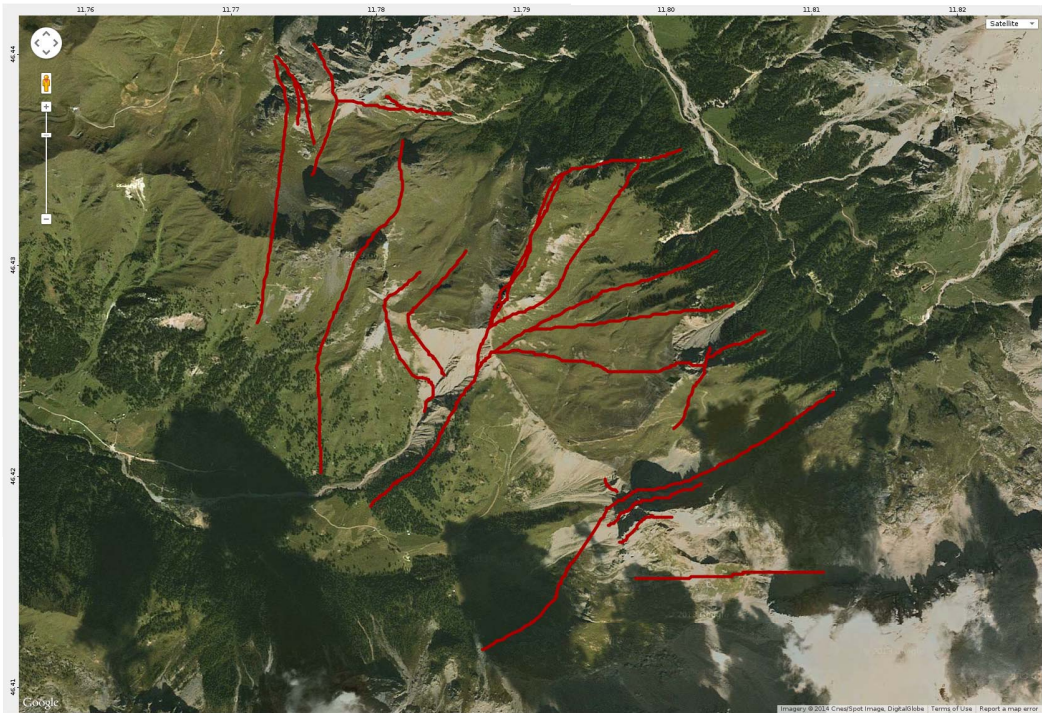

(b)

Fig. 1.: (a) - oblique view of the Digital Elevation Model (DEM) and fault surfaces constructed using the Ribbon tool in Move software, disks represent dips for the various lithologies shown by coloured polygons. (b) - map view of fault traces overlain on Google Satellite image. Data was collected as part of the Innsbruck University Summer School of Alpine Research, from Valle San Nicolò in the Sella Massif, Dolomites Northern Italy. The stratigraphy covers the Dolomites through early rifting and Eoalpine thermotectonics to Neogene indentation.

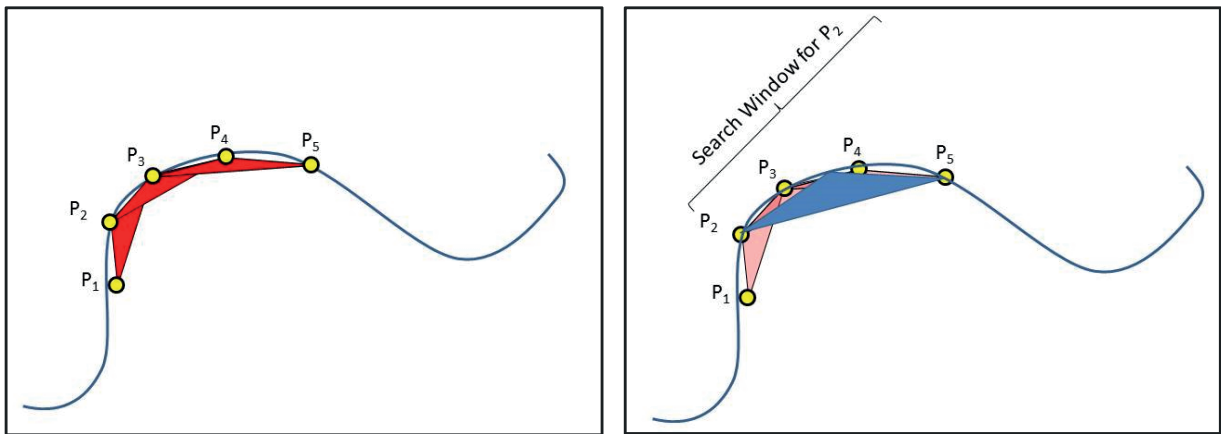

Fig. 2.: Simple representation of a line in space, yellow points (P1-P5) are used in the calculation of dip and dip azimuth. Left - red triangles have been created from every three points. Right - the blue triangle has been created from an average measurement within the selected search window.

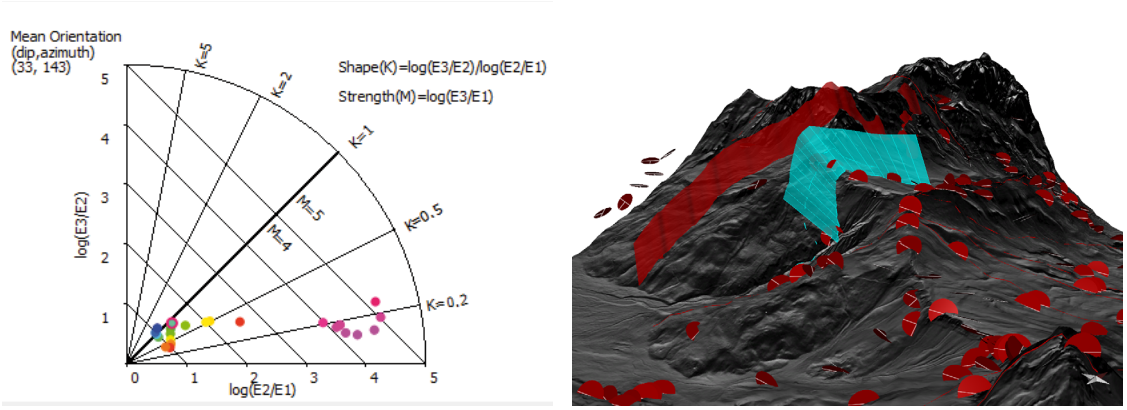

(a) (b)

Fig. 3.: (a) - Fisher plot illustrating the mean principal orientation of dip domains classified after Woodcock (1977). (b) - example of constructed ribbons based on line data on a 3D topography.

constrain the shape and orientation of 3D surfaces in a geologically reasonable way. It is therefore essential for the user to already have a distinct idea of the major geological structure e.g. provided by field orientation data, before starting the Ribbon creation process.

The case studies presented (e.g. Fig. 1. and Fig. 4.) address the practical application of the Ribbon construction as a very efficient method to create 3D surfaces based on dip domains calculated from geological line structures. Although all case study examples presented here demonstrate the use of the tool from surface data, this method can be used in the subsurface on any line with a 3D geometry.

References

Woodcock, N.H. (1977). Specification of fabric shapes using an Eigenvalue method. Bull. geol. Soc. Am. 88, 1231-1236 (47, 48, 49).

Woodcock, N.H. & Naylor, M.A. (1983). Randomness testing in three-dimensional orientation data. J. Struct. Geol. 5, 539-548 (48,49).

Groshong Jr., R.H. (1999). 3D Structural Geology: a Practical Guide to Surface and Subsurface Map Interpretation. Springer Verlag, Berlin.

Fernandez, O., Munoz, J. A., Arbues, P., Falivene, O., Marzo, M. (2004). 3-D reconstruction of geological surfaces: an example of growth strata and turbidite systems from the Ainsa basin (Pyrenees, Spain). AAPG Bulletin, 88, n.8, 1049-1068.

Fernandez, O. (2005). Obtaining and evaluating strike and dip measurements from 3D georeferenced data. Jour. of Structural Geology, 27, p855-858.

Ellis, J., Mannino, I., Johnston, J., Feliks, M.E.J., Younger, P.L. and Vaughan, A.P.M. (2014). Shiremoor Geothermal Heat Project: reducing uncertainty around fault geometry and permeability using MoveTM for structural model building and stress analysis. European Geosciences Union General Assembly 2014, Vienna, 27th April–2nd May 2014. EGU2014-15069.

Acknowledgements

Fig. 1 and 3. “Regione del Veneto – L. R. n. 28/76 – Formazione della Carta Tecnica Regionale” and” Autonome Provinz Bozen – Sud Tirol – Amt fur raumbezogene und statische Informatik/Provincia Autonoma di Bolzano – Alto Adige – Ufficio Informatica geografica e statistica” is acknowledged for the contribution of the DEM.

Figure 4. data curtsey of Cluff Geothermal.

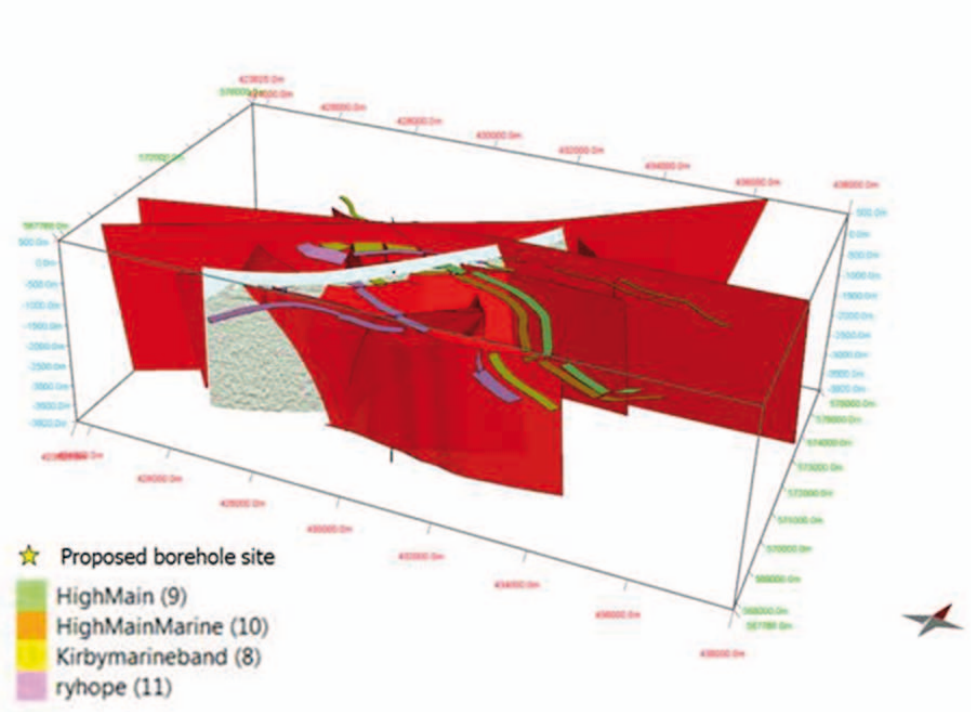

(a)

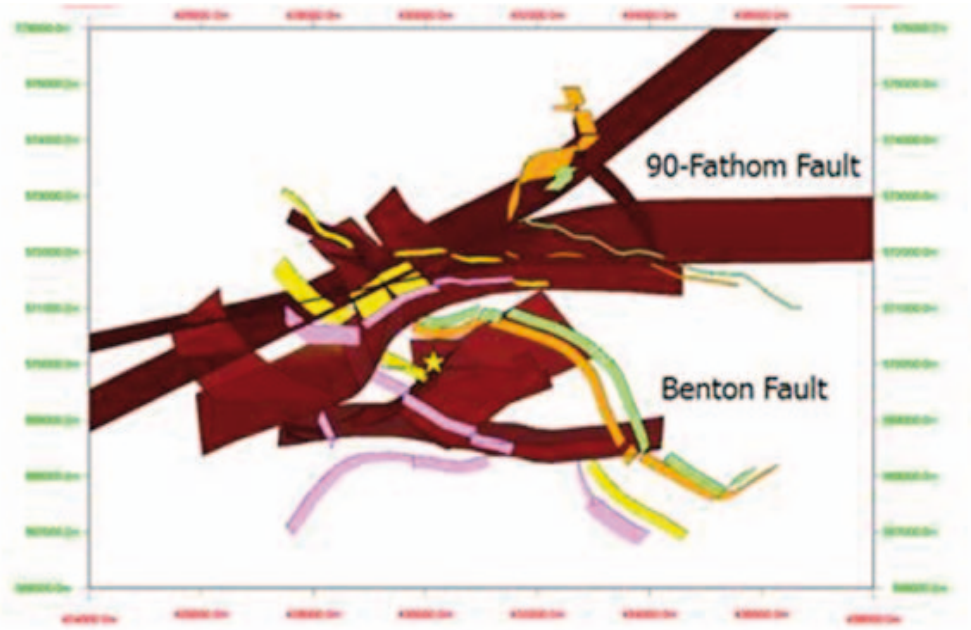

(b)

Fig. 4.: Coal seams construed using surface mapping data and the Ribbon Tool where used to define fault locations and offsets. Oblique (a) and Map (b) view of faults. Fault colour saturation varies with lighting direction (Ellis et al. 2014).

A new method to study the energy budget of rock fragmentation

Øystein Thordén Haug[1], Matthias Rosenau[1], Zahra Amirzada[1], Karen Leever[1], Onno Oncken[1]

[1] *GFZ German Research Centre for Geosciences, Helmholtz Centre Potsdam, Telegrafenberg, D-14473 Potsdam, Germany.*
e-mail: *thorden@gfz-potsdam.de*
session: *Methods and Materials*

Introduction

Fragmentation is a process occurring in several natural systems, e.g. gravitational rock movement [Wang and Tonnon (2010); Locat et al. (2006)]. Despite being a common process, little is known about what governs fragmentation and how it affects the energy of the system. For instance in gravitational rock movements, it is still debated whether fragmentation acts as an energy source [Davies and McSavaney (2009)] or an energy sink [Crosta et al. (2007)]. Our lack of understanding is mainly due to the lack of observations, i.e. the process of fragmentation cannot be quantitatively observed in progress in nature. To overcome this limitation, we have developed a new method where the fragmentation of a new rock analogue material is studied in a controlled laboratory environment. The material strength is scaled to natural rocks and it behaves in a brittle manner (Figure 1a). It is, therefore, ideal for the study of fragmentation under controlled laboratory conditions

Analogue Material

The material is produced by mixing well sorted fluvial sand (average grain size $\sim 300\mu m$) with 2 wt% gypsum powder, while dry. Then, $\sim$10 wt% water is added to the mixture and thoroughly stirred, until a homogeneous material is achieved. The material is left to harden for 2 days. The material properties have been determined by triaxial tests and ring shear tests. The tests show that the primary strength of the material (i.e. its cohesion) can be controlled by the amount of gypsum added to the mixture (Figure 1b). However, the other frictional properties (static friction coefficient, dynamic friction coefficient) remain similar to that of the sand.

Experimental setup

Fragmentation of a sample is induced by impacting on a horizontal plane after being accelerated down a 1 meter slope of 45°. A sketch of the experimental setup is given in Figure 2. The experiments are monitored by two digital optical cameras: one that captures the kinematics of the models at a frequency of 50 Hz, and one that takes a high resolution still image of the final deposits. This ensures both good temporal and spatial resolution. Quantitative measures from the experiments are extracted from the images by binarizing them, i.e. setting all the fragments to 1 and setting everything else to 0.

The energy consumed by fractures is most often characterized by the production of new surface area. Information of the new surface area created in the fragmentation can be measured from the fragment size distribution (FSD). However, to measure the FSD is tedious and difficult. Observations of the FSD (Figure 3), suggests

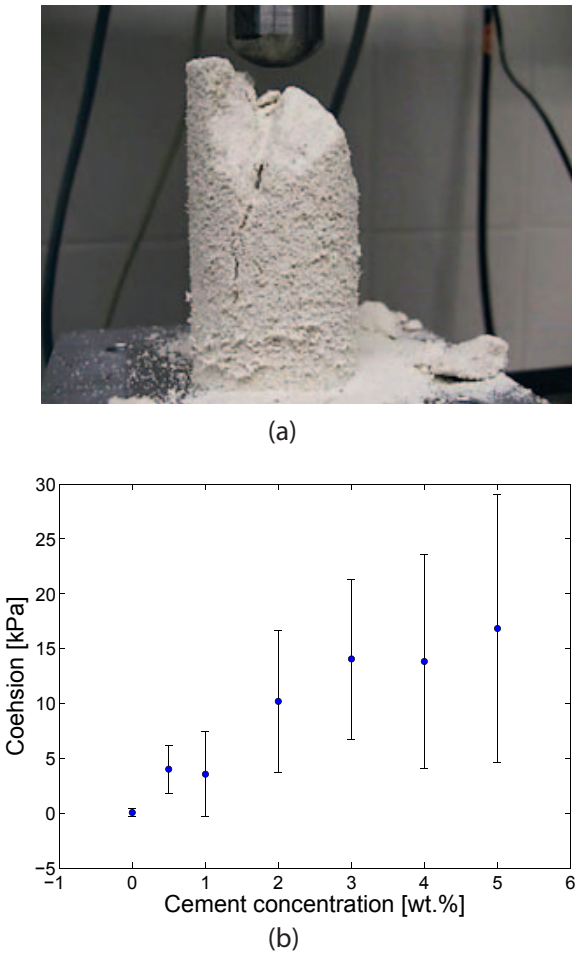

Fig. 1.: Picture of the material after deformation. The material behaves in a brittle manner. (b) The cohesion of the material is controlled by the amount of gypsum powder added to the mixture.

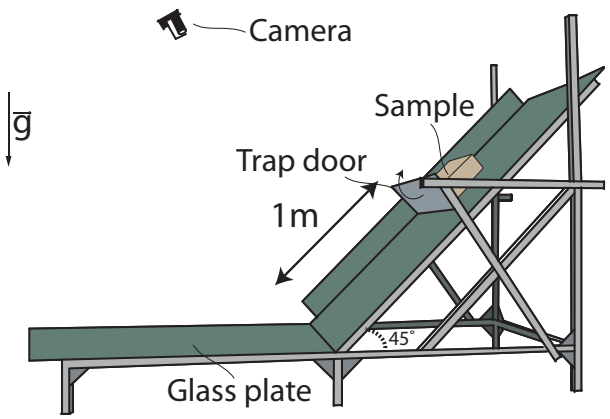

Fig. 2.: Sketch of experimental setup

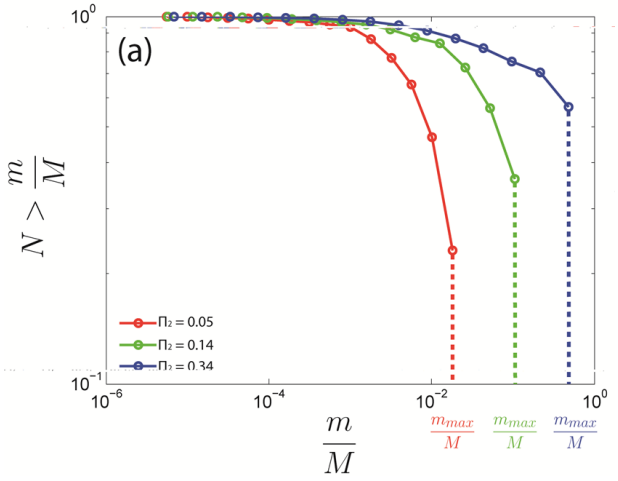

Fig. 3.: Three fragment size distribution for different degrees of fragmentation. The parameter m_{max}/M is observed to act as both a scale parameter and a shape parameter for the distributions.

that the parameter m_{max}/M acts as both a scale parameter and a shape parameter for the FSD, suggesting that we can characterize the fragmentation process with m_{max}/M.

References

Crosta, G. B., Frattini, P., Fusi, N., Feb. 2007. Fragmentation in the Val Pola rock avalanche, Italian Alps. Journal of Geophysical Research 112, F01006.

Davies, T. R., McSaveney, M. J., 2009. The role of rock fragmentation in the motion of large landslides. Engineering Geology 109 (1-2), 67-79.

Locat, P., Couture, R., Leroueil, S., Locat, J., Jaboyedo, M., 2006. Fragmentation energy in rock avalanches. Canadian Geotechnical Journal 43 (8), 830-851.

Wang, Y., Tonon, F., Jul. 2010. Discrete Element Modeling of Rock Fragmentation upon impact in Rock Fall Analysis. Rock Mechanics and Rock Engineering 44 (1), 23-35.

Fringes projection for 3D displacement analysis of experimental dry granular avalanches

Carlos Mares[1], Bernardino Barrientos-García[1], Mariano Cerca[2], Damiano Sarocchi[3], Luis Angel Rodriguez Sedano[4]

[1] *Centro de Investigaciones en Optica*
[2] *Centro de Geociencias, UNAM*
[3] *Instituto de Geología, UASLP*
[4] *Posgrado en Ciencias de la Tierra, UNAM*
e-mail: *mcerca@geociencias.unam.mx*
session: *Methods and Materials*

Introduction

Granular avalanches are common phenomena in nature, and when they occur on a large scale, represent major geological hazards (Dikau et al., 1996; Jakob and Hungr, 2005). Examples of granular avalanches are pyroclastic flows or debris flows (Sulpizio et al., 2010; Sarocchi et al., 2011). Experimental knowledge of the detailed kinematics of these phenomena is of great importance, because it allows developing more detailed rheological models, as well as more efficient simulation algorithms. Indirectly, the observations made in experiments can also contribute to an efficient hazard manage for civil protection.

The method proposed here allows a study over time, at high-speed, of the three-dimensional evolution of a dry- experimental avalanche body. Such study provides more detailed information on grain size segregation and velocity changes inside the avalanche during its development. We present a variation of the optical method based on fringes projection that allows obtaining full field 3D displacements for a model surface by analyzing color images (Barrientos et al., 2008; Mares 2011). The three deformation components are obtained by decomposing the spatial information in the three color channels (RGB). The advantages of this technical variation include that the finite deformation components on- and out-of-the plane are obtained simultaneously (in only one image), and thus it can be applied to fast laboratory processes (fractions of second).

Experimental setup and methods

The experimental granular materials simulating avalanches were made of natural mixtures of volcanic materials with monodispersal and polidispersal grain sizes, and the physical experiments were performed in two different flumes of 1 and 5.5 m long.

The small flume consist of a plexiglass ramp with inclination of 42° and with lateral confining walls. A mixture of low density granular material (pumice) of 1.5 kg was thrown in the upper part of the ramp and monitored by the fringe projection technique. The mean velocity on the ramp plane was of ca. 2.2 m/s.

For the analysis of the granular flow in the small flume a colored (green) fringe pattern with a 6.45 mm period was projected on the ramp, using a high definition Panasonic PT-AE2000 projector and digital images were recorded using a Photron MiniUX100 camera at a frame rate of 1000 images per second. The optical setup for resolving the relief of the flow is presented in figure 1.

Both the camera and the projector were placed

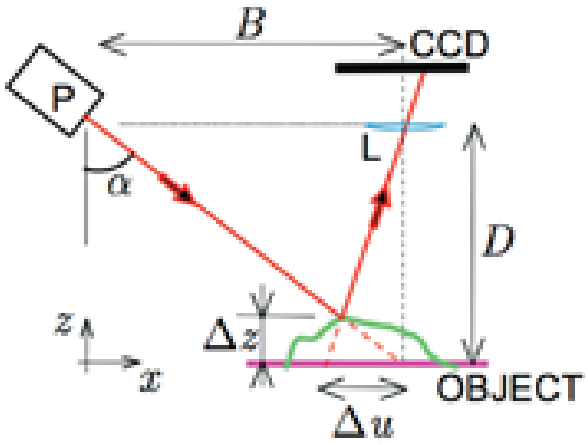

Fig. 1.: Optical set up.

at the same distance from the ramp (1050 cm) and the angle among the camera and the projector was 14.7°. The camera was placed perpendicular to the ramp plane and the total area of analysis was of 710×105 mm2. The images recorded were decomposed in channels R, G, and B. The G channel image contains the information needed to compute the fringe analysis and out-of-plane deformation whilst pairs of the R channel images were cross correlated to obtain the in-plane displacement.

The large flume is equipped with a series of sensors for kinematic, pressure, sound and high speed video analysis. The information from the analysis with the fringes method, supplemented with data provided by the large flume sensors, allow interesting insights about the processes governing granular avalanches.

Results

Results of the granular flow in the small flume are shown in figures 2, 3, and 4. The total experimental time was 1800 milliseconds. Figure 2 presents the out-of-the plane deformation using a red-blue color scale and taking the experimental ramp as the reference plane. Occasionally during the experiment two horizontal bands appear that artifacts of the Fourier method unrelated to flow. Height values (mm) are referred to the initial inclined plane.

Figure 3 is the difference of the out-of-plane deformation computed among two images separated by 2 milliseconds. These results allow to visualize small changes in height during flow and highlight the activity of the deformation front before 360 milliseconds.

Figure 4 is a summary of the kinematics of the experiment. In figure 4a, mz is the height of the flow and can be seen as a measure of the granular material volume in the flume, which is maximum at 380 milliseconds. The flume is filled with the material for about 30 milliseconds and posteriorly the volume decreases.

In sdz (Figure 4a) is shown the evolution of the standard deviation of the displacements. At the beginning of the flow the displacement of particles in the front is characterized by rolling and saltation and their chaotic behavior induce a high variability in the measurements. The maximum variability is observed to end at 400 milliseconds when the flow front reaches the right end of the inspected area. The width of the front increases through its displacement from left to right implying a greater area with unstable particles and a higher standard deviation of the measurement. From 400 to 800 milliseconds the flume is full of material and the flow reaches a laminar and partially steady state. Between 800 and 1400 milliseconds there is an unstable discharge tail of the flow that causes again an increment of the standard deviation of the measurements. The length of the tail increases gradually and the unstable displacement reaches a maximum at 1400 milliseconds. Later, the standard deviation decreases with the flow waning.

MAX (figure 4a) is the maximum deformation and was computed by the average of the 5000 pixels with the largest values of deformation at a given time. The maximum deformation was obtained at 180 milliseconds and then the flow stabilizes. Decreasing of the maximum deformation might be associated to granular segregation of the front. A slight increase is observed again at 1000 milliseconds associated probably to flow tail.

Figure 4b, mdz in the average of the deform-

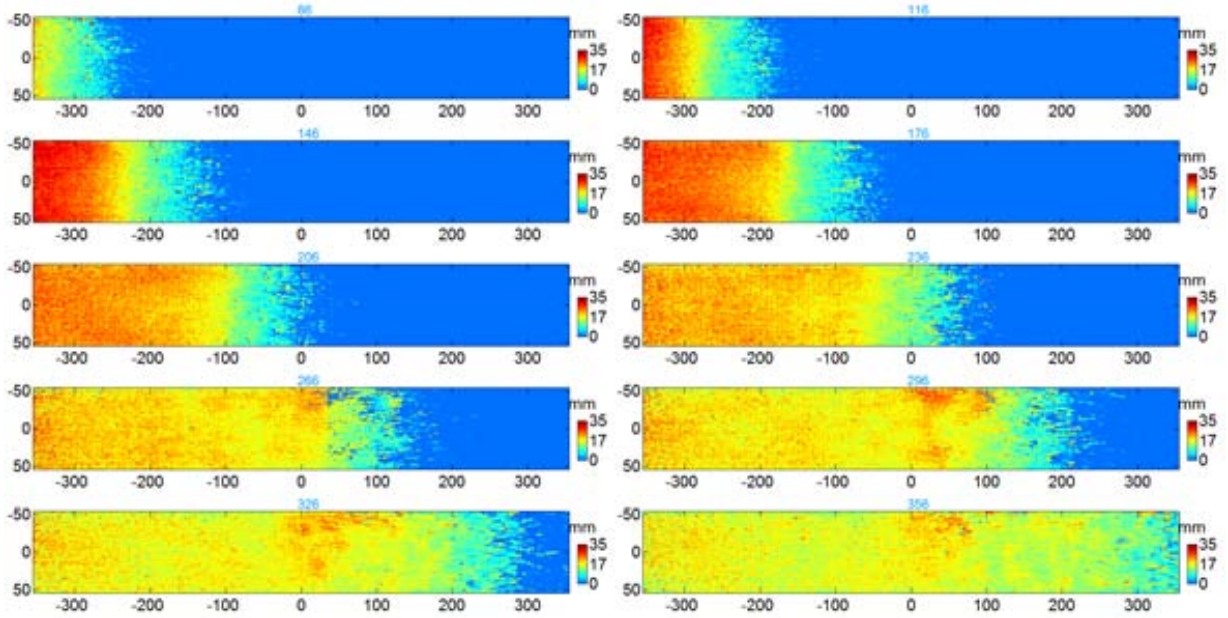

Fig. 2.: Position (mm) vs height (mm) in color of the experimental avalanche. The label in blue indicates the time of the image (in milliseconds).

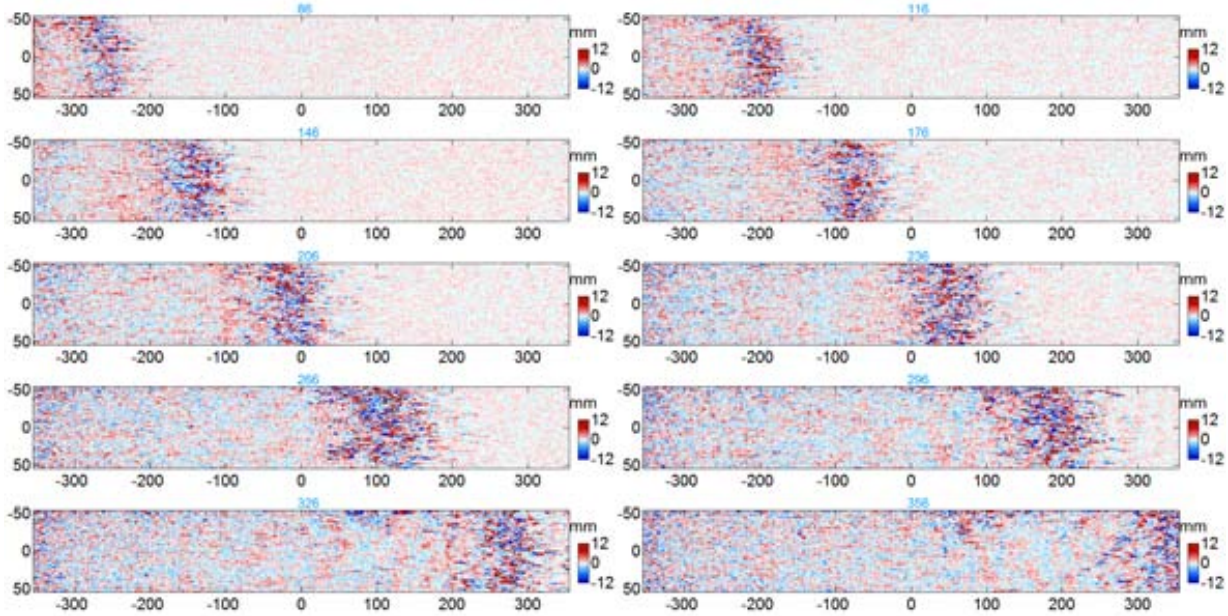

Fig. 3.: Difference of the out-of-plane deformation, obtained by comparison among two images separated by 2 milliseconds.

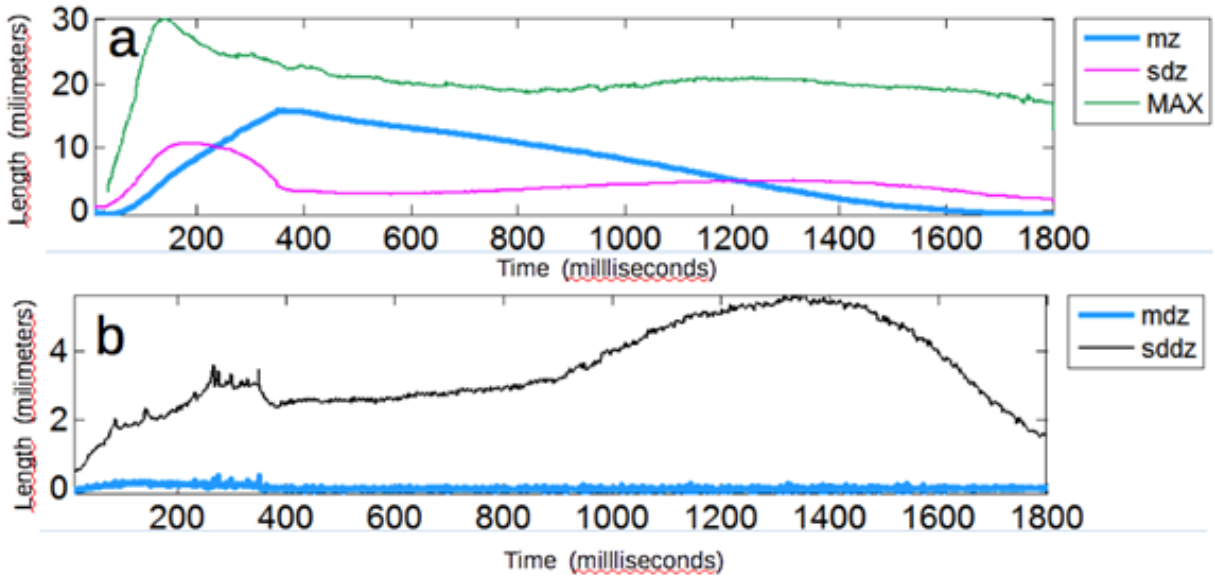

Fig. 4.: (a) mz, height of the flow in mm; sdz, standard deviation of the displacements (mm); MAX maximum deformation (mm). (b) mdz, average of the deformation differences; sdz, standard deviation of the deformation differences.

ation differences that increases gradually up to 400 milliseconds. As in the case of the maximum deformation is associated to the unstable (rolling and salting) particles of the front and tail of the flow. A better image of the unsteady flow particles is shown by the sdz, which is the standard deviation of the deformation differences. The largest values are conspicuously associated to the front and tail of the flow that are the states of greatest instability.

Figure 5 shows a summary of the PIV computed for the first 360 milliseconds of the experiment. The higher velocity is related to the front of the flow. Note that the difference in maximum and minimum velocity increases as the flow evolves.

Finally, we conclude that the optical method based on fringes projection and cross correlation of images is a suitable method allowing to obtain the full field 3D displacements of a granular avalanche. This study provides detailed information on grain size segregation and velocity changes inside the avalanche during its development.

References

Barrientos, B., Cerca, M., García-Márquez, J., and Hernández-Bernal, C. 2008. Three-dimensional displacement fields measured in a deforming granular-media surface by combined fringe projection and speckle photography. Journal of Optics A: Pure and Applied Optics 10 (10), 104027

Dikau, R., Brunsden, D., Schrott, L., Ibsen, M.L. 1996. Landslides recognition. Ed. John Wiley & Sons. 251 p.

Jakob and Hungr. 2005. Debris-flow Hazards and Related Phenomena. Ed. Springer, 738 p.

Mares, C., Barrientos, B., & Blanco, A. 2011. Measurement of transient deformation by color encoding. Optics express, 19(25), 25712-25722.

Sarocchi, D., Sulpizio, R., Macías, J.L., Saucedo, R. 2011. The 17 July 1999 block-and-ash flow at Colima volcano: new insights on volcanic granular flows from textural analysis. (ISSN: 0377-0273). Journal of Volcanology and Geothermal Research. 204: 40-56. http://dx.doi.org/10.1016/j.jvolgeores.2011.04.013

R. Sulpizio, L. Capra, D. Sarocchi, R. Saucedo, J.C. Gavilanes, N. Varley. 2010. Predicting the block and ash flow inundation areas at Fuego de Colima volcano (Colima, Mexico) based on the present day status. Journal of Volcanology and Geothermal Research. 193: 49-66.

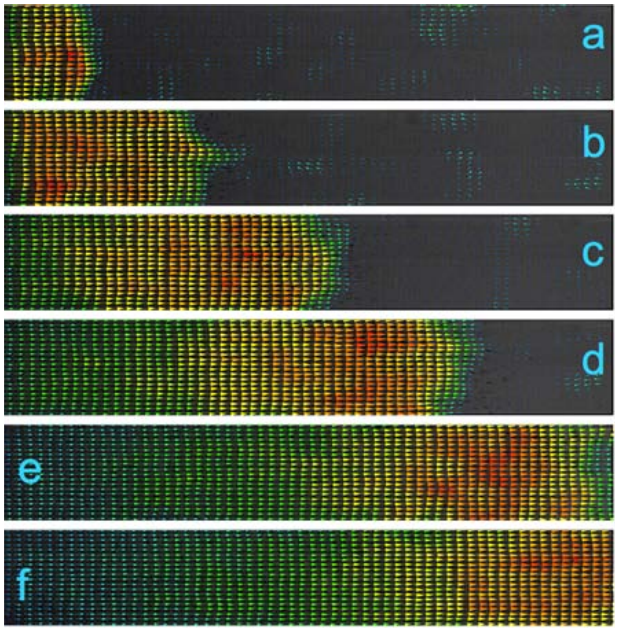

Fig. 5.: Description of the instantaneous velocimetry of the flow from the displacements obtained by the cross-correlation of pair of images separated by 2 millisecond: (a) 65 ms, max velocity 2.2 m/s (red colors), min velocity 0.9 m/s (green colors), (b) 130 ms, max 2.5 m/s, min 0.92 m/s, (c) 195 ms, max 2.7 m/s, min 0.8 m/s, (d) 260 ms, max 2.7 m/s, min 0.92 m/s, (e) 325 ms, max 2.93 m/s, min 0.4 m/s, (f) 350 ms, max 3 m/s, min 0.55 m/s.

A 3-D Lagrangian finite element algorithm with contour-based re-meshing for simulating large-strain hydrodynamic instabilities in visco-elastic fluids

Marina von Tscharner[1], Stefan Schmalholz [1]

[1] *Université de Lausanne, Institut des sciences de la Terre, Quartier UNIL-Mouline, Bâtiment Géopolis, CH-1015 Lausanne*
e-mail: *marina.vontscharner@unil.ch*
session: *Methods and Materials*

Many three-dimensional (3-D) structures in rock, which formed during the deformation of the Earth's crust and lithosphere, are controlled by a difference in mechanical strength between rock units and are often the result of a geometrical instability. Such structures are, for example, folds, pinch-and-swell structures (due to necking) or cuspate-lobate structures (mullions). These structures occur from the centimeter to the kilometer scale and the related deformation processes control the formation of, for example, fold-and-thrust belts and extensional sedimentary basins or the deformation of the basement-cover interface. The 2-D deformation processes causing these structures are relatively well studied. However, several processes during large-strain 3-D deformation are still incompletely understood. One of these 3-D processes is the lateral propagation of these structures, such as cusp propagation in a direction orthogonal to the shortening direction or neck propagation in direction orthogonal to the extension direction. We study the 3-D evolution of geometrical instabilities with numerical simulations based on the finite element method (FEM). Simulating geometrical instabilities caused by sharp variations of mechanical strength between rock units requires a numerical algorithm that can accurately resolve material interfaces for large differences in material properties (e.g. between limestone and shale) and for large deformations. Therefore, our FEM code combines a numerical contour-line technique and a deformable Lagrangian mesh with re-meshing. With this combined method it is possible to accurately follow the initial material contours with the FEM mesh and to accurately resolve the geometrical instabilities. The algorithm can simulate 3-D deformation for a visco-elasto-plastic rheology. Stresses are limited by a yield stress using a visco-plastic formulation and the viscous rheology is described by a power-law flow law. The 3-D FEM code is applied to model 3-D power-law folding and power-law Rayleigh-Taylor instabilities (diapirs) with different re-meshing scenarios. The results are tested with the analytical solution for small amplitudes and with 2-D numerical results for large amplitudes. Thereby, the small initial geometrical perturbations for folding and necking are exactly followed by the FEM mesh. In order to test and measure the numerical properties for an Eulerian mesh we use the analytical solution for a two-dimensional viscous inclusion in pure shear (Fig. 1). We present high resolution 2-D (i.e. cylindrical 3-D with only one element in the third direction) and moderate resolution 3-D results that are applied to the formation of fold nappes (Fig. 2) and to necking during slab detachment (Fig. 3).

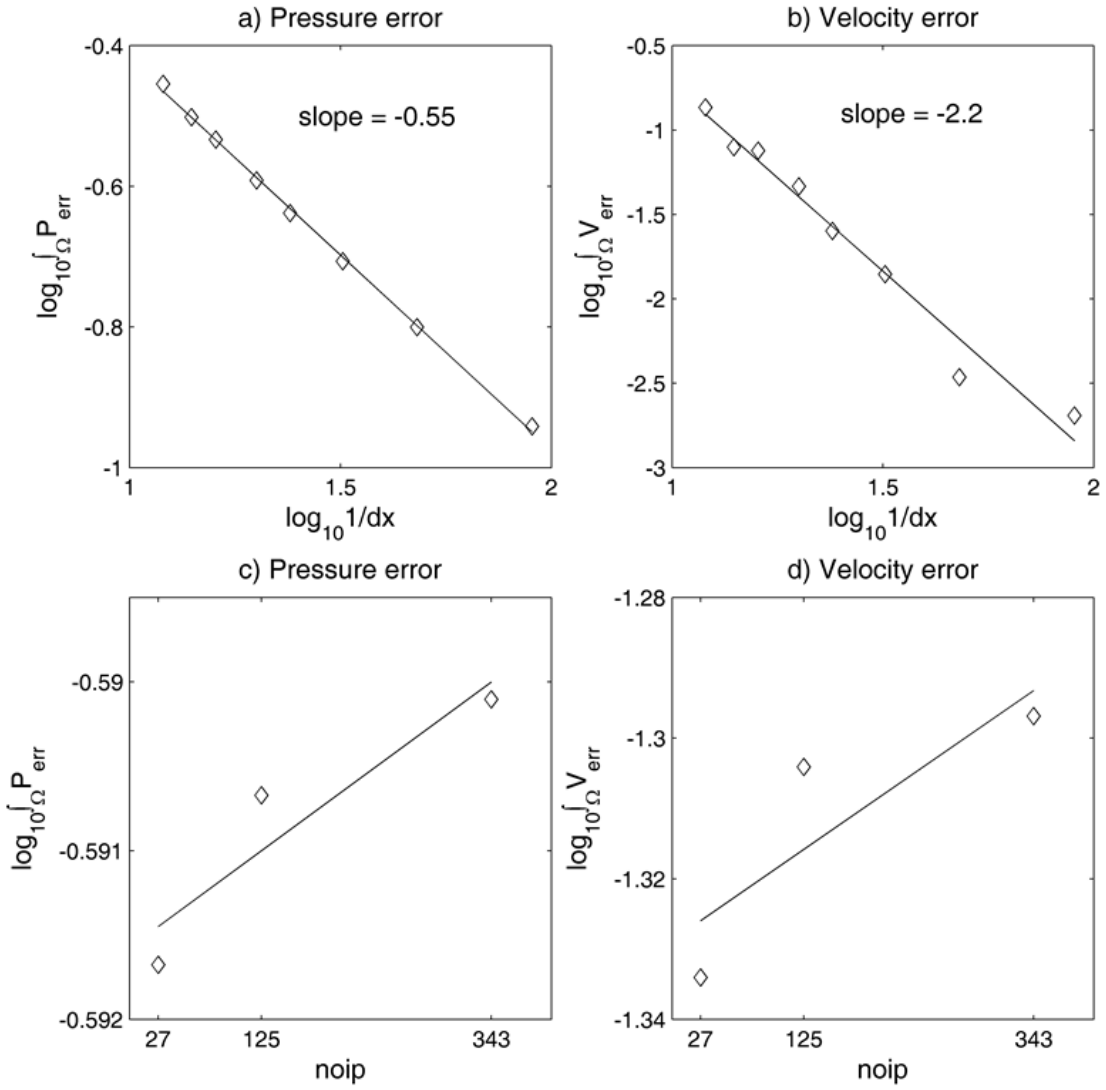

Fig. 1.: Convergence test for a rigid viscous inclusion in a weak matrix under pure shear. Integrated error in pressure and velocity over the model domain versus the nodal FEM resolution (a and b) and versus the number of integration points per element (c and d). We us either $27 = 3^3$,$125 = 5^3$ or $343 = 7^3$ integration points.

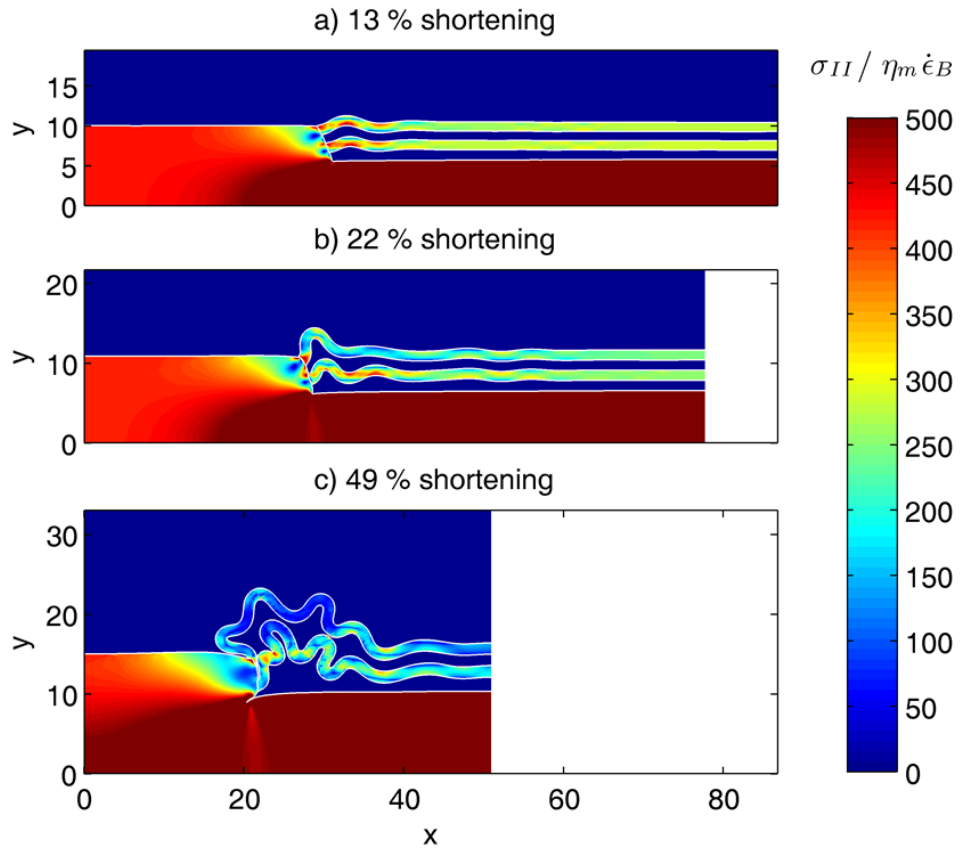

Fig. 2.: Geometrical evolution for fold nappe formation for 13, 22 and 49% shortening. The colors indicate the distribution of dimensionless second invariant of stress tensor. The competent sedimentary layers are first buckeled and then sheared over the basement to form a recumbent fold nappe.

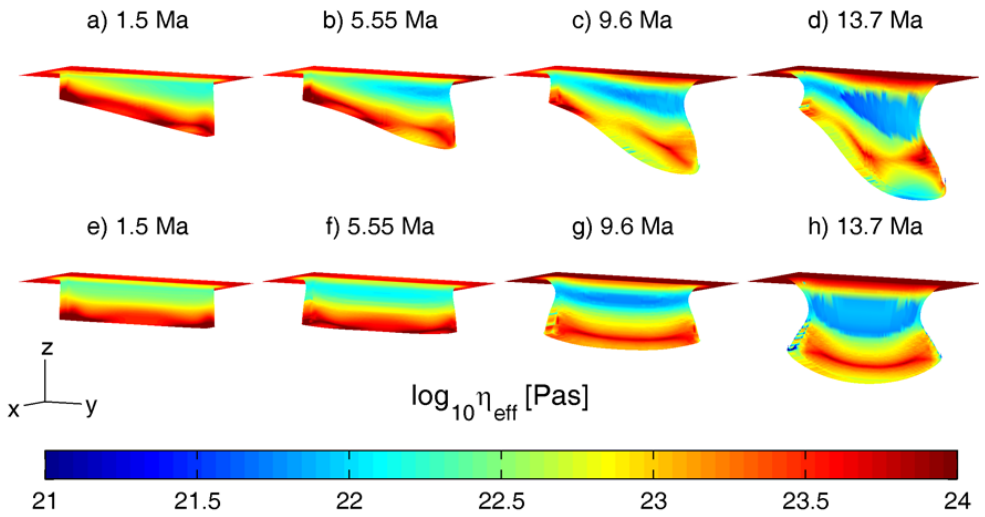

Fig. 3.: The 3-D geometric evolution of an initially symmetric (a-c) and asymmetric (d-f) slab of 800 km width for different times. The colors on the slab surface indicate the effective viscosity in Pa.s.

Some Remarks on wet gypsum as a viscous material for physical modeling

Ali Yassaghi[1]

[1] *Department of Geology, Tarbiat Modares University, P.O. Box 14115-175, Tehran, Iran*
e-mail: *yassaghi@modares.ac.ir*
session: *Methods and Materials*

Dry sand, wet clay and silicone polymers are most common modeling materials in physical modeling (Eisenstadt et al., 1995). Typically, the sand and clay represent competent (brittle rocks), whereas the silicone polymers simulate incompetent (ductile rocks). In this paper we present remarks on application of wet gypsum to simulate mechanical behavior of ductile rocks in modeling deformed structures. For this, physical modeling in which wet gypsum and wet clay are used as modeling material are presented to model folding and fracturing. This study is not intended to represent development of any particular natural geological structures, but to recommend wet gypsum as a ductile analogue material.

Dry gypsum powder (plaster of Paris) has been used to simulate tensile fractures and faults (e.g., Gabrielsen and Clausen, 2001). The viscosity of wet gypsum, however, is less than normal gypsum plaster. This is because, it prepares by simultaneously adding water and shaking that cause to slow down drying time from few minutes to more than a day. Thus, it can be used as ductile material for physical modeling (Fig. 1). In our physical modeling, wet clay considered as competent material and wet gypsum as incompetent material. This is because they both have the advantage to sustain open fractures, and when the water contents can be carefully controlled, the material properties can be controlled to some extent. The chief technical limitations of applying wet gypsum are the influence of the modeling sidewalls and the difficulties that arise by filling the box. Increasing the size of the model set-up will reduce the effects of the sidewalls.

Fig. 1.: Wet gypsum as ductile material in physical modeling.

For analogue modeling of folds, wet gypsum plaster is used with wet clay in order to accommodate competence contrast necessary for development of folds. Variation of the wet gypsum thickness, as ductile material, controls the style of folding from surface to depth (Fig. 2), as well as its behavior to act as detachment horizon during folding (Fig. 3). The resultant structures similar to various detachment folds develop in fold-thrust belts. In addition, applying various thickness of wet clay while keeping the thickness of wet gypsum, results in change on fold geometry from harmonic for the case of constant clay thickness (Fig. 4a) to polyharmonic for the case of various clay thickness (Fig. 4b). This shows that the wet clay can act as competent material during the folding.

For study of fractures wet gypsum allows to understanding fault growth processes and to detect areas of high small-scale strain such as fault

Fig. 2.: Variation of wet gypsum as viscous material on fold style from surface to depth.

Fig. 3.: The effect of wet gypsum to act as detachment horizon during folding.

Fig. 4.: Harmonic(a) and polyharmonic folding (b).

linkage zones. Various tensile and shear fractures is develop on the wet gypsum during shortening. Pull apart and push up are common structures develop along the shear fractures that are comparable with the natural examples. However, fractures are less developed in wet gypsum than wet clay reflecting the marked difference in viscosity of wet gypsum with respect to wet clay (Fig. 6).

References

Gabrielsen, R.H., and Clausen, J.A., 2001, horses and duplexes in extentional regimes: A scaled-modeling contribution, in Koyi, H.A., and Mancktelow, N>S., eds,Tectonic Modeling : a volume in in Honor of Hans Ramberg. Geological Society of America, Memoir, vol. 193, pp. 207-220.

Eisenstadt, G., Vendeville, B.C., Withjack, M.O., 1995. Introduction to Experimental Modeling of Tectonic Processes. Continuing Education Course Notes. Geological Society of America, unpaginated.

Fig. 5.: development of tensile and shear fractures in wet gypsum.

Fig. 6.: Showing the greater development of fractures in wet clay than wet gypsum.

Scientific Programme

GeoMod2014 - Conference Outline

Time	31. August	1. September	2. September	3. September
08:45 - 09:00	-	Welcome	-	-
09:00 - 11:00	-	(Seismo-)tectonics (orals)	Volcanism and Volcanotectonics (orals)	Rheology (orals)
11:00 - 13:00	-	(Seismo-)tectonics (posters)	Volcanism and Volcanotectonics (poster)	Rheology (poster)
13:00 - 14:00	-	Lunch break	Lunch break	Lunch break
14:00 - 16:00	-	Tectonics and Surface processes (orals)	Geodynamics (orals)	Fluids and Deformations (orals)
16:00 - 18:00	-	Tectonics and Surface processes (poster)	Geodynamics (posters)	Fluids and Deformations (poster)
18:00 - 21:00	Ice Breaker Party	-	-	-
19:00 - 22:00	-		Joint Conference Dinner	-

GeoMod2014 - Short course on "Constitutive Laws: from Observation to Implementation in Models" by Onno Oncken, Mathias Rosenau, Fabio Corbi, Georg Dresen Erik Rybacki, Stephan Sobolev, and Sascha Brune
Thursday 4 September: 09:00 - 18:00
Friday 5 September: 09:00 - 14:00

GeoMod2014 - Hands-on tutorial on "ASPECT: a next-generation geodynamic modelling software" by Anne Glerum and Juliane Dannberg
Thursday 4 September: 09:00 - 18:00: Tutorial
Friday 5 September: 09:00 - 18:00: ASPECT Strategy Workshop (for Advanced Users) - voluntary

GeoMod2014 Conference Programme (31 August - 3 September)

Sunday 31 August 2014

18:00 - 21:00: Ice Breaker Party at the 'Theaterschiff Potsdam' (Schiffbauergasse 9b, 14467 Potsdam)

Monday 1 September 2014

08:45 - 09:00: Welcome by Prof. Dr. Dr. h.c. Reinhard Hüttl and Prof. Dr. Onno Oncken

09:00 - 11:00: (Seismo-)tectonics Orals (chairs: B. Kaus, O. Oncken)

- 09:00 - 09:30: **Kelin Wang:** *Thermal Expressions of Stick-slip and Creeping Subduction Megathrusts* (keynote)
- 09:30 - 10:00: **Bertrand Maillot:** *The long-term Evolution of Fold-and-Thrust Belts: Consistency of Numerical Approaches and Physical Experiments* (keynote)
- 10:00 - 10:20: **Tasca Santimano** et al.: *Smart or Beautiful? Accretionary wedge evolution seen as a competition between minimum work and critical taper*
- 10:20 - 10:40: **Lorenzo Bonini** et al.: *The role of pre-existing frictional weaknesses on the propagation of extensional faults*
- 10:40 - 11:00: **Ylona van Dinther** et al.: *Seismo-thermo-mechanical modeling of subduction zone seismicity*

11:00 - 13:00: (Seismo-)tectonics Posters (chairs: B. Kaus, O. Oncken)

13:00 - 14:00: Lunch break

14:00 - 16:00: Tectonics and Surface processes Orals (chairs: F. Graveleau, N. Hovius)

- 14:00 - 14:30: **Ritske Huismans:** *Interaction and feedback between surface processes and mountain building* (keynote)
- 14:30 - 15:00: **Stéphane Dominguez:** *Joint analogue modelling of marine and terrestrial geological processes: state of the art and new developments* (keynote)
- 15:00 - 15:15: **Utsav Mannu** et al.: *Dynamic Modelling of Accretionary Prisms and Stratigraphy of Forearc basins*
- 15:15 - 15:30: **Karen Leever:** *3D Analogue Modelling of the Effect of Fan Sedimentation on Accretionary Wedge Dynamics – the Magdalena Fan case, South Caribbean Margin, Colombia*
- 15:30 - 15:45: **Frank Zwaan**, Guido Schreurs: *4D Transfer Zone Modeling in Continental Rift Systems*
- 15:45 - 16:00: **Sergei Medvedev**, Ebbe H. Hartz: *Evolution of topography of post-Devonian Scandinavia: Effects and rates of erosion*

16:00 - 18:00: Tectonics and Surface processes Posters (chairs: F. Graveleau, N. Hovius)

Tuesday 2 September 2014

09:00 - 11:00: Volcanism and Volcanotectonics Orals (chairs: O. Galland, E. Holohan)

- 09:00 - 09:30: **Rikke Pedersen:** *Surface deformation simulations of volcanic and tectonic processes in Iceland* (keynote)
- 09:30 - 10:00: **Olivier Roche**, Yarko Niño: *Mechanisms of entrainment of a granular substrate by pyroclastic density currents: insights from laboratory experiments and models, and implications for flow dynamics* (keynote)
- 10:00 - 10:15: **Rosanne Heistek** et al.: *Temporal changes in mantle wedge geometry and magma generation processes in the Central Andes: towards linking petrological data to thermomechanical models*
- 10:15 - 10:30: **Francesco Maccaferri** et al.: *The gravitational unloading due to rift depression: A mechanism for the formation of off-rift volcanoes in (continental) rift zones*
- 10:30 - 10:45: **Lola Chanceaux**, Thierry Menand: *Solidification effects on sill formation: an experimental approach*
- 10:45 - 11:00: Max Gallagher, **Ben Kennedy** et al.: *Megatsunami generation from caldera subsidence*

11:00 - 13:00: Volcanism and Volcanotectonics Posters (chairs: O. Galland, E. Holohan)

13:00 - 14:00: Lunch break

14:00 - 16:00: Geodynamics Orals (chairs: F. Funiciello, S. Sobolev)

- 14:00 - 14:30: **Anne Davaille:** *Plumes to Plate Tectonics: Insights from Laboratory Experiments* (keynote)
- 14:30 - 15:00: **Bernhard Steinberger** et al.: *On the relation between plate tectonics, large-scale mantle flow and mantle plumes: Some recent results and many open questions* (keynote)
- 15:00 - 15:15: **Paul J. Tackley** et al.: *Influence of Melting on the Long-Term Thermo-Chemical Evolution of Earth's Deep Mantle*
- 15:15 - 15:30: **Maria V. Chertova** et al.: *3-D numerical modeling of subduction evolution of the western Mediterranean region*
- 15:30 - 15:45: Tobias Baumann, **Boris Kaus**, A. Popov: *Constraining the rheology of the lithosphere through geodynamic inverse modelling*
- 15:45 - 16:00: **Elisa Calignano** et al.: *Strain localization during compression of a laterally heterogeneous lithosphere*

16:00 - 18:00: Geodynamics Posters (chairs: F. Funiciello, S. Sobolev), Methods and Materials Posters (chairs: M. Frehner, M. Rosenau)

19:00 - 22:00 Joint conference dinner in Potsdam on the ship 'Belvedere' (Lange Brücke 6, 14467 Potsdam)

Wednesday 3 September 2014

09:00 - 11:00: Rheology Orals (chairs: G. Dresen, H. Sone)

- 09:00 - 09:30: **Yuri Fialko:** *Numerical models of ductile roots of mature strike-slip faults* (keynote)
- 09:30 - 10:00: **Laurent Montési:** *Localization processes on Earth, Mars, and Venus* (keynote)
- 10:00 - 10:20: **Suzon Jammes** et al.: *Localization of deformation in a polymineralic material*
- 10:20 - 10:40: **Sebastian P. Müller** et al.: *Rheology of bubble- and crystal-bearing magma: new analogue experimental data and an effective-medium model*
- 10:40 - 11:00: **Maria A. Nikolinakou** et al.: *Modeling stress evolution around a rising salt diapir*

11:00 - 13:00: Rheology Posters (chairs: G. Dresen, H. Sone)

13:00 - 14:00: Lunch break

14:00 - 16:00: Fluids and Deformations Orals (chairs: S. Miller, M. Moreno)

- 14:00 - 14:30: **Boris Galvan** et al.: *Towards a general simulation tool for complex fluid-rock lithospheric processes: merging pre-processing, processing and post-processing in state-of-the-art computational devices* (keynote)
- 14:30 - 15:00: **Takeshi Tsuji:** *Digital rock physics: Insight into fluid flow and elastic deformation of porous media* (keynote)
- 15:00 - 15:15: **Thomas Heinze** et al.: *Numerical Modelling of earthquake swarms in the Vogtland / West- Bohemia*
- 15:15 - 15:30: **Samuel Angiboust** et al.: *Effect of Fluid Circulation on Intermediate-Depths Subduction Dynamics: From Field Observations to Numerical Modelling*
- 15:30 - 15:45: Magdalena Scheck-Wenderoth, **Judith Sippel** et al.: *Heat transport mechanisms at different scales – a 3D modelling workflow*
- 15:45 - 16:00: **Antoine Jacquey** et al.: *Modelling of fractured reservoirs: Fluid-rock interactions within fault domains*

16:00 - 18:00: Fluids and deformations Posters (chairs: S. Miller, M. Moreno)

The posters will be presented during the entire conference. Each poster session starts with a 1-2 min. short presentation of all participating posters.

GeoMod2014 - Short course on "Constitutive Laws: from Observation to Implementation in Models"

Thursday 4 September 2014

Morning Session: Onno Oncken, Mathias Rosenau, and Fabio Corbi

- 09:00 - 10:00: **Onno Oncken:** Observing deformation kinematics and localization: Observations from the field, geophysical imaging, and geodetic monitoring
- 10:00 - 10:15: Coffee Break
- 10:15 - 11:00: **Mathias Rosenau:** Rheology of rock analogues 1: Elastoplasticity and its application in seismotectonic simulation
- 11:00 - 11:15: Coffee Break
- 11:15 - 12:00: **Fabio Corbi:** Rheology of rock analogues 2: Viscoelasticity and its application in seismotectonic simulation
- 12:00 - 13:00: **Visit to the GFZ Analogue Lab**

13:00 - 14:00: Lunch break

Afternoon Session: Georg Dresen and Erik Rybackii

- 14:00 - 15:15: Rheology of the lower crust : Reconciling laboratory data and field observations
- 15:15 - 15:30: Coffee Break
- 15:30 - 16:45: **Visit to the GFZ rock mechanics lab**
- 16:45 - 17:00: Coffee Break
- 17:00 - 18:00: Rock fracture processes and stick slip sliding –What do we learn from analyzing nanofemto seismicity?

Friday 5 September 2014

Morning Session: Stephan Sobolev and Sascha Brune

- 09:00 - 10:00: **Stephan Sobolev:** Rheology and geodynamic modeling: key controls in plate tectonics and beyond
- 10:00 - 10:15: Coffee Break
- 10:15 - 11:30: **Sascha Brune:** Rock rheology in numerical models: PC exercises and application to rift dynamics
- 11:30 - 11:45 Coffee Break
- 11:45 - 12:30: **Stephan Sobolev:** Rheology and cross-scale modeling: towards understanding of great earthquakes
- 12:30 - 13:00: Discussion

13:00 - 14:00: Lunch and end of the short course

GeoMod2014 – Hands-on tutorial on"ASPECT: a next-generation geodynamic modelling software" by Anne Glerum and Juliane Dannberg

Thursday 4 September 2014

08:30 - 9:00: Registration

- 09:00 - 10:00: **Tutorial 1:** First Steps – Compiling and Running ASPECT, **Lecture:** How to run and visualize simple models
- 10:00 - 11:15: **Lecture** ASPECT – A next-generation geodynamic modelling software, **Tutorial 2:** Convection in a 2D box
- 11:15 - 11:30: Coffee Break
- 11:30 - 13:00: **Tutorial 3:** Using the adaptive mesh refinement and spherical shell geometry **Lecture:** How to run and visualize simple models

13:00 - 14:00: Lunch break

- 14:00 - 15:15: **Tutorial 4:** Using the adaptive mesh refinement and spherical shell geometry and using the function parser
- 15:15 - 15:30: Coffee Break
- 15:30 - 17:00: **Tutorial 5:** Averaging at the example of subduction and using a “sticky air” layer
- 17:00 - 18:00: **Voluntary:** Installing ASPECT on personal computers

18:30: Joint Dinner (to be payed by the participants)

Friday 5 September 2014

09:00 - 18:00: ASPECT Strategy Workshop for Advanced Users: Perspectives for Modelling with ASPECT

Index